ICRP ref: 4861-1748-4323

Annals of the ICRP

ICRP PUBLICATION XXX

Paediatric Mesh-type Reference Computational Phantoms

Editor-in-Chief
C.H. CLEMENT

Associate Editor
T. YASUMUNE

Authors on behalf of ICRP
C.H. Kim, C. Choi, W.E. Bolch, N. Petoussi-Henss, M. Zankl, C. Lee, B. Shin, Y.S. Yeom, T.T. Nguyen, H. Han, B.S. Chung, K. Eckerman, R. Qiu, S. Kim, G. Son

PUBLISHED FOR

The International Commission on Radiological Protection

by

SAGE

Please cite this issue as 'ICRP, 20xx. Paediatric Mesh-type Reference Computational Phantoms. ICRP Publication XXX. Ann. ICRP xx(x).'

CONTENTS

ABSTRACT 4

MAIN POINTS 6

1. INTRODUCTION 7

2. IMPROVEMENTS IN PAEDIATRIC MESH-TYPE REFERENCE COMPUTATIONAL PHANTOMS 11

3. CONVERSION OF THE PAEDIATRIC VOXEL-TYPE REFERENCE COMPUTATIONAL PHANTOMS TO MESH FORMAT 14
   - 3.1. Simple organs and tissues 14
   - 3.2. Skeletal system 16
   - 3.3. Colon 17
   - 3.4. Thyroid 19
   - 3.5. Lymphatic nodes 20
   - 3.6. Extrathoracic region 21
   - 3.7. Eyes 22
   - 3.8. Teeth 24
   - 3.9. Blood in large vessels 25
   - 3.10. Muscle 26
   - 3.11. Exterior body contour 27

4. INCLUSION OF BLOOD IN ORGANS AND TISSUES 29
   - 4.1. Calculation of mass, density and elemental composition of organs and tissues inclusive of blood content 29
   - 4.2. Phantom adjustment for blood inclusion 33
   - 4.3. Definition of residual soft tissue (RST) 33

5. INCLUSION OF THIN TARGET AND SOURCE REGIONS 35
   - 5.1. Skin 35
   - 5.2. Alimentary tract 35
   - 5.3. Respiratory tract 37
   - 5.4. Urinary bladder 39

6. DESCRIPTION OF THE PAEDIATRIC MESH-TYPE REFERENCE COMPUTATIONAL PHANTOMS 41
   - 6.1. General phantom characteristics 41
   - 6.2. Geometric comparison with the P143 phantoms 44
   - 6.3. Computational performance in Monte Carlo codes 47

7. DOSIMETRIC IMPACT OF THE PAEDIATRIC MESH-TYPE REFERENCE COMPUTATIONAL PHANTOMS 50
   - 7.1. External exposures 50
   - 7.2. Internal exposures 51

REFERENCES 54

ANNEX A. LIST OF ORGAN ID, MEDIUM AND MASS OF EACH ORGAN/TISSUE 60

ANNEX B. LIST OF MEDIA AND THEIR ELEMENTAL COMPOSITIONS 71

ANNEX C. LIST OF ANATOMICAL SOURCE REGIONS, ACRONYMS AND IDENTIFICATION NUMBERS 91

ANNEX D. LIST OF ANATOMICAL TARGET REGIONS, ACRONYMS AND IDENTIFICATION NUMBERS 94

ANNEX E. ORGAN DEPTH DISTRIBUTIONS OF SELECTED ORGANS/TISSUES 96
ANNEX F. CHORD-LENGTH DISTRIBUTIONS BETWEEN SELECTED ORGAN PAIRS (SOURCE/TARGET TISSUES) 162
ANNEX G. CROSS-SECTIONAL IMAGES 188
G.1.Images of the newborn male mesh-type reference computational phantom 188
G.2.Images of the newborn female mesh-type reference computational phantom 191
G.3.Images of the 1-year-old male mesh-type reference computational phantom 194
G.4.Images of the 1-year-old female mesh-type reference computational phantom 197
G.5.Images of the 5-year-old male mesh-type reference computational phantom 200
G.6.Images of the 5-year-old female mesh-type reference computational phantom 203
G.7.Images of the 10-year-old male mesh-type reference computational phantom 206
G.8.Images of the 10-year-old female mesh-type reference computational phantom 209
G.9.Images of the 15-year-old male mesh-type reference computational phantom 212
G.10.Images of the 15-year-old female mesh-type reference computational phantom 215
ANNEX H. COMPARISON OF DOSE COEFFICIENTS FOR EXTERNAL EXPOSURE 218
H.1.References 254
ANNEX I. COMPARISON OF SPECIFIC ABSORBED FRACTIONS 255
I.1.References 280
ANNEX J. DESCRIPTION OF ELECTRONIC FILES 281
J.1.Data files in Phantom_data 281
J.2.Data files in *MC_examples* 284
J.3.References 284
ACKNOWLEDGEMENTS 286

ICRP Publication XXX

PAEDIATRIC MESH-TYPE REFERENCE COMPUTATIONAL PHANTOMS

ICRP PUBLICATION XXX

Approved by the Commission in MMMMM 20XX

ABSTRACT

Abstract– Following the issuance of the 2007 Recommendations in *Publication 103*, the Commission released the adult (male and female) and paediatric (newborn, 1-, 5-, 10- and 15-year-old male and female) reference computational phantoms in *Publications 110* and *143*, respectively, for use in effective dose calculations. These phantoms are voxel models represented in the form of a 3D array of cuboidal voxels, which were constructed from computed tomography images of people and adjusted to be consistent with the reference anatomical parameters given in *Publication 89*. The voxel phantoms provide anatomical improvements over the mathematical equation-based stylised phantoms used for the previous dose coefficient (DC) calculations prior to the 2007 Recommendations. Nevertheless, the voxel phantoms, due to the nature of voxel geometry and finite voxel resolutions, have limitations in representing small and thin organs and tissues, necessitating additional supplementary stylised models such as those defined for the respiratory tract airways, the alimentary tract organ walls and stem cell layers, lens of the eye and the skin basal layer.

To address the limitations of the voxel phantoms, Task Group 103 was charged with developing mesh-type reference computational phantoms (MRCPs) by converting the voxel phantoms into a high-quality/fidelity mesh format with anatomical improvements for the complex organs and tissues which were not fully represented in the voxel phantoms. The MRCPs for adult male and female were then developed and recently released in *Publication 145*. Following the release of the adult MRCPs, the current publication describes the construction of the paediatric MRCPs, the counterparts of the *Publication 143* voxel phantoms. The paediatric MRCPs, like the adult MRCPs, were developed to have all the source and target tissues required for calculation of effective dose, including the micrometre-scale regions, assimilating the supplementary stylised models. These phantoms can be directly used in general-purpose Monte Carlo codes such as Geant4, PHITS and MCNP6, fully maintaining the high fidelity of the mesh geometry in Monte Carlo dose calculations.

To investigate the impact of the paediatric MRCPs, the DCs of organ dose and effective dose and specific absorbed fractions (SAFs) for some selected external and internal exposures were calculated and compared with the values calculated using the *Publication 143* phantoms and the *Publications 66* and *100* mathematical models for the respiratory and alimentary tracts and

the reference values of *Publication 1XX*. While some differences in the DCs and SAFs were observed for anatomically improved organs and weakly penetrating radiations, they were found not to be much different, indicating that the reference DCs obtained from the *Publication 143* voxel phantoms for both external and internal exposures remain valid in the current ICRP dosimetry system. The *Publication 143* voxel phantoms remain the primary ICRP/ICRU reference models for the calculation of reference DCs based on *Publication 103* methodology. The paediatric MRCPs will be used for all calculations of reference DCs following the next set of general recommendations and provide a resource for wider use in radiological protection applications.

Keywords: Phantoms; Tetrahedral mesh; Polygon mesh; Dose coefficients; Internal and external exposures

MAIN POINTS

- **This publication presents paediatric mesh-type reference computational phantoms (MRCPs) representing the Reference Male and Female at 0 year (i.e. newborn), 1 year, 5 years, 10 years and 15 years of age, which are counterparts of the paediatric voxel-type reference computational phantoms in *Publication 143* (ICRP, 2020a) developed based on computed tomography images of real people.**

- **The paediatric MRCPs were constructed by converting the *Publication 143* voxel phantoms to a high-quality mesh format, assimilating the supplementary stylised models used in conjunction with the voxel phantoms to overcome limitations of voxel geometry and adding tissue layers that are considered to contain cells at risk of radiogenic cancer.**

- **The paediatric MRCPs include all the necessary source and target tissues defined by the ICRP system for effective dose calculations, including the micrometre-thick source and target layers of the alimentary and respiratory tracts, skin and urinary bladder, as well as lens dose calculations.**

- **The paediatric MRCPs were found to provide dose coefficients and specific absorbed fractions that are generally not much different from those of the *Publication 143* voxel phantoms for both external and internal exposures, while some differences were observed for anatomically improved organs and weakly penetrating radiations (e.g. photons <50 keV and electrons).**

- **The *Publication 143* voxel phantoms remain the primary ICRP/ICRU reference models for the calculation of reference dose coefficients based on *Publication 103* methodology (ICRP, 2007), but the paediatric MRCPs will be used for all calculations of reference dose coefficients following the next set of general recommendations and also serve as a resource for wider use in radiological protection applications.**

1. INTRODUCTION

(1) A system of radiological protection requires appropriate dose quantities for use in the control of radiation exposures to individuals, including workers and members of the public, to prevent tissue reactions and to optimise protection from stochastic effects. For these purposes, the latest ICRP recommendations published in *Publication 103* (ICRP, 2007) described two protection quantities: equivalent dose (H_T) and effective dose (E), both given in sievert (Sv). These protection quantities are derived from absorbed dose (D_T), which is the basic physical dose quantity in the unit of gray (Gy; joule per kilogram). H_T is calculated from D_T averaged over an organ/tissue (hereafter 'organ') considering the relative effectiveness of different radiation types in causing stochastic effects. E is defined as the weighted sum of the values of H_T (i.e. weighted by the tissue weighting factors (w_T) over all organs considered to be sensitive to the induction of stochastic effects) (ICRP, 1991a). In accordance with the definition in *Publication 103* (ICRP, 2007), E is computed from the gender-averaged H_T values of the Reference Male and Female at specified ages as defined in *Publication 89* (ICRP, 2002). E is the risk-related quantity in radiation protection and is used as the central protection quantity in the optimisation of protection for workers and members of the public, the setting of control criteria (dose limits, dose constraints and reference levels) and the demonstration of regulatory compliance.

(2) For the calculation of the above dose quantities, the Commission adopted adult male and female reference computational phantoms as described in *Publication 110* (ICRP, 2009). The *Publication 110* phantoms, to be referred in this report as P110 phantoms, were constructed from computed tomography (CT) data of two subjects anatomically similar to the Reference Persons and adjusted to be consistent with the reference adult anatomical parameters given in *Publication 89* (ICRP, 2002). These phantoms, coupled with Monte Carlo radiation transport codes, were used to calculate the dose coefficients (DCs) for external idealised exposures in *Publication 116* (ICRP, 2010), external environmental exposures in *Publication 144* (ICRP, 2020b) and specific absorbed fractions (SAFs) in *Publication 133* (ICRP, 2016). The SAFs in *Publication 133* were subsequently used in the computation of the DCs for internal exposures due to occupational intakes of radionuclides in a series of publications (ICRP, 2015, 2016, 2017a,b, 2019).

(3) The Commission also adopted ten paediatric male and female reference computational phantoms representing for ages of 0 year (i.e. newborn), 1 year, 5 years, 10 years and 15 years in *Publication 143* (ICRP, 2020a). The *Publication 143* phantoms, to be referred in this report as P143 phantoms, were also constructed from CT data and adjusted taking into account the reference paediatric anatomical parameters from *Publication 89* (ICRP, 2002). The P143 phantoms were used to calculate the DCs for external environmental exposures in *Publication 144* (ICRP, 2020b) and are currently being used by a joint Task Group of ICRP Committees 2 and 3 to estimate the DCs for common diagnostic x-ray imaging examinations. In addition, these phantoms were employed to calculate the paediatric SAFs in *Publication 1XX* (ICRP, 2022). The SAFs listed in *Publication 133* and *1XX* are currently being used for the computation of the DCs for internal exposures due to environmental intakes of radionuclides by the public and to patients from radiopharmaceuticals administered in diagnostic nuclear medicine.

(4) The P110 and P143 phantoms are voxel models represented in the form of a 3D array of cuboidal voxels. Such voxel phantoms, based on CT images of human bodies, provide higher realism of human anatomy than previous stylised (or mathematical) phantoms in which external body and internal organ shapes are modelled using mathematical equations such as spheres, cylinders and ellipsoids. Prior to the 2007 Recommendations, the Commission relied

on various stylised phantoms (Snyder et al., 1969, 1978; Cristy, 1980; Kramer et al., 1982; Cristy and Eckerman, 1987; Stabin et al., 1995) for the calculation of the ICRP reference DCs for external and internal exposures issued in *Publications 30*, *53*, *56*, *60*, *61*, *66*, *67*, *68*, *69*, *71*, *72*, *74*, *80* and *100* (ICRP, 1979, 1988, 1990, 1991a,b, 1994a, 1993, 1994b, 1995a,b, 1996a,b, 1998, 2006).

(5) While providing anatomical improvements over the stylised phantoms, the ICRP voxel phantoms have limitations in the representation of small organ structures and very thin tissue layers. The voxel phantoms, composed of millimetre-scale voxels, cannot explicitly represent the micrometre-scale radiosensitive target regions and source regions in the respiratory and alimentary tracts, skin, lens of the eye and urinary bladder (the source regions here indicate the organs, tissues and body regions where radionuclides reside or pass that could thus irradiate target regions). With the limitations of these phantoms acknowledged in *Publications 133* and *1XX* (ICRP, 2016, 2022), the SAFs for electrons and alpha particles emitted from the source regions in the respiratory and alimentary tracts were computed by employing supplementary organ-specific stylised models. For the same reason, in *Publication 116* (ICRP, 2010), the DCs from external idealised exposures for lens of the eye and local skin were computed by additional simulations with supplementary stylised models.

(6) In order to overcome the limitations of the ICRP voxel phantoms associated with their intrinsic limitations of using voxels, to avoid the use of supplementary stylised models and to provide therefore all-in-one anatomical computational phantoms, the Commission started to develop mesh-type reference computational phantoms (MRCPs) by converting the voxel phantoms to high-quality/fidelity mesh-based phantoms. Note that the mesh geometry, either polygonal mesh (PM) or tetrahedral mesh (TM), is considered at the time of writing this report as the most advanced geometry used to construct computational phantoms beyond voxel geometry (Kainz et al., 2019).

(7) Recently, many researchers have been motivated to develop computational phantoms in the PM geometry [or sometimes combined with non-uniform rational B-spline (NURBS) geometry] for both adults (Christ et al., 2009; Zhang et al., 2009; Cassola et al., 2010; Lee et al., 2010; Segars et al., 2010; Hurtado et al., 2012; Gosselin et al., 2014; Dong et al., 2015; Lombardo et al., 2018; Pi et al., 2018) and children and adolescents (Lee et al., 2007, 2008, 2010; Christ et al., 2009; de Melo Lima et al., 2011; Cassola et al., 2013; Gosselin et al., 2014; Norris et al., 2014; Ma et al., 2017; Pi et al., 2018), providing more realistic representations of the human bodies than the voxel phantoms. These phantoms, however, need to be voxelised to be used in Monte Carlo codes, which leads to the recurrence of the limitations of the voxel phantoms. The aim of this Task Group, therefore, is to develop ICRP reference computational phantoms in the advanced mesh geometry which can be directly used in Monte Carlo codes, fully maintaining the advantages of the mesh geometry in Monte Carlo dose calculations.

(8) *Publication 145* (ICRP, 2020c) was the first report of this Task Group, which describes the development of adult male and female MRCPs constructed as the mesh counterparts of the P110 phantoms (ICRP, 2009). The current report, as the second report of the Task Group, describes the development of the paediatric series of MRCPs for newborn, 1 year, 5 years, 10 years and 15 years, depicting (1) the conversion of the P143 phantoms to the mesh format, including the remodelling or modification of complex organs; (2) the addition of some tissue structures such as the target cell layers for the respiratory and alimentary tracts, skin, urinary bladder, eyes and teeth; and (3) the impact of the paediatric MRCPs in the estimation of DCs within the ICRP system.

(9) The MRCPs, while closely preserving the original topology and shape of most of the organs of the voxel phantoms, present substantial improvements in the anatomy of small organs and include all the necessary source and target tissues defined by the ICRP system, assimilating

the supplementary stylised models such as those defined for the respiratory tract airways, the alimentary tract organ walls and stem cell layers, the lens of the eye and the skin basal layer. The MRCPs, which are in the TM format, are no longer bounded by the limitations of voxel geometry for the representation of very small and/or thin structures. These phantoms can also be used directly in the general-purpose Monte Carlo codes (e.g. Geant4, PHITS and MCNP6) without any additional processing (i.e. voxelisation) as needed for earlier work with mesh phantoms (Yeom et al., 2019b, 2020).

(10) For the calculation of reference equivalent and effective DCs based on *Publication 103* (ICRP, 2007) methodology, the P110 and P143 voxel phantoms (ICRP, 2009, 2020a) remain the primary ICRP/ICRU reference anatomical models. The MRCPs will replace the voxel phantoms for all calculations of reference DCs following the next set of general recommendations. The MRCPs have applications beyond the calculation of reference DCs. The new mesh phantoms are highly deformable and can be used to create phantoms of various body sizes and postures for use in retrospective emergency or accidental dose reconstruction (Lee et al., 2019; Yeom et al., 2019a; Choi et al., 2020). The deformation capability of the phantoms can also facilitate the virtual calibration of whole-body counters to account for the body size of individuals in efficiency calibration. The mesh phantoms can also be used directly to produce physical phantoms with 3D printing technology (Kim et al., 2022). In addition, it is relatively easy to model detailed structures in the phantoms and, therefore, the new phantoms could find applications in medicine and other areas requiring sophisticated organ models. One of the aims of this report is to assist those who wish to implement the phantoms for their own applications; therefore, detailed data on the phantoms in the PM format as well as the TM format are provided in the supplementary electronic data that accompany the printed publication, together with some input examples of the Monte Carlo codes.

(11) Chapter 1 explains the main background for the construction of the paediatric MRCPs. Chapter 2 focuses on the organs of the P143 phantoms for which the anatomical description has been significantly improved in the paediatric MRCPs. Chapter 3 describes the general procedure for the conversion of the P143 phantoms to the mesh format, including the remodelling or modification of complex organs. Chapter 4 describes the adjustment of the converted mesh models to the reference values for the mass, density and elemental composition of organs inclusive of blood content. Chapter 5 describes the inclusion of the thin target and source regions in the skin, alimentary tract, respiratory tract and urinary bladder. Chapter 6 describes the general characteristics of the paediatric MRCPs. Finally, Chapter 7 investigates the impact of the improved morphology of the paediatric MRCPs on the calculation of DCs for external and internal exposures.

(12) A detailed description of the paediatric MRCPs is given in Annexes A-F. Annex A presents a list of the organs/structures [identification number (ID) list], together with the assigned media, densities and masses. Annex B presents a list of the phantom media and their elemental compositions. Annexes C and D list the source and target regions, respectively, together with their acronyms and IDs. Annex E provides depth distributions for selected organs from the front, back, left, right, top and bottom, along with the respective data for the P143 phantoms. Annex F provides chord-length distributions between selected pairs of source and target organs, along with the data for the P143 phantoms. Annex G presents selected transverse, sagittal and coronal slice images of the paediatric MRCPs. In Annexes H and I, the DCs and SAFs calculated with the paediatric MRCPs for some selected idealised external and internal exposure cases are compared with the values calculated with the P143 phantoms and the *Publication 1XX* values (ICRP, 2022). Annex J describes the contents of the supplementary electronic data that accompany the printed publication, including the detailed phantom data

and examples of input files for three general-purpose Monte Carlo codes (i.e. Geant4, PHITS and MCNP6) which are widely used for dose calculation in the field of radiation protection.

2. IMPROVEMENTS IN PAEDIATRIC MESH-TYPE REFERENCE COMPUTATIONAL PHANTOMS

(13) Following the development of the P110 adult voxel phantoms (ICRP, 2009), the Commission released the P143 paediatric voxel phantoms (see Fig. 2.1) for computation of the protection quantities for children and adolescents. The P143 phantoms comprise ten phantoms representing the reference male and female at the five different ages defined for the Reference Person—newborn, 1 year, 5 years, 10 years and 15 years. These phantoms were derived from a corresponding series of boundary representation (BREP) paediatric phantoms with NURBS/PM surfaces based on human CT images developed in collaboration between the University of Florida (UF) and the National Cancer Institute (NCI) (Lee et al., 2010), which were adjusted to conform with *Publication 89* reference data on the paediatric anatomical parameters (ICRP, 2002) and then voxelised to be used with Monte Carlo simulation codes. The male and female phantoms of newborn, 1-, 5- and 10-year-old are anatomically identical, except for the reproductive system organs (e.g. gonads). Their voxel resolution (for the x, y and z axes) ranges from $0.0663 \times 0.0663 \times 0.0663$ cm^3 for the newborn to $0.1250 \times 0.1250 \times 0.2832$ cm^3 for the 15-year-old male (ICRP, 2020a).

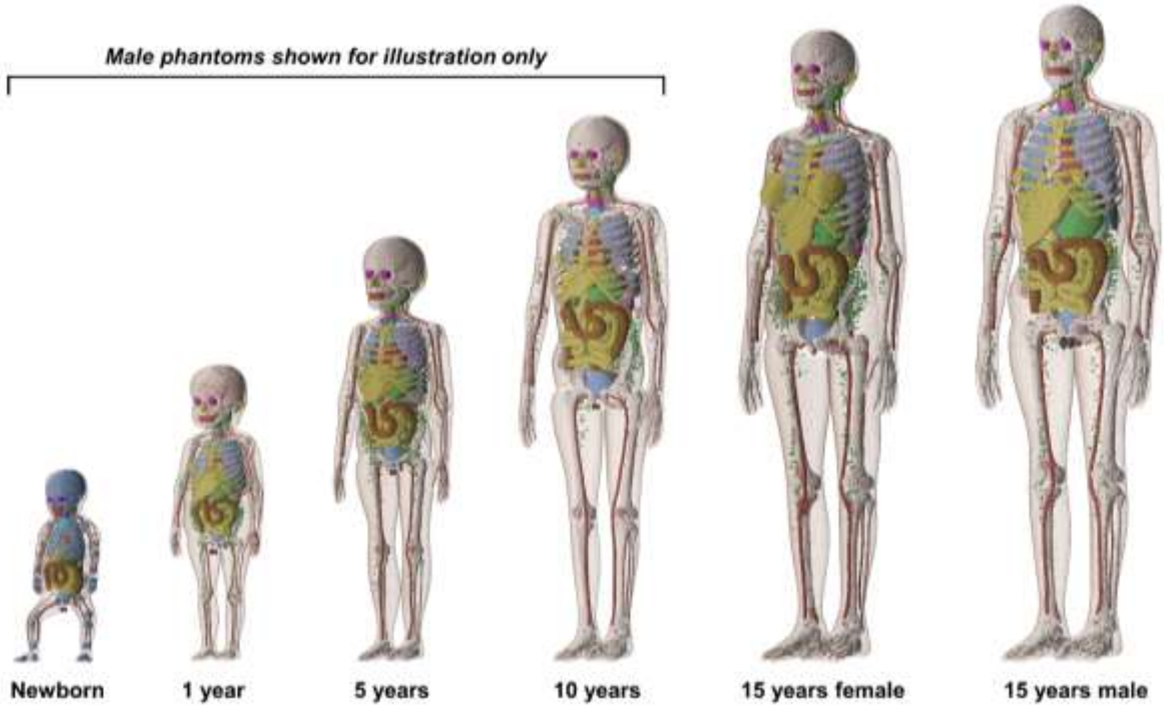

Fig. 2.1. P143 paediatric voxel phantoms (ICRP, 2020a). The figure shows only male phantoms for 10 years and younger and does not display muscle and adipose tissue for better visualisation of internal organs.

(14) While providing significant anatomical improvements over the previous stylised models, the P143 phantoms have limitations, mainly resulting from the inherent nature of voxel geometry and finite voxel resolutions. Small organ structures (e.g. lens of the eye) and very thin tissue layers (e.g. stem cell targets in alimentary and respiratory tract organs) are not fully modelled and for calculations of dose coefficients, some organs are represented by supplementary stylised models. These limitations and some phantom characteristics were addressed in the paediatric MRCPs, as summarised in the following paragraphs.

(15) In the P143 phantoms, the skin is represented by the outermost single voxel layer of each transverse slice, resulting in many spaces between adjacent transverse slices. Through these spaces, radiation incident at nonzero angles relative to the transverse slices can directly reach some radiosensitive organs (such as breasts, spongiosa and testes), leading to a significant overestimation of DCs for those tissues for weakly penetrating radiations. Furthermore, the skin masses of the P143 phantoms do not conform ideally with their reference values; the skin masses of the newborn, 1-year-old and 15-year-old phantoms are smaller by up to ~33%, whereas those of the 5-year-old and 10-year-old phantoms are larger by up to ~20%, than the reference skin masses in *Publication 89*. In the paediatric MRCPs developed in the present work as in the adult MRCPs of *Publication 145* (ICRP, 2020c), the skin is modelled as a continuous layer and the mass exactly matches the reference value. Similarly, the limitations of other thin structures (e.g. cortical bone and alimentary tract organs) were also addressed in the same way.

(16) For the skin, the basal cell layer of the epidermis is assumed to be the target for radiogenic risk (ICRP, 1977, 2010, 2015). This skin target layer, however, could not be separately represented in the P143 phantoms due to their voxel resolutions being limited to hundreds of micrometres to several millimetres. Consequently, the entire skin (= epidermis plus dermis) is defined as a single voxel layer and used to approximate dose to the skin target layer. Considering the small w_T of the skin (= 0.01), this approximation is acceptable for calculation of the effective dose for most penetrating radiations. For external exposures to weakly penetrating radiations (e.g. alpha and beta particles and low-energy photons), however, this approximation could lead to significant errors in both skin dose and effective dose calculations (Yeom et al., 2016, 2017). In the paediatric MRCPs as in the adult MRCPs, this problem was addressed by defining the target layer in the skin.

(17) The computation of specific absorbed fractions (SAFs) for the respiratory and alimentary tracts (ICRP, 1994a, 2006) requires the modelling of the cell layers of radiosensitive tissues and similarly scaled source regions (ICRP, 1994a, 2006). However, these target and source regions were not modelled in the P143 phantoms due to the finite voxel resolutions. For computation of the paediatric SAFs in *Publication 1XX* (ICRP, 2022), therefore, a number of mathematical equations-based stylised models used in *Publications 66* and 100 to describe the respiratory and alimentary tract organs, respectively, were separately employed for charged particles. In the paediatric MRCPs as in the adult MRCPs, the target and source regions in the respiratory and alimentary tracts were defined (Choi et al., 2022a,b), allowing the calculation of SAFs directly using the reference phantoms without using separate supplementary models.

(18) Similarly, for the urinary bladder, the basal cells of the lining epithelium are assumed to be the relevant target cells for radiogenic risk (Colin et al., 2009) and taken as the target region for calculation of the SAFs for non-penetrating radiations (i.e. alpha and beta particles), emitted from the bladder contents (Eckerman and Veinot, 2018). In the paediatric MRCPs as in the adult MRCPs, therefore, the target layer in the urinary bladder wall was explicitly defined to conform with following the age-dependent target depth and thickness data.

(19) The complex structure of the eye was not represented in the P143 phantoms due to the finite voxel resolutions. In the adult MRCPs (ICRP, 2020c), this issue was addressed by incorporating the detailed eye model of Behrens et al. (2009) which had been adopted in *Publication 116* (ICRP, 2010) for calculation of the lens DCs of adults for idealised external radiation fields. The direct use of scaled versions of the adult eye model for children and adolescents, however, would not adequately represent age-related changes in the dimensions of the eye and the lens. In the present work, therefore, a set of paediatric eye models were first developed following the approach used for the development of the Behrens' eye model and then incorporated into the paediatric MRCPs (Han et al., 2021).

(20) The teeth of the P143 phantoms consist of a single homogeneous region with a simplified geometry (i.e. ellipsoid). In the paediatric MRCPs, detailed tooth models were incorporated based on existing high-quality tooth models (Shin et al., 2021). The tooth models of the paediatric MRCPs include four inner tooth structures (i.e. enamel, dentin, pulp and cementum) and reflect the anatomical changes with age. These revised models are well suited for retrospective dosimetry based on electron paramagnetic resonance (EPR) (IAEA, 2002; Shin et al., 2021).

(21) The shapes and/or topologies of some organs (i.e. the thyroid, extrathoracic (ET) region, sacrum, muscle and exterior body contour of all phantoms; the liver of the newborn phantoms; the crania of the newborn and 1-year-old phantoms; and the spine and hand/foot bones of 1-year-old and older phantoms) were modified to achieve better anatomical realism. The mass and density of the colon contents were adjusted to the reference values of *Publication 89* (ICRP, 2002), and the position of the colon was also altered to provide a better representation of typical anatomy. The mass of the blood in the large vessels was significantly increased, improving the anatomical representations.

(22) The organ masses of the P143 phantoms are based on the reference masses listed in Table 2.8 of *Publication 89* (ICRP, 2002), which represent only the organ parenchymal masses (i.e. excluding the intra-organ blood masses). Note that in a living person, a significant portion of the total blood is situated in the small vessels and capillaries in the organs, which should be considered in phantom construction. In the paediatric MRCPs as in the adult MRCPs, therefore, the organs were adjusted to the reference masses including the intra-organ blood content based on the blood distribution in Wayson et al. (2018) adopted in the calculation of the paediatric SAFs (ICRP, 2021). In the SAF calculations using the P110 (ICRP, 2009) and P143 (ICRP, 2020a) voxel phantoms, scaling of SAFs for self-irradiation geometries was performed (ICRP, 2016, 2022). Such scaling will not be necessary with the MRCPs, the organ masses of which are consistent with the reference masses inclusive of blood content.

3. CONVERSION OF THE PAEDIATRIC VOXEL-TYPE REFERENCE COMPUTATIONAL PHANTOMS TO MESH FORMAT

(23) Fig. 3.1 shows how the paediatric MRCPs were developed from the P143 phantoms. Detailed explanations for each step will be given in the following chapters.

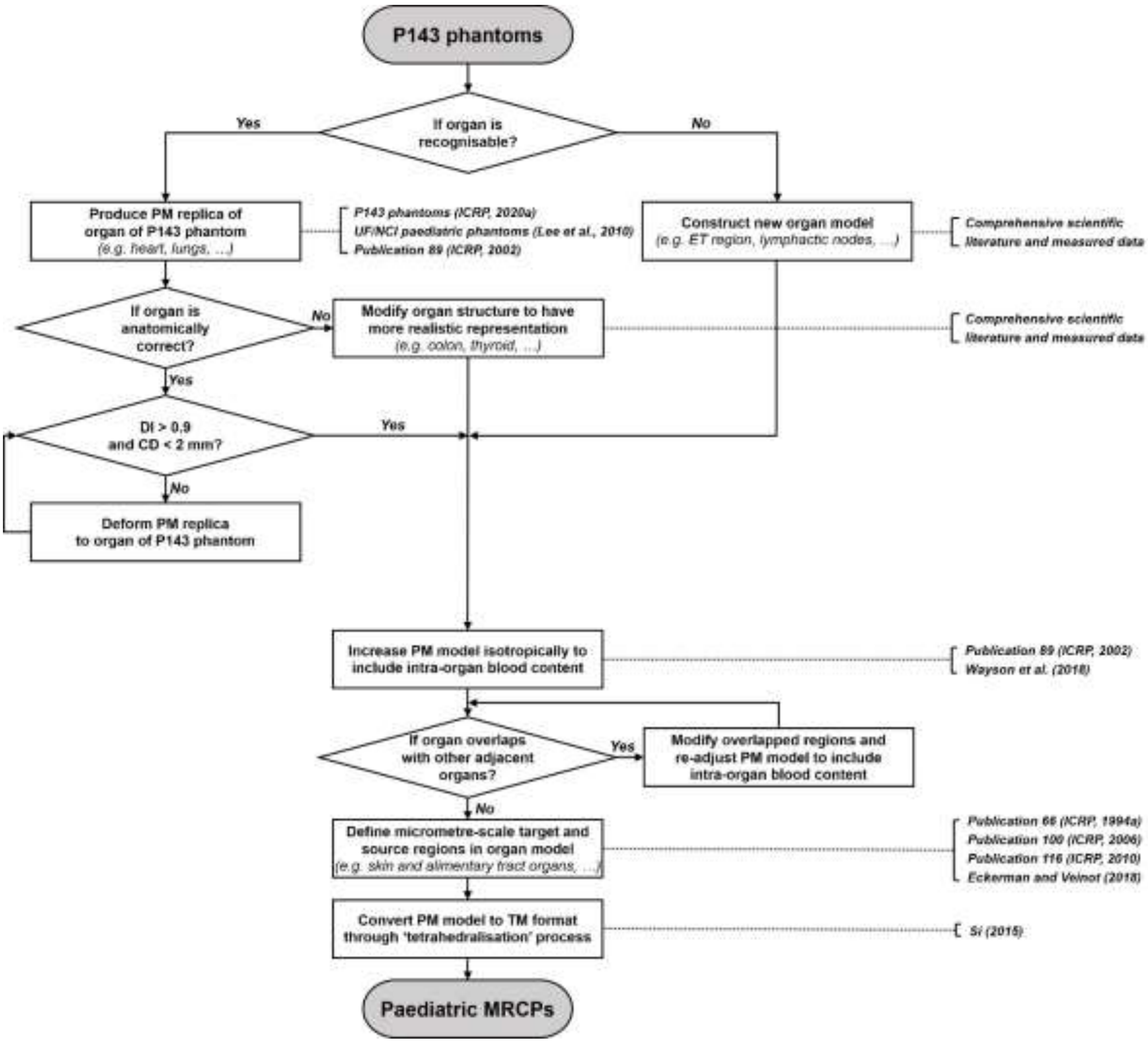

Fig. 3.1. Schematic for constructing the paediatric MRCPs from the P143 phantoms (ICRP, 2020a).

3.1. Simple organs and tissues

(24) Most of the organs of the paediatric MRCPs [i.e. adrenal glands, trachea, main bronchi (= generation 1), brain, breasts, gall bladder, stomach, small intestine, heart, kidneys, liver, lungs, oesophagus, gonads (testes or ovaries), pancreas, pituitary gland, prostate, salivary glands, spinal cord, spleen, tongue, thymus, tonsils, ureters, urinary bladder and uterus], which have an easily recognisable and anatomically reasonable shape, were reproduced using both the P143 phantoms (ICRP, 2020a) and the UF/NCI paediatric phantom series (Lee et al., 2010) which are the source of the P143 phantoms. First, the UF/NCI phantoms were used to produce

initial polygonal mesh (PM) models of the simple organs, which were then refined using the approaches employed for the adult MRCPs (ICRP, 2020c). The refined models were then matched to the organs of the P143 phantoms, which are consistent with the reference values in *Publication 89* (ICRP, 2002), to faithfully preserve the original organ topology. Subsequently, the models were further adjusted to allow for the intra-organ blood content. The PM models were converted to the TM format at the final stage of phantom construction with the other organ models.

(25) During the conversion process, the PM models were matched to the P143 phantoms by monitoring two indices which show the geometric similarity of two models: Dice index (DI), the overlapping volume fraction of two objects and centroid distance (CD), the distance between the centroids of two objects. The matching criteria were set for the DI value to be higher than 0.9 of the maximum achievable Dice index (MADI) and for the CD values to be less than 2 mm. Note that the MADI was introduced to account for the intrinsic difference in the geometry format (i.e. voxel vs. PM) of the two models (ICRP, 2020c).

(26) *Publication 89* (ICRP, 2002) provides sex-averaged reference masses for most of the organs for the ages up to and including 10 years, i.e. the same reference masses for the same age regardless of sex. Only for two organs (i.e. brain for 5 and 10 years and thymus for 10 years), it provides sex-specific reference masses, i.e. the different reference masses depending on sex. However, the P143 phantoms of these ages were developed using sex-averaged masses for all the organs, except for the reproductive system organs (e.g. gonads). In the present work, the paediatric MRCPs were developed using sex-specific reference organ masses where available. Therefore, the refined PM models of the brain and thymus were additionally adjusted to match the sex-specific reference organ masses.

(27) In the P143 phantoms, some organs and contents (e.g. brain and heart contents for newborn, thymus for 1 year and gastro-intestinal contents for all ages) have masses significantly different from the reference values given in *Publication 89*, mainly due to the small space allowed for these organs and contents (Lee et al., 2010). In the paediatric MRCPs, these organs and contents were adjusted to match the reference values. During the adjustment process, these tissues were isotropically enlarged, preserving their original shapes and centroids, with slight adjustment of the adjacent organs.

(28) In the P143 phantoms, the oesophagus contents are not defined, and in principle estimation of the SAFs of the oesophagus wall for radiations from the oesophagus contents is not possible. This limitation was addressed in the paediatric MRCPs following the same approach used for the adult MRCPs (ICRP, 2020c); that is, the oesophagus contents were defined in the middle of the oesophagus with the volume derived from the morphological information (i.e. length and diameter) given in *Publication 100* (ICRP, 2006). To maintain the oesophagus wall volume, the outer diameter of the oesophagus wall was slightly increased (i.e. by 3-7 mm).

(29) The liver of the P143 newborn phantoms is somewhat unrealistically long in the vertical direction, as a result of extending the liver model downwards to match the reference mass of *Publication 89* (ICRP, 2002). To address this issue, the liver was reproduced directly from the original CT image data which had been used for the construction of the P143 phantoms. The liver was then adjusted to match the reference mass, isotropically enlarged to preserve the original shape of the liver. During this reconstruction of the liver for the newborn phantoms, the lower part of the ribs had to be moved outwards slightly (i.e. in the lateral direction); the resulting rib cage was found to be within the range of typical shapes (Devlieger et al., 1991).

(30) In the present work, the organ models were mostly visualised, handled and refined with the *Rapidform*^{TM} software (INUS Technology INC., Korea), with two exceptions: the conversion of NURBS surfaces to PM surfaces and the generation of the blood and colon

passages and the eyes, which were accomplished with the *Rhinoceros 5.0* software (Robert McNeel, USA).

3.2. Skeletal system

(31) The majority of the bones of the paediatric MRCPs (i.e. upper humeri, lower humeri, ulnae, radii, clavicles, cranium, upper femora, lower femora, tibiae, fibulae, patellae, mandible, pelvis, ribs, scapulae and sternum) were produced directly from the UF/NCI phantom series (Lee et al., 2010) using the same procedure as for the simple organs described in Section 3.1. Some bones which were not properly represented in the UF/NCI phantoms were modified or remodelled by using other existing high-quality models and analysing scientific literature and measured data (Choi et al., 2021).

(32) The spine models (cervical, thoracic and lumbar regions) of the 1-year-old and older MRCPs were replaced with high-quality PM models produced from serially sectioned photographic images of adult male and female cadavers (Park et al., 2005) after several adjustments. These adult models are considered to be applicable to children and adolescents, except for the newborn, since ossification of the individual vertebrae of the spine is complete within about five months after birth (Taylor, 1975) and only the anterior-posterior curvature of the spine changes with growth. First, the adult models were scaled down in all directions, matching the spine height of the P143 phantoms. The individual vertebrae were then translated and rotated, matching the original spine topology (i.e. position and curvature) of the P143 phantoms. Finally, the individual vertebrae were scaled isotropically to match the reference mass of *Publication 89* (ICRP, 2002). Likewise, the hand and foot bones of the 1-year-old and older MRCPs were replaced with high-quality PM models based on micro-CT images of adult male and female cadavers (http://dk.kisti.re.kr/) in a similar way as for the spine. Note that the models were available for both male and female and thus were used separately.

(33) The crania of the newborn and 1-year-old MRCPs were modified according to data on fontanelle sizes and suture widths determined from the scientific literature. The anterior fontanelle sizes of the newborn and 1 year were taken from the data provided by Noorizadeh et al. (2015) and Duc and Largo (1986), respectively. The posterior fontanelle size of the newborn was obtained from the data of Faix (1982). Note that the posterior fontanelle is closed 2-3 months after birth (Usman et al., 2011), which was thus defined only in the newborn MRCPs. The suture widths were determined by scaling the newborn and 1-year-old values in proportion to the head circumferences (Li et al., 2015). The crania of the newborn and 1-year-old MRCPs were matched to the target values within 5% difference.

(34) Some minor improvements were also made to several bones. The sacra were modified to take account of anatomical changes in the sacral crest and foramina with growth (Kim et al., 2014). The sterna of the 1-, 5- and 10-year-old MRCPs were extended in the vertical direction to conform to the locations of the ribs. The mandibles of the 1- and 10-year-old MRCPs were slightly adjusted for normal occlusion of the teeth.

(35) The bones of the paediatric MRCPs were finally divided into cortical bone, spongiosa and medullary cavity, in a similar way as for the P143 phantoms.

(36) The costal cartilage, intervertebral disks and pre-osseous cartilage were directly produced from the UF/NCI phantoms. The intervertebral disks of the 1-, 5-, 10- and 15-year-old phantoms were adjusted to their positions in the new spine models produced from the high-quality PM models (Park et al., 2005). For the newborn and 1-year-old MRCPs, the fontanelle cartilage was adjusted to the modified cranium. The other cartilages, which were not explicitly

modelled in the paediatric MRCPs, were included in the residual soft tissue (RST) which will be discussed in Section 4.3.

(37) Fig. 3.2 shows the skeletal system of the newborn and 10-year-old male MRCPs, including the cortical bone, spongiosa, medullary cavity and explicitly defined cartilage.

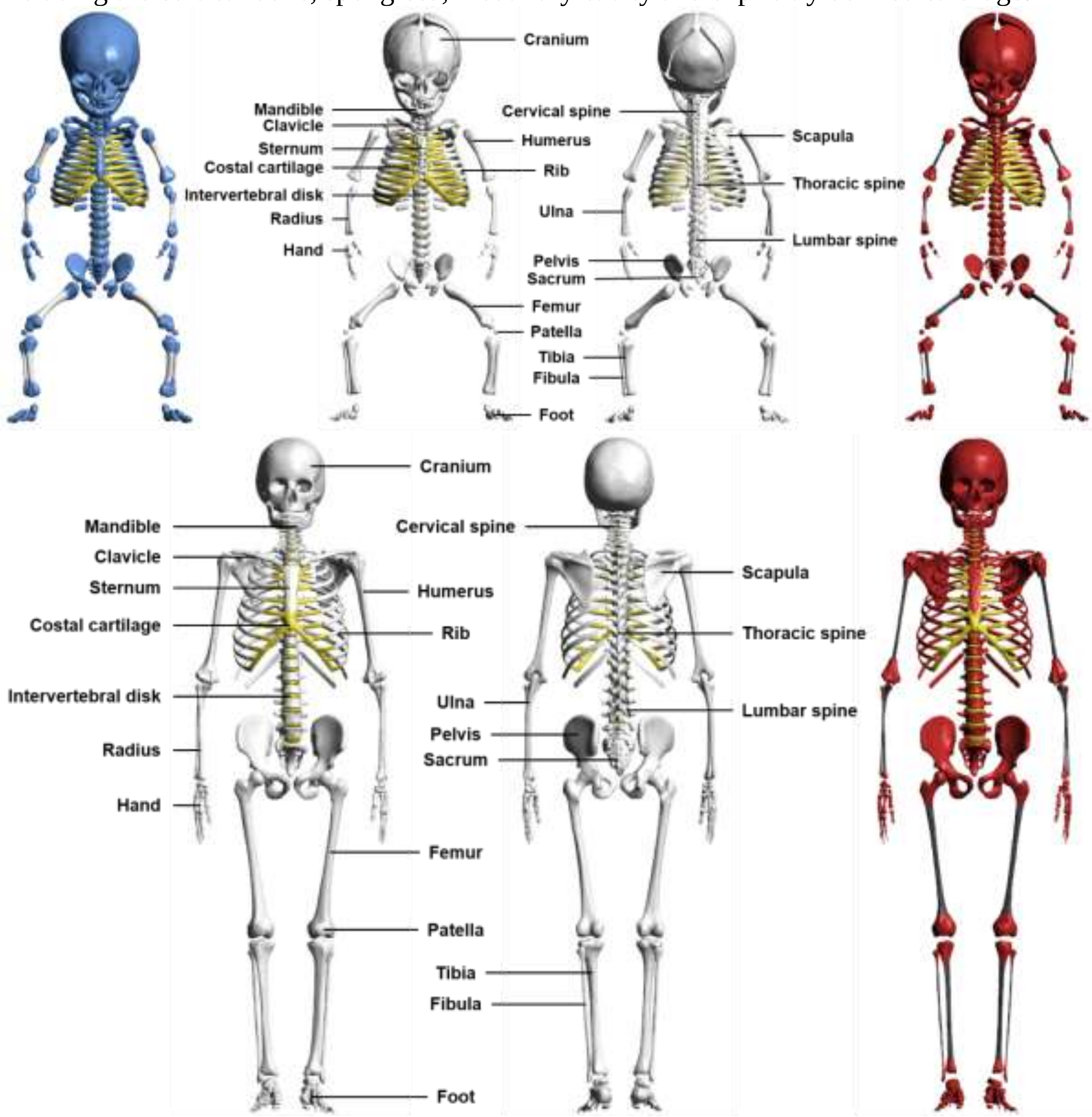

Fig. 3.2. Skeletal system of newborn male (upper) and 10-year-old male (lower) MRCPs: cortical bone (white), spongiosa (red), medullary cavity (black), costal cartilage and intervertebral disks (yellow) and pre-osseous cartilage (blue).

3.3. Colon

(38) In the P143 phantoms (ICRP, 2020a), the wall of the colon has the reference mass and length given in *Publication 89* (ICRP, 2002). However, either the mass or the density of the colon contents was significantly different from the reference values, due to the limitation of the modelling approach using a simple cylinder (Lee et al., 2010). In addition, the middle part of the transverse colon showed significant curvature.

(39) For the paediatric MRCPs, therefore, the colon was remodelled (Choi et al., 2022a). First, the colon was modelled as a connection of three truncated curved cones, representing the right, left and rectosigmoid colons, for the wall and the contents, respectively, as shown in Table 3.1. The top and bottom radii of each truncated cone were determined by a numerical approach, involving iteration of calculations, to connect the three truncated cones most smoothly while matching all the reference values (i.e. mass, length and density of the right, left and rectosigmoid colon, for both the wall and the contents). The details of the numerical approach can be found in Choi et al. (2022a). The colon model was then subdivided into six regions based on the length data given in *Publication 89* (ICRP, 2002): the right colon into the ascending and the transverse right colon; the left colon into the transverse left and the descending colon; and the rectosigmoid colon into the sigmoid colon and the rectum. Finally, the colon was produced in the NURBS format and then converted to the PM format for incorporation into the paediatric MRCPs, while addressing the issue of the transverse colon curvature.

(40) Fig. 3.3 shows the developed colon of the 10-year-old male MRCP, together with the P143 phantom.

Table 3.1. Schematic and dimensions of the colon models for the paediatric ages (Choi et al., 2022a).

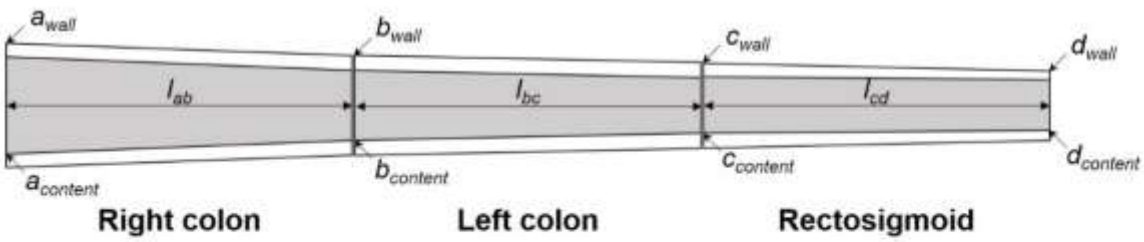

Phantoms	Radius (cm)								Length (cm)		
	a_{wall}	b_{wall}	c_{wall}	d_{wall}	$a_{content}$	$b_{content}$	$c_{content}$	$d_{content}$	l_{ab}	l_{bc}	l_{cd}
Newborn male/female	1.011	0.681	0.587	0.554	0.938	0.495	0.468	0.526	14	16	15
1-year male/female	1.214	0.861	0.734	0.630	1.069	0.562	0.522	0.562	18	21	21
5-year male/female	1.368	1.074	0.953	0.617	1.054	0.560	0.530	0.560	23	26	26
10-year male/female	1.555	1.231	1.145	0.678	1.128	0.604	0.578	0.604	28	31	31
15-year male	1.901	1.499	1.298	0.866	1.430	0.760	0.696	0.760	30	35	35
15-year female	1.856	1.452	1.249	0.861	1.430	0.760	0.696	0.760	30	35	35

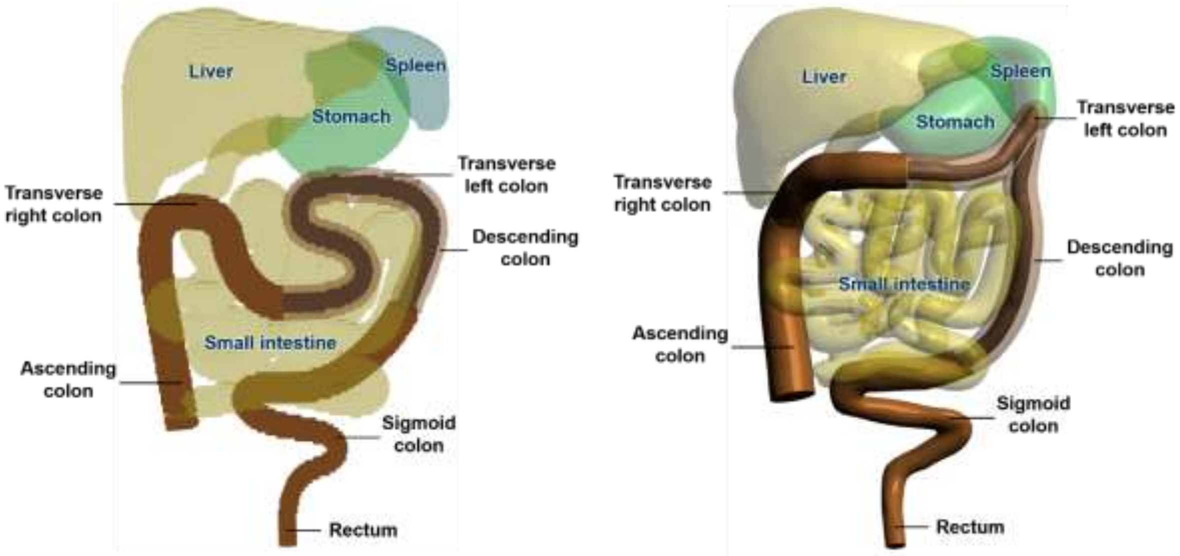

Fig. 3.3. Colon of the P143 phantom (left) and the paediatric MRCP (right) for the 10-year-old male with adjacent organs.

3.4. Thyroid

(41) The thyroids of the P143 phantoms show some anatomical abnormalities (e.g. the thickness of the thyroid isthmus for all phantoms and the position of the thyroid for the newborn and 1-year-old phantoms).

(42) For the paediatric MRCPs, the thyroid was therefore modified to have typical shape and position (Yeom et al., 2022). First, the isthmus thickness, width and height were determined from the scientific literature. The isthmus thickness at each age was taken from the data provided by Sea et al. (2019). The isthmus width and height of the newborn were obtained from the data of Ozguner et al. (2014) and those of the 1, 5, 10 and 15 years, due to the absence of data, were derived by linear interpolation between the newborn (Ozguner et al., 2014) and adult data (Tong and Rubenfeld, 1972; Harjeet et al., 2004; Joshi et al., 2010; Ozgur et al., 2011; Won et al., 2013). The thyroid shape hardly changes after reaching adulthood (Harjeet et al., 2004; Sultana et al., 2011; Won et al., 2013) and, therefore, the adult age was set as 18 years for the interpolation. The thyroid isthmus of the paediatric MRCPs was matched to the target values within 5% difference. Then, the thyroid was placed in the typical position (i.e. in front of the second and third tracheal cartilage) (Ellis, 2007; Naqshi et al., 2016), matching the depth beneath the skin surface to the target values derived from the equations given in Likhtarev et al. (1995), again within 5% difference.

(43) Fig. 3.4 shows the thyroid of the 1-year-old male MRCP, along with the P143 phantom.

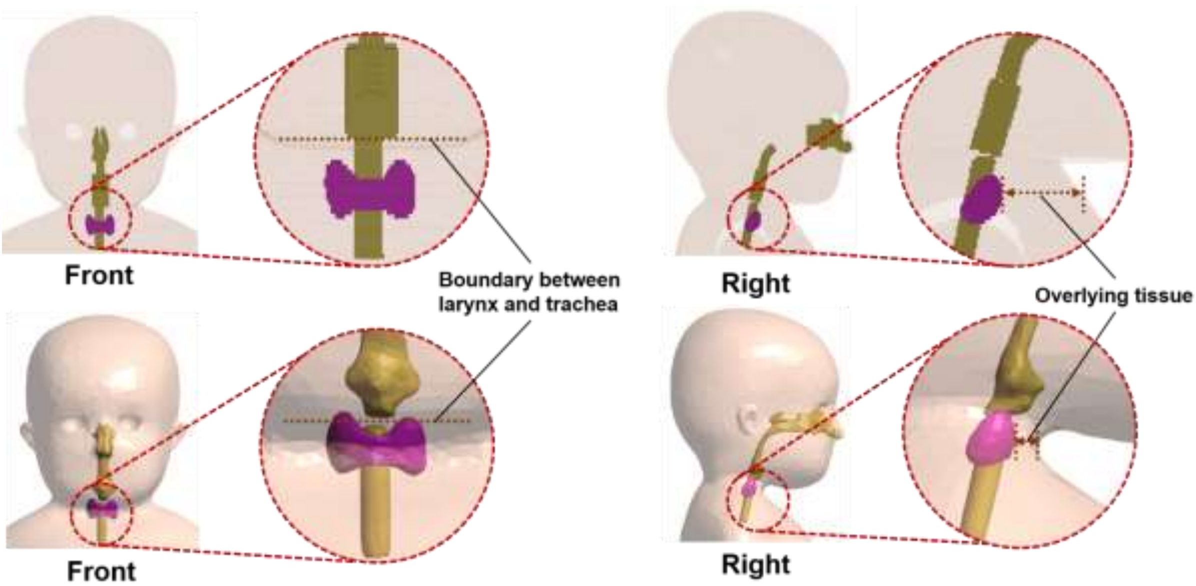

Fig. 3.4. Thyroid of the P143 phantom (upper) and the paediatric MRCP (lower), shown for the 1-year-old male.

3.5. Lymphatic nodes

(44) Due to the complexity of their distribution, the lymphatic nodes had to be generated using a modelling approach. The lymphatic nodes of the paediatric MRCPs were generated by employing the same method used for the adult MRCPs (ICRP, 2020c), but using the paediatric lymphatic node data given in Table 3.2, which were derived from data from *Publications 23* and *89* (ICRP, 1975, 2002) and were also employed for the SAF calculations in *Publication 1XX* (ICRP, 2022).

(45) Fig. 3.5 shows the lymphatic nodes of the 15-year-old male MRCP, together with the corresponding P143 phantom.

Table 3.2. Lymphatic node numbers and masses for the paediatric ages derived from the data of *Publications 23* and *89* (ICRP, 1975, 2002).

Lymphatic node site	Derived nodal numbers	Mass (g)					
		Newborn male/female	1-year male/female	5-year male/female	10-year male/female	15-year male	15-year female
Extrathoracic	55	1.251	2.192	4.356	7.224	12.807	11.589
Cervical	19	0.432	0.757	1.505	2.495	4.424	4.003
Thoracic	55	0.523	0.916	1.822	3.021	5.356	4.846
Breast (left and right)	38	0.865	1.514	3.010	4.991	8.849	8.007
Mesentery (left and right)	350	1.251	2.192	4.356	7.224	12.807	11.589
Axillary (left and right)	23	0.865	1.514	3.010	4.991	8.849	8.007
Cubital (left and right)	38	7.963	13.947	27.721	45.969	81.502	73.746
Inguinal (left and right)	38	0.865	1.514	3.010	4.991	8.849	8.007
Popliteal (left and right)	38	0.865	1.514	3.010	4.991	8.849	8.007

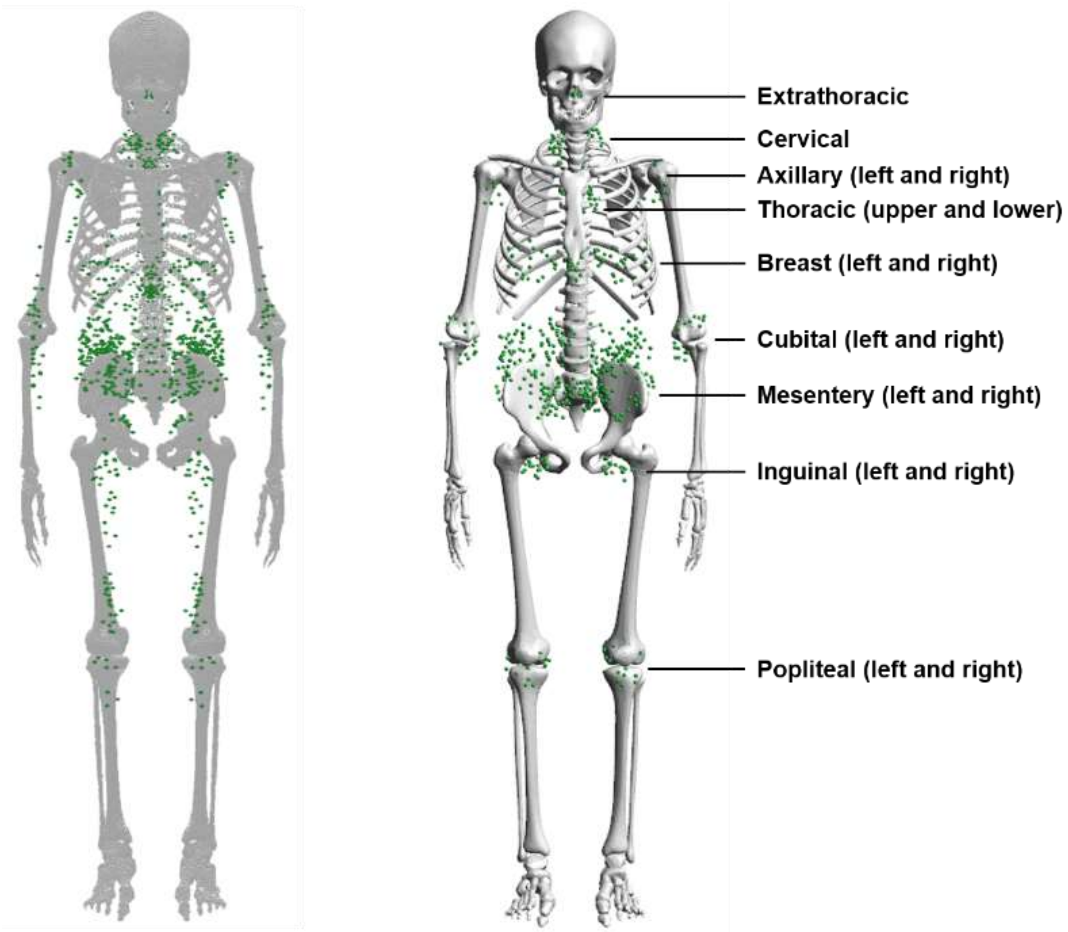

Fig. 3.5. Lymphatic nodes of the P143 phantom (left) and the paediatric MRCP (right) for the 15-year-old male.

3.6. Extrathoracic region

(46) The extrathoracic (ET) region consisting of the anterior nose (ET_1) and the posterior nasal passages, pharynx and larynx (ET_2) is not properly represented in the P143 phantoms (ICRP, 2020a), mainly because its intricate and narrow conduit geometry was not clearly distinguishable in the original CT image data. In addition, the larynx was not included in the ET2 region but tagged as cartilage during the modification of the UF/NCI phantoms to the P143 phantoms.

(47) For the paediatric MRCPs, the ET region was, therefore, remodelled (Choi et al., 2022b). First, the anterior nose and the posterior nasal passage were manually modified, referring to Kozak et al. (2014). Then, the remaining parts (i.e. pharynx and larynx) were replaced with new models which were produced by scaling down those of the adult MRCPs (ICRP, 2020c), taking account of differences in the trachea mass between the adults and children (ICRP, 1994a). Note that the adult models were available for both male and female and thus were used separately. The details of the scaling process can be found in Choi et al. (2022b). The modified regions (i.e. anterior nose and posterior nasal passage) and replaced regions (pharynx and larynx) were then connected, and were finally divided into the ET wall and inner air, matching the volume ratio of the adult models due to the absence of reference values for children and adolescents in *Publication 89* (2002).

(48) Fig. 3.6 shows the ET region of the paediatric MRCP for 5-year-old male, along with that of the P143 phantom.

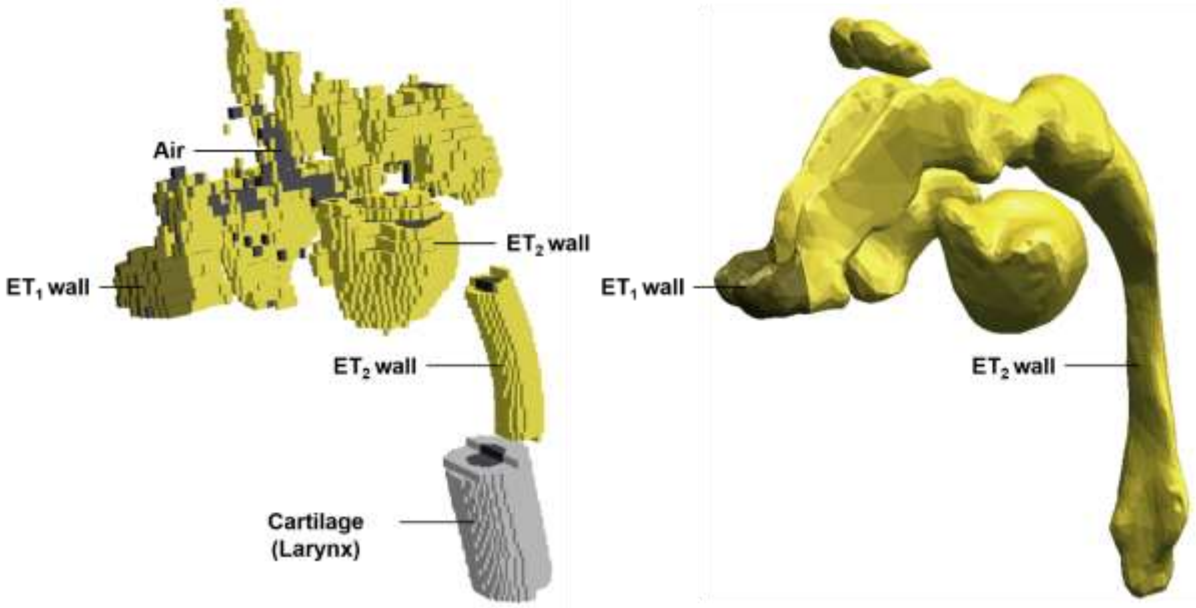

Fig. 3.6. Extrathoracic region (ET1 and ET2) of the P143 phantom (left) and the paediatric MRCP (right) for the 5-year-old male.

3.7. Eyes

(49) Due to their finite voxel resolutions (i.e. hundreds of micrometres to several millimetres), the detailed structures of the eyes could not be fully modelled in the P143 phantoms (ICRP, 2020a).

(50) For the adult MRCPs (ICRP, 2020c), this issue was addressed by incorporating the detailed eye model of Behrens et al. (2009), which was adopted in *Publication 116* (ICRP, 2010) for the calculation of the reference lens dose coefficients for adults. This eye model, however, is not appropriate for the lens dose assessment of children and adolescents, considering that the ocular dimensions of paediatric eyes are significantly different from scaled versions of adult eyes (Ronneburger et al., 2006; Augusteyn, 2010).

(51) Therefore, a set of detailed eye models for children and adolescents at five different ages (i.e. newborn, 1 year, 5 years, 10 years and 15 years) were developed for the paediatric MRCPs following the approach used for the development of the Behrens' eye model, based on nine ocular parameters of the eye: anterior chamber depth along the optical axis (ACD), lens thickness along the optical axis (LT), radius of curvature of the anterior surface of the lens (RAL), radius of curvature of the posterior surface of the lens (RPL), radius of curvature of the anterior surface of the cornea (RAC), corneal thickness along the optical axis (CT), corneal diameter (CD), equatorial diameter of the lens (ED) and radius of curvature of the anterior surface of the sclera (RAS) (Han et al., 2021).

(52) The nine ocular parameters for children and adolescents were first determined by analysing the scientific literature and measured data, as shown in Table 3.3. Among these parameters, the ACD and LT are the most important parameters that mainly influence lens doses from external exposures. The ACD and LT of 5 years and younger were taken from the data provided by Larsen (1971a,b). The ACD and LT of 10 years and 15 years were determined

by using the regression equations provided by Zadnik et al. (2004). Note that the regression equations were derived from the data measured with children aged 6-14 years and, therefore, the ACD and LT of 14 years were taken as the values of 15 years. The remaining parameters were determined in a similar way to that applied to the ACD and LT or through other procedures as discussed by Han et al. (2021).

(53) According to the nine ocular parameters, the eye models were produced in the NURBS format and then converted to the PM format. The eye models in the PM format were finally refined and installed in the paediatric MRCPs, matching the centroid positions of the eyes of the P143 phantoms, as shown in Fig. 3.7.

Table 3.3. Schematic and nine ocular parameters (unit: mm) of the eye models for the paediatric ages (Han et al., 2021).

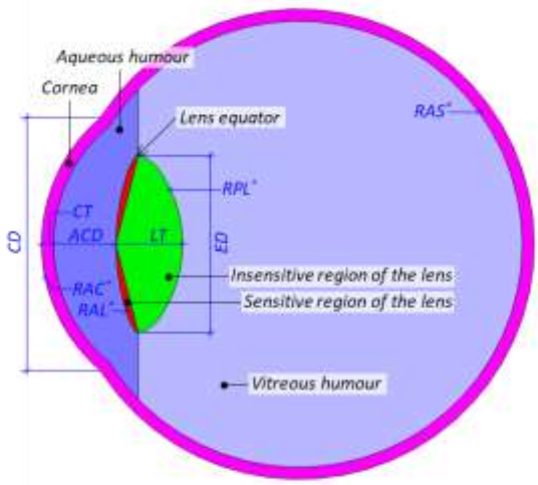

Parameters	Newborn	1 year	5 years	10 years	15 years	References
ACD	1.83	2.75	2.90	3.16	3.21	Larsen (1971a,b)
LT	3.96	3.66	3.61	3.41	3.44	Zadnik et al. (2004)
RAL	6.33	9.23	10.51	11.45	11.72	Mutti et al. (1998)
RPL	4.48	5.27	6.05	6.24	6.55	Frane et al. (2000)
RAC	7.11	7.82	7.72	7.72	7.72	Frane et al. (2000) Ehlers et al. (1976) Friedman et al. (1996)
CT	0.55	0.55	0.56	0.57	0.57	PEDIG (2011)
CD	9.66	11.15	11.80	11.80	11.80	Müller and Doughty (2002) Charles and Brown (1975)
ED	5.95	7.40	8.20	8.37	8.43	Atchison et al. (2008) Dilmen (2002) Goldstein et al. (1998) Ishii et al. (2013) Paquette (2009) Sukonpan and Phupong (2009)
RAS	9.10	9.45	10.96	11.30	11.63	Reference eye mass†

†RAS was determined to match the blood-inclusive reference mass of the eyes derived from *Publication 89* (ICRP, 2002) and Wayson et al. (2018).

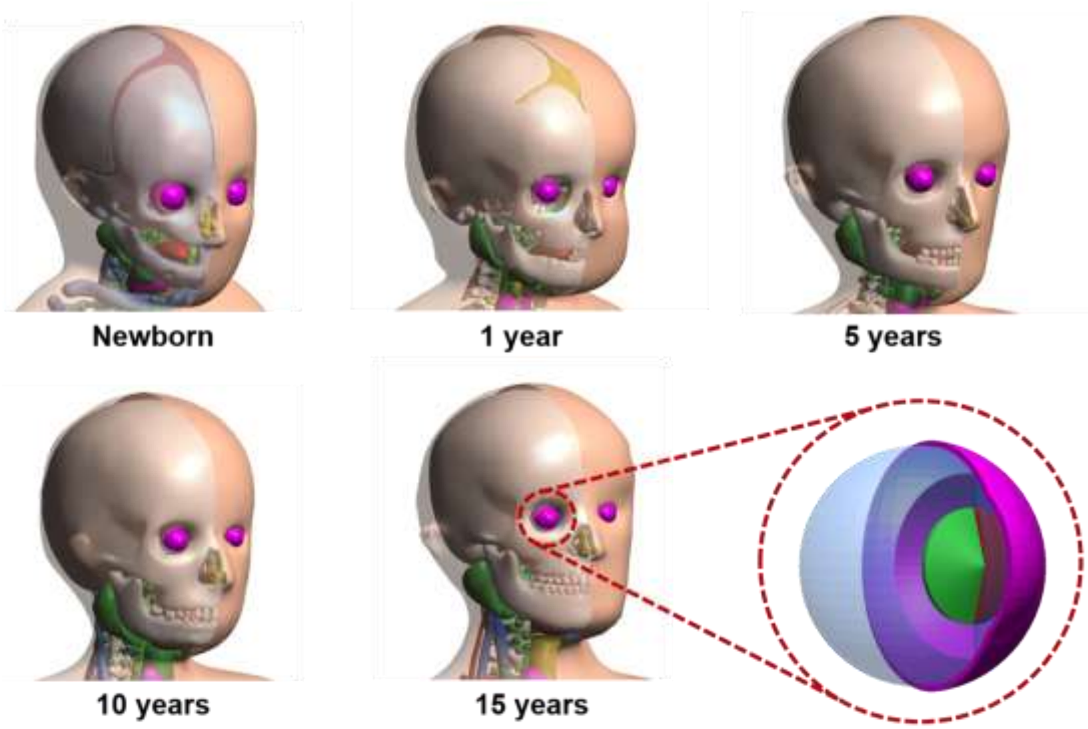

Fig. 3.7. Detailed eye models inserted in the paediatric MRCPs for all ages.

3.8. Teeth

(54) In the P143 phantoms, the teeth are defined as a single homogeneous region with a simplified geometry (i.e. ellipsoid). A more realistic representation was considered important for applications including retrospective dosimetry based on electron paramagnetic resonance (EPR).

(55) Detailed tooth models including the inner tooth tissues (i.e. enamel, dentin, pulp and cementum) were developed for each paediatric age and sex (Shin et al., 2021). The target masses of the tooth tissues for each age and sex were determined by analysing the scientific literature. First, the entire teeth mass was determined by adopting the reference values given in *Publication 89* (ICRP, 2002). The individual tooth masses were then determined using the tooth mass fractions to the entire teeth derived from the data of Ogorelec et al. (1997). Finally, the masses of the enamel, dentin (including cementum) and pulp for each tooth were determined based on the data of *Publication 23* (ICRP, 1975) and Bayle et al. (2009) for the permanent teeth and the deciduous teeth, respectively.

(56) The detailed tooth models were then developed by employing existing high-quality PM tooth models as preliminary models. The preliminary models for the permanent teeth were constructed from the micro-CT images of adult male and female (http://dk.kisti.re.kr) and that for the deciduous teeth was constructed by 3D scanning a mould of the teeth crowns of a child and modelling the teeth roots based on image references (https://www.turbosquid.com/3d-models/primary-teeth-dentition-max/953912). The permanent tooth models, but not the deciduous tooth model, are available for both male and female and thus were used separately. First, each tooth of the preliminary models was scaled to match the target tooth mass. In the scaled tooth model, the inner tooth tissues were modelled referring to anatomical structures represented by Schwartz (1995), matching the target tooth-tissue masses. The cementum was

separated from the dentin according to the age-dependent cementum thickness (Zander et al., 1958). In total, 332 detailed tooth models (i.e. newborn: 20, 1 year: 28, 5 years: 48, 10 years: 38 and 15 years: 32 for each sex) were produced individually, which were finally inserted in the paediatric MRCPs.

(57) Fig. 3.8 shows, as an example, the detailed tooth models of the 15-year-old male MRCP, including the internal structures.

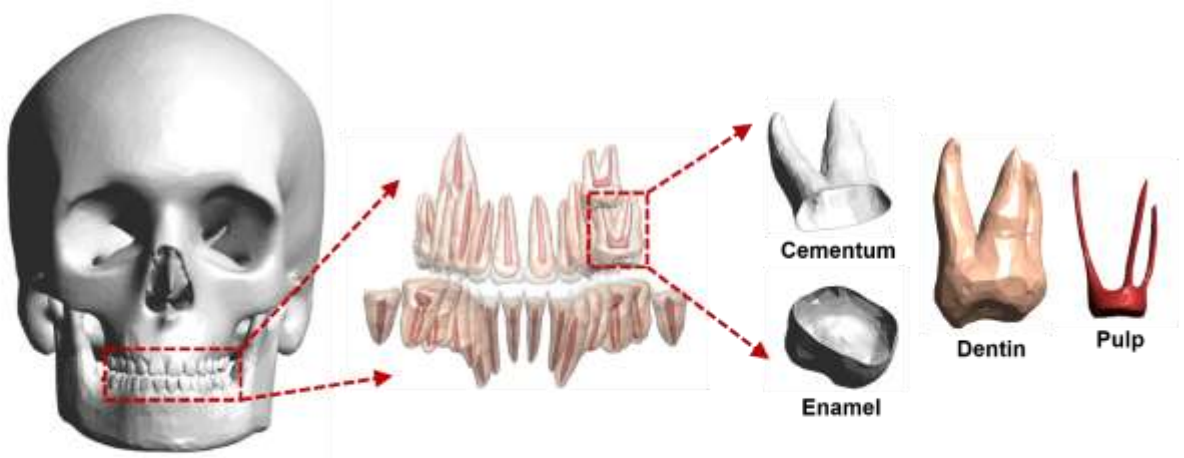

Fig. 3.8. Detailed tooth models of the 15-year-old male MRCP.

3.9. Blood in large vessels

(58) In the P143 phantoms, only a small portion of the blood in the large blood vessels was modelled because of the finite voxel resolutions of the original CT image data (Wayson, 2012; ICRP, 2020a). Consequently, the masses of the blood explicitly defined in the phantoms are significantly smaller than their reference values. Note that these values are not given in *Publication 89* (ICRP, 2002) but can be estimated based on the reference regional volume fractions derived by Wayson et al. (2018) and adopted in the calculation of the paediatric SAFs in *Publication 1XX* (ICRP, 2022).

(59) For the paediatric MRCPs, therefore, the blood in the large vessels was remodelled. First, the flow lines of the blood in the large vessels were manually generated, referring to the high-quality 3D blood models provided by BioDigital Human (http://www.biodigital.com). Next, the blood models were constructed in the NURBS format along the flow lines and then were converted to the PM format. Finally, the PM models were adjusted to match the reference masses.

(60) Fig. 3.9 shows the blood model for the 5-year-old male MRCP, together with the blood model of the corresponding P143 phantom. Note that the intra-organ vasculature was not modelled in the MRCPs and the blood in the intra-organ vasculature was assumed to be homogeneously distributed with the organ parenchyma.

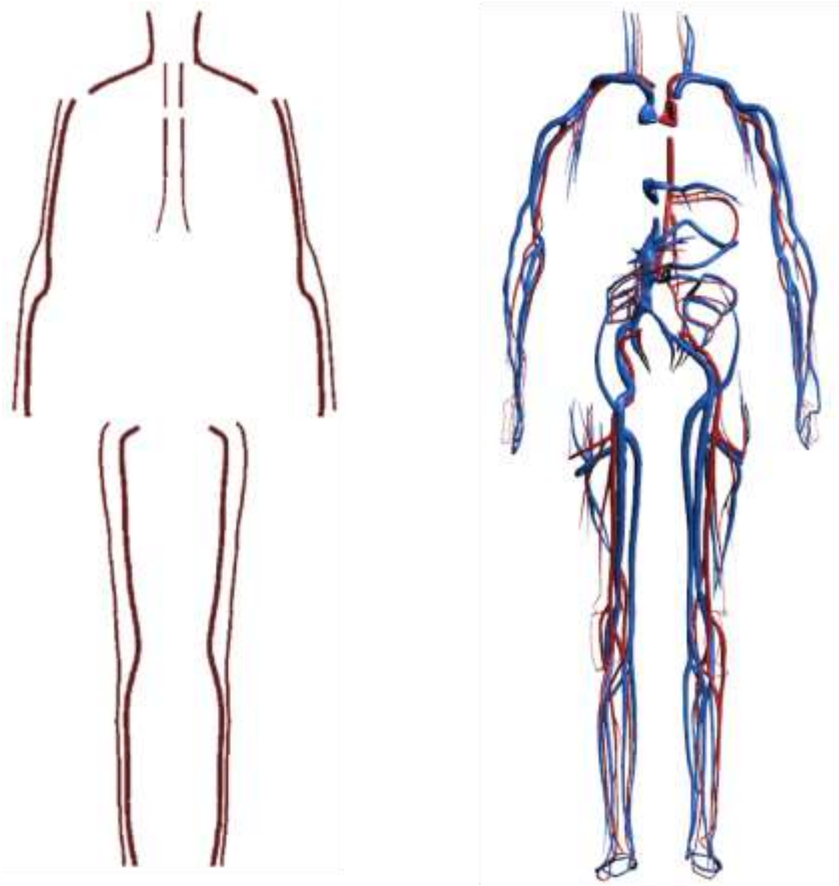

Fig. 3.9. Blood in large vessels of the P143 phantom (left) and the paediatric MRCP (right) for the 5-year-old male. In the MRCP, the blood in the large arteries (red) and the large veins (blue) was modelled separately.

3.10. Muscle

(61) The muscle of the P143 phantoms (ICRP, 2020a) was developed by using a voxel growing algorithm (Stepusin, 2016), by which the complex and heterogeneous anatomical structures of the various muscles of the body could not be modelled delicately.

(62) In the present work, the muscle was modelled using the construction procedure described by Choi et al. (2019). First, the exterior surface of the muscle was produced by replicating and reducing the skin model, and the interior surface of the muscle was generated by producing a surface which covers all of the internal organs except for the blood in the large vessels and the lymphatic nodes. Then, a preliminary muscle model was produced by merging the exterior and interior surfaces of the muscle and then subtracting the blood in the large vessels and the lymphatic nodes. Finally, the preliminary muscle model was adjusted to provide a more anatomically realistic representation, referring to the anatomy text of Drake et al. (2004).

(63) Fig. 3.10 shows the muscle model for the 1-year-old male phantom, along with the model of the corresponding P143 phantom.

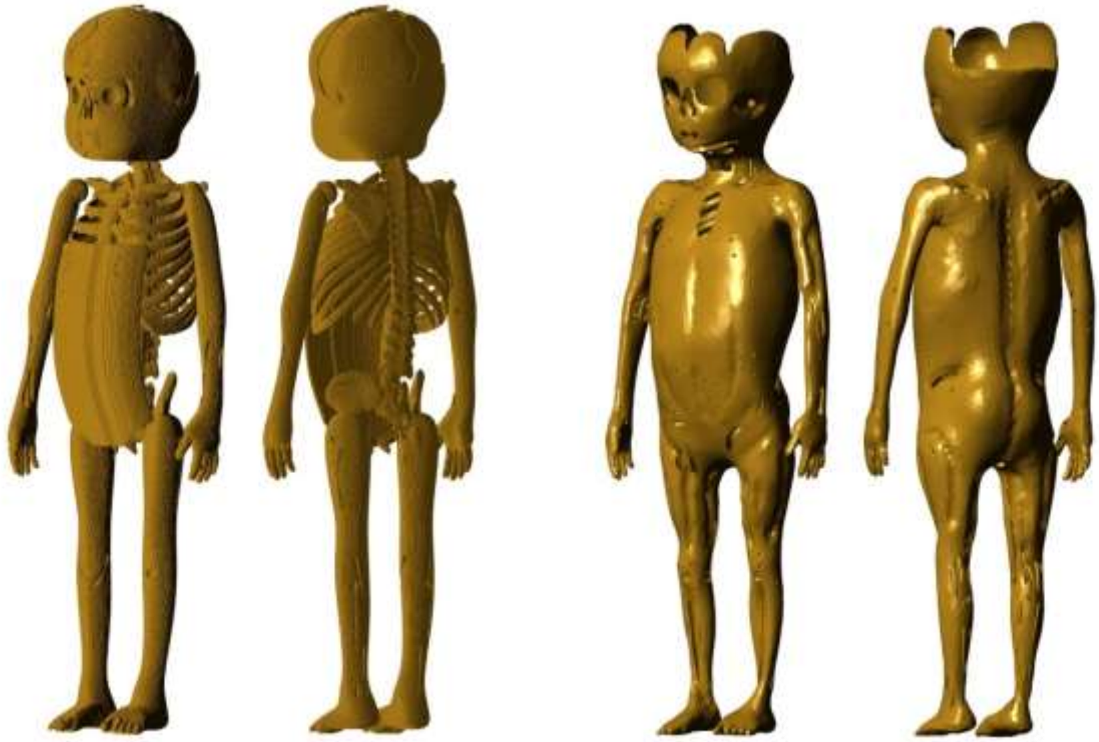

Fig. 3.10. Muscle of the P143 phantom (left) and the paediatric MRCP (right) for 1-year-old male.

3.11. Exterior body contour

(64) The exterior body contours of the P143 phantoms (ICRP, 2020a) were produced for the head, torso and limbs separately, matching eight reference anthropometric dimensions (i.e. standing and sitting height; arm length; biacromial breadth; and head, neck, waist and buttock circumference), but the individual body parts (i.e. head, torso and limbs) were not realistically connected, especially at the hip and the shoulder joints.

(65) For the paediatric MRCPs, therefore, the connected regions were deformed to obtain a more realistic shape. To maintain the total volume of the exterior body contour, the remaining regions were slightly adjusted while matching the reference anthropometric dimensions to within 5% of deviation (see Table 3.4).

(66) Fig. 3.11 shows the exterior body contour of the 5-year-old male MRCP, together with that of the corresponding P143 phantom.

Table 3.4. Anthropometric dimensions (unit: cm) of the paediatric MRCPs, along with reference values given in the P143 phantom (ICRP, 2020a).

Phantoms		Standing height			Sitting height			Arm length			Biacromial breadth		
		Ref.	MRCP	Diff. (%)	Ref.	MRCP	Diff. (%)	Ref.	MRCP	Diff. (%)	Ref.	MRCP	Diff. (%)
Newborn	Male	51.0	–	–	34.0	33.0	-2.9						
	Female	51.0	–	–	34.0	33.0	-2.9						
1 year	Male	76.0	76.0	0.0	48.8	47.3	-3.1	32.6	32.0	-1.8			
	Female	76.0	76.0	0.0	48.8	47.3	-3.1	32.6	32.0	-1.8			
5 years	Male	109.0	109.0	0.0	60.4	61.0	1.0	47.1	47.0	-0.2	25.0	25.3	1.1
	Female	109.0	109.0	0.0	60.4	61.0	1.0	47.1	47.0	-0.2	25.0	25.4	1.4
10 years	Male	138.0	138.0	0.0	73.4	75.2	2.5	61.0	61.1	0.2	31.2	30.3	-2.8
	Female	138.0	138.0	0.0	73.4	75.2	2.5	61.0	61.1	0.2	31.2	30.1	-3.6
15 years	Male	167.0	167.0	0.0	88.8	86.5	-2.6	75.0	75.1	0.1	38.8	40.3	4.0

Female	161.0	161.0	0.0	85.5	83.0	-2.9	70.7	71.8	1.6	36.3	35.3	-2.9

Phantoms		Head circumference			Neck circumference			Waist circumference			Buttock circumference		
		Ref.	MRCP	Diff. (%)	Ref.	MRCP	Diff. (%)	Ref.	MRCP	Diff. (%)	Ref.	MRCP	Diff. (%)
Newborn	Male	33.1	34.5	4.3									
	Female	33.1	34.5	4.3									
1 year	Male	47.3	47.2	1.1									
	Female	47.3	47.2	1.1									
5 years	Male	51.1	52.4	2.6	24.9	25.8	3.7	55.0	53.8	-2.2	57.9	57.0	-1.6
	Female	51.1	52.4	2.6	24.9	25.8	3.8	55.0	54.3	-1.3	57.9	57.4	-0.9
10 years	Male	52.8	53.4	1.1	27.9	28.4	1.6	66.7	65.7	-1.5	75.2	72.6	-3.4
	Female	52.8	53.4	1.1	27.9	28.6	2.4	66.7	65.7	-1.5	75.2	72.3	-3.8
15 years	Male	55.4	54.0	-2.5	32.8	33.8	3.1	80.1	79.0	-1.3	92.5	88.9	-3.9
	Female	54.3	53.5	-1.5	30.8	32.0	3.8	78.8	76.6	-2.8	93.4	89.8	-3.8

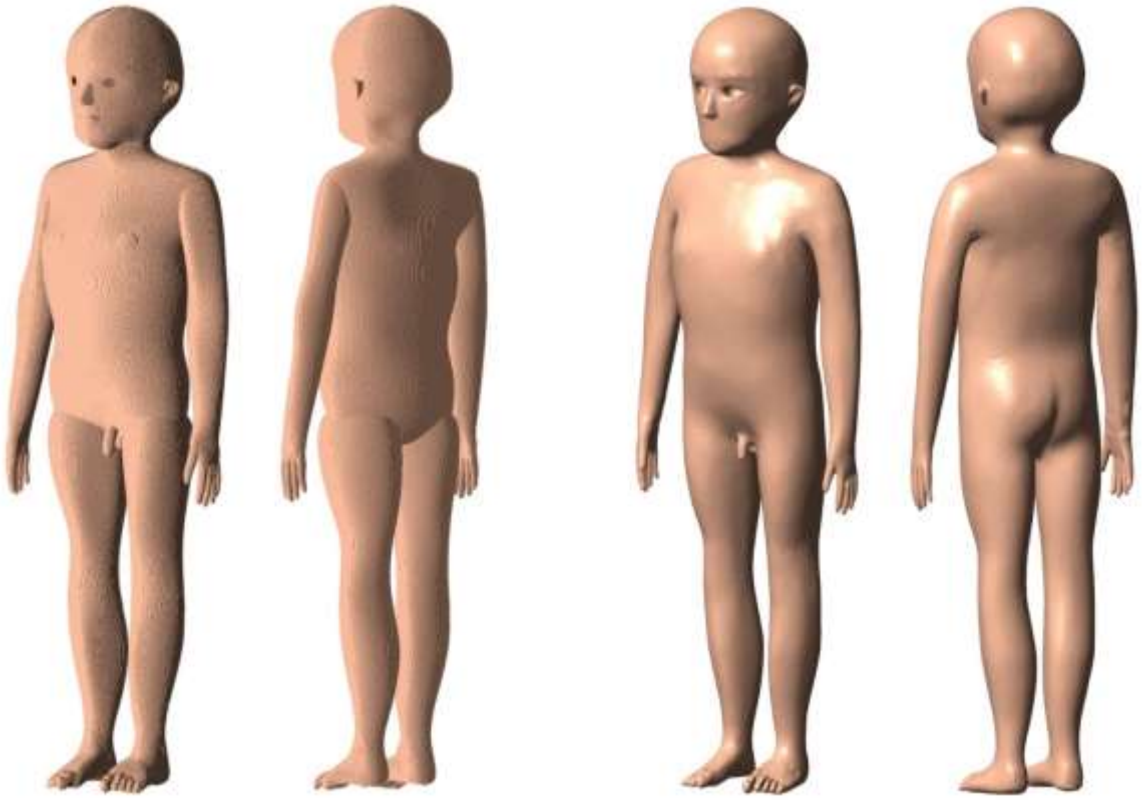

Fig. 3.11. Exterior body contour of the P143 phantom (left) and the paediatric MRCP (right) for 5-year-old male.

4. INCLUSION OF BLOOD IN ORGANS AND TISSUES

(67) The organs of the P143 phantoms (ICRP, 2020a) are based on the reference values for organ parenchyma (i.e. excluding the intra-organ blood content), given in Table 2.8 of *Publication 89* (ICRP, 2002). In a living person, however, a considerable amount of blood is situated in the small vessels and capillaries in the organs. The most realistic phantom design would represent the organ parenchyma and intra-organ vasculature separately, but this is technically challenging due to the complexity and wide distribution of the vasculature. Consideration of the blood content is nevertheless necessary in phantom construction, especially for the purpose of internal dosimetry when the blood is considered as a source region (ICRP, 2016, 2022; Wayson et al., 2018). In addition, the increase in the organ masses due to the inclusion of the blood content can affect the SAF calculations, especially for the self-irradiation resulting from weakly penetrating radiations (ICRP, 2016, 2022).

(68) For the paediatric MRCPs as for the adult MRCPs, therefore, the organ masses, densities and elemental compositions were recalculated to include intra-organ blood content. The organs of the MRCPs were then adjusted to the new blood-inclusive reference organ masses.

(69) The reference organ parenchymal masses in Table 2.8 of *Publication 89* (ICRP, 2002) were used to calculate the blood-inclusive reference organ masses, with two exceptions. The breast parenchymal masses for the ages of 10 years and younger, which are not given in the table, were derived using a similar method to that used for the P143 phantoms; that is, the breast parenchymal masses were calculated by adopting the glandular tissue masses of the stylised phantoms (Cristy and Eckerman, 1987) and considering the glandular tissue fraction in *Publication 89*. The active marrow parenchymal masses were adopted, with slight adjustment, from the P143 phantoms which differ from the reference values in *Publication 89*.

4.1. Calculation of mass, density and elemental composition of organs and tissues inclusive of blood content

(70) The blood-content masses were calculated for the organs listed in Table 2.8 of *Publication 89* (ICRP, 2002) based on the age-dependent regional blood volume fractions derived by Wayson et al. (2018), which are replicated in Table 4.1.

(71) For the organs for which the regional blood volume fraction is explicitly given in the table [i.e. fat, brain, stomach/oesophagus, small intestine, colon, right heart, left heart, coronary tissues, kidneys, liver, pulmonary, bronchial tissue, skeletal muscle, pancreas, active marrow, trabecular bone, cortical bone, other skeletal tissues, skin, spleen, thyroid, lymph nodes, gonads (testes or ovaries), adrenal glands and urinary bladder], the blood-content masses were simply calculated as the product of their regional blood volume fractions and the total blood mass. Among them, for the organs for which the regional blood fractions are grouped into a single value in Table 4.1 (i.e. stomach/oesophagus and other skeletal tissues), the blood masses were assigned in proportion to their masses. Likewise, for the organs for which regional blood fraction is not explicitly given in the table, but listed in Table 2.8 of *Publication 89* (ICRP, 2002) (i.e. tongue, salivary glands, gall bladder wall, breasts, eyes, pituitary gland, larynx, trachea, thymus, tonsils, ureters, urethra, epididymis, prostate, fallopian tubes, uterus and remaining tissues), which are represented as ‘all other tissues’ in Table 4.1, the blood masses were assigned in proportion to their masses. Note that for this calculation, the mass of the remaining tissues was reduced by the mass of the lymphatic nodes, as the regional blood fraction of the lymphatic nodes is given separately, as shown in Table 4.1.

(72) The calculated values of blood content are listed in Table 4.2, together with the reference masses of organ parenchyma. Note that all the organs of 'all other tissues' have slightly different blood-content masses in males and females, even for 10 years and younger, due to the different organ masses of the sex-specific organs and thus different mass proportions.

Table 4.1. Regional blood volume fractions for children and adolescents (Wayson et al., 2018).

Organ	Blood content (% total blood volume)					
	Newborn male/female	1-year male/female	5-year male/female	10-year male/female	15-year male	15-year female
Fat	2.212	4.958	4.061	4.159	3.602	6.608
Brain	5.413	5.276	4.311	2.670	1.568	1.370
Stomach/oesophagus	0.767	0.745	0.935	0.987	0.932	0.866
Small intestine	2.837	2.809	3.805	3.933	3.591	3.327
Colon	1.596	1.641	2.062	2.217	2.107	1.852
Right heart	4.500	4.500	4.500	4.500	4.500	4.500
Left heart	4.500	4.500	4.500	4.500	4.500	4.500
Coronary tissues	1.088	0.951	0.846	0.857	0.831	0.897
Kidneys	0.704	1.759	2.159	2.171	1.905	1.763
Liver	12.922	11.359	10.268	9.188	8.530	9.379
Lungs						
Pulmonary	10.500	10.500	10.500	10.500	10.500	10.500
Bronchial tissue	2.000	2.000	2.000	2.000	2.000	2.000
Skeletal muscle	6.667	5.535	8.538	10.306	13.684	10.303
Pancreas	0.430	0.502	0.460	0.484	0.557	0.505
Skeletal tissues						
Active marrow	5.190	4.969	4.918	4.916	4.841	4.983
Trabecular bone	3.639	4.388	4.376	4.397	4.051	4.352
Cortical bone	1.294	1.584	1.607	1.612	1.387	1.490
Other skeletal tissues	0.659	0.660	0.672	0.797	0.856	0.858
Skin	3.067	2.066	1.761	1.557	2.147	2.240
Spleen	1.505	1.576	1.422	1.398	1.433	1.414
Thyroid	0.066	0.032	0.031	0.045	0.043	0.043
Lymphatic nodes	0.163	0.165	0.164	0.168	0.181	0.177
Gonads	0.012	0.009	0.008	0.007	0.022	0.011
Adrenals	0.415	0.097	0.063	0.054	0.051	0.042
Urinary bladder	0.028	0.022	0.020	0.019	0.019	0.018
All other tissues	3.826	3.397	2.013	2.558	2.162	2.002
Aorta and large arteries	6.000	6.000	6.000	6.000	6.000	6.000
Large veins	18.000	18.000	18.000	18.000	18.000	18.000

Table 4.2. Reference masses of organ parenchyma and their respective blood content for children and adolescents.

Organs	Newborn male		Newborn female		1-year male		1-year female		5-year male		5-year female		10-year male		10-year female		15-year male		15-year female	
	Organ/ tissue only (g)	Blood content (g)	Organ/ tissue only (g)	Blood content (g)	Organ/ tissue only (g)	Blood content (g)	Organ/ tissue only (g)	Blood content (g)	Organ/ tissue only (g)	Blood content (g)	Organ/ tissue only (g)	Blood content (g)	Organ/ tissue only (g)	Blood content (g)	Organ/ tissue only (g)	Blood content (g)	Organ/ tissue only (g)	Blood content (g)	Organ/ tissue only (g)	Blood content (g)
Adipose tissue	890.000	6.414	890.000	6.414	3600.000	26.277	3600.000	26.277	5000.000	60.913	5000.000	60.913	7500.000	103.969	7500.000	103.969	9500.000	172.915	16000.000	231.288
Adrenals	6.000	1.203	6.000	1.203	4.000	0.512	4.000	0.512	5.000	0.948	5.000	0.948	7.000	1.360	7.000	1.360	10.000	2.430	9.000	1.469
Tongue	3.500	0.298	3.500	0.297	10.000	0.414	10.000	0.413	19.000	0.762	19.000	0.650	32.000	1.448	32.000	1.285	56.000	3.154	53.000	1.901
Salivary glands	6.000	0.512	6.000	0.509	24.000	0.993	24.000	0.992	34.000	1.363	34.000	1.163	44.000	1.991	44.000	1.767	68.000	3.830	65.000	2.331
Oesophagus, Wall	2.000	0.494	2.000	0.494	5.000	0.789	5.000	0.789	10.000	2.338	10.000	2.338	18.000	4.311	18.000	4.311	30.000	8.951	30.000	6.061
Oesophagus, Contents	2.022		2.022		3.786		3.786		7.135		7.135		11.908		11.908		21.842		21.033	
Stomach, Wall	7.000	1.730	7.000	1.730	20.000	3.157	20.000	3.157	50.000	11.691	50.000	11.691	85.000	20.356	85.000	20.356	120.000	35.805	120.000	24.242
Stomach, Contents	40.000		40.000		67.000		67.000		83.000		83.000		117.000		117.000		200.000		200.000	
Small intestine, Wall	30.000	8.226	30.000	8.226	85.000	14.889	85.000	14.889	220.000	57.081	220.000	57.081	370.000	98.325	370.000	98.325	520.000	172.343	520.000	116.429
Small intestine, Contents	56.000		56.000		93.000		93.000		117.000		117.000		163.000		163.000		280.000		280.000	
Right colon, Wall	7.000	1.906	7.000	1.906	20.000	3.479	20.000	3.479	49.000	12.627	49.000	12.627	85.000	22.435	85.000	22.435	122.000	41.125	122.000	26.358
Right colon, Contents	24.000		24.000		40.000		40.000		50.000		50.000		70.000		70.000		120.000		120.000	
Left colon, Wall	7.000	1.906	7.000	1.906	20.000	3.479	20.000	3.479	49.000	12.627	49.000	12.627	85.000	22.435	85.000	22.435	122.000	41.125	122.000	26.358
Left colon, Contents	12.000		12.000		20.000		20.000		25.000		25.000		35.000		35.000		60.000		60.000	
Rectosigmoid, Wall	3.000	0.817	3.000	0.817	10.000	1.740	10.000	1.740	22.000	5.669	22.000	5.669	40.000	10.557	40.000	10.557	56.000	18.877	56.000	12.099
Rectosigmoid, Contents	12.000		12.000		20.000		20.000		25.000		25.000		35.000		35.000		60.000		60.000	
Liver	130.000	37.475	130.000	37.475	330.000	60.205	330.000	60.205	570.000	154.019	570.000	154.019	830.000	229.688	830.000	229.688	1300.000	409.440	1300.000	328.278
Gallbladder, Wall	0.500	0.043	0.500	0.042	1.400	0.058	1.400	0.058	2.600	0.104	2.600	0.089	4.400	0.199	4.400	0.177	7.700	0.434	7.300	0.262
Gallbladder, Contents	2.800		2.800		8.000		8.000		15.000		15.000		26.000		26.000		45.000		42.000	
Pancreas	6.000	1.248	6.000	1.248	20.000	2.659	20.000	2.659	35.000	6.892	35.000	6.892	60.000	12.100	60.000	12.100	110.000	26.726	100.000	17.677
Brain	380.000	15.698	380.000	15.698	950.000	27.965	950.000	27.965	1310.000	64.657	1180.000	64.657	1400.000	66.751	1220.000	66.751	1420.000	75.284	1300.000	47.939
Breasts	0.268	0.023	0.268	0.023	1.830	0.076	1.830	0.076	3.775	0.151	3.775	0.129	6.500	0.294	6.500	0.261	15.000	0.845	250.000	8.965
Blood in heart chambers	26.000	26.000	26.000	26.000	48.000	48.000	48.000	48.000	135.000	135.000	135.000	135.000	230.000	230.000	230.000	230.000	430.000	430.000	320.000	320.000
Heart – tissue only	20.000	3.157	20.000	3.157	50.000	5.043	50.000	5.043	85.000	12.696	85.000	12.696	140.000	21.416	140.000	21.416	230.000	39.892	220.000	31.410
Blood	290.000		290.000		530.000		530.000		1500.000		1500.000		2500.000		2500.000		4800.000		3500.000	
Eyes	6.000	0.511	6.000	0.511	7.000	0.289	7.000	0.289	11.000	0.409	11.000	0.409	12.000	0.512	12.000	0.512	13.000	0.599	13.000	0.599
Skin	175.000	8.895	175.000	8.895	350.000	10.952	350.000	10.952	570.000	26.415	570.000	26.415	820.000	38.916	820.000	38.916	2000.000	103.076	1700.000	78.392
Muscle, skeletal	800.000	19.334	800.000	19.334	1900.000	29.338	1900.000	29.338	5600.000	128.075	5600.000	128.075	11000.000	257.653	11000.000	257.653	24000.000	656.842	17000.000	360.601
Pituitary gland	0.100	0.009	0.100	0.008	0.150	0.006	0.150	0.006	0.250	0.010	0.250	0.009	0.350	0.016	0.350	0.014	0.500	0.028	0.500	0.018
Larynx	1.300	0.111	1.300	0.110	4.000	0.166	4.000	0.165	7.000	0.281	7.000	0.239	12.000	0.543	12.000	0.482	22.000	1.239	15.000	0.538
Trachea	0.500	0.043	0.500	0.042	1.500	0.062	1.500	0.062	2.500	0.100	2.500	0.085	4.500	0.204	4.500	0.181	7.500	0.422	6.000	0.215

Blood in lung	30.000	30.000	30.000	30.000	70.000	70.000	70.000	70.000	175.000	175.000	175.000	175.000	290.000	290.000	290.000	290.000	570.000	570.000	460.000	460.000
Lung – tissue only	30.000		30.000		80.000		80.000		125.000		125.000		210.000		210.000		330.000		290.000	
Bone, cortical	69.581	3.753	69.581	3.753	268.189	8.398	268.189	8.398	717.993	24.106	717.993	24.106	1669.036	40.307	1669.036	40.307	3180.576	66.574	2915.480	52.151
Bone, trabecular	100.419	10.552	100.419	10.552	321.811	23.255	321.811	23.255	542.007	65.636	542.007	65.636	630.964	109.927	630.964	109.927	869.424	194.467	784.520	152.336
Marrow, active	50.000	15.051	50.000	15.051	155.548	26.336	155.548	26.336	374.931	73.772	374.931	73.772	754.144	122.896	754.144	122.896	1053.496	232.349	1049.098	174.408
Marrow, inactive		0.000		0.000	14.452	0.119	14.452	0.119	125.069	1.586	125.069	1.586	505.856	6.974	505.856	6.974	1506.504	21.749	1330.902	16.432
Cartilage	130.000	1.648	130.000	1.648	360.000	2.965	360.000	2.965	600.000	7.610	600.000	7.610	820.000	11.304	820.000	11.304	1140.000	16.458	920.000	11.359
Teeth	0.700	0.009	0.700	0.009	5.000	0.041	5.000	0.041	15.000	0.190	15.000	0.190	30.000	0.414	30.000	0.414	45.000	0.650	35.000	0.432
Miscellaneous	20.000	0.254	20.000	0.254	45.000	0.371	45.000	0.371	55.000	0.698	55.000	0.698	90.000	1.241	90.000	1.241	155.000	2.238	145.000	1.790
Spleen	9.500	4.365	9.500	4.365	29.000	8.352	29.000	8.352	50.000	21.329	50.000	21.329	80.000	34.951	80.000	34.951	130.000	68.786	130.000	49.494
Thymus	13.000	1.108	13.000	1.104	30.000	1.242	30.000	1.240	30.000	1.202	30.000	1.026	40.000	1.810	35.000	1.406	35.000	1.972	30.000	1.076
Thyroid	1.300	0.190	1.300	0.190	1.800	0.168	1.800	0.168	3.400	0.471	3.400	0.471	7.900	1.120	7.900	1.120	12.000	2.041	12.000	1.497
Tonsils (2 palatine)	0.100	0.009	0.100	0.008	0.500	0.021	0.500	0.021	2.000	0.080	2.000	0.068	3.000	0.136	3.000	0.121	3.000	0.169	3.000	0.108
Kidneys (2)	25.000	2.042	25.000	2.042	70.000	9.323	70.000	9.323	110.000	32.390	110.000	32.390	180.000	54.284	180.000	54.284	250.000	91.438	240.000	61.707
Ureters (2)	0.770	0.066	0.770	0.065	2.200	0.091	2.200	0.091	4.200	0.168	4.200	0.144	7.000	0.317	7.000	0.281	12.000	0.676	12.000	0.430
Urinary bladder, Wall	4.000	0.080	4.000	0.080	9.000	0.115	9.000	0.115	16.000	0.304	16.000	0.304	25.000	0.487	25.000	0.487	40.000	0.907	35.000	0.619
Urinary bladder, Contents	12.400		12.400		32.900		32.900		64.700		64.700		103.000		103.000		160.000		140.000	
Urethra	0.480	0.041	0.140	0.012	1.400	0.058	0.420	0.017	2.600	0.104	0.780	0.027	4.400	0.199	1.300	0.052	7.700	0.434	2.300	0.082
Testes (2)	0.850	0.036			1.500	0.046			1.700	0.115			2.000	0.179			16.000	1.037		
Epididymes (2)	0.250	0.021			0.350	0.014			0.450	0.018			0.600	0.027			1.600	0.090		
Prostate	0.800	0.068			1.000	0.041			1.200	0.048			1.600	0.072			4.300	0.242		
Ovaries (2)			0.300	0.036			0.800	0.046			2.000	0.115			3.500	0.179			6.000	0.386
Fallopian tubes (2)			0.250	0.021			0.250	0.010			0.350	0.012			0.500	0.020			1.100	0.039
Uterus			4.000	0.340			1.500	0.062			3.000	0.103			4.000	0.161			30.000	1.076
Lymphatic node	14.300	0.471	14.300	0.471	25.000	0.873	25.000	0.873	48.800	2.453	48.800	2.453	80.900	4.202	80.900	4.202	142.700	8.693	130.800	6.212
Blood, arteries		17.400		17.400		31.800		31.800		90.000		90.000		150.000		150.000		288.000		210.000
Blood, veins		52.200		52.200		95.400		95.400		270.000		270.000		450.000		450.000		864.000		630.000
Remaining tissues	96.560	14.584	94.250	14.351	349.684	10.424	350.964	10.453	632.690	37.892	762.510	38.542	1240.942	73.675	1425.242	74.722	1589.158	121.649	1465.967	24.937
Total body (kg)	3.5	0.29	3.5	0.29	10	0.53	10	0.53	19	1.5	19	1.5	32	2.5	32	2.5	56	4.8	53	3.5

(73) Subsequently, the densities and elemental compositions of the organs inclusive of blood content were calculated using data given in the scientific literature (White et al., 1987; ICRU, 1992; ICRP, 2002), assuming that the blood content is uniformly distributed within the organs. The density and hydrogen mass percentage of the blood-inclusive brain, for example, were calculated by using the following equations:

$$\rho_{brain}^{with-blood} = \frac{m_{brain}^{ICRP89} + m_{blood-in-brain}}{\frac{m_{brain}^{ICRP89}}{\rho_{brain}^{ICRU46}} + \frac{m_{blood-in-brain}}{\rho_{blood}^{ICRU46}}} \tag{1}$$

$$(\%H)_{brain}^{with-blood} = \frac{(\%H)_{brain}^{ICRU46} m_{brain}^{ICRP89} + (\%H)_{blood}^{ICRU46} m_{blood-in-brain}}{m_{brain}^{ICRP89} + m_{blood-in-brain}} \tag{2}$$

where $\rho_{brain}^{with-blood}$ is the density of the blood-inclusive brain, ρ_{brain}^{ICRU46} is the density of the brain parenchyma as given in ICRU *Report 46* (ICRU, 1992), ρ_{blood}^{ICRU46} is the density of the blood as given in ICRU *Report 46* (ICRU, 1992), m_{brain}^{ICRP89} is the mass of the brain parenchyma as given in *Publication 89* (ICRP, 2002), $m_{blood-in-brain}$ is the calculated mass of the blood in the brain, $(\%\mathrm{H})_{brain}^{with-blood}$ is the hydrogen mass percentage in the blood-inclusive brain, $(\%H)_{brain}^{ICRU46}$ is the hydrogen mass percentage in the brain parenchyma as given in ICRU *Report 46* (ICRU, 1992) and $(\%H)_{blood}^{ICRU46}$ is the hydrogen mass percentage in the blood. The mass percentages of all other elements in the blood-inclusive tissues have been assessed accordingly. The calculated densities and elemental compositions are given in Tables B.1–B.10.

4.2. Phantom adjustment for blood inclusion

(74) The volumes of the organs, produced in the PM format, were subsequently adjusted to match the blood-inclusive reference masses based on the blood-inclusive density, following the same procedure applied to the adult MRCPs (ICRP, 2020c). First, the PM models were isotropically increased, preserving the original shape and centroid of the organs. After enlargement, resulting overlaps between some of the neighbouring organs were eliminated by preferentially modifying the larger organs, rather than the smaller ones, to minimise the geometric distortion of the organs.

(75) To evaluate the change of topology in the organs due to the inclusion of the blood content, the geometric similarity was again investigated by calculating the DI and CD values for the organs, as discussed in Section 6.2.

4.3. Definition of residual soft tissue (RST)

(76) In the paediatric MRCPs, several organs listed in Table 4.2 (i.e. adipose tissue, urethra, epididymis, fallopian tubes and some parts of cartilage) are not explicitly defined, while several organs implicitly included in 'remaining tissues and regions' [i.e. main bronchi (= generation 1), spinal cord, urine, oesophagus contents, ET region and inner air] are defined in the phantoms. Consequently, the total body masses of the phantoms are smaller than the reference masses. For this reason, as done for other ICRP reference phantoms (ICRP, 2009, 2020a,c), the total body masses of the paediatric MRCPs were matched to the reference masses by defining an additional compensating tissue, called 'residual soft tissue (RST)'. The RST is a homogeneous mixture of all the organs not explicitly defined in the phantoms, a commonly

used approach in the field of phantom development to match the target body mass (ICRP, 2009, 2020c; Lee et al., 2010; Kim et al., 2011; Yeom et al., 2013).

5. INCLUSION OF THIN TARGET AND SOURCE REGIONS

5.1. Skin

(77) In the skin, the basal cells of the epidermis and hair follicles are considered as the relevant target cells at radiogenic risk for stochastic effects. The target cells for adults are assumed to be at a depth of 50 to 100 μm below the skin surface (ICRP, 1977, 2010, 2015) and, in the present work, the same depth was assumed for adolescents. The skin target region for 10 years and younger was assumed to be slightly wider (i.e. 40–100 μm below the skin surface) considering that the epidermis thickness is thinner but the hair follicles are more densely distributed over the skin at younger ages. Note that a substantial proportion of the stem cells that are the assumed targets are not in the inter-follicular basal layer between hair follicles but in the hair follicles themselves that penetrate through the dermis (ICRP, 1991a, 2012). In the paediatric MRCPs, therefore, the target layer was defined at a depth of 40–100 μm for 10 years and younger and 50–100 μm for 15 years.

(78) Fig. 5.1 shows the skin of the 1-year-old female and 15-year-old male phantoms, including the target layer.

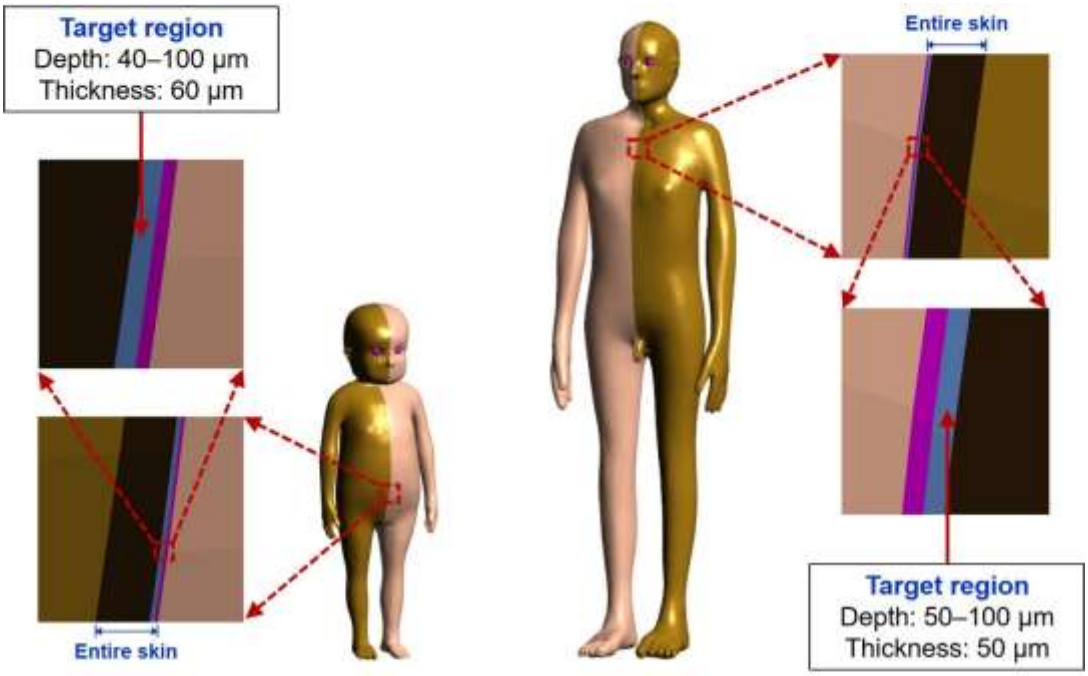

Fig. 5.1. Skin target region of the 1-year-old female (left) and 15-year-old male (right) MRCPs.

5.2. Alimentary tract

(79) The target and source regions were defined for the alimentary tract organs (i.e. oral cavity, oesophagus, stomach, small intestine and colon) of the paediatric MRCPs (Choi et al., 2022a), following the morphometric data given in *Publication 100* (ICRP, 2006), which are summarised in Table 5.1. Except for the oral cavity, the target and source regions of all the alimentary tract organs were simply defined according to their depth and thickness. Note that in *Publication 100*, the depth and thickness of all the target and source regions for adults, with

one exception, are assumed to be applicable to children and adolescents; the exception is the source region in the villi of the small intestine for 5 years and younger, the thickness of which is considered to be 100 µm thinner than that for adults (= 500 µm). This thickness variation of the villus layer with age was reflected in the paediatric MRCPs.

Table 5.1. Information on source (upper) and target (lower) regions of alimentary tract organs from the data of *Publication 100* (ICRP, 2006).

Alimentary tract organ	Source region	Source location¶
Oral cavity	Food (or liquid)	5 mm (on top of the tongue, outward)
	Retention on teeth	10 µm (on inner and outer surfaces of the teeth, outward)
Oesophagus	Contents (fast)	*
	Luminal surface (slow)	**
Stomach	Mucosa	0–300 µm (outward)
	Contents	*
Small intestine	Villi	0–400†/500†† µm (inward)
	Mucosa	0–200 µm (outward)
	Contents	*
Right colon	Mucosa	0–300 µm (outward)
	Contents	*
Left colon	Mucosa	0–300 µm (outward)
	Contents	*
Rectosigmoid	Mucosa	0–300 µm (outward)
	Contents	*
Alimentary tract organ	**Target region**	**Target location¶**
Oral cavity	Roof of mouth	190–200 µm (from the top surface of the food, outward)
	Tongue	190–200 µm (from the surface of the tongue, inward)
	Lips and cheek	190–200 µm (from the outer surface of retention on teeth, outward)
Oesophagus	Basal cells	190–200 µm (outward)
Stomach	Stem cells	60–100 µm (outward)
Small intestine	Stem cells	130–150 µm (outward)
Right colon	Stem cells	280–300 µm (outward)
Left colon	Stem cells	280–300 µm (outward)
Rectosigmoid	Stem cells	280–300 µm (outward)

¶ Default depth is from the luminal surface.
* Volume of the contents is the source region.
** Surface of the contents is the source region.
† Depth of the small intestine villi for newborn, 1 year and 5 years.
†† Depth of the small intestine villi for 10 years and 15 years.

(80) For the oral cavity, two source regions were defined in the paediatric MRCPs: food (or liquid) on the top of the tongue and radionuclides retained on the surface of the teeth. The food volume has been estimated only for the adults (= 20 cm^3) (ICRP, 2006); for the paediatric MRCPs, therefore, the food volume was estimated by scaling in proportion to the area of the

tongue, assuming that the thickness of the food region (= 5 mm) is identical for all ages. The food region was then modelled in the paediatric MRCPs using the same modelling approach used for the adult MRCPs (ICRP, 2020c). The source region for radionuclides retained on teeth was defined by adding a 10-µm-thick layer on the exposed surfaces of the teeth. The target region in the oral cavity was defined in three parts (i.e. roof of mouth, tongue and lips, and cheek) by defining a 10-µm-thick layer at a depth of 190 µm from the source regions.

(81) Fig. 5.2 shows, as examples, the target and source regions defined in the oral cavity and small intestine of the 15-year-old male phantom.

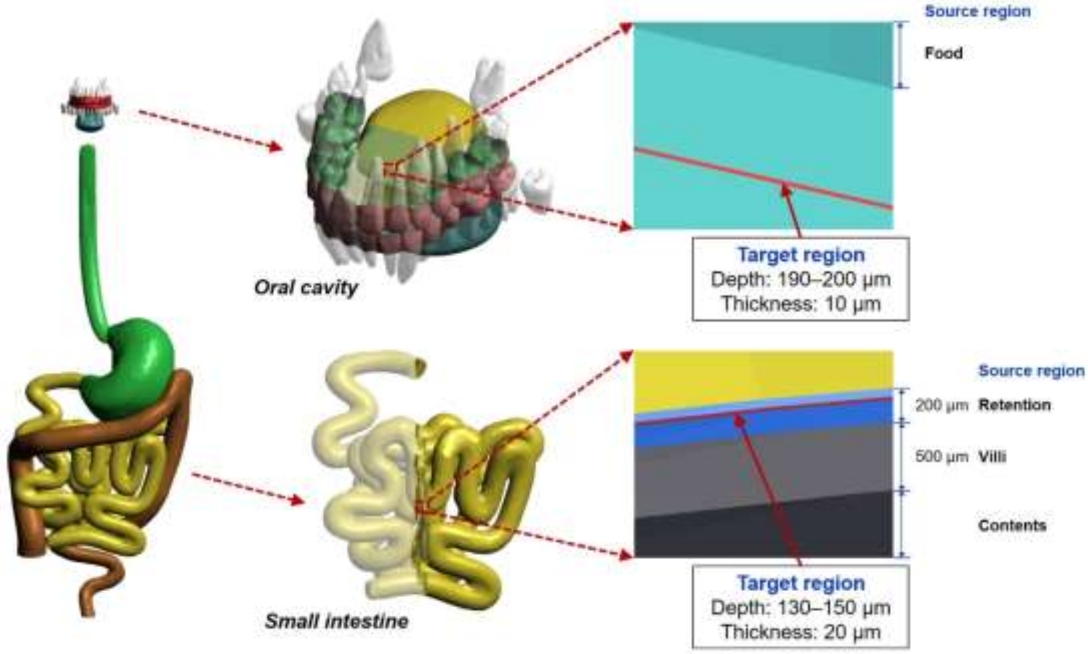

Fig. 5.2. Target and source regions of the oral cavity and small intestine in the 15-year-old male MRCP.

5.3. Respiratory tract

(82) For the paediatric MRCPs as for the adult MRCPs, the target and source regions were defined in the respiratory tract tissues (Choi et al., 2022b), following the morphometric data of *Publication 66* (ICRP, 1994a), which are summarised in Table 5.2. The respiratory tract tissues comprise ET region (i.e. ET1 and ET2), trachea, bronchi (BB), bronchioles (bb) and alveolar-interstitium (AI). In the present work, the AI was not explicitly defined in the phantoms but was assumed to be homogeneously distributed in the lungs.

Table 5.2. Information on source (upper) and target (lower) regions of respiratory tract organs from the data of *Publication 66* (ICRP, 1994a).

Respiratory tract organ	Source region	Source location[¶]
ET_1	Surface	0–8 µm (outward)
ET_2	Surface	0–15 µm (inward)
	Bound	0–55 µm (outward)
	Sequestered	55–65 µm (outward)
BB	Fast mucus	6–11 µm (inward)

	Slow mucus	0–6 μm (inward)
	Bound	0–60 μm (outward)
	Sequestered	60–70 μm (outward)
	AI	*
bb	Fast mucus	4–6 μm (inward)
	Slow mucus	0–4 μm (inward)
	Bound	0–20 μm (outward)
	Sequestered	20–25 μm (outward)
	AI	*

Respiratory tract organ	Target region	Target location[¶]
ET_1	Basal cells	40–50 μm (outward)
ET_2	Basal cells	40–50 μm (outward)
BB	Basal cells	35–50 μm (outward)
	Secretory cells	10–40 μm (outward)
bb	Secretory cells	4–12 μm (outward)

[¶] Default depth is from the airway surface.
[*] AI as a source region is determined by radiation types and energies.

(83) For the ET_1, ET_2, trachea and main BB (i.e. generation 1) regions, the target and source regions were simply defined according to their depth and thickness. This approach, however, could not be used for the other generations of the BB (i.e. generations 2–8) and all the subsequent generations of the bb (i.e. generations 9–15), which are not represented in the P143 phantoms (ICRP, 2020a). These airways were modelled in constructive solid geometry (CSG) format based on airway dimensions (i.e. lengths and diameters) derived using the scaling method of *Publication 66*, using the computer program applied for the adult MRCPs (Kim et al., 2017). The total lengths of the airway branches for each generation were matched to their reference values within 10% difference. Note that as an exception, the newborn airway dimensions were derived by scaling the adult male values in proportion to the cube root of lung volume; this is because the scaling method of *Publication 66*, for which limited data on newborn subjects were used, proved insufficient for the newborn.

(84) The airways generated in the CSG format could have been converted to PM format for easy incorporation into the paediatric MRCPs, but the resulting airways would require a very large number of facets and a large computer memory allocation (i.e. >50 GB) (Kim et al., 2017). In the present work, therefore, the airways in the CSG format were not converted to the PM format, but directly incorporated into the paediatric MRCPs using the overlying approach used for the adult MRCPs (Kim et al., 2017; ICRP, 2020c). Note that the overlying approach makes it possible to perform dose calculation for the airways with a minimal addition of memory usage and computation time.

(85) Fig. 5.3 shows the target and source regions of the ET_2 of the 5-year-old female phantom and the airway model produced in the lungs of the 5-year-old male phantom with the target and source regions of the bb.

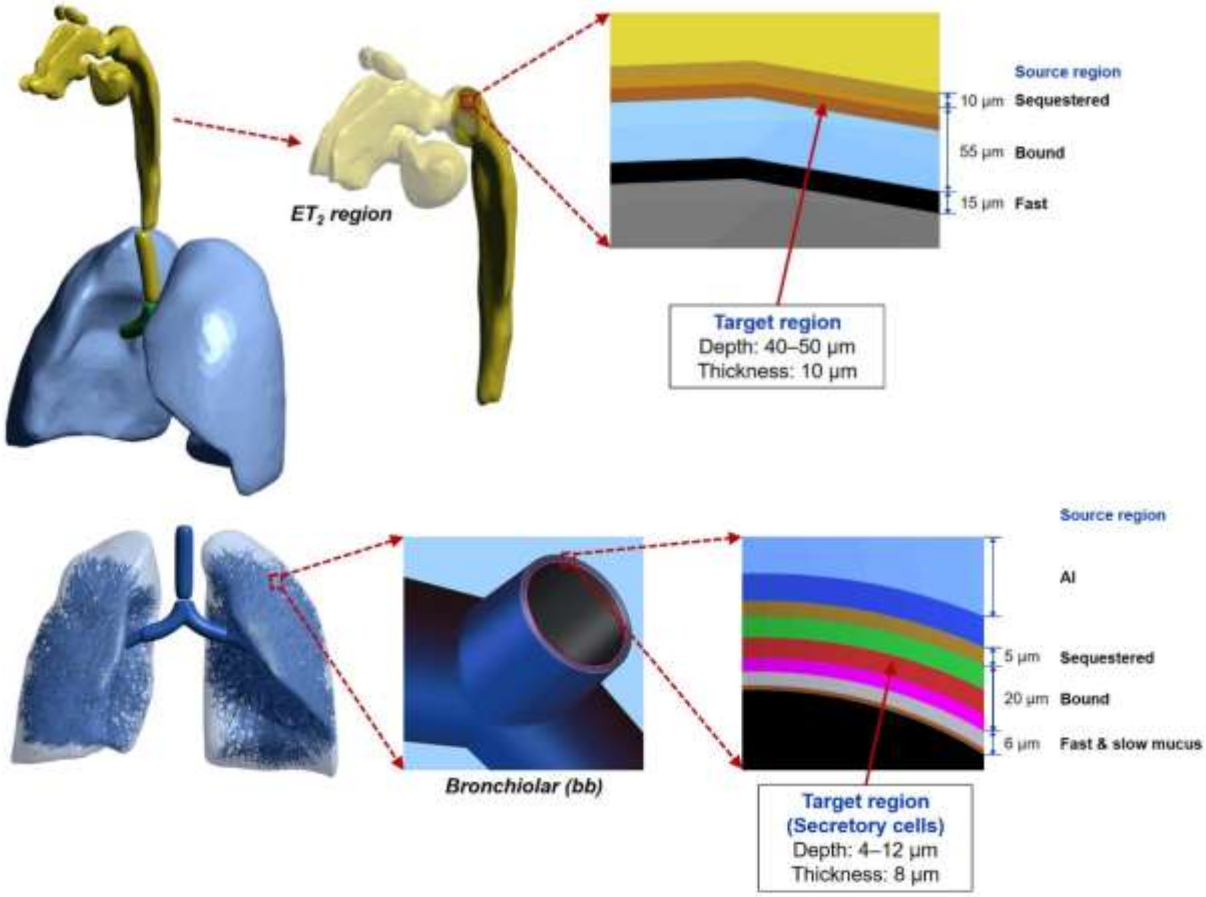

Fig. 5.3. Target and source regions of the ET$_2$ region in the 5-year-old female MRCP (upper) and lung airway of the 5-year-old male MRCP including the target and source regions (lower).

5.4. Urinary bladder

(86) The basal cells in the epithelium of the urinary bladder are considered to be the relevant target cells for carcinogenesis (Colin et al., 2009). Eckerman and Veinot (2018) derived the depth and thickness of the target layer of the urinary bladder for adults, which were used to define the target layer of the urinary bladder in the adult MRCPs (ICRP, 2020c). In their subsequent study, the values for children and adolescents were also derived, as shown in Table 5.3. In the paediatric MRCPs, these values were adopted to define the target layer of the urinary bladder.

(87) Fig. 5.4 shows the urinary bladder of the 10-year-old male phantom including the source and target regions.

Table 5.3. Depth and thickness of target layer of urinary bladder for children and adolescents.

Age	Sex	Depth (µm)	Thickness (µm)
Newborn	Male Female	54	178
1 year	Male Female	71	167
5 years	Male Female	86	107

10 years	Male Female	99	113
15 years	Male	116	122
	Female	111	116

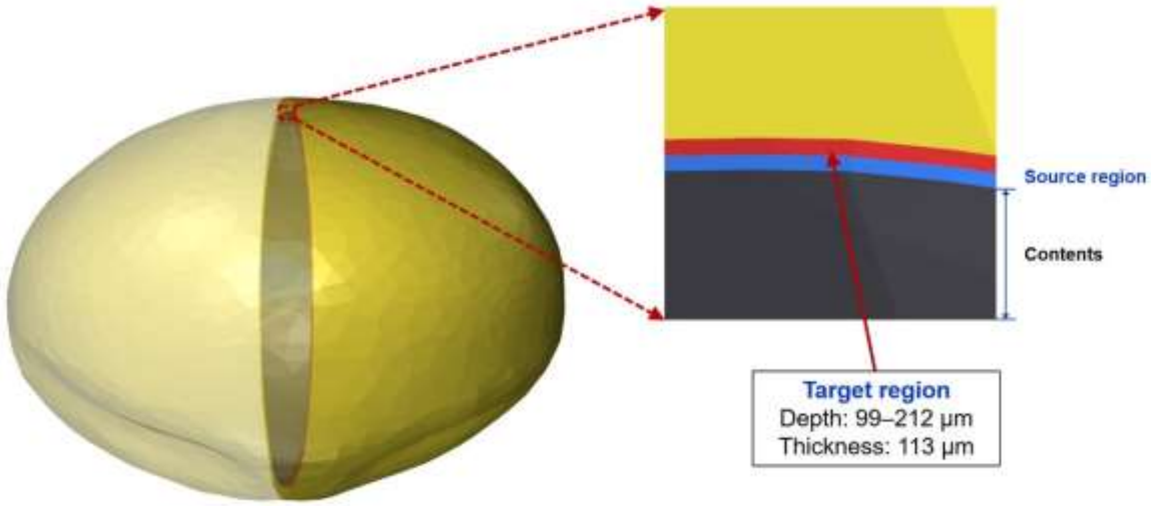

Fig. 5.4. Source and target regions of the urinary bladder in the 10-year-old male MRCP.

6. DESCRIPTION OF THE PAEDIATRIC MESH-TYPE REFERENCE COMPUTATIONAL PHANTOMS

6.1. General phantom characteristics

(88) Fig. 6.1 shows the paediatric MRCPs and Table 6.1 gives the standing height and total body mass of these phantoms, which are consistent with the reference values in *Publication 89* (ICRP, 2002).

(89) The paediatric MRCPs include all the radiosensitive organs required for dose assessment from ionising radiation exposures for radiological protection purpose (ICRP, 2007). These phantoms also include the micrometre-scale target and source regions in the respiratory and alimentary tracts, skin, eye lens and urinary bladder, assimilating the supplementary organ-specific stylised models. The new phantoms at 10 years and younger, unlike the P143 phantoms, have different masses and/or shapes for several organs, besides the sex-specific organs, due to the adoption of individual sex-specific organ masses (i.e. brain for 5 and 10 years and thymus for 10 years) and high-quality organ models (i.e. spine, hand/foot bones, ET region and teeth). Note that the complex microstructures of skeletal target tissues [i.e. red bone marrow (RBM) and endosteum] in trabecular spongiosa and medullary cavity are not explicitly modelled; thus, skeletal dosimetry should be performed by employing the approximation techniques, i.e. simplified approach and fluence-to-dose response functions, which are described in Section 3.4 and Annex D of *Publication 116* (ICRP, 2010), respectively.

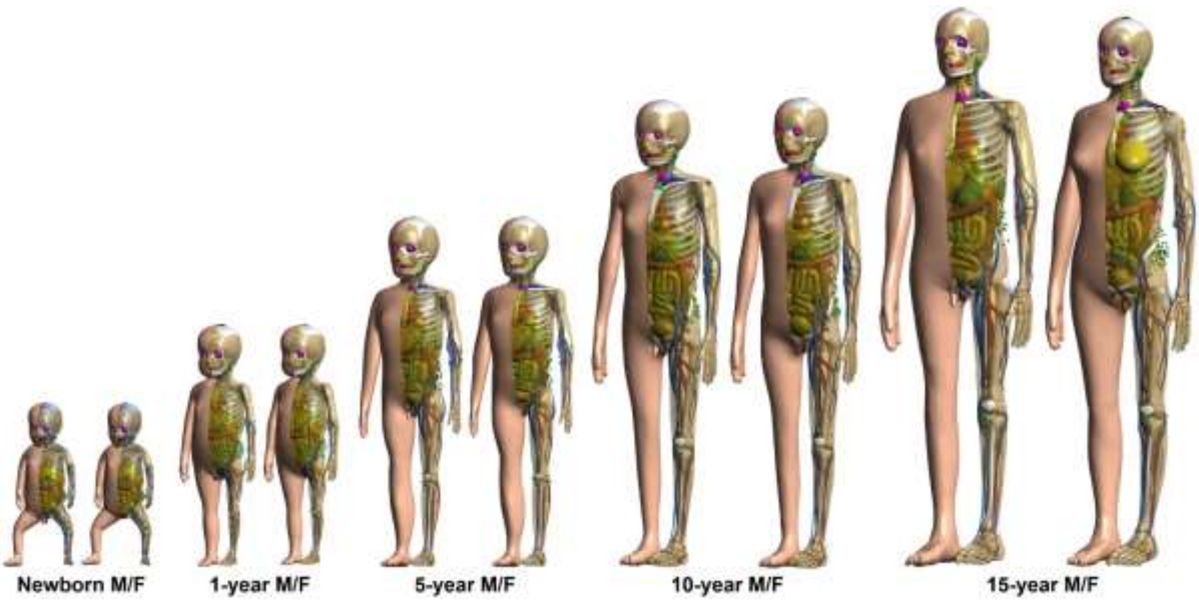

Fig. 6.1. Paediatric male (M) and female (F) MRCPs.

Table 6.1. Standing height and total body mass of the paediatric MRCPs.

Age	Standing height (cm)		Total body mass (kg)	
	Male	Female	Male	Female
Newborn	–	–	3.50	3.50
1 year	76.0	76.0	10.0	10.0
5 years	109.0	109.0	19.0	19.0

10 years	138.0	138.0	32.0	32.0
15 years	167.0	161.0	56.0	53.0

(90) The final geometric format of the paediatric MRCPs, as for the adult MRCPs of *Publication 145* (ICRP, 2020c), is the TM format. Table 6.2 lists the number and average volume of tetrahedra composing the phantoms and the sizes of the phantom files. Note that at the final stage of phantom construction, the phantoms produced in the PM format were converted into the TM format through a 'tetrahedralisation' process; that is, the phantoms were filled with millions of tetrahedra, while maintaining the original organ shapes of the PM-format phantoms. For this, a computer program dedicated to phantom tetrahedralisation was used (Han et al., 2020), which is based on the TetGen code (Si, 2015).

(91) The TM-format phantoms, when compared with the PM-format phantoms, show much faster computation speed in Monte Carlo dose calculations (i.e. by a factor of tens to hundreds for photons, electrons, neutrons and protons in the energy range of 10 keV–10 GeV) (Yeom et al., 2014). In addition, the TM-format phantoms show better compatibility with Monte Carlo codes; the TM-format phantoms can be used in major Monte Carlo codes such as Geant4, PHITS and MCNP6 without any user-plugin tools, while the PM-format phantoms can be used only in Geant4 (Han et al., 2018). The present publication also provides the PM-format phantoms with detailed information to support users who are interested in modifying the phantoms, for example, to produce phantoms with different body sizes and/or postures for individualised dosimetry.

Table 6.2. Numerical information on paediatric MRCPs.

Phantoms		Number of tetrahedra	Average volume of tetrahedra (mm^3)	File size (ASCII) (MB)
Newborn	Male	7,556,192	0.45	423
	Female	7,650,313	0.44	407
1 year	Male	6,715,716	1.47	373
	Female	6,943,945	1.42	387
5 years	Male	8,178,096	2.27	462
	Female	8,440,293	2.19	478
10 years	Male	6,925,977	4.48	385
	Female	7,103,129	4.37	396
15 years	Male	7,366,440	7.43	412
	Female	7,519,627	6.96	422

(92) The masses of the organs of the paediatric MRCPs are in accordance with the reference values inclusive of blood content (see Table 4.2) within 0.1% deviation. Tables A.1–A.2 list the organ IDs, medium and mass for each organ of the paediatric MRCPs. Tables B.1–B.10 list the elemental composition and density for each organ. Table C.1 lists the anatomical source regions, their acronyms and corresponding ID numbers. Table D.1 lists the anatomical target regions, their acronyms and corresponding organ ID numbers.

(93) For dose calculations for the organs in which micron-scale target regions are explicitly defined (e.g. alimentary and respiratory tract organs), due to their small target volumes, longer computation times are generally required to achieve an acceptable statistical precision when compared to calculations for other organs. To save computation time, entire regions instead of the thin target regions can be used in dose calculations for cases where the entire regions of the organs provide dose values similar to those calculated using the target regions (Yeom et al., 2019b, 2020; ICRP, 2020c). For example, for external exposures to penetrating radiations (e.g. photons and neutrons), where low dose gradients are generally observed in the organs, the absorbed doses to the thin target regions tend to be close to those to the entire regions, and thus

the entire regions can be used instead of the thin target regions; exceptions are the skin and lens of the eye, for which the thin target regions should be considered, because charged-particle equilibrium (CPE) is not always established in these superficial tissues. For external exposures to weakly penetrating radiations (e.g. alpha particles and protons), the radiosensitive regions should be used for dose calculation because significant spatial dose gradients could be observed, depending on the particle energies and organ topologies. The dose discrepancies between the thin target regions and the entire regions for external exposures are discussed by Yeom et al. (2019b, 2020). For internal exposures to penetrating radiations, dose calculations for entire regions can replace those for thin target regions to estimate cross-fire irradiation doses (e.g. lungs $\leftarrow$ liver).

(94) However, in cases where subregions of the same organs are considered as source regions (e.g. source region: BB bound region; target region: BB secretory region), the thin target regions should be used in dose calculation, again due to the lack of CPE. For internal exposures to weakly penetrating radiations which could establish steep dose gradients in the organs, it is recommended to calculate doses using the thin target regions.

(95) The paediatric MRCPs overcome the limitations of the P143 phantoms resulting from the inherent nature of voxel geometry and finite voxel resolutions. Fig. 6.2 shows, as an example, the 15-year-old female MRCP, along with the 15-year-old female P143 phantom, viewed in superior-inferior direction. It can be seen that the organs of the P143 voxel phantom are represented with stair-stepped surfaces, whereas those of the mesh phantom are represented with smooth surfaces. Moreover, in the voxel phantom, several radiosensitive organs (e.g. breasts and muscle) are not fully covered by skin voxels and are, thus, directly exposed to the air. This limitation is addressed in the mesh phantoms, preventing significant overestimations in dose calculations for these organs for external exposures to weakly penetrating radiations. Similarly, in the voxel phantoms, the spongiosa is not fully covered by the cortical bone, which is also addressed in the mesh phantoms (see Fig. 6.3).

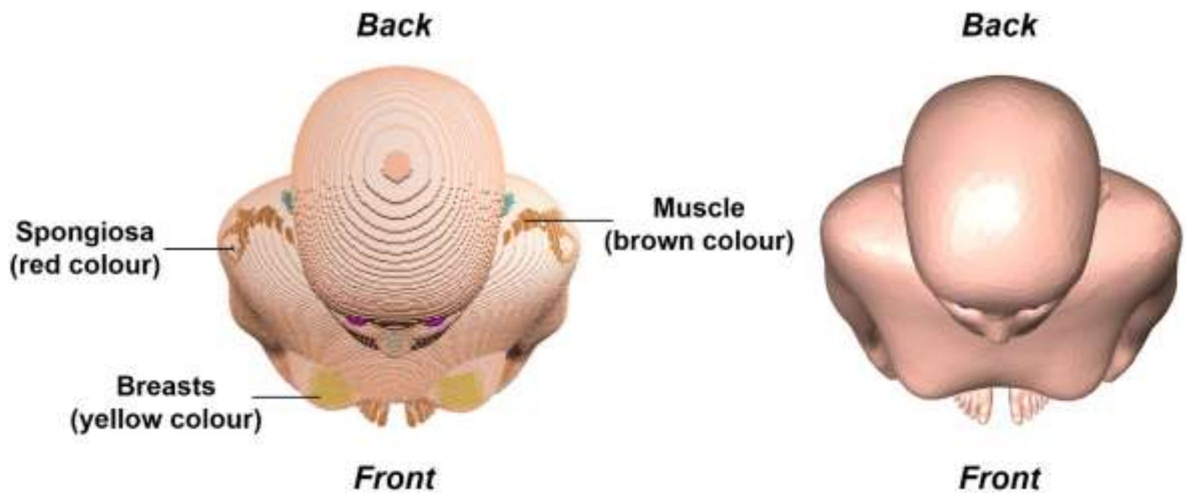

Fig. 6.2. P143 phantom (left) and paediatric MRCP (right) for 15-year-old female viewed in superior-inferior direction: spongiosa (red), muscle (brown) and breasts (yellow) in P143 phantom.

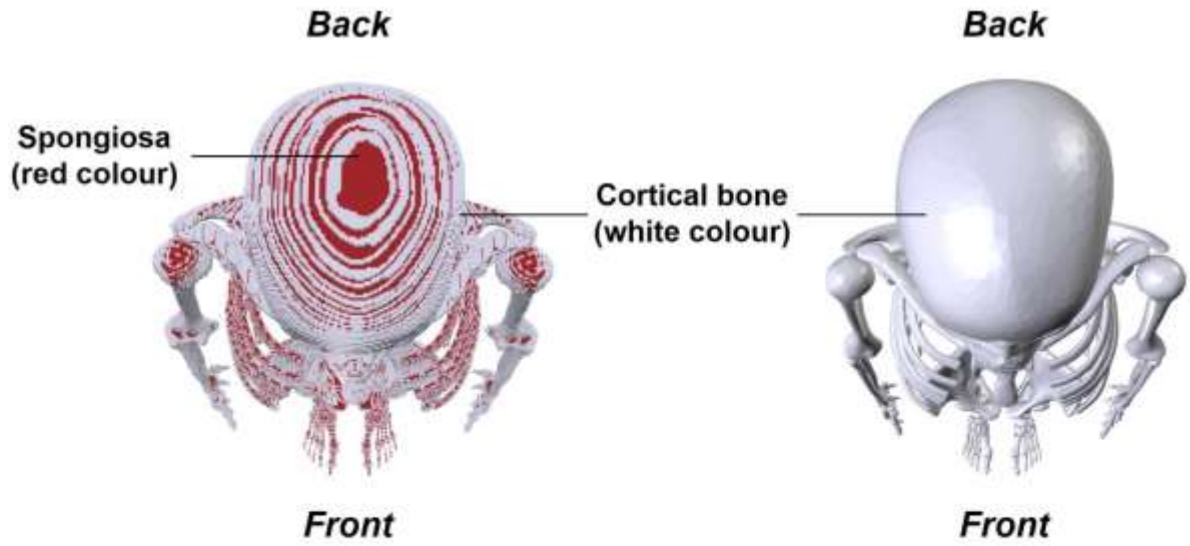

Fig. 6.3. Skeletal system of P143 phantom (left) and paediatric MRCP (right) for 15-year-old female viewed in superior-inferior direction: spongiosa (red) and cortical bone (white).

6.2. Geometric comparison with the P143 phantoms

(96) In order to investigate the geometric similarity between the paediatric MRCPs developed in the present work and the P143 phantoms (ICRP, 2020a), the DI and CD of the organs were calculated as shown in Table 6.3.

(97) The DI and CD values are mostly higher than 0.7 and lower than 10 mm, respectively, with some exceptions. For the spine models, except for the newborn, relatively large dissimilarity is found, which is due mainly to the fact that the spine models of the paediatric MRCPs, except for the newborn, were not directly converted from the P143 phantoms, but constructed based on the PM models of Park et al. (2005). For the colon models, the relatively large dissimilarity is attributed to the fact that the colon models were reproduced with different colon shapes. Large dissimilarity is also found for the organs which were modelled in the present work (i.e. thyroid and ET region models). The large dissimilarity observed for the ureters is mainly due to the shape of the organ; the ureters are very thin and a slight shift in the location results in a very small DI value. Large dissimilarity is also found for some small organs due to the shift of their positions caused by the changes in the adjacent large organs. For example, the low DI values for the spleen of the newborn phantoms and the uterus of the 1-year-old female phantom can be attributed to their shifting due to the change of the colon models. The other large dissimilarities in specific phantoms generally reflect the procedures used in the phantom construction process.

(98) The organ depth distributions (ODDs) and the chord length distributions (CLDs) of the paediatric MRCPs were compared with those of the P143 phantoms, as shown in Annexes E and F. The ODD represents the distance from the body surface to the organ and the CLD represents the distance from the source organ to the target organ, which mainly influence the doses from external and internal exposures, respectively. Although the organs of the paediatric MRCPs were adjusted for blood inclusion, the comparison results show that the ODDs and CLDs of the paediatric MRCPs are generally in good agreement with those of the P143 phantoms for most of the organs.

(99) The results of the geometric similarity investigation show that, in overall, the paediatric MRCPs preserve the shape and location of the organs in the P143 phantoms, and thus they are expected to provide similar dose values for penetrating radiations in both external and internal exposures. For weakly penetrating radiations, however, they will provide significantly different dose values, more accurate and reliable, especially for the organs with large dissimilarities (e.g. colon and thyroid).

Table 6.3. Dice index (DI) and centroid distance (CD) comparing the paediatric MRCPs and the P143 phantoms (ICRP, 2020a).

Organs	Newborn male		Newborn female		1-year male		1-year female		5-year male		5-year female		10-year male		10-year female		15-year male		15-year female	
	DI	CD (cm)	DI	CD (cm)	DI	CD (cm)	DI	CD (cm)	DI	CD (cm)	DI	CD (cm)	DI	CD (cm)	DI	CD (cm)	DI	CD (cm)	DI	CD (cm)
Humeri	0.92	0.02	0.92	0.02	0.95	0.01	0.94	0.08	0.93	0.17	0.93	0.18	0.95	0.18	0.95	0.19	0.91	0.48	0.88	0.29
Ulnae and radii	0.89	0.05	0.89	0.06	0.93	0.05	0.93	0.06	0.91	0.18	0.91	0.18	0.94	0.12	0.94	0.12	0.91	0.26	0.90	0.20
Wrists and hand bones	0.88	0.02	0.88	0.02	0.58	0.30	0.59	0.22	0.66	0.44	0.66	0.44	0.67	0.08	0.67	0.08	0.69	0.64	0.74	0.27
Clavicles	0.87	0.01	0.87	0.01	0.87	0.03	0.87	0.03	0.85	0.07	0.85	0.07	0.81	0.06	0.81	0.06	0.70	0.28	0.83	0.23
Cranium	0.44	0.26	0.44	0.27	0.75	0.14	0.75	0.14	0.78	0.63	0.88	0.40	0.74	0.20	0.78	0.13	0.84	0.33	0.84	0.24
Femora	0.92	0.01	0.92	0.01	0.95	0.02	0.95	0.02	0.93	0.10	0.93	0.10	0.93	0.12	0.93	0.12	0.92	0.38	0.90	0.17
Tibiae, fibulae and patellae	0.91	0.04	0.91	0.03	0.95	0.01	0.95	0.01	0.93	0.12	0.93	0.12	0.95	0.10	0.95	0.10	0.92	0.40	0.91	0.07
Ankles and foot bones	0.89	0.08	0.88	0.08	0.70	0.19	0.70	0.51	0.50	0.63	0.58	0.55	0.53	0.96	0.54	0.96	0.58	1.25	0.72	1.15
Mandible	0.67	0.02	0.67	0.03	0.69	0.32	0.69	0.31	0.72	0.55	0.72	0.50	0.50	0.66	0.49	0.70	0.75	0.16	0.73	0.35
Pelvis	0.91	0.02	0.91	0.02	0.94	0.01	0.94	0.01	0.92	0.07	0.92	0.07	0.91	0.08	0.90	0.08	0.83	0.26	0.86	0.17
Ribs	0.14	0.20	0.14	0.20	0.87	0.07	0.87	0.08	0.85	0.04	0.85	0.04	0.78	0.05	0.77	0.05	0.66	0.25	0.74	0.39
Scapulae	0.66	0.17	0.66	0.17	0.93	0.03	0.93	0.03	0.90	0.14	0.90	0.14	0.89	0.14	0.89	0.14	0.73	0.64	0.81	0.19
Cervical spine	0.87	0.05	0.87	0.05	0.35	0.35	0.40	0.21	0.54	0.13	0.59	0.14	0.59	0.20	0.56	0.20	0.61	0.37	0.64	0.48
Thoracic spine	0.87	0.07	0.87	0.07	0.48	0.65	0.47	0.53	0.64	0.73	0.65	0.73	0.70	0.54	0.70	0.54	0.53	0.40	0.56	0.69
Lumbar spine	0.90	0.02	0.90	0.02	0.55	0.18	0.55	0.09	0.66	0.27	0.66	0.27	0.74	0.27	0.74	0.27	0.76	0.15	0.72	0.50
Sacrum	0.83	0.08	0.83	0.08	0.43	0.49	0.42	0.49	0.87	0.15	0.87	0.15	0.70	0.52	0.70	0.52	0.85	0.25	0.78	0.44
Sternum	0.33	0.26	0.33	0.26	0.50	0.82	0.50	0.82	0.68	1.17	0.68	1.17	0.76	1.08	0.76	1.08	0.86	0.44	0.85	0.13
Teeth									0.28	0.40	0.28	0.44	0.35	0.36	0.35	0.36	0.39	0.35	0.44	0.34
Tongue	0.33	1.32	0.33	1.23	0.46	1.39	0.43	1.49	0.57	1.26	0.54	1.33	0.71	0.96	0.72	0.87	0.84	0.40	0.77	0.76
Oesophagus	0.60	0.11	0.60	0.12	0.66	0.13	0.67	0.15	0.68	0.18	0.63	0.52	0.67	0.12	0.66	0.18	0.64	0.93	0.67	0.48
Stomach	0.80	0.26	0.80	0.26	0.95	0.13	0.95	0.13	0.96	0.01	0.96	0.01	0.95	0.04	0.95	0.04	0.96	0.09	0.95	0.17
Small intestine	0.76	0.19	0.75	0.19	0.79	0.12	0.79	0.12	0.73	0.50	0.73	0.49	0.92	0.27	0.92	0.26	0.86	0.25	0.88	0.11
Colon	0.54	1.11	0.54	1.11	0.42	1.12	0.41	1.12	0.48	1.43	0.49	1.43	0.43	1.61	0.43	1.61	0.58	0.79	0.51	2.10
Salivary glands	0.93	0.02	0.93	0.02	0.77	0.21	0.77	0.22	0.94	0.03	0.94	0.03	0.69	0.43	0.82	0.23	0.86	0.19	0.89	0.09
Tonsils	0.88	0.01	0.88	0.01	0.92	0.01	0.91	0.01	0.92	0.02	0.71	0.20	0.92	0.01	0.65	0.20	0.39	0.51	0.89	0.04
Liver	0.73	0.64	0.73	0.64	0.91	0.18	0.91	0.19	0.88	0.18	0.88	0.18	0.88	0.26	0.88	0.26	0.86	0.55	0.88	0.17
Gall bladder	0.97	0.00	0.97	0.00	0.94	0.08	0.94	0.08	0.95	0.04	0.94	0.05	0.95	0.02	0.95	0.03	0.95	0.03	0.95	0.01
Pancreas	0.66	0.60	0.66	0.60	0.92	0.04	0.92	0.04	0.89	0.08	0.89	0.08	0.91	0.04	0.91	0.04	0.85	0.26	0.87	0.09
Heart	0.69	0.24	0.69	0.23	0.97	0.01	0.97	0.01	0.96	0.05	0.96	0.05	0.96	0.05	0.96	0.05	0.94	0.17	0.96	0.08
Kidneys	0.97	0.01	0.97	0.01	0.95	0.01	0.95	0.01	0.89	0.08	0.89	0.08	0.90	0.01	0.90	0.01	0.86	0.25	0.88	0.15
Ureters	0.59	0.07	0.42	0.34	0.16	0.24	0.16	0.24	0.51	0.03	0.50	0.06	0.47	0.12	0.45	0.34	0.52	0.50	0.56	0.09
Urinary bladder	0.92	0.02	0.90	0.05	0.64	0.11	0.62	0.27	0.95	0.14	0.96	0.03	0.97	0.01	0.98	0.01	0.97	0.04	0.96	0.05
Gonads	0.95	0.01	0.88	0.01	0.94	0.01	0.89	0.05	0.88	0.10	0.92	0.03	0.91	0.02	0.88	0.08	0.93	0.08	0.90	0.40
Prostate / uterus	0.94	0.02	0.93	0.02	0.52	0.41	0.00	1.02	0.82	0.15	0.85	0.10	0.92	0.02	0.92	0.01	0.90	0.03	0.84	0.13
Adrenals	0.91	0.01	0.90	0.01	0.88	0.06	0.88	0.06	0.81	0.07	0.81	0.07	0.81	0.09	0.81	0.09	0.77	0.36	0.86	0.09
Breasts	0.86	0.02	0.87	0.01	0.90	0.02	0.90	0.02	0.87	0.08	0.87	0.08	0.66	0.05	0.90	0.04	0.90	0.23	0.92	0.07
Brain	0.85	0.50	0.85	0.50	0.98	0.03	0.98	0.03	0.94	0.29	0.98	0.03	0.94	0.29	0.98	0.02	0.97	0.14	0.97	0.05
Pituitary glands	0.91	0.00	0.91	0.00	0.90	0.01	0.90	0.01	0.87	0.03	0.87	0.03	0.85	0.02	0.85	0.02	0.78	0.12	0.85	0.05
Spinal	0.82	0.27	0.82	0.28	0.42	0.95	0.42	0.37	0.65	1.97	0.64	2.45	0.87	0.65	0.87	0.68	0.43	0.55	0.48	0.72
Spleen	0.45	0.74	0.45	0.74	0.83	0.28	0.83	0.28	0.82	0.09	0.82	0.09	0.82	0.11	0.82	0.11	0.79	0.09	0.82	0.20
Thymus	0.95	0.02	0.95	0.02	0.65	0.15	0.65	0.15	0.89	0.17	0.89	0.17	0.91	0.07	0.92	0.09	0.90	0.20	0.91	0.17
Thyroid	0.39	0.58	0.39	0.58	0.02	1.44	0.02	1.44	0.23	0.95	0.20	0.96	0.32	1.11	0.32	1.12	0.38	0.98	0.18	1.30
ET	0.46	1.12	0.52	0.80	0.41	1.91	0.45	1.47	0.72	0.79	0.70	0.88	0.70	0.89	0.70	0.71	0.55	2.45	0.47	2.18
Trachea	0.93	0.03	0.89	0.08	0.93	0.09	0.93	0.09	0.84	0.10	0.84	0.10	0.90	0.10	0.90	0.10	0.92	0.09	0.91	0.08
Lungs	0.81	0.10	0.81	0.10	0.94	0.17	0.94	0.17	0.90	0.17	0.90	0.17	0.96	0.12	0.96	0.12	0.93	0.37	0.92	0.14

6.3. Computational performance in Monte Carlo codes

(100) The TM geometry of the paediatric MRCPs can be directly implemented in general-purpose Monte Carlo codes such as Geant4 (version 8.0 and later versions), PHITS (version 2.82 and later versions) and MCNP6 (version 1.0 and later versions) (ICRP, 2020c). The features of these codes that enable implementation of the TM geometry have been significantly improved in the last few years (Allison et al., 2016; Furuta et al., 2017; Martz et al., 2017). In this section, as an example, the computational performance of the 5-year-old male MRCP and P143 phantom (ICRP, 2020a) were compared in terms of run time and memory usage.

(101) Computational performances were measured for Geant4 (version 10.06.p01), PHITS (version 3.10) and MCNP6 (version 2.0) on a single core of the Intel® Xeon® CPU E5-2698 v4 (@ 2.20 GHz and 512 GB memory). Run time was measured for photons, electrons and neutrons in the left-lateral (LLAT) irradiation geometry by simulating 10^5 primary particles with energies of 10^{-2}–10^4 MeV for photons and electrons and 10^{-9}–10^4 MeV for neutrons. The run time results were obtained by averaging values from multiple measurements to achieve relative errors less than 5%.

(102) For Geant4, the physics library of *G4EmLivermorePhysics* was used for the transportation of photons and electrons, and the physics models and cross-sections of *NeutronHPThermalScattering*, *NeutronHPElastic*, *ParticleHPInelastic*, *Neutron-HPCapture* and *NeutronHPFission* were used for the transportation of neutrons. A range cut-off of 1 μm was applied for the production of secondary particles. For PHITS, the *EGS5* physics library was used for the transportation of photons and electrons and the *JENDL-4.0* physics library and the event generator mode version 2 were used for the transportation of neutrons. For the MCNP6 code, the default physics libraries based on Lawrence Livermore National Laboratory evaluated data were used for the transportation of photons and electrons and the *ENDF70* physics library was used for the transportation of neutrons. For the energy cut-off values, considering the range cut-off value of 1 μm used for Geant4 calculations, the equivalent energy cut-off values were applied in the PHITS and MCNP6 codes. Variance reduction techniques were not used.

(103) Fig. 6.4 compares the run time measured for the 5-year-old male MRCP and P143 phantom implemented in Geant4, PHITS and MCNP6. The results of Geant4 show that for photons, the run time of the MRCP is longer than that of the P143 phantom when the energy is lower than 1 MeV, by up to 7.0 times, and shorter when the energy is higher, by up to 4.3 times. For electrons, similar differences were found: the run time of the MRCP is longer when the energy is lower than 10 MeV, by up to 5.2 times, and shorter when the energy is higher, by up to 3.2 times. For neutrons, it can be seen that the run time of the MRCP phantom is similar in the energy range of 10^{-5}–1 MeV and longer than that of the P143 phantom in the other energy ranges, by up to a factor of ~4 and ~2 at the lower and higher energies, respectively.

(104) For PHITS, the run time of the MRCP is generally shorter than that of the P143 phantom for all three radiation types. Unlike Geant4, the run time of the MRCP is shorter at low energies; the maximum difference is ~4 times for both photons and electrons at 0.01 MeV and ~2 times for neutrons at 10^{-9} MeV. For photons and electrons with energies higher than 1 MeV, on the other hand, the run time of the MRCP is similar to that of the P143 phantom. This high computation speed of the MRCP at low energies is due to the fact that the computation speed of the TM geometry in PHITS is accelerated by using the octree decomposition technique (Furuta et al., 2017).

(105) For MCNP6, the run time of the MRCP is significantly longer than that of the P143 phantom for all three radiation types. The differences are 3–11 times except for high-energy (≥ 100 MeV) photons and electrons for which even larger differences (20–27) are found. Such slow computation speeds for the MRCP are due mainly to the fact that MCNP6 uses features dedicated to unstructured mesh geometry; that is, MCNP6 is overly sophisticated for implementing simple TM geometry, although it can additionally implement pentahedral and hexahedral mesh geometry (Martz et al., 2017). Note that Geant4 and PHITS have features dedicated to TM geometry.

(106) The run times of the MRCP were compared between Geant4, PHITS and MCNP6. Geant4 shows the shortest run time of the three codes for photons and electrons. For photons, PHITS and MCNP6 take 1.8–7.8 and 6.3–24.1 times longer than Geant4, respectively. For electrons, PHITS and MCNP6 take 1.4–7.0 and 6.3–26.0 times longer than Geant4. On the other hand, for neutrons, except for the highest energy point, PHITS shows the shortest run time of the three codes; Geant4 and MCNP6 take 1.7–3.3 and 1.6–3.4 times longer run time than PHITS. At the highest energy point (i.e. 10^4 MeV), the run time of MCNP6 is shorter than that of Geant4 and PHITS by a factor of 3.0 and 2.4.

(107) Table 6.4 compares the memory usage required for implementing the 5-year-old male MRCP and P143 phantom in Geant4, PHITS and MCNP6. It can be seen that PHITS requires relatively small memory for the implementation of the MRCP, which is because the memory space is dynamically allocated in PHITS (Han et al., 2018). In addition, while PHITS requires smaller memory usage for the MRCP than for the P143 phantom, in the other codes, the memory usage for the MRCP is larger than that for the P143 phantom by a factor of approximately 12.1 for Geant4 and 2.4 for MCNP6. However, the memory usage for the MRCP for all three codes is much smaller than 16 GB, which is within the capacity of personal computers.

Table 6.4. Memory usage required to implement 5-year-old male MRCP and P143 phantom in Geant4, PHITS and MCNP6.

	Geant4	PHITS	MCNP6
MRCP	8.5 GB	1.4 GB	4.5 GB
P143 phantom	0.7 GB	2.2 GB	1.9 GB

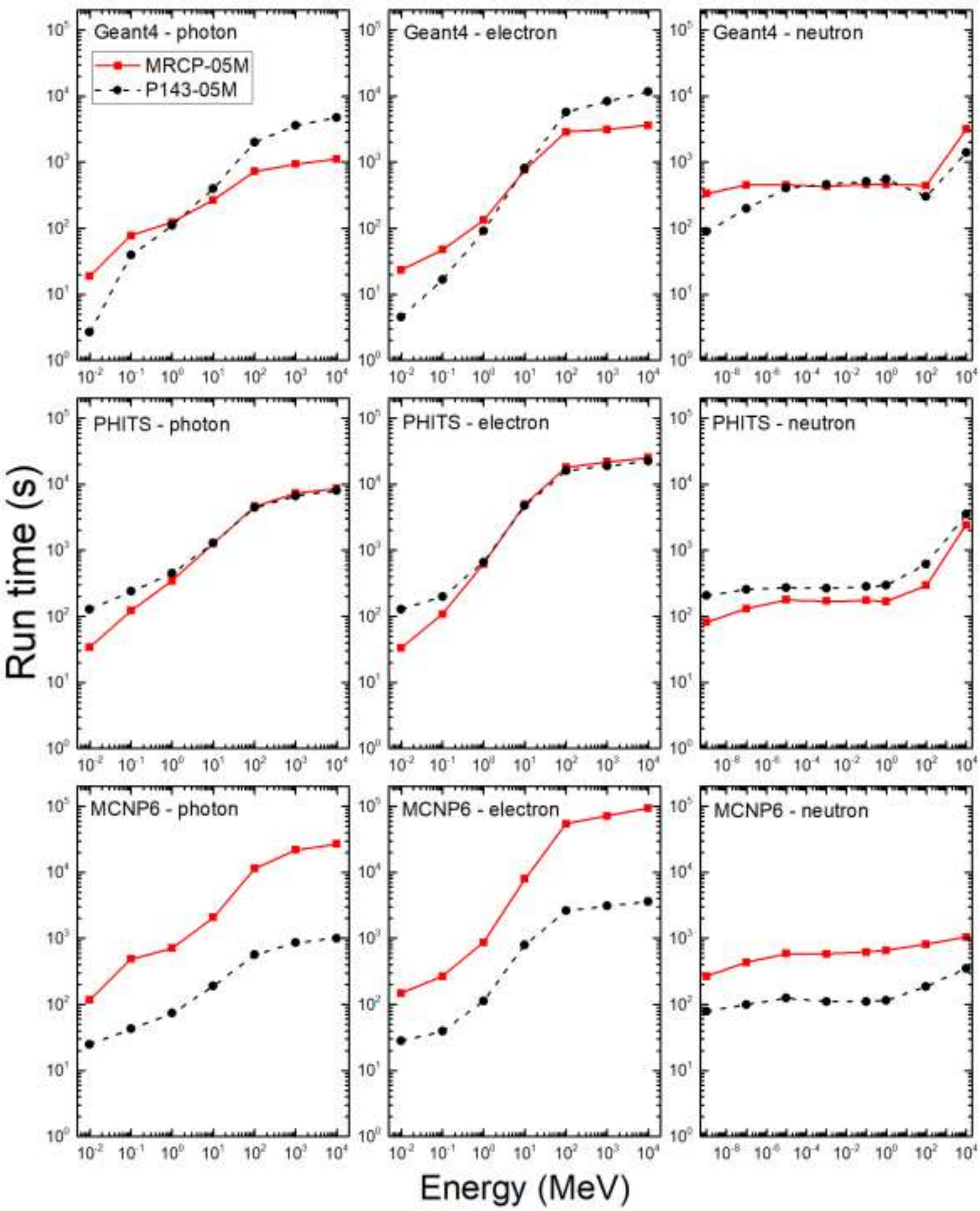

Fig. 6.4. Run time measured for the 5-year-old male MRCP and P143 phantom, implemented in Geant4, PHITS and MCNP6, for transporting 105 source particles in the left-lateral (LLAT) irradiation geometry.

7. DOSIMETRIC IMPACT OF THE PAEDIATRIC MESH-TYPE REFERENCE COMPUTATIONAL PHANTOMS

(108) This chapter discusses the dosimetric impact of the paediatric mesh-type reference computational phantoms (MRCPs) for external and internal exposure geometries, compared with the P143 phantoms (ICRP, 2020a) and the *Publications 66* and *100* mathematical models for the respiratory and alimentary tracts (ICRP, 1994a, 2006) which have been used to estimate reference dose coefficients (DCs) under the current ICRP dosimetry system (ICRP, 2007). In the present work, the Geant4 code (version 10.06.p02) (Allisons et al., 2016) was used for all the calculations, and the MCNP6 (version 2.0) (Martz et al., 2017) and PHITS (version 3.10) (Furuta et al., 2017) codes were used for some limited cases for spot checking purposes.

7.1. External exposures

(109) Organ DCs were calculated for idealised external exposures, in terms of mean absorbed dose per fluence (pGy cm^2), for six organs [i.e. RBM, colon, lungs, stomach, breasts and skin] and four radiation types (i.e. photons, neutrons, electrons and helium ions) and then compared with values calculated using the P143 phantoms (see Annex H for calculation details). All the selected organs have the highest w_T (= 0.12) except skin; the skin, despite the small w_T (= 0.01), could significantly affect the effective dose calculation for external exposures to weakly penetrating radiations of low energies (Yeom et al., 2016, 2017) and its DCs themselves are important in the current ICRP dosimetry system (ICRP, 2007).

(110) The comparison of the values shows that for uncharged particles (i.e. photons and neutrons), the DCs calculated using the MRCPs tend to be close to the values obtained using the P143 phantoms and the differences are less than 10% for most cases. Exceptions are observed for photons at low energies (<20 keV), for which relatively large differences are found. For the low-energy photons, the colon DCs tend to show the largest differences, which is as expected because the colon was significantly modified in the MRCPs. The RBM DCs of the MRCPs tend to be smaller than those of the P143 phantoms, which is because in the MRCPs, in contrast to the P143 phantoms, the spongiosa region is fully covered by the cortical bone.

(111) For charged particles (i.e. electrons and helium ions), the DCs calculated using the MRCPs are close to the values of the P143 phantoms for electrons ≥20 MeV (≥2 MeV for the skin) and helium ions ≥500 MeV/u (≥50 MeV/u for the skin). At lower energies, on the other hand, significant differences are observed for the breast, RBM and skin. The breast DCs of the 10- and 15-year-old MRCPs, for example, are significantly smaller (i.e. up to four orders of magnitude) than those of the P143 phantoms, which is due to the fact that the breasts are fully covered by skin in the MRCPs but not in the P143 phantoms. The RBM DCs of the MRCPs tend to be significantly smaller, which is because, as mentioned earlier, the spongiosa region is fully covered by the cortical bone in the MRCPs. The skin DCs of the MRCPs and the P143 phantoms are significantly different (i.e. up to five orders of magnitude), which is due to the consideration of the micron-scale radiosensitive skin target layer in the MRCPs which was not possible for the P143 phantoms due to the resolution of the voxel geometry.

(112) The effective DCs were also calculated using the MRCPs, in terms of effective dose per fluence (pSv cm^2), and then compared with the values obtained using the P143 phantoms. For uncharged particles, the DCs calculated using the MRCPs are very close to those obtained using the P143 phantoms and the differences are less than 5% for most cases. Only for photons at low energies (<50 keV), relatively large differences are found, but these are still less than

45%. For charged particles, the differences of DCs between the MRCPs and P143 phantoms are very small for electrons >10 MeV and helium ions >200 MeV/u (i.e. mostly less than 5%). At lower energies, however, large differences are observed (i.e. up to four orders of magnitude), which is due mainly to the differences in the skin DCs resulting from the consideration of the radiosensitive skin target layer in the MRCPs. Note that the skin dose, despite the small w_T (= 0.01), dominates contributions to effective dose for low-energy charged particles which do not reach the internal organs.

(113) The DCs for the entire lens were calculated for photons using the paediatric MRCPs and the calculated values were compared with those obtained using the P143 phantoms (see Annex H for calculation details). For the AP geometry in which the lens dose is of primary concern, significant differences are observed by up to 2.5 times, except for the newborn, due to the different depth of the lens between the MRCPs and P143 phantoms. In other irradiation geometries, except at very low energies (<20 keV), the lens DCs calculated using the MRCPs are close to those obtained using the P143 phantoms (i.e. differences <20%). For electrons, considering that the P143 phantoms will not be used for the calculation of lens DCs for electrons, the lens DCs of the paediatric MRCPs were compared with those calculated with the adult MRCPs, which shows that the differences are generally less than 15%. Exceptions are observed for PA geometry where the head size has a large influence; large differences by up to a factor of ~3. The DCs for the radiosensitive region of the lens were also calculated and compared with those of the entire lens (Han et al., 2021). The results show that for photons, the DCs of the radiosensitive region of the lens are very close to those of the entire lens (i.e. differences <10%) for the larger part of the energy range considered (0.02–1.5 MeV). For the electrons at low energies (<2 MeV), however, the DCs of the radiosensitive region of the lens are found significantly larger than those of the entire lens (e.g. by up to ~5 times at 0.8 MeV). This is in agreement with the findings of *Publication 116* (ICRP, 2010) using the detailed eye model of Behrens et al. (2009).

(114) In the paediatric MRCPs, the sub-regions of the teeth (i.e. enamel, cementum, dentin and pulp) were explicitly modelled, in particular to support electron paramagnetic resonance (EPR) retrospective dosimetry. Shin et al. (2021) calculated DCs for the enamel of the teeth, in terms of dose per air kerma, for the AP and RLAT geometries using the MRCPs and then compared the calculated values with DCs for the entire teeth obtained using the P143 phantoms. The results of the study show that the differences in DCs are very large; that is, the differences are a few tens of times for most phantoms at 10 and 20 keV for the AP and RLAT geometry, respectively. In the same study, the calculated values were also compared with those calculated by Ulanovsky et al. (2005) who used a modified Golem phantom (Zankl and Wittmann, 2001) which is the predecessor of the P110 adult male phantom and by Ulanovsky and Wieser (2007) who used a modified 5-year-old mathematical phantom, the results of which generally confirmed that the paediatric MRCPs produce reasonable values for the enamel DCs.

7.2. Internal exposures

(115) Specific absorbed fractions (SAFs) were calculated for photons and electrons and then compared with values calculated using the P143 phantoms as well as *Publication 1XX* values (ICRP, 2022) which were calculated using the P143 phantoms and the MCNPX code (version 2.7) (Pelowitz, 2008) (see Annex I for calculation details). Note that the SAFs obtained from the P143 phantom for self-irradiation were scaled to account for blood content, as were the *Publication 133* and *1XX* values (ICRP, 2016, 2022). The calculated SAFs cover four source

organs (i.e. liver, lungs, cortical bone and thyroid) and four target organs selected for each source organ considering contributions to effective dose.

(116) For most cases, the SAFs calculated using the P143 phantoms in the present work are in good agreement with the P1XX values; the differences are mostly less than 10%, which mainly result from the differences in physics models or cross-section data between the Geant4 code used in the present work and the MCNPX code used in *Publication 1XX*. For photons and electrons at low energies (<20 keV), however, very large differences are found, which is due mainly to the fact that the P1XX values at these low energies were calculated by a special data-smoothing algorithm involving extrapolation (Schwarz et al., 2021), not by direct Monte Carlo simulations. Therefore, the following paragraphs mainly compare the SAFs calculated using the same Monte Carlo code (i.e. Geant4 code) to solely focus on the dosimetric impact of the anatomical and geometrical improvements in the paediatric MRCPs compared to the P143 phantoms.

(117) The comparison of the values for photons shows that for the liver, lungs and cortical bone as source organ, the SAFs of the MRCPs and P143 phantoms are marginally different, except at energies <50 keV for which the SAFs of the MRCPs tend to have higher values than those of the P143 phantoms. This tendency is mainly attributable to the closer distance between the source and target organs enlarged by the inclusion of blood content in the MRCPs.

(118) The opposite tendency is also observed. For example, the (RBM ← liver) SAFs of the MRCPs are generally smaller than those of the P143 phantoms at the lowest energy considered (i.e. 10 keV), which is due to the fact that the spongiosa of the MRCPs, unlike that of the P143 phantoms, is fully covered by the cortical bone which effectively shields low-energy photons. For another example, the (muscle ← cortical bone) SAFs of the MRCPs are much smaller than those of the P143 phantoms for all cases. This is explained because in the MRCPs, the muscle was modelled to have a realistic shape while in the P143 phantoms, the muscle was produced from the surface of the bones by a simple voxel growing algorithm (Stepusin, 2016); consequently, the muscle of the P143 phantoms is closer to the bones, resulting in larger SAFs.

(119) Photon SAFs obtained using the MRCPs and P143 phantoms show relatively large differences when the thyroid is the source organ, which is because in the MRCPs, the thyroid was relocated to its typical position in the neck. The (ET ← thyroid) SAFs of the MRCPs tend to be greater than those of the P143 phantoms; this is because in the MRCPs, the larynx, the location of which is very close to the thyroid, was modelled as a part of the ET region.

(120) Electron SAFs calculated using the MRCPs are close to those obtained using the P143 phantoms for the self-irradiation cases (e.g. thyroid ← thyroid), while for the cross-fire-irradiation cases, the differences are very large (i.e. up to more than four orders of magnitude) in some cases. The pattern of differences is similar to that for low-energy photons for most cases, but the differences are much larger for most cases. For example, the (muscle ← cortical bone) SAFs of the newborn MRCPs are smaller than those of the P143 newborn phantoms by up to a factor of ~2 for photons but by up to a factor of ~80 for electrons. Nevertheless, the committed effective DCs are not expected to be much different, which is due to the fact that the self-irradiation SAFs, not cross-fire-irradiation SAFs, dominantly affect the calculation of committed effective DCs due to the limited range of electrons for most radionuclides.

(121) Electron SAFs calculated using the MRCPs for the alimentary tract were compared with the P1XX values (ICRP, 2022) calculated using the *Publication 100* (ICRP, 2006) stylised models (Choi et al., 2022a). Although the absorbed fractions (AFs) are in good agreement for most cases, some differences in SAFs are observed due mainly to differences in target masses between the MRCPs and the stylised models. However, for some cases (i.e. oral mucosa ← food; oral mucosa ← teeth surface; small intestine ← contents; and large intestine ← contents), significant differences in AFs, as well as in SAFs, are observed, which are attributed to the

differences in the inter-organ distances and organ dimensions. For example, for the small intestine as target region and its contents as source region, the AFs obtained using the MRCPs are larger than the P1XX values, resulting in even larger SAFs with the smaller target mass. These differences result because the lumen diameter of the MRCPs is smaller than that of the stylised models, leading to less energy being absorbed in the contents (i.e. self-absorption) and thus more energy being deposited in the target region.

(122) Electron SAFs calculated using the MRCPs for the respiratory tract were compared with the P1XX values calculated with the *Publication 66* (ICRP, 1994a) stylised models (Choi et al., 2022b). The SAFs of the MRCPs are generally larger than the P1XX values, due mainly to the smaller target masses of the MRCPs. For the bronchiole (bb) region, when compared to the P1XX values, the SAFs of the MRCPs are increased by not only the smaller target masses but also the electron cross-fire from other branches. For the AI source region, rather complex differences are observed due mainly to differences in geometries and densities between the MRCPs and the stylised models.

REFERENCES

Allison, J., Amako, K., Apostolakis, J., et al., 2016. Recent developments in Geant4. Nucl. Instrum. Methods Phys. Res. Sect. A. 835, 186–225.

Atchison, D.A., Markwell, E.L., Kasthurirangan, S., et al., 2008. Age-related changes in optical and biometric characteristics of emmetropic eyes. J. Vis. 8, 1–20.

Augusteyn, R.C., 2010. On the growth and internal structure of the human lens. Exp. Eye Res. 90, 643–654.

Bayle, P., Braga, J., Mazurier, A., et al., 2009. Brief communication: High-resolution assessment of the dental developmental pattern and characterization of tooth tissue proportions in the late Upper Paleolithic child from La Madeleine, France. Am. J. Phys. Anthropol. 138, 493–498.

Behrens, R., Dietze, G., Zankl, M., 2009. Dose conversion coefficients for electron exposure of the human eye lens. Phys. Med. Biol. 54, 4069–4087.

Cassola, V.F., Kramer, R., de Melo Lima, V.J., et al., 2013. Development of newborn and 1-year-old reference phantoms based on polygon mesh surfaces. J. Radiol. Prot. 33, 669–691.

Cassola, V.F., de Melo Lima, V.J., Kramer, R., et al., 2010. FASH and MASH: female and male adult human phantoms based on polygon mesh surfaces: I. Development of the anatomy. Phys. Med. Biol. 55, 133–162.

Charles, M.W., Brown, N., 1975. Dimensions of the human eye relevant to radiation protection (dosimetry). Phys. Med. Biol. 20, 202–218.

Choi, C., Nguyen, T.T., Yeom, Y.S., et al., 2019. Mesh-type reference Korean phantoms (MRKPs) for adult male and female for use in radiation protection dosimetry. Phys. Med. Biol. 64, 085020.

Choi, C., Yeom, Y.S., Lee, H., et al., 2020. Body-size-dependent phantom library constructed from ICRP mesh-type reference computational phantoms. Phys. Med. Biol. 65, 125014.

Choi, C., Shin, B., Yeom, Y.S., et al., 2021. Development of Skeletal Systems for ICRP Pediatric Mesh-type Reference Computational Phantoms. J. Radiol. Prot. 41, 139–161.

Choi, C., 2022a. Development of Alimentary Tract Model for ICRP Pediatric Mesh-type Reference Computational Phantoms (under review).

Choi, C., 2022b. Development of Respiratory Tract Model for ICRP Pediatric Mesh-type Reference Computational Phantoms (will be submitted in the second quarter of 2022).

Christ, A., Kainz, W., Hahn, E.G., et al., 2009. The Virtual Family–development of surface-based anatomical models of two adults and two children for dosimetric simulations. Phys. Med. Biol. 55, N23–38.

Colin, P., Koenig, P., Ouzzane, A., et al., 2009. Environmental factors involved in carcinogenesis of urothelial cell carcinomas of the upper urinary tract. BJU Int. 104, 1436–1440.

Cristy, M., 1980. Mathematical phantoms representing children of various ages for use in estimates of internal dose. ORNL Report TM-367. Oak Ridge National Laboratory, Oak Ridge, TN.

Cristy, M., Eckerman, K.F., 1987. Specific absorbed fractions of energy at various ages from internal photon sources. Part I: Methods. ORNL Report TM-8381/V1. Oak Ridge National Laboratory, Oak Ridge, TN.

de Melo Lima, V.J., Vassola, V.F., Kramer, R., et al., 2011. Development of 5- and 10-year-old pediatric phantoms based on polygon mesh surfaces. Med. Phys. 38, 4723–4736.

Devlieger, H., Daniels, H., Marchal, G., et al., 1991. The diaphragm of the newborn infant: anatomical and ultrasonographic studies. J. Dev. Physiol. 16, 321–329.

Dilmen, G., Koktener, A., Turhan, T.O., et al., 2002. Growth of the fetal lens and orbit. Int. J. Genecol. Obstet. 76, 267–271.

Dong, L., Li, T., Liu, C., 2015. Construction of hybrid Chinese reference adult phantoms and estimation of dose conversion coefficients for muons. Radiat. Prot. Dosim. 164, 219–227.

Drake, R.L., Vogl, A.W., Mitchell, A.W.M., 2004. Gray's Anatomy for Students 1st edn. Amsterdam:Elsevier.

Duc, G., Largo, R.H., 1986. Anterior fontanel: size and closure in term and preterm infants. Pediatrics 78, 904–908.

Eckerman, K.F., Veinot, K.G., 2018. Transitional epithelium of urinary bladder: dosimetric data for cells at risk. IEEE Trans. Radiat. Plasma Med. Sci. 3, 61–64.

Ehlers, N., Sorensen, T., Bramsen, T., et al., 1976. Central corneal thickness in newborns and children. Acta Ophtalmol. 54, 285–290.

Ellis, H, 2007. Anatomy of the thyroid and parathyroid glands. Surgery (Oxford). 25, 467–468.

Faix, R.G., 1982. Fontanelle size in black and white term newborn infants. J. Pediatr. 100, 304–306.

Frane, S.L., Sholtz, R.I., Lin, W.K., et al., 2000. Ocular components before and after acquired, nonaccommodative esotropia. Optometry Vis. Sci. 77, 633–636.

Friedman, N.E., Mutti, D.O., Zadnik, K., 1996. Corneal changes in schoolchildren. Optom. Vis. Sci. 73, 552-557.

Furuta, T., Sato, T., Han, M.C., et al., 2017. Implementation of tetrahedral-mesh geometry in Monte Carlo radiation transport code PHITS. Phys. Med. Biol. 62, 4798–4810.

Goldstein, I. Tamir, A., Zimmer, E.Z., et al., 1998. Growth of the fetal orbit and lens in normal pregnancies. Ultrasound Obstet. Gynecol. 12, 175–179.

Gosselin, M.C., Neufeld, E., Moser, H., et al., 2014. Development of a new generation of high-resolution anatomical models for medical device evaluation: the Virtual population 3.0. Phys. Med. Biol. 59, 5287–5303.

Han, H., Yeom, Y.S., Choi, C., et al., 2020. POLY2TET: a computer program for conversion of computational human phantoms from polygonal mesh to tetrahedral mesh. J. Radiol. Prot. 40, 962–979.

Han, H., Yeom, Y.S., Nguyen, T.T., et al., 2021. Development of Detailed Pediatric Eye Models for Lens Dose Calculations. J. Radiol. Prot. 41, 305–325.

Han, M.C., Yeom, Y.S., Lee, H.S., et al., 2018. Multi-threading performance of Geant4, MCNP6, and PHITS Monte Carlo codes for tetrahedral-mesh geometry. Phys. Med. Biol. 63, 09NT02.

Harjeet, A., Sahni, D., Jit, I., et al., 2004. Shape, measurements and weight of the thyroid gland in northwest Indians. Surg. Radio. Anat. 26, 91–95.

Hurtado, J.L., Lee, C., Lodwick, D., et al., 2012. Hybrid computational phantoms representing the reference adult male and adult female: construction and applications to retrospective dosimetry. Health Phys. 102, 292–304.

IAEA, 2002. Use of electron paramagnetic resonance dosimetry with tooth enamel for retrospective dose assessment. IAEA TECDOC-1331.

ICRP, 1975. Report on the Task Group on Reference Man. ICRP Publication 23. Pergamon Press, Oxford.

ICRP, 1977. Recommendations of the International Commission on Radiological Protection. ICRP Publication 26. Ann. ICRP 1(3).

ICRP, 1979. Limits for Intakes of Radionuclides by Workers. Part 1. ICRP Publication 30. Ann. ICRP 2 (3/4).

ICRP, 1988. Radiation Dose to Patients from Radiopharmaceuticals. ICRP Publication 53. Ann. ICRP 18 (1–4).

ICRP, 1990. Age-dependent Doses to Members of the Public from Intake of Radionuclides – Part 1. ICRP Publication 56. Ann. ICRP 20 (2).

ICRP, 1991a. 1990 Recommendations of the International Commission on Radiological Protection. ICRP Publication 60. Ann. ICRP 21 (1–3).

ICRP, 1991b. Annuals Limits on Intake of Radionuclides by Workers Based on the 1990 Recommendations. ICRP Publication 61. Ann. ICRP 21 (4).

ICRP, 1993. Age-dependent Doses to Members of the Public from Intake of Radionuclides – Part 2 Ingestion Dose Coefficients. ICRP Publication 67. Ann. ICRP 23 (3/4).

ICRP, 1994a. Human Respiratory Tract Model for Radiological Protection. ICRP Publication 66. Ann. ICRP 24 (1–3).

ICRP, 1994b. Dose Coefficients for Intakes of Radionuclides by Workers. ICRP Publication 68. Ann. ICRP 24 (4).

ICRP, 1995a. Age-dependent Doses to Members of the Public from Intake of Radionuclides – Part 3 Ingestion Dose Coefficients. ICRP Publication 69. Ann. ICRP 25 (1).

ICRP, 1995b. Age-dependent Doses to Members of the Public from Intake of Radionuclides – Part 4 Inhalation Dose Coefficients. ICRP Publication 71. Ann. ICRP 25 (3–4).

ICRP, 1996a. Age-dependent Doses to the Members of the Public from Intake of Radionuclides – Part 5 Compilation of Ingestion and Inhalation Coefficients. ICRP Publication 72. Ann. ICRP 26 (1).

ICRP, 1996b. Conversion Coefficients for use in Radiological Protection against External Radiation. ICRP Publication 74. Ann. ICRP 26 (3/4).

ICRP, 1998. Radiation Dose to Patients from Radiopharmaceuticals (Addendum to ICRP Publication 53). ICRP Publication 80. Ann. ICRP 28 (3).

ICRP, 2002. Basic Anatomical and Physiological Data for Use in Radiological Protection Reference Values. ICRP Publication 89. Ann. ICRP 32 (3–4).

ICRP, 2006. Human Alimentary Tract Model for Radiological Protection. ICRP Publication 100. Ann. ICRP 36 (1–2).

ICRP, 2007. The 2007 Recommendations of the International Commission on Radiological Protection. ICRP Publication 103. Ann. ICRP 37 (2–4).

ICRP, 2009. Adult Reference Computational Phantoms. ICRP Publication 110. Ann. ICRP 39 (2).

ICRP, 2010. Conversion Coefficients for Radiological Protection Quantities for External Radiation Exposures. ICRP Publication 116, Ann. ICRP 40 (2–5).

ICRP, 2012. ICRP Statement on Tissue Reaction and Early and Late Effects of Radiation in Normal Tissues and Organs – Threshold Doses for Tissue Reactions in a Radiation Protection Context. ICRP Publication 118. Ann. ICRP 41(1/2).

ICRP, 2015. Occupational Intakes of Radionuclides: Part 1. ICRP Publication 130. Ann. ICRP 44(2).

ICRP, 2016. The ICRP Computational Framework for Internal Dose Assessment for Reference Adults: Specific Absorbed Fractions. ICRP Publication 133. Ann. ICRP 45(2).

ICRP, 2017a. Occupational Intakes of Radionuclides: Part 2. ICRP Publication 134. Ann. ICRP 45(3/4).

ICRP, 2017b. Occupational Intakes of Radionuclides: Part 3. ICRP Publication 137. Ann. ICRP 46(3/4).

ICRP, 2019. Occupational Intakes of Radionuclides: Part 4. ICRP Publication 141. Ann. ICRP 48(2/3).

ICRP, 2020a. Paediatric Reference Computational Phantoms. ICRP Publication 143. Ann. ICRP 49(1).

ICRP, 2020b. Dose Coefficients for External Exposures to Environmental Sources. ICRP Publication 144. Ann. ICRP 49(2).

ICRP, 2020c. Adult Mesh-type Reference Computational Phantoms. ICRP Publication 145. Ann. ICRP 49(3).

ICRP, 2022. Internal Dose Assessment for Reference Children: Specific Absorbed Fractions. ICRP Publication 1XX. Ann. ICRP XX(X) (will be published in 2022).

ICRU, 1992. Photon, Electron, Proton, and Neutron Interaction Data for Body Tissues. ICRU Report 46. International Commission on Radiation Units and Measurements, Bethesda, MD.

Ishii, K., Yamanari, M., Iwata, H., et al., 2013. Relationship between changes in crystalline lens shape and axial elongation in young children. Invest. Ophtalmol. Vis. Sci. 54, 771–777.

Joshi, S.D., Joshi, S.S., Daimi, S.R., et al., 2010. The thyroid gland and its variations: a cadaveric study. Folia Morphol. 69, 47–50.

Kainz, W., Neufeld, E., Bolch, W.E. et al., 2019. Advances in Computational Human Phantoms and Their Applications in Biomedical Engineering. A Topical Review IEEE Transactions on Radiation and Plasma Medical Sciences. 3, 1–23.

Kim, C.H., Jeong, J.H., Bolch, W.E., et al., 2011. A polygon-surface reference Korean male phantom (PSRK-Man) and its direct implementation in Geant4 Monte Carlo simulation. Phys. Med. Biol. 56, 3137–3161.

Kim, D.W., Lee, S.J., Choi, E.J., et al., 2014. Morphologic diversities of sacral canal in children; three-dimensional computed tomographic study. Korean J. Pain. 27, 253–259.

Kim, H.S., Yeom, Y.S., Nguyen, T.T., et al., 2017. Inclusion of thin target and source regions in alimentary and respiratory tract systems of mesh-type ICRP adult reference phantoms. Phys. Med. Biol. 62, 2132–2152.

Kim, H.S., 2022. Physical Phantoms Constructed from the ICRP Adult Mesh-type Reference Computational Phantoms (will be submitted in 2022).

Kozak, F.K., Ospina, J.C., 2014. Characteristics of normal and abnormal postnatal craniofacial growth and development. Cummings Pediatric Otolaryngology, Elsevier. 55–80.

Kramer, R., Zankl, M., Williams, G., et al., 1982. The calculation of Dose from External Photon Exposures Using Reference Human Phantoms and Monte Carlo Methods. Part I: The male (Adam) and Female (Eva) Adult Mathematical Phantoms. GSF-Report S-885. GSF – National Research Center for Environment and Health, Neuherberg.

Larsen, J., 1971a. The sagittal growth of the eye: 1. Ultrasonic measurement of the depth of the anterior chamber from birth to puberty, Acta Ophthalmol. 49, 239–262.

Larsen, J., 1971b. The sagittal growth of the eye: 2. Ultrasonic measurement of the axial diameter of the lens and the anterior segment from birth to puberty. Acta Ophthalmol. 49, 427–440.

Lee, C., Lodwick, D., Hasenauer, D., et al., 2007. Hybrid computational phantoms of the male and female newborn patient: NURBS-based whole-body models. Phys. Med. Biol. 52, 3309–3333.

Lee, C., Lodwick, D., Williams, J.L., et al., 2008. Hybrid computational phantoms of the 15-year male and female adolescent: Applications to CT organ dosimetry for patients of variable morphometry. Med. Phys. 35, 2366–2382.

Lee, C., Lodwick, D., Hurtado, J., et al., 2010. The UF family of reference hybrid phantoms for computational radiation dosimetry. Phys. Med. Biol. 55, 339–363.

Lee, H., Yeom, Y.S., Nguyen, T.T., et al., 2019. Percentile-specific computational phantoms constructed from ICRP mesh-type reference computational phantoms (MRCPs). Phys. Med. Biol. 64. 045005.

Li, Z., Park, B.K., Liu, W., et al., 2015. A statistical skull geometry model for children 0–3 years old. PLoS One 10, 1–13.

Likhtarev, I.A., Gulko, G.M., Sobolev, B.G., et al., 1995. Evaluation of the 131I thyroid-monitoring measurements performed in Ukraine during May and June of 1986. Health Physics. 69, 6–15.

Lombardo, P.A., Vanhavere, F., Lebacq, A.L., et al., 2018. Development and validation of the realistic anthropomorphic flexible (RAF) phantom. Health Phys. 114, 489–499.

Ma, R., Qiu, R., Li, J., 2017. Development of mesh-type Chinese pediatric reference phantoms series. 6th International Workshop on Computational Human Phantoms.

Martz, R.L., 2017. The MCNP6 book on unstructured mesh geometry: a user's guide for MCNP6.2. Report LA-UR-17-22442. Los Alamos National Laboratory, Los Alamos, NM.

Müller, A., Doughty, M.J., 2002. Assessments of corneal endothelial cell density in growing children and its relationship to horizontal corneal diameter. Optom. Vis. Sci. 79, 762–770.

Mutti, D.O., Zadnik, K., Fusaro, R.E., et al., 1998. Optical and structural development of the crystalline lens in childhood. Invest. Ophthalmol. Vis. Sci. 39, 120–133.

Naqshi, B.F., Seth, S., Shah, A.B., et al., 2016. Thyroid Hemiagenesis with Agenesis of Isthmus a Case Report. J. Med. Sci. Clin. Res. 4, 10799–10801.

Noorizadeh, N., Kazemi, K., Grebe, R., et al., 2015. Evaluation of anterior fontanel size and area in the newborn using CT images. J. Intell. Fuzzy. Syst. 29, 443–450.

Norris, H., Zhang, Y., Bond, J., et al., 2017. A set of 4D pediatric XCAT reference phantoms for multimodality research. Med. Phys. 41, 033701.

Ogorelec, Z., 1997. The Growth of Human Teeth: A Simple Description of its Kinetics. Acta Stomatol. Croat. 31, 389–395.

Ozguner, G., Sulak, O., 2014. Size and location of thyroid gland in the fetal period. Surg. Radiol. Anat. 36, 359–367.

Ozgur, Z., Celik, S., Govsa, F., et al., 2011. Anatomical and surgical aspects of the lobes of the thyroid glands. Eur. Arch. Otorhinolaryngol. 268, 1357–1363.

Paquette, L.B., Jackson, H.A., Tavaré, C.J., et al., 2009. In utero eye development documented by fetal MR imaging. Am. J. Neuroradiol. 30, 1787–1791.

Park, J.S., Chung, M.S., Hwang, S.B., et al., 2005. Visible Korean Human: Improved Serially Sectioned Images of the Entire Body. IEEE Trans. Med. Imaging 24, 352–360.

PEDIG, 2011. Central Corneal Thickness in Children. Arch. Ophthalmol. 129, 1132–1138.

Pelowitz, D.B., 2008. MCNPX User's Manual, Version 2.6.0. LA-CP-07-1473. Los Alamos National Laboratory, Los Alamos, NM.

Pi, Y., Liu, T., Xu, X.G., 2018. Development of A Set of Mesh-based And Age-dependent Chinese Phantoms and Application for Ct Dose Calculations. Radiat. Prot. Dosim. 179, 370–382.

Ronneburger, A., Basarab, J., Howland, H.C., 2006. Growth of the cornea from infancy to adolescence. Ophtalmic Physiol. Opt. 26, 80–87.

Schwartz, J.H., 1995. Skeleton keys: an introduction to human skeletal morphology, development, and analysis. Oxford: Oxford University Press.

Schwarz, B. C., Godwin, W. J., Wayson, M. B., et al. 2021. Specific absorbed fractions for a revised series of the UF/NCI pediatric reference phantoms: internal photon sources. Phys. Med. Biol. 66, 035006.

Sea, J.H., Ji, H., You, S.K., et al. 2019. Age-dependent reference values of the thyroid gland in pediatric population; from routine computed tomography data. Clin. Imag. 56, 88–92.

Segars, W.P., Sturgeon, G., Mendonca, S., et al. 2010. 4D XCAT phantom for multimodality imaging research. Med. Phys. 37, 4902–4915.

Shin, B., Choi, C., Yeom, Y.S., et al. 2021. Detailed Tooth Models for ICRP Mesh-type Reference Computational Phantoms. J. Radiol. Prot. 41, 669–688.

Si, H., 2015. TetGen, a Delaunay-Based Quality Tetrahedral Mesh Generator. ACM Trans. Math. Softw. 41, 1–36.

Snyder, W.S., Ford, M.R., Warner, G.G., et al., 1969. Estimates of Absorbed Fractions for Monoenergetic Photon Sources Uniformly Distributed in Various Organs of a Heterogeneous Phantom. J. Nucl. Med. 10: Suppl. No. 3, 7–52.

Snyder, W.S., Ford, M.R., Warner, G.G., 1978. Estimates of Specific Absorbed Fractions for Monoenergetic Photon Sources Uniformly Distributed in Various Organs of a Heterogeneous Phantom. MIRD Pamphlet No. 5, Revised. Society of Nuclear Medicine, New York.

Stabin, M.G., Watson, E.E., Cristy, M., et al., 1995. Mathematical models and specific absorbed fractions of photon energy in the nonpregnant adult female and at the end of each trimester of pregnancy. ORNL Report TM-12907. Oak Ridge National Laboratory, Oak Ridge, TN.

Stepusin, E.J., 2016. Pre-Computed Monte Carlo Dosimetry and Reporting for Computed 782 Tomography. Biomedical Engineering, University of Florida, Dissertation.

Sukonpan, K., Phupong, V., 2009. A biometric study of the fetal orbit and lens in normal pregnancies. J. Clin. Ultrasound 37, 69–74.

Sultana, S.Z., Khalil, M., Khan, M.K., et al., 2011. Morphometry of isthmus of thyroid gland in Bangladeshi cadaver. Mymensingh Med. J. 20, 366–370.

Taylor, J.R., 1975. Growth of human intervertebral discs and vertebral bodies. J. Anat. 120, 49–68.

Tong, E.C.K., Rubenfeld, S., 1972. Scan measurements of normal and enlarged thyroid gland. Am. J. Roentgenol. Radium Ther. Nucl. Med. 1–5, 706–708.

Ulanovsky, A., Wieser, A., Zankl, M., et al., 2005, Photon dose conversion coefficients for human teeth in standard irradiation geometries. Health. Phys. 89, 645–659.

Ulanovsky, A. and Wieser, A., 2007, External exposure of deciduous tooth enamel to photons: dose conversion coefficients for standard radiation fields. Radiat. Environ. Biophys. 46, 339–348.

Usman, N., Dilkash, N.A., Khan, S., et al. 2011. Study of Relationship Between Changes in Size of Posterior Fontanelle with Gestational Age. Natl. J. Integr. Res. Med. 2, 1–3.

Wayson, M.B., 2012. Computational internal dosimetry methods as applied to the University of Florida series of hybrid phantoms. Biomedical Engineering, University of Florida, Dissertation.

Wayson, M.B., Leggetti, R.W., Jokisch, D.W., et al., 2018. Suggested reference values for regional blood volumes in children and adolescents. Phys. Med. Biol. 63, 155022.

White, D.R., Woodard, H.Q. and Hammond, S.M., 1987. Average soft-tissue and bone models for use in radiation dosimetry. Br. J. Radiol. 60, 907–9013.

Won, H.S., Han, S.H. Oh, C.S., et al., 2013. The location and morphometry of the thyroid isthmus in adult Korean cadavers. Anat. Sci. Int. 88, 212–216.

Yeom, Y.S., Han, M.C., Kim, C.H., et al., 2013. Conversion of ICRP male reference phantom to polygon-surface phantom. Phys. Med. Biol. 58, 6985–7007.

Yeom, Y.S., Jeong, J.H., Han, M.C., et al., 2014. Tetrahedral-mesh-based computational human phantom for fast Monte Carlo dose calculations. Phys. Med. Biol. 59, 3173–3185.

Yeom, Y.S., Kim, C.H., Nguyen, T.T., et al., 2016. Construction of new skin models and calculation of skin dose coefficients for electron exposures. J. Korean Phys. Soc. 69, 512–517.

Yeom, Y.S., Nguyen, T.T., Choi, C., et al., 2017. Implications of using a 50-μm-thick skin target layer in skin dose coefficient calculation for photons, protons, and helium ions. Nucl. Eng. Technol. 49, 1495–1504.

Yeom, Y.S., Han, H., Choi, C. et al., 2019a. Posture-dependent dose coefficients of mesh-type ICRP reference computational phantoms for photon external exposures. Phys. Med. Biol. 64, 075018.

Yeom, Y.S., Choi, C., Han, H. et al., 2019b. Dose coefficients of mesh-type ICRP reference computational phantoms for idealized external exposures of photons and electron. Nucl. Eng. Technol. 51, 843–852.

Yeom, Y.S., Choi, C., Han, H. et al., 2020. Dose coefficients of mesh-type ICRP reference computational phantoms for external exposures of neutrons, protons, and helium ions. Nucl. Eng. Technol. 52, 1545–1556.

Yeom, Y.S., 2022. Development of Thyroid Model for ICRP Pediatric Mesh-type Reference Computational Phantoms (under review).

Zadnik, K., Mutti, D.O., Mitchell, G.L., et al., 2004. Normal eye growth in emmetropic schoolchildren. Optom. Vis. Sci. 81, 819–828.

Zander, H.A., Hürzeler, B., 1958. Continuous cementum apposition. J. Dental. Research. 37, 1035–1044.

Zankl, M. and Wittmann, A., 2001. The adult male voxel model “Golem” segmented from whole-body CT patient data. Radiat. Environ. Biophys. 40, 153–162.

Zhang, J., Na, Y., Caracappa, P., et al., 2009. RPI-AM and RPI-AF, a pair of mesh-based, size-adjustable adult male and female computational phantoms using ICRP-89 parameters and their calculations for organ doses from monoenergetic photon beams. Phys. Med. Biol. 54, 5885–5908.

ANNEX A. LIST OF ORGAN ID, MEDIUM AND MASS OF EACH ORGAN/TISSUE

Table A.1. List of organ ID, medium and mass of organs/tissues for the TM-version of the newborn, 1-year-old, 5-year-old, 10-year-old and 15-year-old male and female phantoms.

Organ ID	Organ/tissue	Medium	Mass (g)									
			Newborn		1 year		5 years		10 years		15 years	
			Male	Female	Male	Female	Male	Female	Male	Female	Male	Female
100	Adrenal, left	1	3.601	3.601	2.256	2.256	2.974	2.975	4.180	4.180	6.215	5.236
200	Adrenal, right	1	3.601	3.601	2.256	2.256	2.974	2.975	4.180	4.180	6.215	5.236
300	ET$_1$, 0 ~ 8 μm	2	0.000741	0.000738	0.00124	0.00125	0.00268	0.00259	0.00260	0.00259	0.0106	0.00194
301	ET$_1$, 8 ~ 40 μm	2	0.00304	0.00303	0.00504	0.00510	0.0109	0.0105	0.0105	0.0105	0.0425	0.00790
302	ET$_1$, 40 ~ 50 μm	2	0.000976	0.000972	0.00160	0.00163	0.00345	0.00333	0.00334	0.00332	0.0134	0.00251
303	ET$_1$, 50 μm ~ surface	2	0.0968	0.0954	0.218	0.212	0.316	0.330	0.667	0.664	4.145	0.729
400	ET$_2$, -15 ~ 0 μm	73	0.0327	0.0330	0.0692	0.0693	0.127	0.129	0.138	0.136	0.200	0.148
401	ET$_2$, 0 ~ 40 μm	2	0.0938	0.0945	0.198	0.197	0.364	0.367	0.395	0.387	0.572	0.422
402	ET$_2$, 40 ~ 50 μm	2	0.0237	0.0239	0.0498	0.0496	0.0917	0.0925	0.0995	0.0973	0.144	0.106
403	ET$_2$, 50 ~ 55 μm	2	0.0119	0.0120	0.0249	0.0249	0.0460	0.0463	0.0498	0.0488	0.0720	0.0531
404	ET$_2$, 55 ~ 65 μm	2	0.0238	0.0240	0.0500	0.0498	0.0921	0.0928	0.100	0.098	0.144	0.106
405	ET$_2$, 65 μm ~ surface	2	2.144	1.685	6.934	6.031	16.626	19.227	19.647	22.187	30.927	24.777
500	Oral mucosa, tongue	3	0.00810	0.00811	0.0187	0.0186	0.0311	0.0313	0.0509	0.0502	0.0767	0.0719
501	Oral mucosa, mouth floor	3	0.00980	0.00980	0.0143	0.0143	0.0190	0.0187	0.0245	0.0244	0.0317	0.0292
600	Oral mucosa, lips and cheeks	3	0.00649	0.00641	0.00450	0.00425	0.0133	0.0144	0.0211	0.0212	0.0212	0.0178
700	Trachea	2	0.542	0.542	1.561	1.561	2.600	2.583	4.701	4.677	7.930	6.212
800	BB$_1^*$, -11 ~ -6 μm	73	0.00159	0.00159	0.00302	0.00302	0.00220	0.00220	0.00499	0.00499	0.00916	0.00858
801	BB$_1^*$, -6 ~ 0 μm	2	0.00204	0.00203	0.00387	0.00385	0.00282	0.00281	0.00639	0.00636	0.0117	0.0109
802	BB$_1^*$, 0 ~ 10 μm	2	0.00342	0.00341	0.00648	0.00645	0.00473	0.00471	0.0107	0.0106	0.0196	0.0183
803	BB$_1^*$, 10 ~ 35 μm	2	0.00863	0.00860	0.0163	0.0163	0.0120	0.0119	0.0268	0.0267	0.0492	0.0458
804	BB$_1^*$, 35 ~ 40 μm	2	0.00174	0.00173	0.00329	0.00327	0.00243	0.00242	0.00539	0.00537	0.00987	0.00920
805	BB$_1^*$, 40 ~ 50 μm	2	0.00349	0.00348	0.00660	0.00657	0.00489	0.00487	0.0108	0.0108	0.0198	0.0184
806	BB$_1^*$, 50 ~ 60 μm	2	0.00352	0.00350	0.00663	0.00660	0.00493	0.00490	0.0109	0.0108	0.0198	0.0185
807	BB$_1^*$, 60 ~ 70 μm	2	0.00353	0.00352	0.00667	0.00663	0.00497	0.00494	0.0109	0.0108	0.0199	0.0185
808	BB$_1^*$, 70 μm ~ surface	2	0.352	0.350	1.920	1.911	3.383	3.367	2.823	2.809	7.237	6.639
900	Blood in large arteries, head	4	0.0766	0.0766	0.153	0.155	0.282	0.285	0.625	0.644	1.333	0.722
910	Blood in large veins, head	4	0.280	0.281	0.507	0.511	1.850	1.830	1.913	1.923	3.474	3.320
1000	Blood in large arteries, trunk	4	9.296	9.251	14.943	14.921	37.204	37.063	58.078	58.644	103.887	85.067
1010	Blood in large veins, trunk	4	23.049	22.888	39.286	39.435	103.180	103.365	134.162	137.193	242.655	171.713
1100	Blood in large arteries, arms	4	1.826	1.849	3.247	3.282	7.361	7.321	12.278	11.728	29.990	25.736
1110	Blood in large veins, arms	4	7.149	7.272	14.267	14.534	46.392	46.454	90.648	88.267	142.125	96.255
1200	Blood in large arteries, legs	4	6.200	6.223	13.469	13.455	45.100	45.278	78.914	78.872	152.559	98.425
1210	Blood in large veins, legs	4	21.720	21.760	41.378	40.957	118.413	118.174	222.953	222.299	474.985	358.632
1300	Humeri, upper, cortical	5	1.924	1.924	12.671	12.671	28.834	28.834	88.307	88.307	153.118	124.843
1400	Humeri, upper, spongiosa	6	3.545	3.545	8.730	8.730	20.156	20.156	52.648	52.648	172.915	133.667
1500	Humeri, upper, medullary cavity	7	0.322	0.322	0.863	0.863	3.765	3.765	9.795	9.795	19.317	15.042
1600	Humeri, lower, cortical	5	1.850	1.850	9.035	9.035	22.274	22.274	67.363	67.363	167.635	133.909
1700	Humeri, lower, spongiosa	8	2.768	2.768	4.519	4.519	11.026	11.026	26.263	26.263	70.768	55.192
1800	Humeri, lower, medullary cavity	9	0.322	0.322	0.809	0.809	3.564	3.564	9.766	9.766	16.556	12.753
1900	Radii, cortical	5	1.213	1.214	5.616	5.615	14.849	14.849	44.007	44.007	97.596	84.248
1910	Ulnae, cortical	5	1.551	1.551	7.415	7.415	18.778	18.778	56.671	56.672	124.440	105.367

2000	Radii, spongiosa	10	1.697	1.698	1.117	1.117	3.314	3.314	7.239	7.239	37.902	28.355
2010	Ulnae, spongiosa	11	2.159	2.159	1.812	1.812	5.492	5.492	12.632	12.632	54.219	41.425
2100	Radii, medullary cavity	12	0.122	0.122	0.359	0.359	2.301	2.301	6.288	6.288	6.590	5.643
2110	Ulnae, medullary cavity	13	0.143	0.143	0.589	0.589	2.626	2.626	6.912	6.912	8.386	6.994
2200	Wrists and hand bones, cortical	5	0.841	0.841	5.399	5.399	9.335	9.335	32.585	32.585	130.632	108.276
2300	Wrists and hand bones, spongiosa	14	3.175	3.175	14.073	14.073	16.482	16.482	37.057	37.057	59.944	48.594
2400	Clavicles, cortical	5	0.915	0.915	1.368	1.368	6.181	6.181	14.383	14.383	43.288	56.937
2500	Clavicles, spongiosa	15	1.673	1.673	1.963	1.964	7.957	7.957	17.017	17.017	21.095	26.604
2600	Cranium, cortical	5	21.449	21.460	91.486	91.486	229.093	229.118	328.089	328.082	544.127	450.603
2700	Cranium, spongiosa	16	78.766	78.789	289.874	289.963	520.373	520.560	497.534	497.175	493.256	391.553
2800	Femora, upper, cortical	5	3.755	3.755	14.111	14.111	49.468	49.468	164.695	164.714	314.770	236.151
2900	Femora, upper, spongiosa	17	5.772	5.772	8.867	8.863	26.096	26.096	75.472	75.472	251.197	186.875
3000	Femora, upper, medullary cavity	18	0.737	0.737	0.994	0.994	8.215	8.215	25.189	25.189	49.294	34.927
3100	Femora, lower, cortical	5	5.511	5.511	20.536	20.536	48.062	48.062	152.121	152.143	243.605	255.040
3200	Femora, lower, spongiosa	19	4.777	4.777	8.765	8.769	28.737	28.737	90.514	90.514	308.417	271.337
3300	Femora, lower, medullary cavity	20	1.174	1.174	1.568	1.568	5.794	5.794	16.906	16.906	36.212	38.343
3400	Tibiae, cortical	5	4.503	4.503	26.332	26.331	73.040	73.040	240.889	240.889	381.346	325.556
3410	Fibulae, cortical	5	1.158	1.158	3.024	3.024	10.254	10.254	32.677	32.677	72.322	54.325
3420	Patellae, cortical	5	0.0374	0.0374	0.162	0.162	1.189	1.189	2.595	2.595	21.420	17.537
3500	Tibiae, spongiosa	21	6.624	6.624	7.275	7.275	23.028	23.028	62.567	62.567	264.537	227.056
3510	Fibulae, spongiosa	22	1.394	1.394	0.565	0.565	2.789	2.789	7.385	7.385	31.687	24.536
3520	Patellae, spongiosa	23	0.171	0.171	0.575	0.575	5.569	5.569	12.630	12.630	22.257	17.825
3600	Tibiae, medullary cavity	24	0.673	0.673	2.203	2.203	8.261	8.261	26.272	26.272	59.424	48.773
3610	Fibulae, medullary cavity	25	0.107	0.107	0.204	0.204	1.871	1.871	5.576	5.576	8.185	5.809
3700	Ankles and foot, cortical	5	1.289	1.289	7.235	7.235	33.249	33.249	93.863	93.863	217.341	176.948
3800	Ankles and foot, spongiosa	26	4.926	4.926	20.331	20.331	70.793	70.793	159.839	159.839	387.180	306.517
3900	Mandible, cortical	5	1.700	1.700	7.164	7.164	19.289	19.282	24.910	24.909	59.285	47.273
4000	Mandible, spongiosa	27	5.693	5.693	13.095	13.095	29.495	29.477	27.505	27.504	37.750	28.847
4100	Pelvis, cortical	5	6.147	6.147	21.200	21.202	58.226	58.226	128.933	128.933	188.605	215.135
4200	Pelvis, spongiosa	28	8.689	8.689	34.395	34.395	99.470	99.470	285.898	285.898	512.498	553.247
4300	Ribs, cortical	5	6.389	6.389	20.410	20.410	38.511	38.511	70.415	70.415	169.281	186.406
4400	Ribs, spongiosa	29	21.362	21.362	58.121	58.121	79.112	79.112	138.704	138.704	198.249	208.053
4500	Scapulae, cortical	5	2.447	2.447	9.647	9.647	29.302	29.302	59.267	59.267	124.479	172.602
4600	Scapulae, spongiosa	30	4.457	4.457	14.863	14.863	42.719	42.719	90.282	90.282	110.814	147.468
4700	Cervical spine, cortical	5	3.774	3.774	3.276	3.275	6.992	6.992	14.127	14.127	33.755	42.945
4800	Cervical spine, spongiosa	31	7.135	7.135	9.103	9.103	14.083	14.083	30.749	30.749	56.493	68.327
4900	Thoracic spine, cortical	5	8.531	8.538	11.501	11.501	33.105	33.105	68.387	68.387	90.861	84.062
5000	Thoracic spine, spongiosa	32	10.497	10.499	28.110	28.110	74.596	74.596	211.317	211.317	264.347	230.516
5100	Lumbar spine, cortical	5	2.728	2.728	7.073	7.073	16.796	16.796	36.752	36.752	35.528	41.247
5200	Lumbar spine, spongiosa	33	7.849	7.849	21.948	21.936	58.995	58.995	161.646	161.646	255.535	270.609
5300	Sacrum, cortical	5	1.084	1.084	5.453	5.453	11.696	11.696	16.667	16.667	69.681	86.543
5400	Sacrum, spongiosa	34	3.140	3.140	15.116	15.116	34.521	34.521	55.236	55.236	118.649	140.213
5500	Sternum, cortical	5	0.168	0.168	0.630	0.630	2.469	2.469	5.282	5.282	22.161	15.671
5600	Sternum, spongiosa	35	0.677	0.677	2.103	2.103	8.505	8.505	20.823	20.823	42.389	28.431
5700	Cartilage, head	36	53.068	52.989	5.027	5.027						
5800	Cartilage, trunk	36	48.202	48.202	36.850	36.850	55.137	55.137	129.154	129.154	152.190	162.007
5900	Cartilage, arms	36	11.539	11.539								
6000	Cartilage, legs	36	15.378	15.378								
6100	Brain	37	395.660	395.660	978.101	978.101	1374.203	1244.203	1467.081	1287.082	1496.739	1348.990
6200	Breast, left, adipose tissue	38	0.0870	0.0870	0.571	0.572	1.178	1.171	2.038	2.028	4.758	77.618
6300	Breast, left, glandular tissue	39	0.0580	0.0580	0.381	0.381	0.785	0.781	1.359	1.352	3.172	51.751
6400	Breast, right, adipose tissue	38	0.0870	0.0870	0.571	0.572	1.178	1.171	2.038	2.028	4.758	77.616
6500	Breast, right, glandular tissue	39	0.0580	0.0580	0.381	0.381	0.785	0.781	1.359	1.352	3.172	51.751

6600	Eye lens, sensitive, left	40	0.0162	0.0162	0.0169	0.0169	0.0202	0.0202	0.0184	0.0184	0.0203	0.0203
6601	Eye lens, insensitive, left	41	0.0673	0.0673	0.0978	0.0978	0.114	0.114	0.113	0.113	0.117	0.117
6700	Cornea, left	42	0.582	0.582	0.629	0.629	0.870	0.870	0.941	0.941	0.996	0.996
6701	Aqueous, left	43	0.174	0.174	0.275	0.275	0.294	0.294	0.327	0.327	0.344	0.344
6702	Vitreous, left	44	2.413	2.413	2.624	2.624	4.403	4.403	4.853	4.853	5.322	5.322
6800	Eye lens, sensitive, right	40	0.0162	0.0162	0.0169	0.0169	0.0202	0.0202	0.0184	0.0184	0.0203	0.0203
6801	Eye lens, insensitive, right	41	0.0673	0.0673	0.0978	0.0978	0.114	0.114	0.113	0.113	0.117	0.117
6900	Cornea, right	42	0.582	0.582	0.629	0.629	0.870	0.870	0.942	0.941	0.996	0.996
6901	Aqueous, right	43	0.174	0.174	0.275	0.275	0.294	0.294	0.327	0.327	0.344	0.344
6902	Vitreous, right	44	2.413	2.413	2.624	2.624	4.403	4.403	4.853	4.853	5.322	5.322
7000	Gall bladder wall	45	0.542	0.542	1.457	1.458	2.704	2.686	4.597	4.576	8.141	7.555
7100	Gall bladder contents	46	2.800	2.800	8.000	8.000	15.000	15.000	26.000	26.000	45.000	42.000
7200	Stomach wall, 0 ~ 60 µm	47	0.408	0.408	0.814	0.814	0.745	0.745	0.998	0.998	2.407	1.602
7201	Stomach wall, 60 ~ 100 µm	47	0.273	0.273	0.407	0.407	0.489	0.489	0.667	0.667	1.605	1.070
7202	Stomach wall, 100 ~ 300 µm	47	1.384	1.384	2.056	2.056	2.469	2.469	3.361	3.361	8.068	5.385
7203	Stomach wall, 300 µm ~ surface	47	6.663	6.665	19.881	19.881	57.962	57.962	100.420	100.408	143.657	136.315
7300	Stomach contents	49	40.000	40.000	67.000	67.000	83.000	83.000	117.000	117.000	200.000	200.000
7400	Small intestine wall, 0 ~ 130 µm	48	3.220	3.218	4.934	4.934	6.595	6.595	8.740	8.698	12.504	12.460
7401	Small intestine wall, 130 ~ 150 µm	48	0.503	0.503	0.770	0.770	1.031	1.031	1.365	1.365	1.948	1.941
7402	Small intestine wall, 150 ~ 200 µm	48	1.267	1.267	1.939	1.939	2.597	2.597	3.435	3.435	4.897	4.880
7403	Small intestine wall, 200 µm ~ surface	48	33.226	33.215	92.166	92.256	266.743	266.743	454.794	454.418	673.314	616.548
7500	Small intestine contents, -400/-500[†] ~ 0 µm	49	9.275	9.273	14.320	14.320	19.024	19.024	31.330	31.371	45.272	45.187
7501	Small intestine contents, centre ~ -400/-500[†] µm	49	46.725	46.727	78.680	78.680	97.976	97.976	131.670	131.670	234.729	234.813
7600	Ascending colon wall, 0 ~ 280 µm	48	1.140	1.140	1.572	1.572	1.907	1.907	2.588	2.588	3.641	3.658
7601	Ascending colon wall, 280 ~ 300 µm	48	0.0832	0.0832	0.114	0.114	0.139	0.139	0.188	0.188	0.264	0.265
7602	Ascending colon wall, 300 µm ~ surface	48	2.795	2.795	9.364	9.370	26.671	26.673	50.903	50.876	76.362	68.667
7700	Ascending colon contents	49	15.594	15.594	26.017	26.017	31.346	31.346	45.283	45.283	77.810	77.810
7800	Transverse colon wall, right, 0 ~ 280 µm	48	0.842	0.842	1.200	1.200	1.580	1.580	1.924	1.924	2.662	2.673
7801	Transverse colon wall, right, 280 ~ 300 µm	48	0.0618	0.0618	0.0878	0.0878	0.116	0.116	0.140	0.140	0.193	0.194
7802	Transverse colon wall, right, 300 µm ~ surface	48	3.989	3.989	11.135	11.138	31.214	31.228	51.687	51.707	79.877	72.880
7900	Transverse colon contents, right	49	8.406	8.406	13.983	13.983	18.654	18.654	24.717	24.717	42.190	42.190
8000	Transverse colon wall, left, 0 ~ 280 µm	48	0.651	0.651	1.029	1.029	1.101	1.101	1.486	1.486	2.191	2.147
8001	Transverse colon wall, left, 280 ~ 300 µm	48	0.0481	0.0481	0.0757	0.0757	0.0808	0.0808	0.109	0.109	0.160	0.157
8002	Transverse colon wall, left, 300 µm ~ surface	48	3.802	3.802	10.300	10.300	27.086	27.083	45.608	45.608	74.084	67.632
8100	Transverse colon contents, left	49	5.418	5.418	8.933	8.933	10.920	10.920	15.054	15.054	27.012	27.012
8200	Descending colon wall, 0 ~ 280 µm	48	0.780	0.780	1.232	1.232	1.504	1.504	2.013	2.013	2.693	2.687
8201	Descending colon wall, 280 ~ 300 µm	48	0.0575	0.0575	0.0906	0.0906	0.110	0.110	0.148	0.148	0.197	0.196
8202	Descending colon wall, 300 µm ~ surface	48	3.572	3.572	10.753	10.753	31.744	31.746	58.010	58.063	83.743	75.444
8300	Descending colon contents	49	6.582	6.582	11.067	11.067	14.081	14.081	19.946	19.946	32.988	32.988
8400	Sigmoid colon wall, 0 ~ 280 µm	48	0.965	0.965	1.558	1.568	1.811	1.811	2.452	2.452	3.260	3.220
8401	Sigmoid colon wall, 280 ~ 300 µm	48	0.0710	0.0710	0.115	0.115	0.133	0.133	0.180	0.180	0.238	0.235
8402	Sigmoid colon wall, 300 µm ~ surface	48	2.223	2.223	7.999	7.987	22.780	22.776	42.083	42.101	61.660	55.580
8500	Sigmoid colon contents	49	8.521	8.521	13.983	13.983	17.992	17.992	24.519	24.519	41.771	41.771
8600	Rectum wall, 0 ~ 280 µm	48	0.418	0.418	0.657	0.657	0.717	0.717	1.033	1.033	1.492	1.440
8601	Rectum wall, 280 ~ 300 µm	48	0.0309	0.0309	0.0484	0.0484	0.0527	0.0527	0.0758	0.0758	0.109	0.105
8602	Rectum wall, 300 µm ~ surface	48	0.111	0.111	1.363	1.363	2.176	2.175	4.708	4.710	8.110	7.527
8603	Rectum contents	49	3.479	3.479	6.017	6.017	7.008	7.008	10.481	10.481	18.229	18.229
8700	Heart wall	50	23.157	23.157	55.043	55.043	97.696	97.617	161.495	161.495	269.653	251.488
8800	Blood in heart chamber	4	26.000	26.000	48.000	48.000	134.999	134.999	230.000	230.000	430.000	320.000
8900	Kidney, left, cortex	51	9.460	9.460	27.763	27.763	49.837	49.847	82.031	82.031	119.394	105.694
9000	Kidney, left, medulla	51	3.379	3.379	9.915	9.915	17.799	17.810	29.299	29.299	42.641	37.747
9100	Kidney, left, pelvis	51	0.676	0.676	1.983	1.983	3.560	3.561	5.859	5.859	8.528	7.550
9200	Kidney, right, cortex	51	9.460	9.460	27.763	27.763	49.852	49.848	82.031	82.031	119.394	105.694

9300	Kidney, right, medulla	51	3.379	3.379	9.915	9.915	17.784	17.810	29.299	29.299	42.641	37.747
9400	Kidney, right, pelvis	51	0.676	0.676	1.983	1.983	3.560	3.561	5.859	5.859	8.528	7.550
9500	Liver	52	167.410	167.410	390.445	390.445	724.407	723.337	1059.764	1059.773	1707.819	1628.966
9700	Lung (AI), left	53	28.689	28.690	68.837	68.832	139.438	139.441	222.219	222.238	389.511	330.576
9900	Lung (AI), right	53	31.311	31.310	81.163	81.163	160.562	160.559	277.781	277.762	510.489	419.425
10000	Lymphatic nodes, ET	54	1.243	1.243	2.176	2.176	4.310	4.311	7.157	7.157	12.733	11.522
10100	Lymphatic nodes, thoracic	54	1.243	1.243	2.176	2.176	4.310	4.311	7.157	7.157	12.733	11.522
10200	Lymphatic nodes, head	54	0.429	0.429	0.752	0.752	1.489	1.489	2.473	2.472	4.399	3.980
10300	Lymphatic nodes, trunk	54	10.144	10.145	17.763	17.763	35.189	35.193	58.429	58.429	103.944	94.065
10400	Lymphatic nodes, arms	54	0.858	0.859	1.503	1.503	2.978	2.978	4.945	4.945	8.797	7.961
10500	Lymphatic nodes, legs	54	0.858	0.859	1.503	1.503	2.978	2.978	4.945	4.945	8.797	7.961
10600	Muscle, head	55	125.222	111.243	263.904	237.341	410.315	451.105	402.331	459.190	501.080	420.428
10700	Muscle, trunk	55	404.474	400.177	938.124	845.801	2429.028	2352.725	5411.448	5432.564	11448.780	7993.776
10800	Muscle, arms	55	80.200	85.671	203.970	220.014	516.123	515.041	1174.835	1081.028	2704.937	1525.566
10900	Muscle, legs	55	209.857	222.675	523.216	626.048	2372.297	2407.881	4269.153	4284.462	10002.930	7420.928
11000	Oesophagus wall, 0 ~ 190 µm	47	0.344	0.344	0.545	0.567	0.918	0.895	1.598	1.569	2.169	1.784
11001	Oesophagus wall, 190 ~ 200 µm	47	0.0188	0.0188	0.0296	0.0308	0.0496	0.0483	0.0858	0.0843	0.116	0.096
11002	Oesophagus wall, 200 µm ~ surface	47	2.132	2.132	5.214	5.192	11.370	11.390	20.609	20.657	36.640	34.197
11003	Oesophagus contents	49	2.022	2.022	3.786	3.786	7.135	7.135	11.908	11.908	21.842	21.033
11100	Ovary, left	56		0.168		0.423		1.058		1.839		3.193
11200	Ovary, right	56		0.168		0.423		1.058		1.839		3.193
11300	Pancreas	57	7.248	7.248	22.651	22.651	41.892	41.880	72.126	72.126	136.661	117.631
11400	Pituitary gland	45	0.108	0.108	0.156	0.156	0.260	0.259	0.366	0.364	0.529	0.518
11500	Prostate	58	0.868		1.040		1.247		1.672		4.546	
11600	RST, head	59	169.932	182.852	546.567	568.696	469.432	531.111	476.102	572.644	426.945	741.522
11700	RST, trunk	59	638.601	626.472	2629.911	2733.559	3273.639	3432.305	6672.482	6629.690	8266.877	10427.278
11800	RST, arms	59	56.999	53.600	209.725	225.132	667.281	608.369	597.727	678.047	1079.522	1778.736
11900	RST, legs	59	138.552	138.785	906.740	766.638	1839.962	1806.911	1822.673	1870.086	2565.001	5471.857
12000	Salivary glands, left	45	3.254	3.253	12.485	12.494	17.666	17.571	22.981	22.862	35.947	33.647
12100	Salivary glands, right	45	3.254	3.253	12.485	12.494	17.665	17.571	22.981	22.862	35.947	33.647
12200	Skin, head, insensitive	60	39.192	38.826	67.228	67.956	79.918	79.684	80.634	82.635	146.485	132.439
12201	Skin, head, sensitive, 40/50‡ ~ 100 µm	60	2.977	2.979	5.491	5.490	6.833	6.809	7.058	7.038	6.239	6.255
12300	Skin, trunk, insensitive	60	63.649	62.579	118.490	117.558	173.372	173.809	276.681	274.960	661.753	548.780
12301	Skin, trunk, sensitive, 40/50‡ ~ 100 µm	60	4.830	4.746	9.626	9.550	14.799	14.767	23.849	23.689	27.877	26.467
12400	Skin, arms, insensitive	60	26.252	26.302	51.837	53.757	95.991	94.607	145.191	145.694	401.730	318.655
12401	Skin, arms, sensitive, 40/50‡ ~ 100 µm	60	2.055	2.077	4.320	4.427	8.328	8.171	12.673	12.534	17.195	15.205
12500	Skin, legs, insensitive	60	41.719	43.118	96.053	94.424	199.966	201.347	287.831	287.273	807.546	697.557
12501	Skin, legs, sensitive, 40/50‡ ~ 100 µm	60	3.220	3.269	7.907	7.789	17.196	17.220	24.975	25.076	34.251	33.011
12600	Spinal cord	45	6.107	6.065	10.641	10.669	23.825	23.123	45.695	45.338	40.217	54.218
12700	Spleen	61	13.865	13.865	37.352	37.352	71.306	71.262	114.975	114.975	198.771	179.324
12800	Erupted, upper, front, buccal, permanent, enamel	62							0.352	0.350	0.650	0.564
12801	Erupted, upper, front, lingual, permanent, enamel	62							0.354	0.356	0.823	0.580
12802	Erupted, upper, front, buccal, deciduous, enamel	63			0.0709	0.0689	0.193	0.193	0.0680	0.0649		
12803	Erupted, upper, front, lingual, deciduous, enamel	63			0.0598	0.0617	0.165	0.165	0.0873	0.0903		
12804	Erupted, upper, front-left, buccal, permanent, enamel	62							0.117	0.108	0.317	0.219
12805	Erupted, upper, front-left, lingual, permanent, enamel	62							0.0766	0.0859	0.224	0.201
12806	Erupted, upper, front-right, buccal, permanent, enamel	62							0.0755	0.125	0.317	0.201
12807	Erupted, upper, front-right, lingual, permanent, enamel	62							0.118	0.0693	0.224	0.219
12808	Erupted, upper, left, buccal, permanent, enamel	62							0.303	0.250	0.513	0.426
12809	Erupted, upper, left, lingual, permanent, enamel	62							0.145	0.198	0.494	0.356
12810	Erupted, upper, left, buccal, deciduous, enamel	63					0.149	0.149	0.0983	0.0804		
12811	Erupted, upper, left, lingual, deciduous, enamel	63					0.159	0.159	0.0569	0.0749		
12812	Erupted, upper, right, buccal, permanent, enamel	62							0.216	0.218	0.477	0.381

12813	Erupted, upper, right, lingual, permanent, enamel	62							0.232	0.229	0.531	0.400
12814	Erupted, upper, right, buccal, deciduous, enamel	63					0.149	0.149	0.0760	0.0705		
12815	Erupted, upper, right, lingual, deciduous, enamel	63					0.158	0.158	0.0792	0.0848		
12816	Erupted, lower, front, buccal, permanent, enamel	62							0.532	0.516	0.605	0.444
12817	Erupted, lower, front, lingual, permanent, enamel	62							0.412	0.427	0.541	0.445
12818	Erupted, lower, front, buccal, deciduous, enamel	63			0.0453	0.0506	0.135	0.135				
12819	Erupted, lower, front, lingual, deciduous, enamel	63			0.0425	0.0373	0.138	0.138				
12820	Erupted, lower, front-left, buccal, permanent, enamel	62									0.239	0.181
12821	Erupted, lower, front-left, lingual, permanent, enamel	62									0.228	0.182
12822	Erupted, lower, front-right, buccal, permanent, enamel	62									0.244	0.200
12823	Erupted, lower, front-right, lingual, permanent, enamel	62									0.224	0.163
12824	Erupted, lower, left, buccal, permanent, enamel	62							0.176	0.270	0.536	0.334
12825	Erupted, lower, left, lingual, permanent, enamel	62							0.302	0.208	0.494	0.466
12826	Erupted, lower, left, buccal, deciduous, enamel	63					0.175	0.175	0.146	0.141		
12827	Erupted, lower, left, lingual, deciduous, enamel	63					0.234	0.234	0.111	0.116		
12828	Erupted, lower, right, buccal, permanent, enamel	62							0.232	0.237	0.593	0.396
12829	Erupted, lower, right, lingual, permanent, enamel	62							0.246	0.241	0.437	0.404
12830	Erupted, lower, right, buccal, deciduous, enamel	63					0.197	0.197	0.140	0.121		
12831	Erupted, lower, right, lingual, deciduous, enamel	63					0.213	0.213	0.117	0.136		
12832	Erupted, upper, front, permanent, dentin	64							2.387	2.385	4.944	3.835
12833	Erupted, upper, front, deciduous, dentin	65			0.299	0.300	0.821	0.820	0.350	0.350		
12834	Erupted, upper, front-left, permanent, dentin	64							0.655	0.654	1.809	1.406
12835	Erupted, upper, front-right, permanent, dentin	64							0.653	0.653	1.816	1.410
12836	Erupted, upper, left, permanent, dentin	64							1.518	1.511	3.391	2.625
12837	Erupted, upper, left, deciduous, dentin	65					0.708	0.708	0.350	0.354		
12838	Erupted, upper, right, permanent, dentin	64							1.513	1.512	3.392	2.636
12839	Erupted, upper, right, deciduous, dentin	65					0.708	0.708	0.355	0.352		
12840	Erupted, lower, front, permanent, dentin	64							3.140	3.160	3.764	2.935
12841	Erupted, lower, front, deciduous, dentin	65			0.199	0.200	0.617	0.617				
12842	Erupted, lower, front-left, permanent, dentin	64									1.559	1.213
12843	Erupted, lower, front-right, permanent, dentin	64									1.558	1.211
12844	Erupted, lower, left, permanent, dentin	64							1.628	1.627	3.465	2.690
12845	Erupted, lower, left, deciduous, dentin	65					0.948	0.948	0.591	0.590		
12846	Erupted, lower, right, permanent, dentin	64							1.624	1.630	3.462	2.681
12847	Erupted, lower, right, deciduous, dentin	65					0.948	0.948	0.595	0.593		
12848	Unerupted, permanent, enamel	62			0.146	0.146	1.626	1.626	1.926	1.926	1.218	0.945
12849	Unerupted, deciduous, enamel	63	0.190	0.190	0.952	0.952						
12850	Unerupted, permanent, dentin	64			0.486	0.489	5.402	5.430	6.443	6.436	4.115	3.183
12851	Unerupted, deciduous, dentin	65	0.425	0.426	2.204	2.205						
12852	Permanent, cementum	64			0.0239	0.0203	0.284	0.256	0.786	0.779	1.450	1.138
12853	Deciduous, cementum	65	0.0337	0.0323	0.125	0.122	0.242	0.242	0.125	0.128		
12854	Permanent, pulp	66			0.0146	0.0146	0.163	0.163	0.582	0.582	0.993	0.771
12855	Deciduous, pulp	66	0.0607	0.0607	0.374	0.374	0.661	0.661	0.313	0.313		
12856	Teeth, retention region	67			0.00345	0.00345	0.0211	0.0212	0.0382	0.0386	0.0505	0.0412
12900	Testis, left	56	0.443		0.773		0.907		1.090		8.518	
13000	Testis, right	56	0.443		0.773		0.907		1.090		8.518	
13100	Thymus	68	14.101	14.096	31.212	31.228	31.203	31.014	41.791	36.392	37.004	31.049
13200	Thyroid	69	1.490	1.490	1.967	1.968	3.871	3.871	9.022	9.022	14.036	13.505
13300	Tongue, upper (food)	3	3.054	3.053	5.973	5.973	9.148	9.116	12.989	12.950	19.029	18.085
13301	Tongue, lower	3	0.736	0.736	4.422	4.422	10.582	10.502	20.408	20.286	40.045	36.742
13400	Tonsils	45	0.108	0.108	0.521	0.521	2.080	2.068	3.134	3.120	3.172	3.107
13500	Ureter, left	45	0.418	0.418	1.145	1.145	2.184	2.172	3.658	3.641	6.344	6.210
13600	Ureter, right	45	0.418	0.418	1.145	1.145	2.184	2.172	3.658	3.641	6.344	6.210

13700	Urinary bladder wall, insensitive	70	3.571	3.576	8.158	8.169	15.418	15.416	24.211	24.206	39.000	33.933
13701	Urinary bladder wall, sensitive, α[§] ~ β[¶] µm	70	0.510	0.505	0.948	0.947	0.882	0.884	1.288	1.294	1.871	1.656
13800	Urinary bladder contents	71	12.400	12.400	32.900	32.900	64.700	64.700	103.000	103.000	160.000	140.000
13900	Uterus	58		4.337		1.562		3.100		4.158		31.064
14000	Air inside body	72	0.00261	0.00192	0.00925	0.00736	0.0240	0.0229	0.0529	0.0513	0.384	0.127

ET, extrathoracic; AI, alveolar-interstitium; RST, residual soft tissue.
[*] Only the main bronchi (BB_1) was defined in the TM-version phantoms. The other generations of the bronchi (BB) and all generations of the bronchioles (bb) were modelled in constructive solid geometry format.
[†] Newborn, 1 year, 5 years/10 years, 15 years.
[‡] Newborn, 1 year, 5 years, 10 years/15 years.
[§] Newborn: 54, 1 year: 71, 5 years: 86, 10 years: 99, 15 years male: 116, 15 years female: 111.
[¶] Newborn: 232, 1 year: 238, 5 years: 193, 10 years: 212, 15 years male: 238, 15 years female: 227.

Table A.2. List of organ ID, medium and mass of organs/tissues for the PM-version of the newborn, 1-year-old, 5-year-old, 10-year-old and 15-year-old male and female phantoms.

Organ ID	Organ/tissue	Medium	Mass (g)									
			Newborn		1-year-old		5-year-old		10-year-old		15-year-old	
			Male	Female	Male	Female	Male	Female	Male	Female	Male	Female
100	Adrenal, left	1	3.601	3.601	2.256	2.256	2.974	2.975	4.180	4.180	6.215	5.236
200	Adrenal, right	1	3.601	3.601	2.256	2.256	2.974	2.975	4.180	4.180	6.215	5.236
300	ET_1, 8 µm	2	0.000741	0.000738	0.00124	0.00125	0.00268	0.00259	0.00260	0.00259	0.0106	0.00194
301	ET_1, 40 µm	2	0.00304	0.00303	0.00504	0.00510	0.01088	0.01049	0.0105	0.0105	0.0425	0.00790
302	ET_1, 50 µm	2	0.000976	0.000972	0.00160	0.00163	0.00345	0.00333	0.00334	0.00332	0.0134	0.00251
303	ET_1, surface	2	0.0968	0.0954	0.218	0.212	0.316	0.330	0.667	0.664	4.145	0.729
400	ET_2, 0 µm	73	0.0327	0.0330	0.0692	0.0693	0.127	0.129	0.138	0.136	0.200	0.150
401	ET_2, 40 µm	2	0.0938	0.0945	0.198	0.197	0.364	0.367	0.395	0.387	0.572	0.426
402	ET_2, 50 µm	2	0.0237	0.0239	0.0498	0.0496	0.0917	0.0925	0.0995	0.0973	0.144	0.107
403	ET_2, 55 µm	2	0.0119	0.0120	0.0249	0.0249	0.0460	0.0463	0.0498	0.0488	0.0720	0.0537
404	ET_2, 65 µm	2	0.0238	0.0240	0.0500	0.0498	0.0921	0.0928	0.100	0.0977	0.144	0.108
405	ET_2, surface	2	2.144	1.685	6.934	6.031	16.626	19.227	19.647	22.187	30.927	24.770
500	Oral mucosa, tongue	3	0.00810	0.00811	0.0187	0.0186	0.0311	0.0313	0.0509	0.0502	0.0772	0.0719
501	Oral mucosa, mouth floor	3	0.00980	0.00980	0.0143	0.0143	0.0190	0.0187	0.0245	0.0244	0.0317	0.0292
600	Oral mucosa, lips and cheeks	3	0.00649	0.00641	0.00450	0.00425	0.0133	0.0144	0.0211	0.0212	0.0212	0.0178
700	Trachea	2	0.542	0.542	1.561	1.561	2.600	2.583	4.701	4.677	7.930	6.212
800	BB_1^*, -6 µm	73	0.00159	0.00159	0.00302	0.00302	0.00220	0.00220	0.00499	0.00499	0.00916	0.00858
801	BB_1^*, 0 µm	2	0.00204	0.00203	0.00387	0.00385	0.00282	0.00281	0.00639	0.00636	0.0117	0.0109
802	BB_1^*, 10 µm	2	0.00342	0.00341	0.00648	0.00645	0.00473	0.00471	0.0107	0.0106	0.0196	0.0183
803	BB_1^*, 35 µm	2	0.00863	0.00860	0.0163	0.0163	0.0120	0.0119	0.0268	0.0267	0.0492	0.0458
804	BB_1^*, 40 µm	2	0.00174	0.00173	0.00329	0.00327	0.00243	0.00242	0.00539	0.00537	0.00987	0.00920
805	BB_1^*, 50 µm	2	0.00350	0.00348	0.00660	0.00657	0.00489	0.00487	0.0108	0.0108	0.0198	0.0184
806	BB_1^*, 60 µm	2	0.00352	0.00350	0.00663	0.00660	0.00493	0.00490	0.0109	0.0108	0.0198	0.0185
807	BB_1^*, 70 µm	2	0.00353	0.00352	0.00667	0.00663	0.00497	0.00494	0.0109	0.0108	0.0199	0.0185
808	BB_1^*, surface	2	0.352	0.350	1.920	1.911	3.383	3.367	2.823	2.809	7.237	6.639
900	Blood in large arteries	4	17.398	17.400	31.812	31.812	89.946	89.946	149.891	149.895	287.770	209.978
910	Blood in large veins	4	52.197	52.200	95.437	95.438	269.837	269.829	449.648	449.633	863.307	629.936
1300	Humeri, upper, cortical	5	1.924	1.924	12.671	12.671	28.834	28.834	88.307	88.307	153.118	124.843
1400	Humeri, upper, spongiosa	6	3.545	3.545	8.730	8.730	20.156	20.156	52.648	52.648	172.915	133.667
1500	Humeri, upper, medullary cavity	7	0.322	0.322	0.863	0.863	3.765	3.765	9.795	9.795	19.317	15.042
1600	Humeri, lower, cortical	5	1.850	1.850	9.035	9.035	22.274	22.274	67.363	67.363	167.635	133.909
1700	Humeri, lower, spongiosa	8	2.768	2.768	4.519	4.519	11.026	11.026	26.263	26.263	70.768	55.192
1800	Humeri, lower, medullary cavity	9	0.322	0.322	0.809	0.809	3.564	3.564	9.766	9.766	16.556	12.753
1900	Radii, cortical	5	1.213	1.214	5.616	5.615	14.849	14.849	44.007	44.007	97.596	84.248
1910	Ulnae, cortical	5	1.551	1.551	7.415	7.415	18.778	18.778	56.671	56.672	124.440	105.367
2000	Radii, spongiosa	10	1.697	1.698	1.117	1.117	3.314	3.314	7.239	7.239	37.902	28.355
2010	Ulnae, spongiosa	11	2.159	2.159	1.812	1.812	5.492	5.492	12.632	12.632	54.219	41.425
2100	Radii, medullary cavity	12	0.122	0.122	0.359	0.359	2.301	2.301	6.288	6.288	6.590	5.643
2110	Ulnae, medullary cavity	13	0.143	0.143	0.589	0.589	2.626	2.626	6.912	6.912	8.386	6.994
2200	Wrists and hand bones, cortical	5	0.841	0.841	5.399	5.399	9.335	9.335	32.585	32.585	130.632	108.276
2300	Wrists and hand bones, spongiosa	14	3.175	3.175	14.073	14.073	16.482	16.482	37.057	37.057	59.944	48.594
2400	Clavicles, cortical	5	0.915	0.915	1.368	1.368	6.181	6.181	14.383	14.383	43.288	56.937
2500	Clavicles, spongiosa	15	1.673	1.673	1.963	1.964	7.957	7.957	17.017	17.017	21.095	26.604
2600	Cranium, cortical	5	21.449	21.460	91.486	91.486	229.093	229.118	328.089	328.082	544.127	450.594
2700	Cranium, spongiosa	16	78.766	78.789	289.874	289.963	520.373	520.560	497.534	497.175	493.237	391.553
2800	Femora, upper, cortical	5	3.755	3.755	14.111	14.111	49.468	49.468	164.619	164.717	315.080	236.162

2900	Femora, upper, spongiosa	17	5.772	5.772	8.867	8.863	26.096	26.096	75.472	75.472	251.197	186.875
3000	Femora, upper, medullary cavity	18	0.737	0.737	0.994	0.994	8.215	8.215	25.189	25.189	49.294	34.927
3100	Femora, lower, cortical	5	5.511	5.511	20.536	20.536	48.062	48.062	152.143	152.143	243.605	255.040
3200	Femora, lower, spongiosa	19	4.777	4.777	8.765	8.769	28.737	28.737	90.514	90.514	308.417	271.337
3300	Femora, lower, medullary cavity	20	1.174	1.174	1.568	1.568	5.794	5.794	16.906	16.906	36.212	38.343
3400	Tibiae, cortical	5	4.503	4.503	26.332	26.331	73.040	73.040	240.889	240.889	381.346	325.554
3410	Fibulae, cortical	5	1.158	1.158	3.024	3.024	10.254	10.254	32.677	32.677	72.322	54.325
3420	Patellae, cortical	5	0.0374	0.0374	0.162	0.162	1.189	1.189	2.595	2.595	21.420	17.537
3500	Tibiae, spongiosa	21	6.624	6.624	7.275	7.275	23.028	23.028	62.567	62.567	264.537	227.056
3510	Fibulae, spongiosa	22	1.394	1.394	0.565	0.565	2.789	2.789	7.385	7.385	31.687	24.536
3520	Patellae, spongiosa	23	0.171	0.171	0.575	0.575	5.569	5.569	12.630	12.630	22.257	17.825
3600	Tibiae, medullary cavity	24	0.673	0.673	2.203	2.203	8.261	8.261	26.272	26.272	59.424	48.773
3610	Fibulae, medullary cavity	25	0.107	0.107	0.204	0.204	1.871	1.871	5.576	5.576	8.185	5.809
3700	Ankles and foot, cortical	5	1.289	1.289	7.235	7.235	33.249	33.249	93.863	93.863	217.341	176.948
3800	Ankles and foot, spongiosa	26	4.926	4.926	20.331	20.331	70.793	70.793	159.839	159.839	387.180	306.517
3900	Mandible, cortical	5	1.700	1.700	7.164	7.164	19.289	19.282	24.910	24.909	59.285	47.273
4000	Mandible, spongiosa	27	5.693	5.693	13.095	13.095	29.495	29.477	27.505	27.504	37.750	28.847
4100	Pelvis, cortical	5	6.147	6.147	21.202	21.202	58.226	58.226	128.933	128.933	188.606	215.135
4200	Pelvis, spongiosa	28	8.689	8.689	34.395	34.395	99.470	99.470	285.898	285.898	512.498	553.247
4300	Ribs, cortical	5	6.389	6.389	20.409	20.410	38.511	38.511	70.415	70.415	169.281	186.406
4400	Ribs, spongiosa	29	21.362	21.362	58.121	58.121	79.112	79.112	138.704	138.704	198.249	208.053
4500	Scapulae, cortical	5	2.447	2.447	9.647	9.647	29.302	29.302	59.267	59.267	124.479	172.602
4600	Scapulae, spongiosa	30	4.457	4.457	14.863	14.863	42.719	42.719	90.282	90.282	110.814	147.468
4700	Cervical spine, cortical	5	3.774	3.774	3.276	3.275	6.992	6.992	14.127	14.127	33.755	42.945
4800	Cervical spine, spongiosa	31	7.135	7.135	9.103	9.103	14.083	14.083	30.749	30.749	56.493	68.327
4900	Thoracic spine, cortical	5	8.531	8.538	11.501	11.501	33.105	33.105	68.387	68.387	90.861	84.062
5000	Thoracic spine, spongiosa	32	10.497	10.499	28.110	28.110	74.596	74.596	211.317	211.317	264.347	230.516
5100	Lumbar spine, cortical	5	2.728	2.728	7.073	7.073	16.796	16.796	36.752	36.752	35.528	41.247
5200	Lumbar spine, spongiosa	33	7.849	7.849	21.948	21.936	58.995	58.995	161.646	161.646	255.535	270.609
5300	Sacrum, cortical	5	1.084	1.084	5.453	5.453	11.696	11.696	16.667	16.667	69.681	86.543
5400	Sacrum, spongiosa	34	3.140	3.140	15.116	15.116	34.521	34.521	55.236	55.236	118.649	140.213
5500	Sternum, cortical	5	0.168	0.168	0.630	0.630	2.469	2.469	5.282	5.281	22.161	15.671
5600	Sternum, spongiosa	35	0.677	0.677	2.103	2.103	8.505	8.505	20.823	20.823	42.389	28.431
5700	Cartilage, head	36	53.069	52.989	5.027	5.027						
5800	Cartilage, trunk	36	48.202	48.202	36.850	36.850	55.137	55.137	129.154	129.154	152.190	162.007
5900	Cartilage, arms	36	11.539	11.539								
6000	Cartilage, legs	36	15.378	15.378								
6100	Brain	37	395.660	395.660	978.101	978.101	1374.203	1244.203	1467.081	1287.082	1496.739	1348.990
6200	Breast, left, adipose tissue	38	0.0870	0.0870	0.571	0.572	1.178	1.171	2.038	2.028	4.758	77.618
6300	Breast, left, glandular tissue	39	0.0580	0.0580	0.381	0.381	0.785	0.781	1.359	1.352	3.172	51.751
6400	Breast, right, adipose tissue	38	0.0870	0.0870	0.571	0.572	1.178	1.171	2.038	2.028	4.758	77.616
6500	Breast, right, glandular tissue	39	0.0580	0.0580	0.381	0.381	0.785	0.781	1.359	1.352	3.172	51.751
6600	Eye lens, sensitive, left	40	0.0162	0.0162	0.0169	0.0169	0.0202	0.0202	0.0184	0.0184	0.0203	0.0203
6601	Eye lens, insensitive, left	41	0.0673	0.0673	0.0978	0.0978	0.114	0.114	0.113	0.113	0.117	0.117
6700	Cornea, left	42	0.582	0.582	0.629	0.629	0.870	0.870	0.941	0.941	0.996	0.996
6701	Aqueous, left	43	0.174	0.174	0.275	0.275	0.294	0.294	0.327	0.327	0.344	0.344
6702	Vitreous, left	44	2.413	2.413	2.624	2.624	4.403	4.403	4.853	4.853	5.322	5.322
6800	Eye lens, sensitive, right	40	0.0162	0.0162	0.0169	0.0169	0.0202	0.0202	0.0184	0.0184	0.0203	0.0203
6801	Eye lens, insensitive, right	41	0.0673	0.0673	0.0978	0.0978	0.114	0.114	0.113	0.113	0.117	0.117
6900	Cornea, right	42	0.582	0.582	0.629	0.629	0.870	0.870	0.942	0.941	0.996	0.996
6901	Aqueous, right	43	0.174	0.174	0.275	0.275	0.294	0.294	0.327	0.327	0.344	0.344
6902	Vitreous, right	44	2.413	2.413	2.624	2.624	4.403	4.403	4.853	4.853	5.322	5.322
7000	Gall bladder wall	45	0.542	0.542	1.457	1.458	2.704	2.686	4.597	4.576	8.141	7.555

7100	Gall bladder contents	46	2.800	2.800	8.000	8.000	15.000	15.000	26.000	26.000	45.000	42.000
7200	Stomach wall, 60 µm	47	0.408	0.408	0.814	0.814	0.745	0.745	0.998	0.998	2.407	1.602
7201	Stomach wall, 100 µm	47	0.273	0.273	0.407	0.407	0.489	0.489	0.667	0.667	1.605	1.070
7202	Stomach wall, 300 µm	47	1.384	1.384	2.056	2.056	2.469	2.469	3.361	3.361	8.068	5.385
7203	Stomach wall, surface	47	6.663	6.665	19.881	19.881	57.962	57.962	100.420	100.408	143.657	136.315
7300	Stomach contents	49	40.000	40.000	67.000	67.000	83.000	83.000	117.000	117.000	200.000	200.000
7400	Small intestine wall, 130 µm	48	3.220	3.218	4.934	4.934	6.595	6.595	8.740	8.698	12.504	12.460
7401	Small intestine wall, 150 µm	48	0.503	0.503	0.770	0.770	1.031	1.031	1.365	1.365	1.948	1.941
7402	Small intestine wall, 200 µm	48	1.267	1.267	1.939	1.939	2.597	2.597	3.435	3.435	4.897	4.880
7403	Small intestine wall, surface	48	33.226	33.215	92.155	92.304	266.743	266.743	454.781	454.493	673.314	616.548
7500	Small intestine contents, 0 µm	49	9.275	9.273	14.320	14.320	19.024	19.024	31.330	31.370	45.272	45.187
7501	Small intestine contents, -400/-500† µm	49	46.725	46.727	78.680	78.680	97.976	97.976	131.670	131.670	234.729	234.813
7600	Ascending colon wall, 280 µm	48	1.140	1.140	1.572	1.572	1.907	1.907	2.588	2.588	3.641	3.658
7601	Ascending colon wall, 300 µm	48	0.0832	0.0832	0.114	0.114	0.139	0.139	0.188	0.188	0.264	0.265
7602	Ascending colon wall, surface	48	2.795	2.795	9.364	9.370	26.671	26.673	50.903	50.876	76.362	68.667
7700	Ascending colon contents	49	15.594	15.594	26.017	26.017	31.346	31.346	45.283	45.283	77.810	77.810
7800	Transverse colon wall, right, 280 µm	48	0.842	0.842	1.200	1.200	1.580	1.580	1.924	1.924	2.662	2.673
7801	Transverse colon wall, right, 300 µm	48	0.0618	0.0618	0.0878	0.0878	0.116	0.116	0.140	0.140	0.193	0.194
7802	Transverse colon wall, right, surface	48	3.989	3.989	11.135	11.138	31.214	31.228	51.687	51.707	79.877	72.880
7900	Transverse colon contents, right	49	8.406	8.406	13.983	13.983	18.654	18.654	24.717	24.717	42.190	42.190
8000	Transverse colon wall, left, 280 µm	48	0.651	0.651	1.029	1.029	1.101	1.101	1.486	1.486	2.191	2.147
8001	Transverse colon wall, left, 300 µm	48	0.0481	0.0481	0.0757	0.0757	0.0808	0.0808	0.109	0.109	0.160	0.157
8002	Transverse colon wall, left, surface	48	3.802	3.802	10.300	10.300	27.086	27.083	45.608	45.608	74.084	67.632
8100	Transverse colon contents, left	49	5.418	5.418	8.933	8.933	10.920	10.920	15.054	15.054	27.012	27.012
8200	Descending colon wall, 280 µm	48	0.780	0.780	1.232	1.232	1.504	1.504	2.013	2.013	2.693	2.687
8201	Descending colon wall, 300 µm	48	0.0575	0.0575	0.0906	0.0906	0.110	0.110	0.148	0.148	0.197	0.196
8202	Descending colon wall, surface	48	3.572	3.572	10.753	10.753	31.744	31.746	58.010	58.063	83.743	75.444
8300	Descending colon contents	49	6.582	6.582	11.067	11.067	14.081	14.081	19.946	19.946	32.988	32.988
8400	Sigmoid colon wall, 280 µm	48	0.965	0.965	1.558	1.568	1.811	1.811	2.452	2.452	3.260	3.220
8401	Sigmoid colon wall, 300 µm	48	0.0710	0.0710	0.115	0.115	0.133	0.133	0.180	0.180	0.238	0.235
8402	Sigmoid colon wall, surface	48	2.223	2.223	7.999	7.987	22.780	22.776	42.083	42.103	61.660	55.580
8500	Sigmoid colon contents	49	8.521	8.521	13.983	13.983	17.992	17.992	24.519	24.519	41.771	41.771
8600	Rectum wall, 280 µm	48	0.418	0.418	0.657	0.657	0.717	0.717	1.033	1.033	1.492	1.440
8601	Rectum wall, 300 µm	48	0.0309	0.0309	0.0484	0.0484	0.0527	0.0527	0.0758	0.0758	0.109	0.105
8602	Rectum wall, surface	48	0.111	0.111	1.363	1.363	2.176	2.175	4.708	4.710	8.110	7.527
8603	Rectum contents	49	3.479	3.479	6.017	6.017	7.008	7.008	10.481	10.481	18.229	18.229
8700	Heart wall	50	23.157	23.157	55.043	55.043	97.696	97.617	161.495	161.495	269.653	251.488
8800	Blood in heart chamber	4	26.000	26.000	48.000	48.000	134.999	134.999	230.000	230.000	430.000	320.000
8900	Kidney, left, cortex	51	9.460	9.460	27.763	27.763	49.837	49.847	82.031	82.031	119.394	105.694
9000	Kidney, left, medulla	51	3.379	3.379	9.915	9.915	17.799	17.810	29.299	29.299	42.641	37.747
9100	Kidney, left, pelvis	51	0.676	0.676	1.983	1.983	3.560	3.561	5.859	5.859	8.528	7.550
9200	Kidney, right, cortex	51	9.460	9.460	27.763	27.763	49.852	49.848	82.031	82.031	119.394	105.694
9300	Kidney, right, medulla	51	3.379	3.379	9.915	9.915	17.784	17.810	29.299	29.299	42.641	37.747
9400	Kidney, right, pelvis	51	0.676	0.676	1.983	1.983	3.560	3.561	5.859	5.859	8.528	7.550
9500	Liver	52	167.410	167.410	389.892	390.399	724.407	723.337	1059.764	1059.773	1707.819	1628.966
9700	Lung (AI), left	53	28.689	28.690	68.837	68.837	139.438	139.441	222.219	222.238	389.511	330.576
9900	Lung (AI), right	53	31.311	31.310	81.163	81.163	160.562	160.559	277.781	277.762	510.489	419.425
10000	Lymphatic nodes, ET	54	1.243	1.243	2.176	2.176	4.310	4.311	7.157	7.157	12.733	11.522
10100	Lymphatic nodes, thoracic	54	1.243	1.243	2.176	2.176	4.310	4.311	7.157	7.157	12.733	11.522
10200	Lymphatic nodes, head	54	0.429	0.429	0.752	0.752	1.489	1.489	2.473	2.472	4.399	3.980
10300	Lymphatic nodes, trunk	54	10.144	10.145	17.763	17.763	35.189	35.193	58.429	58.429	103.944	94.065
10400	Lymphatic nodes, arms	54	0.858	0.859	1.503	1.503	2.978	2.978	4.945	4.945	8.797	7.961
10500	Lymphatic nodes, legs	54	0.858	0.859	1.503	1.503	2.978	2.978	4.945	4.945	8.797	7.961

10600	Muscle	55	819.752	819.765	1929.207	1929.207	5727.750	5726.753	11257.260	11257.050	24657.360	17360.700
11000	Oesophagus wall, 190 µm	47	0.344	0.344	0.545	0.567	0.918	0.895	1.598	1.569	2.169	1.784
11001	Oesophagus wall, 200 µm	47	0.0188	0.0188	0.0296	0.0308	0.0496	0.0483	0.0858	0.0843	0.116	0.0957
11002	Oesophagus wall, surface	47	2.132	2.132	5.214	5.192	11.370	11.395	20.609	20.657	36.640	34.197
11003	Oesophagus contents	49	2.022	2.022	3.786	3.786	7.135	7.135	11.908	11.908	21.842	21.033
11100	Ovary, left	56		0.168		0.423		1.058		1.839		3.193
11200	Ovary, right	56		0.168		0.423		1.058		1.839		3.193
11300	Pancreas	57	7.248	7.248	22.651	22.651	41.892	41.880	72.126	72.126	136.661	117.631
11400	Pituitary gland	45	0.108	0.108	0.156	0.156	0.260	0.259	0.366	0.364	0.529	0.518
11500	Prostate	58	0.868		1.040		1.247		1.672		4.546	
11600	RST	59	1004.089	1001.707	4293.561	4294.031	6250.308	6378.696	9569.542	9750.656	12343.443	18424.633
12000	Salivary glands, left	45	3.254	3.253	12.485	12.488	17.666	17.571	22.981	22.862	35.947	33.647
12100	Salivary glands, right	45	3.254	3.253	12.485	12.494	17.665	17.571	22.981	22.862	35.947	33.647
12200	Skin, insensitive, surface	60	8.741	8.732	18.255	18.201	31.071	31.014	45.776	45.597	85.650	80.996
12201	Skin, insensitive, 100 µm	60	162.072	162.092	315.357	315.493	518.800	518.943	744.559	744.994	1931.860	1616.478
12300	Skin, sensitive, 40/50‡ µm	60	13.083	13.071	27.340	27.259	46.543	46.458	68.581	68.320	85.566	80.917
12600	Spinal cord	45	6.107	6.065	10.641	10.669	23.825	23.123	45.695	45.338	40.217	54.218
12700	Spleen	61	13.865	13.865	37.352	37.352	71.306	71.262	114.975	114.975	198.771	179.324
12800	Erupted, upper, front, buccal, permanent, enamel	62							0.352	0.350	0.650	0.564
12801	Erupted, upper, front, lingual, permanent, enamel	62							0.354	0.356	0.823	0.580
12802	Erupted, upper, front, buccal, deciduous, enamel	63			0.0709	0.0689	0.193	0.193	0.0680	0.0649		
12803	Erupted, upper, front, lingual, deciduous, enamel	63			0.0598	0.0617	0.165	0.165	0.0873	0.0903		
12804	Erupted, upper, front-left, buccal, permanent, enamel	62							0.117	0.108	0.317	0.219
12805	Erupted, upper, front-left, lingual, permanent, enamel	62							0.0766	0.086	0.224	0.201
12806	Erupted, upper, front-right, buccal, permanent, enamel	62							0.0755	0.125	0.317	0.201
12807	Erupted, upper, front-right, lingual, permanent, enamel	62							0.118	0.0693	0.224	0.219
12808	Erupted, upper, left, buccal, permanent, enamel	62							0.303	0.250	0.513	0.426
12809	Erupted, upper, left, lingual, permanent, enamel	62							0.145	0.198	0.494	0.356
12810	Erupted, upper, left, buccal, deciduous, enamel	63					0.149	0.149	0.0983	0.0804		
12811	Erupted, upper, left, lingual, deciduous, enamel	63					0.159	0.159	0.0569	0.0749		
12812	Erupted, upper, right, buccal, permanent, enamel	62							0.216	0.218	0.477	0.381
12813	Erupted, upper, right, lingual, permanent, enamel	62							0.232	0.229	0.531	0.400
12814	Erupted, upper, right, buccal, deciduous, enamel	63					0.149	0.149	0.0760	0.0705		
12815	Erupted, upper, right, lingual, deciduous, enamel	63					0.158	0.158	0.0792	0.0848		
12816	Erupted, lower, front, buccal, permanent, enamel	62							0.532	0.516	0.605	0.444
12817	Erupted, lower, front, lingual, permanent, enamel	62							0.412	0.427	0.541	0.445
12818	Erupted, lower, front, buccal, deciduous, enamel	63			0.0453	0.0506	0.135	0.135				
12819	Erupted, lower, front, lingual, deciduous, enamel	63			0.0425	0.0373	0.138	0.138				
12820	Erupted, lower, front-left, buccal, permanent, enamel	62									0.239	0.181
12821	Erupted, lower, front-left, lingual, permanent, enamel	62									0.228	0.182
12822	Erupted, lower, front-right, buccal, permanent, enamel	62									0.244	0.200
12823	Erupted, lower, front-right, lingual, permanent, enamel	62									0.224	0.163
12824	Erupted, lower, left, buccal, permanent, enamel	62							0.176	0.270	0.536	0.334
12825	Erupted, lower, left, lingual, permanent, enamel	62							0.302	0.208	0.494	0.466
12826	Erupted, lower, left, buccal, deciduous, enamel	63					0.175	0.175	0.146	0.141		
12827	Erupted, lower, left, lingual, deciduous, enamel	63					0.234	0.234	0.111	0.116		
12828	Erupted, lower, right, buccal, permanent, enamel	62							0.232	0.237	0.593	0.396
12829	Erupted, lower, right, lingual, permanent, enamel	62							0.246	0.241	0.437	0.404
12830	Erupted, lower, right, buccal, deciduous, enamel	63					0.197	0.197	0.140	0.121		
12831	Erupted, lower, right, lingual, deciduous, enamel	63					0.213	0.213	0.117	0.136		
12832	Erupted, upper, front, permanent, dentin	64							2.387	2.385	4.944	3.835
12833	Erupted, upper, front, deciduous, dentin	65			0.299	0.300	0.821	0.820	0.350	0.350		
12834	Erupted, upper, front-left, permanent, dentin	64							0.655	0.654	1.809	1.406

12835	Erupted, upper, front-right, permanent, dentin	64							0.653	0.653	1.816	1.410
12836	Erupted, upper, left, permanent, dentin	64							1.518	1.511	3.391	2.625
12837	Erupted, upper, left, deciduous, dentin	65					0.708	0.708	0.350	0.354		
12838	Erupted, upper, right, permanent, dentin	64							1.513	1.512	3.392	2.636
12839	Erupted, upper, right, deciduous, dentin	65					0.708	0.708	0.355	0.352		
12840	Erupted, lower, front, permanent, dentin	64							3.140	3.160	3.764	2.935
12841	Erupted, lower, front, deciduous, dentin	65			0.199	0.200	0.617	0.617				
12842	Erupted, lower, front-left, permanent, dentin	64									1.559	1.213
12843	Erupted, lower, front-right, permanent, dentin	64									1.558	1.211
12844	Erupted, lower, left, permanent, dentin	64							1.628	1.627	3.465	2.690
12845	Erupted, lower, left, deciduous, dentin	65					0.948	0.948	0.591	0.590		
12846	Erupted, lower, right, permanent, dentin	64							1.624	1.630	3.462	2.681
12847	Erupted, lower, right, deciduous, dentin	65					0.948	0.948	0.595	0.593		
12848	Unerupted, permanent, enamel	62			0.146	0.146	1.626	1.626	1.926	1.926	1.218	0.945
12849	Unerupted, deciduous, enamel	63	0.190	0.190	0.952	0.952						
12850	Unerupted, permanent, dentin	64			0.486	0.489	5.402	5.430	6.443	6.436	4.115	3.183
12851	Unerupted, deciduous, dentin	65	0.425	0.426	2.204	2.205						
12852	Permanent, cementum	64			0.0239	0.0203	0.284	0.256	0.786	0.779	1.450	1.138
12853	Deciduous, cementum	65	0.0337	0.0323	0.125	0.122	0.242	0.242	0.125	0.128		
12854	Permanent, pulp	66			0.0146	0.0146	0.163	0.163	0.582	0.582	0.993	0.771
12855	Deciduous, pulp	66	0.0607	0.0607	0.374	0.374	0.661	0.661	0.313	0.313		
12856	Teeth, retention region	67			0.00345	0.00345	0.0211	0.0212	0.0382	0.0386	0.0505	0.0412
12900	Testis, left	56	0.443		0.773		0.907		1.090		8.518	
13000	Testis, right	56	0.443		0.773		0.907		1.090		8.518	
13100	Thymus	68	14.101	14.096	31.212	31.214	31.203	31.014	41.791	36.392	37.004	31.049
13200	Thyroid	69	1.490	1.490	1.967	1.968	3.871	3.871	9.022	9.022	14.036	13.505
13300	Tongue, upper (food)	3	3.054	3.053	5.973	5.973	9.148	9.116	12.989	12.950	19.029	18.085
13301	Tongue, lower, -200 µm	3	0.574	0.574	4.058	4.060	9.981	9.899	19.428	19.319	38.572	35.361
13301	Tongue, lower, surface	3	0.162	0.162	0.364	0.362	0.601	0.604	0.979	0.967	1.473	1.381
13400	Tonsils	45	0.108	0.108	0.521	0.521	2.080	2.068	3.134	3.120	3.172	3.107
13500	Ureter, left	45	0.418	0.418	1.145	1.145	2.184	2.172	3.658	3.641	6.344	6.210
13600	Ureter, right	45	0.418	0.418	1.145	1.145	2.184	2.172	3.658	3.641	6.344	6.210
13700	Urinary bladder wall, insensitive, surface	70	3.419	3.426	7.760	7.771	14.714	14.711	23.091	23.080	37.233	32.360
13700	Urinary bladder wall, insensitive, α[§] µm	70	0.152	0.151	0.398	0.398	0.703	0.705	1.121	1.125	1.767	1.574
13701	Urinary bladder wall, sensitive, β[¶] µm	70	0.510	0.505	0.948	0.947	0.882	0.884	1.288	1.294	1.871	1.656
13800	Urinary bladder contents	71	12.400	12.400	32.900	32.900	64.700	64.700	103.000	103.000	160.000	140.000
13900	Uterus	58		4.337		1.562		3.100		4.158		31.064
14000	ET_1 contents (air)	72	0.0000380	0.0000309	0.0000894	0.0000940	0.000224	0.000209	0.000240	0.000240	0.00120	0.000117
14000	ET_2 contents, -15 µm (air)	72	0.00202	0.00130	0.00638	0.00449	0.0150	0.0140	0.0179	0.0163	0.0303	0.0183
14000	Trachea contents (air)	72	0.000239	0.000267	0.000440	0.000433	0.000164	0.000165	0.00187	0.00187	0.00285	0.00624
14000	BB_1 contents*, -11 µm (air)	72	0.000312	0.000312	0.000655	0.000655	0.000277	0.000277	0.00163	0.00163	0.00375	0.00366
14000	Stomach contents (air)	72			0.00169	0.00169	0.00833	0.00833	0.0313	0.0313	0.346	0.0984

ET, extrathoracic; AI, alveolar-interstitium; RST, residual soft tissue.

[*] Only the main bronchi (BB_1) was defined in the PM-version phantoms. The other generations of the bronchi (BB) and all generations of the bronchioles (bb) were modelled in constructive solid geometry format.

[†] Newborn, 1 year, 5 years/10 years, 15 years.

[‡] Newborn, 1 year, 5 years, 10 years/15 years.

[§] Newborn: 54, 1 year: 71, 5 years: 86, 10 years: 99, 15 years male: 116, 15 years female: 111.

[¶] Newborn: 232, 1 year: 238, 5 years: 193, 10 years: 212, 15 years male: 238, 15 years female: 227.

ANNEX B. LIST OF MEDIA AND THEIR ELEMENTAL COMPOSITIONS

Table B.1. List of media, their elemental compositions (percent by mass) and their mass densities for the newborn male phantom.

Medium no.		H	C	N	O	Na	Mg	P	S	Cl	K	Ca	Fe	I	Density (g/cm^3)
1	Adrenal	10.5	15.8	2.4	71.2				0.1						1.036
2	ET, Trachea, BB, bb	10.1	13.1	2.3	72.6	0.2		1.0	0.5	0.2					1.065
3	Oral mucosa, Tongue	10.4	10.5	2.5	75.9	0.1		0.1	0.1	0.2	0.2				1.052
4	Blood	10.0	13.1	4.0	72.0	0.1		0.1	0.2	0.2	0.2		0.1		1.070
5	Cortical bone	5.3	15.8	4.2	53.9		0.3	6.6	0.3			13.6			1.544
6	Humeri, upper, spongiosa	8.1	24.9	3.8	53.5		0.1	3.0	0.2	0.1	0.1	6.1	0.1		1.266
7	Humeri, upper, medullary cavity	10.4	33.3	3.4	52.1			0.1	0.2	0.2	0.2		0.1		1.038
8	Humeri, lower, spongiosa	8.1	24.9	3.8	53.5		0.1	3.0	0.2	0.1	0.1	6.1	0.1		1.266
9	Humeri, lower, medullary cavity	10.4	33.3	3.4	52.1			0.1	0.2	0.2	0.2		0.1		1.038
10	Radii, spongiosa	8.1	24.8	3.8	53.5		0.1	3.0	0.2	0.1	0.1	6.2	0.1		1.267
11	Ulnae, spongiosa	8.1	24.9	3.8	53.5		0.1	3.0	0.2	0.1	0.1	6.1	0.1		1.265
12	Radii, medullary cavity	10.4	33.3	3.4	52.1			0.1	0.2	0.2	0.2		0.1		1.038
13	Ulnae, medullary cavity	10.4	33.3	3.4	52.1			0.1	0.2	0.2	0.2		0.1		1.038
14	Wrists and hand bones, spongiosa	8.7	26.9	3.7	53.2		0.1	2.3	0.2	0.1	0.1	4.6	0.1		1.212
15	Clavicles, spongiosa	8.6	26.5	3.7	53.2		0.1	2.5	0.2	0.1	0.1	4.9	0.1		1.222
16	Cranium, spongiosa	7.0	20.8	3.9	54.2		0.2	4.4	0.2	0.1	0.1	9.1			1.377
17	Femora, upper, spongiosa	8.1	24.9	3.8	53.5		0.1	3.0	0.2	0.1	0.1	6.1	0.1		1.266
18	Femora, upper, medullary cavity	10.4	33.3	3.4	52.1			0.1	0.2	0.2	0.2		0.1		1.038
19	Femora, lower, spongiosa	8.1	24.9	3.8	53.5		0.1	3.0	0.2	0.1	0.1	6.1	0.1		1.266
20	Femora, lower, medullary cavity	10.4	33.3	3.4	52.1			0.1	0.2	0.2	0.2		0.1		1.038
21	Tibiae, spongiosa	8.1	24.9	3.8	53.5		0.1	3.0	0.2	0.1	0.1	6.1	0.1		1.266
22	Fibulae, spongiosa	8.1	24.9	3.8	53.5		0.1	3.0	0.2	0.1	0.1	6.1	0.1		1.267
23	Patellae, spongiosa	8.6	26.9	3.7	53.2		0.1	2.3	0.2	0.1	0.1	4.7	0.1		1.212
24	Tibiae, medullary cavity	10.4	33.3	3.4	52.1			0.1	0.2	0.2	0.2		0.1		1.038
25	Fibulae, medullary cavity	10.4	33.3	3.4	52.1			0.1	0.2	0.2	0.2		0.1		1.038
26	Ankles and foot, spongiosa	8.6	26.9	3.7	53.2		0.1	2.3	0.2	0.1	0.1	4.7	0.1		1.212
27	Mandible, spongiosa	8.6	26.9	3.7	53.2		0.1	2.3	0.2	0.1	0.1	4.7	0.1		1.212
28	Pelvis, spongiosa	8.5	26.5	3.7	53.2		0.1	2.5	0.2	0.1	0.1	5.0	0.1		1.223
29	Ribs, spongiosa	8.6	26.9	3.7	53.2		0.1	2.3	0.2	0.1	0.1	4.7	0.1		1.212
30	Scapulae, spongiosa	8.5	26.5	3.7	53.2		0.1	2.5	0.2	0.1	0.1	5.0	0.1		1.224
31	Cervical spine, spongiosa	7.8	23.9	3.8	53.7		0.1	3.4	0.2	0.1	0.1	6.8	0.1		1.293
32	Thoracic spine, spongiosa	7.7	23.5	3.8	53.8		0.1	3.5	0.2	0.1	0.1	7.1	0.1		1.304
33	Lumbar spine, spongiosa	8.1	24.9	3.8	53.5		0.1	3.0	0.2	0.1	0.1	6.1	0.1		1.266
34	Sacrum, spongiosa	8.1	24.9	3.8	53.5		0.1	3.0	0.2	0.1	0.1	6.1	0.1		1.266
35	Sternum, spongiosa	8.6	26.8	3.7	53.2		0.1	2.4	0.2	0.1	0.1	4.7	0.1		1.215
36	Cartilage	9.6	9.9	2.2	74.4	0.5		2.2	0.9	0.3					1.100
37	Brain	10.8	5.8	1.2	81.2	0.2		0.3	0.1	0.2	0.2				1.032
38	Breast, adipose tissue	11.0	28.4	1.2	59.1	0.1			0.1	0.1					0.996
39	Breast, glandular tissue	10.6	31.6	3.1	54.2	0.1		0.1	0.2	0.1					1.024
40	Eye lens, sensitive	9.6	19.5	5.7	64.6	0.1		0.1	0.3	0.1					1.050
41	Eye lens, insensitive	9.6	19.5	5.7	64.6	0.1		0.1	0.3	0.1					1.069
42	Cornea	10.1	12.7	3.7	73.0	0.1		0.1	0.2	0.1					1.076
43	Aqueous	11.1	1.0	0.3	87.6										1.008
44	Vitreous	11.1	1.0	0.3	87.6										1.013
45	Gall bladder wall, Pituitary gland, Salivary glands, Tonsils, Spinal cord, Ureter	10.6	16.0	2.2	71.1				0.1						1.033
46	Gall bladder contents	10.6	16.3	2.0	71.0				0.1						1.030
47	Stomach wall, Oesophagus	10.5	11.8	2.6	74.5	0.1		0.1	0.1	0.2	0.1				1.038
48	Small intestine wall, Colon wall	10.5	11.9	2.6	74.4	0.1		0.1	0.1	0.2	0.1				1.038
49	GI contents	10.0	22.2	2.2	64.4	0.1		0.2	0.3	0.1	0.4	0.1			1.030
50	Heart wall	10.5	8.3	2.1	78.3	0.2		0.1	0.1	0.2	0.2				1.044
51	Kidney	10.6	6.9	1.8	79.8	0.2		0.2	0.1	0.2	0.2				1.033
52	Liver	10.4	10.0	2.5	76.2	0.2		0.2	0.1	0.2	0.2				1.047

53	Lung	10.3	10.3	2.9	75.6	0.1		0.1	0.2	0.2	0.2		0.1		0.618
54	Lymphatic nodes	10.8	4.4	1.2	82.8	0.3			0.1	0.4					1.031
55	Muscle	10.4	10.4	2.4	76.1	0.1		0.1	0.1	0.2	0.2				1.050
56	Gonads	10.6	16.2	2.1	71.0				0.1						1.041
57	Pancreas	10.5	16.2	2.5	69.9	0.2		0.2	0.1	0.2	0.2				1.045
58	Prostate	10.6	16.0	2.2	71.1				0.1						1.033
59	RST	11.0	28.1	1.1	59.5	0.1			0.1	0.1					0.995
60	Skin	10.4	10.5	2.9	75.3	0.2		0.1	0.2	0.3	0.1				1.099
61	Spleen	10.4	10.0	2.9	75.8	0.2		0.2	0.1	0.2	0.2				1.049
62	Permanent, enamel*														
63	Deciduous, enamel	0.4	0.7	0.2	43.4		0.3	18.0				37.0			2.840
64	Permanent, dentin and cementum*														
65	Deciduous, dentin and cementum	1.5	2.8	0.9	47.5		0.8	15.2				31.3			2.185
66	Pulp	10.8	4.1	1.1	83.2	0.3			0.1	0.4					1.021
67	Teeth, retention region*														
68	Thymus	10.6	16.0	2.2	71.1				0.1						1.070
69	Thyroid	10.3	12.1	2.6	74.2	0.2		0.1	0.1	0.2	0.1			0.1	1.053
70	Urinary bladder wall	10.5	9.7	2.6	76.0	0.2		0.2	0.2	0.3	0.3				1.041
71	Urine	10.7	0.3	1.0	87.3	0.4		0.1			0.2				1.010
72	Air inside body			80.0	20.0										0.001
73	Water	11.2			88.8										1.000

ET, extrathoracic; BB, bronchi; bb, bronchioles; RST, residual soft tissue.

* The permanent enamel, dentin, cementum and teeth retention region are not included in the newborn phantoms.

Table B.2. List of media, their elemental compositions (percent by mass) and their mass densities for the newborn female phantom.

Medium no.		H	C	N	O	Na	Mg	P	S	Cl	K	Ca	Fe	I	Density (g/cm^3)
1	Adrenal	10.5	15.8	2.4	71.2				0.1						1.028
2	ET, Trachea, BB, bb	10.1	13.1	2.3	72.6	0.2		1.0	0.5	0.2					1.061
3	Oral mucosa, Tongue	10.4	10.5	2.5	75.9	0.1		0.1	0.1	0.2	0.2				1.052
4	Blood	10.0	13.1	4.0	72.0	0.1		0.1	0.2	0.2	0.2		0.1		1.070
5	Cortical bone	5.3	15.8	4.2	53.9		0.3	6.6	0.3			13.6			1.542
6	Humeri, upper, spongiosa	8.1	24.9	3.8	53.5		0.1	3.0	0.2	0.1	0.1	6.1	0.1		1.265
7	Humeri, upper, medullary cavity	10.4	33.3	3.4	52.1			0.1	0.2	0.2	0.2		0.1		1.037
8	Humeri, lower, spongiosa	8.1	24.9	3.8	53.5		0.1	3.0	0.2	0.1	0.1	6.1	0.1		1.265
9	Humeri, lower, medullary cavity	10.4	33.3	3.4	52.1			0.1	0.2	0.2	0.2		0.1		1.037
10	Radii, spongiosa	8.1	24.8	3.8	53.5		0.1	3.0	0.2	0.1	0.1	6.2	0.1		1.266
11	Ulnae, spongiosa	8.1	24.9	3.8	53.5		0.1	3.0	0.2	0.1	0.1	6.1	0.1		1.264
12	Radii, medullary cavity	10.4	33.3	3.4	52.1			0.1	0.2	0.2	0.2		0.1		1.037
13	Ulnae, medullary cavity	10.4	33.3	3.4	52.1			0.1	0.2	0.2	0.2		0.1		1.037
14	Wrists and hand bones, spongiosa	8.7	26.9	3.7	53.2		0.1	2.3	0.2	0.1	0.1	4.6	0.1		1.211
15	Clavicles, spongiosa	8.5	26.5	3.7	53.3		0.1	2.5	0.2	0.1	0.1	4.9	0.1		1.221
16	Cranium, spongiosa	7.0	20.8	3.9	54.2		0.2	4.4	0.2	0.1	0.1	9.1			1.375
17	Femora, upper, spongiosa	8.1	24.9	3.8	53.5		0.1	3.0	0.2	0.1	0.1	6.1	0.1		1.265
18	Femora, upper, medullary cavity	10.4	33.3	3.4	52.1			0.1	0.2	0.2	0.2		0.1		1.037
19	Femora, lower, spongiosa	8.1	24.9	3.8	53.5		0.1	3.0	0.2	0.1	0.1	6.1	0.1		1.265
20	Femora, lower, medullary cavity	10.4	33.3	3.4	52.1			0.1	0.2	0.2	0.2		0.1		1.037
21	Tibiae, spongiosa	8.1	24.9	3.8	53.5		0.1	3.0	0.2	0.1	0.1	6.1	0.1		1.265
22	Fibulae, spongiosa	8.1	24.9	3.8	53.5		0.1	3.0	0.2	0.1	0.1	6.1	0.1		1.266
23	Patellae, spongiosa	8.6	26.9	3.7	53.2		0.1	2.3	0.2	0.1	0.1	4.7	0.1		1.211
24	Tibiae, medullary cavity	10.4	33.3	3.4	52.1			0.1	0.2	0.2	0.2		0.1		1.037
25	Fibulae, medullary cavity	10.4	33.3	3.4	52.1			0.1	0.2	0.2	0.2		0.1		1.037
26	Ankles and foot, spongiosa	8.6	26.9	3.7	53.2		0.1	2.3	0.2	0.1	0.1	4.7	0.1		1.211
27	Mandible, spongiosa	8.6	26.9	3.7	53.2		0.1	2.3	0.2	0.1	0.1	4.7	0.1		1.211
28	Pelvis, spongiosa	8.5	26.5	3.7	53.3		0.1	2.5	0.2	0.1	0.1	4.9	0.1		1.222
29	Ribs, spongiosa	8.7	26.9	3.7	53.2		0.1	2.3	0.2	0.1	0.1	4.6	0.1		1.211
30	Scapulae, spongiosa	8.5	26.4	3.7	53.3		0.1	2.5	0.2	0.1	0.1	5.0	0.1		1.223
31	Cervical spine, spongiosa	7.8	23.9	3.8	53.7		0.1	3.4	0.2	0.1	0.1	6.8	0.1		1.292
32	Thoracic spine, spongiosa	7.7	23.5	3.8	53.8		0.1	3.5	0.2	0.1	0.1	7.1	0.1		1.303
33	Lumbar spine, spongiosa	8.1	24.9	3.8	53.5		0.1	3.0	0.2	0.1	0.1	6.1	0.1		1.265
34	Sacrum, spongiosa	8.1	24.9	3.8	53.5		0.1	3.0	0.2	0.1	0.1	6.1	0.1		1.265
35	Sternum, spongiosa	8.6	26.8	3.7	53.2		0.1	2.4	0.2	0.1	0.1	4.7	0.1		1.213
36	Cartilage	9.6	9.9	2.2	74.4	0.5		2.2	0.9	0.3					1.100
37	Brain	10.8	5.8	1.2	81.2	0.2		0.3	0.1	0.2	0.2				1.032
38	Breast, adipose tissue	11.0	28.4	1.2	59.1	0.1			0.1	0.1					0.996
39	Breast, glandular tissue	10.6	31.6	3.1	54.2	0.1		0.1	0.2	0.1					1.024
40	Eye lens, sensitive	9.6	19.5	5.7	64.6	0.1		0.1	0.3	0.1					1.050
41	Eye lens, insensitive	9.6	19.5	5.7	64.6	0.1		0.1	0.3	0.1					1.069
42	Cornea	10.1	12.7	3.7	73.0	0.1		0.1	0.2	0.1					1.076
43	Aqueous	11.1	1.0	0.3	87.6										1.008
44	Vitreous	11.1	1.0	0.3	87.6										1.013
45	Gall bladder wall, Pituitary gland, Salivary glands, Tonsils, Spinal cord, Ureter	10.6	16.0	2.2	71.1				0.1						1.024
46	Gall bladder contents	10.6	16.3	2.0	71.0				0.1						1.020
47	Stomach wall, Oesophagus	10.5	11.8	2.6	74.5	0.1		0.1	0.1	0.2	0.1				1.038
48	Small intestine wall, Colon wall	10.5	11.9	2.6	74.4	0.1		0.1	0.1	0.2	0.1				1.038
49	GI contents	10.0	22.2	2.2	64.4	0.1		0.2	0.3	0.1	0.4	0.1			1.030
50	Heart wall	10.5	8.3	2.1	78.3	0.2		0.1	0.1	0.2	0.2				1.044
51	Kidney	10.6	6.9	1.8	79.8	0.2		0.2	0.1	0.2	0.2				1.033
52	Liver	10.4	10.0	2.5	76.2	0.2		0.2	0.1	0.2	0.2				1.047
53	Lung	10.3	10.3	2.9	75.6	0.1		0.1	0.2	0.2	0.2		0.1		0.618
54	Lymphatic nodes	10.8	4.4	1.2	82.8	0.3			0.1	0.4					1.032
55	Muscle	10.4	10.4	2.4	76.1	0.1		0.1	0.1	0.2	0.2				1.050
56	Gonads	10.6	16.0	2.2	71.1				0.1						1.052

57	Pancreas	10.5	16.2	2.5	69.9	0.2		0.2	0.1	0.2	0.2				1.045
58	Uterus	10.6	16.0	2.2	71.1				0.1						1.052
59	RST	11.0	28.1	1.1	59.5	0.1			0.1	0.1					0.994
60	Skin	10.4	10.5	2.9	75.3	0.2		0.1	0.2	0.3	0.1				1.099
61	Spleen	10.4	10.0	2.9	75.8	0.2		0.2	0.1	0.2	0.2				1.049
62	Permanent, enamel*														
63	Deciduous, enamel	0.4	0.7	0.2	43.4		0.3	18.0				37.0			2.840
64	Permanent, dentin and cementum*														
65	Deciduous, dentin and cementum	1.5	2.8	0.9	47.5		0.8	15.2				31.3			2.185
66	Pulp	10.8	4.1	1.1	83.2	0.3			0.1	0.4					1.021
67	Teeth, retention region*														
68	Thymus	10.6	16.0	2.2	71.1				0.1						1.070
69	Thyroid	10.3	12.1	2.6	74.2	0.2		0.1	0.1	0.2	0.1			0.1	1.053
70	Urinary bladder wall	10.5	9.7	2.6	76.0	0.2		0.2	0.2	0.3	0.3				1.041
71	Urine	10.7	0.3	1.0	87.3	0.4		0.1			0.2				1.010
72	Air inside body			80.0	20.0										0.001
73	Water	11.2			88.8										1.000

ET, extrathoracic; BB, bronchi; bb, bronchioles; RST, residual soft tissue.

* The permanent enamel, dentin, cementum and teeth retention region are not included in the newborn phantoms.

Table B.3. List of media, their elemental compositions (percent by mass) and their mass densities for the 1-year-old male phantom.

Medium no.		H	C	N	O	Na	Mg	P	S	Cl	K	Ca	Fe	I	Density (g/cm^3)
1	Adrenal	10.5	23.9	2.8	61.8	0.1		0.2	0.3	0.2	0.2				1.033
2	ET, Trachea, BB, bb	10.0	17.5	2.5	67.6	0.3		1.2	0.6	0.2	0.1				1.065
3	Oral mucosa, Tongue	10.2	14.2	3.4	71.1	0.1		0.2	0.3	0.1	0.4				1.050
4	Blood	10.2	11.0	3.3	74.5	0.1		0.1	0.2	0.3	0.2		0.1		1.060
5	Cortical bone	4.9	16.5	4.3	51.2		0.3	7.5	0.3			15.0			1.587
6	Humeri, upper, spongiosa	7.5	25.3	3.8	50.7		0.1	4.1	0.3	0.1	0.1	8.0			1.329
7	Humeri, upper, medullary cavity	10.5	38.0	3.2	47.5			0.1	0.2	0.2	0.2		0.1		1.031
8	Humeri, lower, spongiosa	7.5	26.0	3.8	49.9		0.1	4.1	0.3	0.1	0.1	8.1			1.332
9	Humeri, lower, medullary cavity	10.6	38.4	3.1	47.1			0.1	0.2	0.2	0.2		0.1		1.030
10	Radii, spongiosa	7.2	25.1	3.8	50.2		0.2	4.4	0.3	0.1	0.1	8.6			1.352
11	Ulnae, spongiosa	6.8	23.0	3.9	50.8		0.2	5.0	0.3	0.1	0.1	9.8			1.396
12	Radii, medullary cavity	10.5	38.7	3.1	46.9			0.1	0.2	0.2	0.2		0.1		1.029
13	Ulnae, medullary cavity	10.6	38.7	3.1	46.8			0.1	0.2	0.2	0.2		0.1		1.029
14	Wrists and hand bones, spongiosa	8.3	33.3	3.2	44.9		0.1	3.3	0.2	0.1	0.1	6.5			1.262
15	Clavicles, spongiosa	8.1	27.8	3.7	50.1		0.1	3.3	0.2	0.1	0.1	6.4	0.1		1.269
16	Cranium, spongiosa	6.8	22.8	3.9	51.1		0.2	4.9	0.3	0.1	0.1	9.8			1.395
17	Femora, upper, spongiosa	7.6	26.0	3.8	50.6		0.1	3.8	0.3	0.1	0.1	7.5	0.1		1.311
18	Femora, upper, medullary cavity	10.5	37.7	3.2	47.8			0.1	0.2	0.2	0.2		0.1		1.031
19	Femora, lower, spongiosa	8.0	28.3	3.6	49.3		0.1	3.4	0.3	0.1	0.1	6.7	0.1		1.279
20	Femora, lower, medullary cavity	10.5	38.3	3.2	47.2			0.1	0.2	0.2	0.2		0.1		1.030
21	Tibiae, spongiosa	7.6	26.5	3.7	49.9		0.1	3.9	0.3	0.1	0.1	7.7	0.1		1.318
22	Fibulae, spongiosa	7.5	26.3	3.7	49.8		0.1	4.1	0.3	0.1	0.1	8.0			1.327
23	Patellae, spongiosa	8.8	31.5	3.5	48.6		0.1	2.4	0.2	0.1	0.1	4.6	0.1		1.201
24	Tibiae, medullary cavity	10.6	38.7	3.1	46.8			0.1	0.2	0.2	0.2		0.1		1.029
25	Fibulae, medullary cavity	10.6	39.0	3.1	46.5			0.1	0.2	0.2	0.2		0.1		1.028
26	Ankles and foot, spongiosa	8.3	33.8	3.1	44.7	0.1	0.1	3.2	0.2	0.1	0.1	6.3			1.255
27	Mandible, spongiosa	7.0	23.5	3.9	50.9		0.2	4.7	0.3	0.1	0.1	9.3			1.376
28	Pelvis, spongiosa	8.8	30.8	3.6	49.4		0.1	2.3	0.2	0.2	0.1	4.4	0.1		1.195
29	Ribs, spongiosa	8.5	29.5	3.6	49.7		0.1	2.7	0.2	0.2	0.1	5.3	0.1		1.228
30	Scapulae, spongiosa	8.2	28.2	3.7	50.0		0.1	3.1	0.2	0.1	0.1	6.2	0.1		1.260
31	Cervical spine, spongiosa	8.9	31.0	3.5	49.4		0.1	2.2	0.2	0.2	0.1	4.3	0.1		1.191
32	Thoracic spine, spongiosa	9.2	32.4	3.5	49.1		0.1	1.7	0.2	0.2	0.2	3.3	0.1		1.155
33	Lumbar spine, spongiosa	8.3	28.7	3.7	49.9		0.1	3.0	0.2	0.1	0.1	5.8	0.1		1.248
34	Sacrum, spongiosa	8.3	28.6	3.7	49.9		0.1	3.0	0.2	0.1	0.1	5.9	0.1		1.250
35	Sternum, spongiosa	8.5	29.5	3.6	49.7		0.1	2.7	0.2	0.2	0.1	5.3	0.1		1.227
36	Cartilage	9.6	9.9	2.2	74.4	0.5		2.2	0.9	0.3					1.100
37	Brain	10.7	9.2	1.6	77.5	0.2		0.3	0.1	0.2	0.2				1.031
38	Breast, adipose tissue	11.3	43.2	0.7	44.5	0.1			0.1	0.1					0.964
39	Breast, glandular tissue	10.6	32.3	3.0	53.6	0.1		0.1	0.2	0.1					1.022
40	Eye lens, sensitive	9.6	19.5	5.7	64.6	0.1		0.1	0.3	0.1					1.050
41	Eye lens, insensitive	9.6	19.5	5.7	64.6	0.1		0.1	0.3	0.1					1.078
42	Cornea	10.2	12.5	3.7	73.1	0.1		0.1	0.2	0.1					1.075
43	Aqueous	11.2	0.4	0.1	88.3										1.005
44	Vitreous	11.2	0.4	0.1	88.3										1.011
45	Gall bladder wall, Pituitary gland, Salivary glands, Tonsils, Spinal cord, Ureter	10.5	25.0	2.7	60.8	0.1		0.2	0.3	0.2	0.2				1.031
46	Gall bladder contents	10.5	25.6	2.7	60.2	0.1		0.2	0.3	0.2	0.2				1.030
47	Stomach wall, Oesophagus	10.6	11.4	2.4	75.0	0.1		0.1	0.1	0.2	0.1				1.034
48	Small intestine wall, Colon wall	10.6	11.4	2.4	75.0	0.1		0.1	0.1	0.2	0.1				1.034
49	GI contents	10.0	22.2	2.2	64.4	0.1		0.2	0.3	0.1	0.4	0.1			1.030
50	Heart wall	10.5	9.0	2.3	77.4	0.1		0.2	0.1	0.2	0.2				1.042
51	Kidney	10.6	9.6	2.2	76.7	0.2		0.2	0.1	0.2	0.2				1.042
52	Liver	10.3	12.3	2.8	73.5	0.1		0.3	0.2	0.2	0.3				1.052
53	Lung	10.2	10.7	3.2	74.7	0.2		0.2	0.3	0.3	0.2				0.400
54	Lymphatic nodes	10.8	4.3	1.2	82.9	0.3			0.1	0.4					1.031
55	Muscle	10.2	14.2	3.4	71.1	0.1		0.2	0.3	0.1	0.4				1.050
56	Gonads	10.6	9.9	2.1	76.5	0.2		0.1	0.2	0.2	0.2				1.041

57	Pancreas	10.6	16.2	2.3	70.0	0.2		0.2	0.1	0.2	0.2				1.042
58	Prostate	10.5	25.0	2.7	60.8	0.1		0.2	0.3	0.2	0.2				1.031
59	RST	11.2	41.0	0.9	46.5	0.1		0.1	0.1	0.1					0.972
60	Skin	10.0	20.1	4.2	64.8	0.2		0.1	0.2	0.3	0.1				1.099
61	Spleen	10.3	11.2	3.2	74.2	0.1		0.3	0.2	0.2	0.3				1.060
62	Permanent, enamel	0.4	0.7	0.2	43.4		0.3	18.0				37.0			3.000
63	Deciduous, enamel	0.4	0.7	0.2	43.4		0.3	18.0				37.0			2.840
64	Permanent, dentin and cementum	1.5	2.8	0.9	47.5		0.8	15.2				31.3			2.140
65	Deciduous, dentin and cementum	1.5	2.8	0.9	47.5		0.8	15.2				31.3			2.185
66	Pulp	10.8	4.1	1.1	83.2	0.3			0.1	0.4					1.021
67	Teeth, retention region	10.0	22.2	2.2	64.4	0.1		0.2	0.3	0.1	0.4	0.1			1.030
68	Thymus	10.5	25.0	2.7	60.8	0.1		0.2	0.3	0.2	0.2				1.026
69	Thyroid	10.4	11.8	2.5	74.5	0.2		0.1	0.1	0.2	0.1			0.1	1.051
70	Urinary bladder wall	10.5	9.6	2.6	76.1	0.2		0.2	0.2	0.3	0.3				1.040
71	Urine	10.7	0.3	1.0	87.3	0.4		0.1			0.2				1.010
72	Air inside body			80.0	20.0										0.001
73	Water	11.2			88.8										1.000

ET, extrathoracic; BB, bronchi; bb, bronchioles; RST, residual soft tissue.

Table B.4 List of media, their elemental compositions (percent by mass) and their mass densities for the 1-year-old female phantom.

Medium no.		H	C	N	O	Na	Mg	P	S	Cl	K	Ca	Fe	I	Density (g/cm^3)
1	Adrenal	10.6	29.2	2.5	56.9	0.1		0.2	0.2	0.1	0.2				1.024
2	ET, Trachea, BB, bb	10.1	20.3	2.3	65.0	0.3		1.2	0.5	0.2	0.1				1.060
3	Oral mucosa, Tongue	10.2	14.2	3.4	71.1	0.1		0.2	0.3	0.1	0.4				1.050
4	Blood	10.2	11.0	3.3	74.5	0.1		0.1	0.2	0.3	0.2		0.1		1.060
5	Cortical bone	4.9	16.9	4.3	50.8		0.3	7.5	0.3			15.0			1.586
6	Humeri, upper, spongiosa	7.5	25.7	3.8	50.3		0.1	4.1	0.3	0.1	0.1	8.0			1.328
7	Humeri, upper, medullary cavity	10.5	38.3	3.2	47.2			0.1	0.2	0.2	0.2		0.1		1.030
8	Humeri, lower, spongiosa	7.5	26.4	3.7	49.5		0.2	4.1	0.3	0.1	0.1	8.1			1.331
9	Humeri, lower, medullary cavity	10.5	38.8	3.1	46.8			0.1	0.2	0.2	0.2		0.1		1.029
10	Radii, spongiosa	7.3	25.5	3.8	49.8		0.2	4.4	0.2	0.1	0.1	8.6			1.351
11	Ulnae, spongiosa	6.8	23.4	3.9	50.4		0.2	5.0	0.3	0.1	0.1	9.8			1.395
12	Radii, medullary cavity	10.5	39.1	3.1	46.5			0.1	0.2	0.2	0.2		0.1		1.029
13	Ulnae, medullary cavity	10.5	39.1	3.1	46.5			0.1	0.2	0.2	0.2		0.1		1.029
14	Wrists and hand bones, spongiosa	8.3	33.8	3.1	44.5		0.1	3.3	0.2	0.1	0.1	6.5			1.261
15	Clavicles, spongiosa	8.1	28.2	3.7	49.7		0.1	3.3	0.2	0.1	0.1	6.4	0.1		1.268
16	Cranium, spongiosa	6.8	23.2	3.9	50.7		0.2	4.9	0.3	0.1	0.1	9.8			1.394
17	Femora, upper, spongiosa	7.7	26.4	3.8	50.2		0.1	3.8	0.2	0.1	0.1	7.5	0.1		1.311
18	Femora, upper, medullary cavity	10.5	38.1	3.2	47.4			0.1	0.2	0.2	0.2		0.1		1.030
19	Femora, lower, spongiosa	8.0	28.8	3.6	48.9		0.1	3.4	0.2	0.1	0.1	6.7	0.1		1.278
20	Femora, lower, medullary cavity	10.5	38.7	3.1	46.9			0.1	0.2	0.2	0.2		0.1		1.029
21	Tibiae, spongiosa	7.6	26.9	3.7	49.5		0.1	3.9	0.3	0.1	0.1	7.7	0.1		1.317
22	Fibulae, spongiosa	7.5	26.7	3.7	49.4		0.1	4.1	0.3	0.1	0.1	8.0			1.326
23	Patellae, spongiosa	8.8	31.9	3.5	48.2		0.1	2.4	0.2	0.1	0.1	4.6	0.1		1.200
24	Tibiae, medullary cavity	10.6	39.1	3.1	46.4			0.1	0.2	0.2	0.2		0.1		1.028
25	Fibulae, medullary cavity	10.6	39.5	3.0	46.1			0.1	0.2	0.2	0.2		0.1		1.028
26	Ankles and foot, spongiosa	8.4	34.2	3.1	44.3		0.1	3.2	0.2	0.1	0.1	6.3			1.254
27	Mandible, spongiosa	7.0	24.0	3.9	50.5		0.2	4.7	0.2	0.1	0.1	9.3			1.375
28	Pelvis, spongiosa	8.9	31.2	3.5	49.0		0.1	2.3	0.2	0.2	0.1	4.4	0.1		1.194
29	Ribs, spongiosa	8.5	29.9	3.6	49.3		0.1	2.7	0.2	0.2	0.1	5.3	0.1		1.227
30	Scapulae, spongiosa	8.2	28.7	3.7	49.6		0.1	3.1	0.2	0.1	0.1	6.1	0.1		1.259
31	Cervical spine, spongiosa	8.9	31.4	3.5	49.0		0.1	2.2	0.2	0.2	0.1	4.3	0.1		1.191
32	Thoracic spine, spongiosa	9.3	32.8	3.4	48.7		0.1	1.7	0.2	0.2	0.2	3.3	0.1		1.154
33	Lumbar spine, spongiosa	8.3	29.1	3.6	49.5		0.1	3.0	0.2	0.2	0.1	5.8	0.1		1.248
34	Sacrum, spongiosa	8.3	29.0	3.7	49.5		0.1	3.0	0.2	0.1	0.1	5.9	0.1		1.249
35	Sternum, spongiosa	8.5	29.9	3.6	49.4		0.1	2.7	0.2	0.1	0.1	5.3	0.1		1.226
36	Cartilage	9.6	9.9	2.2	74.4	0.5		2.2	0.9	0.3					1.100
37	Brain	10.7	9.2	1.6	77.5	0.2		0.3	0.1	0.2	0.2				1.031
38	Breast, adipose tissue	11.3	43.2	0.7	44.5	0.1			0.1	0.1					0.964
39	Breast, glandular tissue	10.6	32.3	3.0	53.6	0.1		0.1	0.2	0.1					1.022
40	Eye lens, sensitive	9.6	19.5	5.7	64.6	0.1		0.1	0.3	0.1					1.050
41	Eye lens, insensitive	9.6	19.5	5.7	64.6	0.1		0.1	0.3	0.1					1.078
42	Cornea	10.2	12.5	3.7	73.1	0.1		0.1	0.2	0.1					1.075
43	Aqueous	11.2	0.4	0.1	88.3										1.005
44	Vitreous	11.2	0.4	0.1	88.3										1.011
45	Gall bladder wall, Pituitary gland, Salivary glands, Tonsils, Spinal cord, Ureter	10.6	30.7	2.4	55.5	0.1		0.2	0.2	0.1	0.2				1.022
46	Gall bladder contents	10.6	31.5	2.4	54.7	0.1		0.2	0.2	0.1	0.2				1.020
47	Stomach wall, Oesophagus	10.6	11.4	2.4	75.0	0.1		0.1	0.1	0.2	0.1				1.034
48	Small intestine wall, Colon wall	10.6	11.4	2.4	75.0	0.1		0.1	0.1	0.2	0.1				1.034
49	GI contents	10.0	22.2	2.2	64.4	0.1		0.2	0.3	0.1	0.4	0.1			1.030
50	Heart wall	10.5	9.0	2.3	77.4	0.1		0.2	0.1	0.2	0.2				1.042
51	Kidney	10.6	9.6	2.2	76.7	0.2		0.2	0.1	0.2	0.2				1.042
52	Liver	10.3	12.3	2.8	73.5	0.1		0.3	0.2	0.2	0.3				1.052
53	Lung	10.2	10.7	3.2	74.7	0.2		0.2	0.3	0.3	0.2				0.400
54	Lymphatic nodes	10.8	4.3	1.2	82.9	0.3			0.1	0.4					1.031
55	Muscle	10.2	14.2	3.4	71.1	0.1		0.2	0.3	0.1	0.4				1.050
56	Gonads	10.5	9.4	2.4	76.7	0.2		0.2	0.2	0.2	0.2				1.051

57	Pancreas	10.6	16.2	2.3	70.0	0.2		0.2	0.1	0.2	0.2				1.042
58	Uterus	10.5	9.4	2.4	76.7	0.2		0.2	0.2	0.2	0.2				1.050
59	RST	11.1	40.6	0.9	46.8	0.1		0.2	0.2	0.1					0.975
60	Skin	10.0	20.1	4.2	64.8	0.2		0.1	0.2	0.3	0.1				1.099
61	Spleen	10.3	11.2	3.2	74.2	0.1		0.3	0.2	0.2	0.3				1.060
62	Permanent, enamel	0.4	0.7	0.2	43.4		0.3	18.0				37.0			3.000
63	Deciduous, enamel	0.4	0.7	0.2	43.4		0.3	18.0				37.0			2.840
64	Permanent, dentin and cementum	1.5	2.8	0.9	47.5		0.8	15.2				31.3			2.140
65	Deciduous, dentin and cementum	1.5	2.8	0.9	47.5		0.8	15.2				31.3			2.185
66	Pulp	10.8	4.1	1.1	83.2	0.3			0.1	0.4					1.021
67	Teeth, retention region	10.0	22.2	2.2	64.4	0.1		0.2	0.3	0.1	0.4	0.1			1.030
68	Thymus	10.6	30.7	2.4	55.5	0.1		0.2	0.2	0.1	0.2				1.026
69	Thyroid	10.4	11.8	2.5	74.5	0.2		0.1	0.1	0.2	0.1			0.1	1.051
70	Urinary bladder wall	10.5	9.6	2.6	76.1	0.2		0.2	0.2	0.3	0.3				1.040
71	Urine	10.7	0.3	1.0	87.3	0.4		0.1			0.2				1.010
72	Air inside body			80.0	20.0										0.001
73	Water	11.2			88.8										1.000

ET, extrathoracic; BB, bronchi; bb, bronchioles; RST, residual soft tissue.

Table B.5. List of media, their elemental compositions (percent by mass) and their mass densities for the 5-year-old male phantom.

Medium no.		H	C	N	O	Na	Mg	P	S	Cl	K	Ca	Fe	I	Density (g/cm^3)
1	Adrenal	10.4	23.3	2.8	62.5	0.1		0.2	0.3	0.2	0.2				1.035
2	ET, Trachea, BB, bb	10.0	17.5	2.5	67.6	0.3		1.2	0.6	0.2	0.1				1.065
3	Oral mucosa, Tongue	10.2	14.2	3.4	71.1	0.1		0.2	0.3	0.1	0.4				1.050
4	Blood	10.2	11.0	3.3	74.5	0.1		0.1	0.2	0.3	0.2		0.1		1.060
5	Cortical bone	4.6	16.1	4.4	48.8	0.1	0.2	8.2	0.3			17.3			1.642
6	Humeri, upper, spongiosa	8.3	30.1	3.5	47.7	0.1	0.1	3.2	0.2	0.1	0.1	6.5	0.1		1.259
7	Humeri, upper, medullary cavity	10.7	41.9	2.8	43.9			0.1	0.2	0.2	0.1		0.1		1.023
8	Humeri, lower, spongiosa	8.5	31.9	3.3	46.3	0.1	0.1	3.0	0.2	0.1	0.1	6.3	0.1		1.249
9	Humeri, lower, medullary cavity	10.7	42.4	2.7	43.4			0.1	0.2	0.2	0.2		0.1		1.022
10	Radii, spongiosa	8.9	35.6	3.0	44.0	0.1	0.1	2.6	0.2	0.1	0.1	5.3			1.210
11	Ulnae, spongiosa	8.5	33.5	3.1	44.8	0.1	0.1	3.1	0.2	0.1	0.1	6.4			1.248
12	Radii, medullary cavity	10.8	46.4	2.3	39.8			0.1	0.2	0.2	0.1		0.1		1.014
13	Ulnae, medullary cavity	10.8	46.3	2.4	39.8			0.1	0.2	0.2	0.1		0.1		1.014
14	Wrists and hand bones, spongiosa	9.0	41.0	2.5	38.5	0.1	0.1	2.7	0.2	0.1		5.8			1.213
15	Clavicles, spongiosa	8.8	32.6	3.3	47.1	0.1		2.5	0.2	0.1	0.1	5.1	0.1		1.207
16	Cranium, spongiosa	7.7	27.0	3.6	48.7	0.1	0.1	4.0	0.2	0.1	0.1	8.4			1.326
17	Femora, upper, spongiosa	8.3	30.2	3.5	47.7	0.1	0.1	3.1	0.2	0.1	0.1	6.5	0.1		1.258
18	Femora, upper, medullary cavity	10.7	41.9	2.8	43.9			0.1	0.2	0.2	0.1		0.1		1.023
19	Femora, lower, spongiosa	8.7	33.0	3.2	46.0	0.1	0.1	2.8	0.2	0.1	0.1	5.7			1.228
20	Femora, lower, medullary cavity	10.7	42.4	2.7	43.5			0.1	0.2	0.2	0.1		0.1		1.022
21	Tibiae, spongiosa	8.8	34.9	3.1	44.2	0.1	0.1	2.7	0.2	0.1	0.1	5.7			1.222
22	Fibulae, spongiosa	9.3	38.1	2.9	43.0	0.1		2.0	0.2	0.1	0.1	4.1	0.1		1.165
23	Patellae, spongiosa	10.0	42.0	2.6	41.5	0.1		1.1	0.2	0.2	0.1	2.2			1.094
24	Tibiae, medullary cavity	10.8	46.3	2.4	39.8			0.1	0.2	0.2	0.1		0.1		1.014
25	Fibulae, medullary cavity	10.8	46.3	2.4	39.8			0.1	0.2	0.2	0.1		0.1		1.014
26	Ankles and foot, spongiosa	8.8	40.1	2.5	39.0	0.1	0.1	2.9	0.2	0.1	0.1	6.1			1.225
27	Mandible, spongiosa	8.0	28.4	3.6	48.3	0.1	0.1	3.6	0.2	0.1	0.1	7.5			1.295
28	Pelvis, spongiosa	9.2	34.3	3.2	46.6	0.1		2.0	0.2	0.2	0.1	4.0	0.1		1.170
29	Ribs, spongiosa	8.8	31.6	3.4	47.9	0.1	0.1	2.5	0.2	0.1	0.1	5.1	0.1		1.209
30	Scapulae, spongiosa	8.6	31.5	3.4	47.5	0.1	0.1	2.7	0.2	0.1	0.1	5.6	0.1		1.228
31	Cervical spine, spongiosa	8.8	31.7	3.4	47.9	0.1	0.1	2.4	0.2	0.2	0.1	5.0	0.1		1.207
32	Thoracic spine, spongiosa	9.3	33.9	3.3	47.4	0.1		1.8	0.2	0.2	0.1	3.6	0.1		1.158
33	Lumbar spine, spongiosa	8.8	31.7	3.4	47.9	0.1	0.1	2.4	0.2	0.2	0.1	5.0	0.1		1.206
34	Sacrum, spongiosa	9.5	35.4	3.2	46.3			1.7	0.2	0.2	0.1	3.3	0.1		1.145
35	Sternum, spongiosa	9.4	34.4	3.3	47.3			1.7	0.2	0.2	0.1	3.3	0.1		1.147
36	Cartilage	9.6	9.9	2.2	74.4	0.5		2.2	0.9	0.3					1.099
37	Brain	10.7	14.3	2.2	71.4	0.2		0.4	0.2	0.3	0.3				1.041
38	Breast, adipose tissue	11.3	43.2	0.7	44.5	0.1			0.1	0.1					0.964
39	Breast, glandular tissue	10.6	32.4	3.0	53.5	0.1		0.1	0.2	0.1					1.021
40	Eye lens, sensitive	9.6	19.5	5.7	64.6	0.1		0.1	0.3	0.1					1.050
41	Eye lens, insensitive	9.6	19.5	5.7	64.6	0.1		0.1	0.3	0.1					1.082
42	Cornea	10.2	12.5	3.7	73.1	0.1		0.1	0.2	0.1					1.075
43	Aqueous	11.2	0.4	0.1	88.3										1.005
44	Vitreous	11.2	0.4	0.1	88.3										1.013
45	Gall bladder wall, Pituitary gland, Salivary glands, Tonsils, Spinal cord, Ureter	10.5	25.0	2.7	60.8	0.1		0.2	0.3	0.2	0.2				1.031
46	Gall bladder contents	10.5	25.6	2.7	60.2	0.1		0.2	0.3	0.2	0.2				1.030
47	Stomach wall, Oesophagus	10.6	11.4	2.4	75.0	0.1		0.1	0.1	0.2	0.1				1.036
48	Small intestine wall, Colon wall	10.5	11.4	2.5	75.0	0.1		0.1	0.1	0.2	0.1				1.036
49	GI contents	10.0	22.2	2.2	64.4	0.1		0.2	0.3	0.1	0.4	0.1			1.030
50	Heart wall	10.5	10.5	2.6	75.5	0.1		0.2	0.1	0.2	0.3				1.043
51	Kidney	10.3	12.7	3.0	72.9	0.2		0.2	0.2	0.2	0.2	0.1			1.052
52	Liver	10.2	13.3	3.1	72.2	0.2		0.2	0.3	0.2	0.3				1.060
53	Lung	10.3	10.8	3.2	74.7	0.1		0.1	0.2	0.3	0.2		0.1		0.401
54	Lymphatic nodes	10.8	4.4	1.2	82.8	0.3			0.1	0.4					1.031
55	Muscle	10.2	14.2	3.4	71.1	0.1		0.2	0.3	0.1	0.4				1.050
56	Gonads	10.6	10.0	2.1	76.4	0.2		0.1	0.2	0.2	0.2				1.041

57	Pancreas	10.5	15.9	2.4	70.3	0.2		0.2	0.1	0.2	0.2				1.043
58	Prostate	10.5	25.0	2.7	60.8	0.1		0.2	0.3	0.2	0.2				1.031
59	RST	11.1	39.1	1.0	48.2	0.1		0.2	0.2	0.1					0.979
60	Skin	10.0	20.0	4.2	64.9	0.2		0.1	0.2	0.3	0.1				1.098
61	Spleen	10.3	11.2	3.2	74.2	0.1		0.3	0.2	0.2	0.3				1.060
62	Permanent, enamel	0.4	0.7	0.2	43.4		0.3	18.0				37.0			3.000
63	Deciduous, enamel	0.4	0.7	0.2	43.4		0.3	18.0				37.0			2.840
64	Permanent, dentin and cementum	1.5	2.8	0.9	47.5		0.8	15.2				31.3			2.140
65	Deciduous, dentin and cementum	1.5	2.8	0.9	47.5		0.8	15.2				31.3			2.185
66	Pulp	10.8	4.1	1.1	83.2	0.3			0.1	0.4					1.021
67	Teeth, retention region	10.0	22.2	2.2	64.4	0.1		0.2	0.3	0.1	0.4	0.1			1.030
68	Thymus	10.5	25.0	2.7	60.8	0.1		0.2	0.3	0.2	0.2				1.026
69	Thyroid	10.4	11.8	2.5	74.5	0.2		0.1	0.1	0.2	0.1			0.1	1.051
70	Urinary bladder wall	10.5	9.6	2.6	76.1	0.2		0.2	0.2	0.3	0.3				1.040
71	Urine	10.7	0.3	1.0	87.3	0.4		0.1			0.2				1.010
72	Air inside body			80.0	20.0										0.001
73	Water	11.2			88.8										1.000

ET, extrathoracic; BB, bronchi; bb, bronchioles; RST, residual soft tissue.

Table B.6. List of media, their elemental compositions (percent by mass) and their mass densities for the 5-year-old female phantom.

Medium no.		H	C	N	O	Na	Mg	P	S	Cl	K	Ca	Fe	I	Density (g/cm^3)
1	Adrenal	10.5	28.2	2.6	57.9	0.1		0.2	0.2	0.1	0.2				1.026
2	ET, Trachea, BB, bb	10.1	20.4	2.3	64.9	0.3		1.2	0.5	0.2	0.1				1.060
3	Oral mucosa, Tongue	10.2	14.2	3.4	71.1	0.1		0.2	0.3	0.1	0.4				1.050
4	Blood	10.2	11.0	3.3	74.5	0.1		0.1	0.2	0.3	0.2		0.1		1.060
5	Cortical bone	4.6	16.4	4.3	48.6	0.1	0.2	8.2	0.3			17.3			1.641
6	Humeri, upper, spongiosa	8.3	30.4	3.5	47.5	0.1	0.1	3.1	0.2	0.1	0.1	6.5	0.1		1.259
7	Humeri, upper, medullary cavity	10.7	42.1	2.8	43.7			0.1	0.2	0.2	0.1		0.1		1.023
8	Humeri, lower, spongiosa	8.5	32.2	3.3	46.1	0.1	0.1	3.0	0.2	0.1	0.1	6.3			1.248
9	Humeri, lower, medullary cavity	10.7	42.6	2.7	43.2			0.1	0.2	0.2	0.2		0.1		1.022
10	Radii, spongiosa	8.9	35.8	3.0	43.8	0.1	0.1	2.6	0.2	0.1	0.1	5.3			1.209
11	Ulnae, spongiosa	8.5	33.7	3.1	44.6	0.1	0.1	3.1	0.2	0.1	0.1	6.4			1.248
12	Radii, medullary cavity	10.8	46.6	2.3	39.6			0.1	0.2	0.2	0.1		0.1		1.014
13	Ulnae, medullary cavity	10.8	46.5	2.4	39.6			0.1	0.2	0.2	0.1		0.1		1.014
14	Wrists and hand bones, spongiosa	9.0	41.2	2.4	38.3	0.1	0.1	2.8	0.2	0.1		5.8			1.212
15	Clavicles, spongiosa	8.8	32.8	3.3	46.9	0.1		2.5	0.2	0.1	0.1	5.1	0.1		1.207
16	Cranium, spongiosa	7.7	27.2	3.6	48.5	0.1	0.1	4.0	0.2	0.1	0.1	8.4			1.326
17	Femora, upper, spongiosa	8.3	30.4	3.5	47.5	0.1	0.1	3.1	0.2	0.1	0.1	6.5	0.1		1.257
18	Femora, upper, medullary cavity	10.7	42.1	2.8	43.7			0.1	0.2	0.2	0.1		0.1		1.023
19	Femora, lower, spongiosa	8.7	33.2	3.2	45.8	0.1	0.1	2.8	0.2	0.1	0.1	5.7			1.228
20	Femora, lower, medullary cavity	10.7	42.6	2.7	43.3			0.1	0.2	0.2	0.1		0.1		1.022
21	Tibiae, spongiosa	8.8	35.2	3.0	44.0	0.1	0.1	2.7	0.2	0.1	0.1	5.7			1.222
22	Fibulae, spongiosa	9.3	38.3	2.9	42.8	0.1		2.0	0.2	0.1	0.1	4.1	0.1		1.165
23	Patellae, spongiosa	10.0	42.2	2.6	41.3	0.1		1.1	0.2	0.1	0.1	2.2	0.1		1.093
24	Tibiae, medullary cavity	10.8	46.6	2.3	39.6			0.1	0.2	0.2	0.1		0.1		1.014
25	Fibulae, medullary cavity	10.8	46.5	2.3	39.6	0.1		0.1	0.2	0.2	0.1		0.1		1.014
26	Ankles and foot, spongiosa	8.8	40.3	2.5	38.8	0.1	0.1	2.9	0.2	0.1	0.1	6.1			1.225
27	Mandible, spongiosa	8.0	28.6	3.6	48.1	0.1	0.1	3.6	0.2	0.1	0.1	7.5			1.295
28	Pelvis, spongiosa	9.2	34.5	3.2	46.4	0.1		2.0	0.2	0.2	0.1	4.0	0.1		1.170
29	Ribs, spongiosa	8.8	31.8	3.4	47.7	0.1	0.1	2.5	0.2	0.1	0.1	5.1	0.1		1.209
30	Scapulae, spongiosa	8.6	31.7	3.4	47.3	0.1	0.1	2.7	0.2	0.1	0.1	5.6	0.1		1.227
31	Cervical spine, spongiosa	8.8	31.9	3.4	47.7	0.1	0.1	2.5	0.2	0.1	0.1	5.0	0.1		1.207
32	Thoracic spine, spongiosa	9.3	34.1	3.3	47.2	0.1		1.8	0.2	0.2	0.1	3.6	0.1		1.157
33	Lumbar spine, spongiosa	8.8	31.9	3.4	47.7	0.1	0.1	2.4	0.2	0.2	0.1	5.0	0.1		1.206
34	Sacrum, spongiosa	9.5	35.6	3.2	46.1			1.7	0.2	0.2	0.1	3.3	0.1		1.145
35	Sternum, spongiosa	9.4	34.6	3.3	47.1			1.7	0.2	0.2	0.1	3.3	0.1		1.146
36	Cartilage	9.6	9.9	2.2	74.4	0.5		2.2	0.9	0.3					1.099
37	Brain	10.7	14.3	2.2	71.4	0.2		0.4	0.2	0.3	0.3				1.041
38	Breast, adipose tissue	11.3	43.4	0.7	44.3	0.1			0.1	0.1					0.963
39	Breast, glandular tissue	10.6	32.5	3.0	53.4	0.1		0.1	0.2	0.1					1.021
40	Eye lens, sensitive	9.6	19.5	5.7	64.6	0.1		0.1	0.3	0.1					1.050
41	Eye lens, insensitive	9.6	19.5	5.7	64.6	0.1		0.1	0.3	0.1					1.082
42	Cornea	10.2	12.5	3.7	73.1	0.1		0.1	0.2	0.1					1.075
43	Aqueous	11.2	0.4	0.1	88.3										1.005
44	Vitreous	11.2	0.4	0.1	88.3										1.013
45	Gall bladder wall, Pituitary gland, Salivary glands, Tonsils, Spinal cord, Ureter	10.6	30.8	2.4	55.4	0.1		0.2	0.2	0.1	0.2				1.021
46	Gall bladder contents	10.6	31.5	2.4	54.7	0.1		0.2	0.2	0.1	0.2				1.020
47	Stomach wall, Oesophagus	10.6	11.4	2.4	75.0	0.1		0.1	0.1	0.2	0.1				1.036
48	Small intestine wall, Colon wall	10.5	11.4	2.5	75.0	0.1		0.1	0.1	0.2	0.1				1.036
49	GI contents	10.0	22.2	2.2	64.4	0.1		0.2	0.3	0.1	0.4	0.1			1.030
50	Heart wall	10.5	10.5	2.6	75.5	0.1		0.2	0.1	0.2	0.3				1.043
51	Kidney	10.3	12.7	3.0	72.9	0.2		0.2	0.2	0.2	0.2	0.1			1.052
52	Liver	10.2	13.3	3.1	72.2	0.2		0.2	0.3	0.2	0.3				1.060
53	Lung	10.3	10.8	3.2	74.7	0.1		0.1	0.2	0.3	0.2		0.1		0.401
54	Lymphatic nodes	10.8	4.4	1.2	82.8	0.3			0.1	0.4					1.031
55	Muscle	10.2	14.2	3.4	71.1	0.1		0.2	0.3	0.1	0.4				1.050
56	Gonads	10.5	9.4	2.4	76.7	0.2		0.2	0.2	0.2	0.2				1.051

57	Pancreas	10.5	15.9	2.4	70.3	0.2		0.2	0.1	0.2	0.2				1.043
58	Uterus	10.5	9.4	2.4	76.7	0.2		0.2	0.2	0.2	0.2				1.050
59	RST	11.1	39.5	1.0	47.8	0.1		0.2	0.2	0.1					0.979
60	Skin	10.0	20.0	4.2	64.9	0.2		0.1	0.2	0.3	0.1				1.098
61	Spleen	10.3	11.2	3.2	74.2	0.1		0.3	0.2	0.2	0.3				1.060
62	Permanent, enamel	0.4	0.7	0.2	43.4		0.3	18.0				37.0			3.000
63	Deciduous, enamel	0.4	0.7	0.2	43.4		0.3	18.0				37.0			2.840
64	Permanent, dentin and cementum	1.5	2.8	0.9	47.5		0.8	15.2				31.3			2.140
65	Deciduous, dentin and cementum	1.5	2.8	0.9	47.5		0.8	15.2				31.3			2.185
66	Pulp	10.8	4.1	1.1	83.2	0.3			0.1	0.4					1.021
67	Teeth, retention region	10.0	22.2	2.2	64.4	0.1		0.2	0.3	0.1	0.4	0.1			1.030
68	Thymus	10.6	30.8	2.4	55.4	0.1		0.2	0.2	0.1	0.2				1.026
69	Thyroid	10.4	11.8	2.5	74.5	0.2		0.1	0.1	0.2	0.1			0.1	1.051
70	Urinary bladder wall	10.5	9.6	2.6	76.1	0.2		0.2	0.2	0.3	0.3				1.040
71	Urine	10.7	0.3	1.0	87.3	0.4		0.1			0.2				1.010
72	Air inside body			80.0	20.0										0.001
73	Water	11.2			88.8										1.000

ET, extrathoracic; BB, bronchi; bb, bronchioles; RST, residual soft tissue.

Table B.7. List of media, their elemental compositions (percent by mass) and their mass densities for the 10-year-old male phantom.

Medium no.		H	C	N	O	Na	Mg	P	S	Cl	K	Ca	Fe	I	Density (g/cm^3)
1	Adrenal	10.5	23.2	2.8	62.5	0.1		0.2	0.3	0.2	0.2				1.035
2	ET, Trachea, BB, bb	10.1	17.5	2.5	67.6	0.3		1.1	0.6	0.2	0.1				1.065
3	Oral mucosa, Tongue	10.2	14.2	3.4	71.1	0.1		0.2	0.3	0.1	0.4				1.050
4	Blood	10.2	11.0	3.3	74.5	0.1		0.1	0.2	0.3	0.2		0.1		1.060
5	Cortical bone	4.3	16.1	4.3	47.2	0.1	0.2	8.9	0.3			18.6			1.701
6	Humeri, upper, spongiosa	9.0	34.5	3.1	45.4	0.1	0.1	2.4	0.2	0.1	0.1	4.9	0.1		1.203
7	Humeri, upper, medullary cavity	10.9	48.8	2.2	37.5			0.1	0.2	0.2	0.1				1.010
8	Humeri, lower, spongiosa	9.3	42.0	2.4	38.7	0.1		2.3	0.2	0.1	0.1	4.8			1.182
9	Humeri, lower, medullary cavity	10.9	49.1	2.1	37.2	0.1		0.1	0.2	0.2	0.1				1.009
10	Radii, spongiosa	9.4	43.6	2.3	37.4	0.1		2.2	0.2	0.1	0.1	4.6			1.174
11	Ulnae, spongiosa	9.1	41.0	2.4	38.7	0.1	0.1	2.7	0.2	0.1	0.1	5.5			1.210
12	Radii, medullary cavity	11.2	56.0	1.5	30.9	0.1			0.1	0.1	0.1				0.996
13	Ulnae, medullary cavity	11.2	56.0	1.5	30.9	0.1			0.1	0.1	0.1				0.996
14	Wrists and hand bones, spongiosa	10.0	50.7	1.6	31.7	0.1		1.8	0.2	0.1		3.8			1.131
15	Clavicles, spongiosa	9.7	39.7	2.8	42.8			1.5	0.2	0.2	0.1	2.9	0.1		1.127
16	Cranium, spongiosa	8.5	32.3	3.2	45.8	0.1	0.1	3.1	0.2	0.1	0.1	6.5			1.259
17	Femora, upper, spongiosa	8.9	34.1	3.2	45.5	0.1		2.5	0.2	0.1	0.1	5.2	0.1		1.211
18	Femora, upper, medullary cavity	10.9	48.8	2.2	37.5			0.1	0.2	0.2	0.1				1.010
19	Femora, lower, spongiosa	9.2	41.2	2.5	39.1	0.1		2.4	0.2	0.1	0.1	5.1			1.194
20	Femora, lower, medullary cavity	10.9	49.1	2.1	37.2	0.1		0.1	0.2	0.2	0.1				1.009
21	Tibiae, spongiosa	9.5	44.1	2.2	37.1	0.1	0.1	2.1	0.2	0.1	0.1	4.4			1.166
22	Fibulae, spongiosa	9.8	46.3	2.1	36.0	0.1		1.7	0.2	0.1	0.1	3.6			1.135
23	Patellae, spongiosa	10.8	53.1	1.6	32.4	0.1		0.5	0.2	0.1	0.1	1.1			1.036
24	Tibiae, medullary cavity	11.2	56.0	1.5	30.9	0.1			0.1	0.1	0.1				0.996
25	Fibulae, medullary cavity	11.2	56.0	1.5	30.9	0.1			0.1	0.1	0.1				0.996
26	Ankles and foot, spongiosa	9.8	49.4	1.7	32.5	0.1		2.0	0.2	0.1		4.2			1.147
27	Mandible, spongiosa	8.8	33.8	3.1	45.2	0.1	0.1	2.8	0.2	0.1	0.1	5.7			1.230
28	Pelvis, spongiosa	9.8	38.6	3.0	44.1			1.3	0.2	0.2	0.1	2.6	0.1		1.117
29	Ribs, spongiosa	9.7	36.7	3.1	45.7			1.4	0.2	0.2	0.2	2.7	0.1		1.125
30	Scapulae, spongiosa	9.4	37.4	2.9	43.8	0.1		1.9	0.2	0.2	0.1	3.9	0.1		1.163
31	Cervical spine, spongiosa	9.6	36.1	3.2	45.9			1.5	0.2	0.2	0.1	3.1	0.1		1.138
32	Thoracic spine, spongiosa	9.9	37.6	3.1	45.4			1.1	0.2	0.2	0.1	2.3	0.1		1.108
33	Lumbar spine, spongiosa	9.5	35.8	3.2	46.0			1.6	0.2	0.2	0.1	3.3	0.1		1.146
34	Sacrum, spongiosa	10.2	40.8	2.9	43.4			0.7	0.2	0.2	0.1	1.4	0.1		1.073
35	Sternum, spongiosa	10.1	38.8	3.0	45.0			0.8	0.2	0.2	0.2	1.6	0.1		1.082
36	Cartilage	9.6	9.9	2.2	74.4	0.5		2.2	0.9	0.3					1.099
37	Brain	10.7	14.3	2.3	71.3	0.2		0.4	0.2	0.3	0.3				1.041
38	Breast, adipose tissue	11.3	43.0	0.7	44.7	0.1			0.1	0.1					0.964
39	Breast, glandular tissue	10.6	32.2	3.0	53.7	0.1		0.1	0.2	0.1					1.022
40	Eye lens, sensitive	9.6	19.5	5.7	64.6	0.1		0.1	0.3	0.1					1.050
41	Eye lens, insensitive	9.6	19.5	5.7	64.6	0.1		0.1	0.3	0.1					1.083
42	Cornea	10.2	12.5	3.7	73.1	0.1		0.1	0.2	0.1					1.075
43	Aqueous	11.2	0.4	0.1	88.3										1.005
44	Vitreous	11.2	0.4	0.1	88.3										1.013
45	Gall bladder wall, Pituitary gland, Salivary glands, Tonsils, Spinal cord, Ureter	10.5	25.0	2.7	60.8	0.1		0.2	0.3	0.2	0.2				1.031
46	Gall bladder contents	10.5	25.6	2.7	60.2	0.1		0.2	0.3	0.2	0.2				1.030
47	Stomach wall, Oesophagus	10.6	11.4	2.4	75.0	0.1		0.1	0.1	0.2	0.1				1.036
48	Small intestine wall, Colon wall	10.5	11.4	2.5	75.0	0.1		0.1	0.1	0.2	0.1				1.036
49	GI contents	10.0	22.2	2.2	64.4	0.1		0.2	0.3	0.1	0.4	0.1			1.030
50	Heart wall	10.5	10.5	2.6	75.5	0.1		0.2	0.1	0.2	0.3				1.043
51	Kidney	10.3	12.7	3.0	72.9	0.2		0.2	0.2	0.2	0.2	0.1			1.052
52	Liver	10.2	13.3	3.1	72.2	0.2		0.2	0.3	0.2	0.3				1.060
53	Lung	10.3	10.8	3.2	74.7	0.1		0.1	0.2	0.3	0.2		0.1		0.429
54	Lymphatic nodes	10.8	4.4	1.2	82.8	0.3			0.1	0.4					1.031
55	Muscle	10.2	14.2	3.4	71.1	0.1		0.2	0.3	0.1	0.4				1.050
56	Gonads	10.6	10.0	2.1	76.4	0.2		0.1	0.2	0.2	0.2				1.042

57	Pancreas	10.5	15.9	2.4	70.3	0.2		0.2	0.1	0.2	0.2				1.043
58	Prostate	10.5	25.0	2.7	60.8	0.1		0.2	0.3	0.2	0.2				1.031
59	RST	11.1	39.1	1.0	48.2	0.1		0.2	0.2	0.1					0.979
60	Skin	10.0	20.0	4.2	64.9	0.2		0.1	0.2	0.3	0.1				1.098
61	Spleen	10.3	11.2	3.2	74.2	0.1		0.3	0.2	0.2	0.3				1.060
62	Permanent, enamel	0.4	0.7	0.2	43.4		0.3	18.0				37.0			3.000
63	Deciduous, enamel	0.4	0.7	0.2	43.4		0.3	18.0				37.0			2.840
64	Permanent, dentin and cementum	1.5	2.8	0.9	47.5		0.8	15.2				31.3			2.140
65	Deciduous, dentin and cementum	1.5	2.8	0.9	47.5		0.8	15.2				31.3			2.185
66	Pulp	10.8	4.1	1.1	83.2	0.3			0.1	0.4					1.021
67	Teeth, retention region	10.0	22.2	2.2	64.4	0.1		0.2	0.3	0.1	0.4	0.1			1.030
68	Thymus	10.5	25.0	2.7	60.8	0.1		0.2	0.3	0.2	0.2				1.026
69	Thyroid	10.4	11.8	2.5	74.5	0.2		0.1	0.1	0.2	0.1			0.1	1.051
70	Urinary bladder wall	10.5	9.6	2.6	76.1	0.2		0.2	0.2	0.3	0.3				1.040
71	Urine	10.7	0.3	1.0	87.3	0.4		0.1			0.2				1.010
72	Air inside body			80.0	20.0										0.001
73	Water	11.2			88.8										1.000

ET, extrathoracic; BB, bronchi; bb, bronchioles; RST, residual soft tissue.

Table B.8. List of media, their elemental compositions (percent by mass) and their mass densities for the 10-year-old female phantom.

Medium no.		H	C	N	O	Na	Mg	P	S	Cl	K	Ca	Fe	I	Density (g/cm^3)
1	Adrenal	10.5	28.2	2.6	57.9	0.1		0.2	0.2	0.1	0.2				1.026
2	ET, Trachea, BB, bb	10.1	20.3	2.4	64.9	0.3		1.2	0.5	0.2	0.1				1.060
3	Oral mucosa, Tongue	10.2	14.2	3.4	71.1	0.1		0.2	0.3	0.1	0.4				1.050
4	Blood	10.2	11.0	3.3	74.5	0.1		0.1	0.2	0.3	0.2		0.1		1.060
5	Cortical bone	4.4	16.3	4.3	47.0	0.1	0.2	8.8	0.3			18.6			1.701
6	Humeri, upper, spongiosa	9.0	34.7	3.1	45.2	0.1	0.1	2.4	0.2	0.1	0.1	4.9	0.1		1.203
7	Humeri, upper, medullary cavity	10.9	49.0	2.2	37.3	0.1		0.1	0.1	0.2	0.1				1.010
8	Humeri, lower, spongiosa	9.3	42.2	2.4	38.5	0.1		2.3	0.2	0.1	0.1	4.8			1.182
9	Humeri, lower, medullary cavity	10.9	49.3	2.1	37.1	0.1		0.1	0.1	0.2	0.1				1.009
10	Radii, spongiosa	9.4	43.7	2.3	37.3	0.1		2.2	0.2	0.1	0.1	4.6			1.174
11	Ulnae, spongiosa	9.1	41.2	2.4	38.6	0.1	0.1	2.7	0.2	0.1		5.5			1.210
12	Radii, medullary cavity	11.2	56.2	1.4	30.8	0.1			0.1	0.1	0.1				0.995
13	Ulnae, medullary cavity	11.2	56.2	1.5	30.7	0.1			0.1	0.1	0.1				0.995
14	Wrists and hand bones, spongiosa	10.0	50.9	1.6	31.6	0.1		1.8	0.1	0.1		3.8			1.131
15	Clavicles, spongiosa	9.8	39.8	2.8	42.6	0.1		1.5	0.2	0.1	0.1	2.9	0.1		1.126
16	Cranium, spongiosa	8.5	32.4	3.2	45.6	0.1	0.1	3.1	0.2	0.1	0.1	6.5	0.1		1.259
17	Femora, upper, spongiosa	8.9	34.3	3.1	45.4	0.1		2.5	0.2	0.1	0.1	5.2	0.1		1.211
18	Femora, upper, medullary cavity	10.9	49.0	2.2	37.3	0.1		0.1	0.1	0.2	0.1				1.010
19	Femora, lower, spongiosa	9.2	41.4	2.4	38.9	0.1	0.1	2.4	0.2	0.1	0.1	5.1			1.194
20	Femora, lower, medullary cavity	10.9	49.3	2.1	37.1	0.1		0.1	0.1	0.2	0.1				1.009
21	Tibiae, spongiosa	9.5	44.3	2.2	37.0	0.1		2.1	0.2	0.1	0.1	4.4			1.165
22	Fibulae, spongiosa	9.8	46.5	2.1	35.8	0.1		1.7	0.2	0.1	0.1	3.6			1.134
23	Patellae, spongiosa	10.8	53.3	1.6	32.3	0.1		0.5	0.1	0.1	0.1	1.1			1.036
24	Tibiae, medullary cavity	11.2	56.2	1.4	30.8	0.1			0.1	0.1	0.1				0.995
25	Fibulae, medullary cavity	11.2	56.2	1.4	30.8	0.1			0.1	0.1	0.1				0.995
26	Ankles and foot, spongiosa	9.8	49.6	1.7	32.3	0.1		2.0	0.2	0.1		4.2			1.147
27	Mandible, spongiosa	8.8	34.0	3.1	45.0	0.1	0.1	2.8	0.2	0.1	0.1	5.7			1.230
28	Pelvis, spongiosa	9.8	38.7	2.9	44.0	0.1		1.3	0.2	0.2	0.1	2.6	0.1		1.116
29	Ribs, spongiosa	9.7	36.9	3.1	45.5			1.4	0.2	0.2	0.2	2.7	0.1		1.125
30	Scapulae, spongiosa	9.4	37.6	2.9	43.7	0.1		1.9	0.2	0.1	0.1	3.9	0.1		1.162
31	Cervical spine, spongiosa	9.6	36.3	3.1	45.7	0.1		1.5	0.2	0.2	0.1	3.1	0.1		1.138
32	Thoracic spine, spongiosa	9.9	37.7	3.1	45.3			1.1	0.2	0.2	0.1	2.3	0.1		1.107
33	Lumbar spine, spongiosa	9.5	35.9	3.2	45.8	0.1		1.6	0.2	0.2	0.1	3.3	0.1		1.146
34	Sacrum, spongiosa	10.2	41.0	2.8	43.2			0.8	0.2	0.2	0.1	1.4	0.1		1.073
35	Sternum, spongiosa	10.1	39.0	3.0	44.9			0.8	0.2	0.2	0.2	1.5	0.1		1.081
36	Cartilage	9.6	9.9	2.2	74.4	0.5		2.2	0.9	0.3					1.099
37	Brain	10.7	14.3	2.2	71.4	0.2		0.4	0.2	0.3	0.3				1.041
38	Breast, adipose tissue	11.3	43.2	0.7	44.5	0.1			0.1	0.1					0.964
39	Breast, glandular tissue	10.6	32.4	3.0	53.5	0.1		0.1	0.2	0.1					1.021
40	Eye lens, sensitive	9.6	19.5	5.7	64.6	0.1		0.1	0.3	0.1					1.050
41	Eye lens, insensitive	9.6	19.5	5.7	64.6	0.1		0.1	0.3	0.1					1.083
42	Cornea	10.2	12.5	3.7	73.1	0.1		0.1	0.2	0.1					1.075
43	Aqueous	11.2	0.4	0.1	88.3										1.005
44	Vitreous	11.2	0.4	0.1	88.3										1.013
45	Gall bladder wall, Pituitary gland, Salivary glands, Tonsils, Spinal cord, Ureter	10.6	30.7	2.4	55.5	0.1		0.2	0.2	0.1	0.2				1.021
46	Gall bladder contents	10.6	31.5	2.4	54.7	0.1		0.2	0.2	0.1	0.2				1.020
47	Stomach wall, Oesophagus	10.6	11.4	2.4	75.0	0.1		0.1	0.1	0.2	0.1				1.036
48	Small intestine wall, Colon wall	10.5	11.4	2.5	75.0	0.1		0.1	0.1	0.2	0.1				1.036
49	GI contents	10.0	22.2	2.2	64.4	0.1		0.2	0.3	0.1	0.4	0.1			1.030
50	Heart wall	10.5	10.5	2.6	75.5	0.1		0.2	0.1	0.2	0.3				1.043
51	Kidney	10.3	12.7	3.0	72.9	0.2		0.2	0.2	0.2	0.2	0.1			1.052
52	Liver	10.2	13.3	3.1	72.2	0.2		0.2	0.3	0.2	0.3				1.060
53	Lung	10.3	10.8	3.2	74.7	0.1		0.1	0.2	0.3	0.2		0.1		0.429
54	Lymphatic nodes	10.8	4.4	1.2	82.8	0.3			0.1	0.4					1.032
55	Muscle	10.2	14.2	3.4	71.1	0.1		0.2	0.3	0.1	0.4				1.050
56	Gonads	10.5	9.4	2.4	76.7	0.2		0.2	0.2	0.2	0.2				1.050

57	Pancreas	10.5	15.9	2.4	70.3	0.2		0.2	0.1	0.2	0.2				1.043
58	Uterus	10.5	9.4	2.4	76.7	0.2		0.2	0.2	0.2	0.2				1.050
59	RST	11.1	39.6	1.0	47.7	0.1		0.2	0.2	0.1					0.979
60	Skin	10.0	20.0	4.2	64.9	0.2		0.1	0.2	0.3	0.1				1.098
61	Spleen	10.3	11.2	3.2	74.2	0.1		0.3	0.2	0.2	0.3				1.060
62	Permanent, enamel	0.4	0.7	0.2	43.4		0.3	18.0				37.0			3.000
63	Deciduous, enamel	0.4	0.7	0.2	43.4		0.3	18.0				37.0			2.840
64	Permanent, dentin and cementum	1.5	2.8	0.9	47.5		0.8	15.2				31.3			2.140
65	Deciduous, dentin and cementum	1.5	2.8	0.9	47.5		0.8	15.2				31.3			2.185
66	Pulp	10.8	4.1	1.1	83.2	0.3			0.1	0.4					1.021
67	Teeth, retention region	10.0	22.2	2.2	64.4	0.1		0.2	0.3	0.1	0.4	0.1			1.030
68	Thymus	10.6	30.7	2.4	55.5	0.1		0.2	0.2	0.1	0.2				1.026
69	Thyroid	10.4	11.8	2.5	74.5	0.2		0.1	0.1	0.2	0.1			0.1	1.051
70	Urinary bladder wall	10.5	9.6	2.6	76.1	0.2		0.2	0.2	0.3	0.3				1.040
71	Urine	10.7	0.3	1.0	87.3	0.4		0.1			0.2				1.010
72	Air inside body			80.0	20.0										0.001
73	Water	11.2			88.8										1.000

ET, extrathoracic; BB, bronchi; bb, bronchioles; RST, residual soft tissue.

Table B.9. List of media, their elemental compositions (percent by mass) and their mass densities for the 15-year-old male phantom.

Medium no.		H	C	N	O	Na	Mg	P	S	Cl	K	Ca	Fe	I	Density (g/cm^3)
1	Adrenal	10.4	22.8	2.8	63.0	0.1		0.2	0.3	0.2	0.2				1.036
2	ET, Trachea, BB, bb	10.1	17.4	2.5	67.7	0.3		1.1	0.6	0.2	0.1				1.065
3	Oral mucosa, Tongue	10.2	14.1	3.4	71.2	0.1		0.2	0.3	0.1	0.4				1.051
4	Blood	10.2	11.0	3.3	74.5	0.1		0.1	0.2	0.3	0.2		0.1		1.060
5	Cortical bone	4.3	16.1	4.3	47.0	0.1	0.2	8.9	0.3			18.8			1.752
6	Humeri, upper, spongiosa	9.9	40.9	2.6	42.1	0.1		1.3	0.2	0.2	0.1	2.6			1.118
7	Humeri, upper, medullary cavity	11.1	52.1	1.8	34.5	0.1			0.1	0.2	0.1				1.003
8	Humeri, lower, spongiosa	9.9	49.7	1.7	32.7	0.1		1.8	0.2	0.1		3.8			1.144
9	Humeri, lower, medullary cavity	11.2	56.4	1.4	30.6	0.1			0.1	0.1	0.1				0.995
10	Radii, spongiosa	10.0	50.6	1.6	32.1	0.1		1.7	0.2	0.1		3.6			1.133
11	Ulnae, spongiosa	9.7	48.2	1.8	33.6	0.1		2.0	0.2	0.1		4.3			1.164
12	Radii, medullary cavity	11.5	62.5	0.8	24.9	0.1			0.1	0.1					0.983
13	Ulnae, medullary cavity	11.5	62.5	0.8	24.9	0.1			0.1	0.1					0.983
14	Wrists and hand bones, spongiosa	10.6	55.1	1.3	29.4	0.1		1.1	0.1	0.1		2.2			1.076
15	Clavicles, spongiosa	9.8	40.7	2.6	41.9	0.1		1.4	0.2	0.2	0.1	2.9	0.1		1.130
16	Cranium, spongiosa	9.0	35.1	3.0	44.7	0.1	0.1	2.5	0.2	0.1	0.1	5.1			1.220
17	Femora, upper, spongiosa	9.6	39.0	2.7	42.9	0.1		1.7	0.2	0.2	0.1	3.4	0.1		1.150
18	Femora, upper, medullary cavity	11.1	52.1	1.8	34.5	0.1			0.1	0.2	0.1				1.003
19	Femora, lower, spongiosa	9.5	46.3	1.9	34.7	0.1	0.1	2.3	0.2	0.1		4.8			1.187
20	Femora, lower, medullary cavity	11.2	56.4	1.4	30.6	0.1			0.1	0.1	0.1				0.995
21	Tibiae, spongiosa	10.6	55.1	1.3	29.4	0.1		1.1	0.1	0.1		2.2			1.077
22	Fibulae, spongiosa	10.0	50.2	1.6	32.4	0.1		1.8	0.1	0.1		3.7			1.138
23	Patellae, spongiosa	10.6	55.1	1.3	29.4	0.1		1.1	0.1	0.1		2.2			1.076
24	Tibiae, medullary cavity	11.5	62.5	0.8	24.9	0.1			0.1	0.1					0.983
25	Fibulae, medullary cavity	11.5	62.5	0.8	24.9	0.1			0.1	0.1					0.983
26	Ankles and foot, spongiosa	10.6	55.1	1.3	29.4	0.1		1.1	0.1	0.1		2.2			1.076
27	Mandible, spongiosa	9.2	36.4	2.9	44.1	0.1		2.2	0.2	0.1	0.1	4.6	0.1		1.198
28	Pelvis, spongiosa	10.2	40.7	2.7	43.1	0.1		0.9	0.2	0.2	0.1	1.7	0.1		1.088
29	Ribs, spongiosa	10.0	37.9	3.0	45.5			1.0	0.2	0.2	0.1	2.0	0.1		1.101
30	Scapulae, spongiosa	9.1	35.6	2.9	44.5	0.1	0.1	2.4	0.2	0.1	0.1	4.9			1.213
31	Cervical spine, spongiosa	9.8	36.7	3.0	45.9	0.1		1.3	0.2	0.2	0.1	2.6	0.1		1.126
32	Thoracic spine, spongiosa	9.9	37.7	3.0	45.6			1.1	0.2	0.2	0.1	2.1	0.1		1.106
33	Lumbar spine, spongiosa	10.1	38.3	3.0	45.4			0.9	0.2	0.2	0.1	1.7	0.1		1.092
34	Sacrum, spongiosa	10.4	42.4	2.6	42.5	0.1		0.5	0.2	0.2	0.1	0.9	0.1		1.056
35	Sternum, spongiosa	10.1	38.7	2.9	45.2	0.1		0.8	0.2	0.2	0.2	1.5	0.1		1.084
36	Cartilage	9.6	9.9	2.2	74.4	0.5		2.2	0.9	0.3					1.099
37	Brain	10.7	14.3	2.2	71.4	0.2		0.4	0.2	0.3	0.3				1.041
38	Breast, adipose tissue	11.2	42.7	0.8	45.0	0.1			0.1	0.1					0.965
39	Breast, glandular tissue	10.6	32.0	3.0	53.9	0.1		0.1	0.2	0.1					1.022
40	Eye lens, sensitive	9.6	19.5	5.7	64.6	0.1		0.1	0.3	0.1					1.050
41	Eye lens, insensitive	9.6	19.5	5.7	64.6	0.1		0.1	0.3	0.1					1.084
42	Cornea	10.2	12.5	3.7	73.1	0.1		0.1	0.2	0.1					1.075
43	Aqueous	11.2	0.5	0.1	88.2										1.005
44	Vitreous	11.2	0.5	0.1	88.2										1.013
45	Gall bladder wall, Pituitary gland, Salivary glands, Tonsils, Spinal cord, Ureter	10.5	24.8	2.7	61.0	0.1		0.2	0.3	0.2	0.2				1.032
46	Gall bladder contents	10.5	25.6	2.7	60.2	0.1		0.2	0.3	0.2	0.2				1.030
47	Stomach wall, Oesophagus	10.5	11.4	2.5	75.0	0.1		0.1	0.1	0.2	0.1				1.037
48	Small intestine wall, Colon wall	10.5	11.4	2.5	75.0	0.1		0.1	0.1	0.2	0.1				1.037
49	GI contents	10.0	22.2	2.2	64.4	0.1		0.2	0.3	0.1	0.4	0.1			1.030
50	Heart wall	10.5	10.5	2.6	75.5	0.1		0.2	0.1	0.2	0.3				1.043
51	Kidney	10.3	12.6	3.1	72.9	0.2		0.2	0.2	0.2	0.2	0.1			1.053
52	Liver	10.2	13.2	3.1	72.3	0.2		0.2	0.3	0.2	0.3				1.060
53	Lung	10.3	10.8	3.2	74.7	0.1		0.1	0.2	0.3	0.2		0.1		0.344
54	Lymphatic nodes	10.8	4.5	1.2	82.7	0.3			0.1	0.4					1.032
55	Muscle	10.2	14.2	3.4	71.1	0.1		0.2	0.3	0.1	0.4				1.050
56	Gonads	10.6	9.9	2.1	76.5	0.2		0.1	0.2	0.2	0.2				1.041

57	Pancreas	10.5	15.8	2.4	70.4	0.2		0.2	0.1	0.2	0.2				1.044
58	Prostate	10.5	24.8	2.7	61.0	0.1		0.2	0.3	0.2	0.2				1.032
59	RST	11.1	38.6	1.0	48.7	0.1		0.2	0.2	0.1					0.981
60	Skin	10.0	19.9	4.2	65.0	0.2		0.1	0.2	0.3	0.1				1.098
61	Spleen	10.3	11.2	3.2	74.3	0.1		0.2	0.2	0.2	0.3				1.060
62	Permanent, enamel	0.4	0.7	0.2	43.4		0.3	18.0				37.0			3.000
63	Deciduous, enamel*														
64	Permanent, dentin and cementum	1.5	2.8	0.9	47.5		0.8	15.2				31.3			2.140
65	Deciduous, dentin and cementum*														
66	Pulp	10.8	4.1	1.1	83.2	0.3			0.1	0.4					1.021
67	Teeth, retention region	10.0	22.2	2.2	64.4	0.1		0.2	0.3	0.1	0.4	0.1			1.030
68	Thymus	10.5	24.8	2.7	61.0	0.1		0.2	0.3	0.2	0.2				1.027
69	Thyroid	10.4	11.8	2.5	74.5	0.2		0.1	0.1	0.2	0.1			0.1	1.051
70	Urinary bladder wall	10.5	9.6	2.6	76.1	0.2		0.2	0.2	0.3	0.3				1.040
71	Urine	10.7	0.3	1.0	87.3	0.4		0.1			0.2				1.010
72	Air inside body			80.0	20.0										0.001
73	Water	11.2			88.8										1.000

ET, extrathoracic; BB, bronchi; bb, bronchioles; RST, residual soft tissue.

* The deciduous enamel, dentin and cementum are not included in the 15-year-old phantoms.

Table B.10. List of media, their elemental compositions (percent by mass) and their mass densities for the 15-year-old female phantom.

Medium no.		H	C	N	O	Na	Mg	P	S	Cl	K	Ca	Fe	I	Density (g/cm^3)
1	Adrenal	10.6	28.6	2.5	57.5	0.1		0.2	0.2	0.1	0.2				1.025
2	ET, Trachea, BB, bb	10.1	20.4	2.3	64.9	0.3		1.2	0.5	0.2	0.1				1.060
3	Oral mucosa, Tongue	10.2	14.2	3.4	71.1	0.1		0.2	0.3	0.1	0.4				1.050
4	Blood	10.2	11.0	3.3	74.5	0.1		0.1	0.2	0.3	0.2		0.1		1.060
5	Cortical bone	4.3	16.3	4.3	46.7	0.1	0.2	9.0	0.3			18.8			1.755
6	Humeri, upper, spongiosa	9.9	41.9	2.6	41.0	0.1		1.3	0.2	0.2	0.1	2.6	0.1		1.118
7	Humeri, upper, medullary cavity	11.1	53.0	1.8	33.7	0.1			0.1	0.1	0.1				1.002
8	Humeri, lower, spongiosa	9.9	50.4	1.7	32.0	0.1		1.8	0.2	0.1		3.8			1.144
9	Humeri, lower, medullary cavity	11.2	57.1	1.4	29.9	0.1			0.1	0.1	0.1				0.994
10	Radii, spongiosa	10.0	51.2	1.6	31.5	0.1		1.7	0.2	0.1		3.6			1.133
11	Ulnae, spongiosa	9.7	48.8	1.8	32.9	0.1		2.1	0.2	0.1		4.3			1.164
12	Radii, medullary cavity	11.5	62.8	0.8	24.6	0.1			0.1	0.1					0.982
13	Ulnae, medullary cavity	11.5	62.8	0.8	24.6	0.1			0.1	0.1					0.982
14	Wrists and hand bones, spongiosa	10.6	55.6	1.3	28.9	0.1		1.1	0.1	0.1		2.2			1.075
15	Clavicles, spongiosa	9.8	41.7	2.6	40.8	0.1		1.5	0.2	0.1	0.1	3.0	0.1		1.131
16	Cranium, spongiosa	9.0	36.1	2.9	43.6	0.1		2.6	0.2	0.1	0.1	5.3			1.224
17	Femora, upper, spongiosa	9.6	40.0	2.7	41.9	0.1		1.7	0.2	0.1	0.1	3.5	0.1		1.152
18	Femora, upper, medullary cavity	11.1	53.0	1.8	33.7	0.1			0.1	0.1	0.1				1.002
19	Femora, lower, spongiosa	9.5	47.0	1.9	34.0	0.1		2.3	0.2	0.1		4.9			1.188
20	Femora, lower, medullary cavity	11.2	57.1	1.4	29.9	0.1			0.1	0.1	0.1				0.994
21	Tibiae, spongiosa	10.6	55.6	1.3	28.9	0.1		1.1	0.1	0.1		2.2			1.076
22	Fibulae, spongiosa	10.0	50.8	1.6	31.7	0.1		1.8	0.2	0.1		3.7			1.138
23	Patellae, spongiosa	10.6	55.6	1.3	28.9	0.1		1.1	0.1	0.1		2.2			1.076
24	Tibiae, medullary cavity	11.5	62.8	0.8	24.6	0.1			0.1	0.1					0.982
25	Fibulae, medullary cavity	11.5	62.8	0.8	24.6	0.1			0.1	0.1					0.982
26	Ankles and foot, spongiosa	10.6	55.6	1.3	28.9	0.1		1.1	0.1	0.1		2.2			1.075
27	Mandible, spongiosa	9.2	37.3	2.9	43.1	0.1		2.3	0.2	0.1	0.1	4.7			1.201
28	Pelvis, spongiosa	10.2	41.8	2.7	42.0			0.9	0.2	0.2	0.1	1.8	0.1		1.088
29	Ribs, spongiosa	10.0	39.0	3.0	44.4			1.0	0.2	0.2	0.1	2.0	0.1		1.102
30	Scapulae, spongiosa	9.0	36.5	2.9	43.4	0.1	0.1	2.5	0.2	0.1	0.1	5.1			1.216
31	Cervical spine, spongiosa	9.8	37.8	3.0	44.8			1.3	0.2	0.2	0.1	2.7	0.1		1.127
32	Thoracic spine, spongiosa	9.9	38.8	3.0	44.4	0.1		1.1	0.2	0.2	0.1	2.1	0.1		1.107
33	Lumbar spine, spongiosa	10.1	39.5	2.9	44.2			0.9	0.2	0.2	0.1	1.8	0.1		1.092
34	Sacrum, spongiosa	10.5	43.5	2.6	41.3			0.5	0.2	0.2	0.1	1.0	0.1		1.055
35	Sternum, spongiosa	10.1	39.9	2.9	44.1			0.8	0.2	0.2	0.1	1.6	0.1		1.084
36	Cartilage	9.6	9.9	2.2	74.4	0.5		2.2	0.9	0.3					1.099
37	Brain	10.7	14.4	2.2	71.3	0.2		0.4	0.2	0.3	0.3				1.041
38	Breast, adipose tissue	11.3	43.3	0.7	44.4	0.1			0.1	0.1					0.963
39	Breast, glandular tissue	10.6	32.4	3.0	53.5	0.1		0.1	0.2	0.1					1.021
40	Eye lens, sensitive	9.6	19.5	5.7	64.6	0.1		0.1	0.3	0.1					1.050
41	Eye lens, insensitive	9.6	19.5	5.7	64.6	0.1		0.1	0.3	0.1					1.084
42	Cornea	10.2	12.5	3.7	73.1	0.1		0.1	0.2	0.1					1.075
43	Aqueous	11.2	0.5	0.1	88.2										1.005
44	Vitreous	11.2	0.5	0.1	88.2										1.013
45	Gall bladder wall, Pituitary gland, Salivary glands, Tonsils, Spinal cord, Ureter	10.6	30.8	2.4	55.4	0.1		0.2	0.2	0.1	0.2				1.021
46	Gall bladder contents	10.6	31.5	2.4	54.7	0.1		0.2	0.2	0.1	0.2				1.020
47	Stomach wall, Oesophagus	10.6	11.4	2.4	75.0	0.1		0.1	0.1	0.2	0.1				1.035
48	Small intestine wall, Colon wall	10.6	11.4	2.4	75.0	0.1		0.1	0.1	0.2	0.1				1.035
49	GI contents	10.0	22.2	2.2	64.4	0.1		0.2	0.3	0.1	0.4	0.1			1.030
50	Heart wall	10.5	10.5	2.6	75.5	0.1		0.2	0.1	0.2	0.3				1.042
51	Kidney	10.3	12.7	3.1	72.8	0.2		0.2	0.2	0.2	0.2	0.1			1.052
52	Liver	10.2	13.3	3.0	72.2	0.2		0.3	0.3	0.2	0.3				1.060
53	Lung	10.3	10.8	3.2	74.7	0.1		0.1	0.2	0.3	0.2		0.1		0.301
54	Lymphatic nodes	10.8	4.4	1.2	82.8	0.3			0.1	0.4					1.031
55	Muscle	10.2	14.2	3.4	71.1	0.1		0.2	0.3	0.1	0.4				1.050
56	Gonads	10.5	9.4	2.4	76.7	0.2		0.2	0.2	0.2	0.2				1.051

57	Pancreas	10.5	16.0	2.4	70.2	0.2		0.2	0.1	0.2	0.2				1.043
58	Uterus	10.5	9.4	2.4	76.7	0.2		0.2	0.2	0.2	0.2				1.050
59	RST	11.2	41.6	0.8	46.0	0.1		0.1	0.1	0.1					0.971
60	Skin	10.0	20.0	4.2	64.9	0.2		0.1	0.2	0.3	0.1				1.098
61	Spleen	10.3	11.2	3.2	74.2	0.1		0.3	0.2	0.2	0.3				1.060
62	Permanent, enamel	0.4	0.7	0.2	43.4		0.3	18.0				37.0			3.000
63	Deciduous, enamel*														
64	Permanent, dentin and cementum	1.5	2.8	0.9	47.5		0.8	15.2				31.3			2.140
65	Deciduous, dentin and cementum*														
66	Pulp	10.8	4.1	1.1	83.2	0.3			0.1	0.4					1.021
67	Teeth, retention region	10.0	22.2	2.2	64.4	0.1		0.2	0.3	0.1	0.4	0.1			1.030
68	Thymus	10.6	30.8	2.4	55.4	0.1		0.2	0.2	0.1	0.2				1.026
69	Thyroid	10.4	11.8	2.5	74.5	0.2		0.1	0.1	0.2	0.1			0.1	1.051
70	Urinary bladder wall	10.5	9.6	2.6	76.1	0.2		0.2	0.2	0.3	0.3				1.040
71	Urine	10.7	0.3	1.0	87.3	0.4		0.1			0.2				1.010
72	Air inside body			80.0	20.0										0.001
73	Water	11.2			88.8										1.000

ET, extrathoracic; BB, bronchi; bb, bronchioles; RST, residual soft tissue.

* The deciduous enamel, dentin and cementum are not included in the 15-year-old phantoms.

ANNEX C. LIST OF ANATOMICAL SOURCE REGIONS, ACRONYMS AND IDENTIFICATION NUMBERS

Table C.1. List of source regions, their acronyms and corresponding identification (ID) numbers in the phantoms.

Source region	Acronym	ID number(s)
Oral cavity	O-cavity	13300
Oral mucosa	O-mucosa	500, 501, 600
Teeth surface*	Teeth-S	12856
Teeth volume	Teeth-V	†
Tongue	Tongue	500, 13300, 13301
Tonsils	Tonsils	13400
Oesophagus fast	Oesophag-f	11003
Oesophagus slow	Oesophag-s	11003
Oesophagus	Oesophagus-w	11000, 11001, 11002
Stomach contents	St-cont	7300
Stomach wall	St-wall	7200, 7201, 7202, 7203
Stomach mucosa	St-mucosa	7200, 7201, 7202
Small intestine contents	SI-cont	7500, 7501
Small intestine villi	SI-villi	7500
Small intestine wall	SI-wall	7400, 7401, 7402, 7403
Small intestine mucosa	SI-mucosa	7400, 7401, 7402
Right colon contents	RC-cont	7700, 7900
Right colon wall	RC-wall	7600, 7601, 7602, 7800, 7801, 7802
Right colon mucosa	RC-mucosa	7600, 7601, 7800, 7801
Left colon contents	LC-cont	8100, 8300
Left colon wall	LC-wall	8000, 8001, 8002, 8200, 8201, 8202
Left colon mucosa	LC-mucosa	8000, 8001, 8200, 8201
Rectosigmoid colon contents	RS-cont	8500, 8603
Rectosigmoid colon wall	RS-wall	8400, 8401, 8402, 8600, 8601, 8602
Rectosigmoid colon mucosa	RS-mucosa	8400, 8401, 8600, 8601
ET_1 surface	ET1-sur	300
ET_2 surface	ET2-sur	400
ET_1 wall	ET1-wall	300, 301, 302, 303
ET_2 wall	ET2-wall	401, 402, 403, 404, 405
ET_2 bound region	ET2-bnd	401, 402, 403
ET_2 sequestered region	ET2-seq	404
Extrathoracic lymph nodes	LN-ET	10000
Bronchial – fast	Bronchi-f	800
Bronchial – slow	Bronchi-s	801
Bronchi bound region	Bronchi-b	802, 803, 804, 805, 806
Bronchi sequestered region	Bronchi-q	807
Bronchiolar – fast	Brchiole-f	810
Bronchiolar – slow	Brchiole-s	811
Bronchiolar bound region	Brchiole-b	812, 813, 814
Bronchiolar sequestered region	Brchiole-q	815
Alveolar-interstitium	AI	9700, 9900
Thoracic lymph nodes	LN-Th	10100
Right lung lobe	RLung	9900
Left lung lobe	LLung	9700
RLung + LLung	Lungs	9700, 9900
Right adrenal gland	RAdrenal	200
Left adrenal gland	LAdrenal	100
RAdrenal + LAdrenal	Adrenals	100, 200

Blood vessels of head	HBlood	900, 910
Blood vessels of trunk	TBlood	1000, 1010
Blood vessels of arms	ABlood	1100, 1110
Blood vessels of legs	LBlood	1200, 1210
Blood in heart	Ht-cont	8800
Total blood	Blood	‡
Cortical bone surface	C-bone-S	§
Cortical bone volume	C-bone-V	§
Trabecular bone surface	T-bone-S	¶
Trabecular bone volume	T-bone-V	¶
Cortical bone marrow	C-marrow	**
Trabecular bone marrow	T-marrow	††
Brain	Brain	6100
Right breast adipose	RBreast-a	6400
Right breast glandular	RBreast-g	6500
Left breast adipose	LBreast-a	6200
Left breast glandular	LBreast-g	6300
RBreast-a + RBreast-g	RBreast	6400, 6500
LBreast-a + LBreast-g	LBreast	6200, 6300
RBreast-a + LBreast-a	Breast-a	6200, 6400
RBreast-g + LBreast-g	Breast-g	6300, 6500
Breast-a + Breast-g	Breast	6200, 6300, 6400, 6500
Lens of eye	Eye-lens	6600, 6601, 6800, 6801
Gall bladder	GB-wall	7000
Gall bladder contents	GB-cont	7100
Heart	Ht-wall	8700
Right kidney cortex	RKidney-C	9200
Right kidney medulla	RKidney-M	9300
Right kidney pelvis	RKidney-P	9400
Right kidney C+M+P	RKidney	9200, 9300, 9400
Left kidney cortex	LKidney-C	8900
Left kidney medulla	LKidney-M	9000
Left kidney pelvis	LKidney-P	9100
Left kidney C+M+P	LKidney	8900, 9000, 9100
RKidney + LKidney	Kidneys	8900, 9000, 9100, 9200, 9300, 9400
Liver	Liver	9500
Systemic lymph nodes	LN-Sys	10200, 10300, 10400, 10500
Muscle	Muscle	10600, 10700, 10800, 10900
Right ovary	ROvary	11200
Left ovary	LOvary	11100
ROvary + LOvary	Ovaries	11100, 11200
Pancreas	Pancreas	11300
Pituitary gland	P-gland	11400
Prostate	Prostate	11500
Salivary glands	S-glands	12000, 12100
Skin	Skin	12200, 12201, 12300, 12301, 12400, 12401, 12500, 12501
Spinal cord	Sp-cord	12600
Spleen	Spleen	12700
Testes	Testes	12900, 13000
Thymus	Thymus	13100
Thyroid	Thyroid	13200
Ureters	Ureters	13500, 13600
Urinary bladder	UB-wall	13700, 13701
Urinary bladder content	UB-cont	13800
Uterus/cervix	Uterus	13900
Adipose/residual tissue	Adipose	11600, 11700, 11800, 11900
Total body tissues (total body minus contents of walled organs)	T-body	‡‡

Soft tissue (T-body – mineral bone)	S-tissue	§§

ET, extrathoracic.

[*] Teeth surface is not included in the newborn phantoms.

[†] Teeth volume of the newborn phantoms is 12849, 12851, 12853 and 12855; teeth volume of the 1-year-old phantoms is 12802, 12803, 12818, 12819, 12833, 12841, 12848, 12849, 12850, 12851, 12852, 12853, 12854 and 12855; teeth volume of the 5-year-old phantoms is 12802, 12803, 12810, 12811, 12814, 12815, 12818, 12819, 12826, 12827, 12830, 12831, 12833, 12837, 12839, 12841, 12845, 12847, 12848, 12850, 12852, 12853, 12854 and 12855; teeth volume of the 10-year-old phantoms is 12800, 12801, 12802, 12803, 12804, 12805, 12806, 12807, 12808, 12809, 12810, 12811, 12812, 12813, 12814, 12815, 12816, 12817, 12824, 12825, 12826, 12827, 12828, 12829, 12830, 12831, 12832, 12833, 12834, 12835, 12836, 12837, 12838, 12839, 12840, 12844, 12845, 12846, 12847, 12848, 12850, 12852, 12853, 12854 and 12855; and teeth volume of the 15-year-old phantoms is 12800, 12801, 12804, 12805, 12806, 12807, 12808, 12809, 12812, 12813, 12816, 12817, 12820, 12821, 12822, 12823, 12824, 12825, 12828, 12829, 12832, 12834, 12835, 12836, 12838, 12840, 12842, 12843, 12844, 12846, 12848, 12850, 12852 and 12854.

[‡] Blood: 900, 910, 1000, 1010, 1100, 1110, 1200, 1210, 8800, plus blood included in the organs and tissues.

[§] Cortical bone mineral: 1300, 1600, 1900, 1910, 2200, 2400, 2600, 2800, 3100, 3400, 3410, 3420, 3700, 3900, 4100, 4300, 4500, 4700, 4900, 5100, 5300, 5500.

[¶] Trabecular bone mineral: mineral bone fraction of 1400, 1700, 2000, 2010, 2300, 2500, 2700, 2900, 3200, 3500, 3510, 3520, 3800, 4000, 4200, 4400, 4600, 4800, 5000, 5200, 5400, 5600.

[**] Cortical bone marrow: 1500, 1800, 2100, 2110, 3000, 3300, 3600, 3610.

[††] Trabecular bone marrow: marrow fraction of 1400, 1500, 1700, 1800, 2000, 2010, 2100, 2110, 2300, 2500, 2700, 2900, 3000, 3200, 3300, 3500, 3510, 3520, 3600, 3610, 3800, 4000, 4200, 4400, 4600, 4800, 5000, 5200, 5400, 5600 (red and yellow marrow).

[‡‡] Total body tissues: 100–7000, 7200–7203, 7400–7403, 7600–7602, 7800–7802, 8000–8002, 8200–8202, 8400–8402, 8600–8602, 8700–11002, 11100–13701, 13900.

[§§] Soft tissue: 100–1210, 1500, 1800, 2100, 2110, 3000, 3300, 3600, 3610, 5700–7000, 7200–7203, 7400–7403, 7600–7602, 7800–7802, 8000–8002, 8200–8202, 8400–8402, 8600–8602, 8700–11002, 11100–12700, 12900–13701, 13900, plus soft tissue fraction of 1400, 1700, 2000, 2010, 2300, 2500, 2700, 2900, 3200, 3500, 3510, 3520, 3800, 4000, 4200, 4400, 4600, 4800, 5000, 5200, 5400, 5600.

ANNEX D. LIST OF ANATOMICAL TARGET REGIONS, ACRONYMS AND IDENTIFICATION NUMBERS

Table D.1. List of target regions, their acronyms and corresponding identification (ID) numbers in the phantoms.

Target region	Acronym	ID number(s)
Red (active) marrow	R-marrow	*
Colon wall	Colon	7600, 7601, 7602, 7800, 7801, 7802, 8000, 8001, 8002, 8200, 8201, 8202, 8400, 8401, 8402, 8600, 8601, 8602
Stem cells of colon	Colon-stem	7601, 7801, 8001, 8201, 8401, 8601
RLung + LLung	Lungs	9700, 9900
Stomach wall	St-wall	7200, 7201, 7202, 7203
Stem cells of stomach	St-stem	7201
Breast-a + Breast-g	Breast	6200, 6300, 6400, 6500
ROvary + LOvary	Ovaries	11100, 11200
Testes	Testes	12900, 13000
Urinary bladder wall	UB-wall	13700, 13701
Urinary bladder basal cells	UB-basal	13701
Oesophagus wall	Oesophagus	11000, 11001, 11002
Oesophagus basal cells	Oesophagus-bas	11001
Liver	Liver	9500
Thyroid	Thyroid	13200
50-µm endosteal region	Endost-BS	†
Brain	Brain	6100
Salivary glands	S-glands	12000, 12100
Skin	Skin	12200, 12201, 12300, 12301, 12400, 12401, 12500, 12501
Basal cells of skin	Skin-bas	12201, 12301, 12401, 12501
RAdrenal + LAdrenal	Adrenals	100, 200
ET region	ET	300, 301, 302, 303, 401, 402, 403, 404, 405
Gall bladder wall	GB-wall	7000
Heart wall	Ht-wall	8700
RKidney + LKidney	Kidneys	8900, 9000, 9100, 9200, 9300, 9400
Systemic lymph nodes	LN-Sys	10200, 10300, 10400, 10500
Muscle	Muscle	10600, 10700, 10800, 10900
Oral mucosa	O-mucosa	500, 501, 600
Pancreas	Pancreas	11300
Prostate	Prostate	11500
Small intestine wall	SI-wall	7400, 7401, 7402, 7403
Stem cells of small intestine	SI-stem	7401
Spleen	Spleen	12700
Thymus	Thymus	13100
Uterus/cervix	Uterus	13900
Tongue	Tongue	500, 13300, 13301
Tonsils	Tonsils	13400
Right colon wall (ascending + right transverse)	RC-wall	7600, 7601, 7602, 7800, 7801, 7802
Left colon wall (left transverse + descending)	LC-wall	8000, 8001, 8002, 8200, 8201, 8202
Rectosigmoid colon wall (sigmoid + rectum)	RS-wall	8400, 8401, 8402, 8600, 8601, 8602
Stem cells of right colon (ascending + right transverse)	RC-stem	7601, 7801
Stem cells of left colon (left transverse + descending)	LC-stem	8001, 8201
Stem cells of rectosigmoid colon (sigmoid + rectum)	RSig-stem	8401, 8601
Basal cells of anterior nasal passages	ET1-bas	302
Basal cells of posterior nasal passages + pharynx	ET2-bas	402
Extrathoracic lymph nodes	LN-ET	10000
Bronchi basal cells	Bronch-bas	804, 805

Bronchi secretory cells	Bronch-sec	803, 804
Bronchiolar secretory cells	Brchiol-sec	813
Alveolar-interstitial	AI	9700, 9900
Thoracic lymph nodes	LN-Th	10100
Right lung lobe	RLung	9900
Left lung lobe	LLung	9700
Right adrenal gland	RAdrenal	200
Left adrenal gland	LAdrenal	100
Right breast adipose	RBreast-a	6400
Right breast glandular	RBreast-g	6500
Left breast adipose	LBreast-a	6200
Left breast glandular	LBreast-g	6300
RBreast-a + RBreast-g	RBreast	6400, 6500
LBreast-a + LBreast-g	LBreast	6200, 6300
RBreast-a + LBreast-a	Breast-a	6200, 6400
RBreast-g + LBreast-g	Breast-g	6300, 6500
Entire lenses of eye	Lens-ent	6600, 6601, 6800, 6801
Sensitive lenses of eye	Lens-sen	6600, 6800
Right kidney cortex	RKidney-C	9200
Right kidney medulla	RKidney-M	9300
Right kidney pelvis	RKidney-P	9400
Right kidney C+M+P	RKidney	9200, 9300, 9400
Left kidney cortex	LKidney-C	8900
Left kidney medulla	LKidney-M	9000
Left kidney pelvis	LKidney-P	9100
Left kidney C+M+P	LKidney	8900, 9000, 9100
Right ovary	ROvary	11200
Left ovary	LOvary	11100
Pituitary gland	P-gland	11400
Spinal cord	Sp-cord	12600
Ureters	Ureters	13500, 13600
Adipose/residual tissue	Adipose	11600, 11700, 11800, 11900

[*] Red bone marrow fraction in organ IDs: 1400, 1500, 1700, 1800, 2000, 2010, 2100, 2110, 2300, 2500, 2700, 2900, 3000, 3200, 3300, 3500, 3510, 3520, 3600, 3610, 3800, 4000, 4200, 4400, 4600, 4800, 5000, 5200, 5400, 5600.

[†] Endosteum fraction in organ IDs: 1400, 1500, 1700, 1800, 2000, 2010, 2100, 2110, 2300, 2500, 2700, 2900, 3000, 3200, 3300, 3500, 3510, 3520, 3600, 3610, 3800, 4000, 4200, 4400, 4600, 4800, 5000, 5200, 5400, 5600.

ANNEX E. ORGAN DEPTH DISTRIBUTIONS OF SELECTED ORGANS/TISSUES

(E 1) In Figs E.1–E.65, organ depth distributions (ODDs) of the paediatric mesh-type reference computational phantoms (MRCPs) and the P143 phantoms are shown for selected organs [i.e. red bone marrow (RBM), colon, lungs, stomach, breast, gonads, urinary bladder, oesophagus, liver, thyroid, brain, salivary glands and skin]. For their ODD calculation, ten million points were randomly sampled in the considered organ and the distances from the sampled points to the outer surface (e.g. front, back, left, etc.) of the phantoms were calculated. The ODDs represent a depth of an organ/tissue below the outer surface of the phantoms, significantly influencing dose calculation for external exposures.

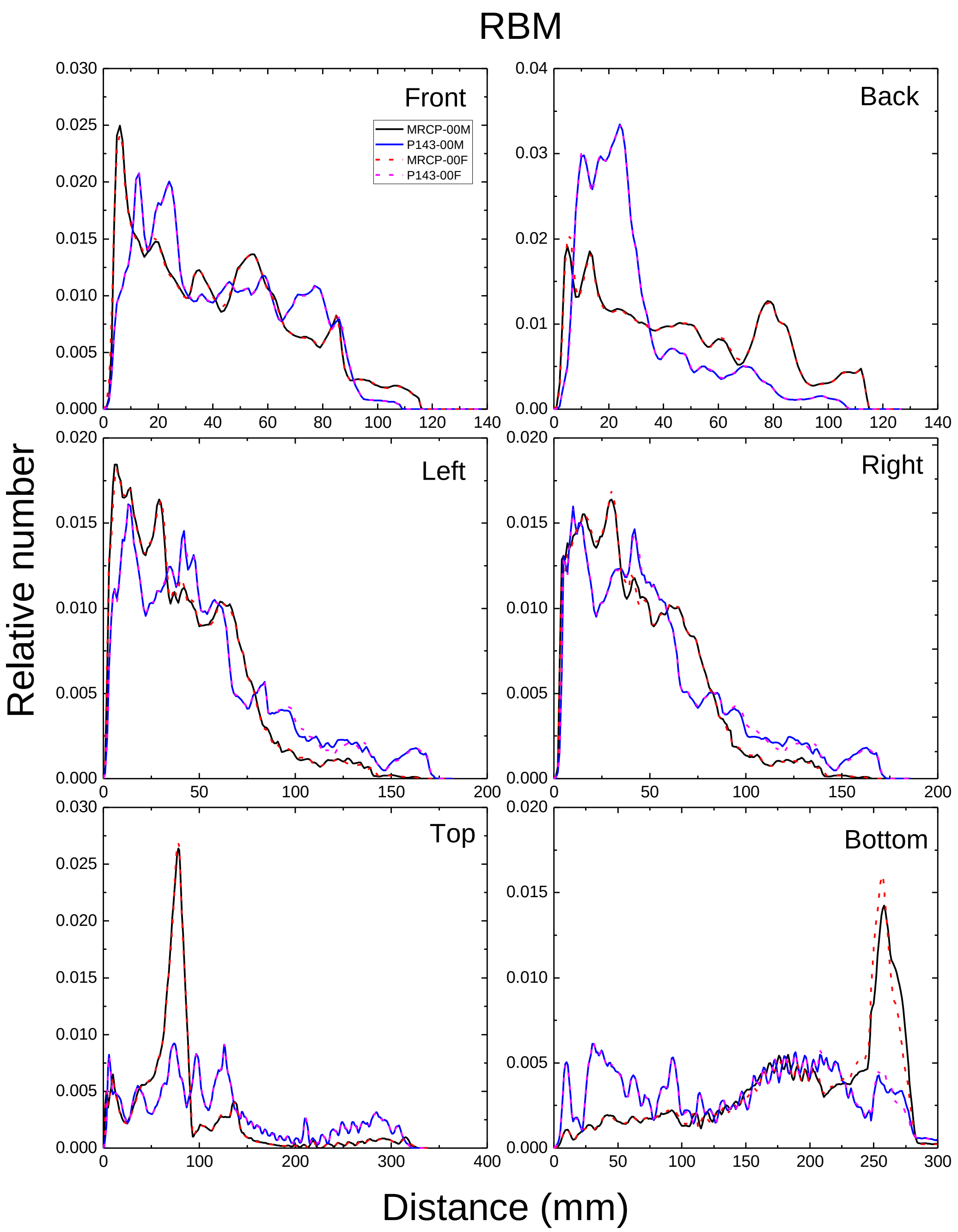

Fig. E.1. Distribution of depths of 10 million randomly sampled points in the red bone marrow (RBM) below the body surface of the newborn male/female phantoms at: front, back, left, right, top and bottom.

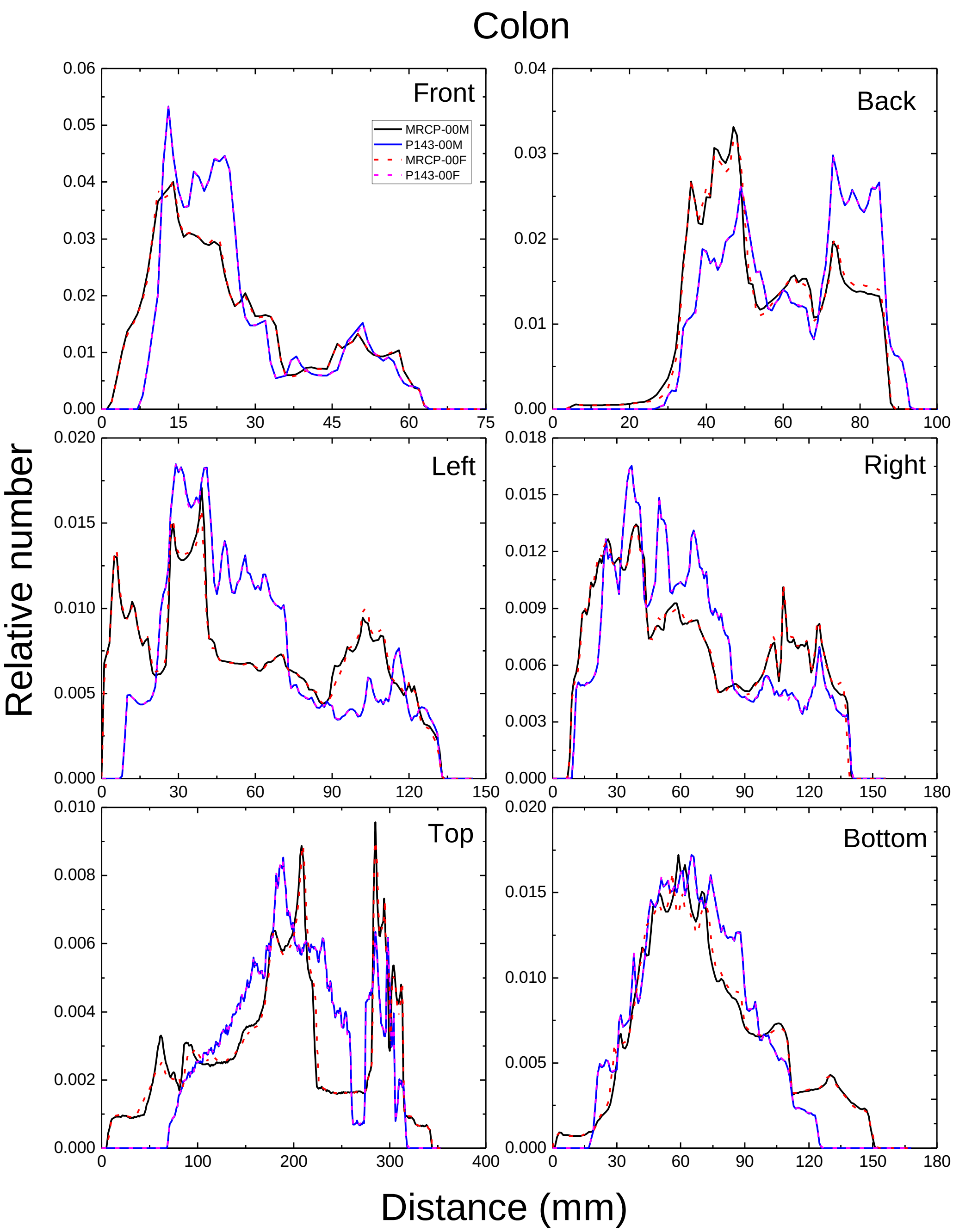

Fig. E.2. Distribution of depths of 10 million randomly sampled points in the colon below the body surface of the newborn male/female phantoms at: front, back, left, right, top and bottom.

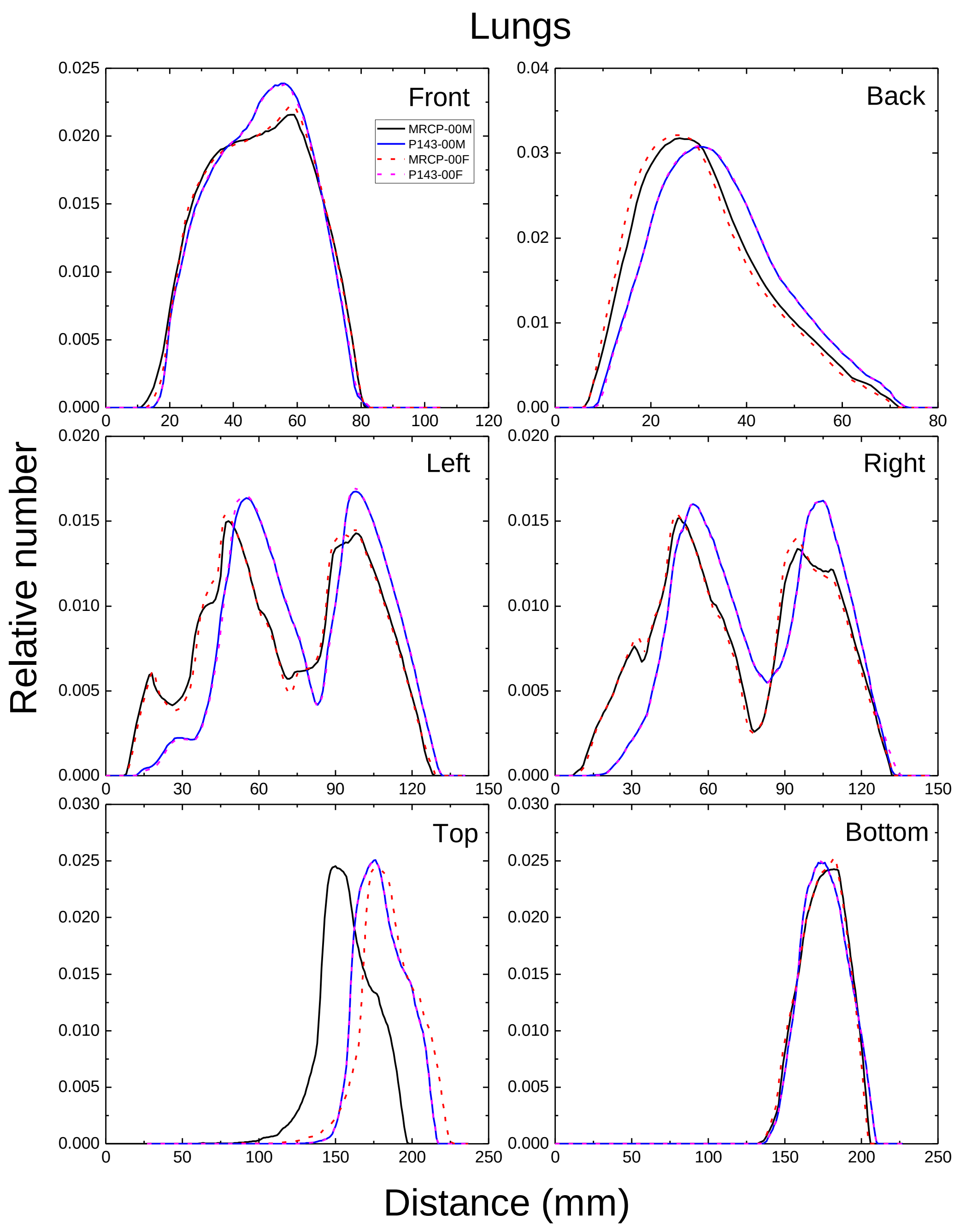

1717

1718 Fig. E.3. Distribution of depths of 10 million randomly sampled points in the lungs below the
1719 body surface of the newborn male/female phantoms at: front, back, left, right, top and bottom.

1720

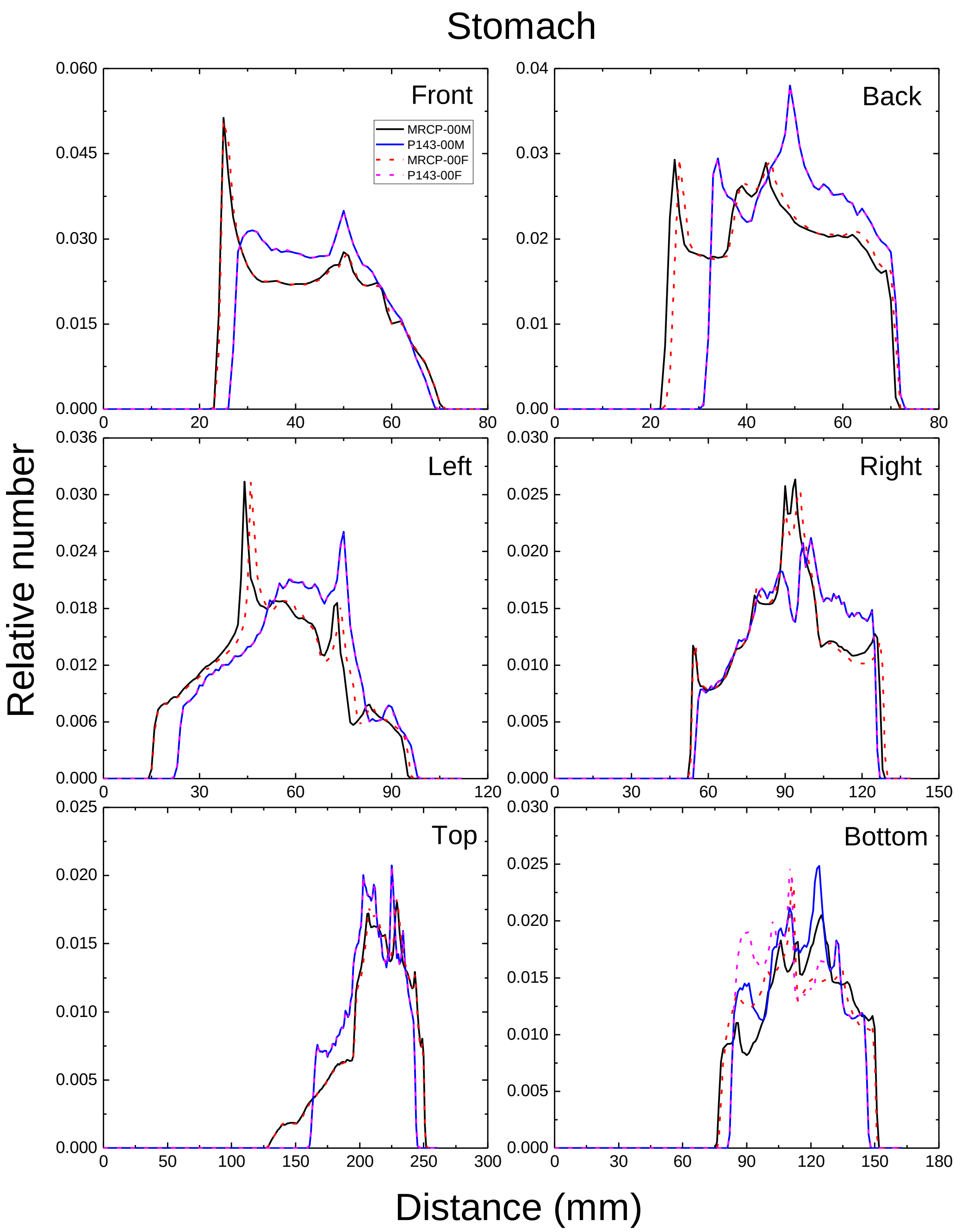

1721
1722 Fig. E.4. Distribution of depths of 10 million randomly sampled points in the stomach below
1723 the body surface of the newborn male/female phantoms at: front, back, left, right, top and
1724 bottom.
1725

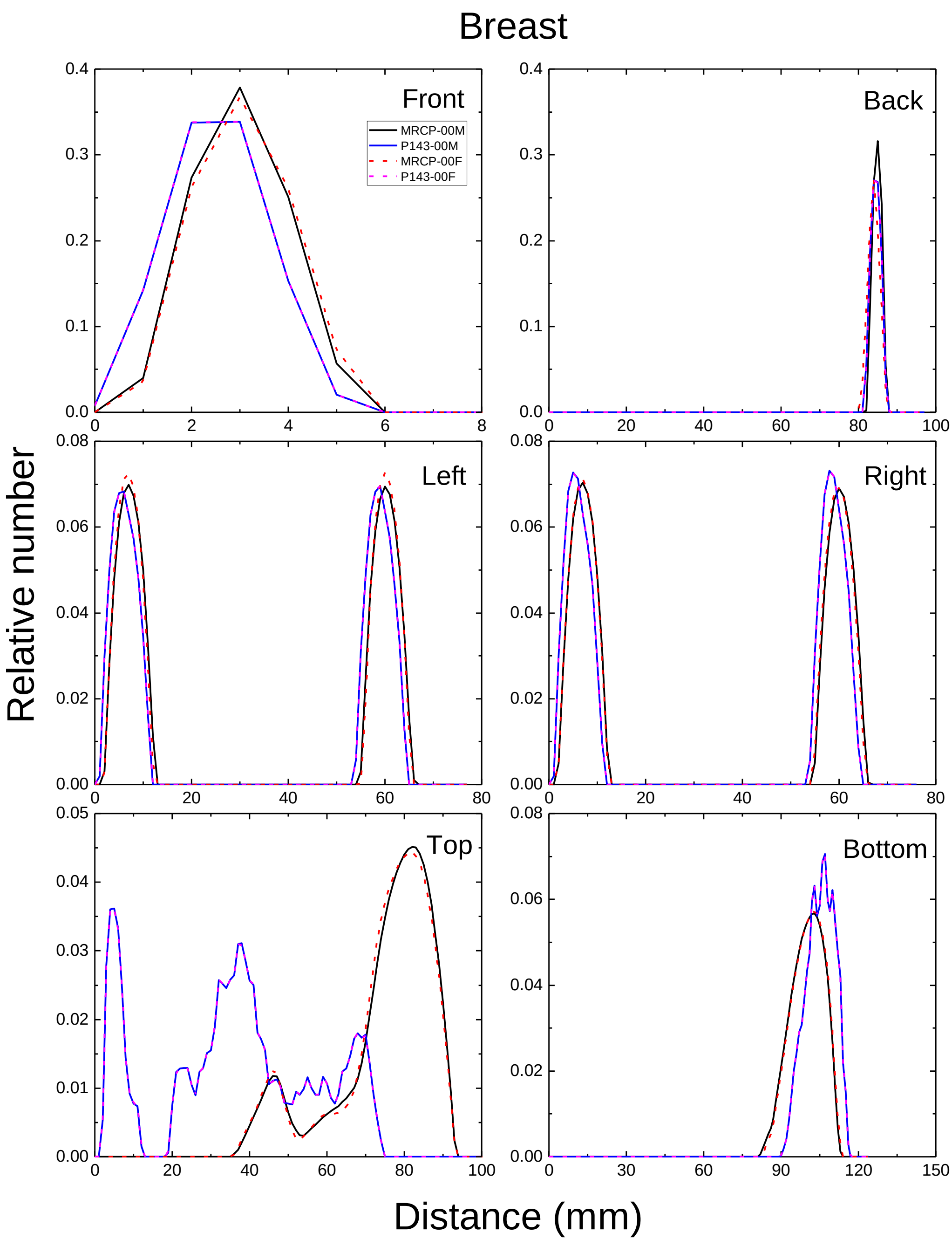

Fig. E.5. Distribution of depths of 10 million randomly sampled points in the breast below the body surface of the newborn male/female phantoms at: front, back, left, right, top and bottom.

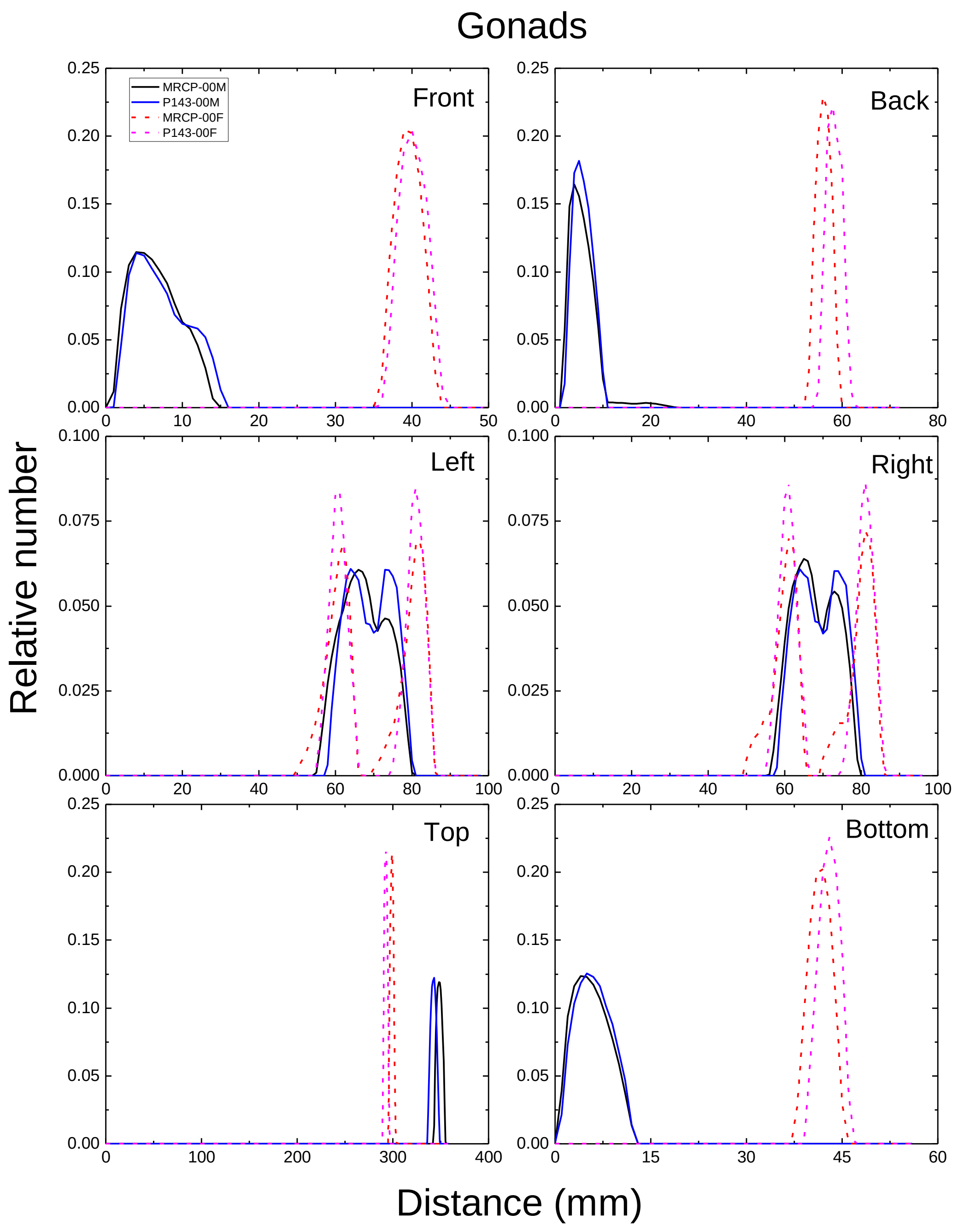

Fig. E.6. Distribution of depths of 10 million randomly sampled points in the gonads below the body surface of the newborn male/female phantoms at: front, back, left, right, top and bottom.

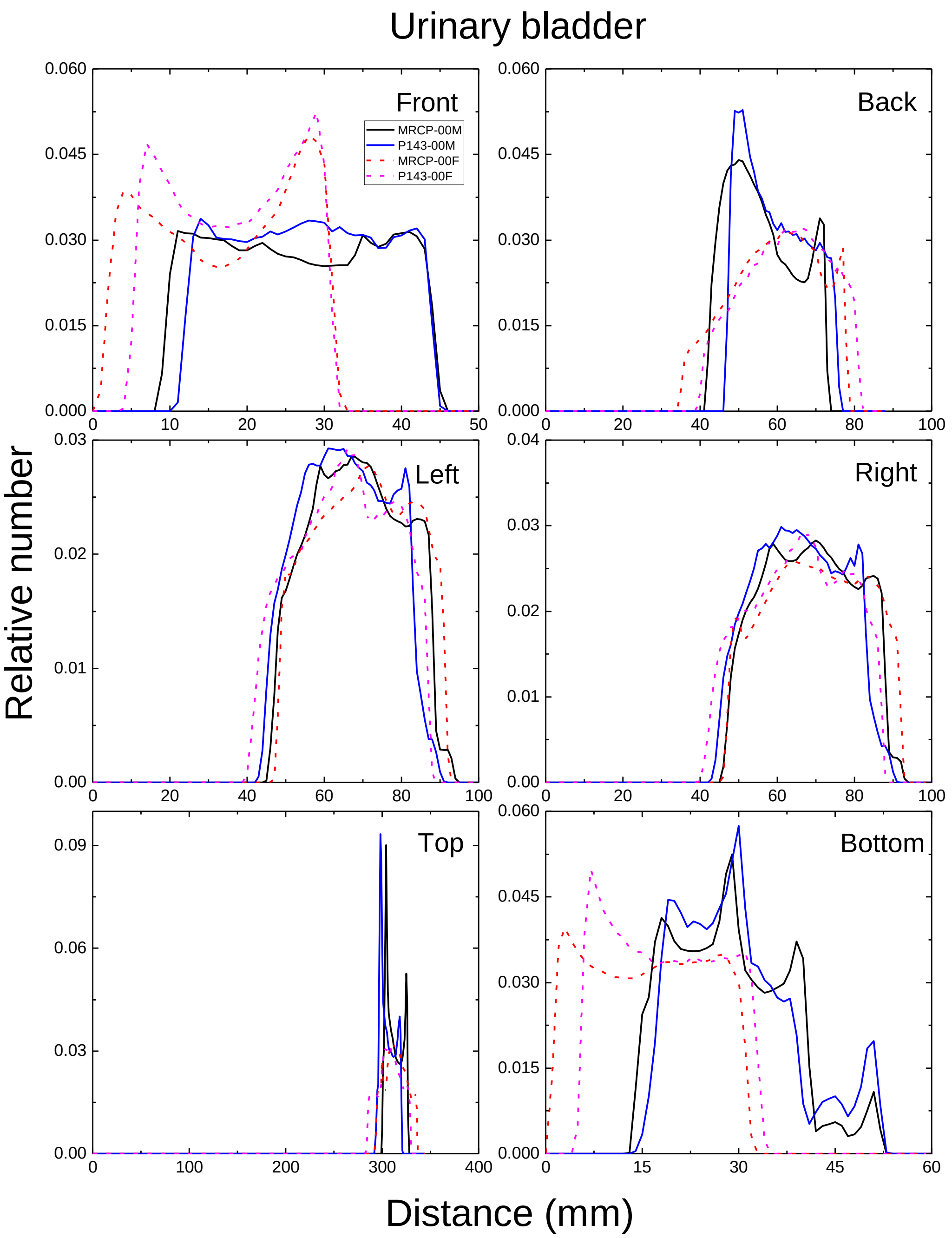

1734
1735 Fig. E.7. Distribution of depths of 10 million randomly sampled points in the urinary bladder
1736 below the body surface of the newborn male/female phantoms at: front, back, left, right, top
1737 and bottom.
1738

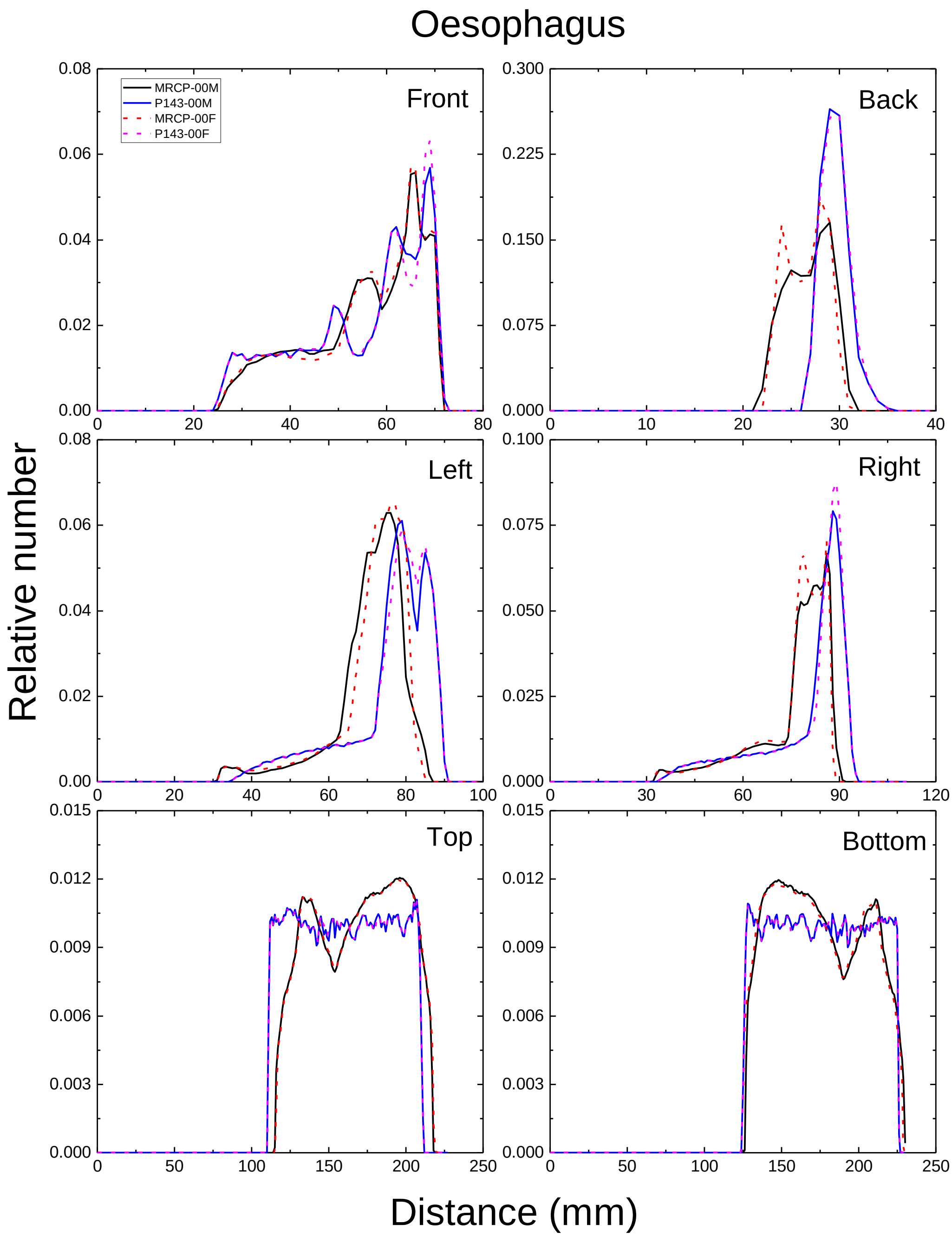

Fig. E.8. Distribution of depths of 10 million randomly sampled points in the oesophagus below the body surface of the newborn male/female phantoms at: front, back, left, right, top and bottom.

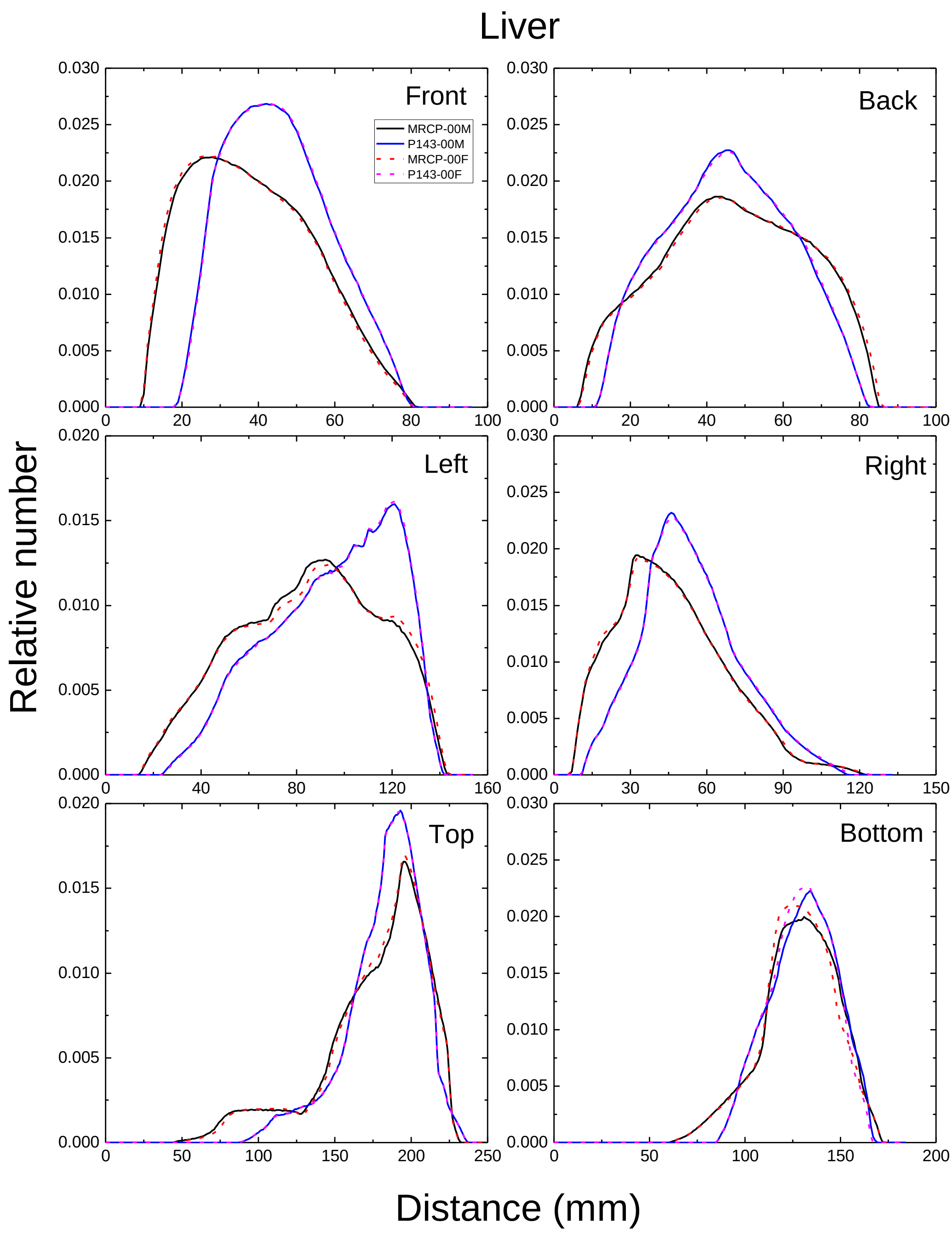

1744
1745 Fig. E.9. Distribution of depths of 10 million randomly sampled points in the liver below the
1746 body surface of the newborn male/female phantoms at: front, back, left, right, top and bottom.
1747

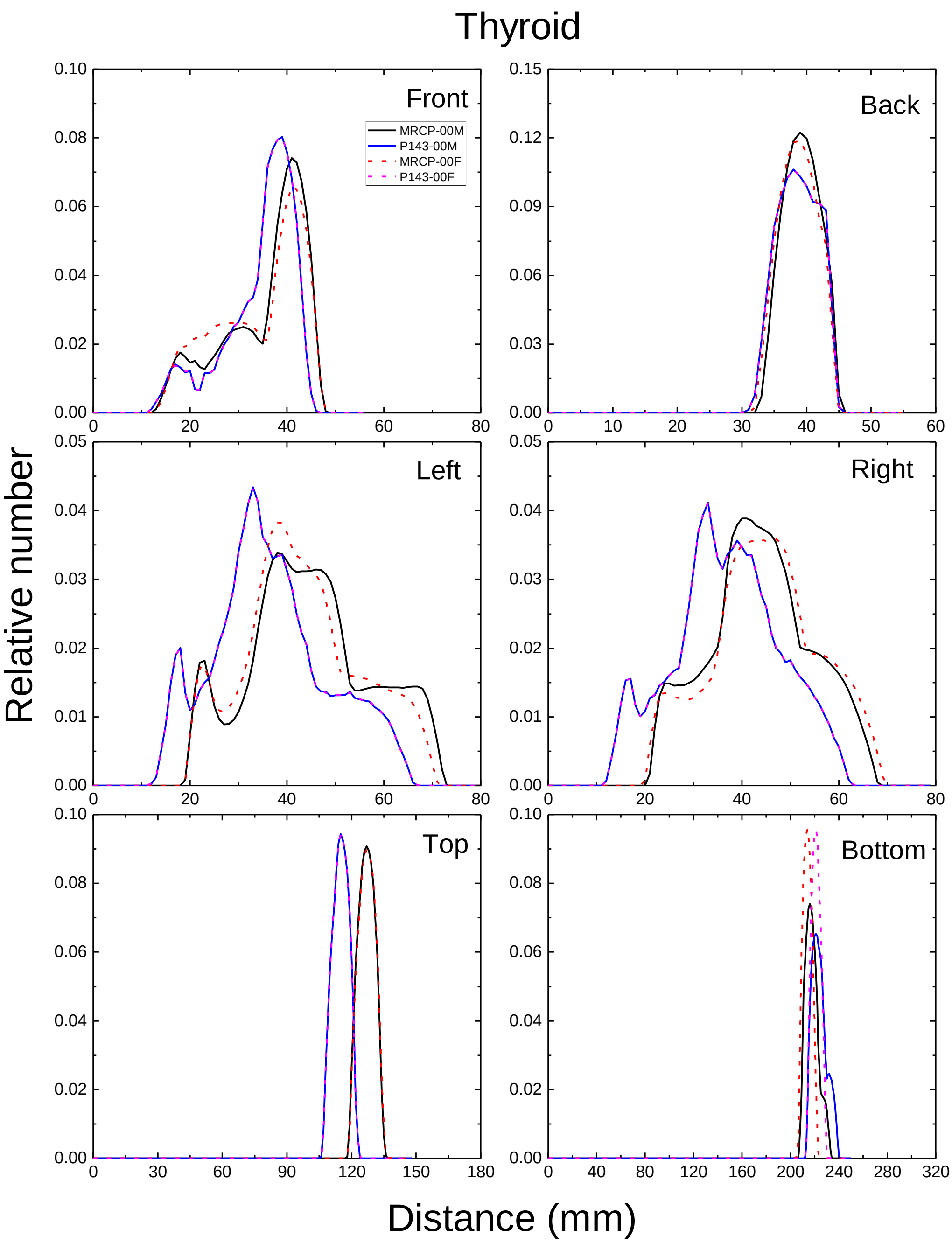

1748
1749 Fig. E.10. Distribution of depths of 10 million randomly sampled points in the thyroid below
1750 the body surface of the newborn male/female phantoms at: front, back, left, right, top and
1751 bottom.
1752

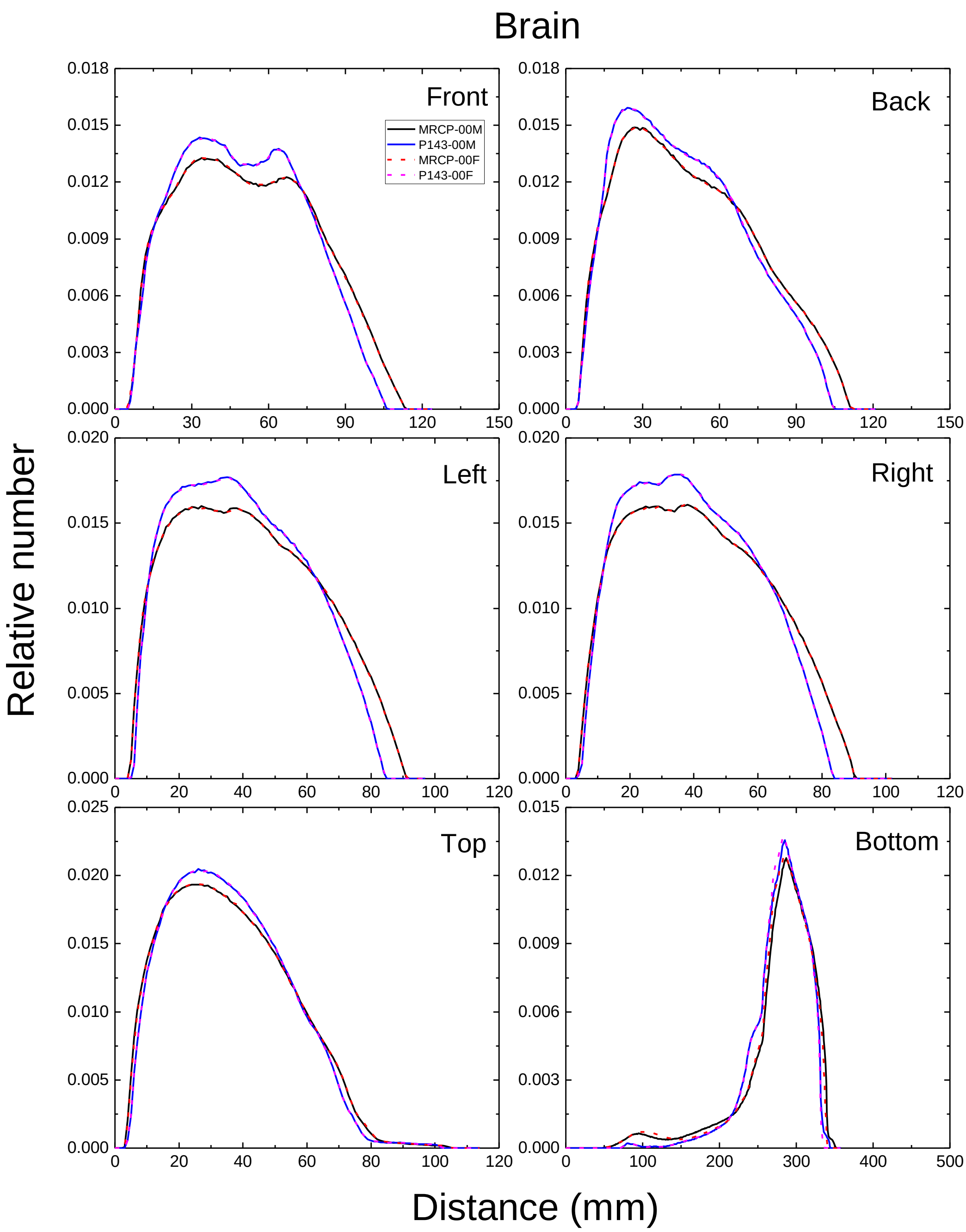

1753
1754 Fig. E.11. Distribution of depths of 10 million randomly sampled points in the brain below the
1755 body surface of the newborn male/female phantoms at: front, back, left, right, top and bottom.
1756

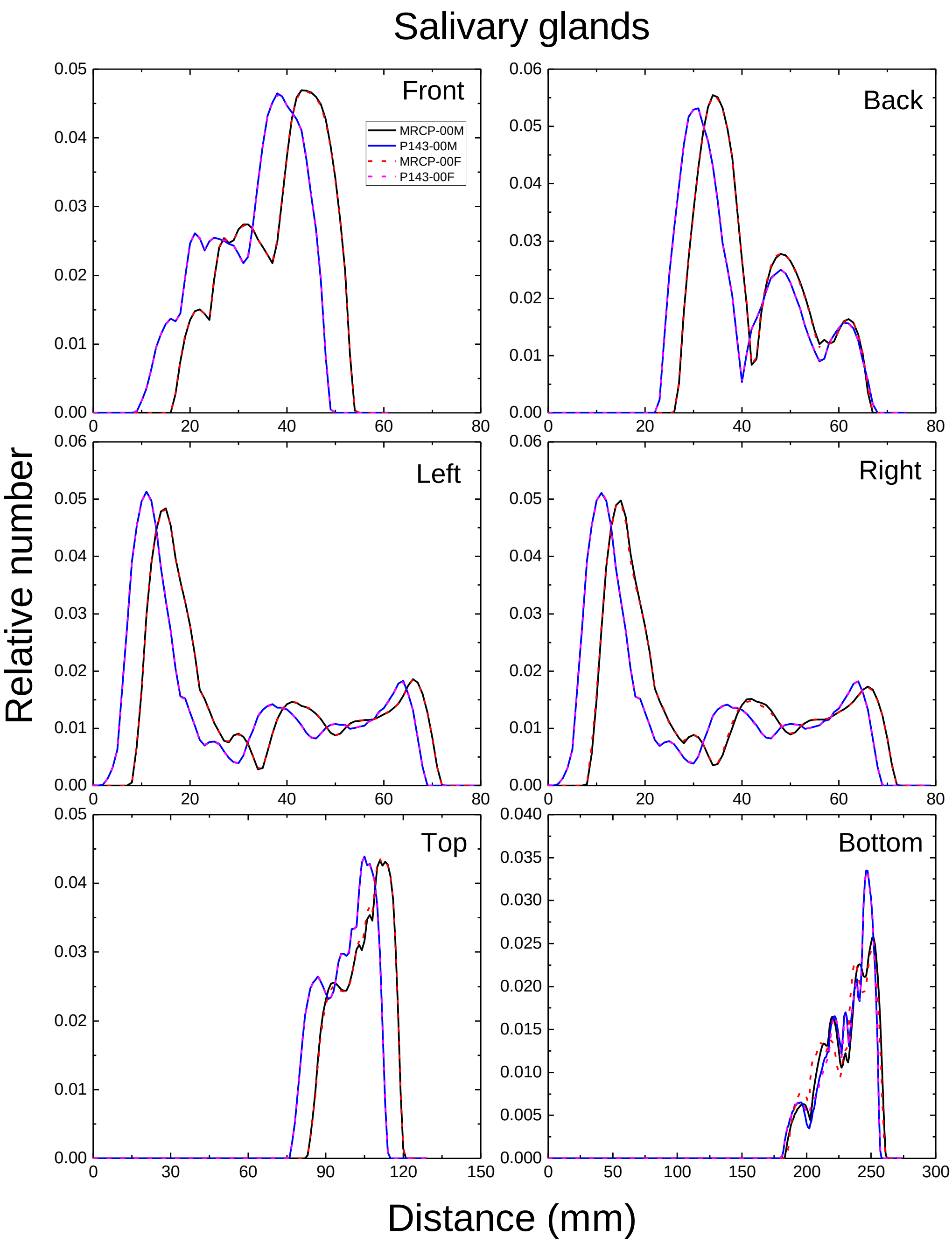

1757
1758 Fig. E.12. Distribution of depths of 10 million randomly sampled points in the salivary glands
1759 below the body surface of the newborn male/female phantoms at: front, back, left, right, top
1760 and bottom.
1761

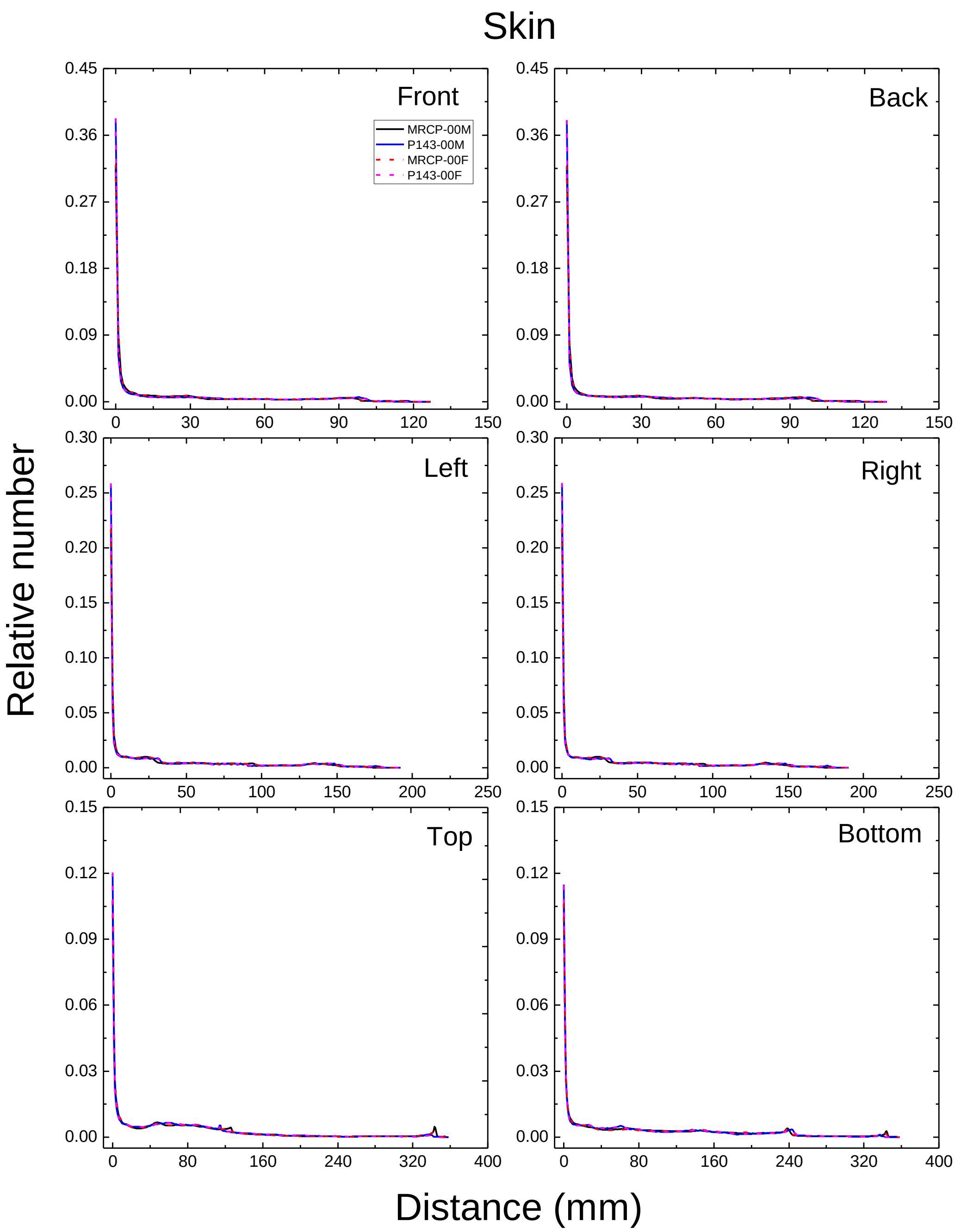

1762
1763 Fig. E.13. Distribution of depths of 10 million randomly sampled points in the skin below the
1764 body surface of the newborn male/female phantoms at: front, back, left, right, top and bottom.
1765

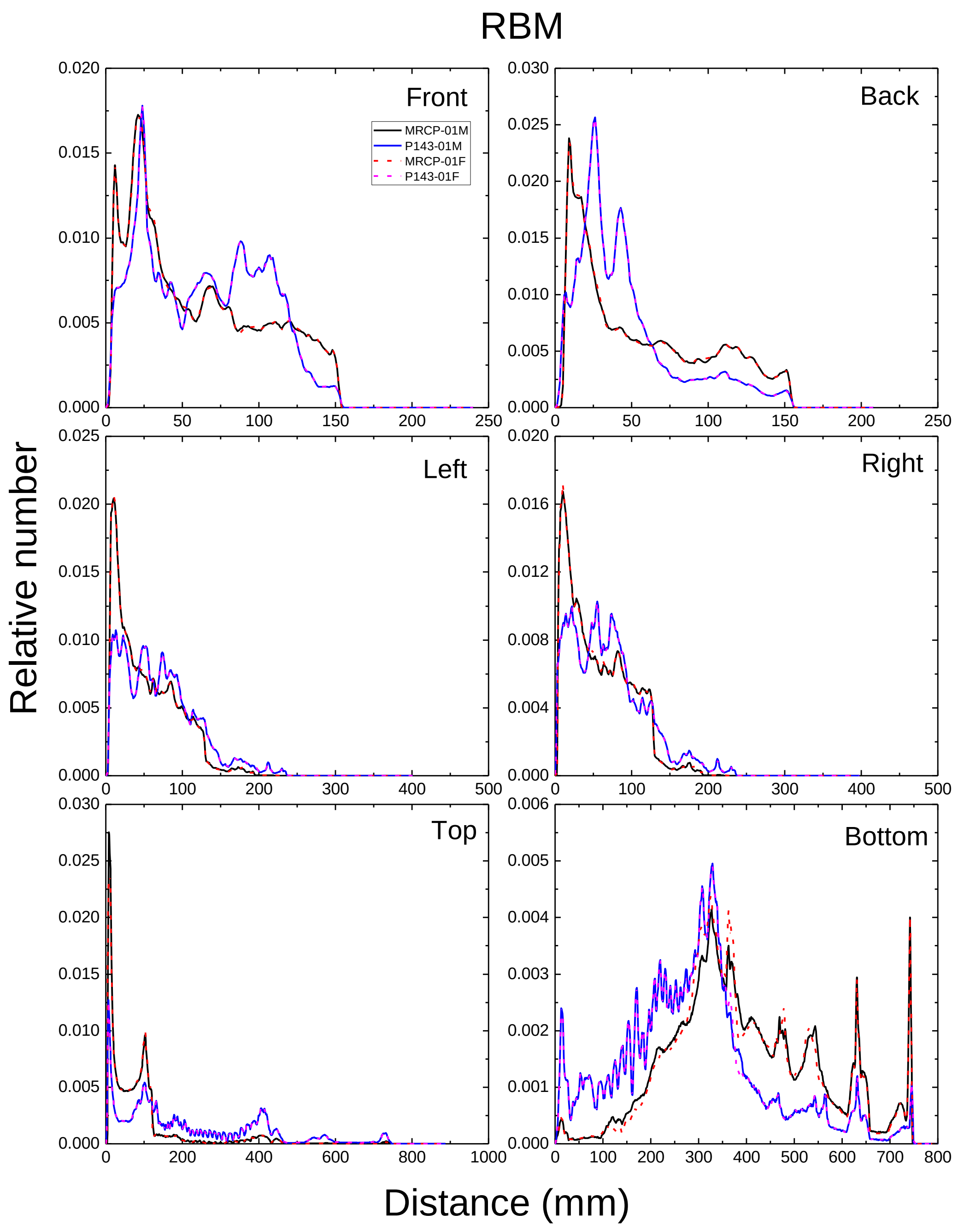

1767 Fig. E.14. Distribution of depths of 10 million randomly sampled points in the red bone marrow
1768 (RBM) below the body surface of the 1-year male/female phantoms at: front, back, left, right,
1769 top and bottom.

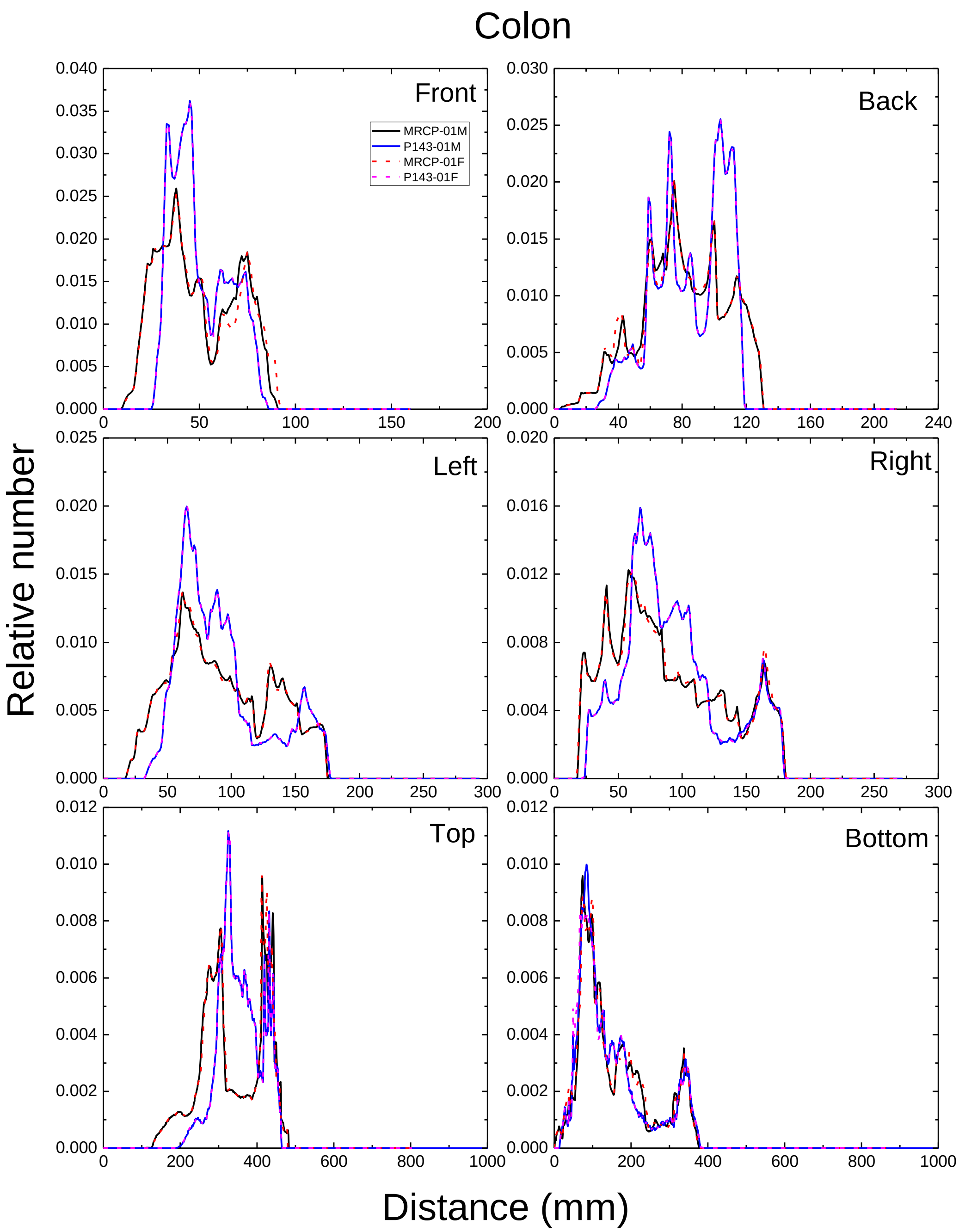

1771
1772 Fig. E.15. Distribution of depths of 10 million randomly sampled points in the colon below the
1773 body surface of the 1-year male/female phantoms at: front, back, left, right, top and bottom.
1774

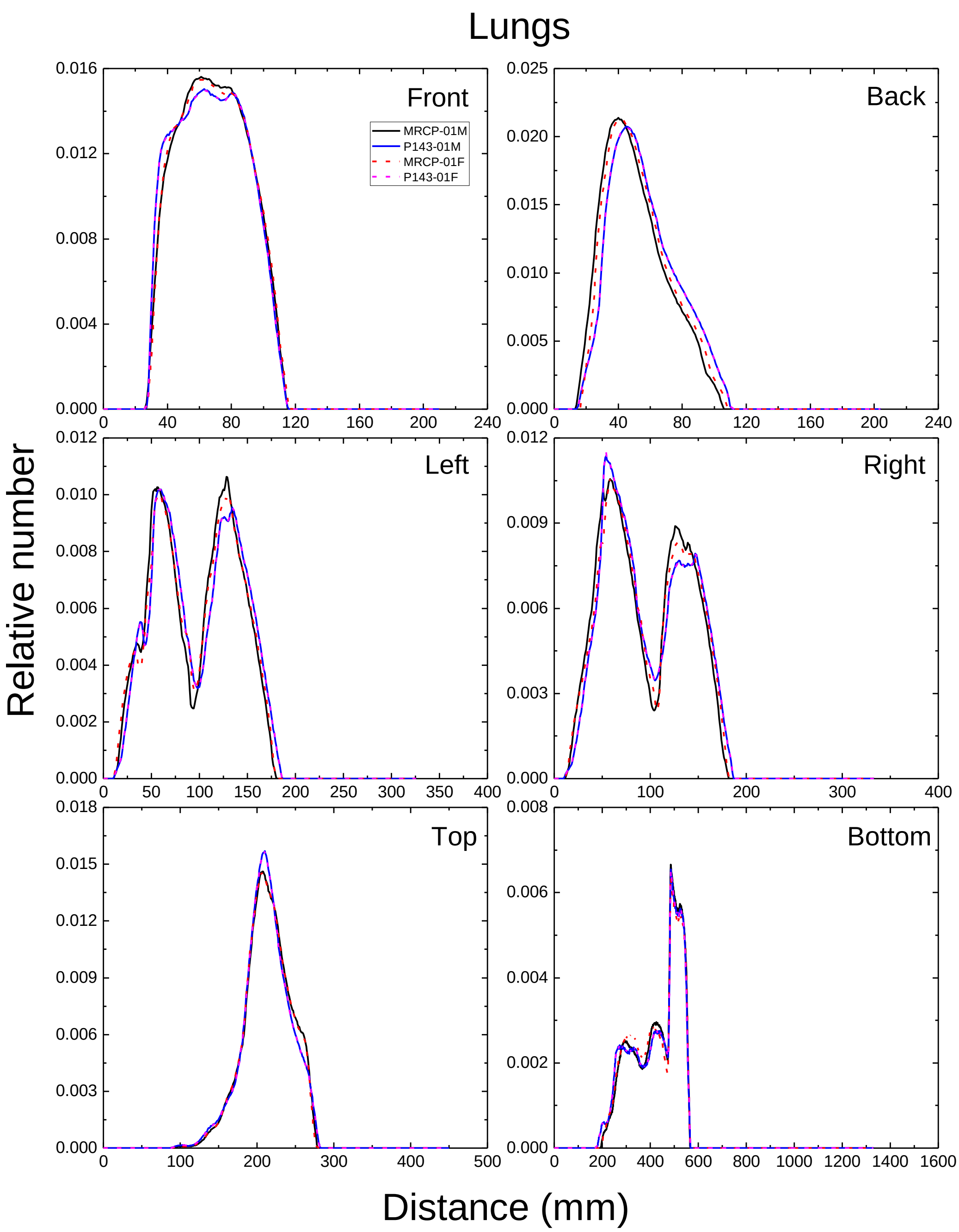

1775
1776 Fig. E.16. Distribution of depths of 10 million randomly sampled points in the lungs below the
1777 body surface of the 1-year male/female phantoms at: front, back, left, right, top and bottom.
1778

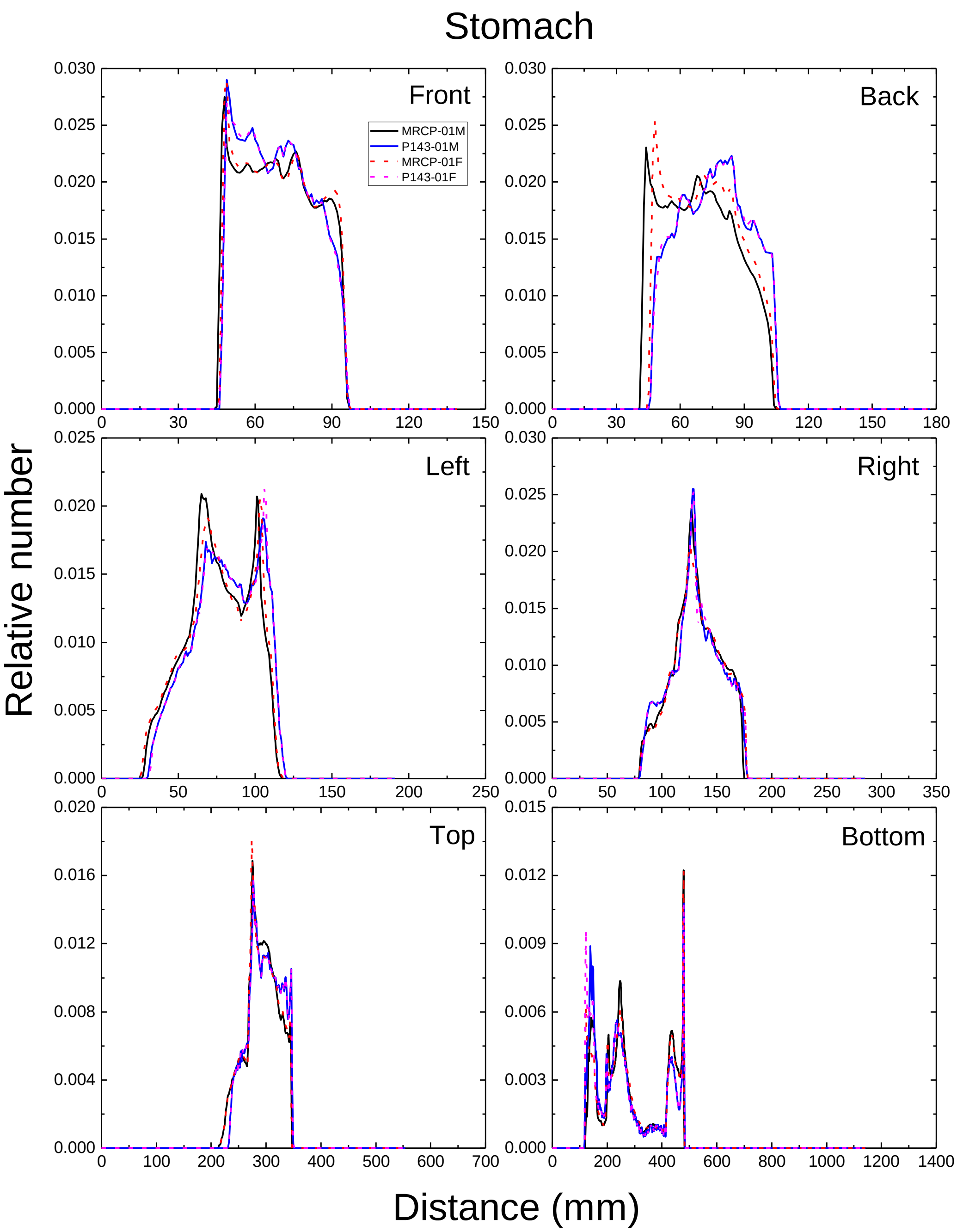

1779
1780 Fig. E.17. Distribution of depths of 10 million randomly sampled points in the stomach below
1781 the body surface of the 1-year male/female phantoms at: front, back, left, right, top and bottom.
1782

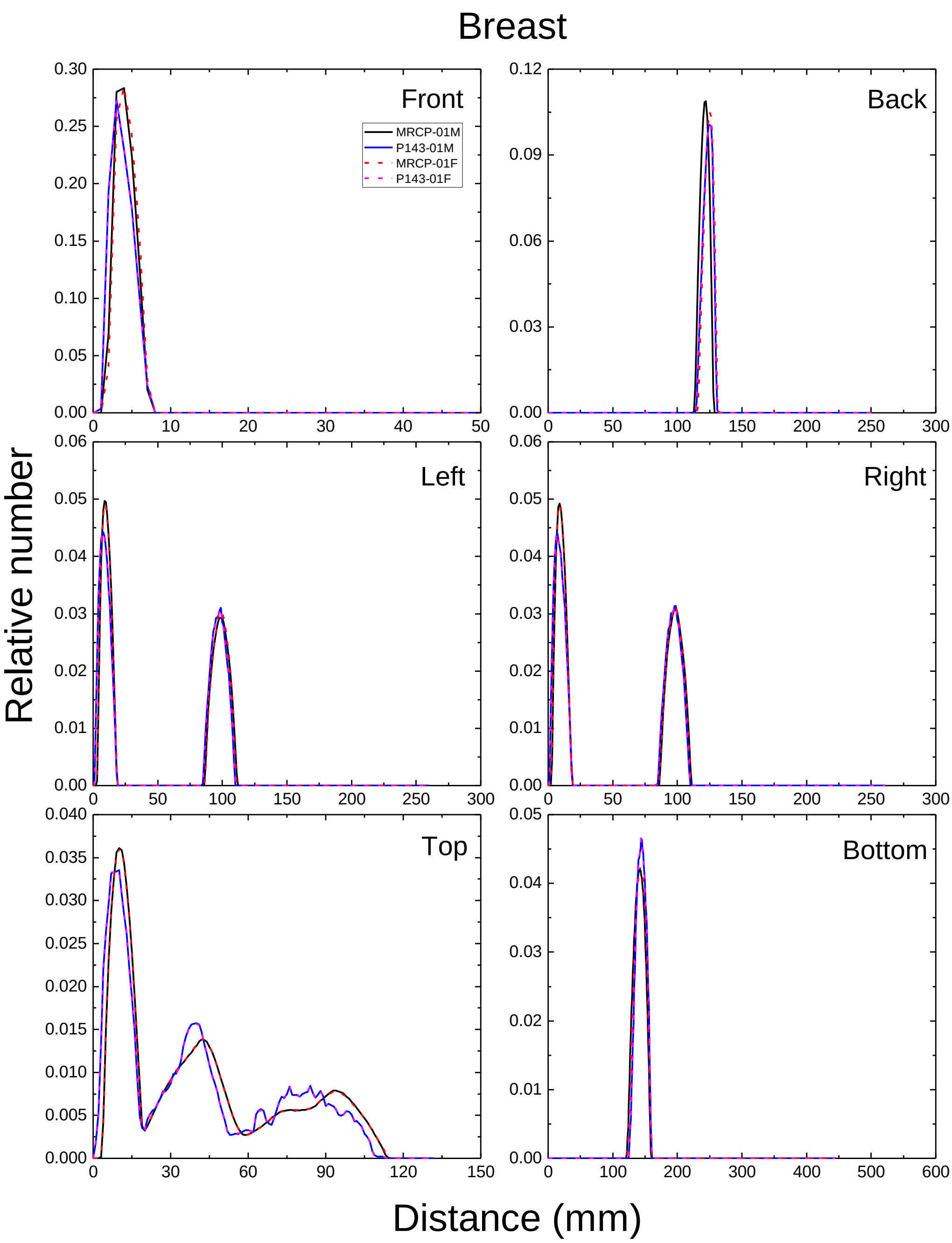

1783

1784 Fig. E.18. Distribution of depths of 10 million randomly sampled points in the breast below the
1785 body surface of the 1-year male/female phantoms at: front, back, left, right, top and bottom.

1786

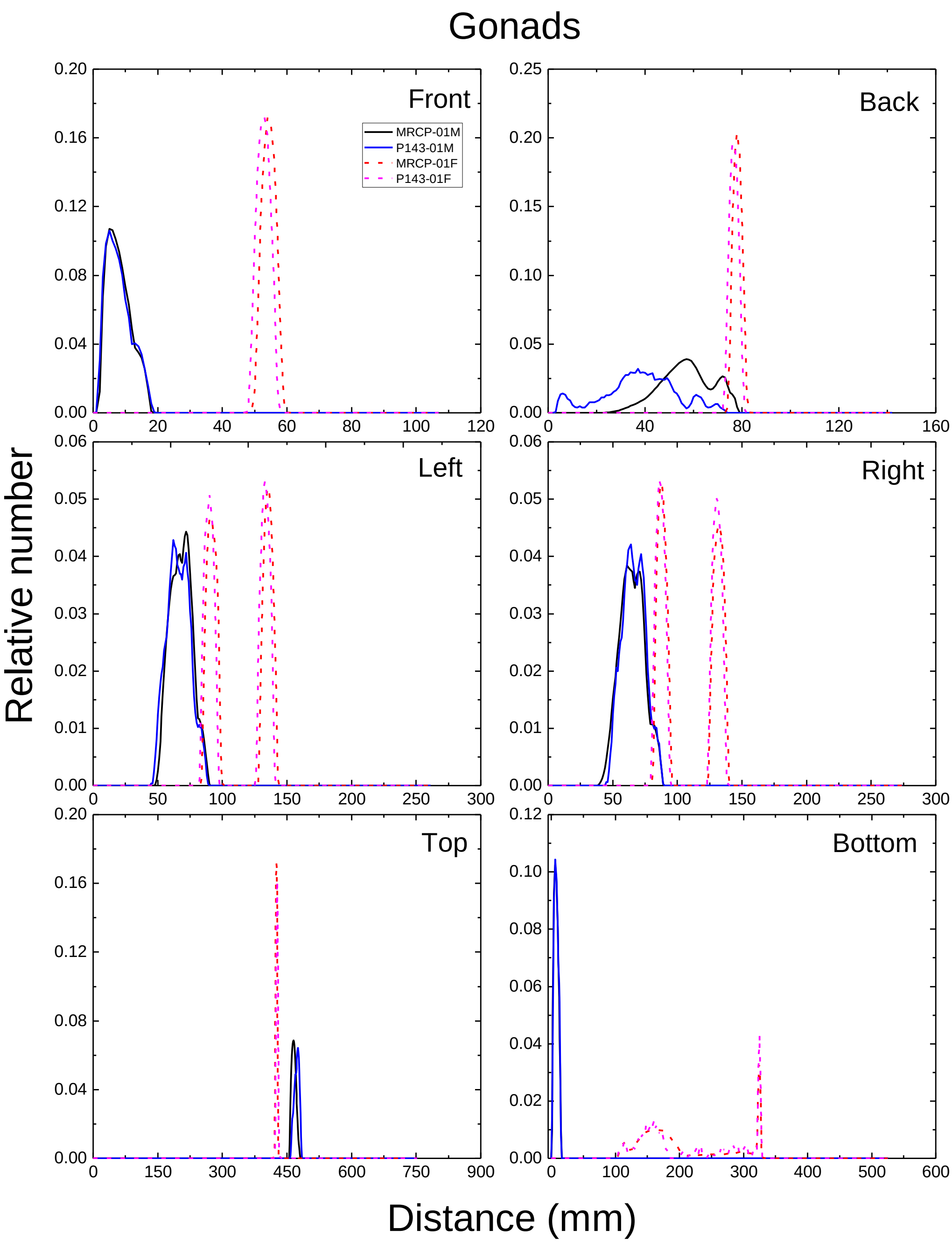

1787
1788 Fig. E.19. Distribution of depths of 10 million randomly sampled points in the gonads below
1789 the body surface of the 1-year male/female phantoms at: front, back, left, right, top and bottom.
1790

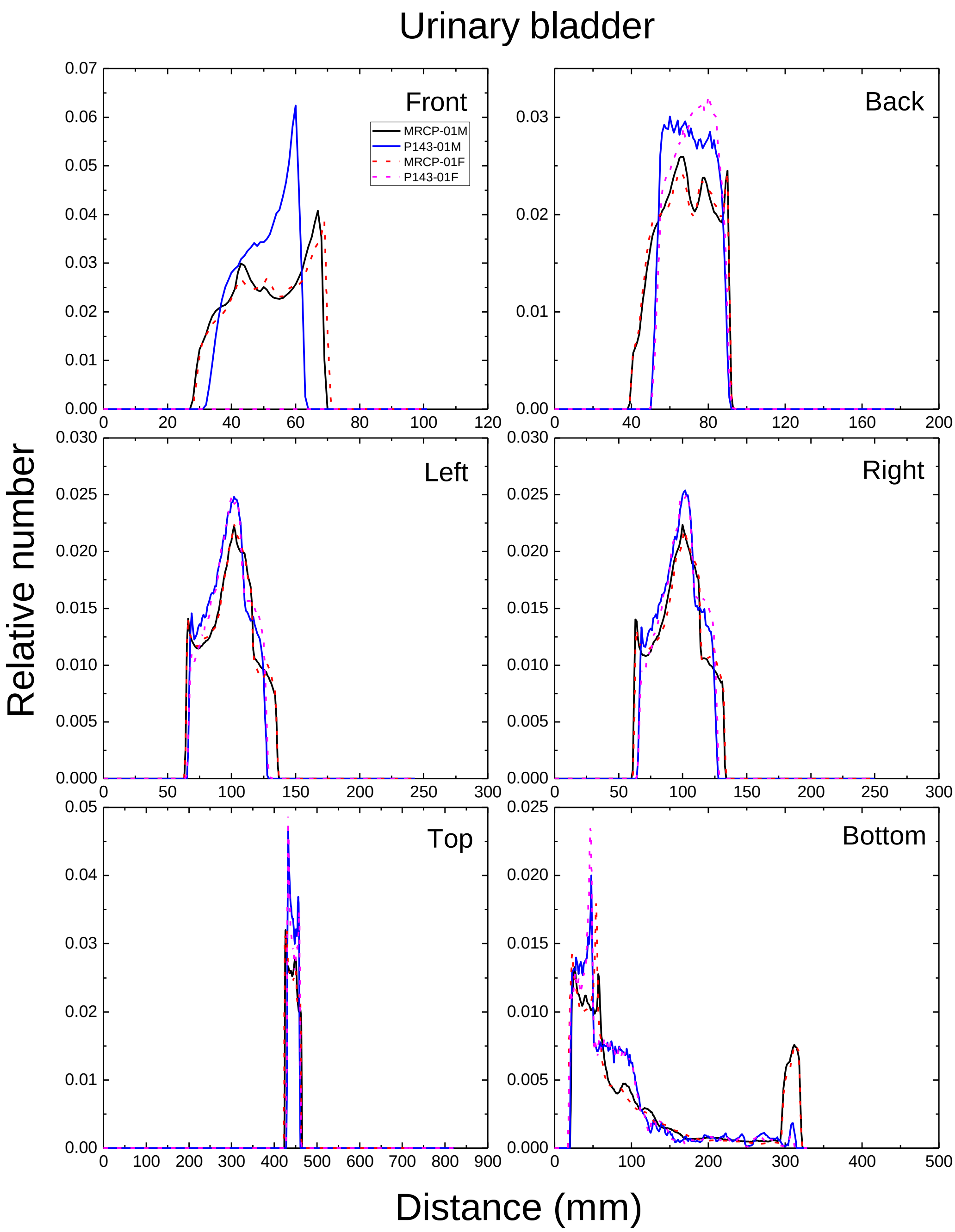

1791
1792 Fig. E.20. Distribution of depths of 10 million randomly sampled points in the urinary bladder
1793 below the body surface of the 1-year male/female phantoms at: front, back, left, right, top and
1794 bottom.
1795

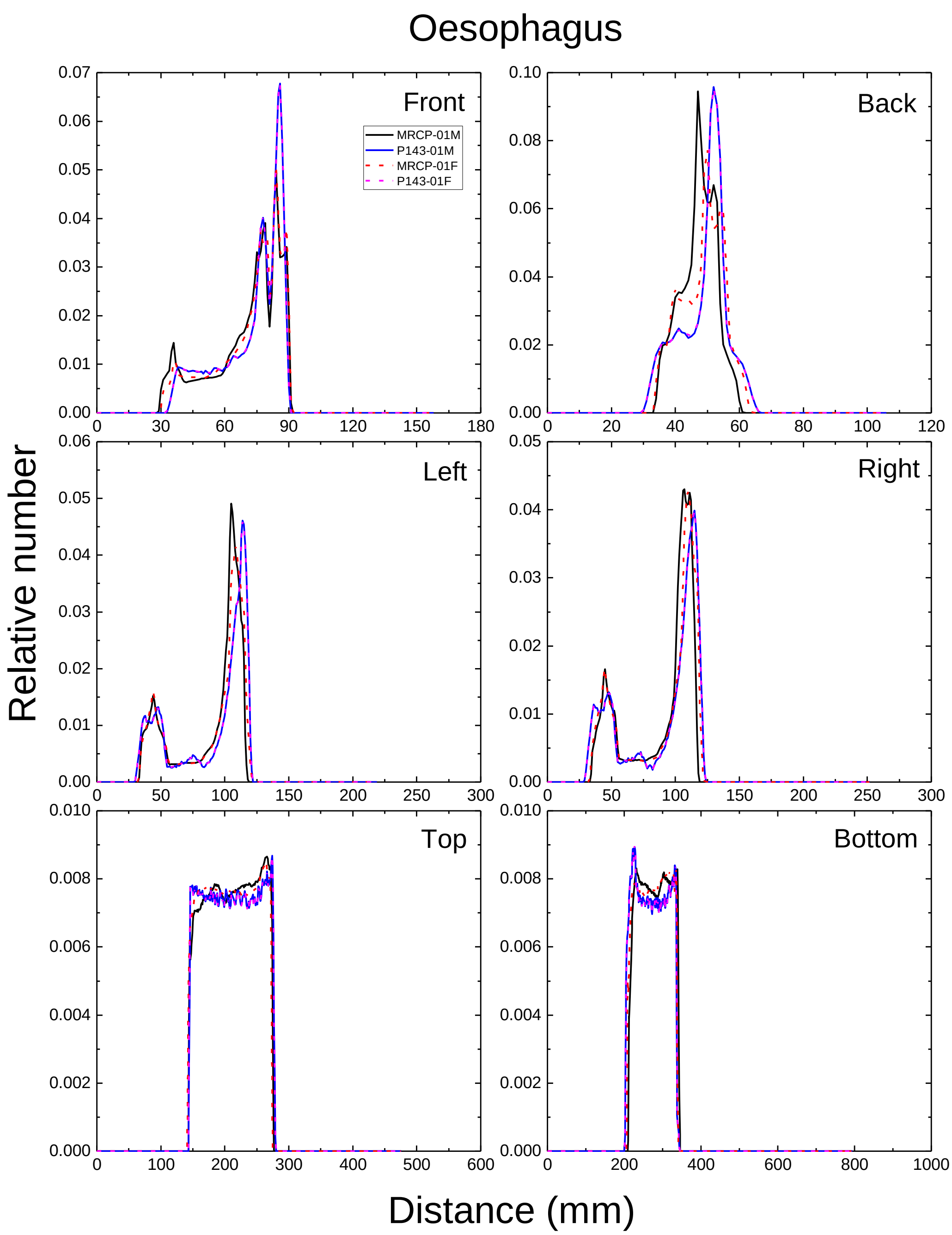

1796
1797 Fig. E.21. Distribution of depths of 10 million randomly sampled points in the oesophagus
1798 below the body surface of the 1-year male/female phantoms at: front, back, left, right, top and
1799 bottom.
1800

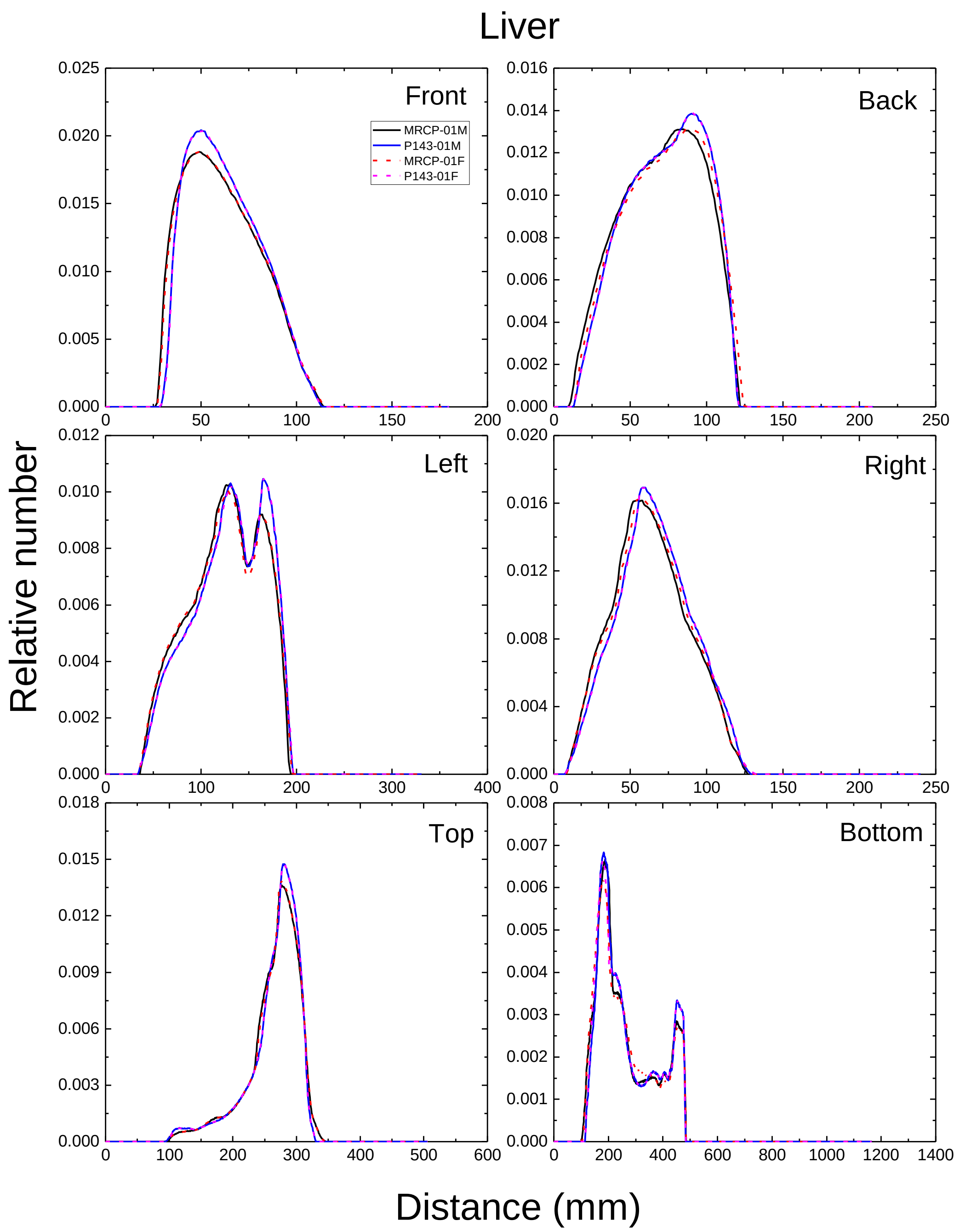

Fig. E.22. Distribution of depths of 10 million randomly sampled points in the liver below the body surface of the 1-year male/female phantoms at: front, back, left, right, top and bottom.

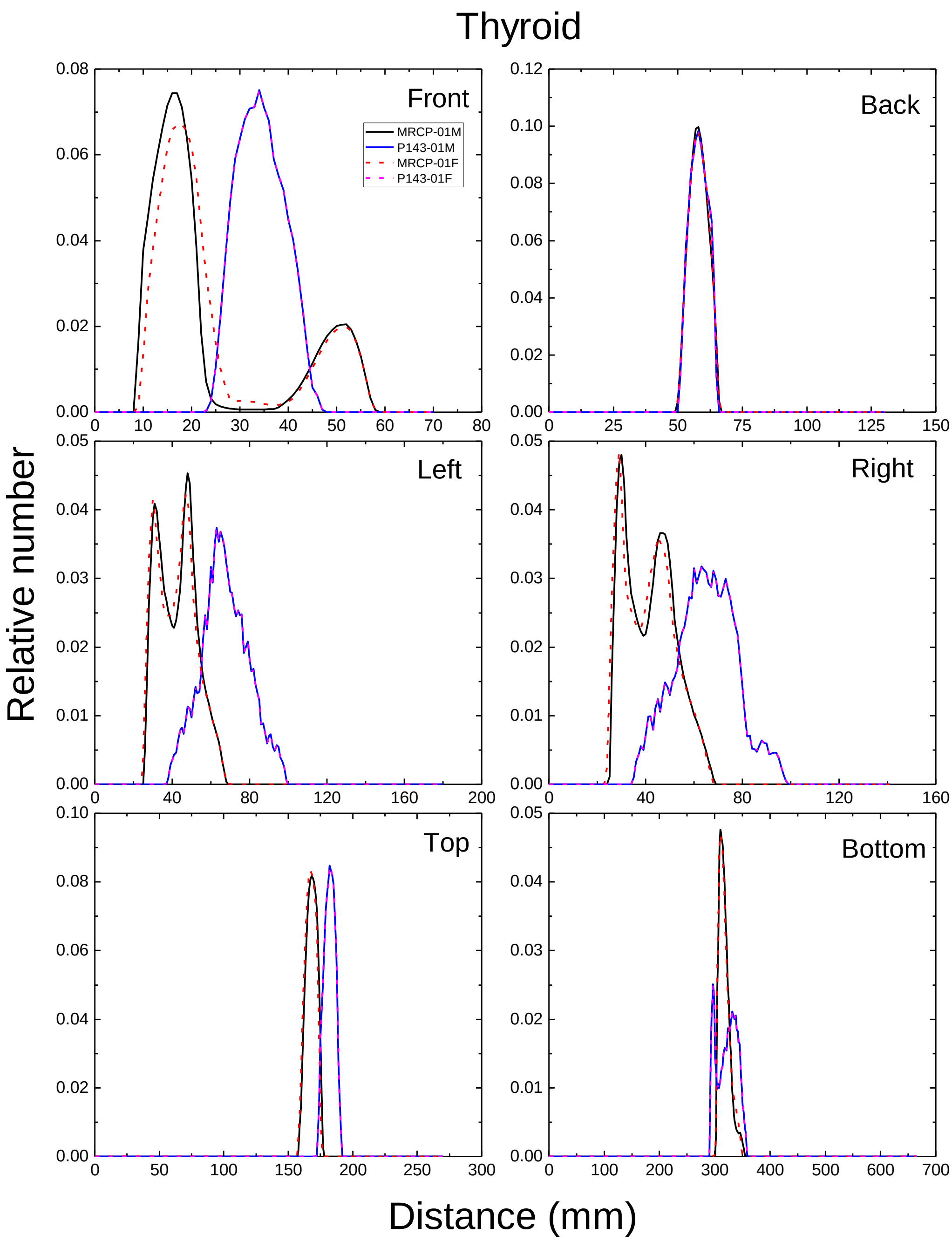

1805
1806 Fig. E.23. Distribution of depths of 10 million randomly sampled points in the thyroid below
1807 the body surface of the 1-year male/female phantoms at: front, back, left, right, top and bottom.
1808

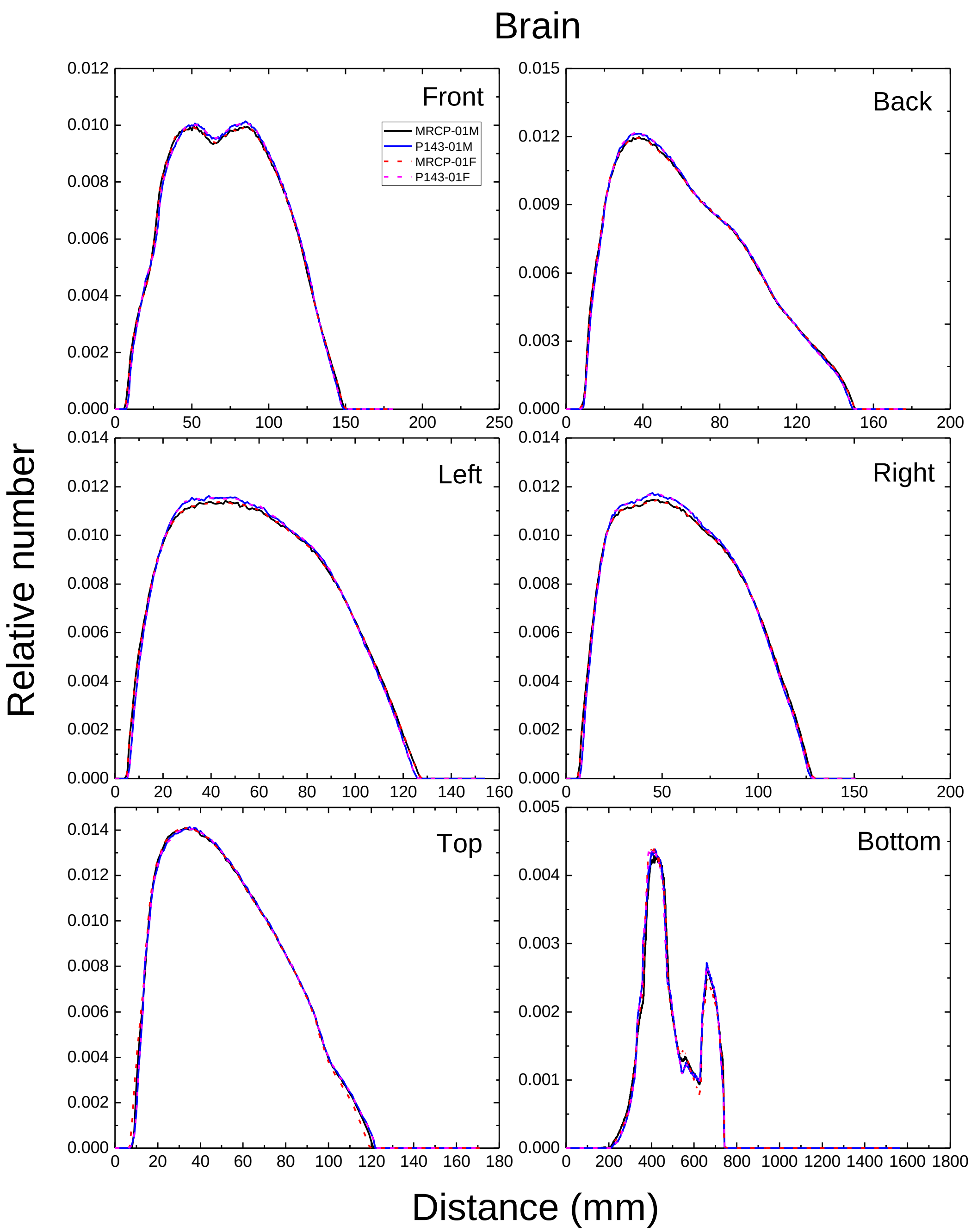

1809
1810 Fig. E.24. Distribution of depths of 10 million randomly sampled points in the brain below the
1811 body surface of the 1-year male/female phantoms at: front, back, left, right, top and bottom.
1812

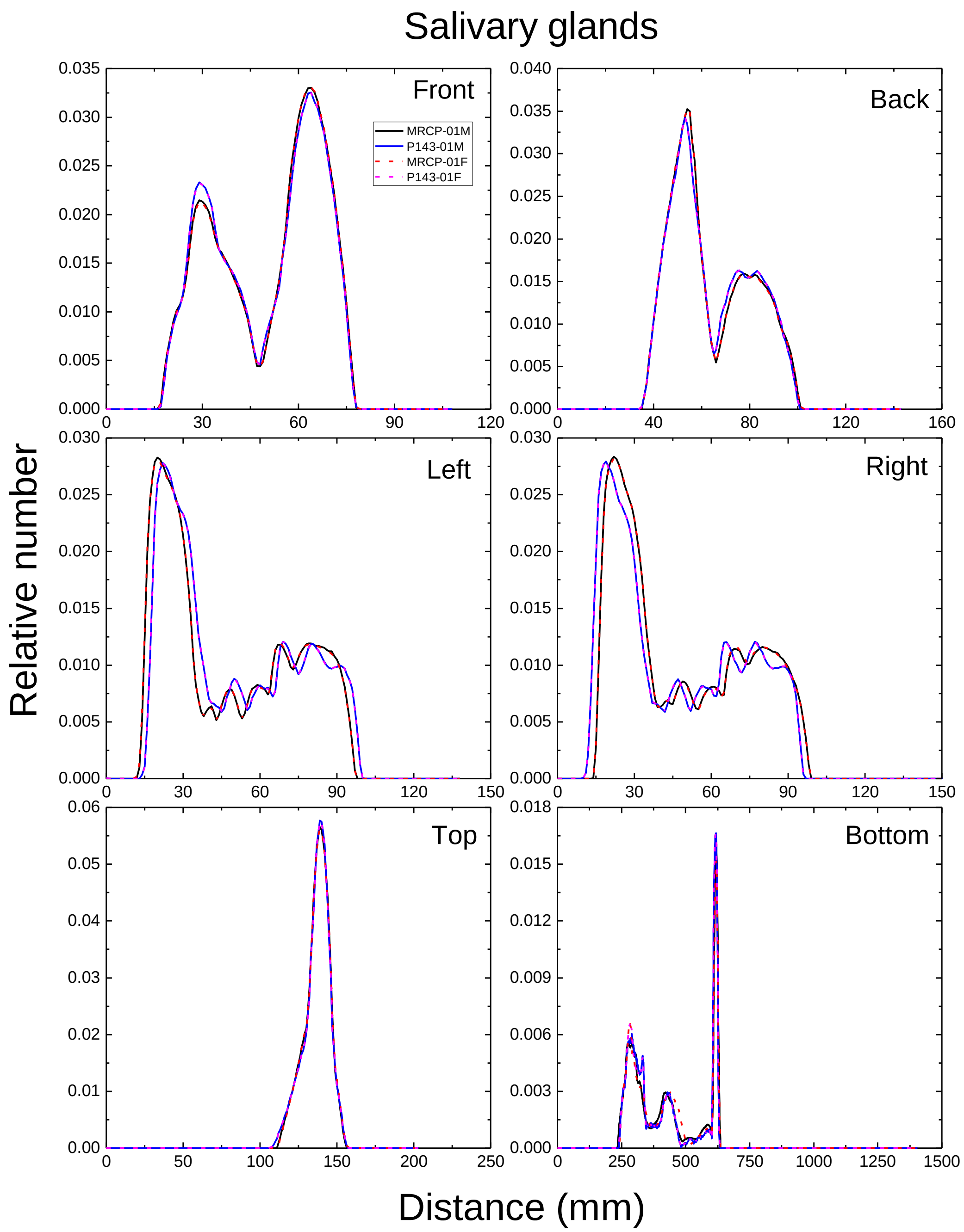

Fig. E.25. Distribution of depths of 10 million randomly sampled points in the salivary glands below the body surface of the 1-year male/female phantoms at: front, back, left, right, top and bottom.

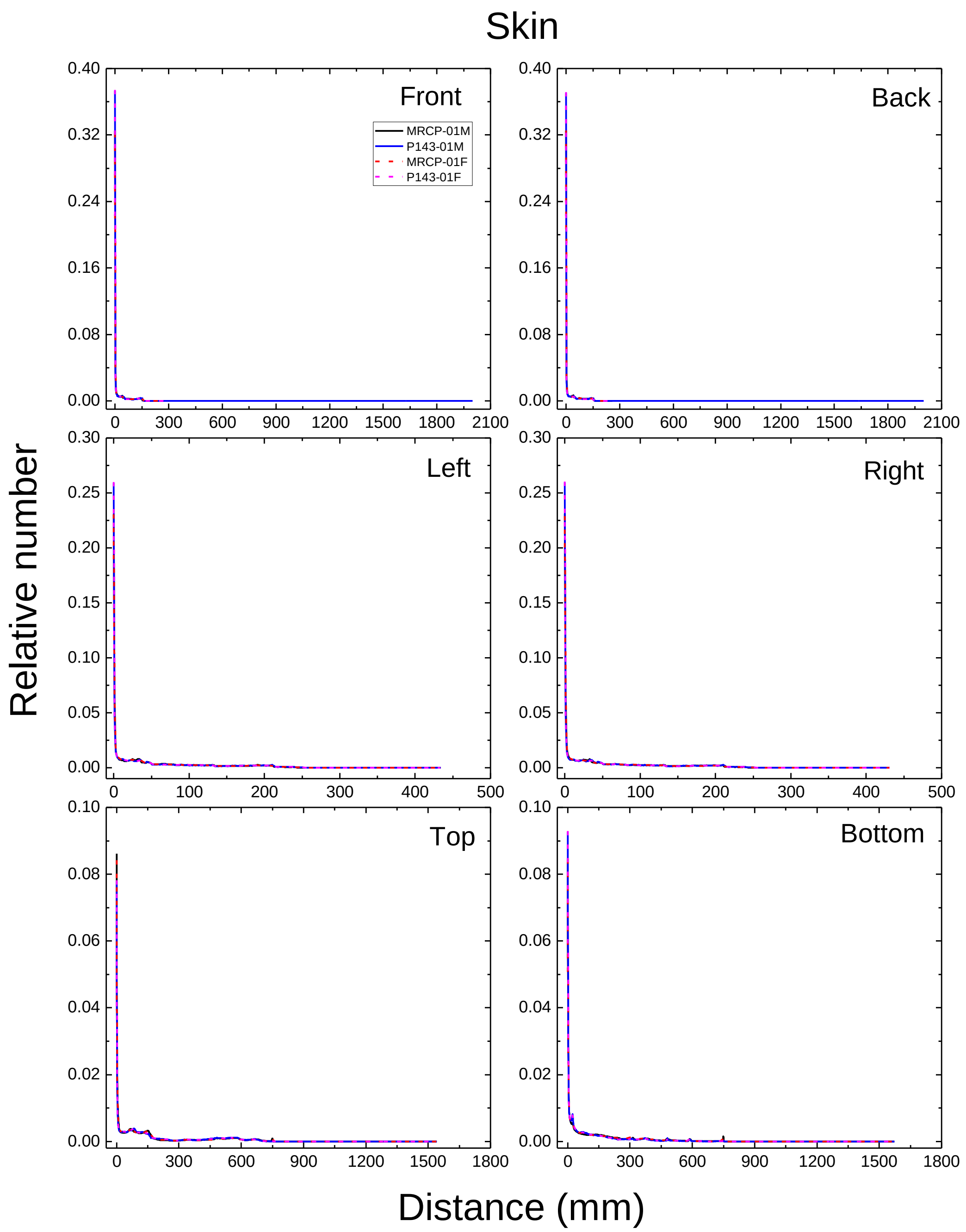

1818
1819 Fig. E.26. Distribution of depths of 10 million randomly sampled points in the skin below the
1820 body surface of the 1-year male/female phantoms at: front, back, left, right, top and bottom.
1821

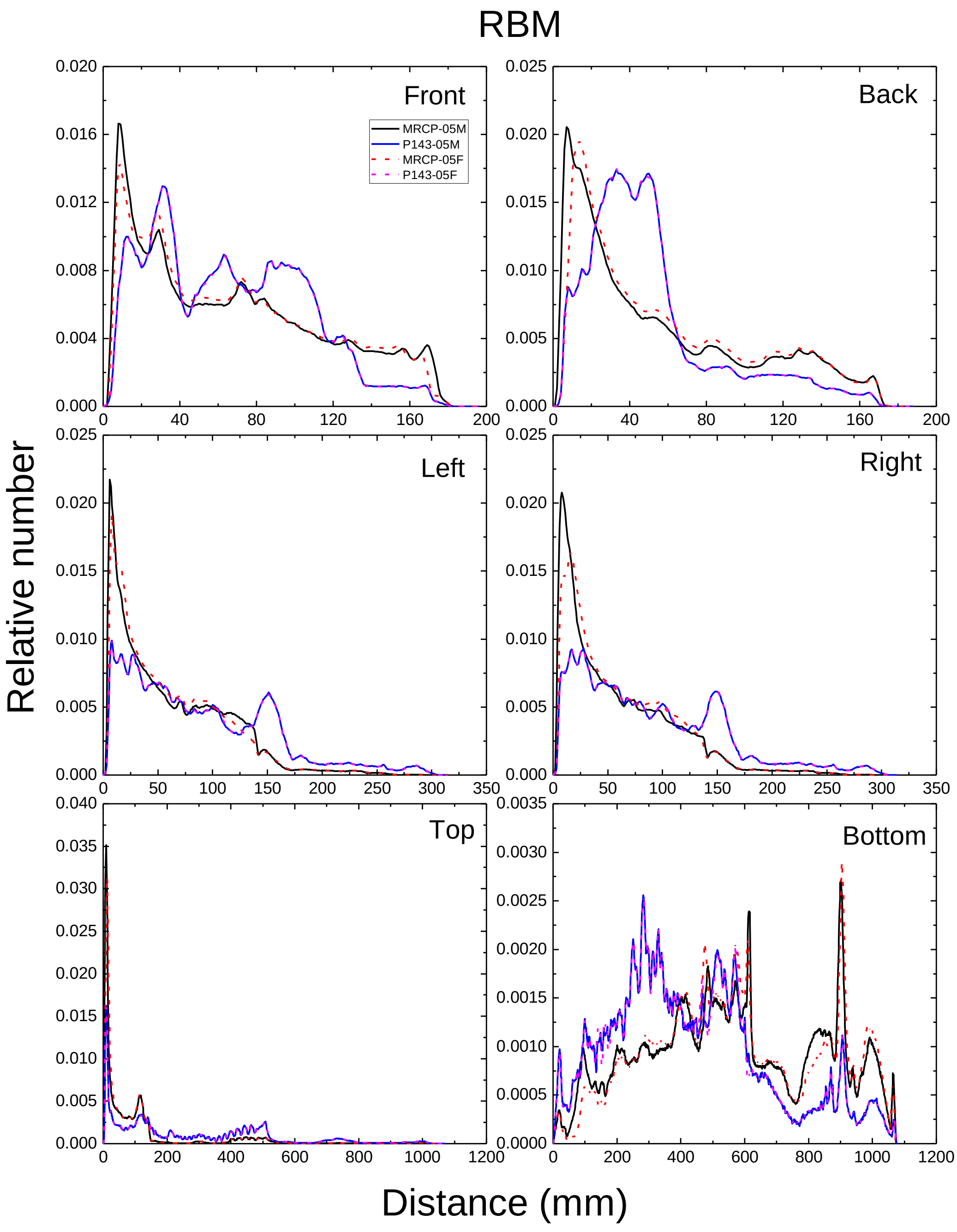

Fig. E.27. Distribution of depths of 10 million randomly sampled points in the red bone marrow (RBM) below the body surface of the 5-year male/female phantoms at: front, back, left, right, top and bottom.

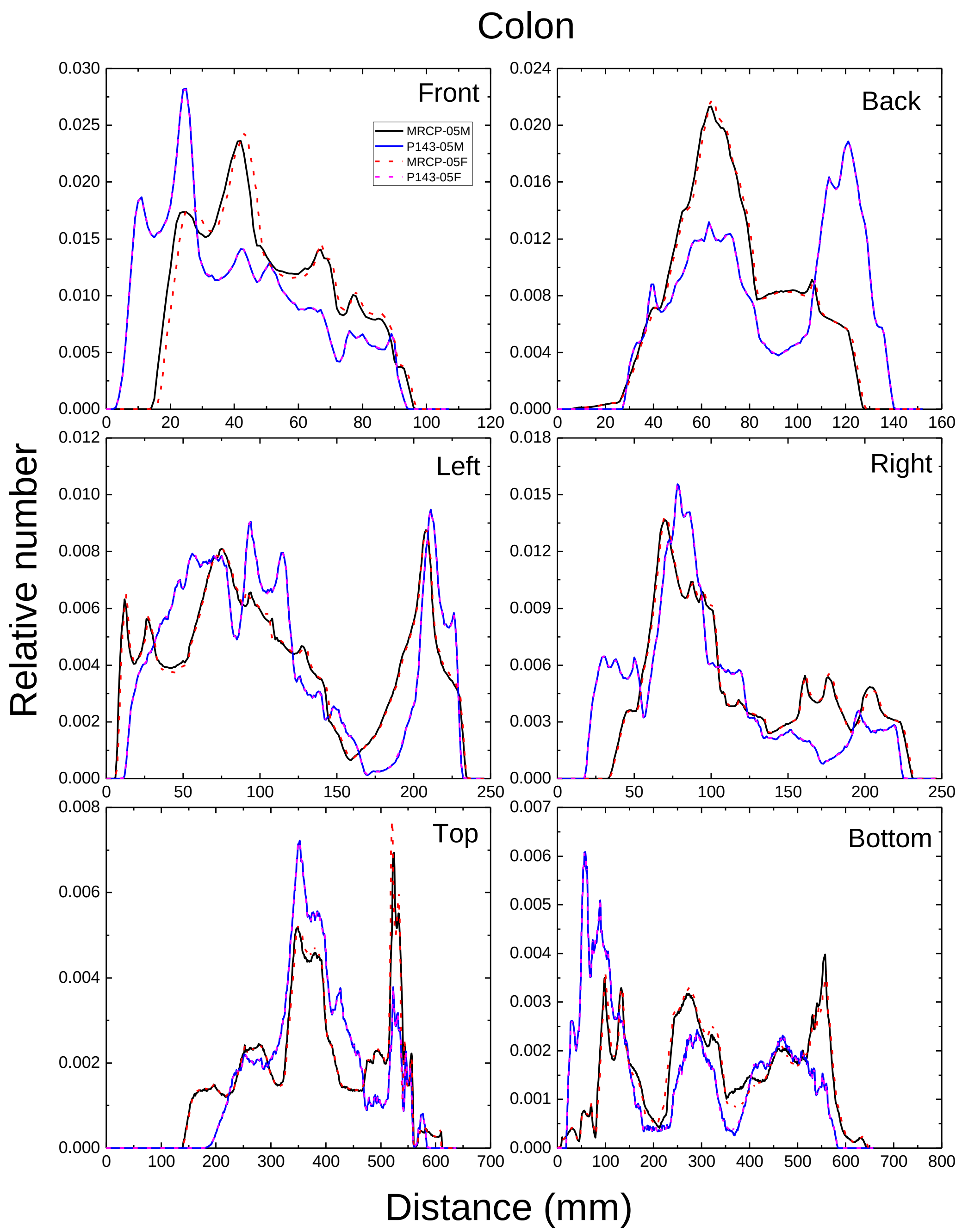

Fig. E.28. Distribution of depths of 10 million randomly sampled points in the colon below the body surface of the 5-year male/female phantoms at: front, back, left, right, top and bottom.

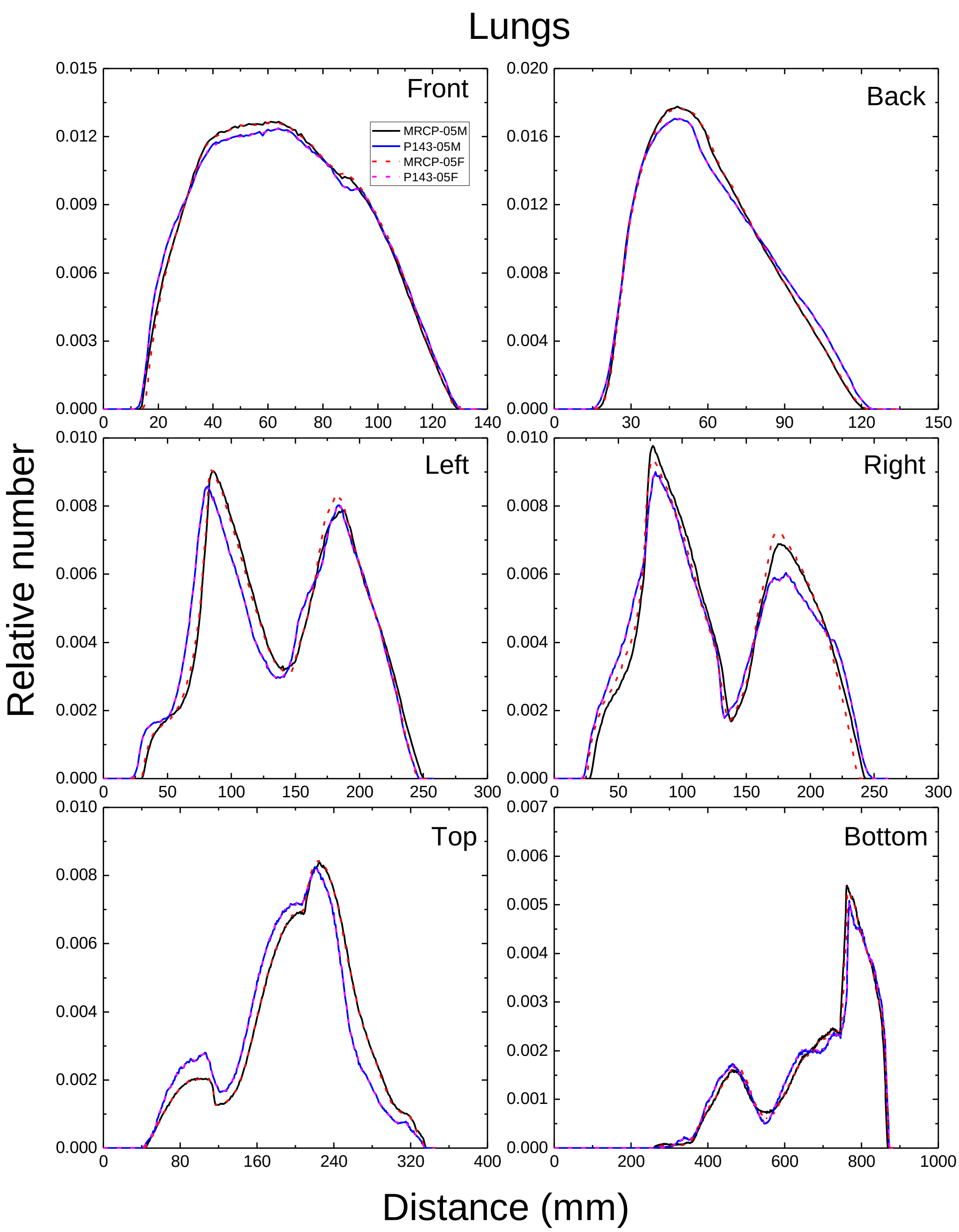

1831
1832 Fig. E.29. Distribution of depths of 10 million randomly sampled points in the lungs below the
1833 body surface of the 5-year male/female phantoms at: front, back, left, right, top and bottom.
1834

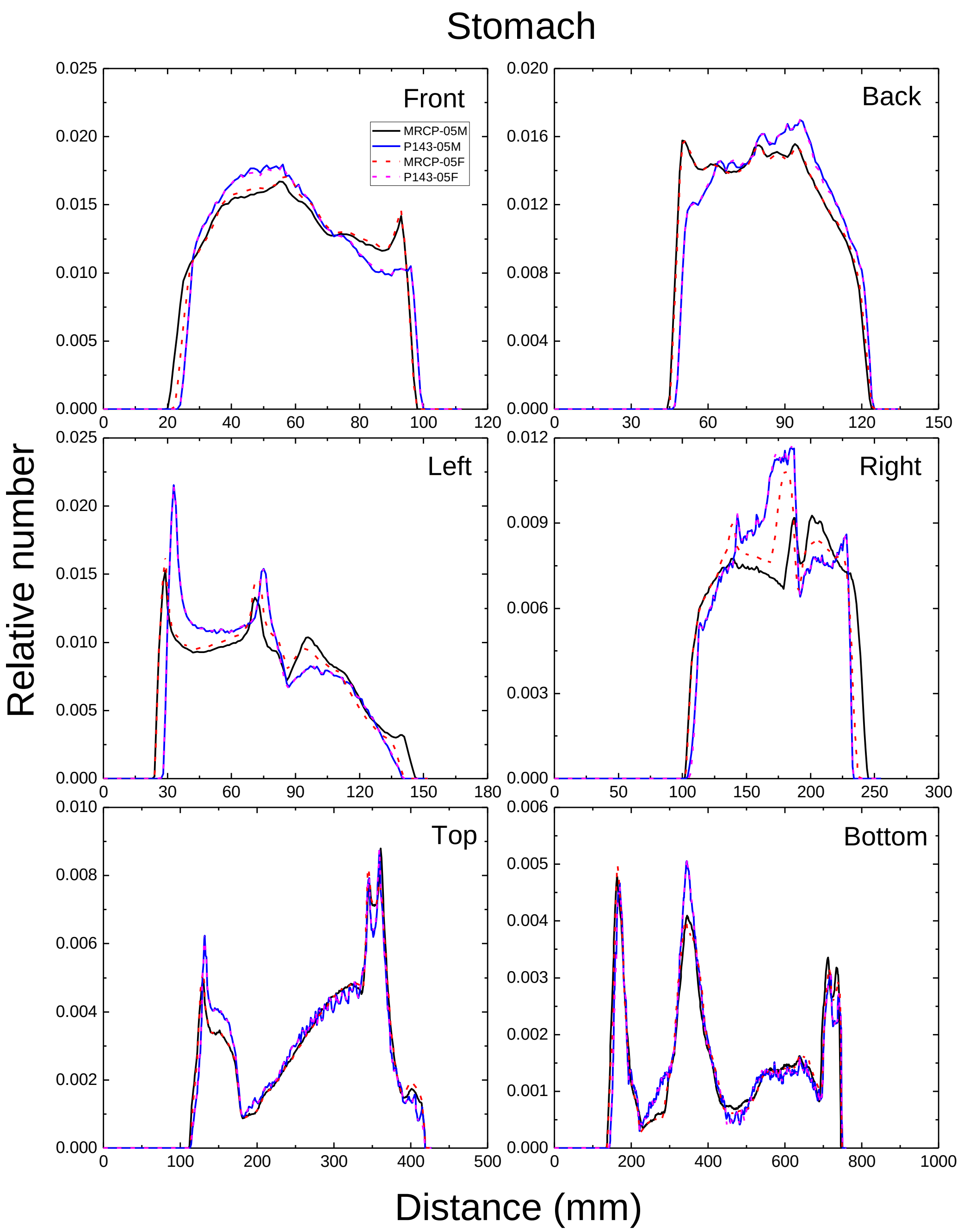

1835
1836 Fig. E.30. Distribution of depths of 10 million randomly sampled points in the stomach below
1837 the body surface of the 5-year male/female phantoms at: front, back, left, right, top and bottom.
1838

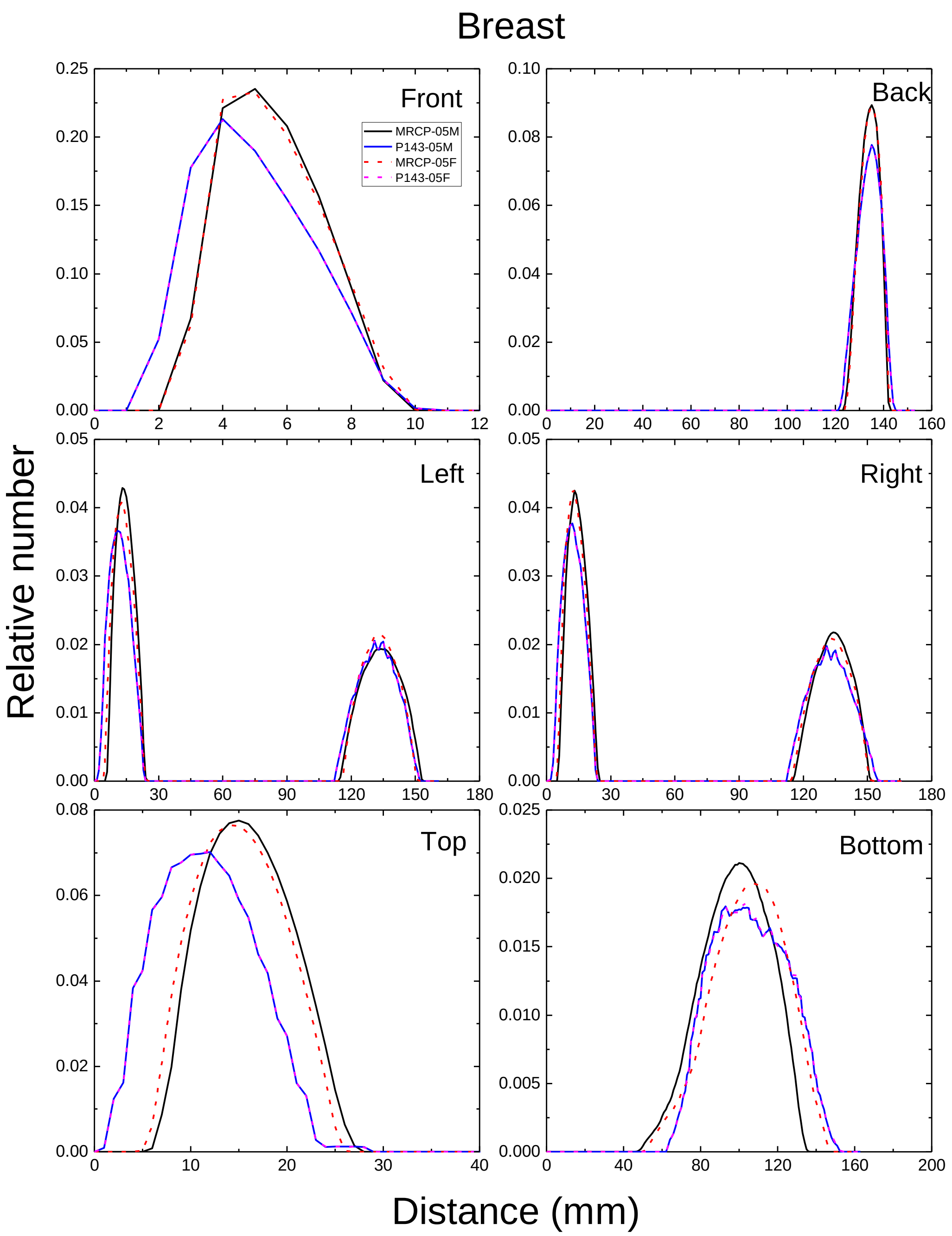

1839
1840 Fig. E.31. Distribution of depths of 10 million randomly sampled points in the breast below the
1841 body surface of the 5-year male/female phantoms at: front, back, left, right, top and bottom.
1842

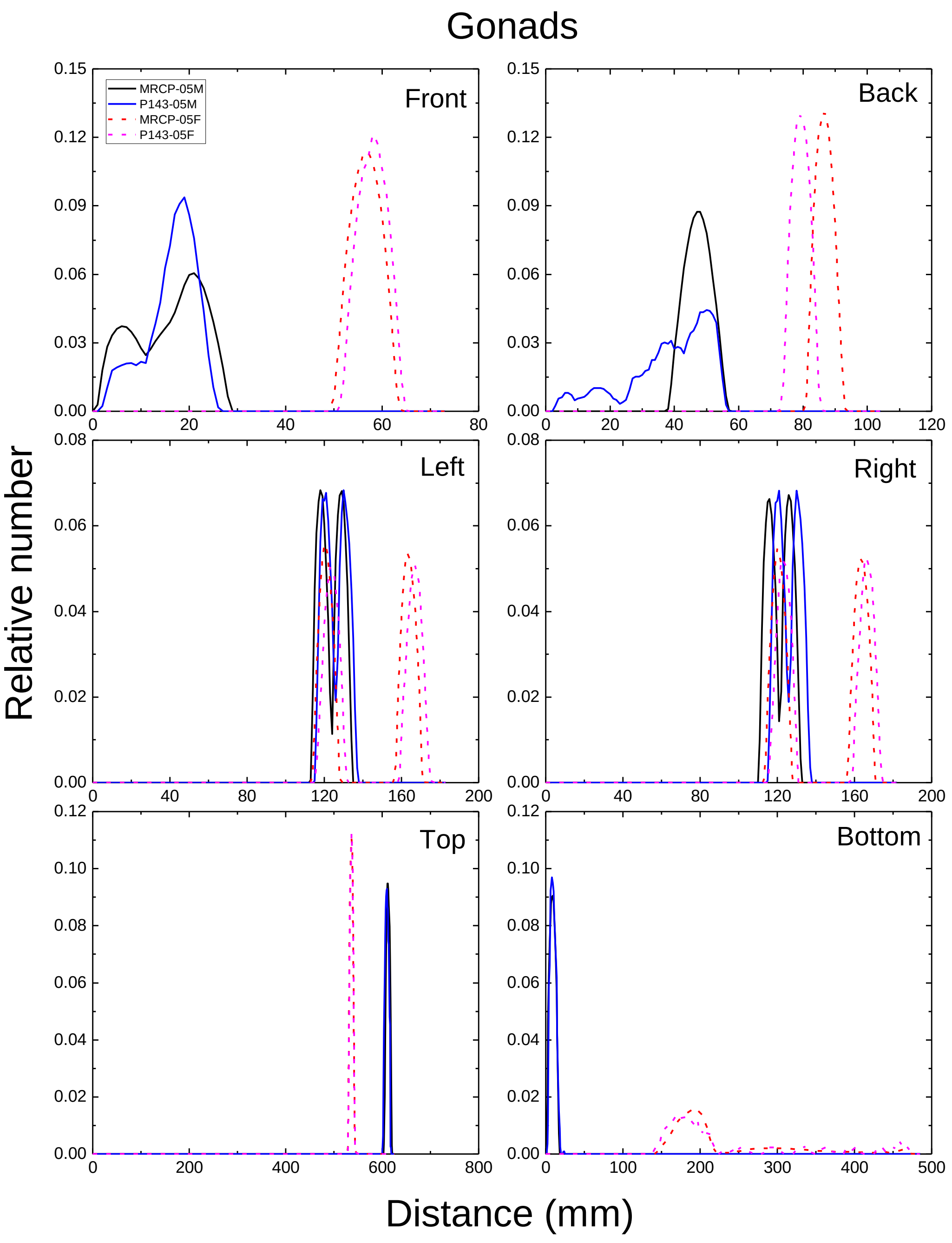

1843
1844 Fig. E.32. Distribution of depths of 10 million randomly sampled points in the gonads below
1845 the body surface of the 5-year male/female phantoms at: front, back, left, right, top and bottom.
1846

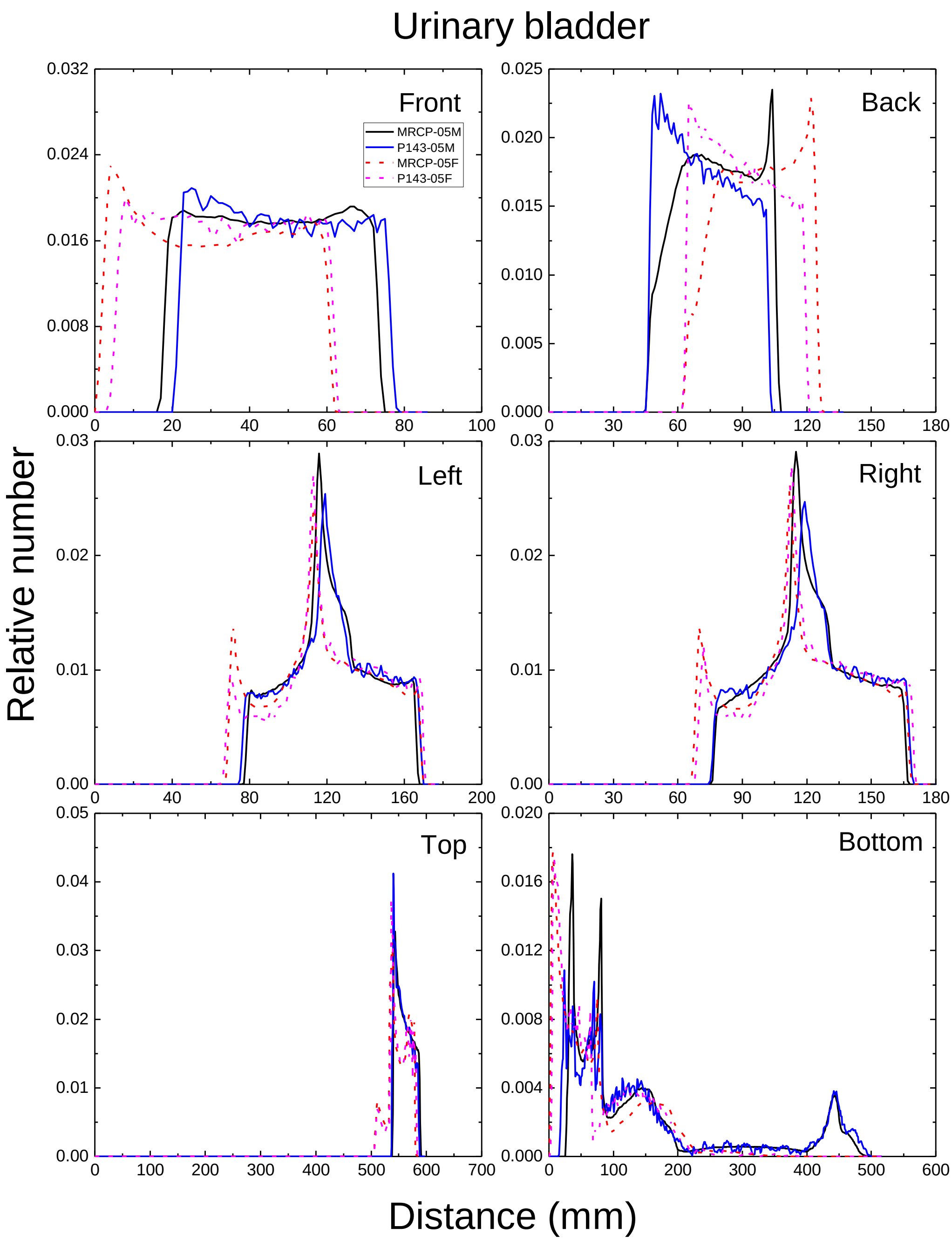

1847
1848 Fig. E.33. Distribution of depths of 10 million randomly sampled points in the urinary bladder
1849 below the body surface of the 5-year male/female phantoms at: front, back, left, right, top and
1850 bottom.
1851

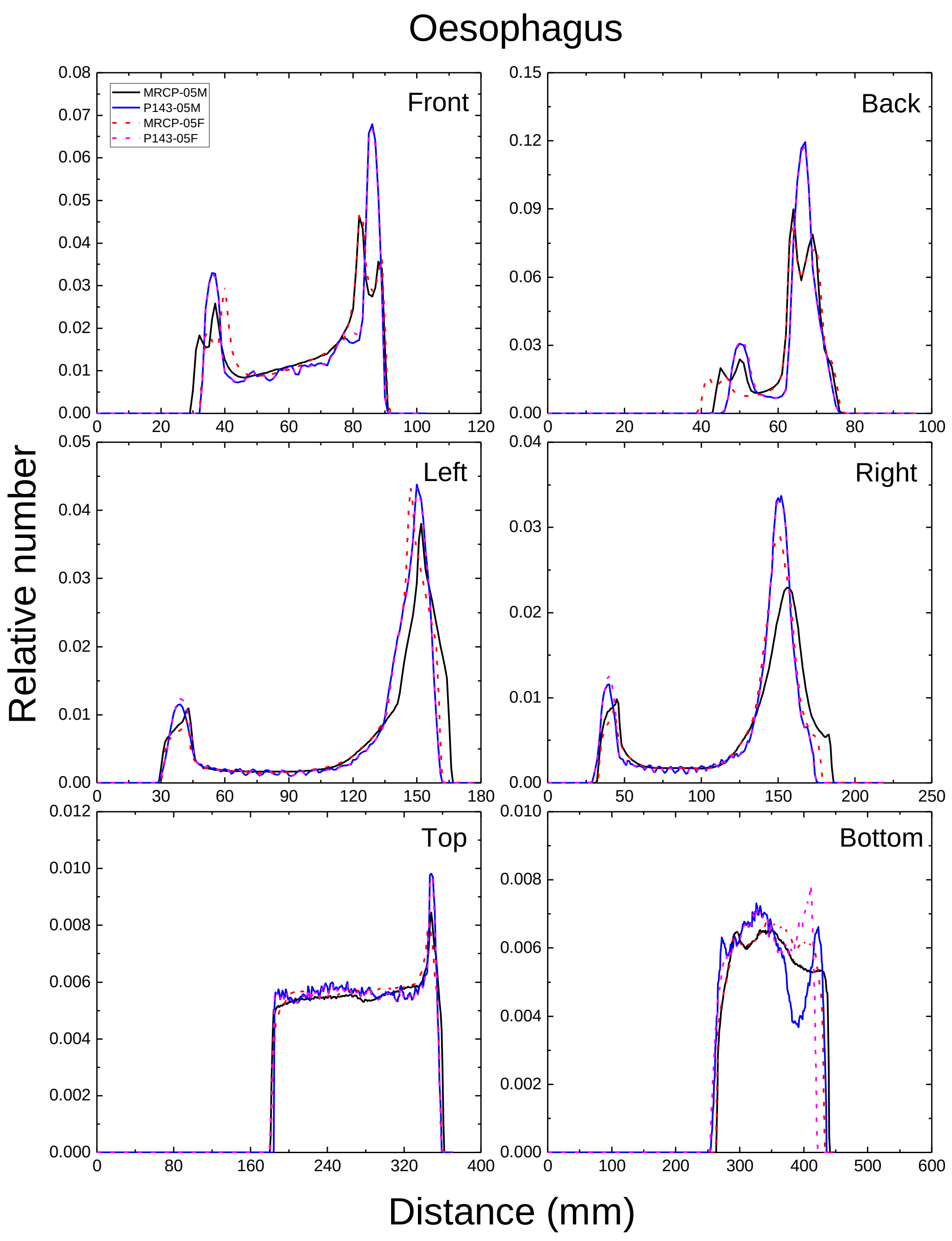

Fig. E.34. Distribution of depths of 10 million randomly sampled points in the oesophagus below the body surface of the 5-year male/female phantoms at: front, back, left, right, top and bottom.

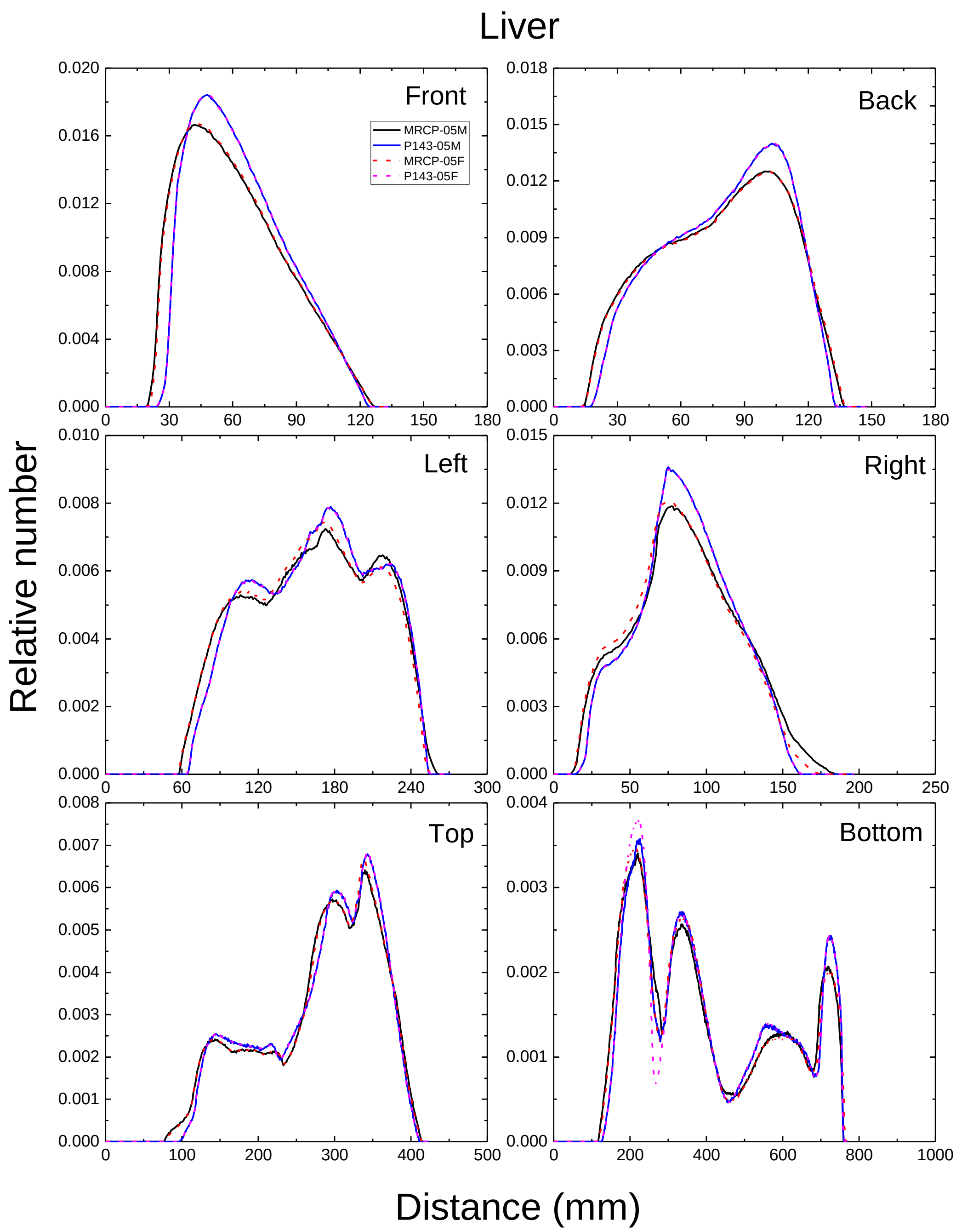

1857
1858 Fig. E.35. Distribution of depths of 10 million randomly sampled points in the liver below the
1859 body surface of the 5-year male/female phantoms at: front, back, left, right, top and bottom.
1860

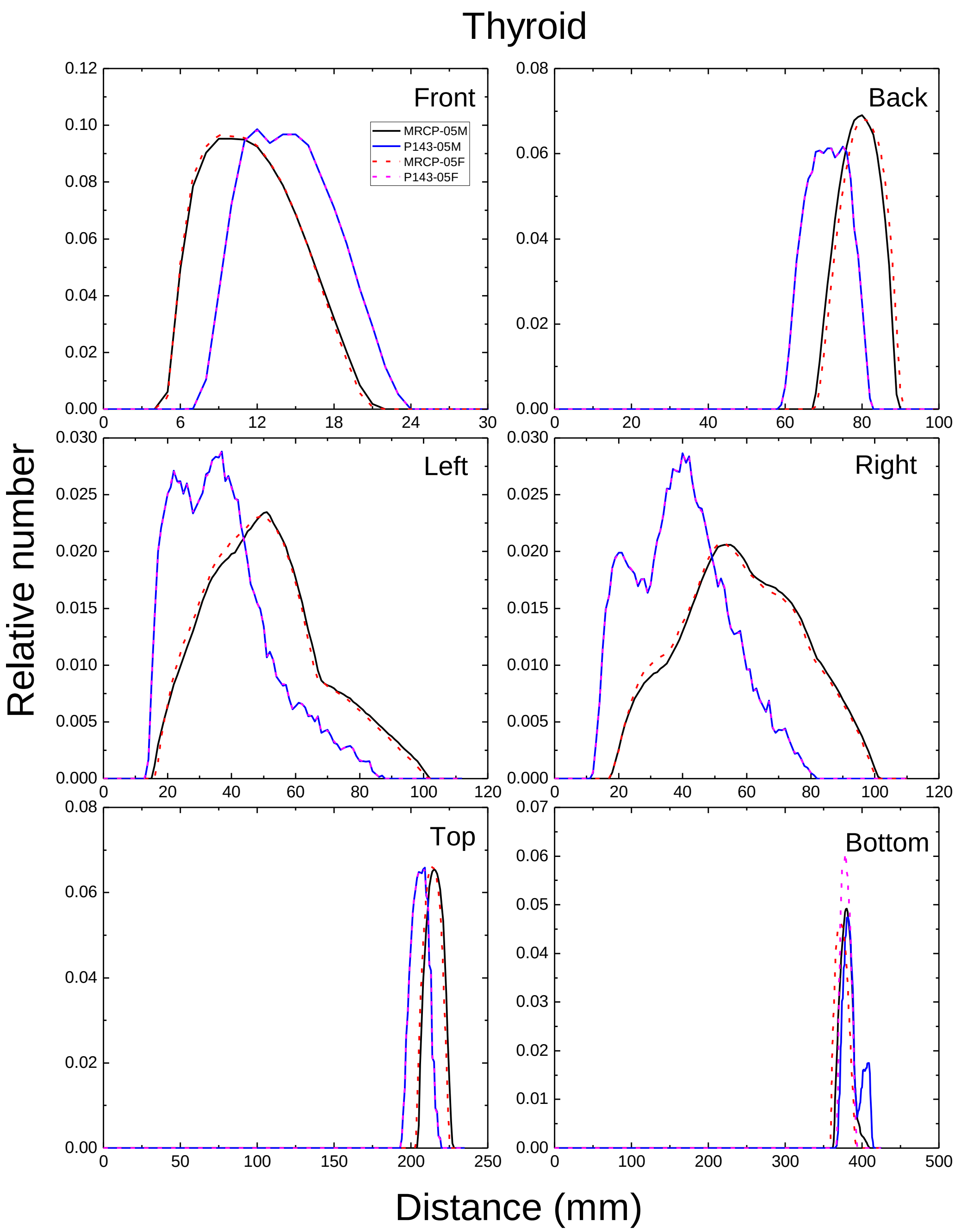

1861
1862 Fig. E.36. Distribution of depths of 10 million randomly sampled points in the thyroid below
1863 the body surface of the 5-year male/female phantoms at: front, back, left, right, top and bottom.
1864

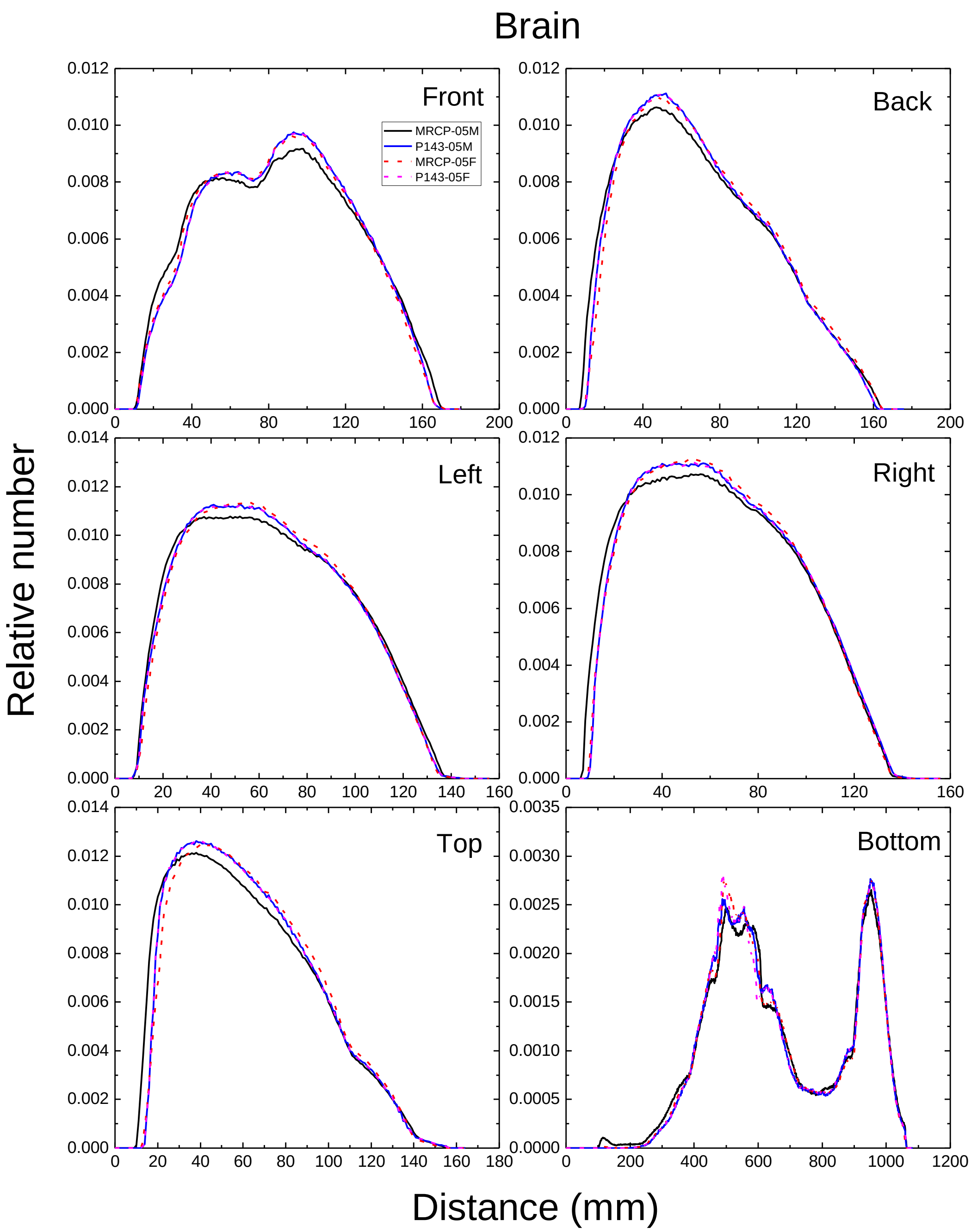

1865
1866 Fig. E.37. Distribution of depths of 10 million randomly sampled points in the brain below the
1867 body surface of the 5-year male/female phantoms at: front, back, left, right, top and bottom.
1868

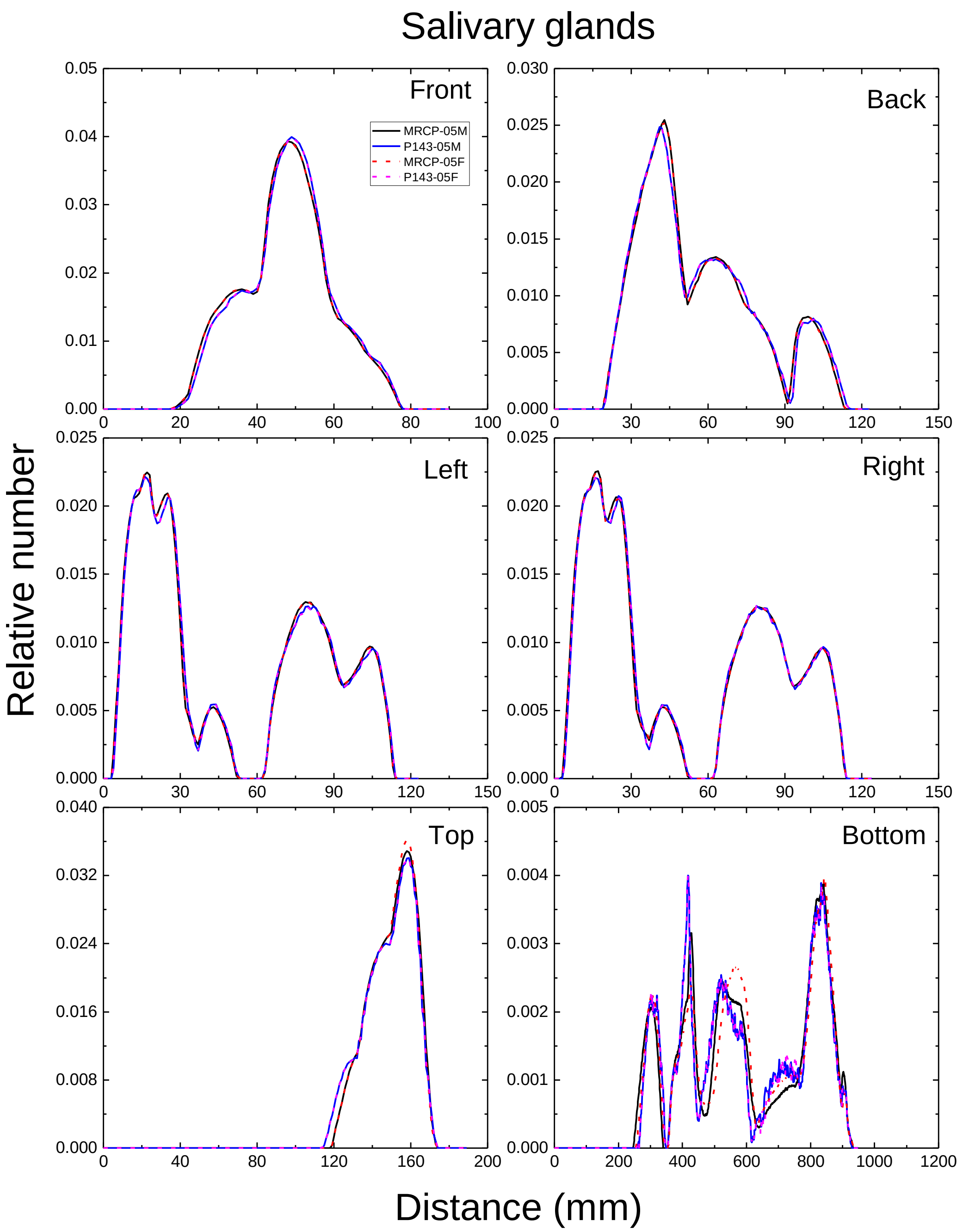

Fig. E.38. Distribution of depths of 10 million randomly sampled points in the salivary glands below the body surface of the 5-year male/female phantoms at: front, back, left, right, top and bottom.

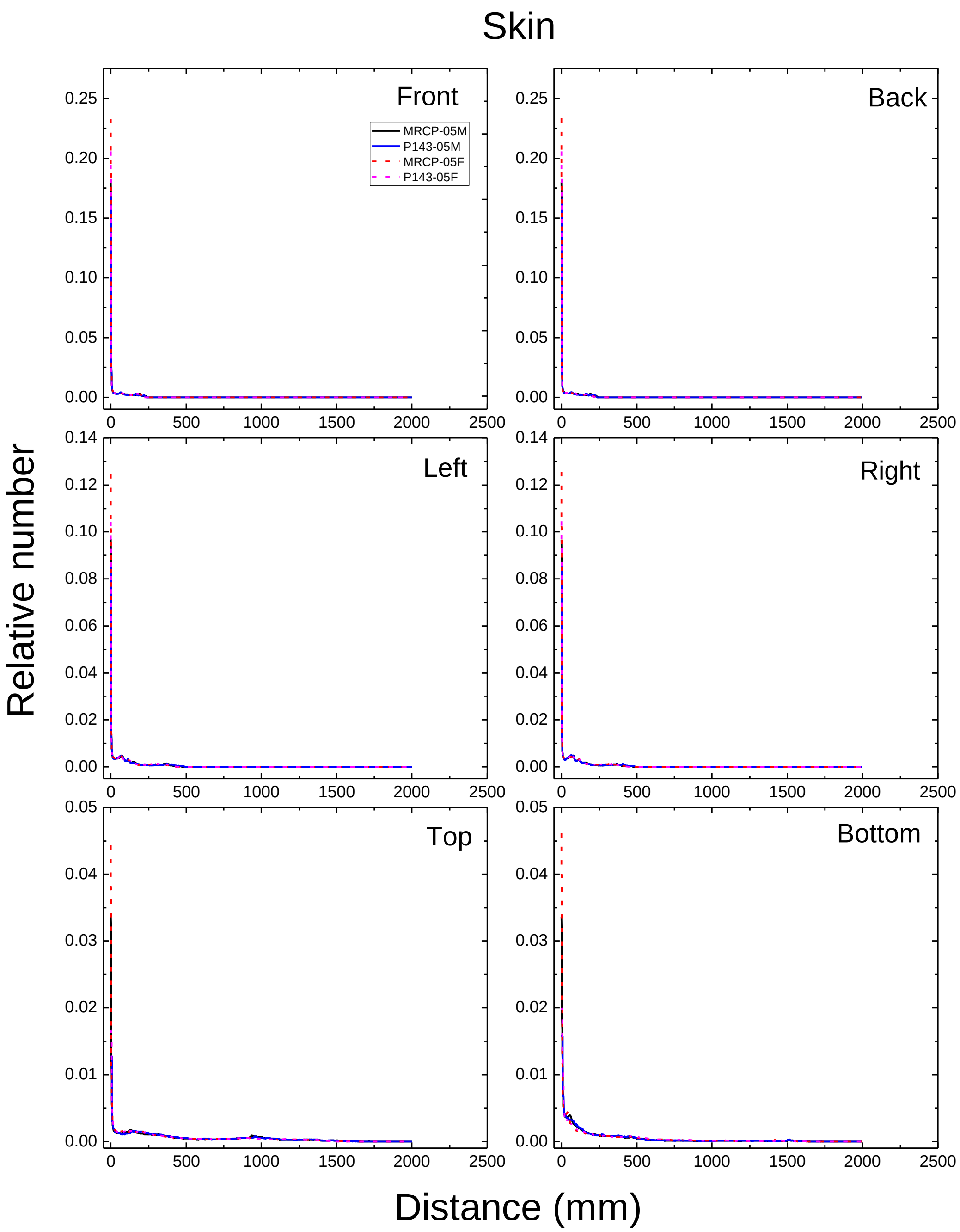

Fig. E.39. Distribution of depths of 10 million randomly sampled points in the skin below the body surface of the 5-year male/female phantoms at: front, back, left, right, top and bottom.

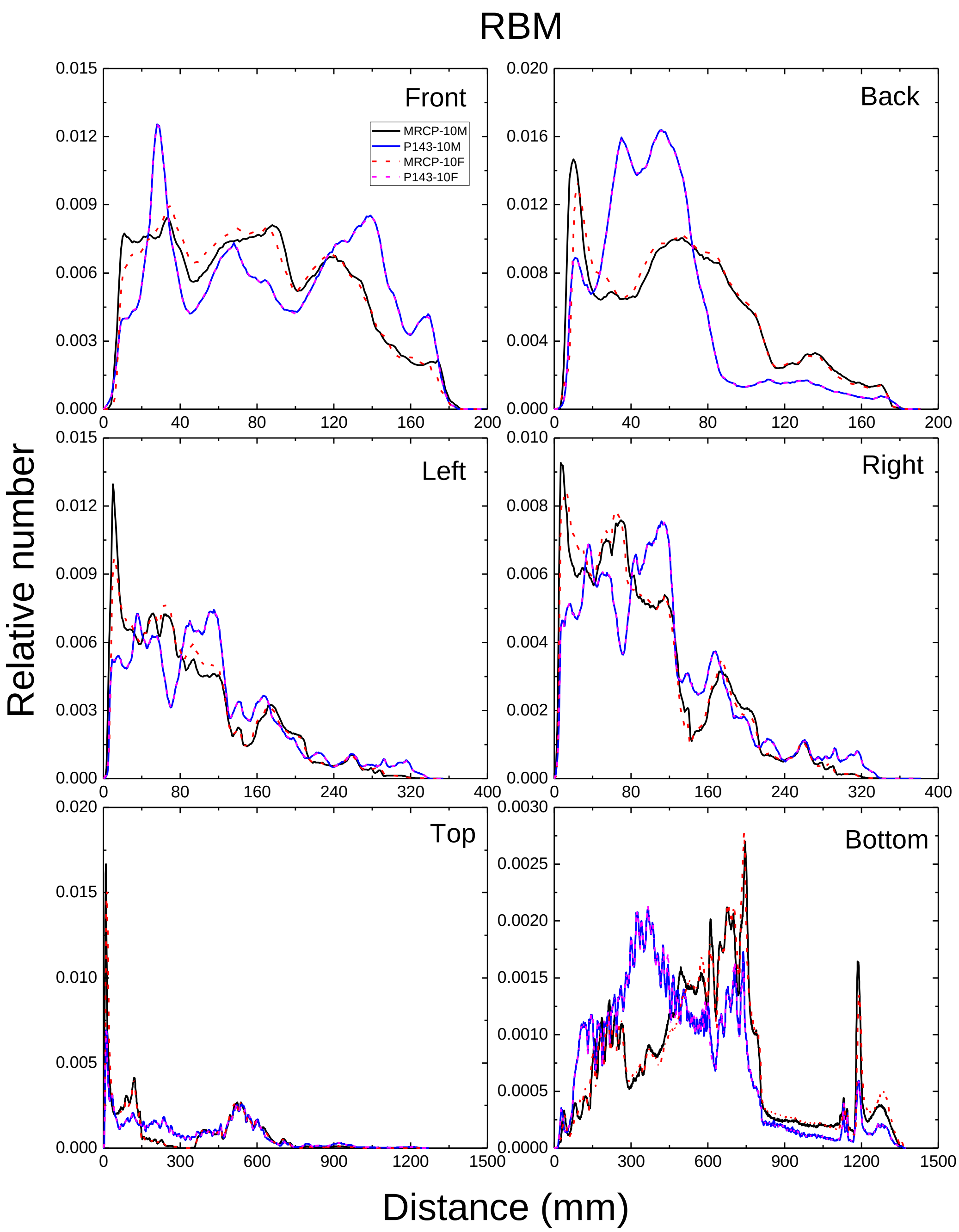

1878
1879 Fig. E.40. Distribution of depths of 10 million randomly sampled points in the red bone marrow
1880 (RBM) below the body surface of the 10-year male/female phantoms at: front, back, left, right,
1881 top and bottom.
1882

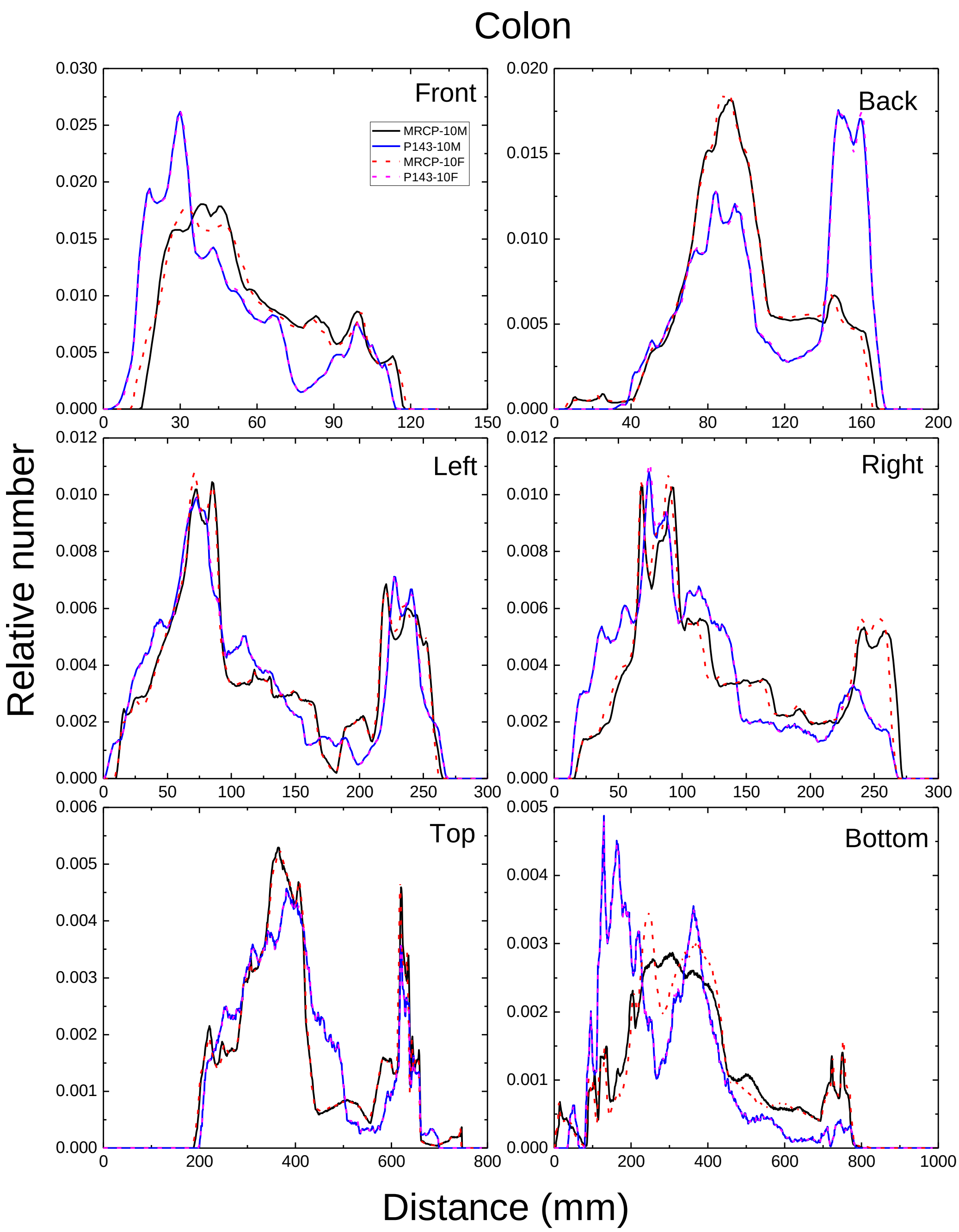

1883
1884 Fig. E.41. Distribution of depths of 10 million randomly sampled points in the colon below the
1885 body surface of the 10-year male/female phantoms at: front, back, left, right, top and bottom.
1886

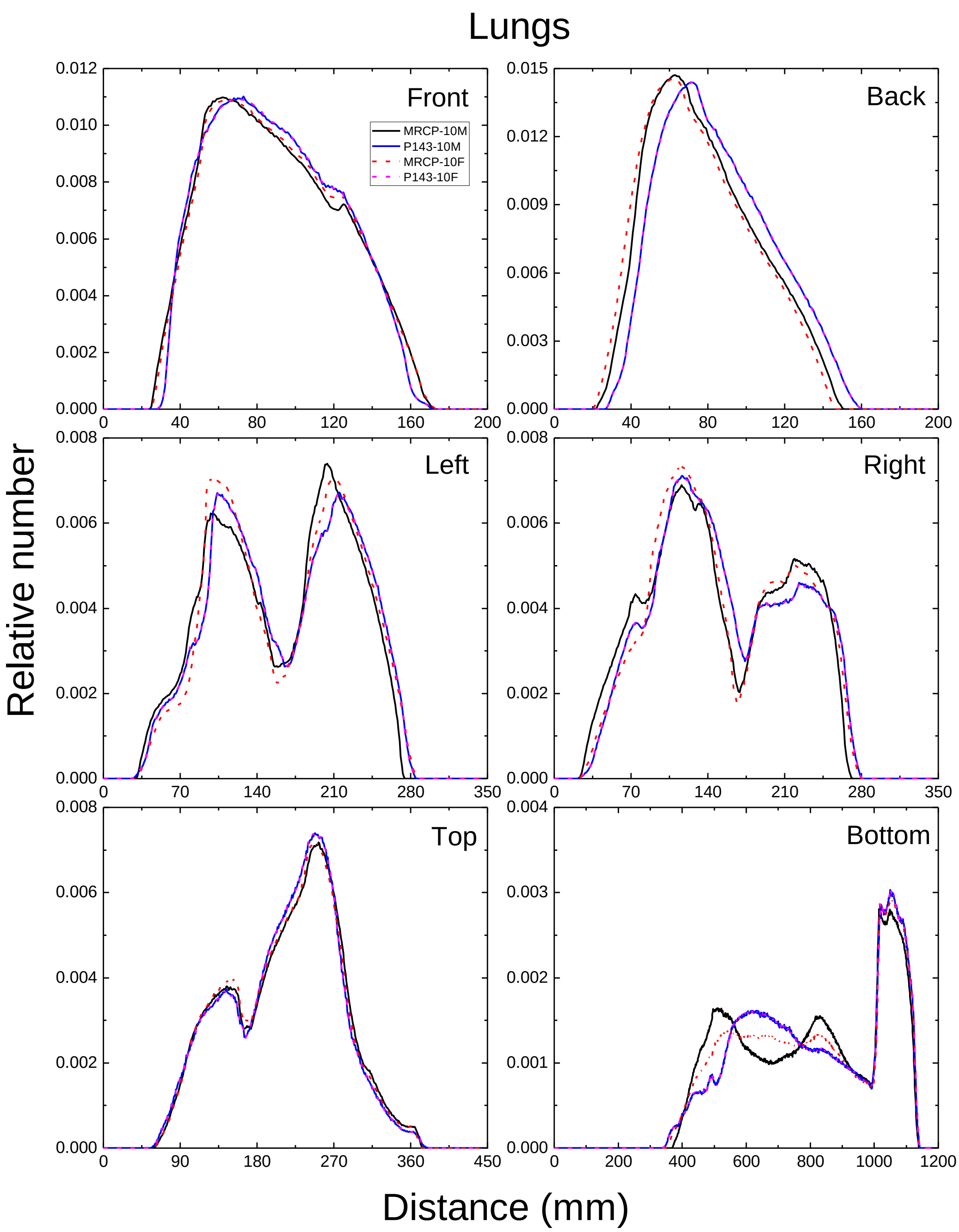

1887
1888 Fig. E.42. Distribution of depths of 10 million randomly sampled points in the lungs below the
1889 body surface of the 10-year male/female phantoms at: front, back, left, right, top and bottom.
1890

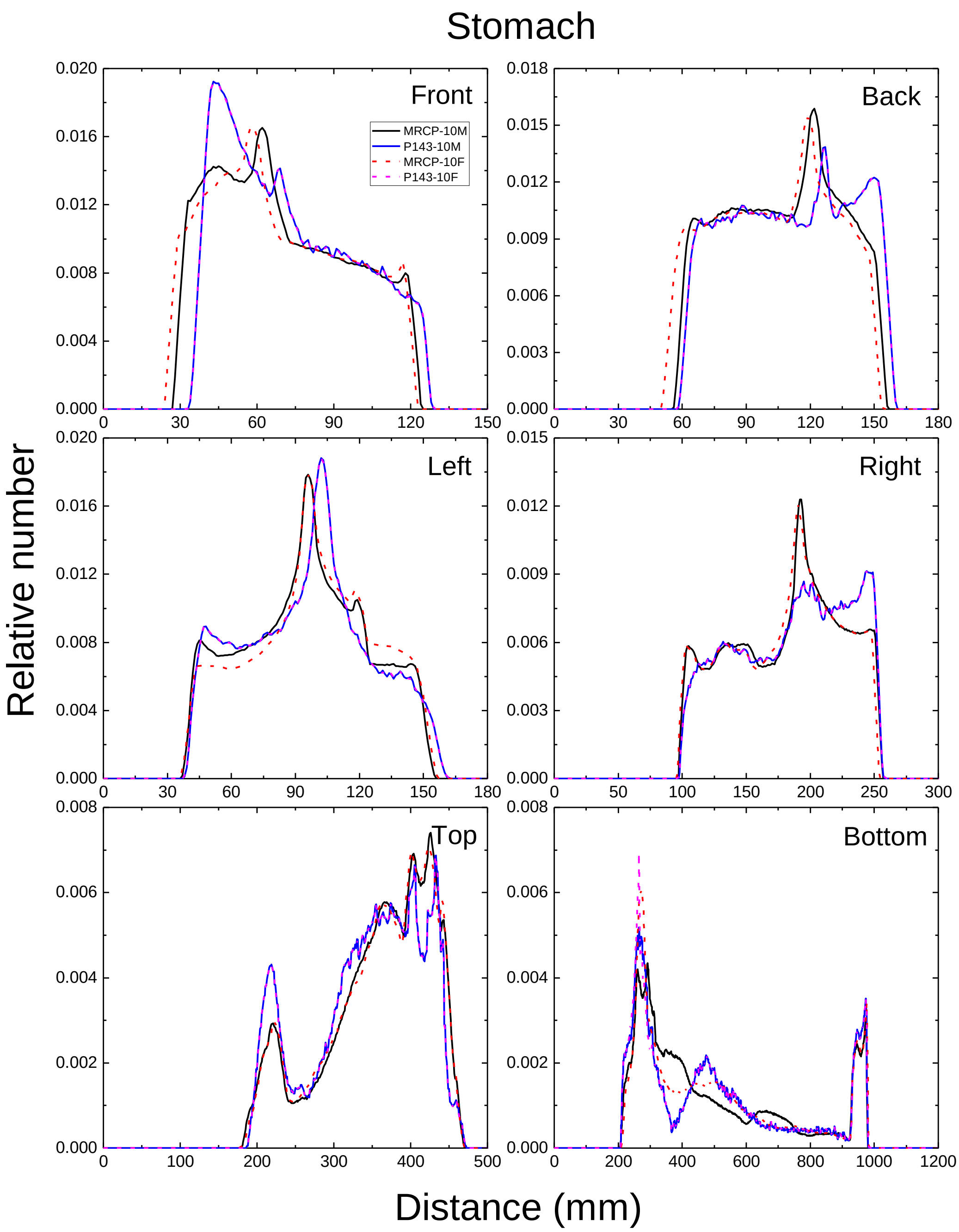

1891
1892 Fig. E.43. Distribution of depths of 10 million randomly sampled points in the stomach below
1893 the body surface of the 10-year male/female phantoms at: front, back, left, right, top and bottom.
1894

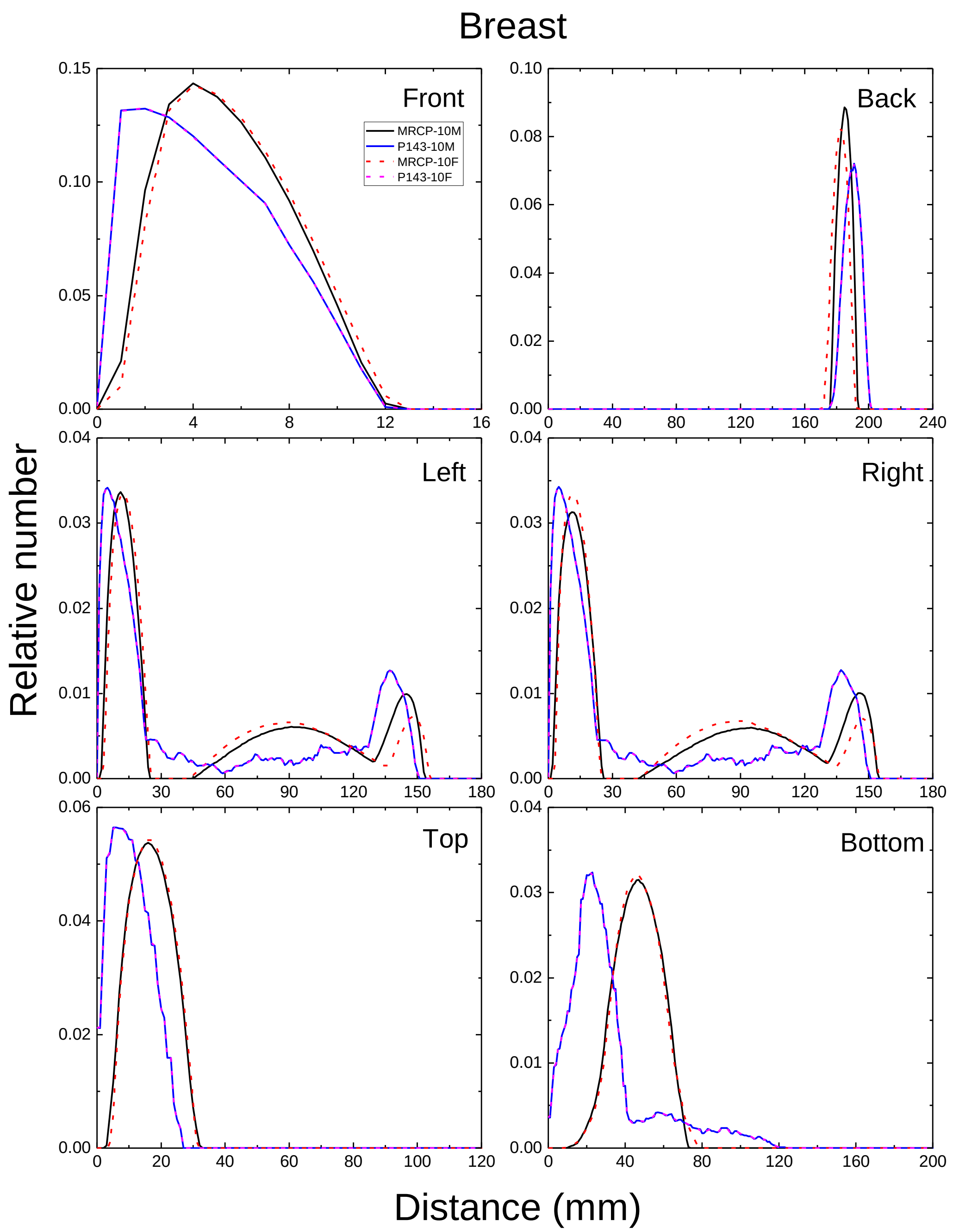

Fig. E.44. Distribution of depths of 10 million randomly sampled points in the breast below the body surface of the 10-year male/female phantoms at: front, back, left, right, top and bottom.

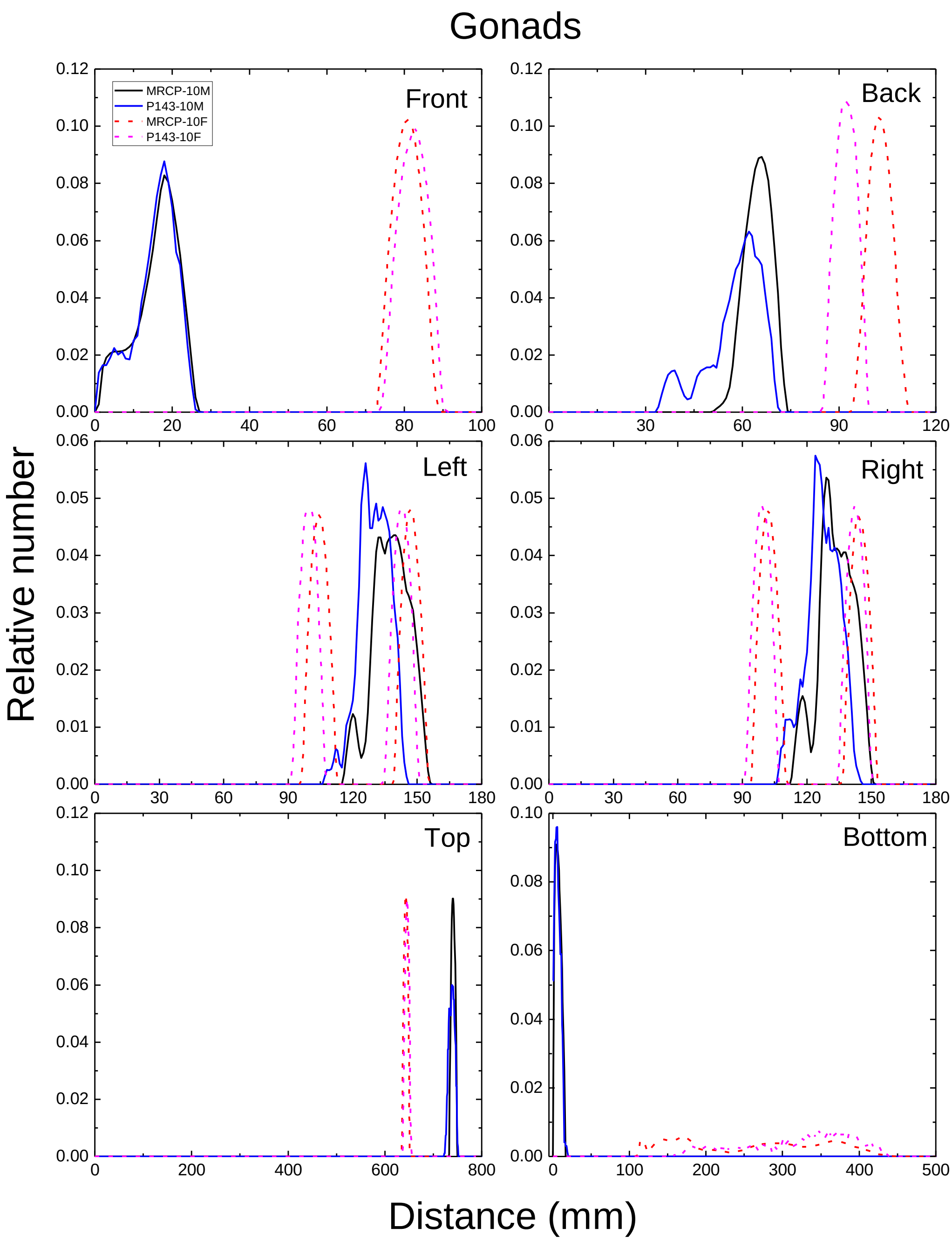

Fig. E.45. Distribution of depths of 10 million randomly sampled points in the gonads below the body surface of the 10-year male/female phantoms at: front, back, left, right, top and bottom.

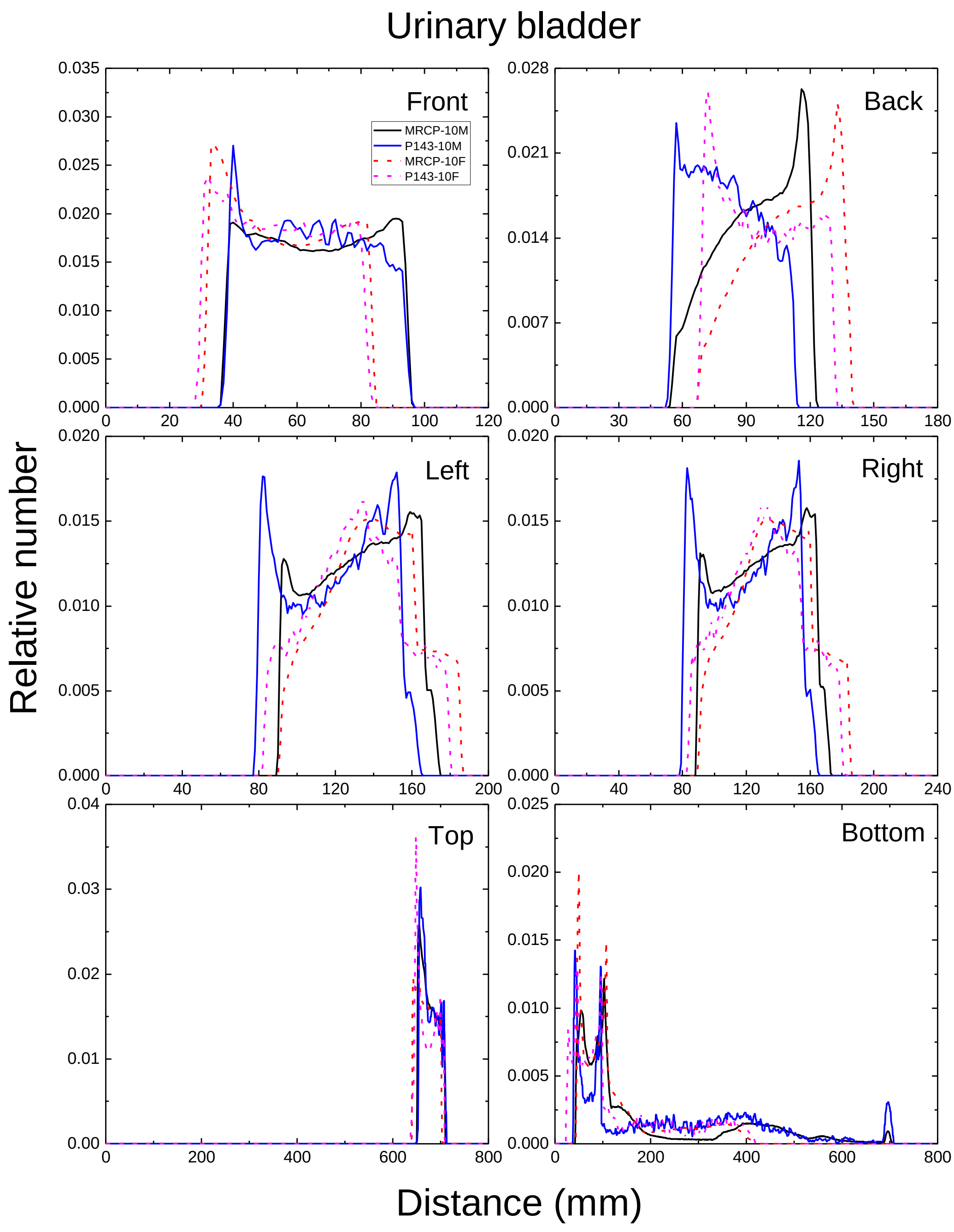

1903
1904 Fig. E.46. Distribution of depths of 10 million randomly sampled points in the urinary bladder
1905 below the body surface of the 10-year male/female phantoms at: front, back, left, right, top and
1906 bottom.
1907

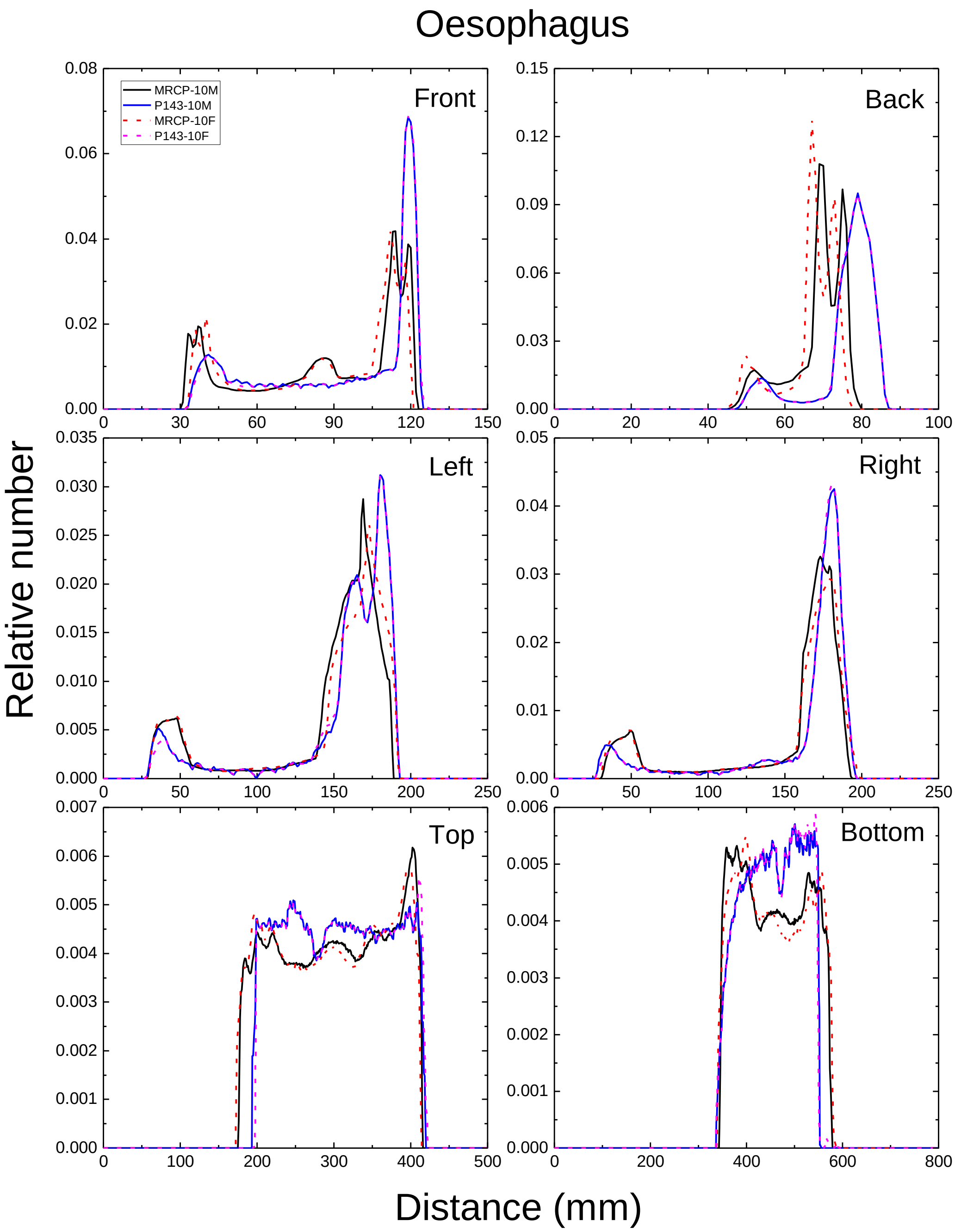

1908

1909 Fig. E.47. Distribution of depths of 10 million randomly sampled points in the oesophagus
1910 below the body surface of the 10-year male/female phantoms at: front, back, left, right, top and
1911 bottom.

1912

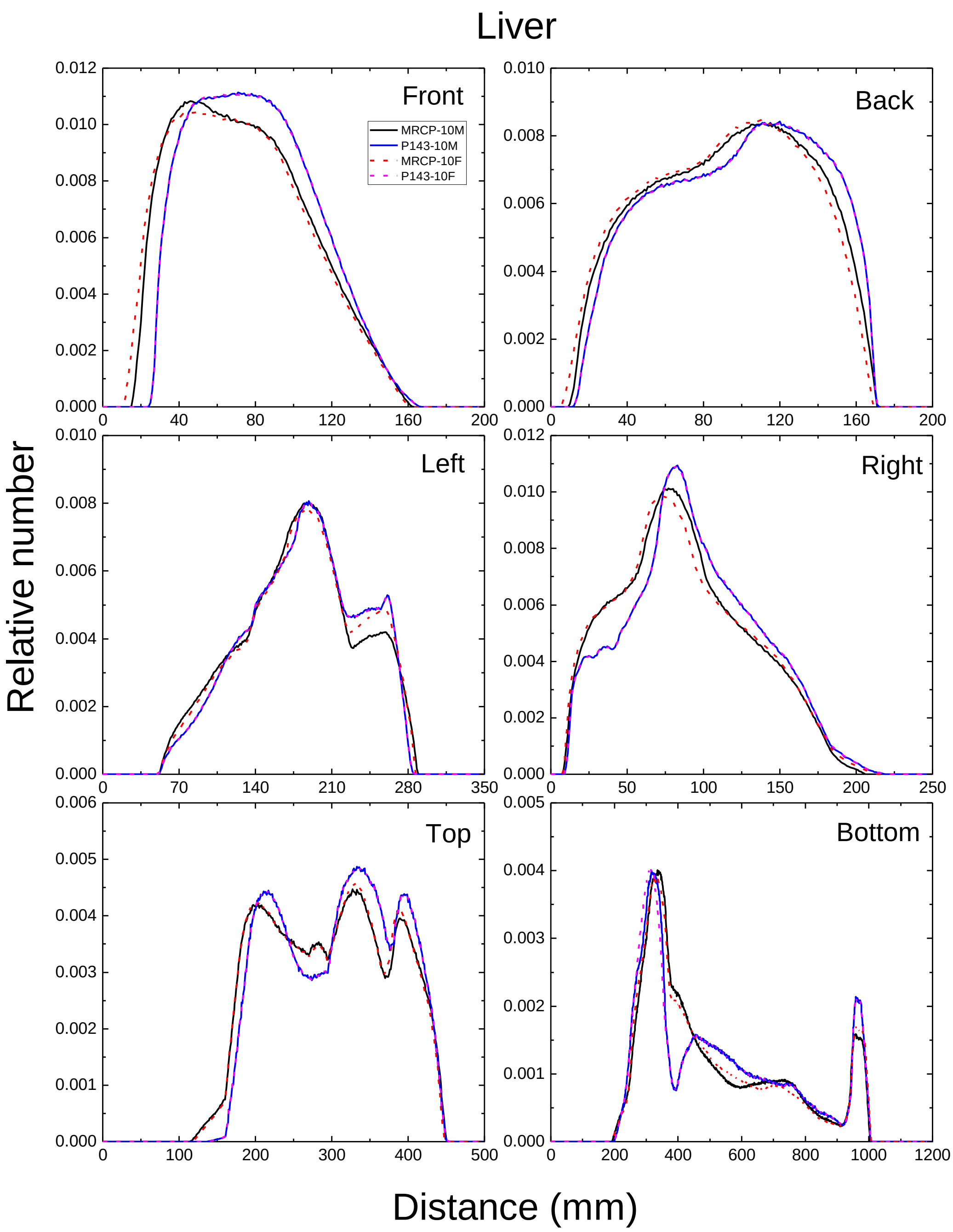

1913
1914 Fig. E.48. Distribution of depths of 10 million randomly sampled points in the liver below the
1915 body surface of the 10-year male/female phantoms at: front, back, left, right, top and bottom.
1916

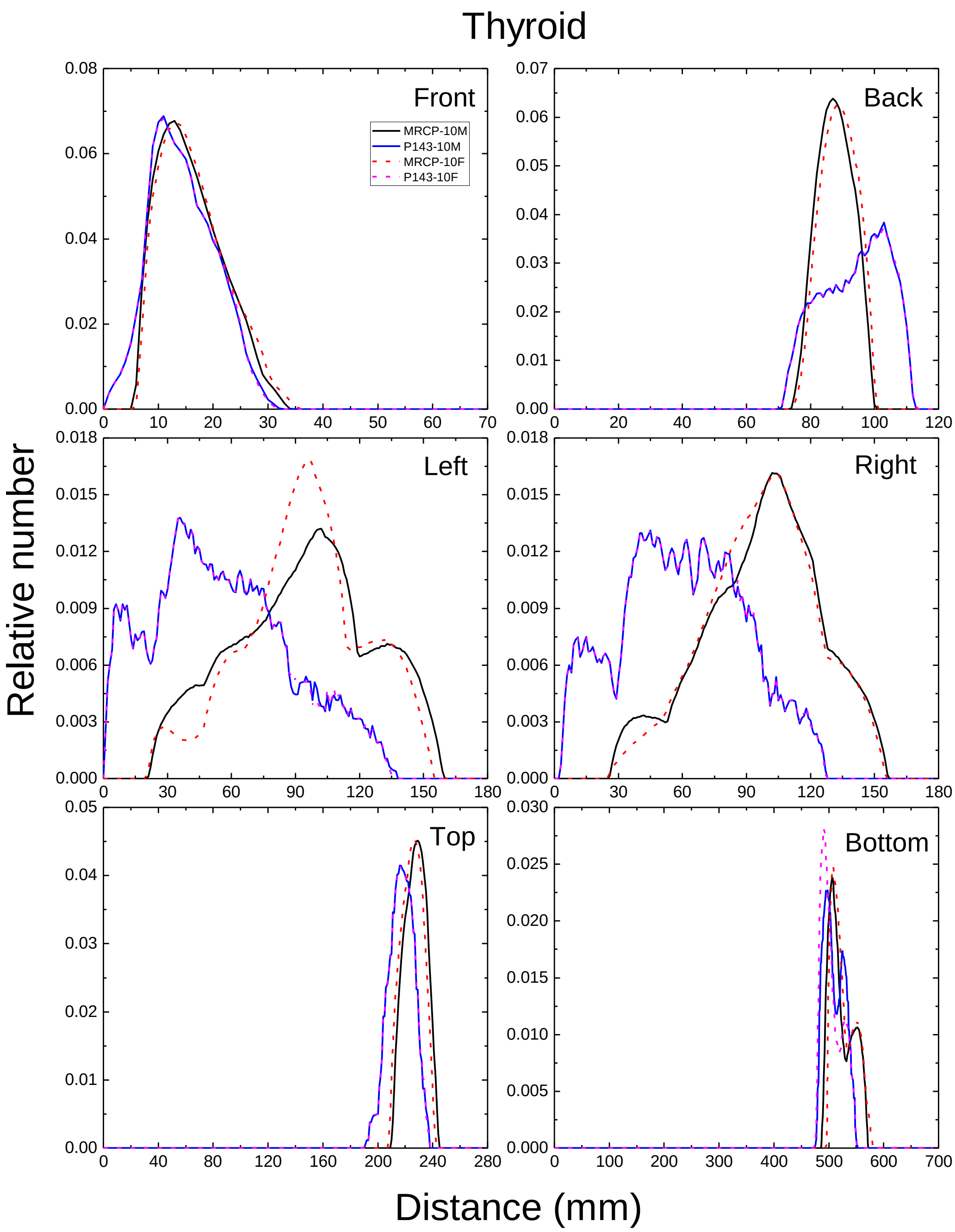

Fig. E.49. Distribution of depths of 10 million randomly sampled points in the thyroid below the body surface of the 10-year male/female phantoms at: front, back, left, right, top and bottom.

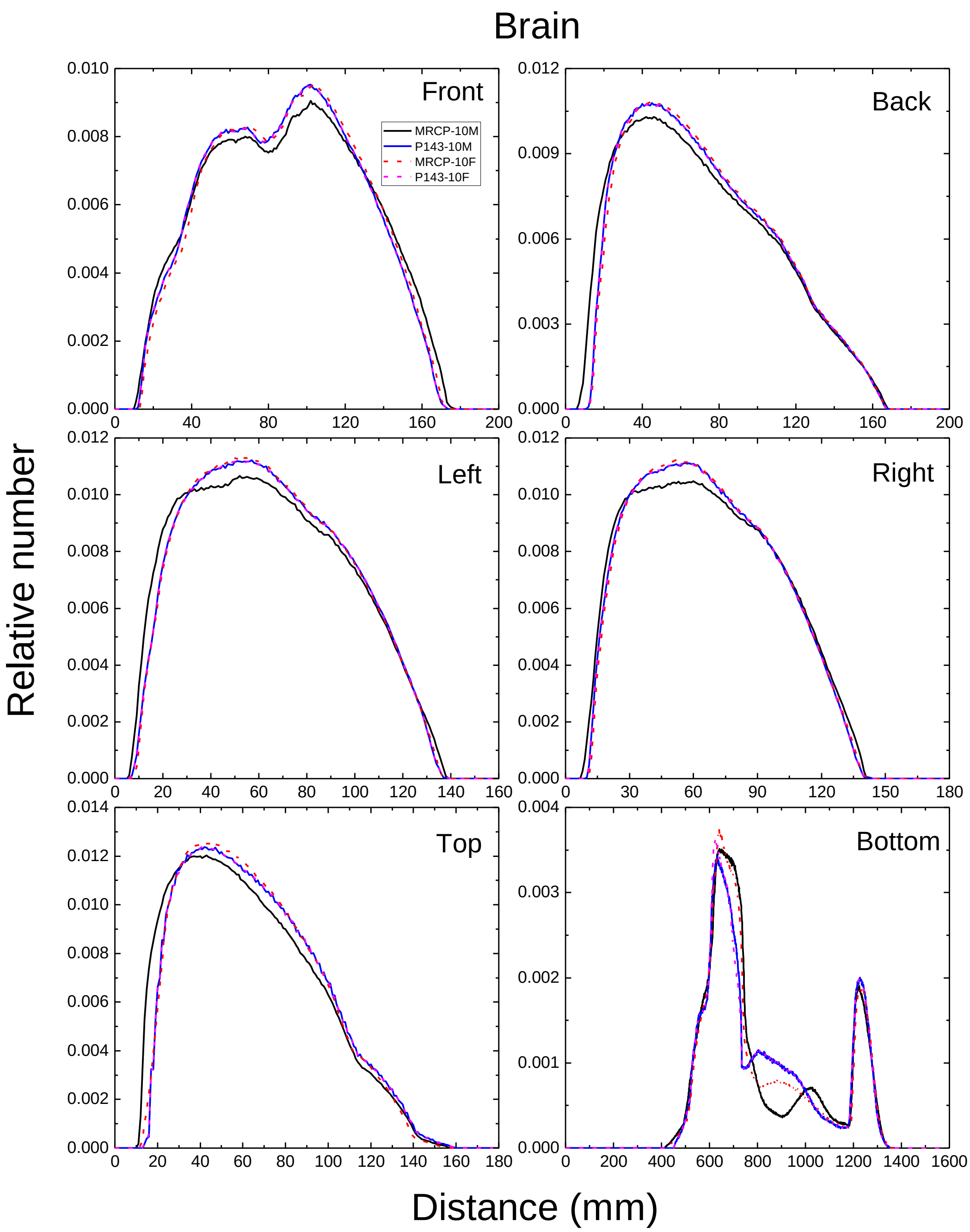

1921
1922 Fig. E.50. Distribution of depths of 10 million randomly sampled points in the brain below the
1923 body surface of the 10-year male/female phantoms at: front, back, left, right, top and bottom.
1924

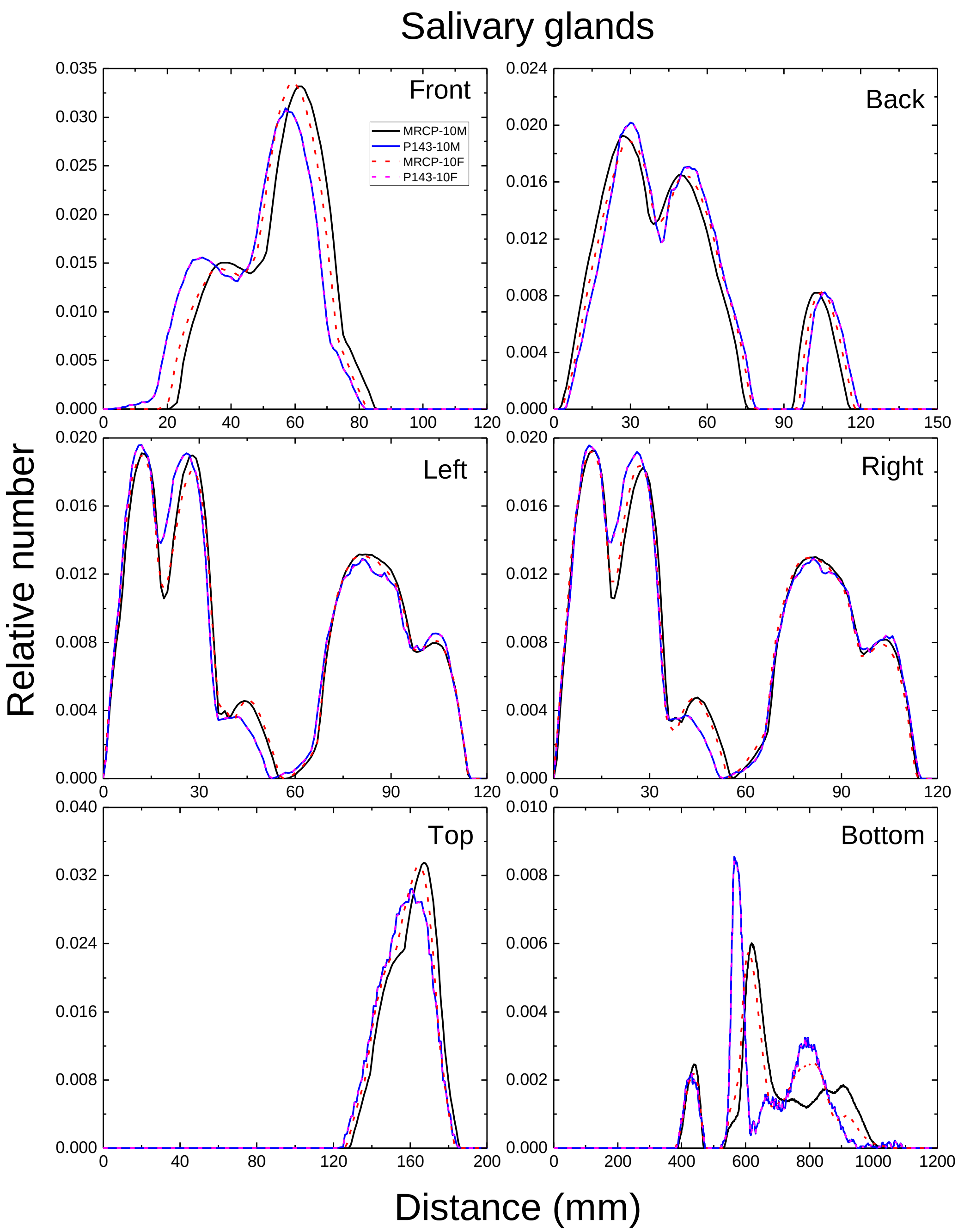

1925
1926 Fig. E.51. Distribution of depths of 10 million randomly sampled points in the salivary glands
1927 below the body surface of the 10-year male/female phantoms at: front, back, left, right, top and
1928 bottom.
1929

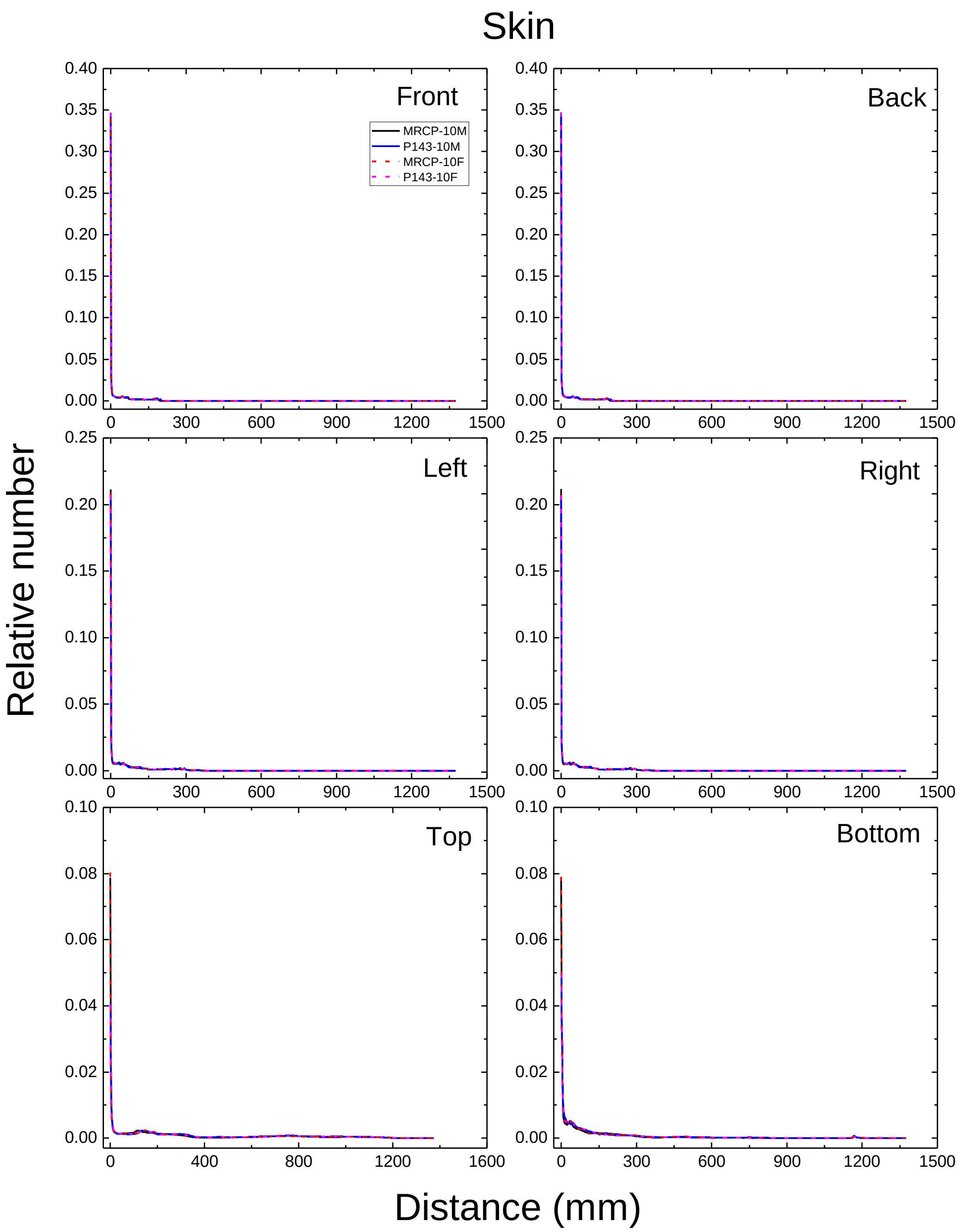

1930
1931 Fig. E.52. Distribution of depths of 10 million randomly sampled points in the skin below the
1932 body surface of the 10-year male/female phantoms at: front, back, left, right, top and bottom.
1933

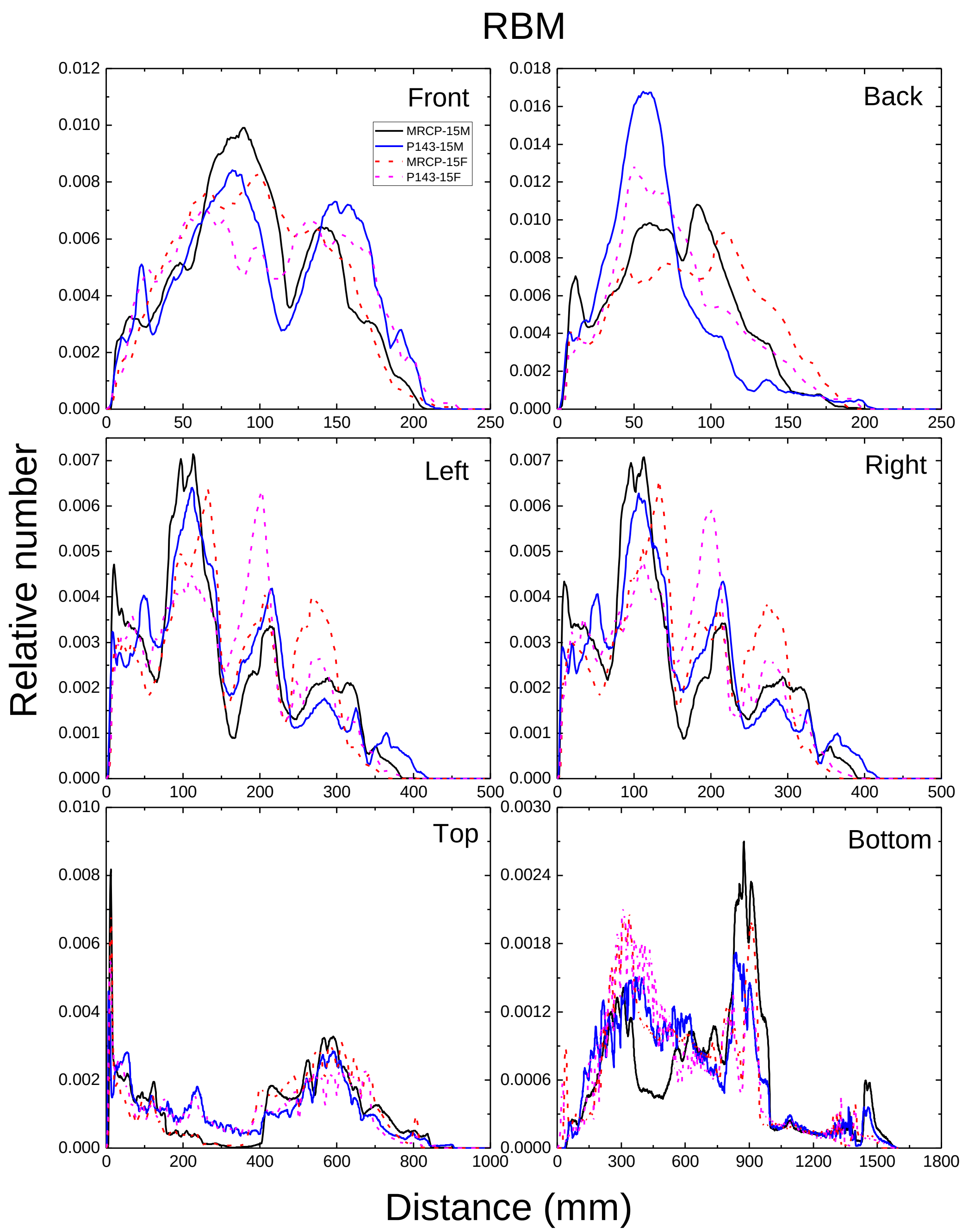

1934
1935 Fig. E.53. Distribution of depths of 10 million randomly sampled points in the red bone marrow
1936 (RBM) below the body surface of the 15-year male/female phantoms at: front, back, left, right,
1937 top and bottom.
1938

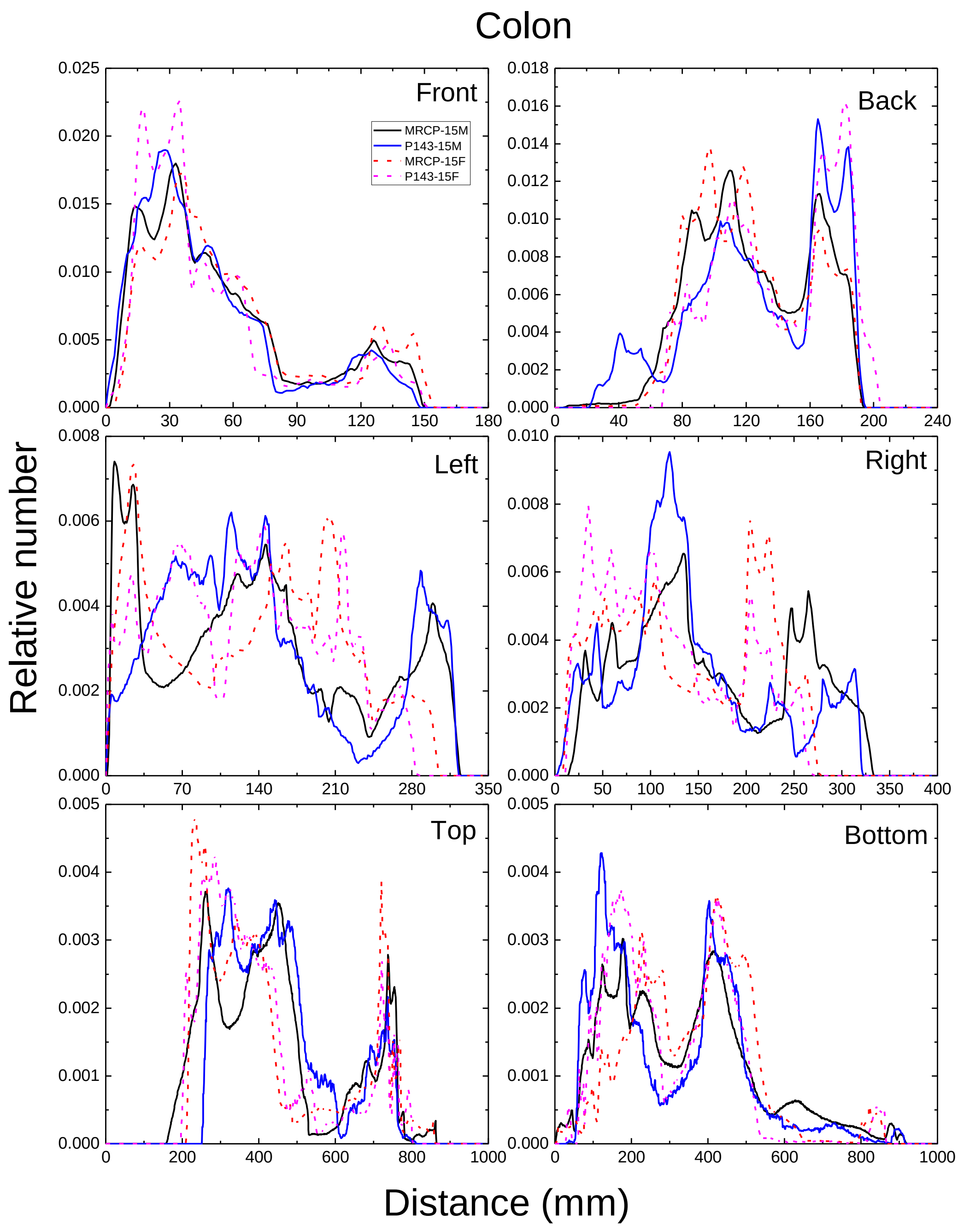

1939
1940 Fig. E.54. Distribution of depths of 10 million randomly sampled points in the colon below the
1941 body surface of the 15-year male/female phantoms at: front, back, left, right, top and bottom.
1942

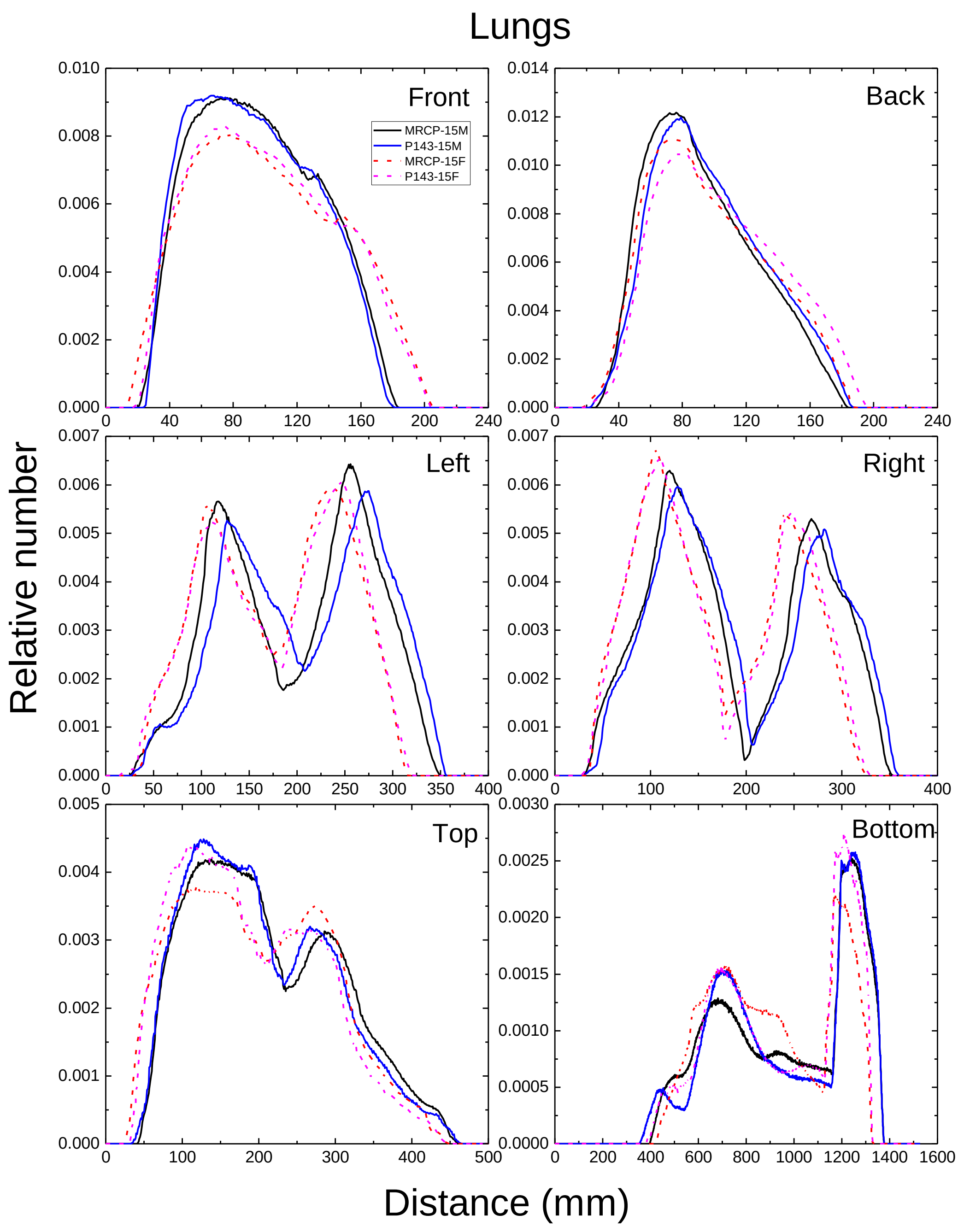

Fig. E.55. Distribution of depths of 10 million randomly sampled points in the lungs below the body surface of the 15-year male/female phantoms at: front, back, left, right, top and bottom.

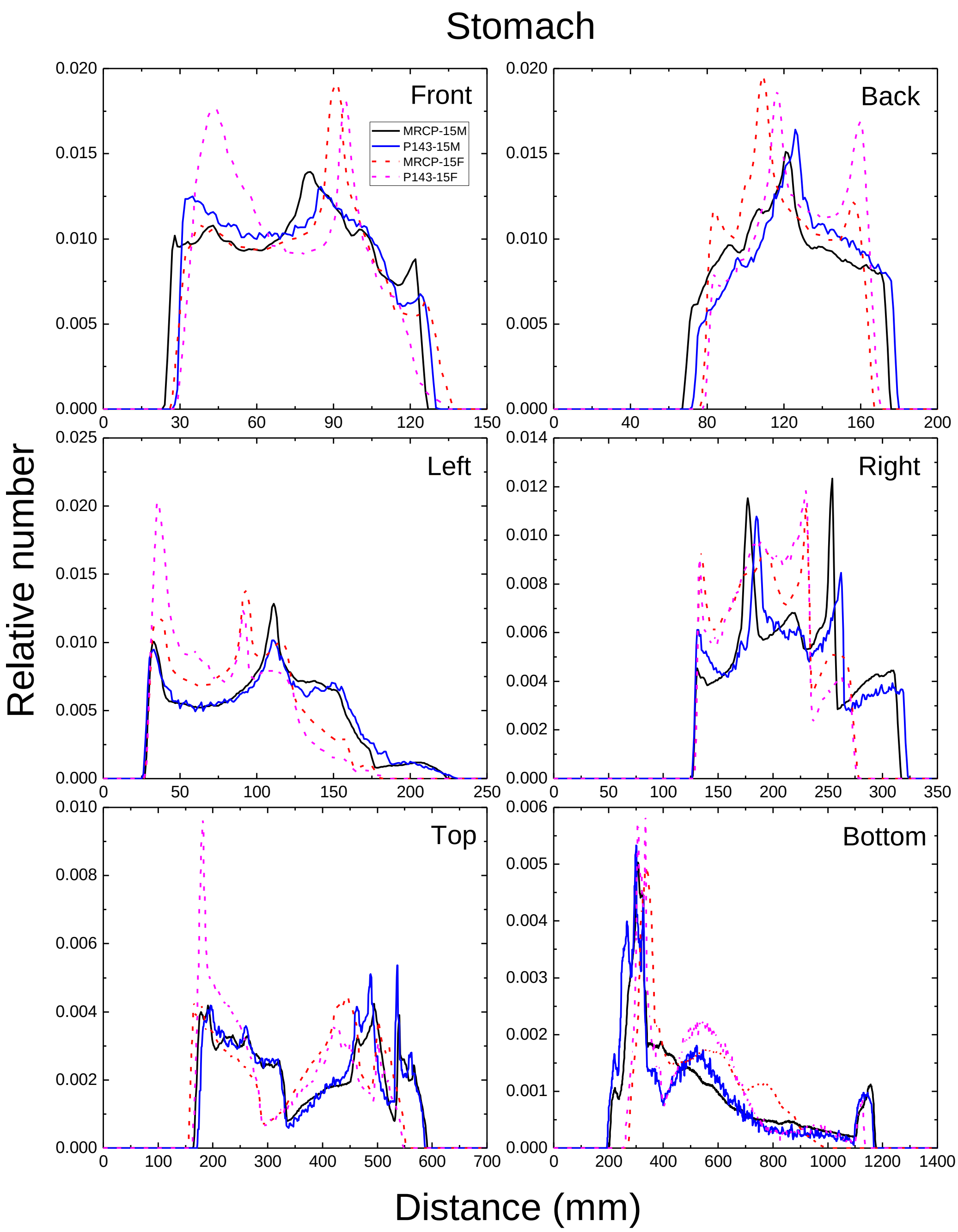

1947
1948 Fig. E.56. Distribution of depths of 10 million randomly sampled points in the stomach below
1949 the body surface of the 15-year male/female phantoms at: front, back, left, right, top and bottom.
1950

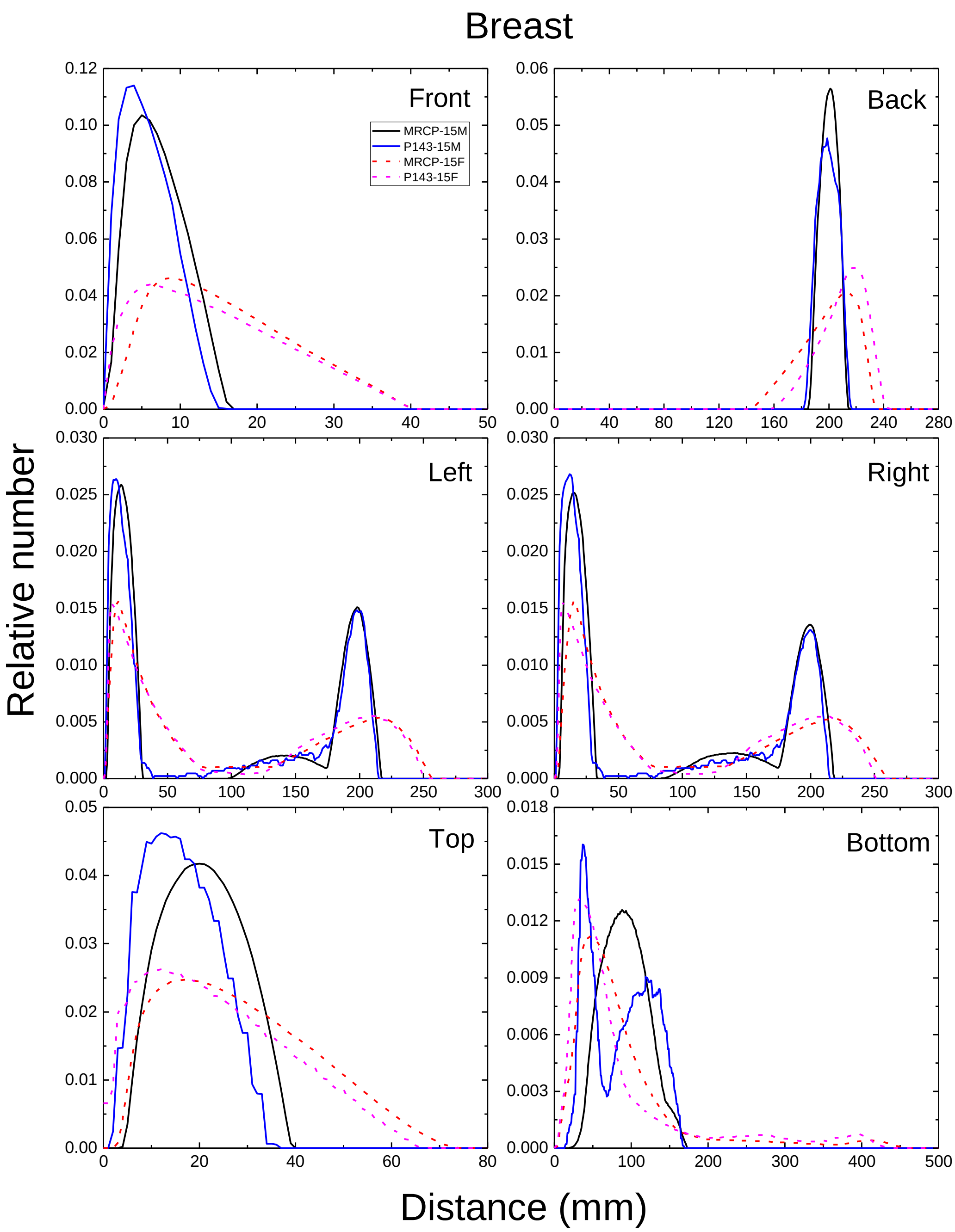

1951
1952 Fig. E.57. Distribution of depths of 10 million randomly sampled points in the breast below the
1953 body surface of the 15-year male/female phantoms at: front, back, left, right, top and bottom.
1954

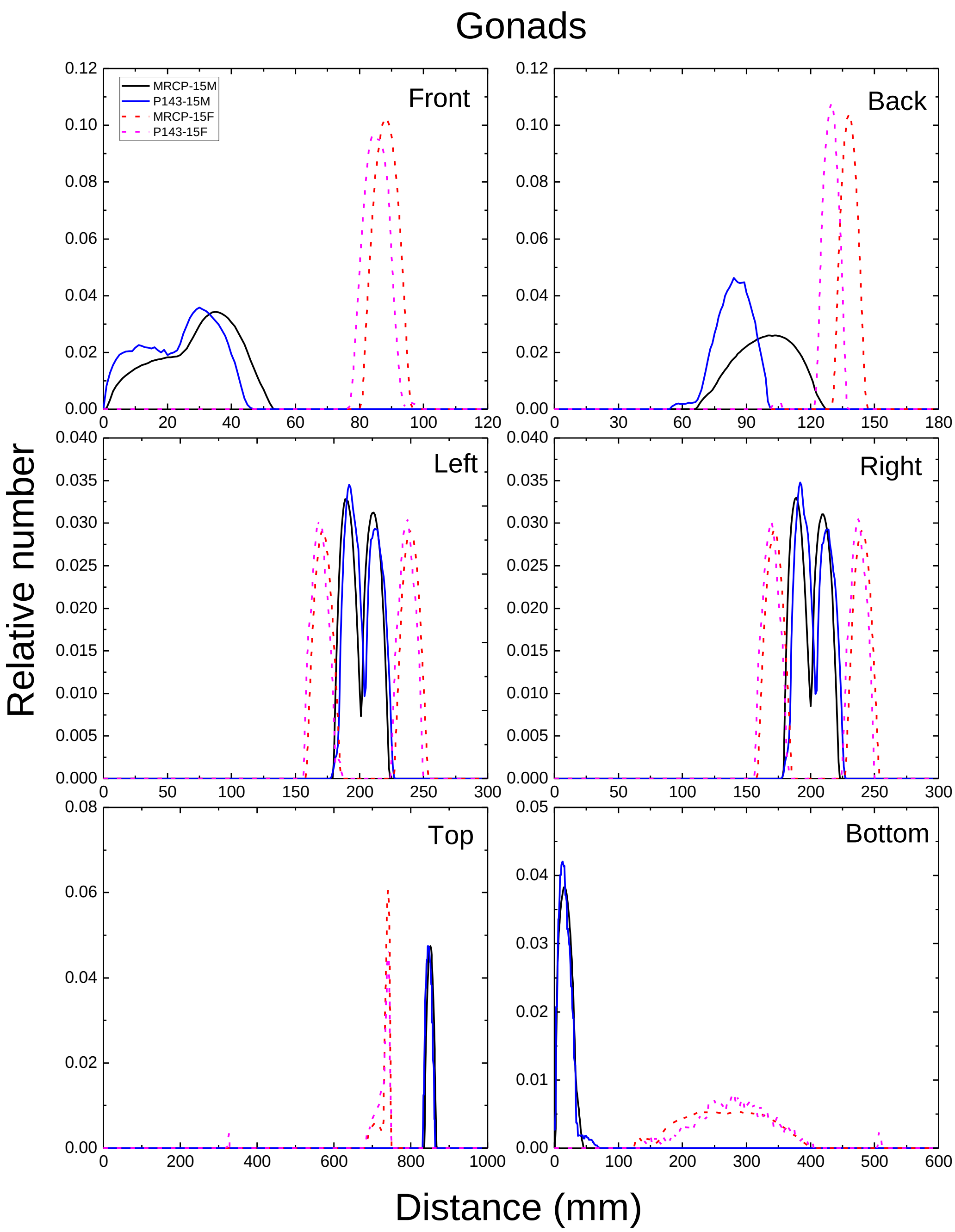

1955
1956 Fig. E.58. Distribution of depths of 10 million randomly sampled points in the gonads below
1957 the body surface of the 15-year male/female phantoms at: front, back, left, right, top and bottom.
1958

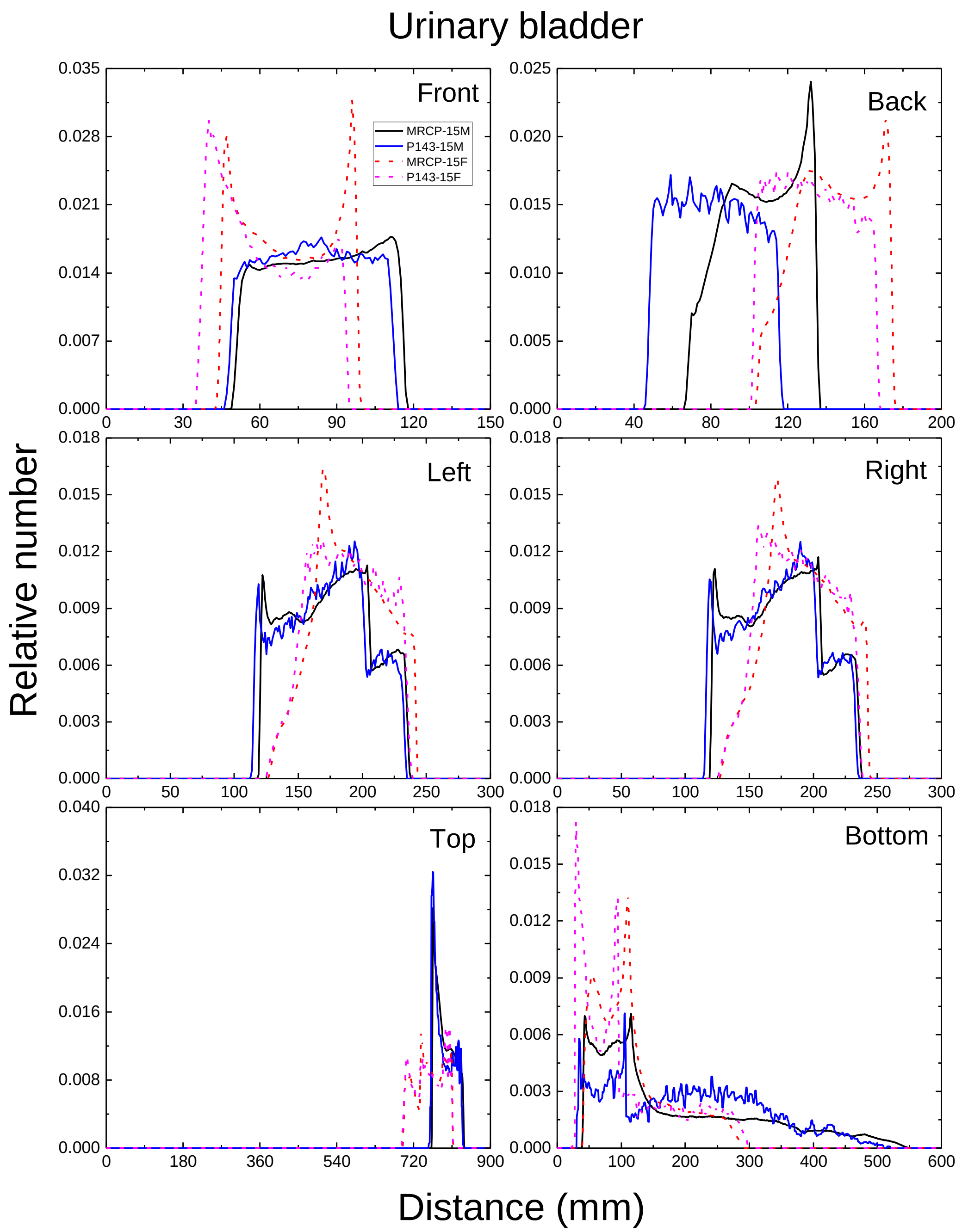

Fig. E.59. Distribution of depths of 10 million randomly sampled points in the urinary bladder below the body surface of the 15-year male/female phantoms at: front, back, left, right, top and bottom.

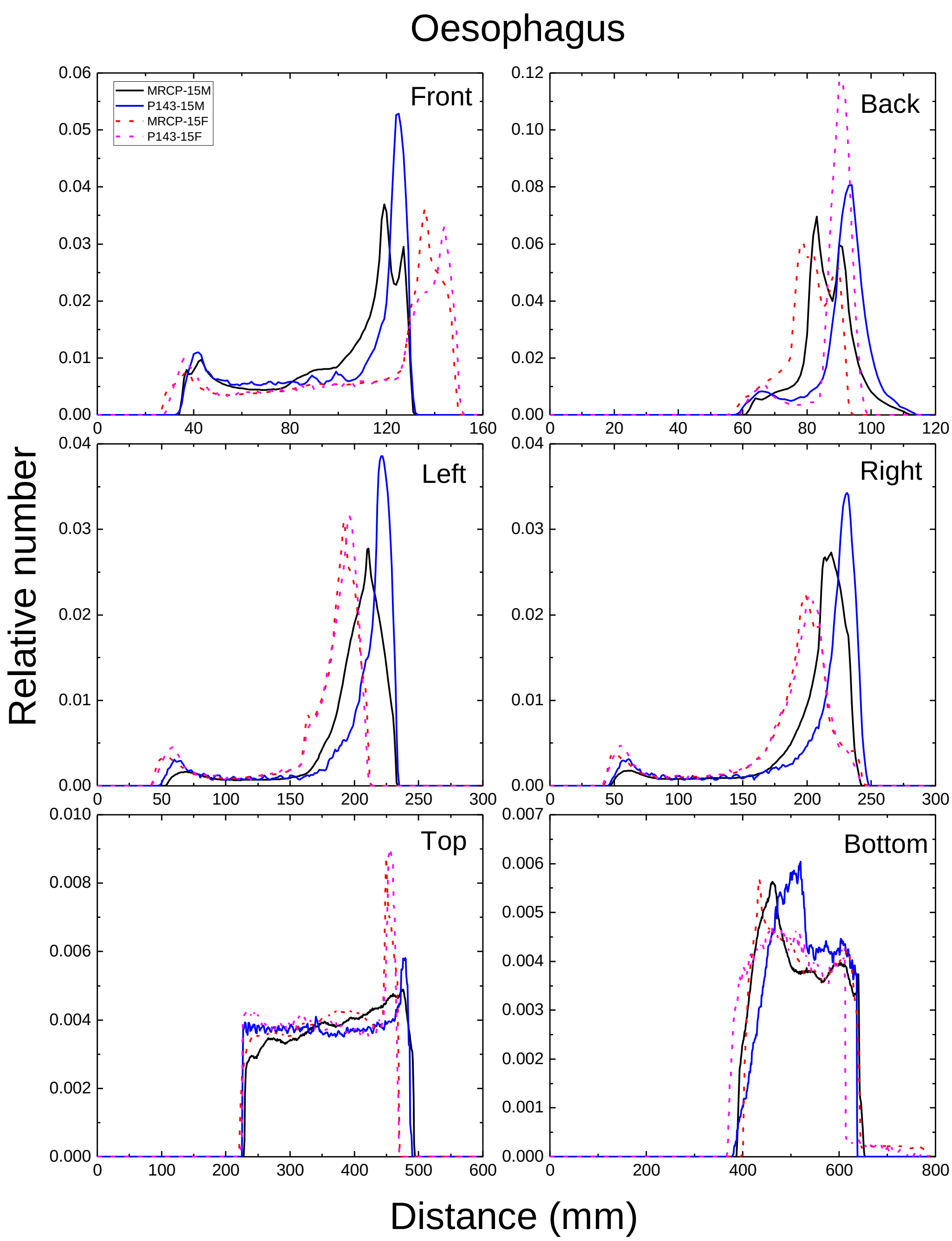

1964
1965 Fig. E.60. Distribution of depths of 10 million randomly sampled points in the oesophagus
1966 below the body surface of the 15-year male/female phantoms at: front, back, left, right, top and
1967 bottom.
1968

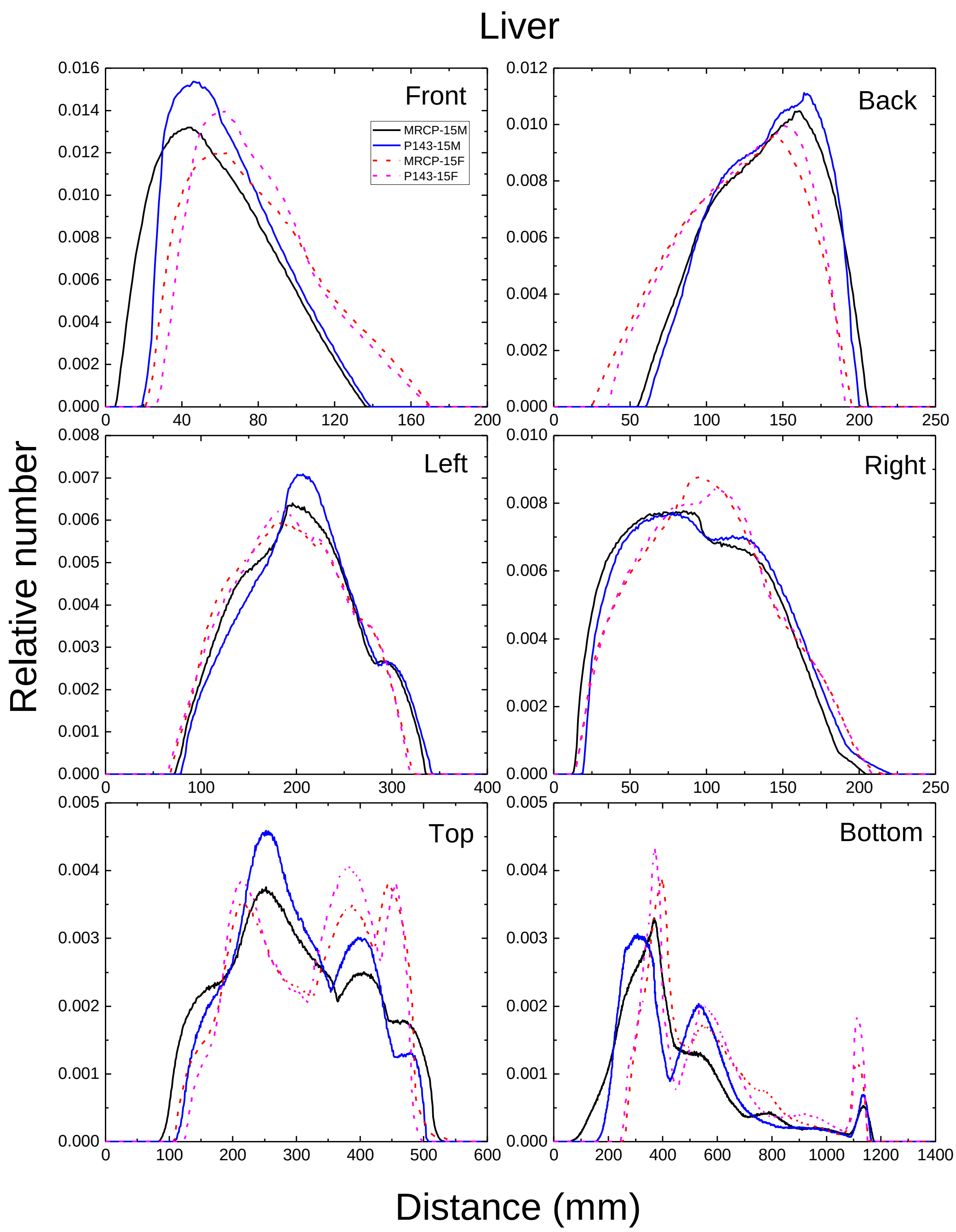

1969
1970 Fig. E.61. Distribution of depths of 10 million randomly sampled points in the liver below the
1971 body surface of the 15-year male/female phantoms at: front, back, left, right, top and bottom.
1972

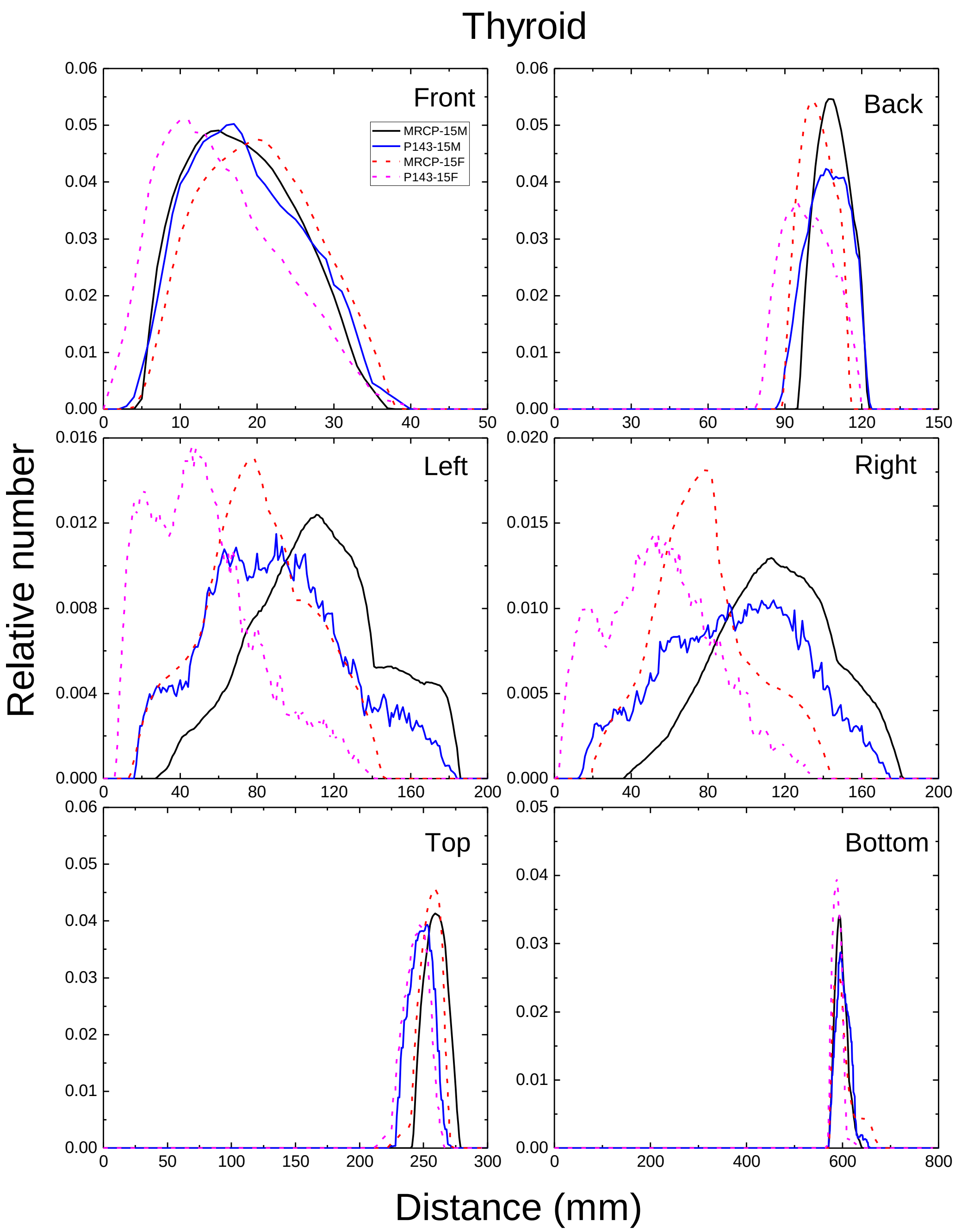

Fig. E.62. Distribution of depths of 10 million randomly sampled points in the thyroid below the body surface of the 15-year male/female phantoms at: front, back, left, right, top and bottom.

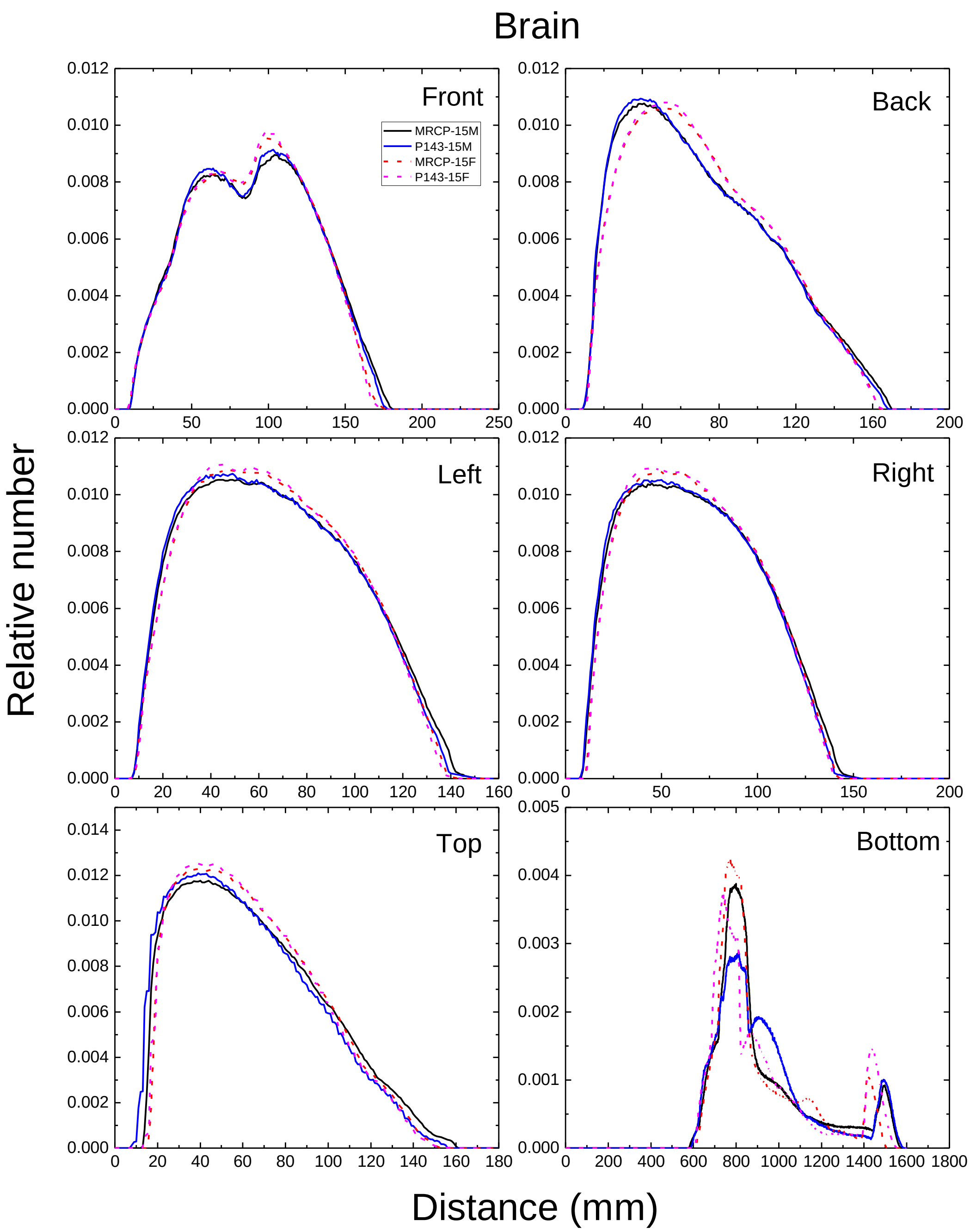

1977
1978 Fig. E.63. Distribution of depths of 10 million randomly sampled points in the brain below the
1979 body surface of the 15-year male/female phantoms at: front, back, left, right, top and bottom.
1980

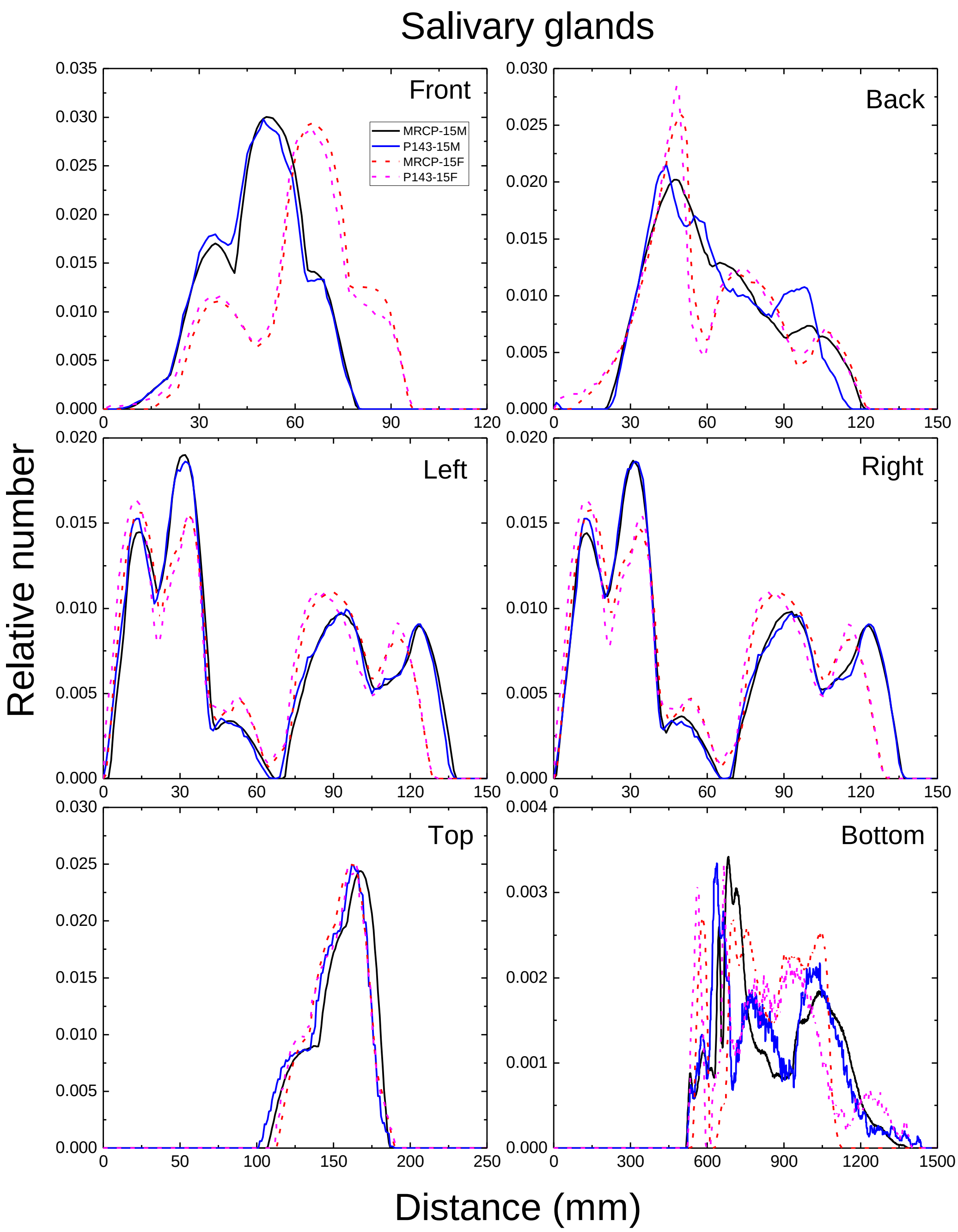

1981
1982 Fig. E.64. Distribution of depths of 10 million randomly sampled points in the salivary glands
1983 below the body surface of the 15-year male/female phantoms at: front, back, left, right, top and
1984 bottom.
1985

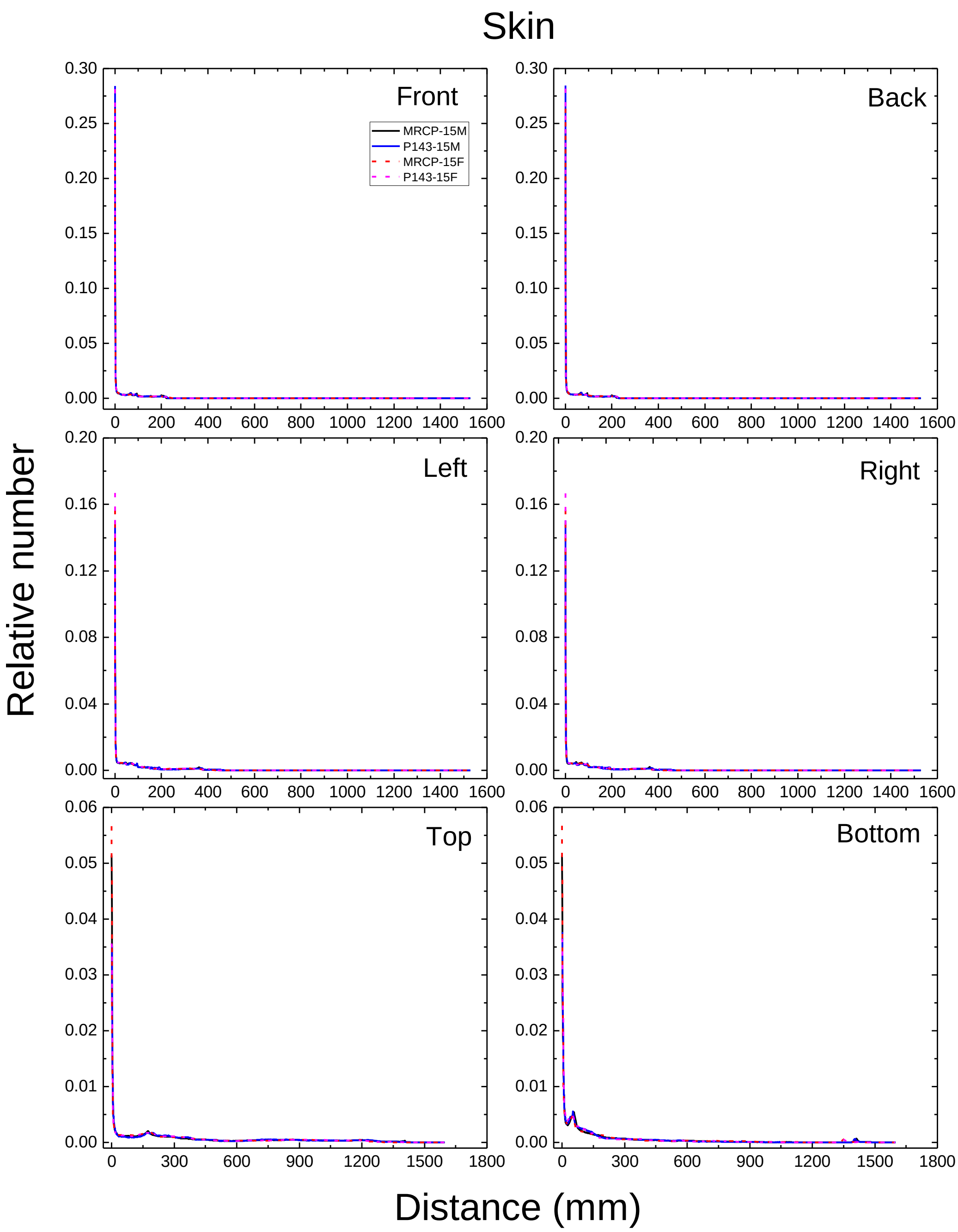

1986
1987 Fig. E.65. Distribution of depths of 10 million randomly sampled points in the skin below the
1988 body surface of the 15-year male/female phantoms at: front, back, left, right, top and bottom.
1989

ANNEX F. CHORD-LENGTH DISTRIBUTIONS BETWEEN SELECTED ORGAN PAIRS (SOURCE/TARGET TISSUES)

(F 1) In Figs F.1–F.25, chord-length distributions (CLDs) of the paediatric mesh-type reference computational phantoms (MRCPs) and the P143 phantoms are shown for the selected organ pairs (i.e. source/target regions): source regions (cortical bone, liver, lungs, thyroid and urinary bladder contents); target regions [red bone marrow (RBM), colon, lungs, stomach, breast, gonads, urinary bladder, oesophagus, liver, thyroid, brain and salivary glands]. For the CLD calculation, ten million-point pairs were randomly sampled in the target and source regions considered, and distances of the point pairs were calculated. The CLDs represent a distance between the target and source regions, significantly influencing dose calculation for internal exposures.

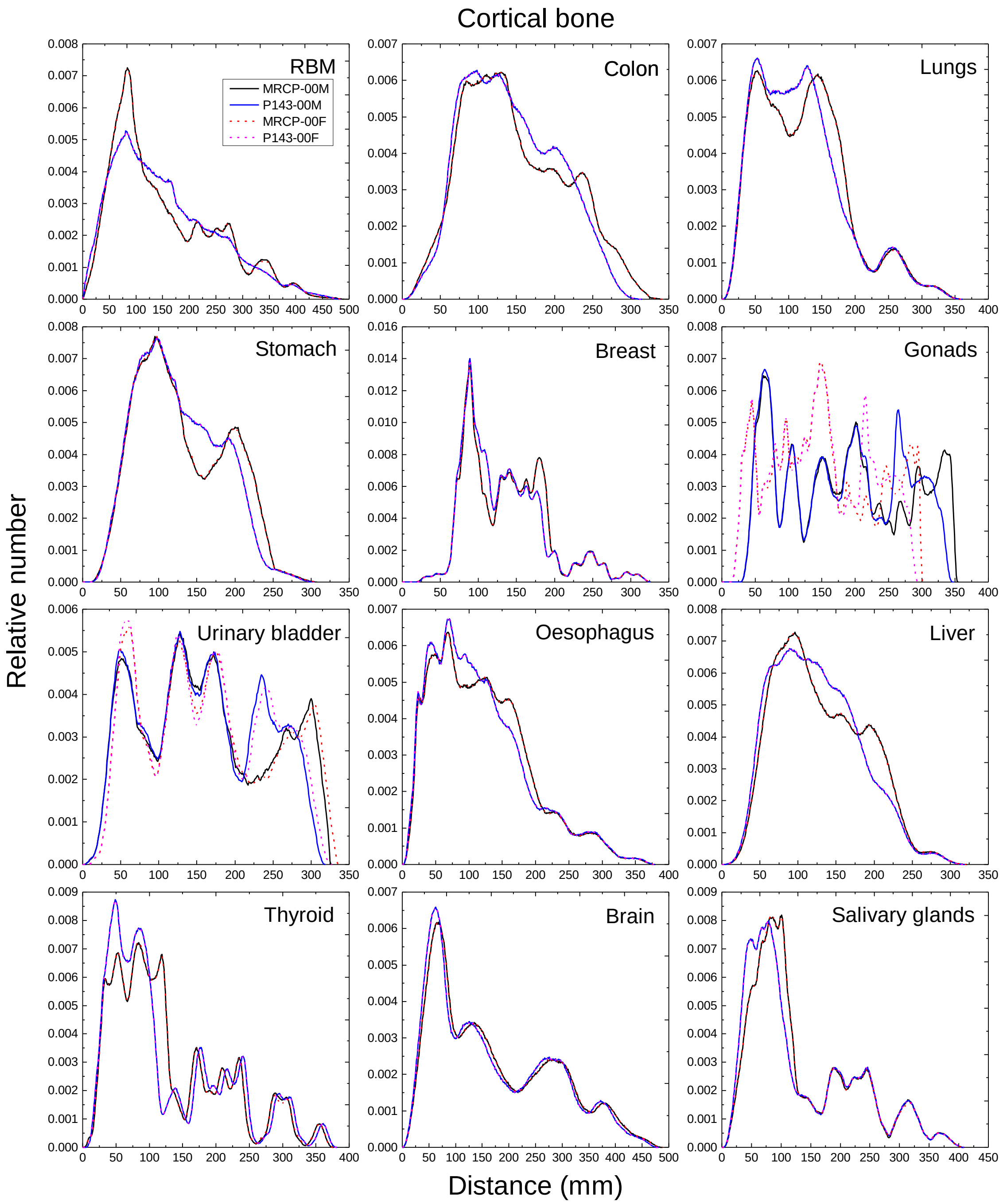

2002
2003 Fig. F.1. Distribution of distances between 10 million randomly sampled point pairs in the
2004 cortical bone (source region) and red bone marrow (RBM), colon, lungs, stomach, breast,
2005 gonads, urinary bladder, oesophagus, liver, thyroid, brain and salivary glands (target regions)
2006 in the newborn male/female phantoms.
2007

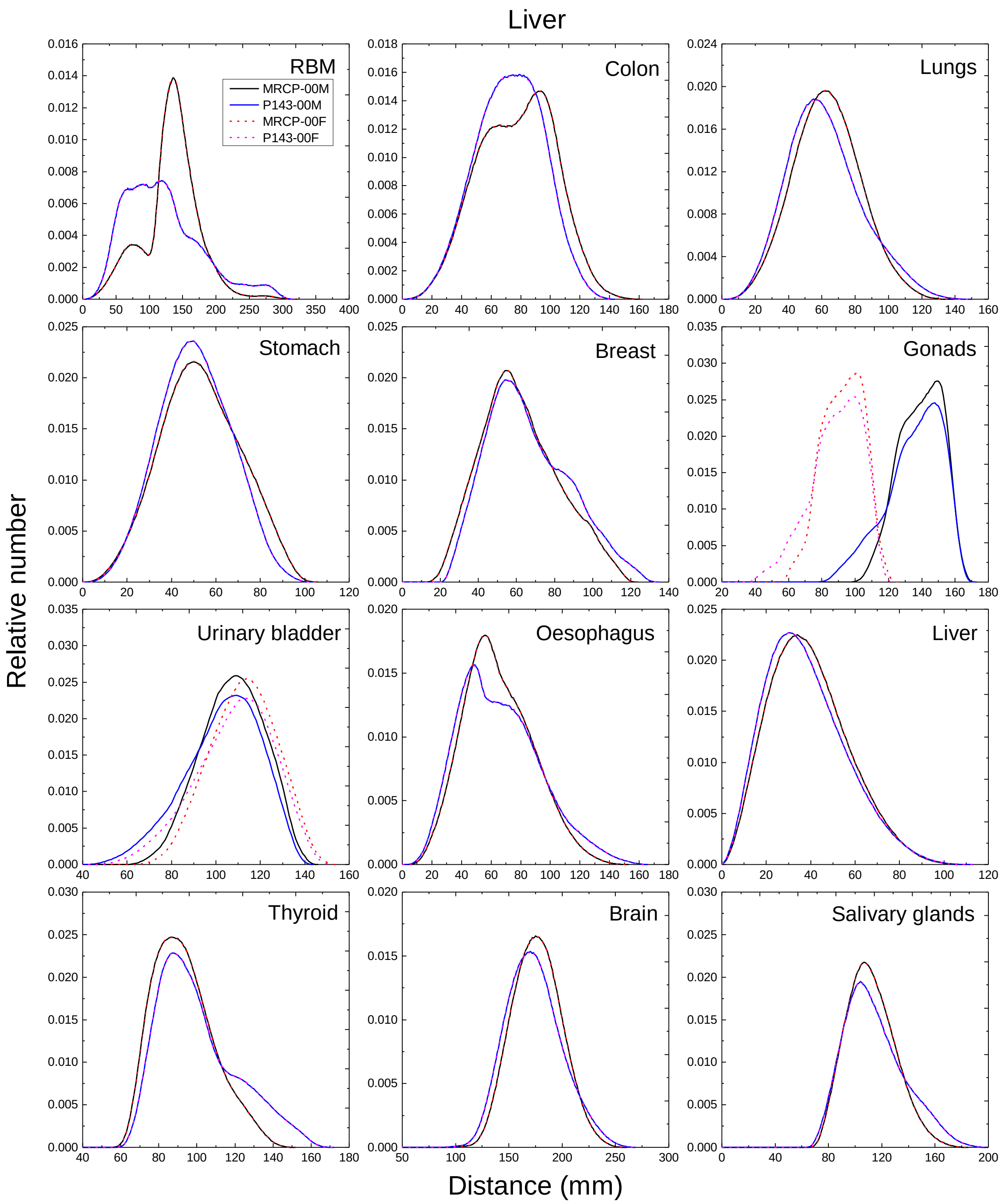

Fig. F.2. Distribution of distances between 10 million randomly sampled point pairs in the liver (source region) and red bone marrow (RBM), colon, lungs, stomach, breast, gonads, urinary bladder, oesophagus, liver, thyroid, brain and salivary glands (target regions) in the newborn male/female phantoms.

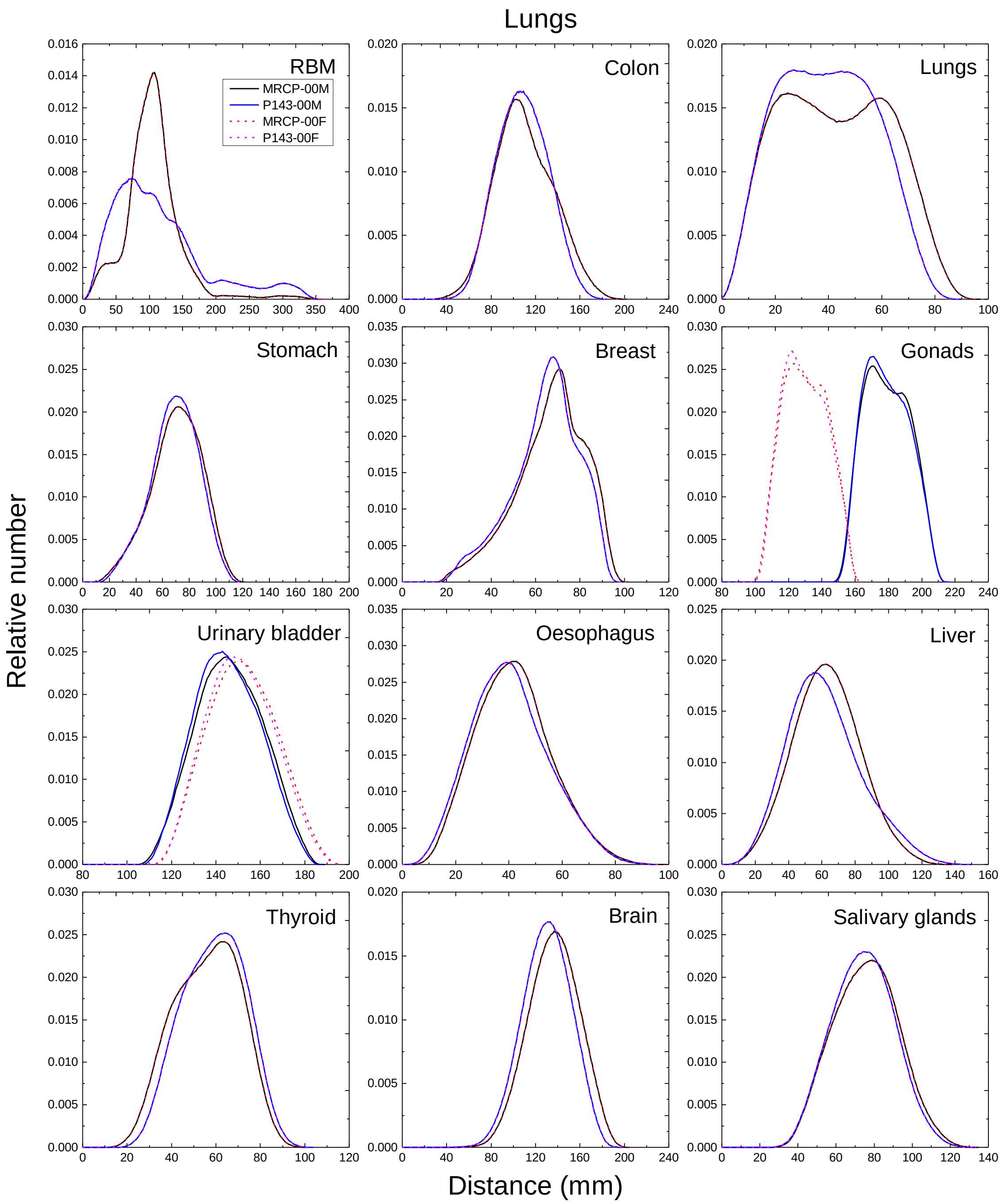

Fig. F.3. Distribution of distances between 10 million randomly sampled point pairs in the lungs (source region) and red bone marrow (RBM), colon, lungs, stomach, breast, gonads, urinary bladder, oesophagus, liver, thyroid, brain and salivary glands (target regions) in the newborn male/female phantoms.

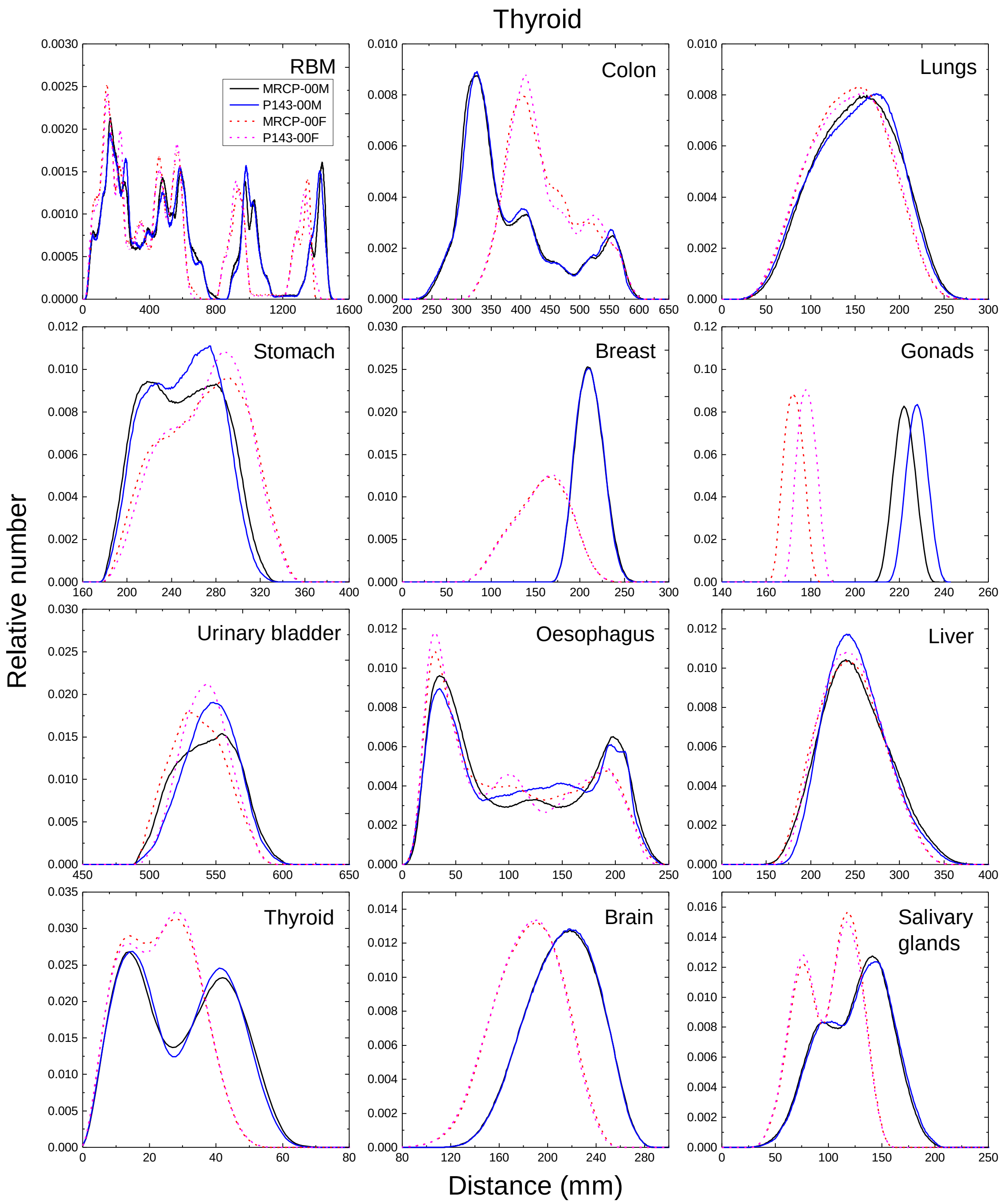

2020
2021 Fig. F.4. Distribution of distances between 10 million randomly sampled point pairs in the
2022 thyroid (source region) and red bone marrow (RBM), colon, lungs, stomach, breast, gonads,
2023 urinary bladder, oesophagus, liver, thyroid, brain and salivary glands (target regions) in the
2024 newborn male/female phantoms.
2025

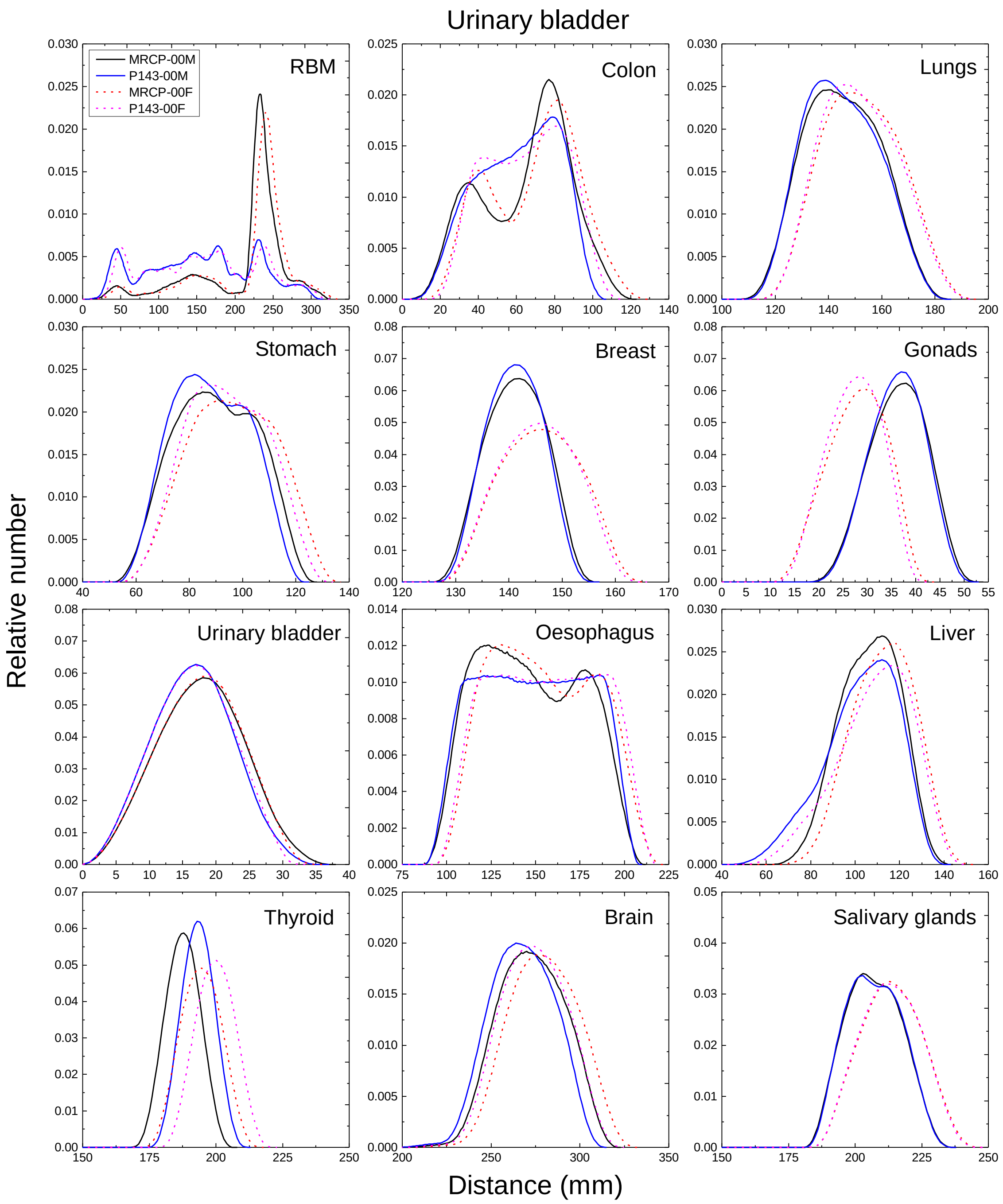

Fig. F.5. Distribution of distances between 10 million randomly sampled point pairs in the urinary bladder contents (source region) and red bone marrow (RBM), colon, lungs, stomach, breast, gonads, urinary bladder, oesophagus, liver, thyroid, brain and salivary glands (target regions) in the newborn male/female phantoms.

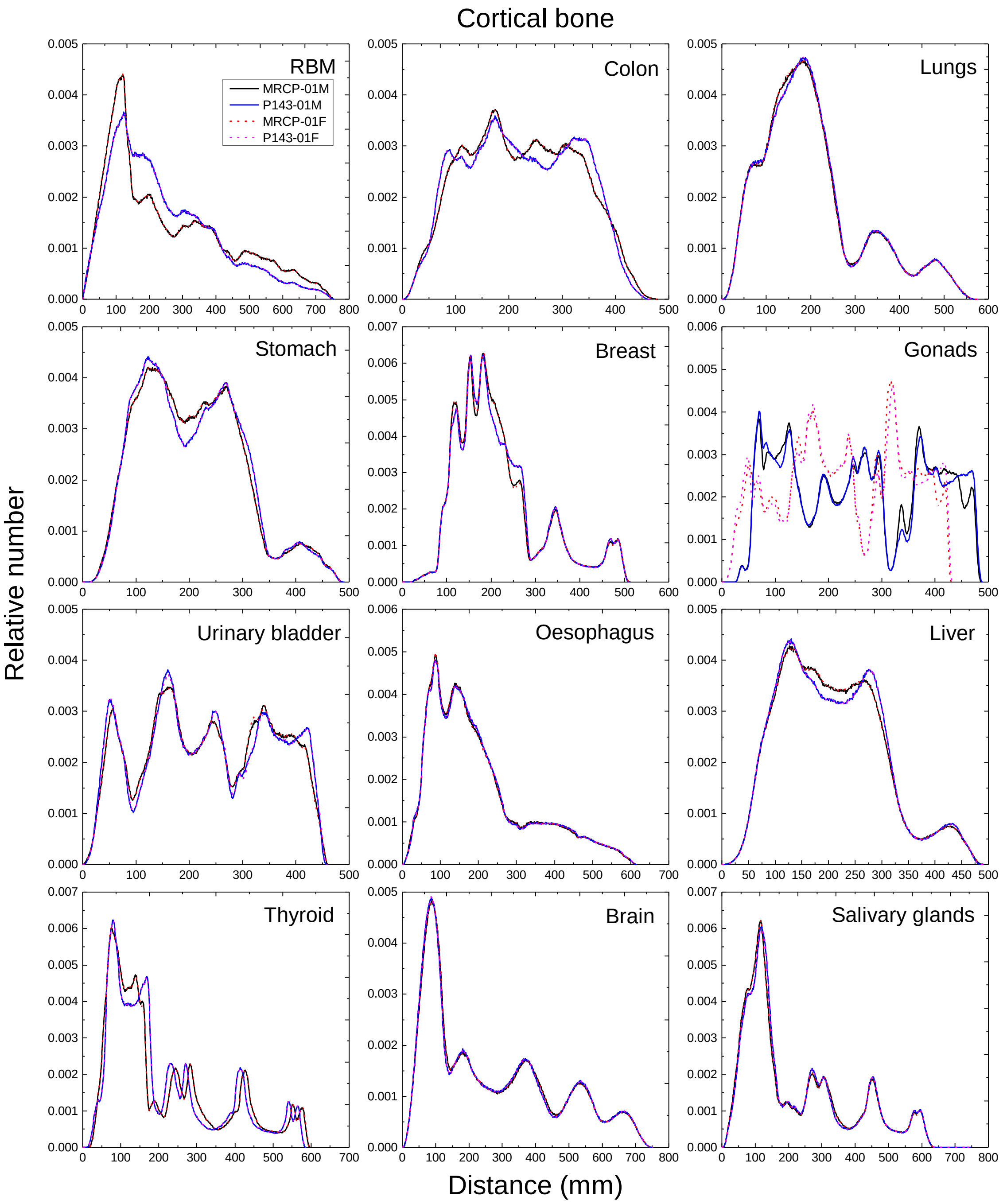

Fig. F.6. Distribution of distances between 10 million randomly sampled point pairs in the cortical bone (source region) and red bone marrow (RBM), colon, lungs, stomach, breast, gonads, urinary bladder, oesophagus, liver, thyroid, brain and salivary glands (target regions) in the 1-year male/female phantoms.

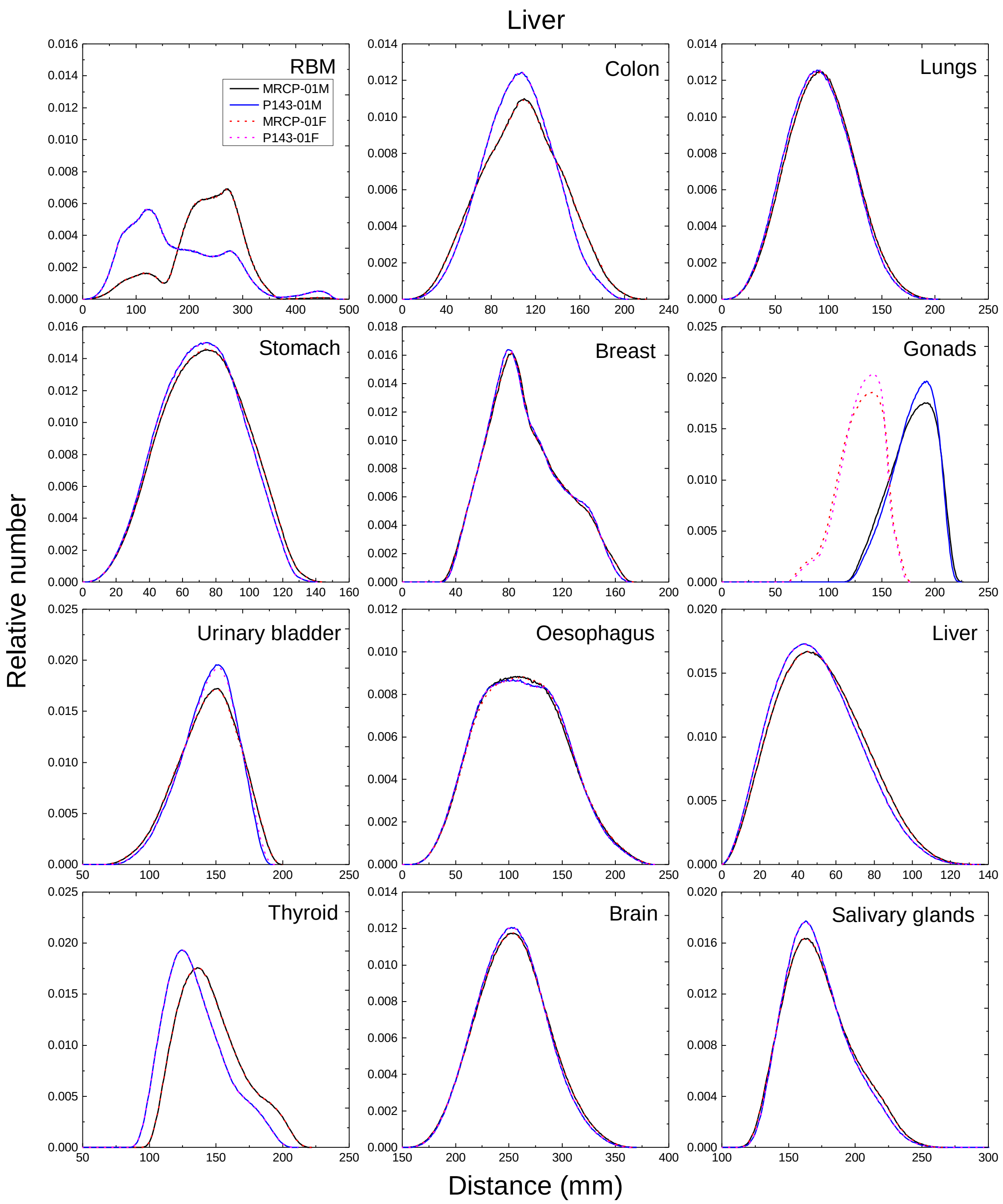

Fig. F.7. Distribution of distances between 10 million randomly sampled point pairs in the liver (source region) and red bone marrow (RBM), colon, lungs, stomach, breast, gonads, urinary bladder, oesophagus, liver, thyroid, brain and salivary glands (target regions) in the 1-year male/female phantoms.

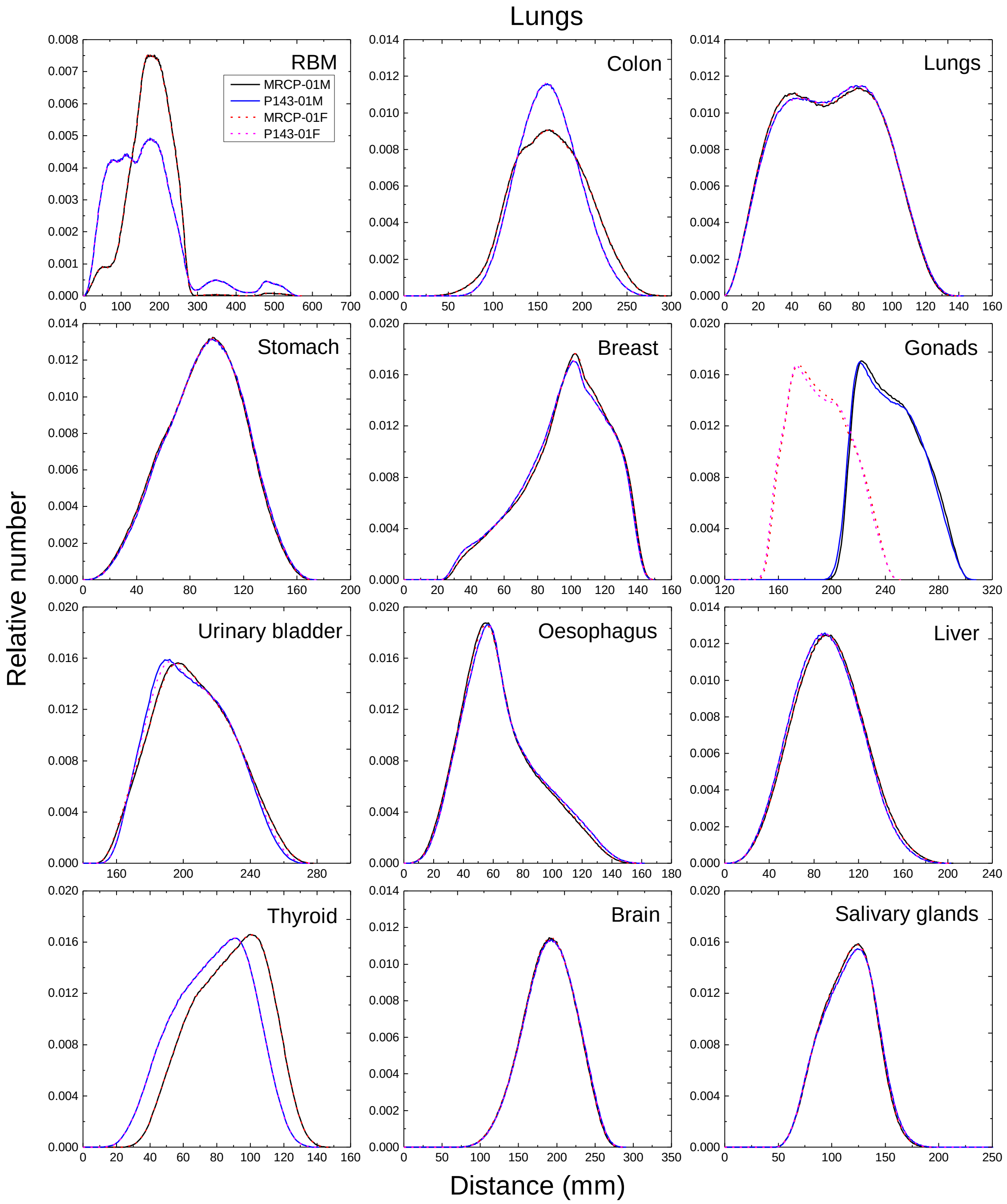

2044
2045 Fig. F.8. Distribution of distances between 10 million randomly sampled point pairs in the
2046 lungs (source region) and red bone marrow (RBM), colon, lungs, stomach, breast, gonads,
2047 urinary bladder, oesophagus, liver, thyroid, brain and salivary glands (target regions) in the 1-
2048 year male/female phantoms.
2049

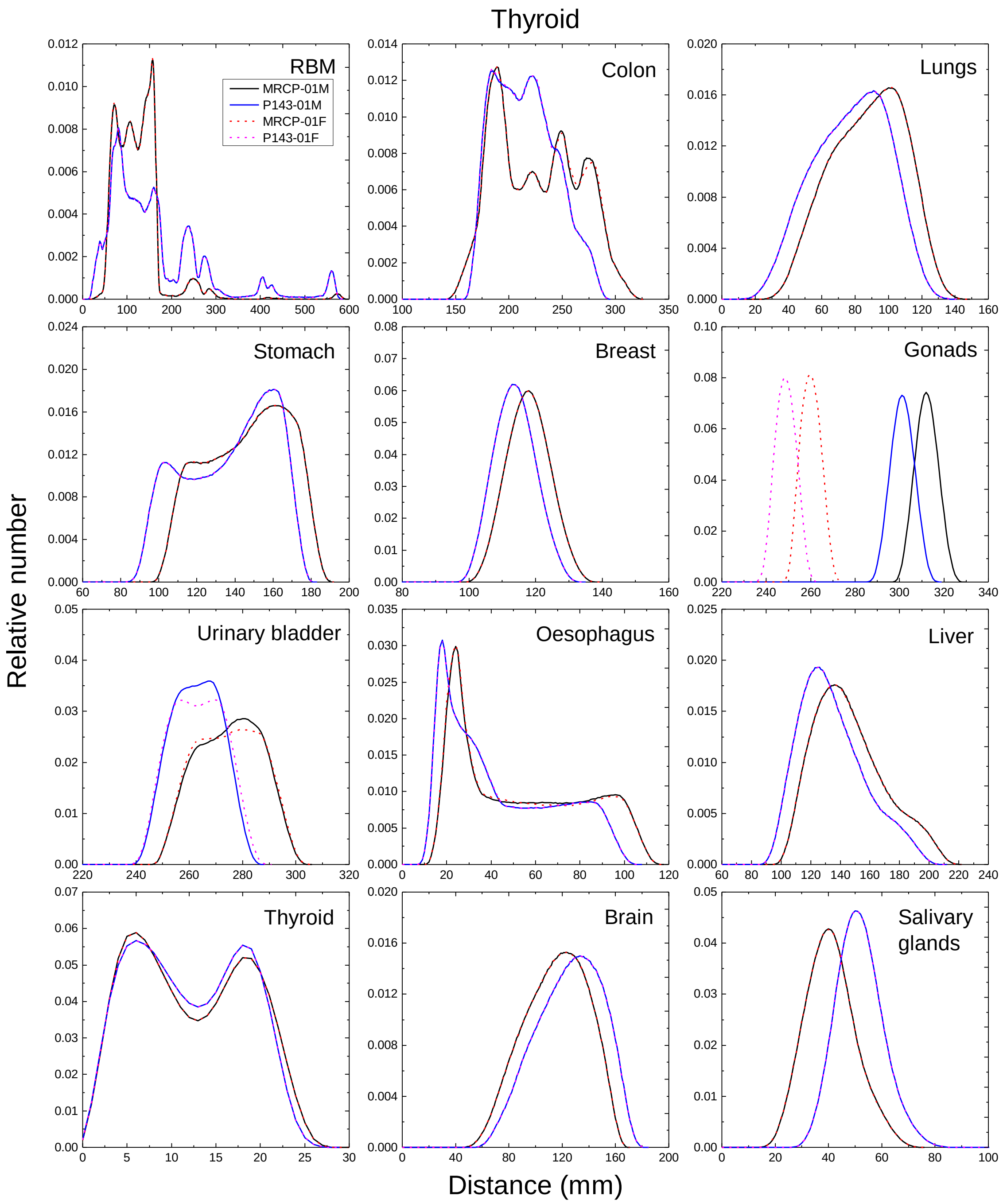

Fig. F.9. Distribution of distances between 10 million randomly sampled point pairs in the thyroid (source region) and red bone marrow (RBM), colon, lungs, stomach, breast, gonads, urinary bladder, oesophagus, liver, thyroid, brain and salivary glands (target regions) in the 1-year male/female phantoms.

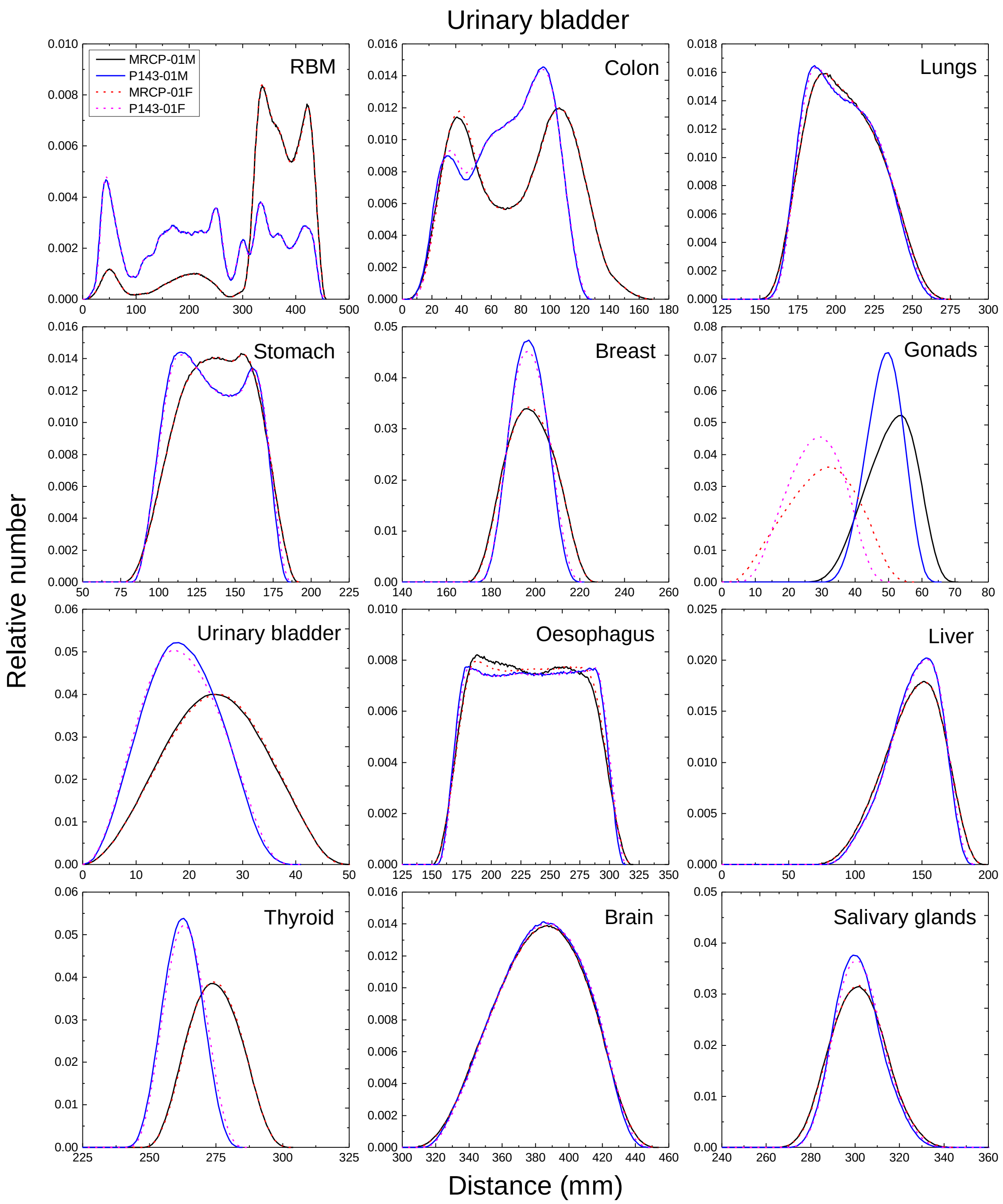

2056
2057 Fig. F.10. Distribution of distances between 10 million randomly sampled point pairs in the
2058 urinary bladder (source region) and red bone marrow (RBM), colon, lungs, stomach, breast,
2059 gonads, urinary bladder, oesophagus, liver, thyroid, brain and salivary glands (target regions)
2060 in the 1-year male/female phantoms.
2061

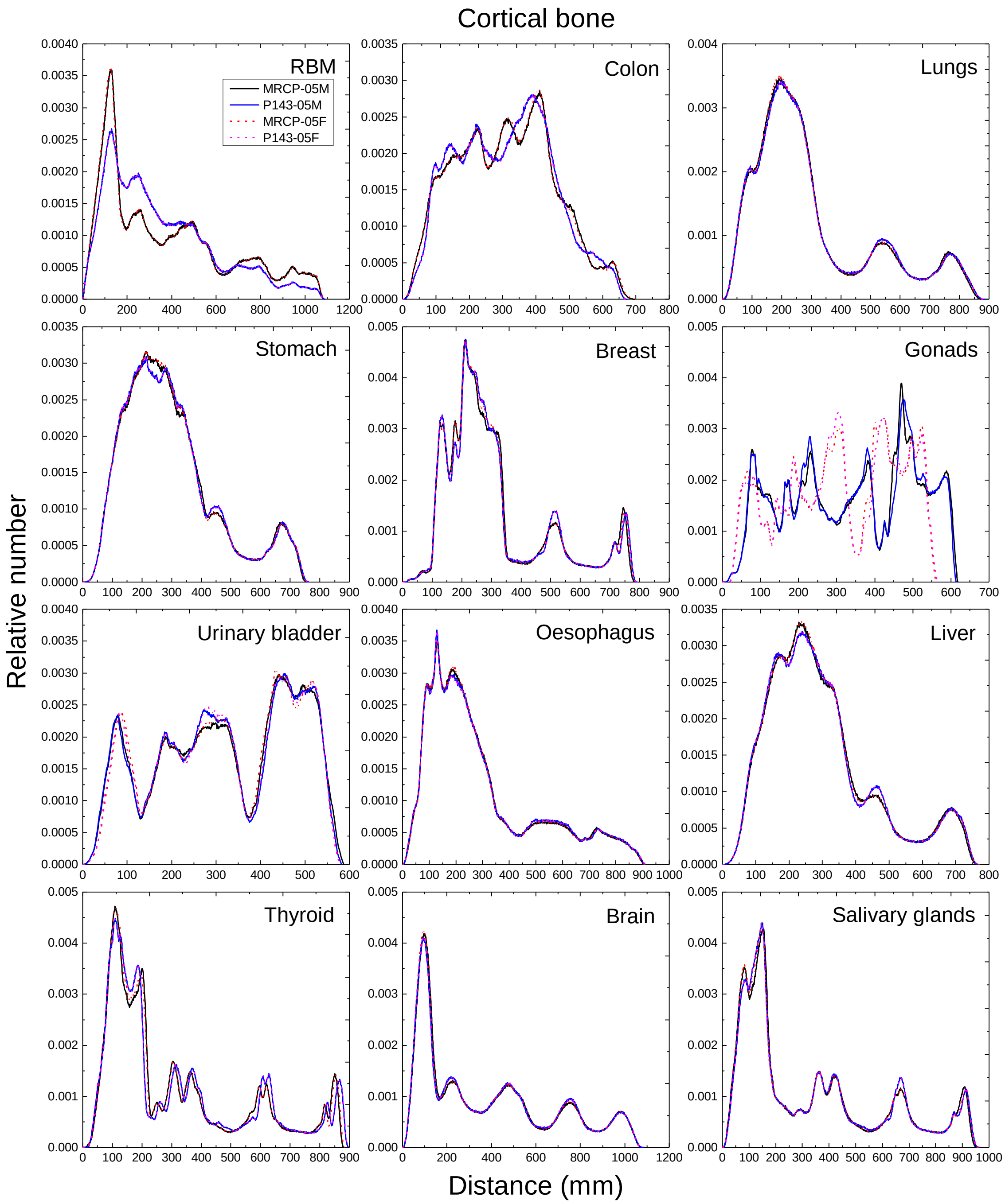

2062

2063 Fig. F.11. Distribution of distances between 10 million randomly sampled point pairs in the
2064 cortical bone (source region) and red bone marrow (RBM), colon, lungs, stomach, breast,
2065 gonads, urinary bladder, oesophagus, liver, thyroid, brain and salivary glands (target regions)
2066 in the 5-year male/female phantoms.

2067

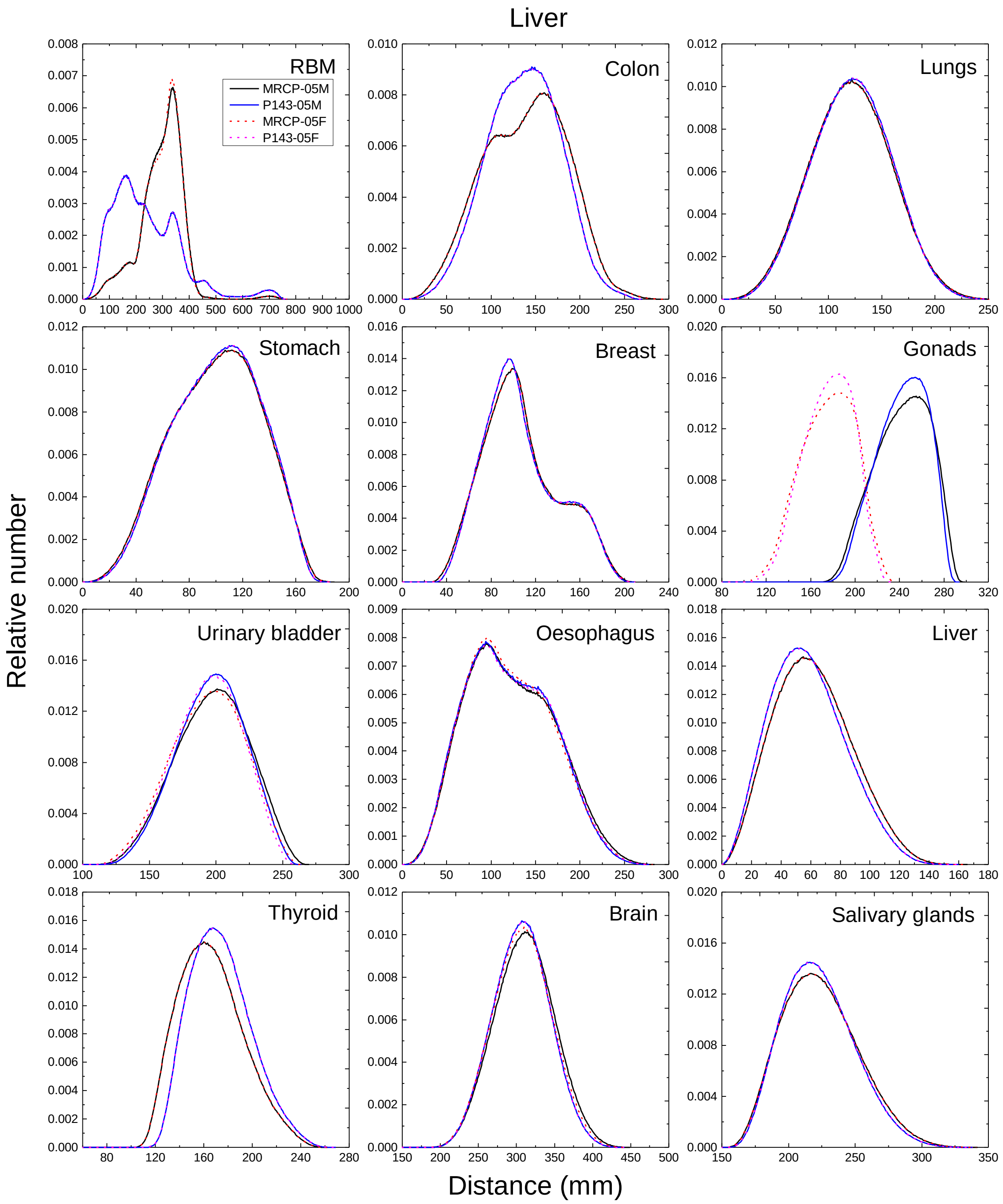

2068
2069 Fig. F.12. Distribution of distances between 10 million randomly sampled point pairs in the
2070 liver (source region) and red bone marrow (RBM), colon, lungs, stomach, breast, gonads,
2071 urinary bladder, oesophagus, liver, thyroid, brain and salivary glands (target regions) in the 5-
2072 year male/female phantoms.
2073

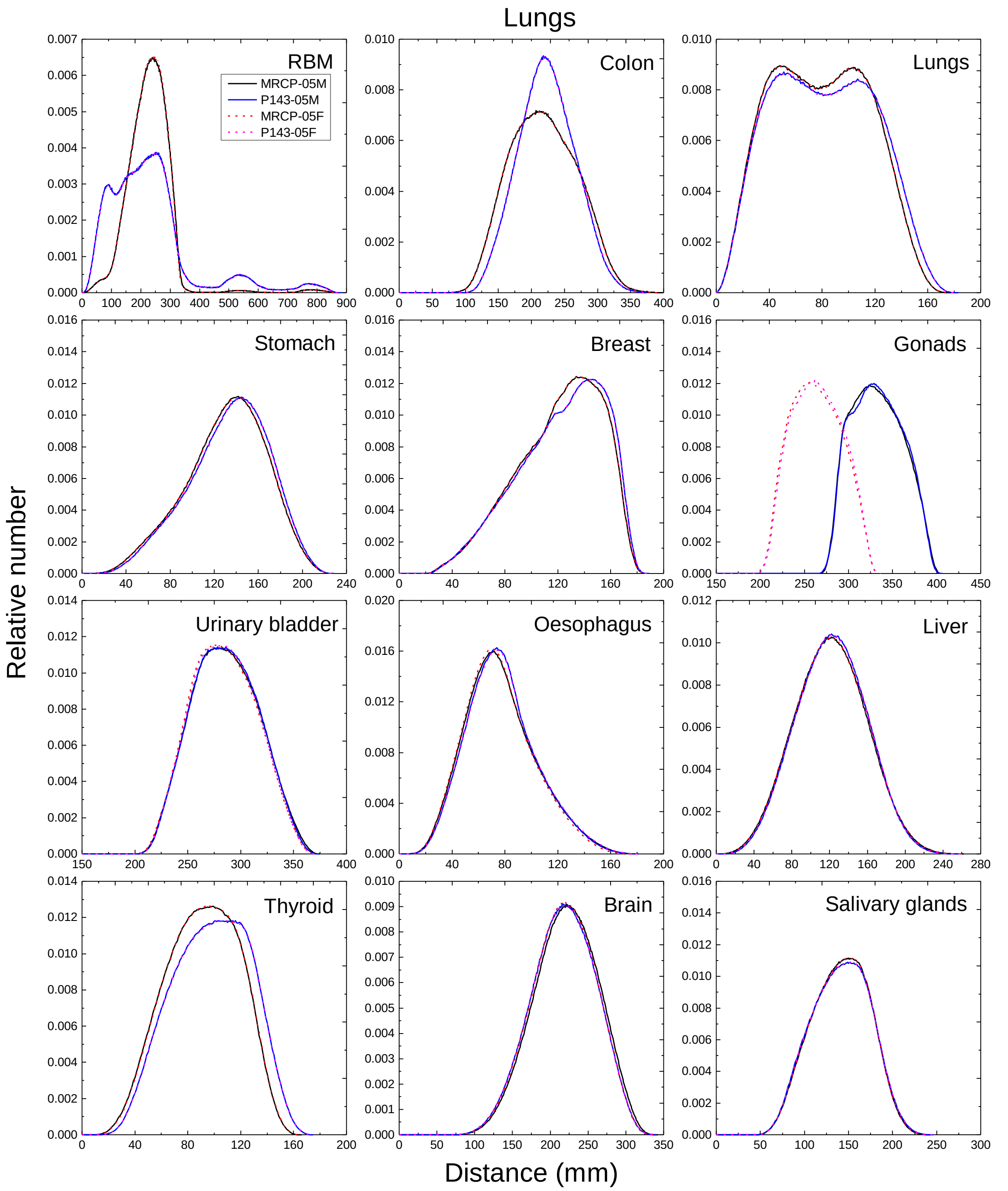

Fig. F.13. Distribution of distances between 10 million randomly sampled point pairs in the lungs (source region) and red bone marrow (RBM), colon, lungs, stomach, breast, gonads, urinary bladder, oesophagus, liver, thyroid, brain and salivary glands (target regions) in the 5-year male/female phantoms.

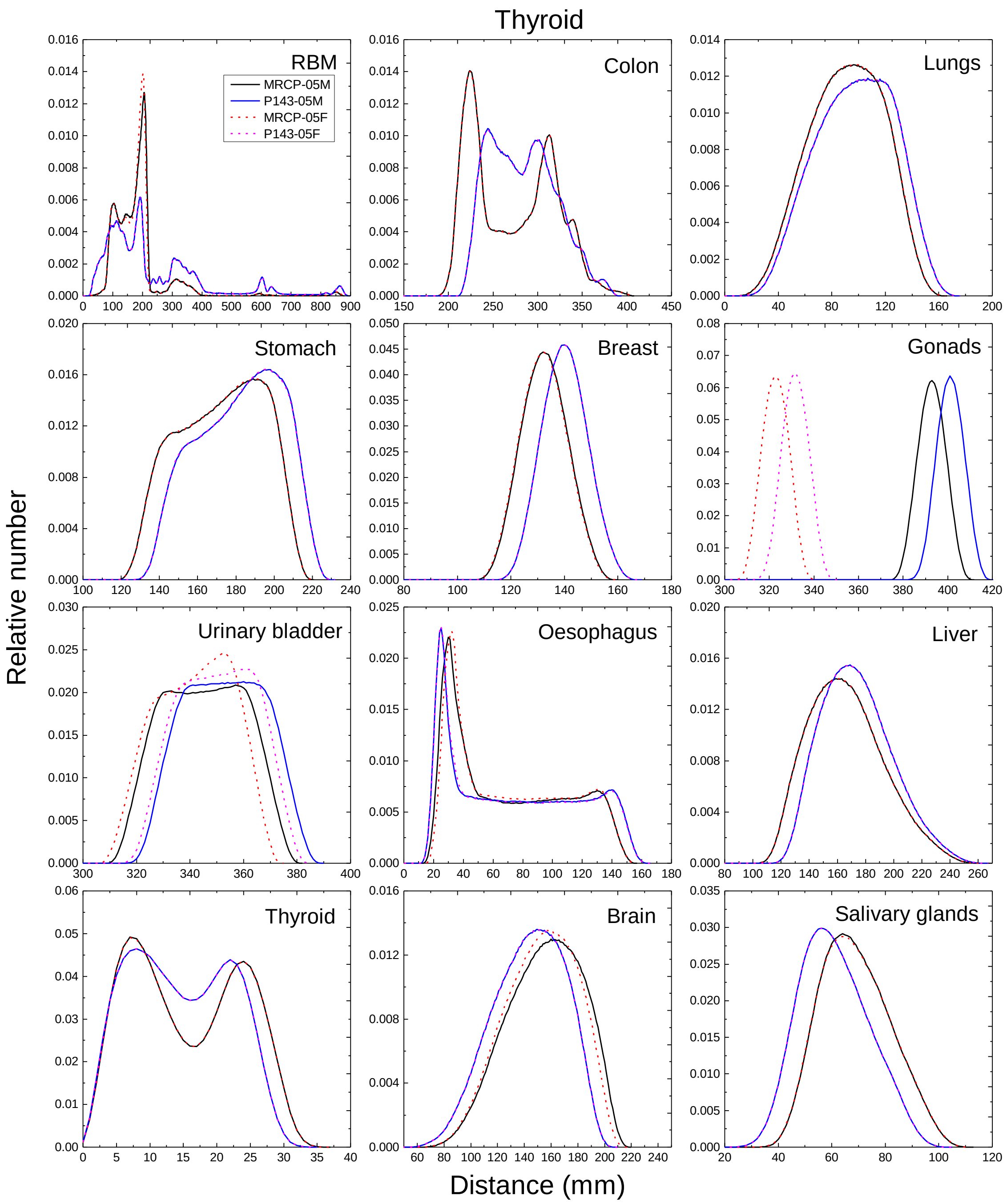

Fig. F.14. Distribution of distances between 10 million randomly sampled point pairs in the thyroid (source region) and red bone marrow (RBM), colon, lungs, stomach, breast, gonads, urinary bladder, oesophagus, liver, thyroid, brain and salivary glands (target regions) in the 5-year male/female phantoms.

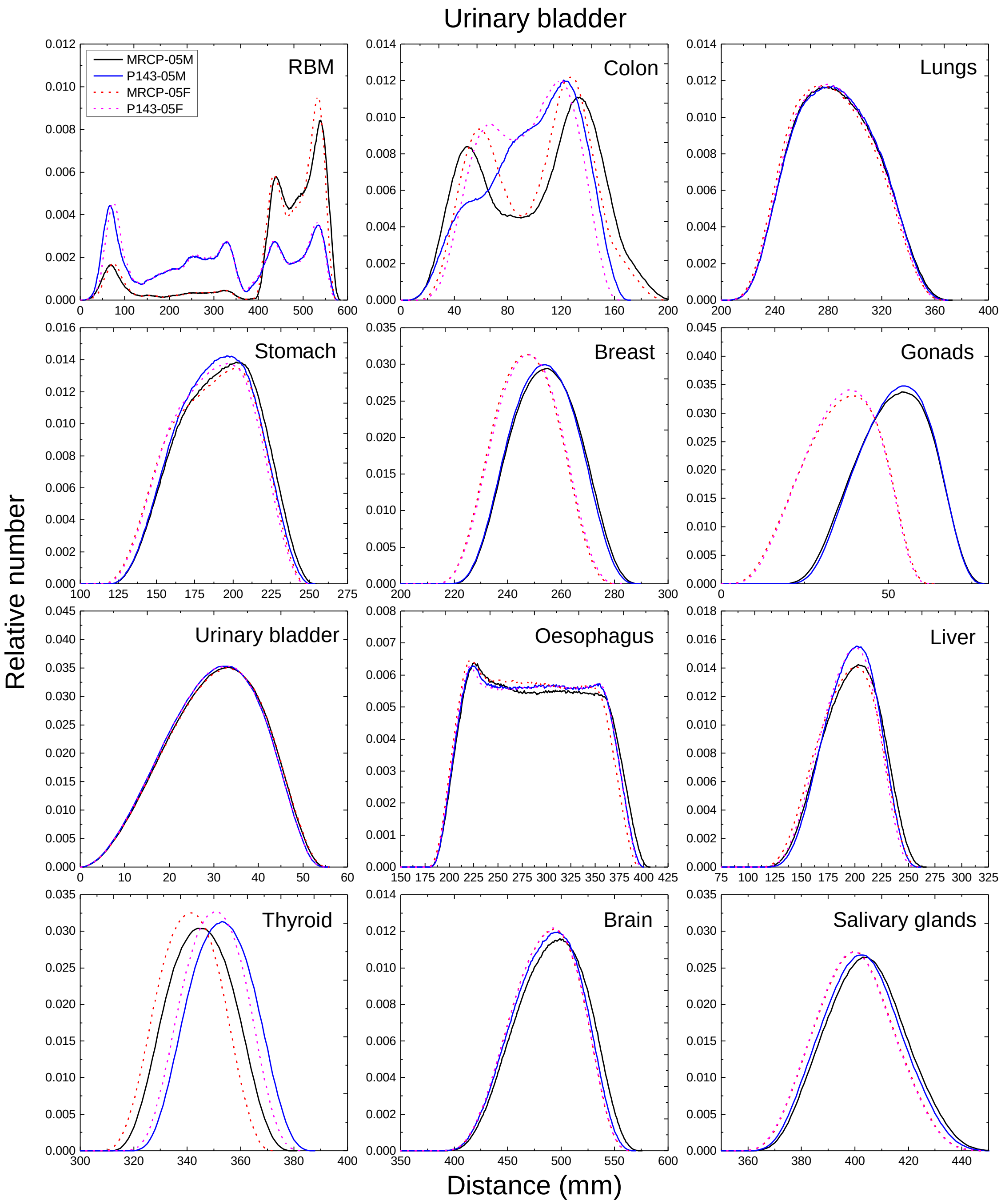

Fig. F.15. Distribution of distances between 10 million randomly sampled point pairs in the urinary bladder (source region) and red bone marrow (RBM), colon, lungs, stomach, breast, gonads, urinary bladder, oesophagus, liver, thyroid, brain and salivary glands (target regions) in the 5-year male/female phantoms.

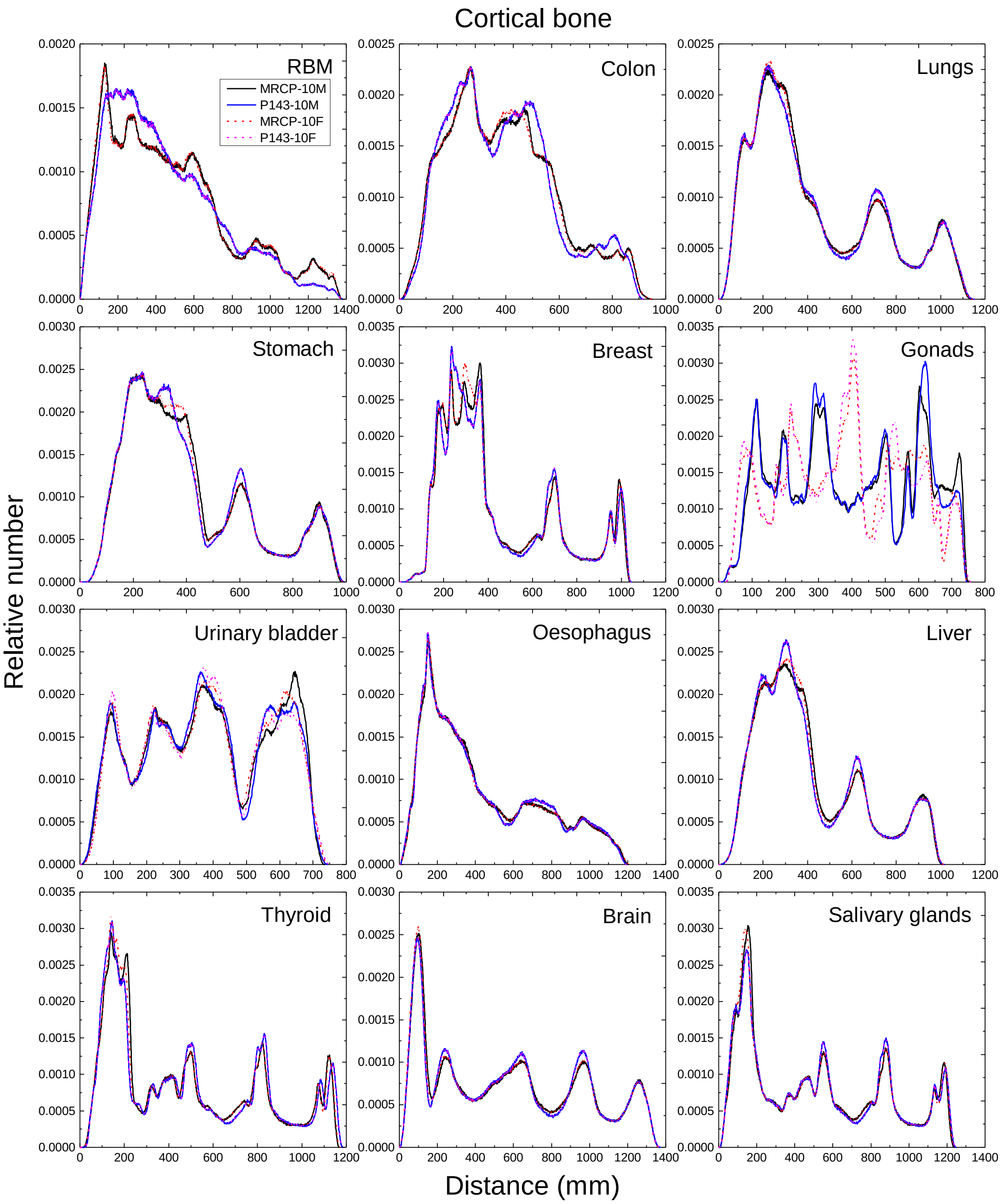

Fig. F.16. Distribution of distances between 10 million randomly sampled point pairs in the cortical bone (source region) and red bone marrow (RBM), colon, lungs, stomach, breast, gonads, urinary bladder, oesophagus, liver, thyroid, brain and salivary glands (target regions) in the 10-year male/female phantoms.

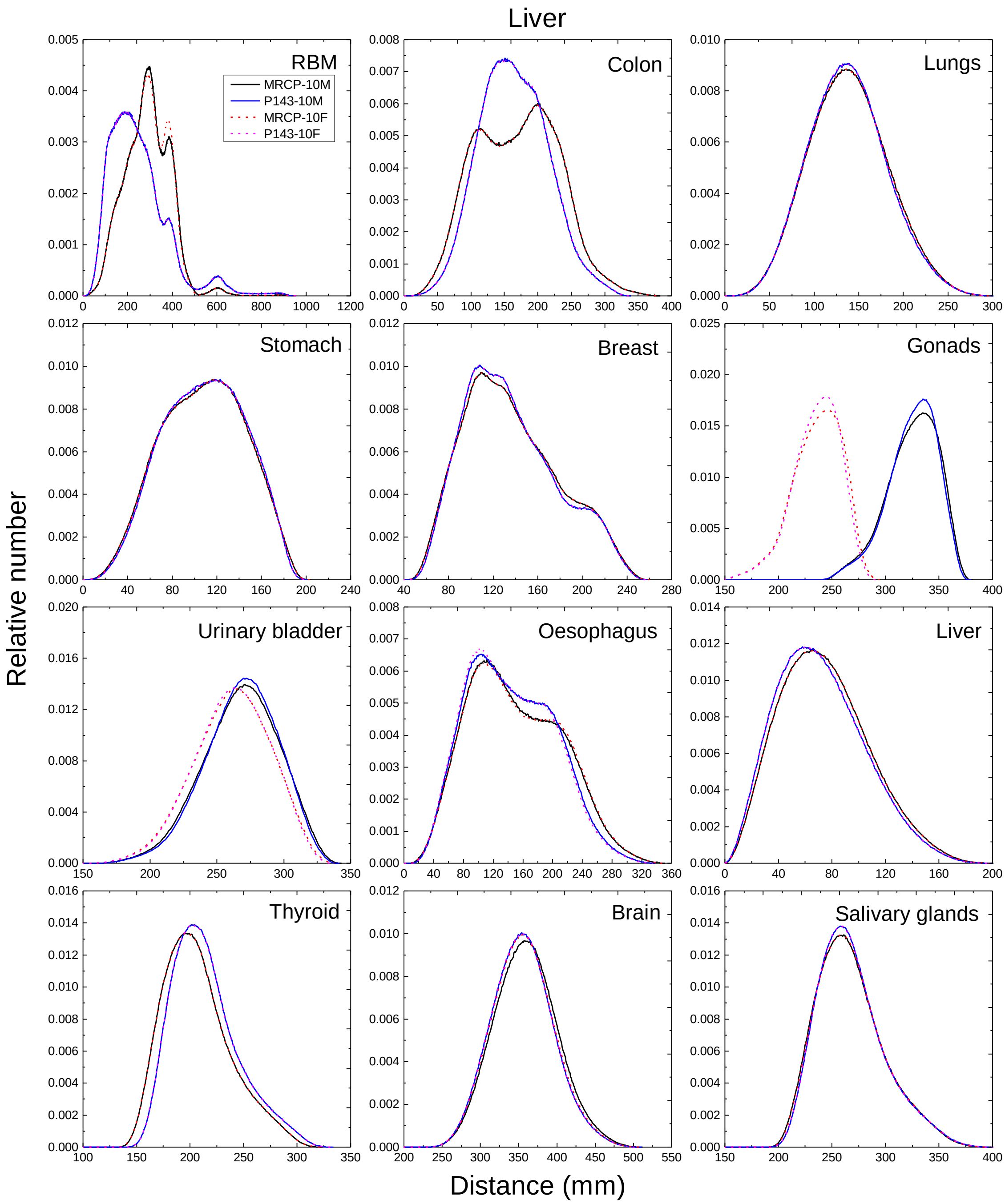

Fig. F.17. Distribution of distances between 10 million randomly sampled point pairs in the liver (source region) and red bone marrow (RBM), colon, lungs, stomach, breast, gonads, urinary bladder, oesophagus, liver, thyroid, brain and salivary glands (target regions) in the 10-year male/female phantoms.

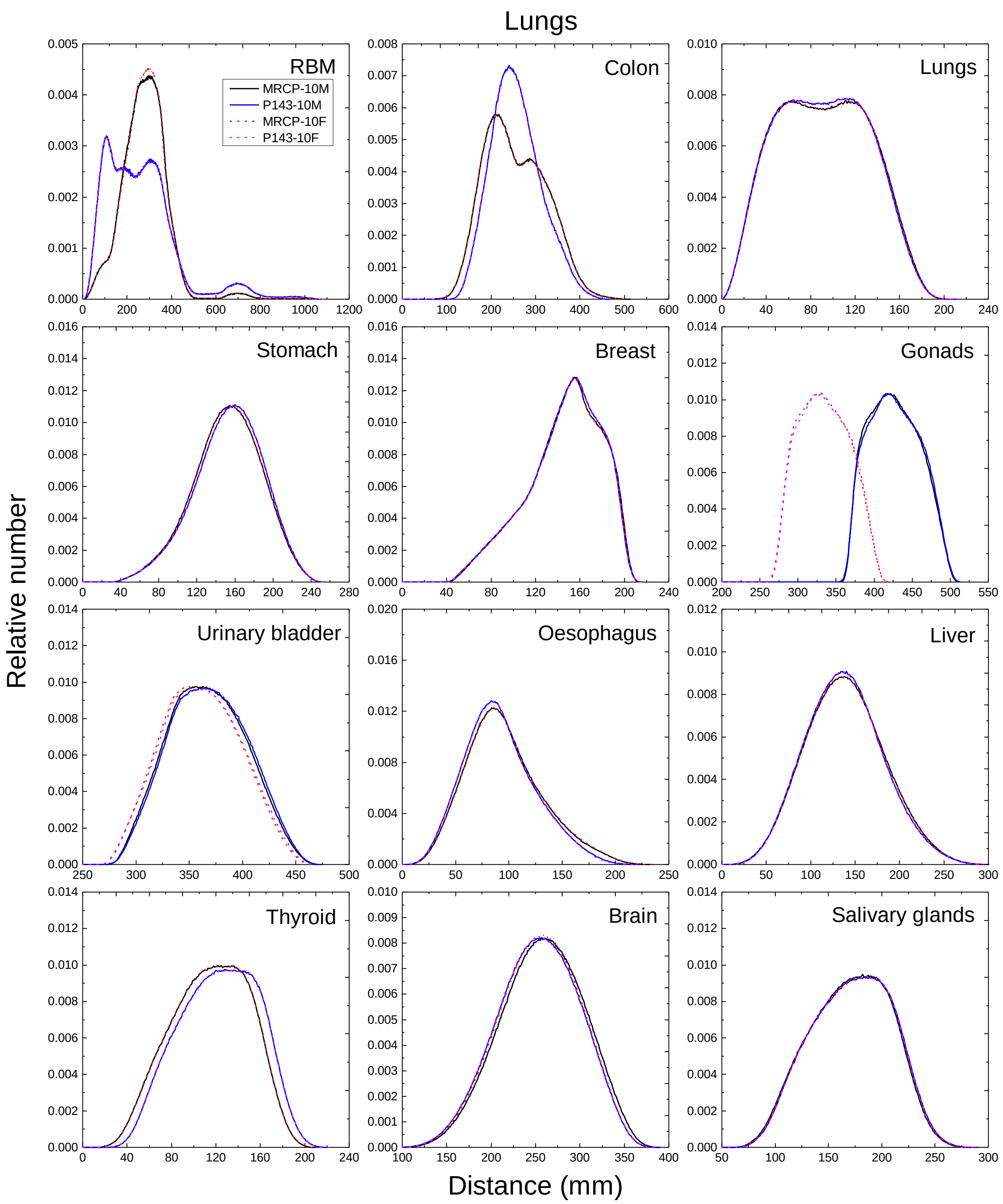

2104
2105 Fig. F.18. Distribution of distances between 10 million randomly sampled point pairs in the
2106 lungs (source region) and red bone marrow (RBM), colon, lungs, stomach, breast, gonads,
2107 urinary bladder, oesophagus, liver, thyroid, brain and salivary glands (target regions) in the 10-
2108 year male/female phantoms.
2109

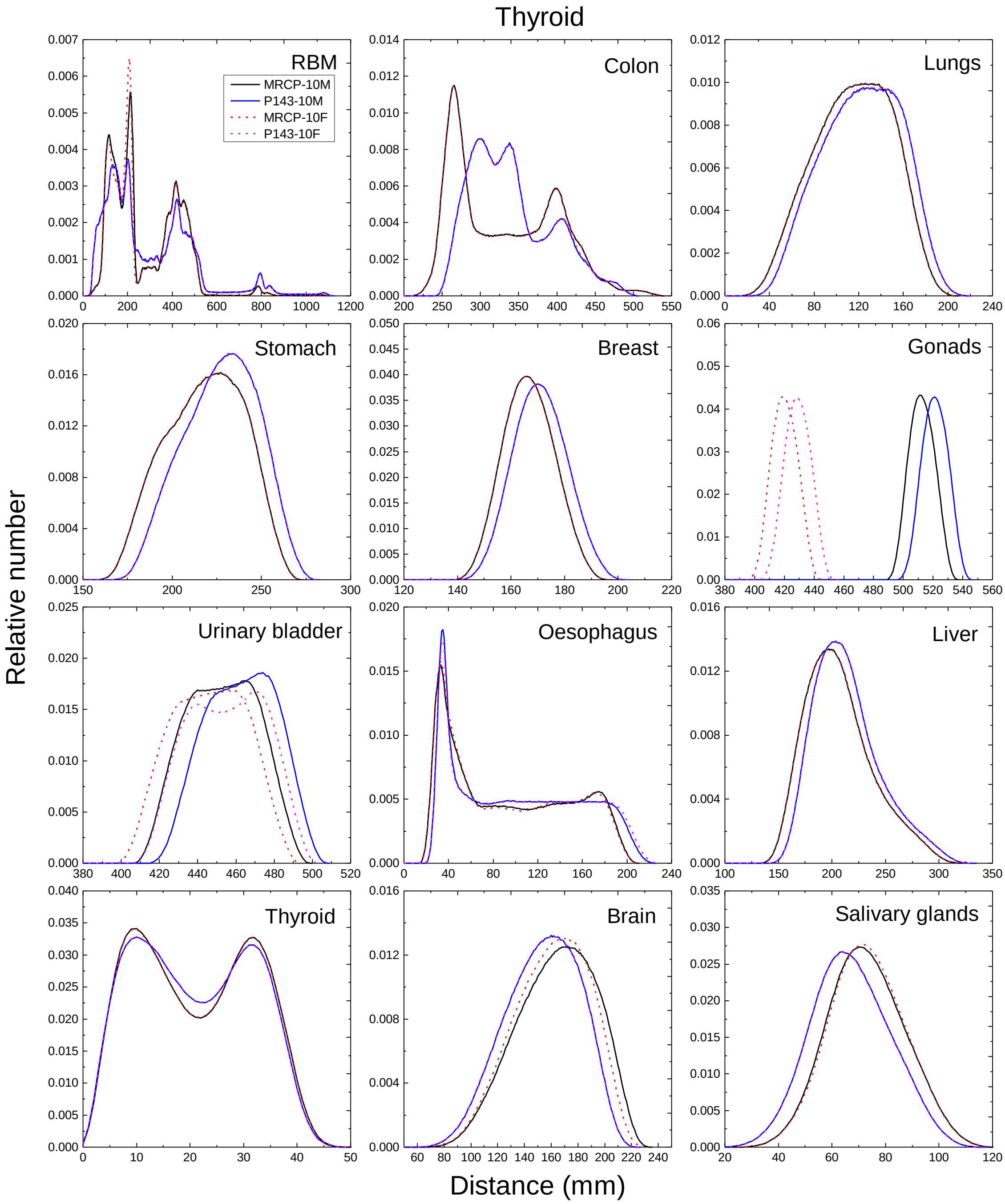

Fig. F.19. Distribution of distances between 10 million randomly sampled point pairs in the thyroid (source region) and red bone marrow (RBM), colon, lungs, stomach, breast, gonads, urinary bladder, oesophagus, liver, thyroid, brain and salivary glands (target regions) in the 10-year male/female phantoms.

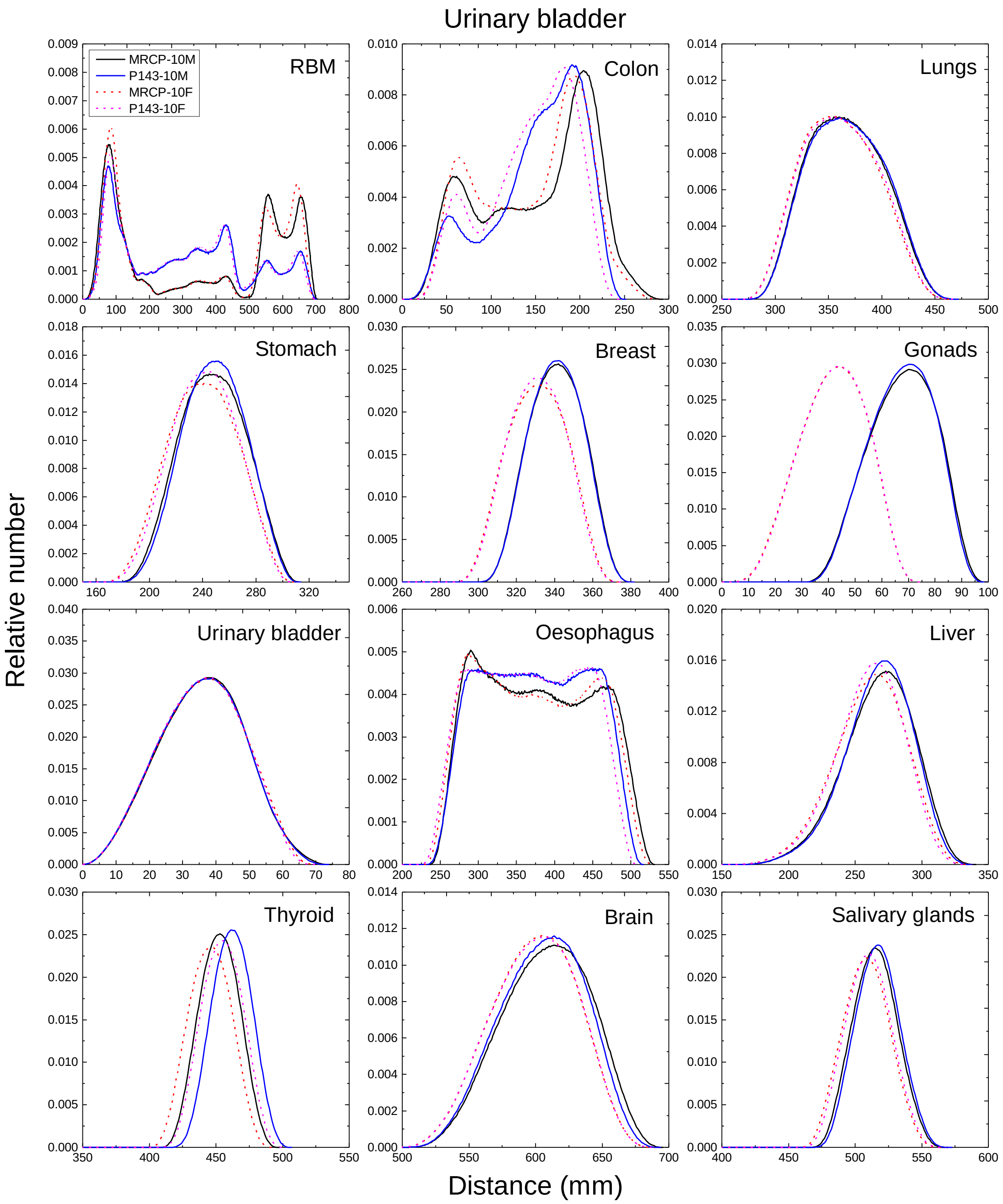

Fig. F.20. Distribution of distances between 10 million randomly sampled point pairs in the urinary bladder (source region) and red bone marrow (RBM), colon, lungs, stomach, breast, gonads, urinary bladder, oesophagus, liver, thyroid, brain and salivary glands (target regions) in the 10-year male/female phantoms.

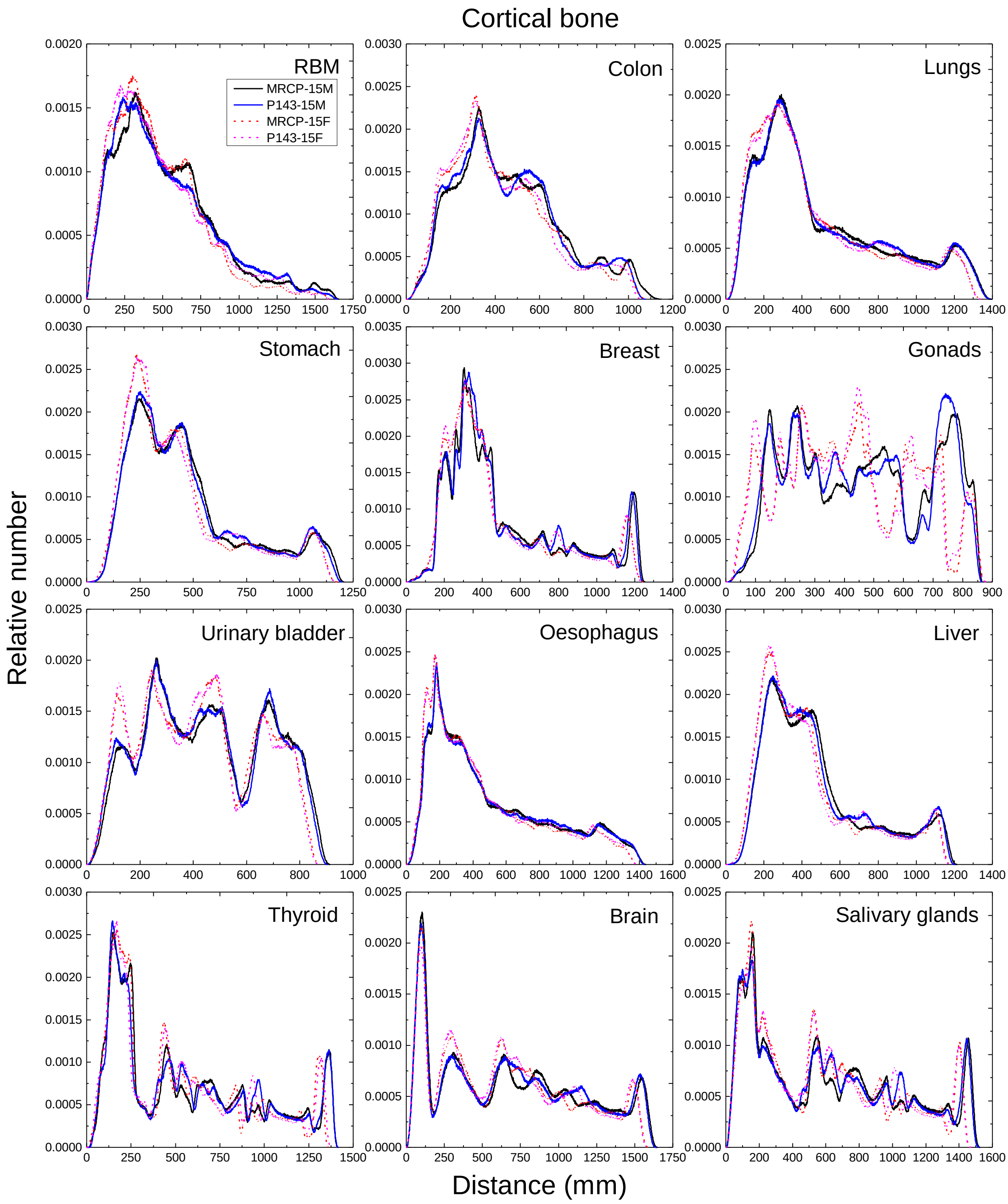

Fig. F.21. Distribution of distances between 10 million randomly sampled point pairs in the cortical bone (source region) and red bone marrow (RBM), colon, lungs, stomach, breast, gonads, urinary bladder, oesophagus, liver, thyroid, brain and salivary glands (target regions) in the 15-year male/female phantoms.

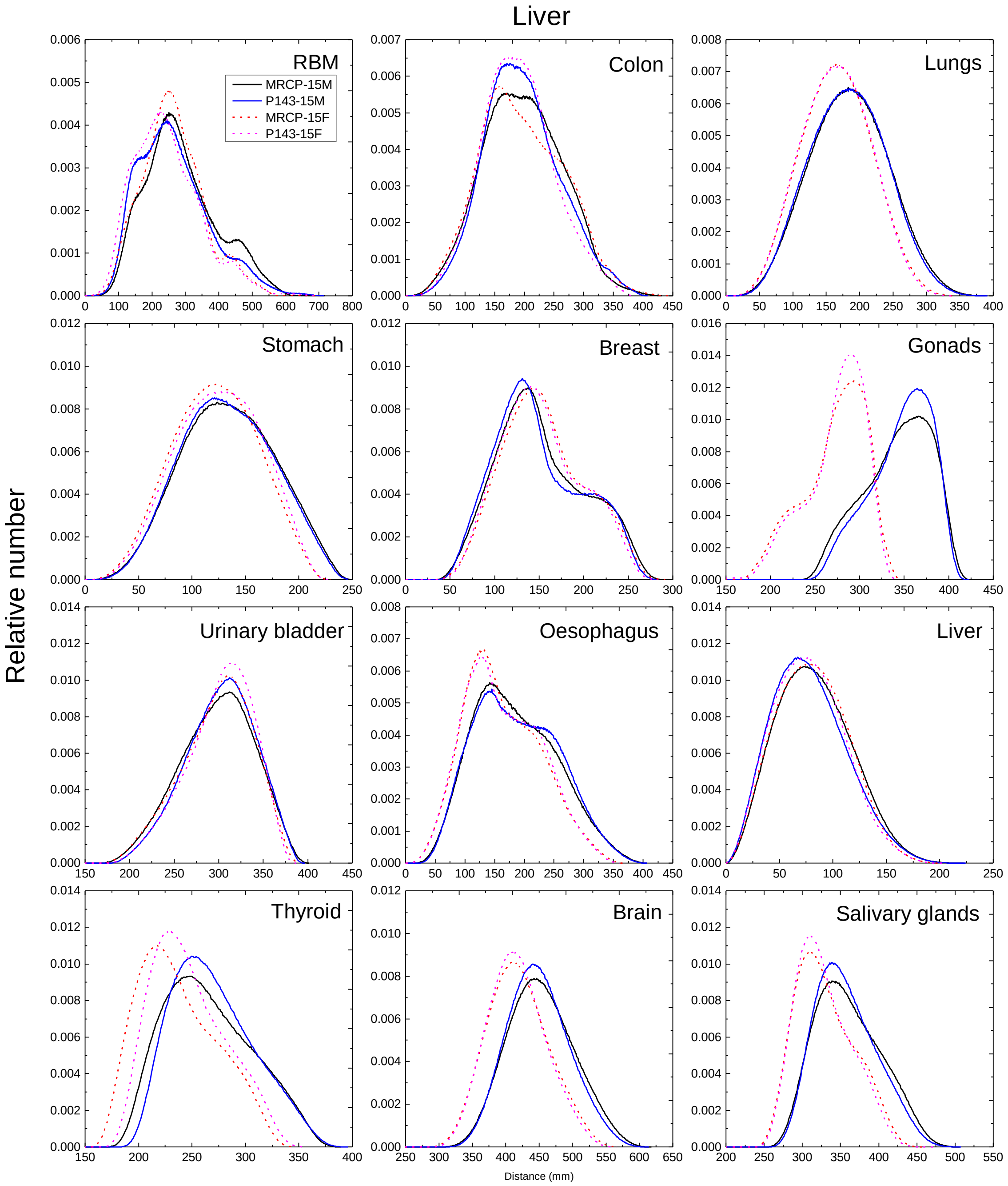

Fig. F.22. Distribution of distances between 10 million randomly sampled point pairs in the liver (source region) and red bone marrow (RBM), colon, lungs, stomach, breast, gonads, urinary bladder, oesophagus, liver, thyroid, brain and salivary glands (target regions) in the 15-year male/female phantoms.

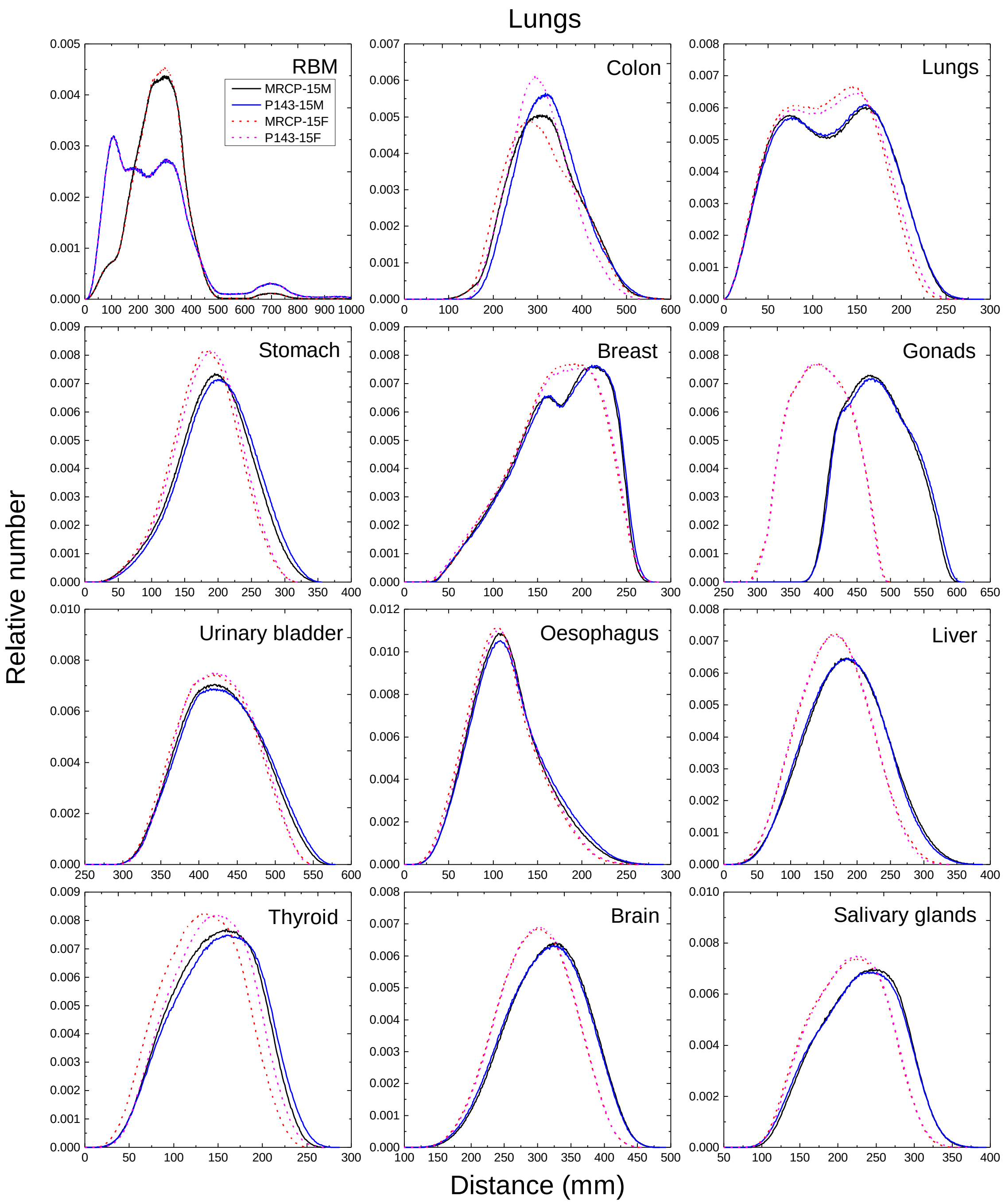

2134
2135 Fig. F.23. Distribution of distances between 10 million randomly sampled point pairs in the
2136 lungs (source region) and red bone marrow (RBM), colon, lungs, stomach, breast, gonads,
2137 urinary bladder, oesophagus, liver, thyroid, brain and salivary glands (target regions) in the 15-
2138 year male/female phantoms.
2139

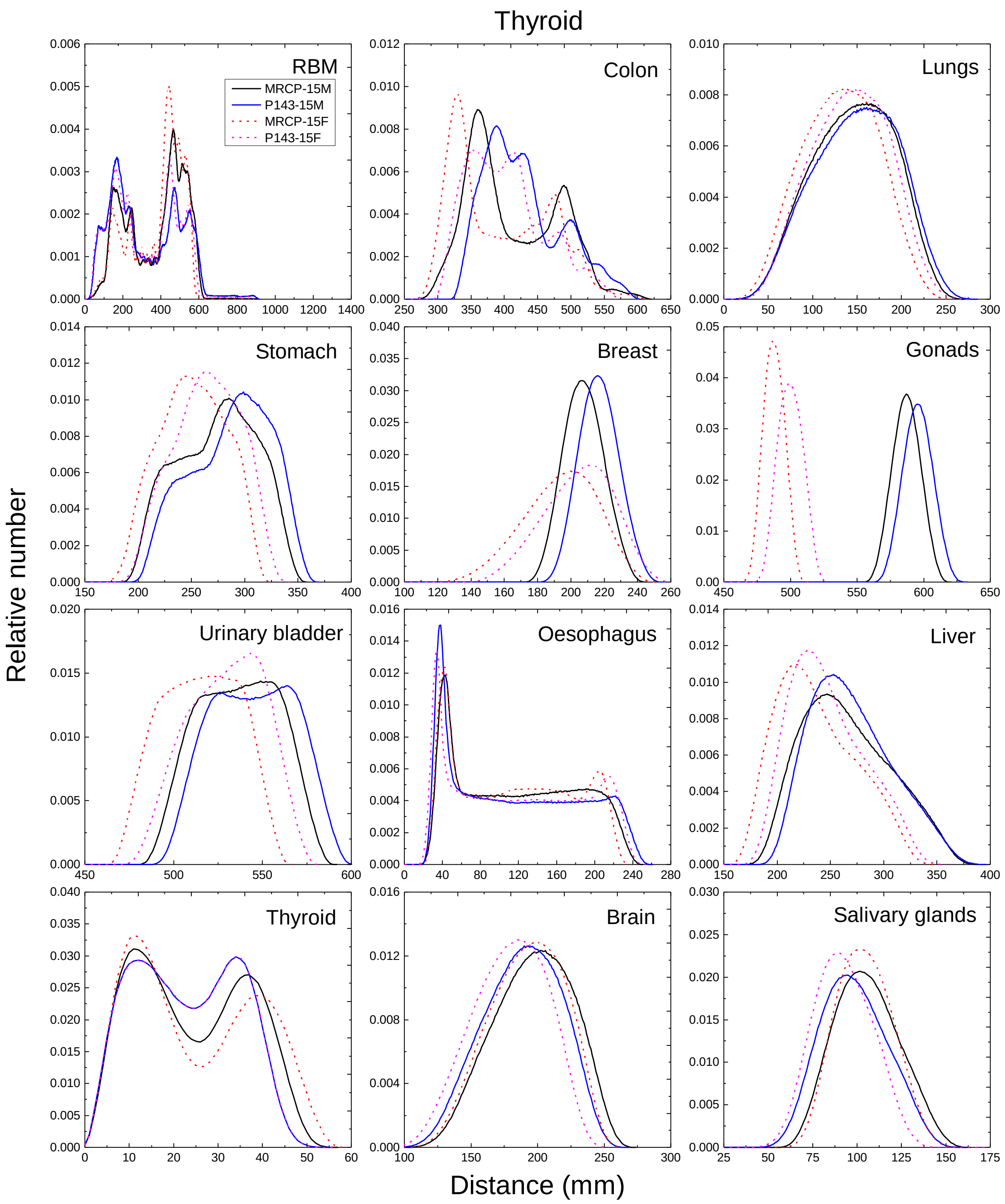

Fig. F.24. Distribution of distances between 10 million randomly sampled point pairs in the thyroid (source region) and red bone marrow (RBM), colon, lungs, stomach, breast, gonads, urinary bladder, oesophagus, liver, thyroid, brain and salivary glands (target regions) in the 15-year male/female phantoms.

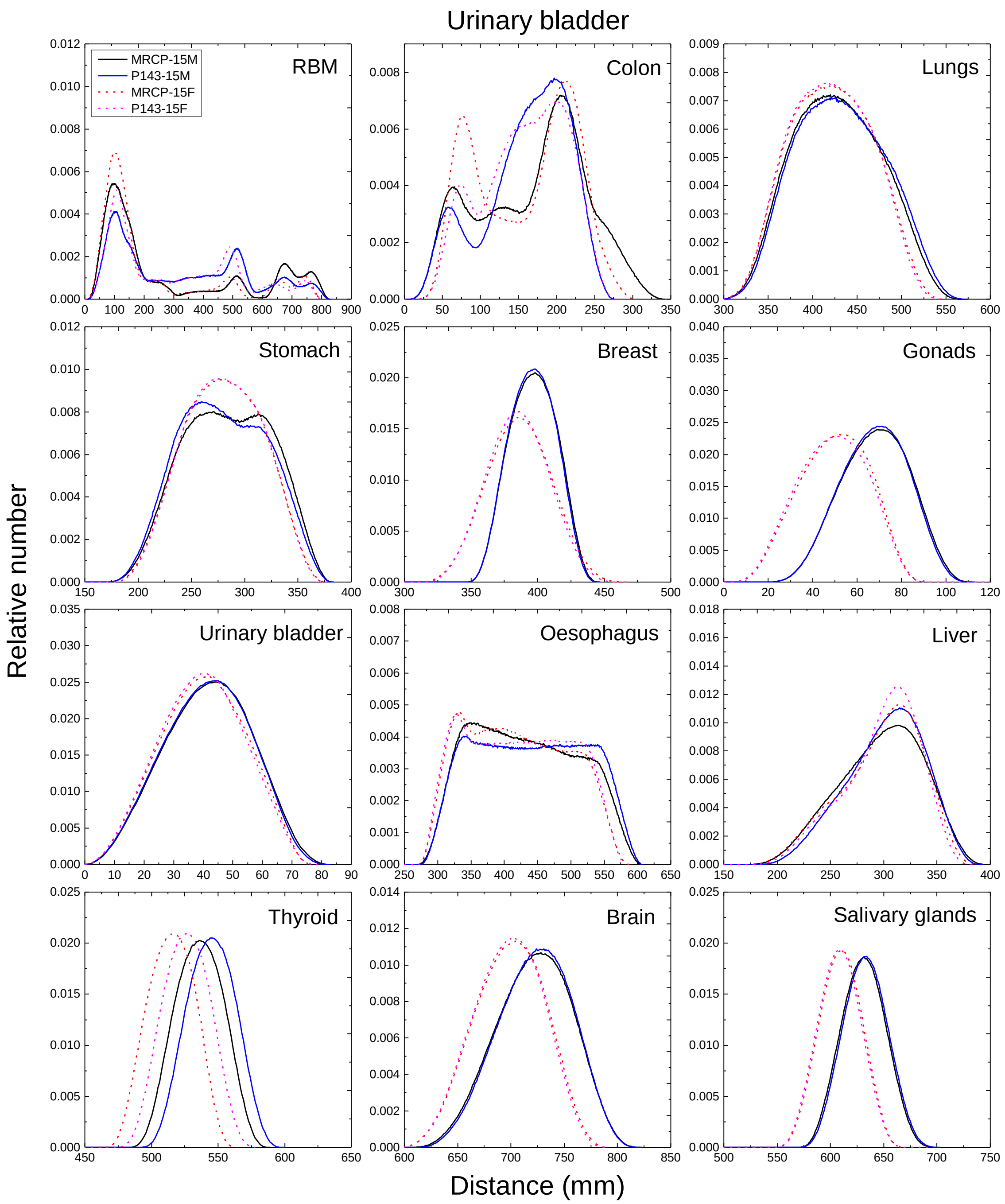

2146
2147 Fig. F.25. Distribution of distances between 10 million randomly sampled point pairs in the
2148 urinary bladder (source region) and red bone marrow (RBM), colon, lungs, stomach, breast,
2149 gonads, urinary bladder, oesophagus, liver, thyroid, brain and salivary glands (target regions)
2150 in the 15-year male/female phantoms.
2151

ANNEX G. CROSS-SECTIONAL IMAGES

G.1. Images of the newborn male mesh-type reference computational phantom

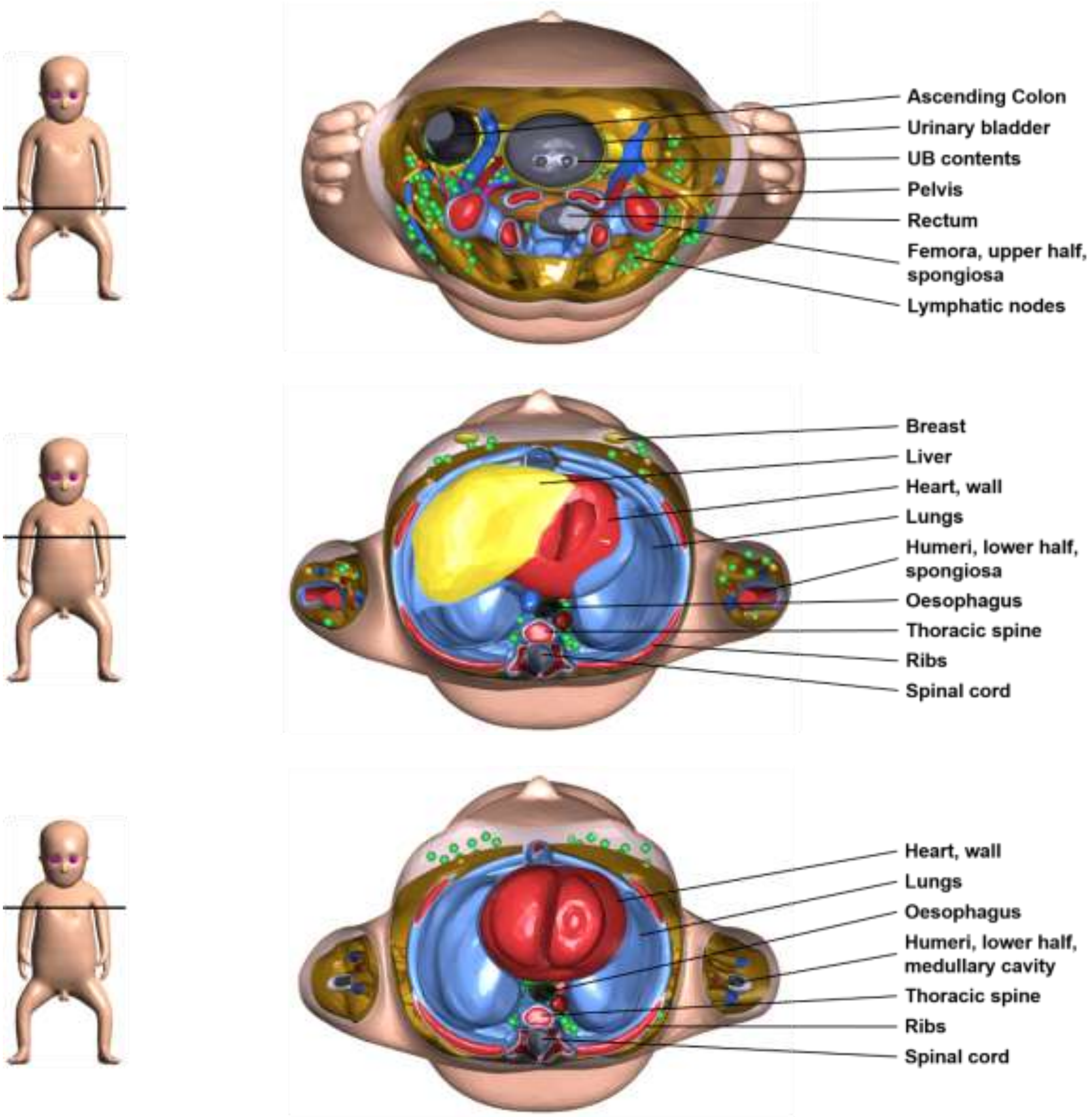

Fig. G.1.1. Transverse (axial) images of the newborn male mesh-type reference computational phantom (*continued on next page*).

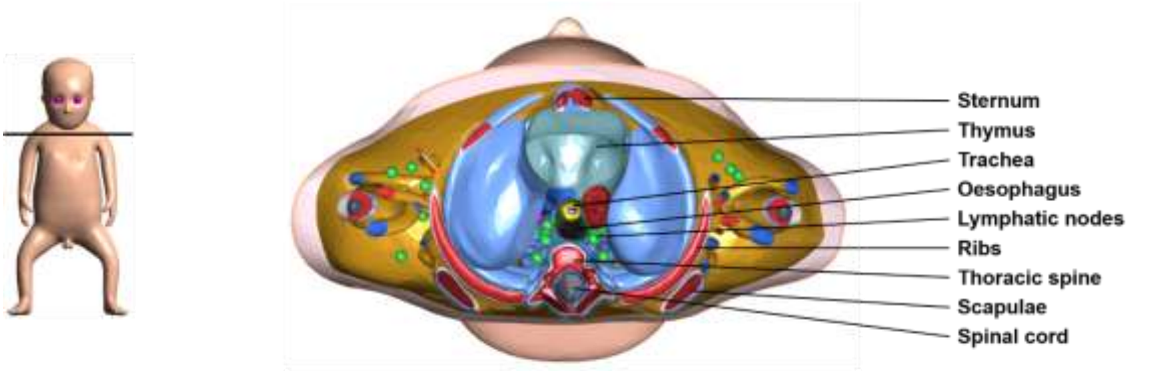

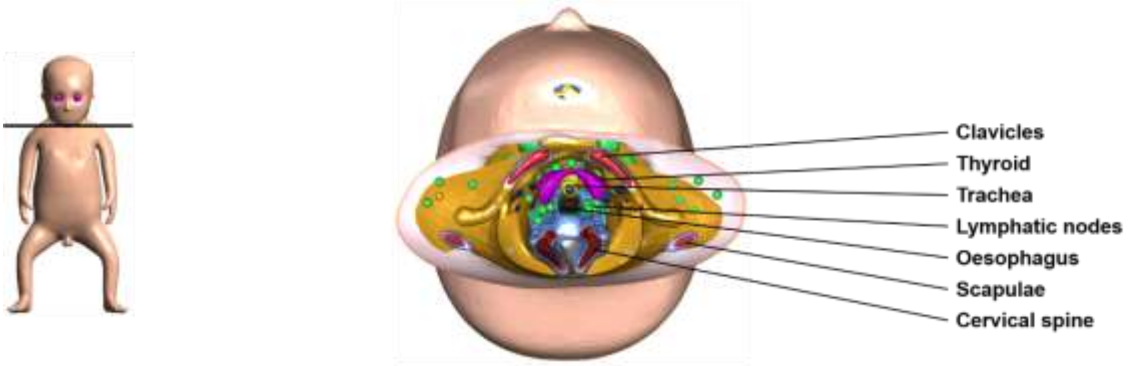

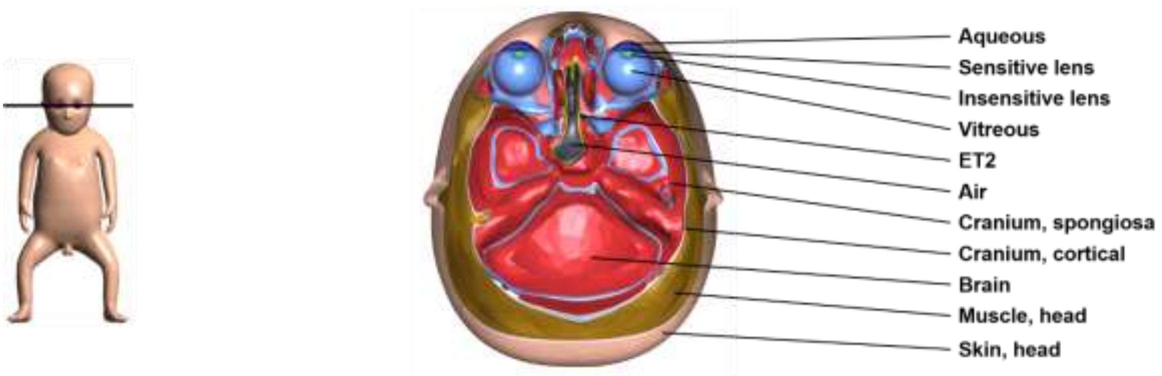

Fig. G.1.1. (*continued*)

2166
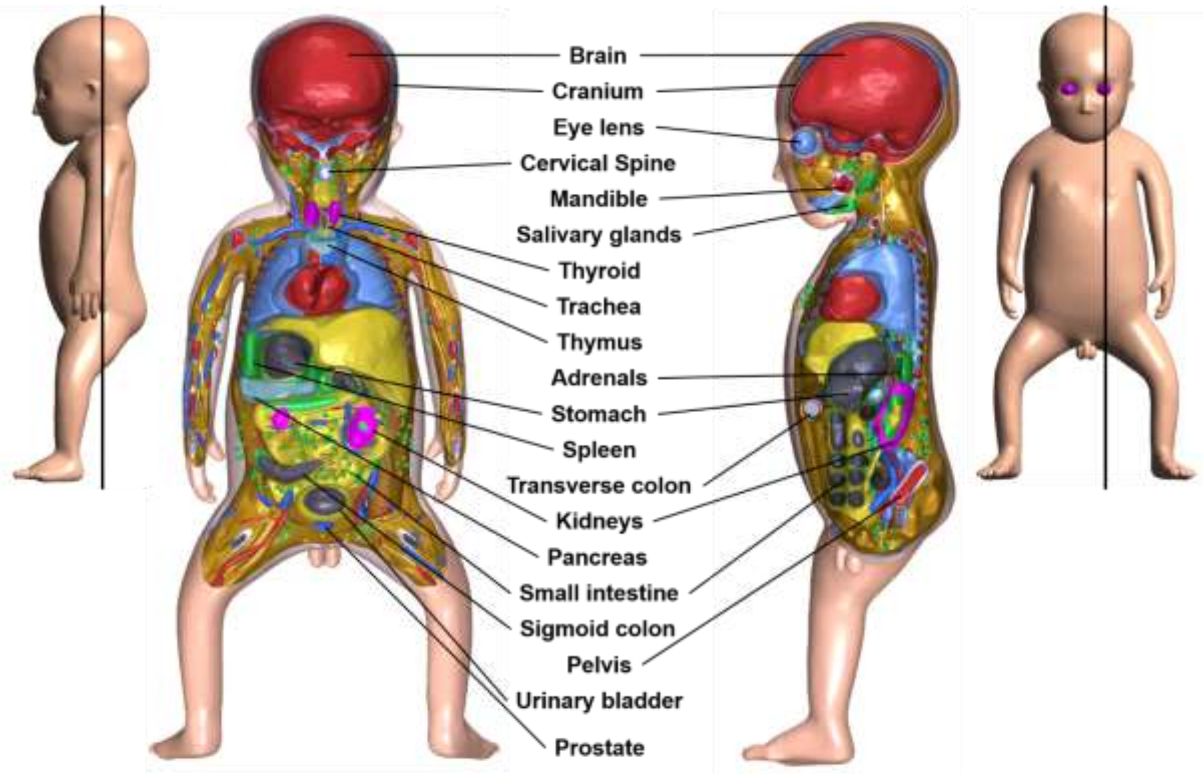

2167 Fig. G.1.2. Coronal and sagittal images of the newborn male mesh-type reference
2168 computational phantom.

2169

G.2. Images of the newborn female mesh-type reference computational phantom

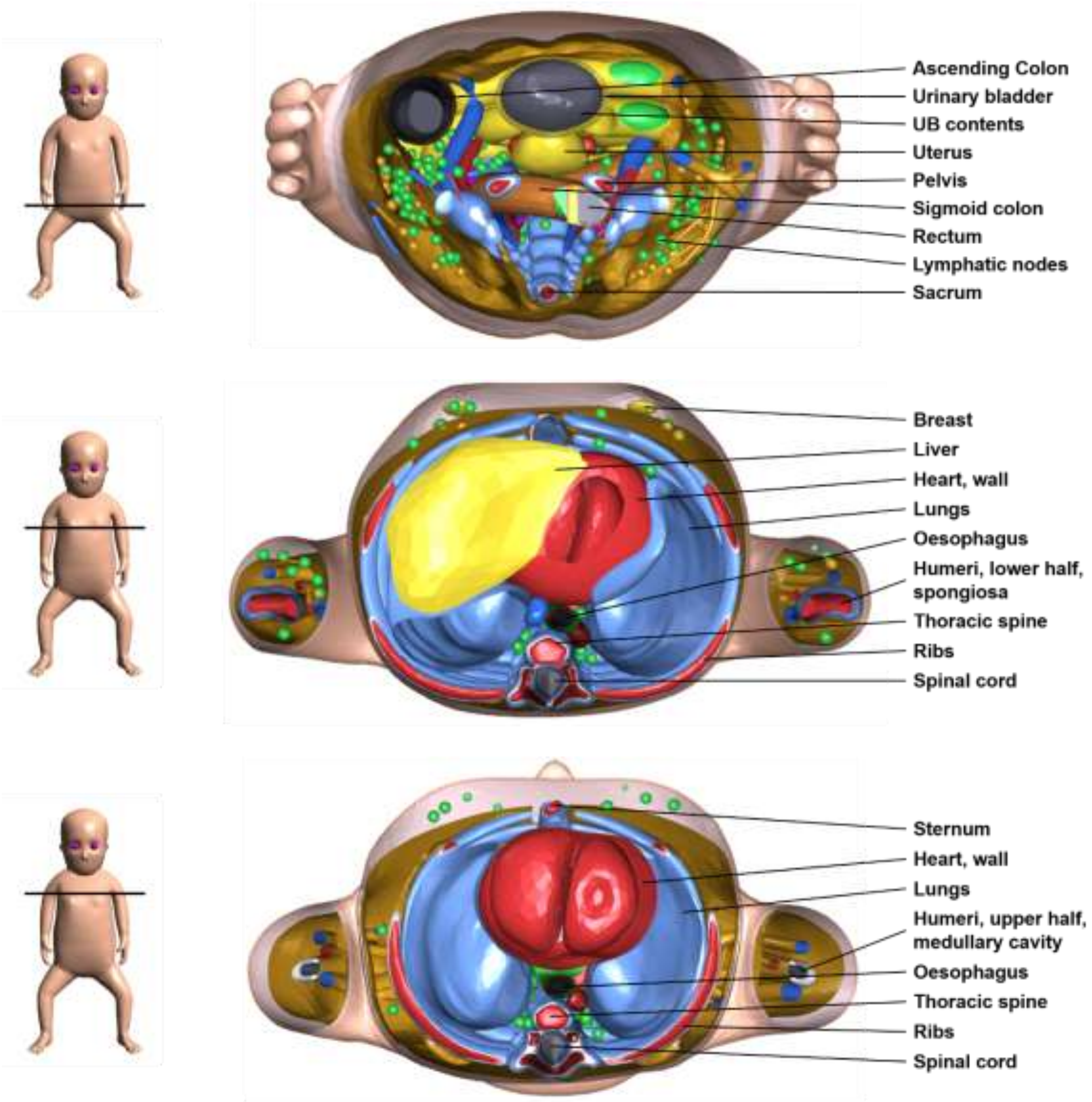

Fig. G.2.1. Transverse (axial) images of the newborn female mesh-type reference computational phantom (*continued on next page*).

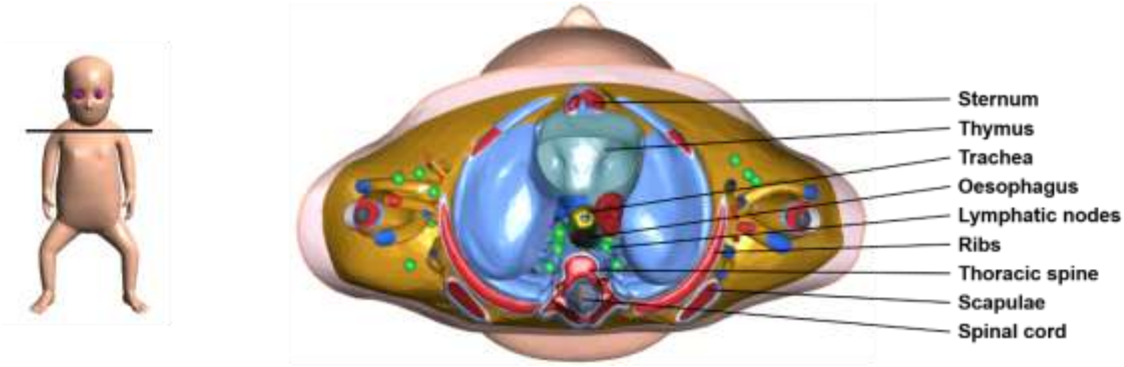

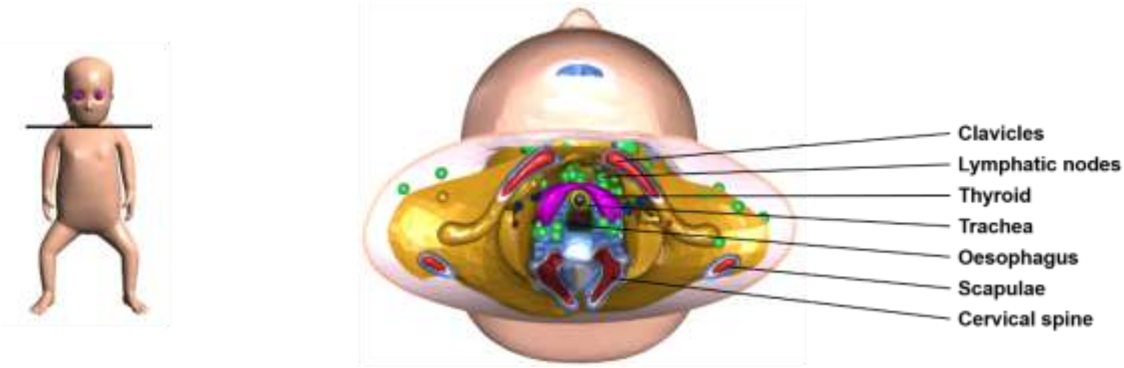

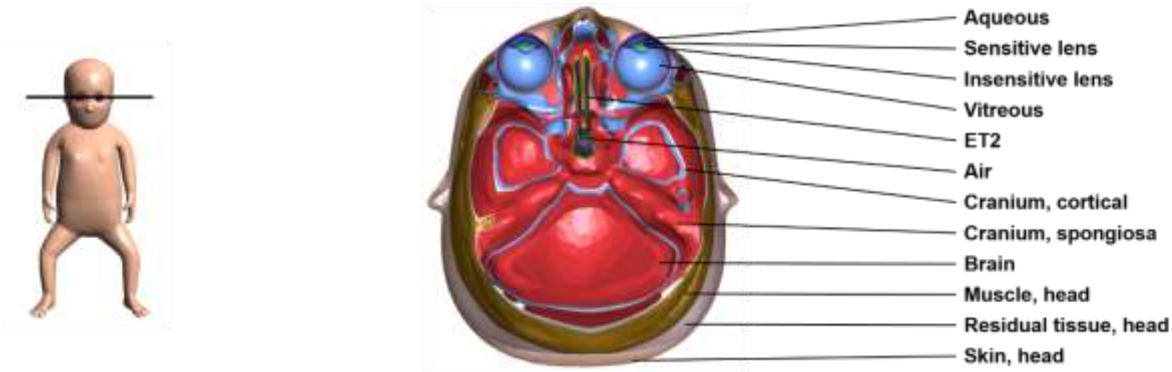

Fig. G.2.1. (*continued*)

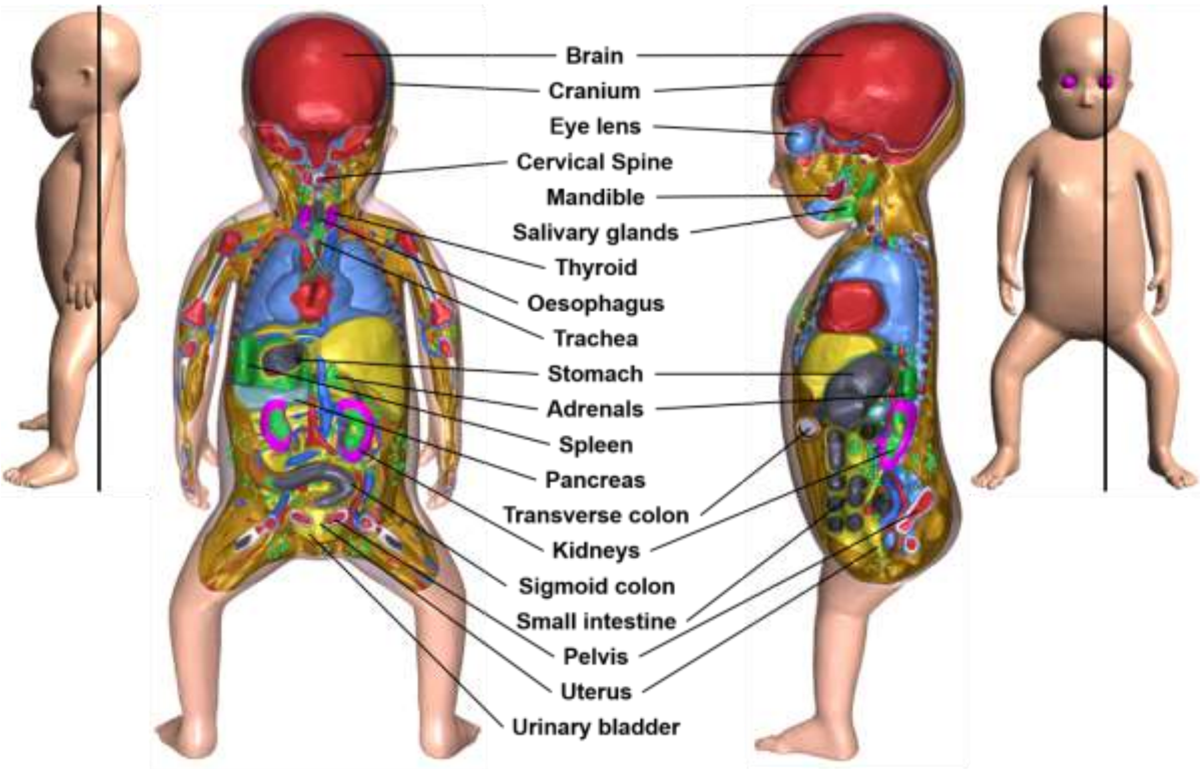

2184 Fig. G.2.2. Coronal and sagittal images of the newborn female mesh-type reference
2185 computational phantom.

G.3. Images of the 1-year-old male mesh-type reference computational phantom

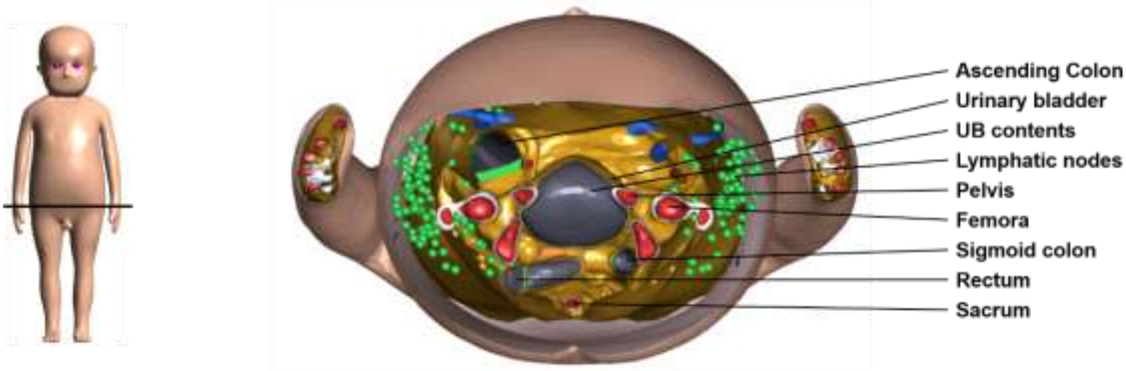

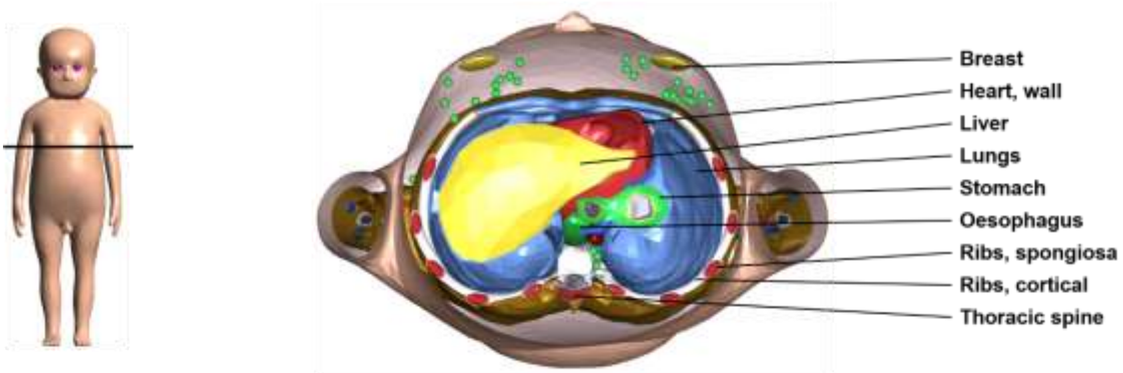

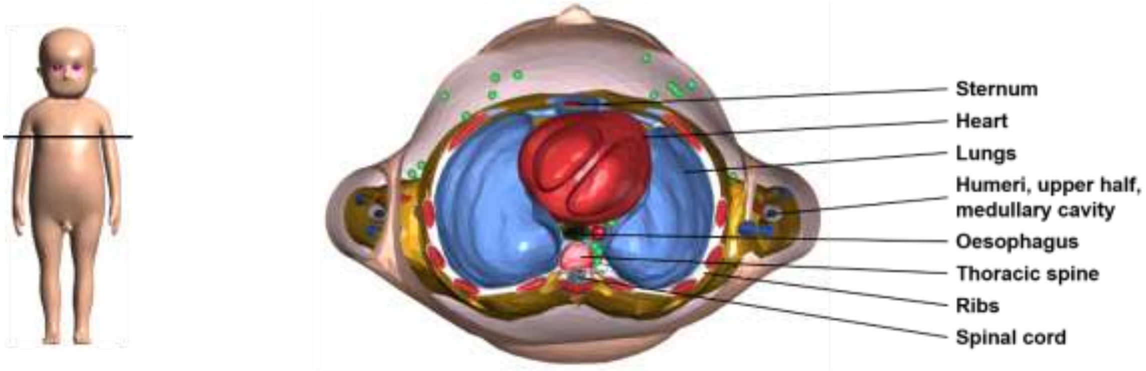

Fig. G.3.1. Transverse (axial) images of the 1-year-old male mesh-type reference computational phantom (*continued on next page*).

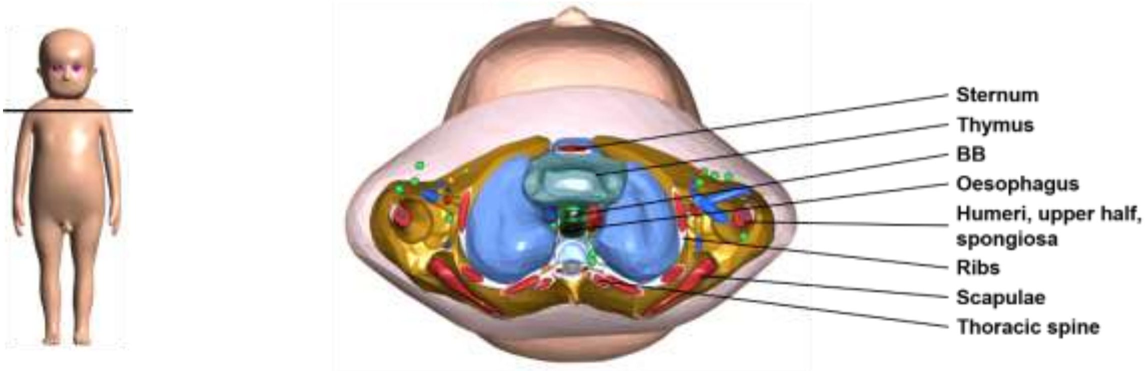

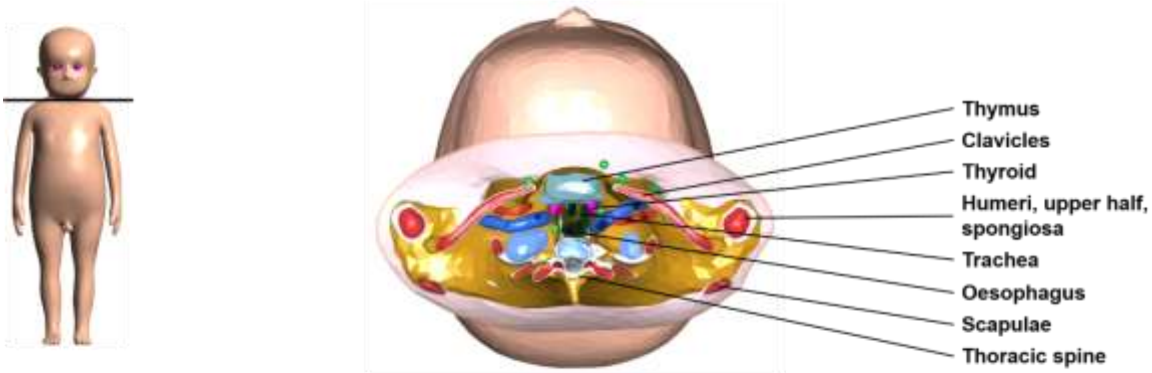

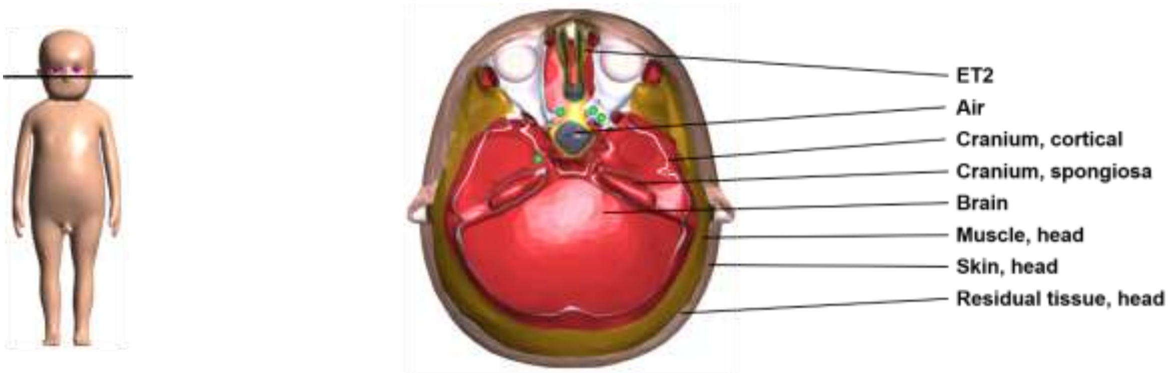

Fig. G.3.1. (*continued*)

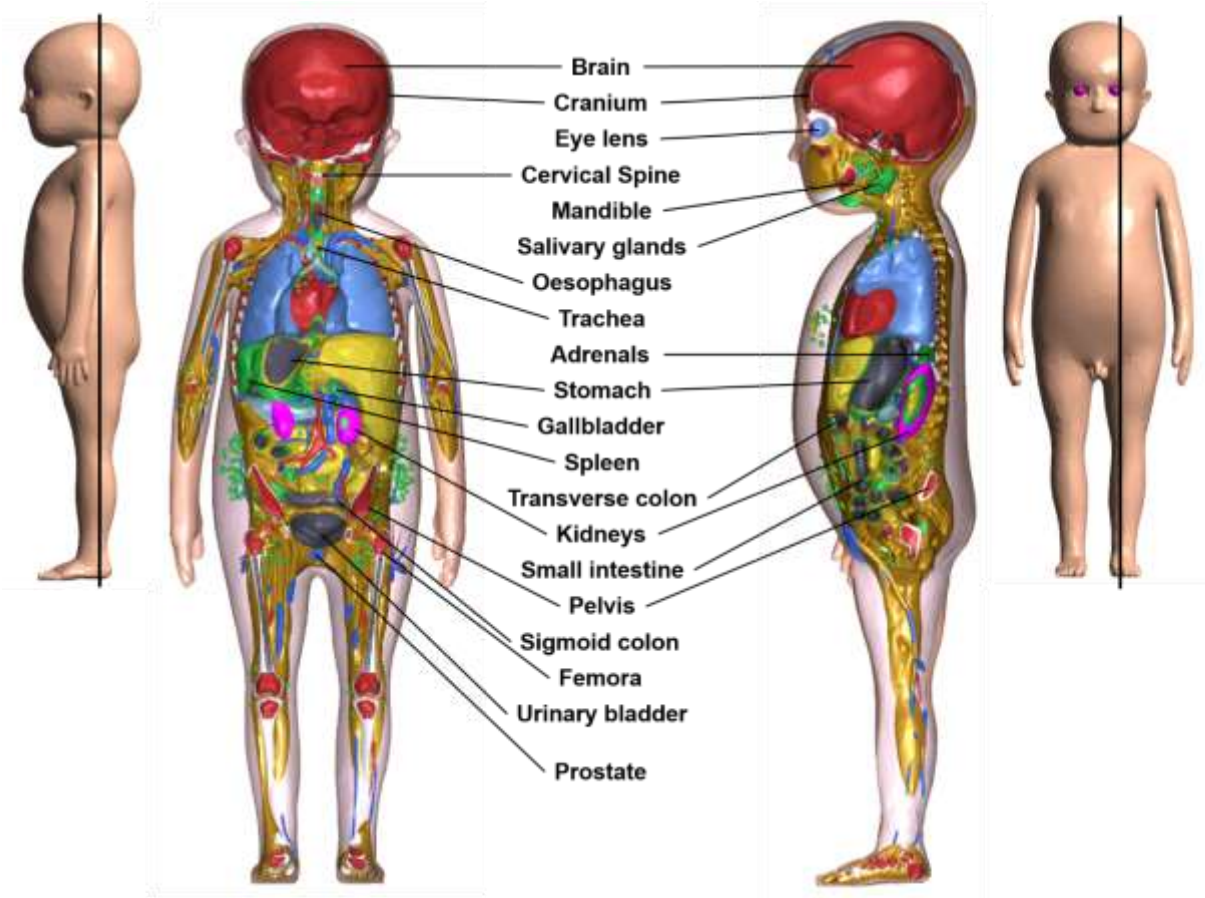

Fig. G.3.2. Coronal and sagittal images of the 1-year-old male mesh-type reference computational phantom.

G.4. Images of the 1-year-old female mesh-type reference computational phantom

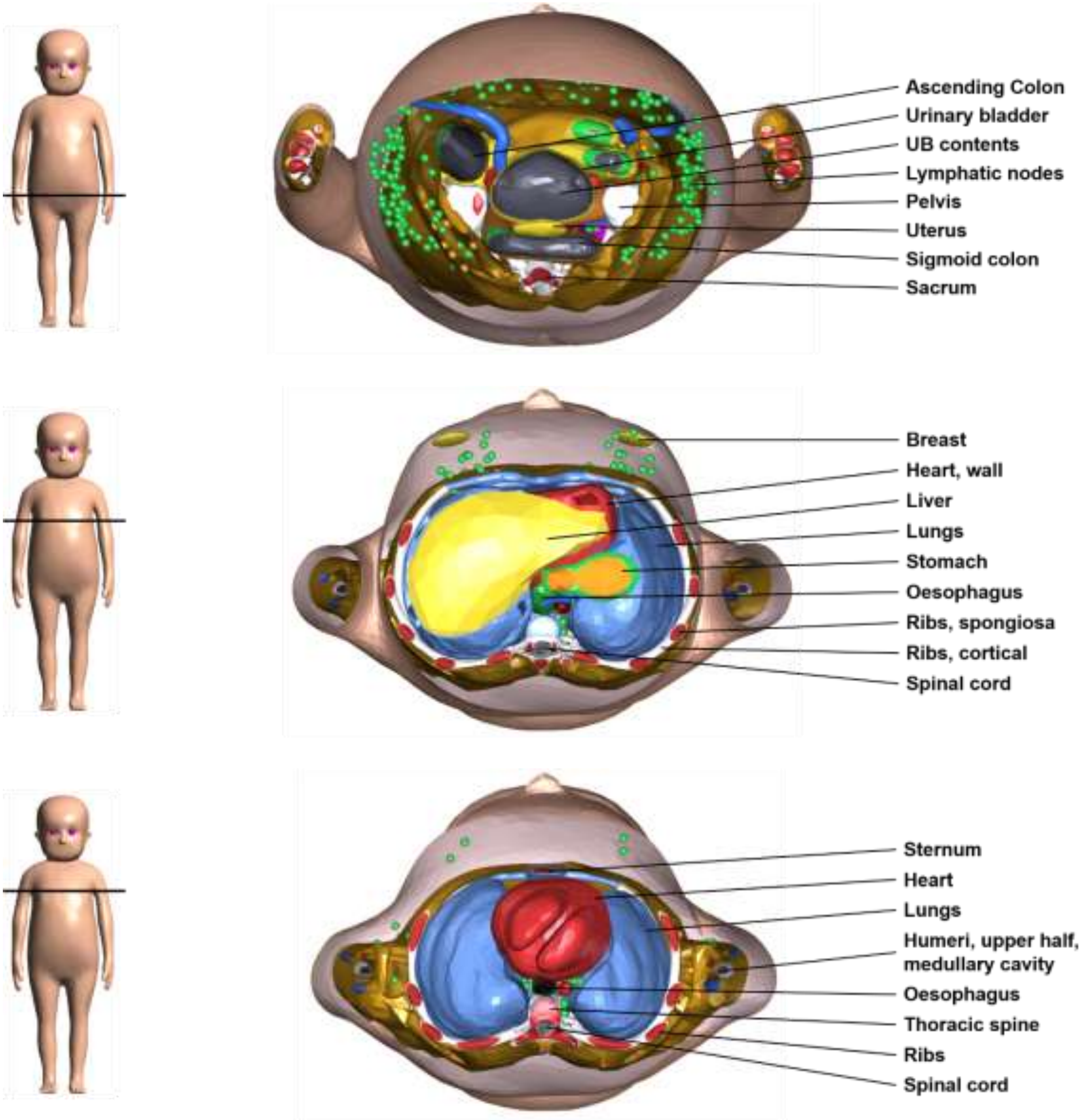

Fig. G.4.1. Transverse (axial) images of the 1-year-old female mesh-type reference computational phantom (*continued on next page*).

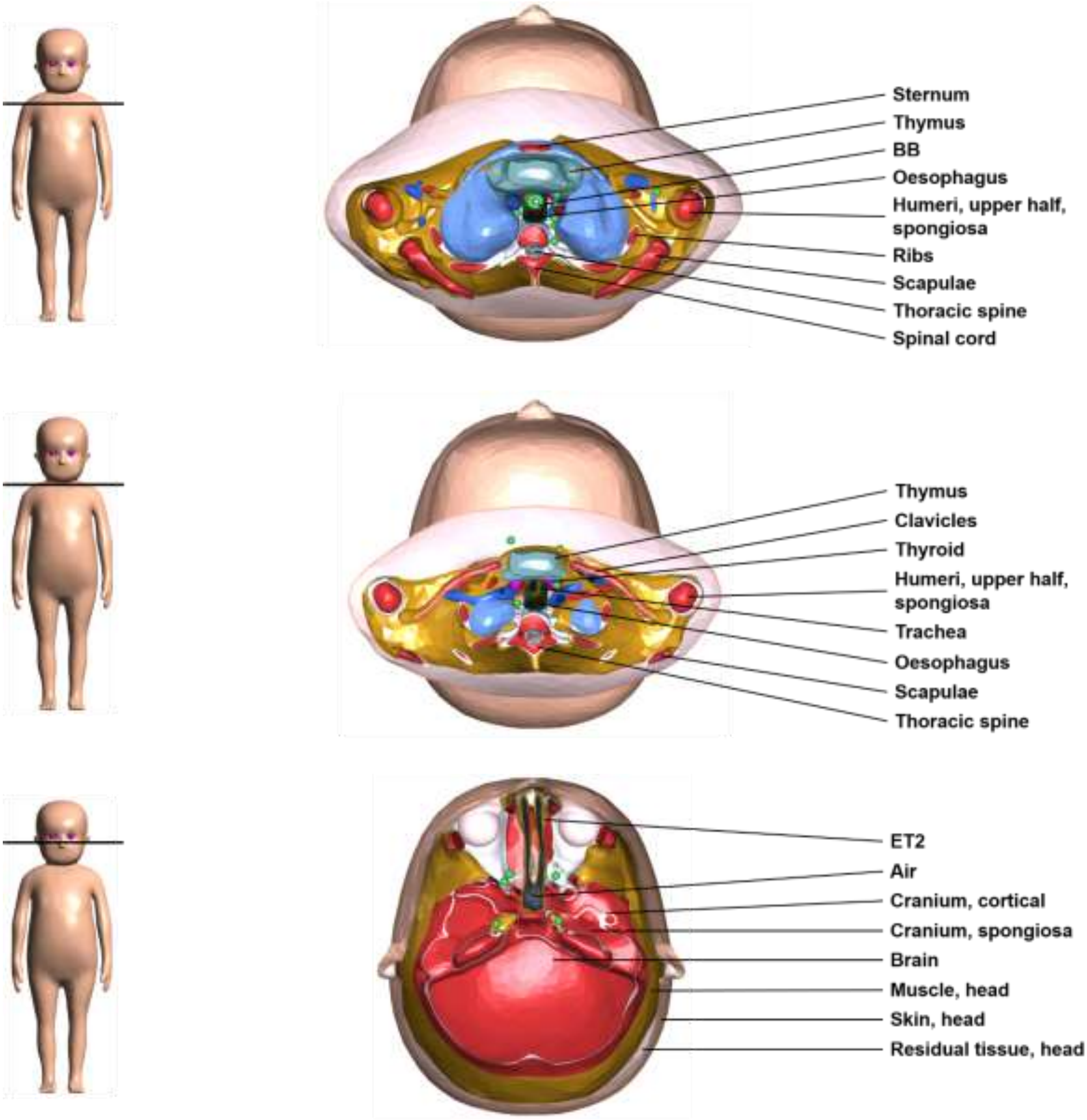

Fig. G.4.1. (*continued*)

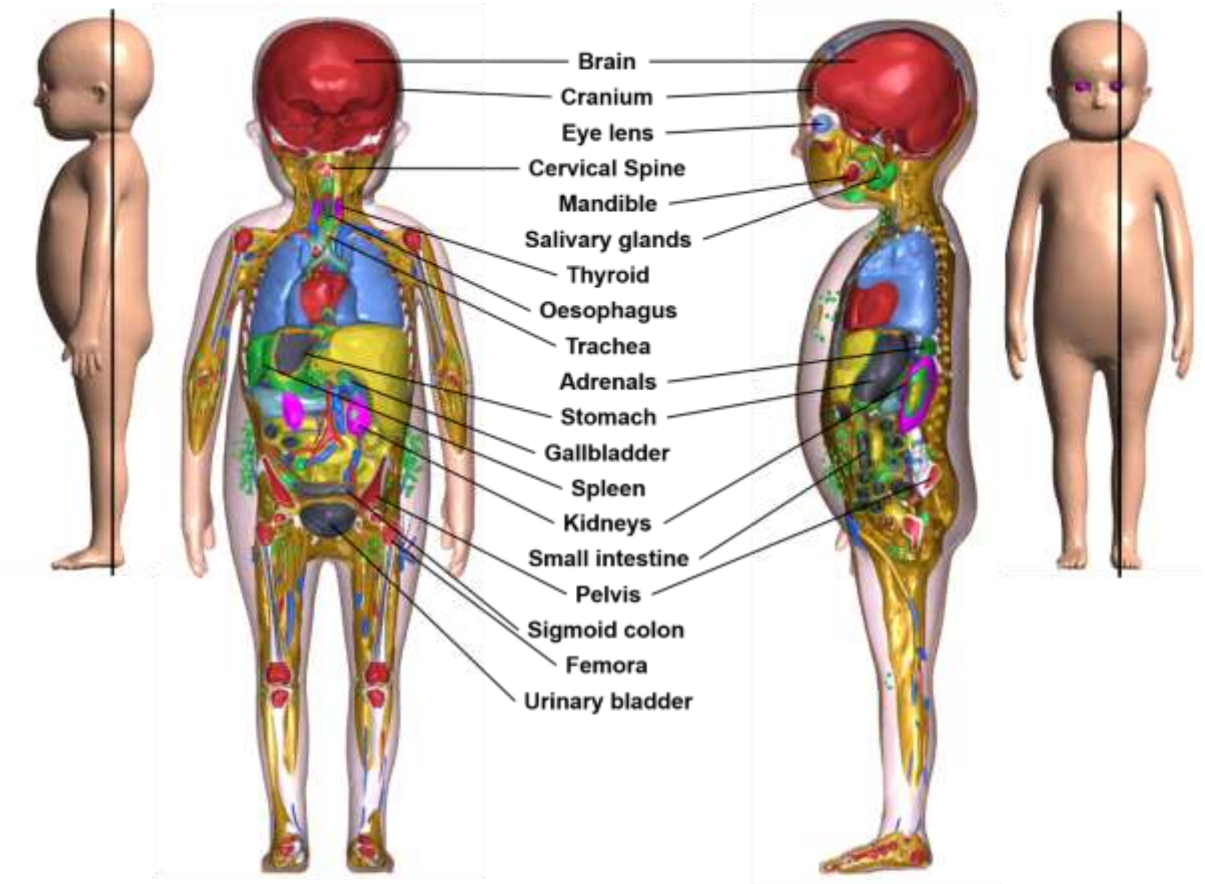

2217

2218 Fig. G.4.2. Coronal and sagittal images of the 1-year-old female mesh-type reference
2219 computational phantom.

2220

G.5. Images of the 5-year-old male mesh-type reference computational phantom

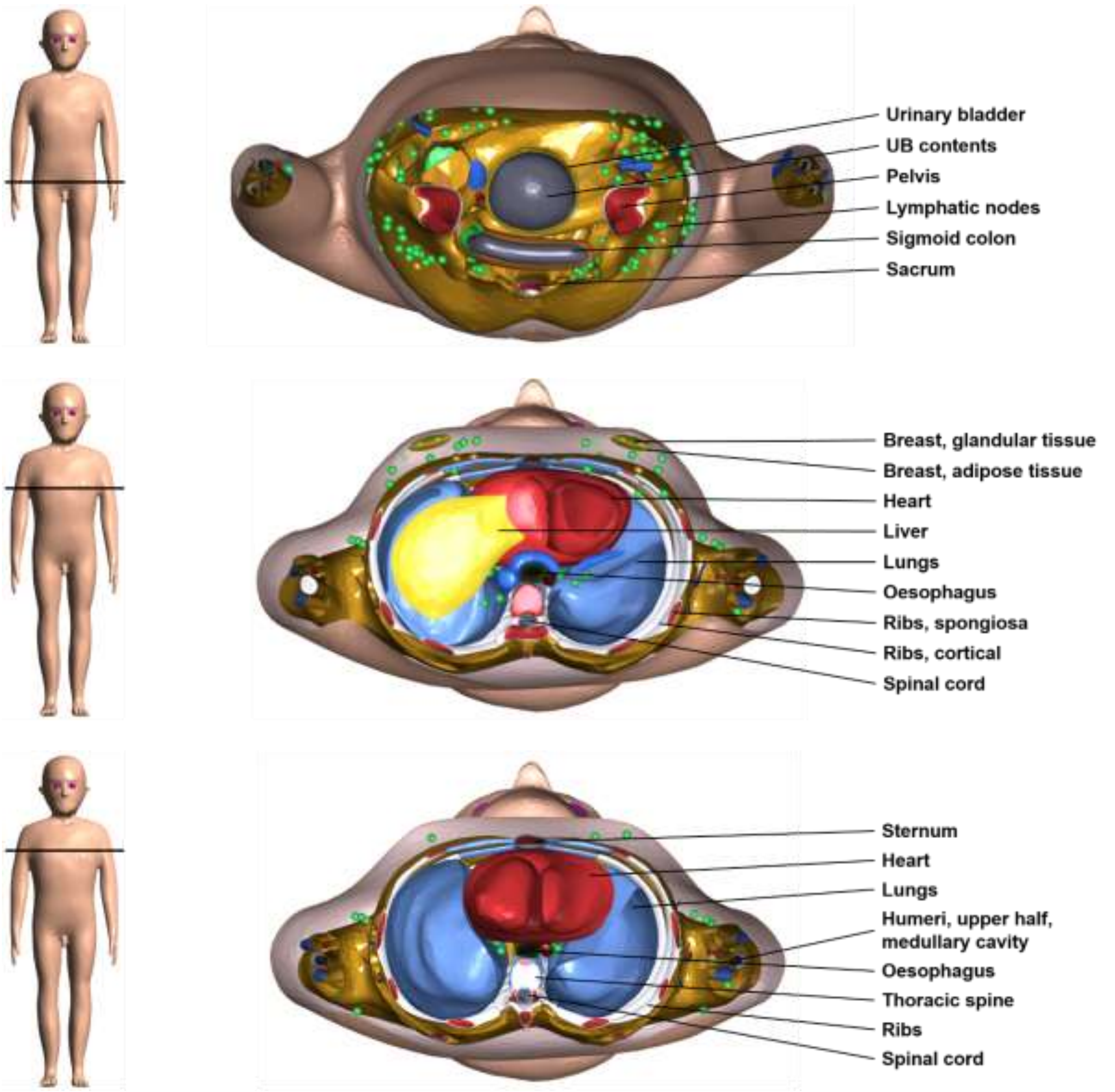

Fig. G.5.1. Transverse (axial) images of the 5-year-old male mesh-type reference computational phantom (*continued on next page*).

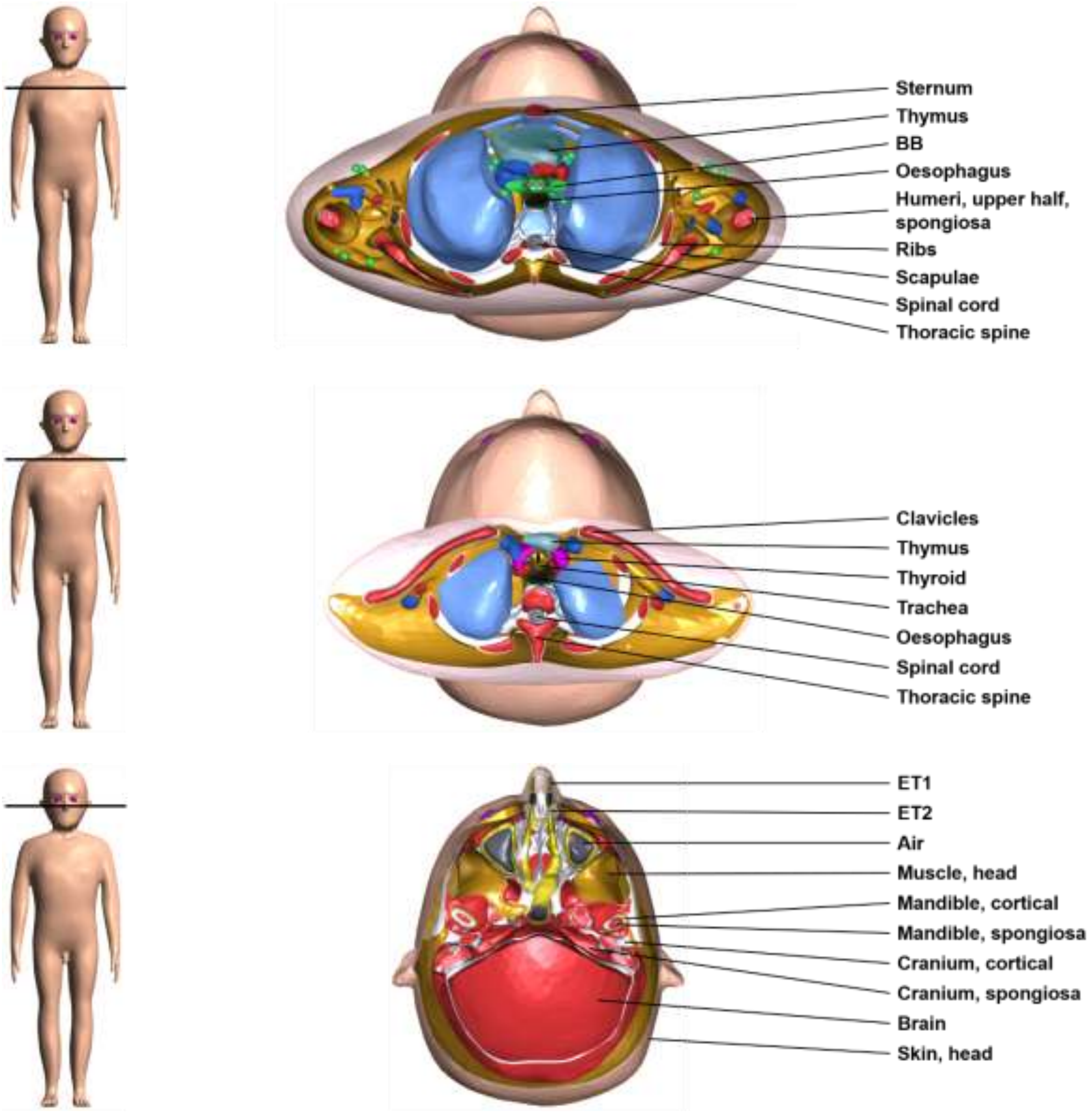

Fig. G.5.1. (*continued*)

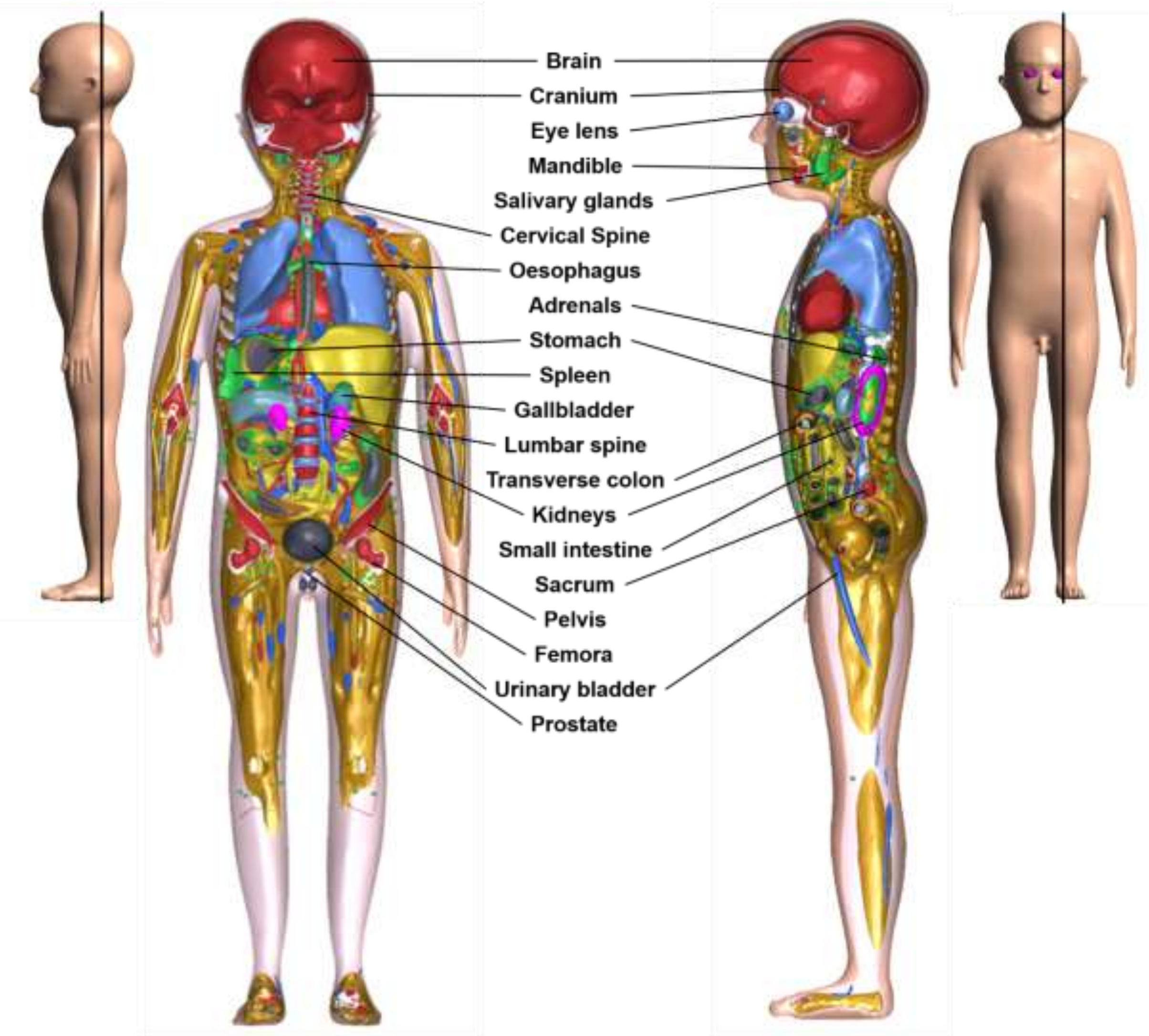

2234

2235 Fig. G.5.2. Coronal and sagittal images of the 5-year-old male mesh-type reference
2236 computational phantom.

2237

G.6. Images of the 5-year-old female mesh-type reference computational phantom

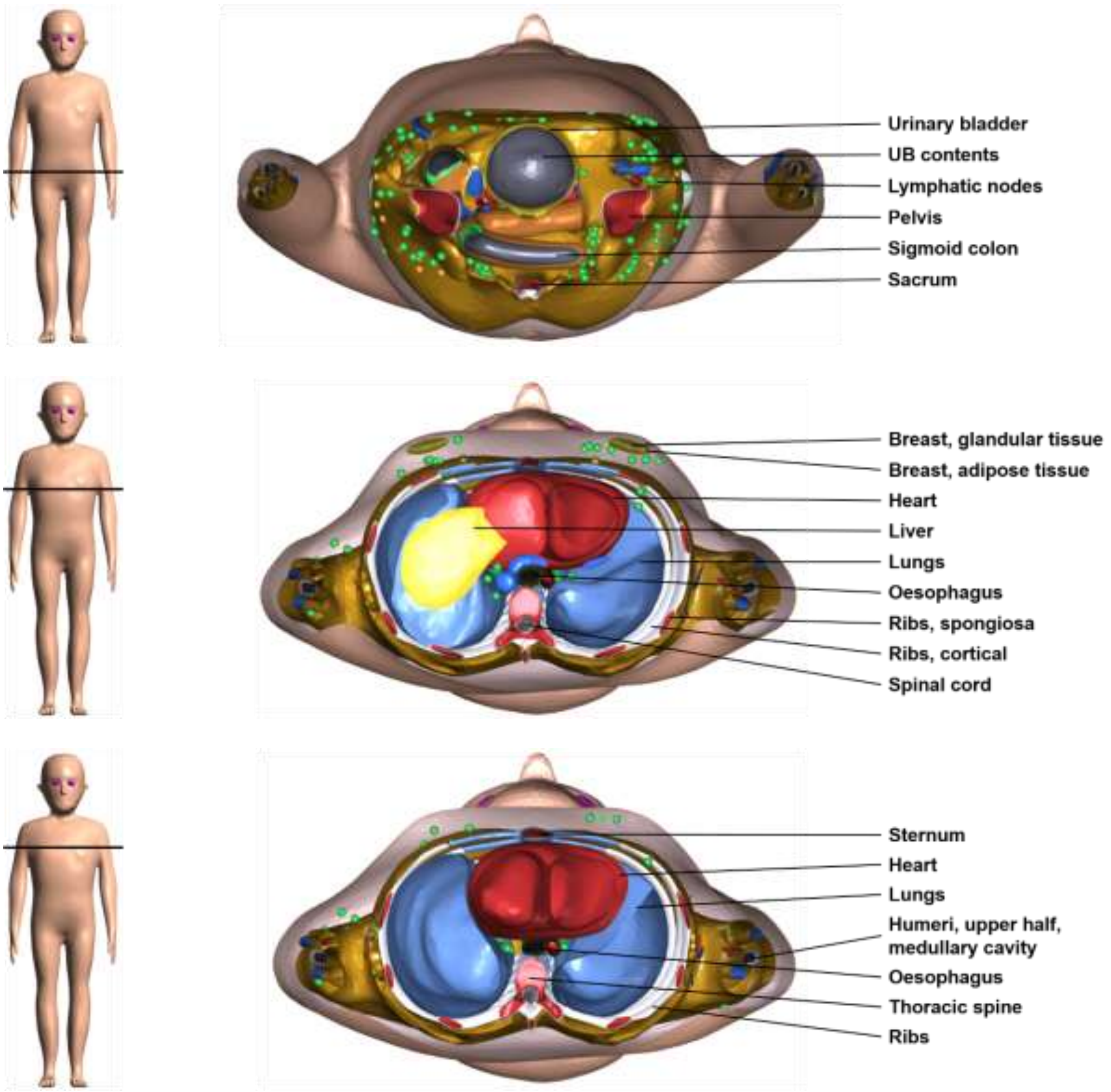

Fig. G.6.1. Transverse (axial) images of the 5-year-old female mesh-type reference computational phantom (*continued on next page*).

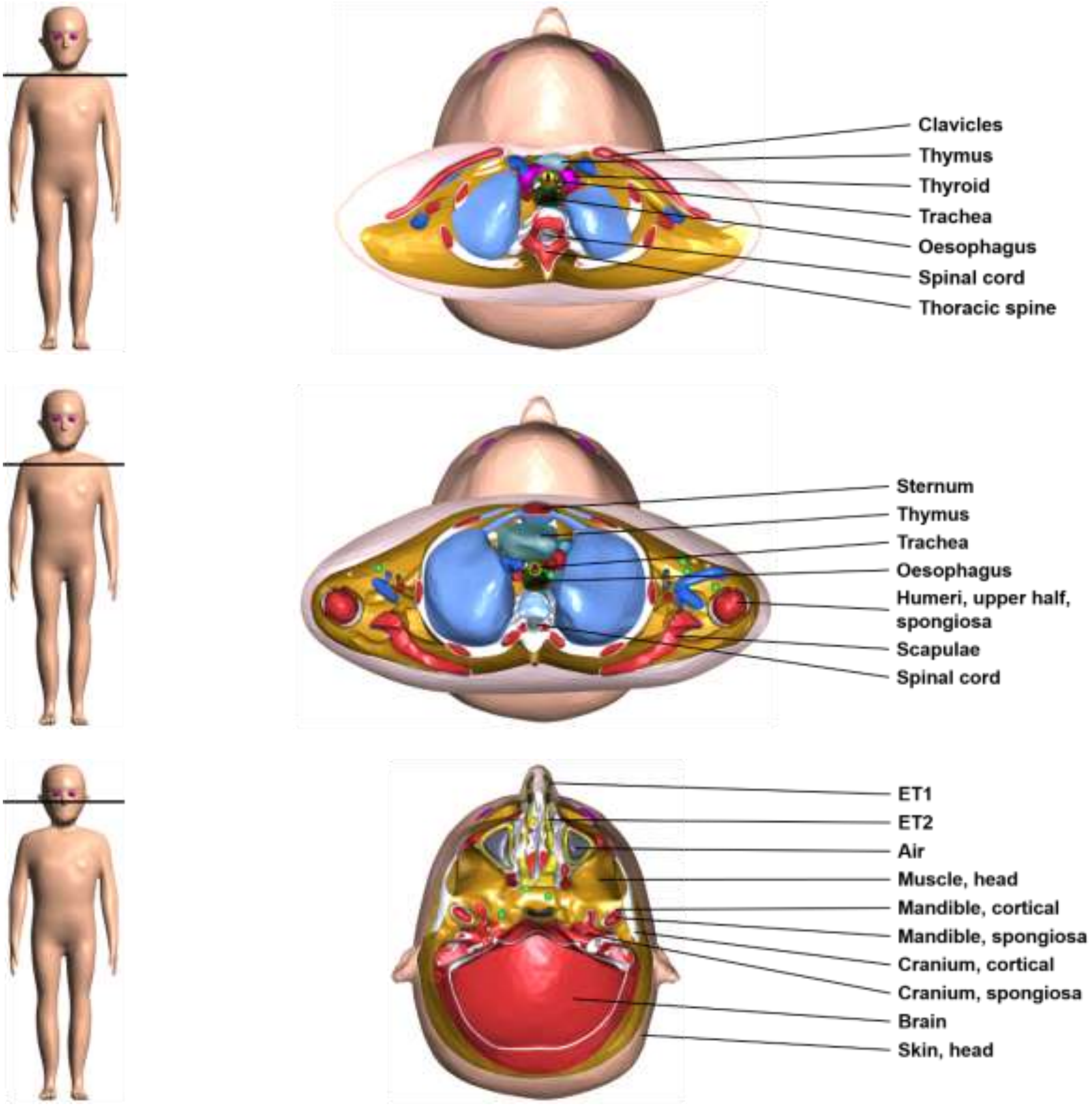

Fig. G.6.1. (*continued*)

2251 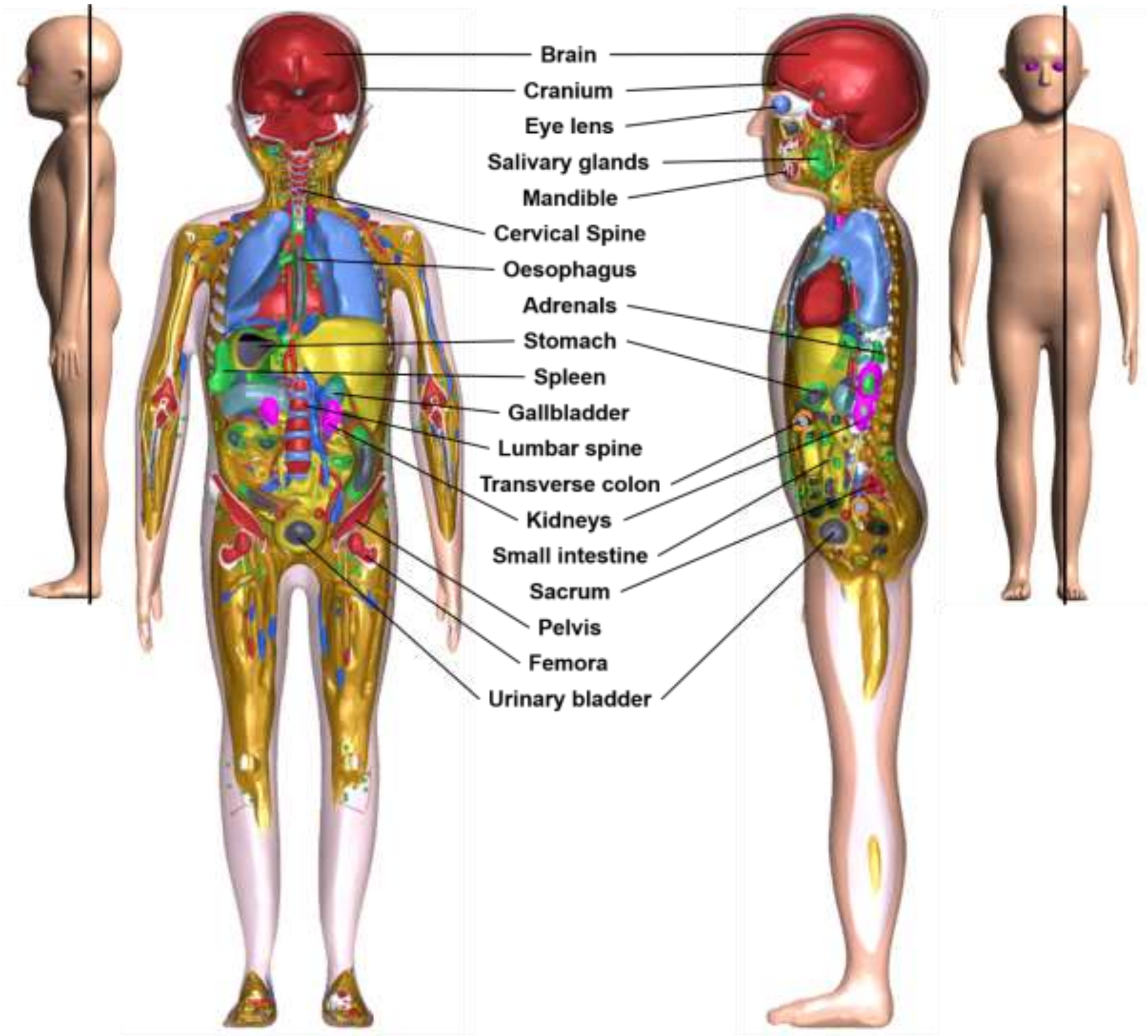

2252 Fig. G.6.2. Coronal and sagittal images of the 5-year-old female mesh-type reference
2253 computational phantom.

2254

G.7. Images of the 10-year-old male mesh-type reference computational phantom

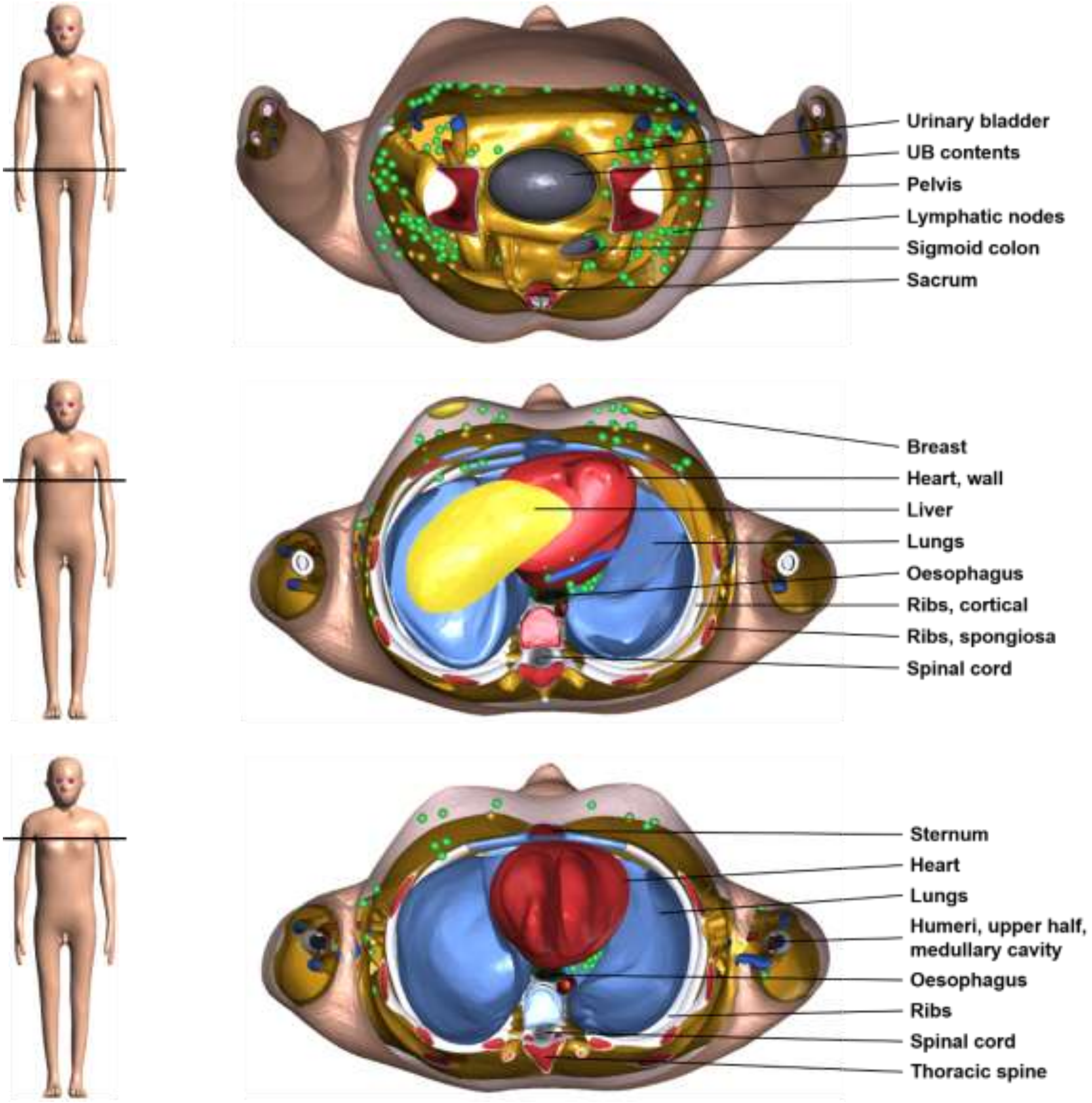

Fig. G.7.1. Transverse (axial) images of the 10-year-old male mesh-type reference computational phantom (*continued on next page*).

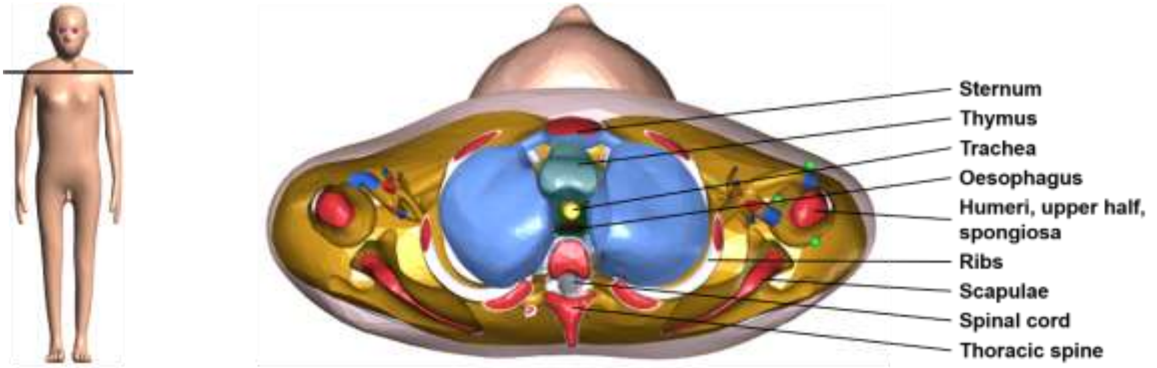

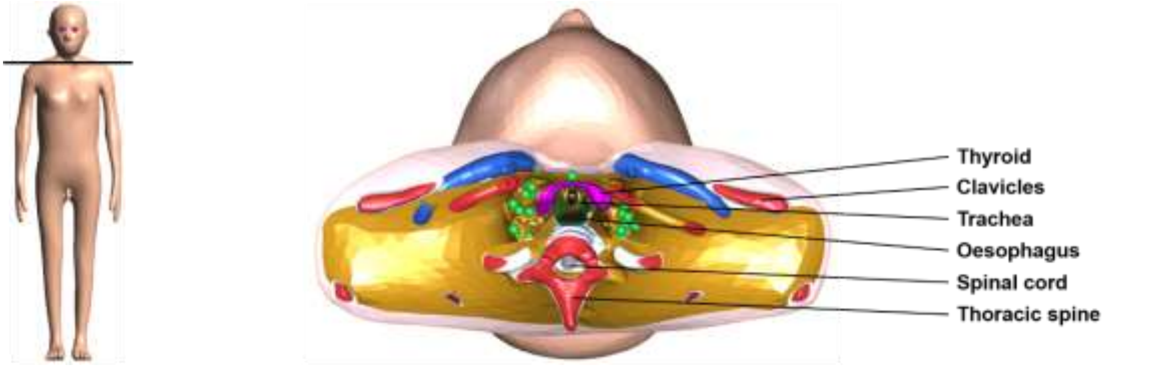

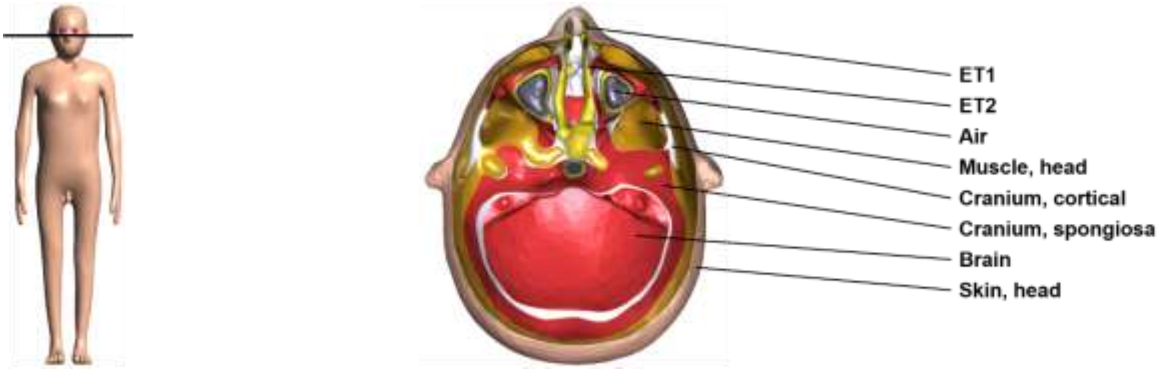

Fig. G.7.1. (*continued*)

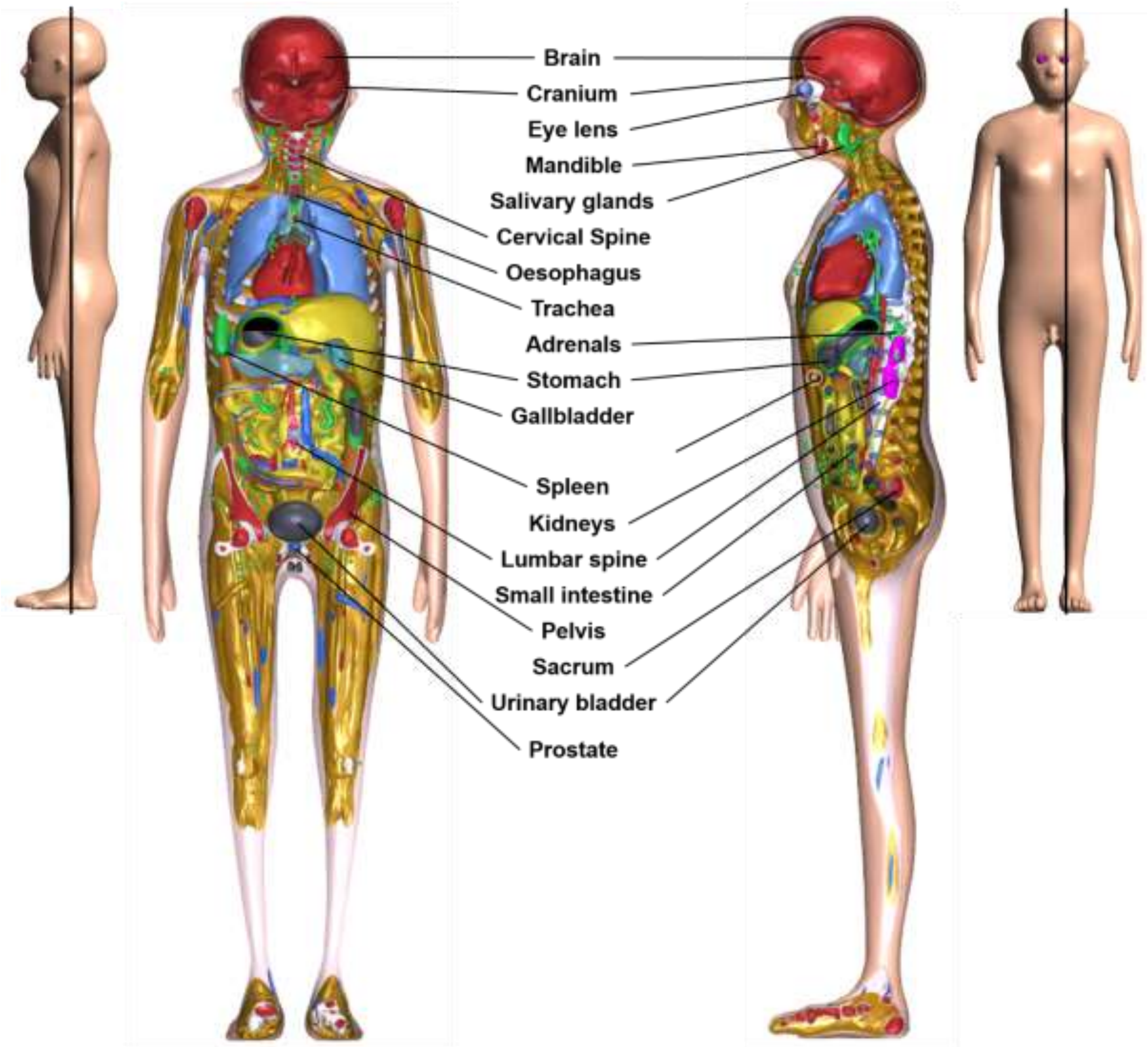

2268

2269 Fig. G.7.2. Coronal and sagittal images of the 10-year-old male mesh-type reference
2270 computational phantom.

2271

G.8. Images of the 10-year-old female mesh-type reference computational phantom

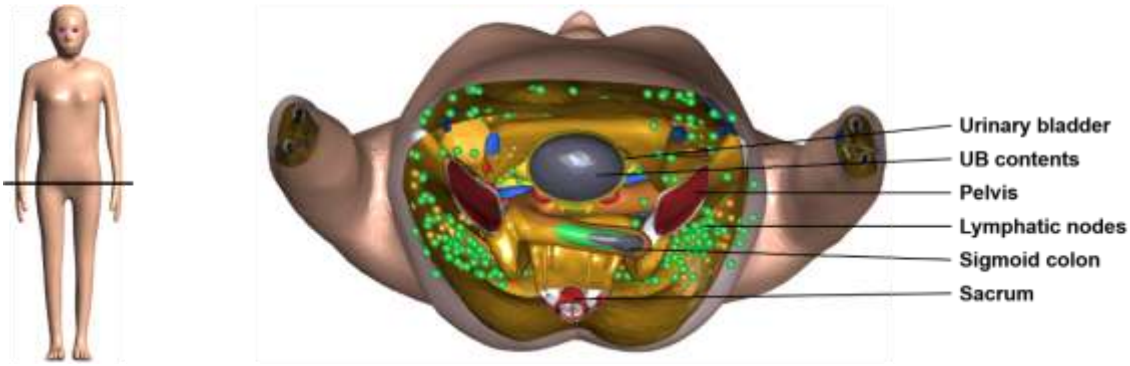

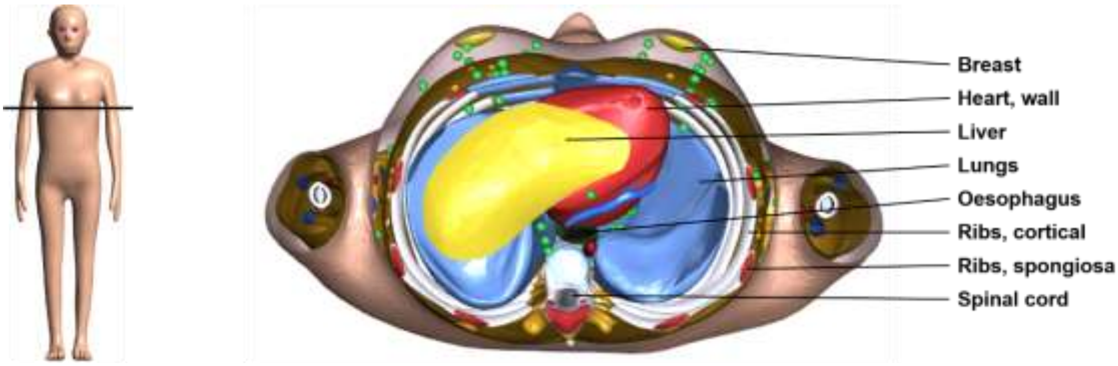

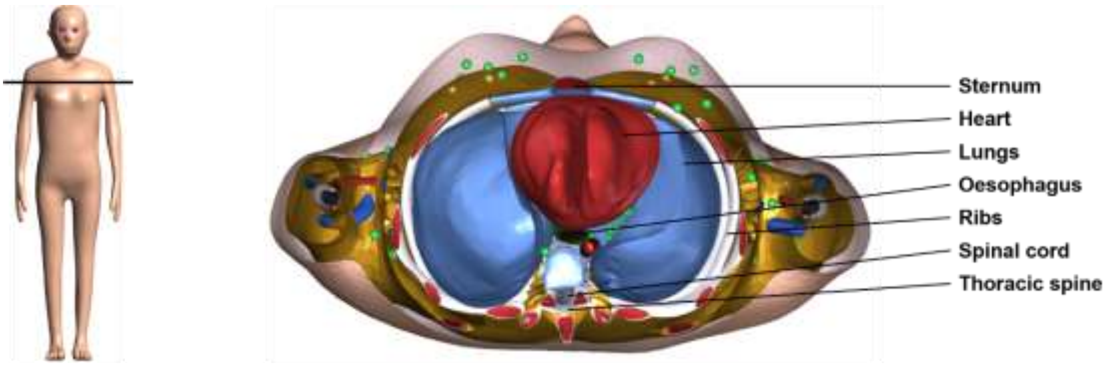

Fig. G.8.1. Transverse (axial) images of the 10-year-old female mesh-type reference computational phantom (*continued on next page*).

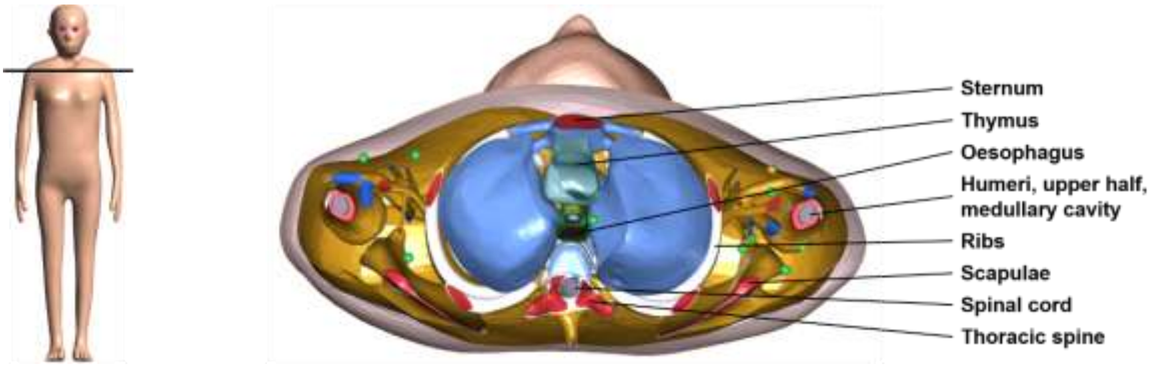

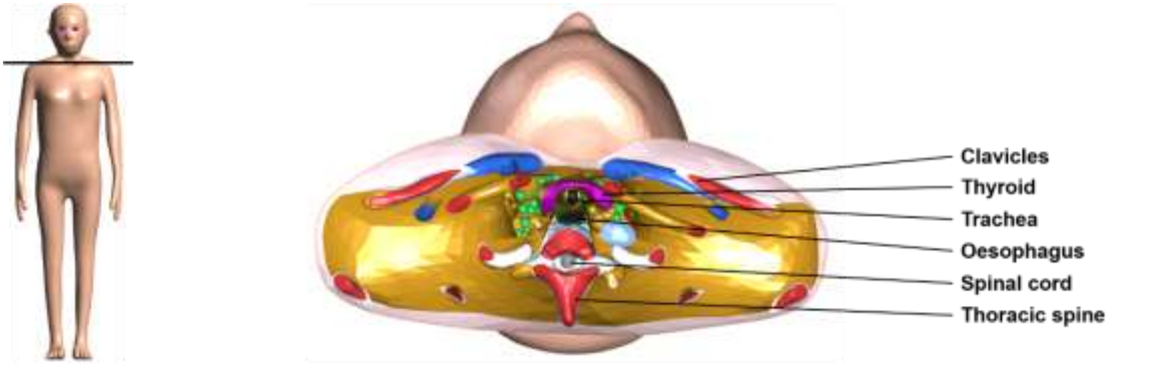

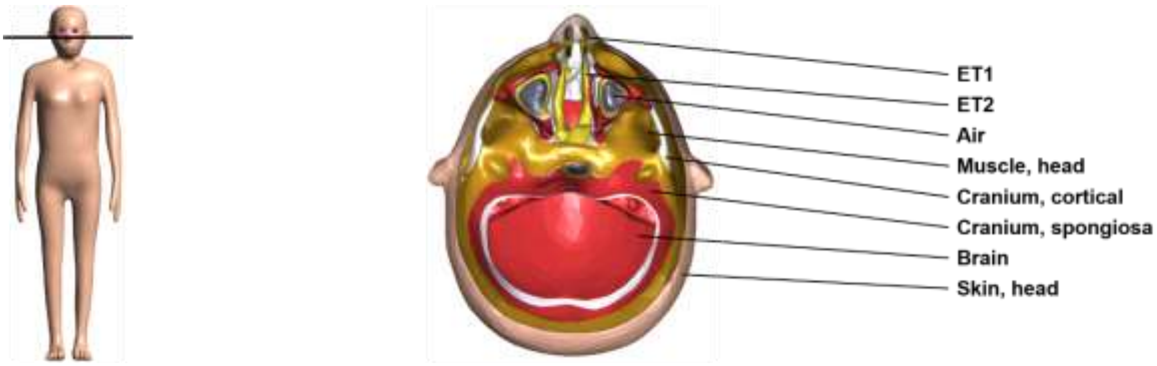

Fig. G.8.1. (*continued*)

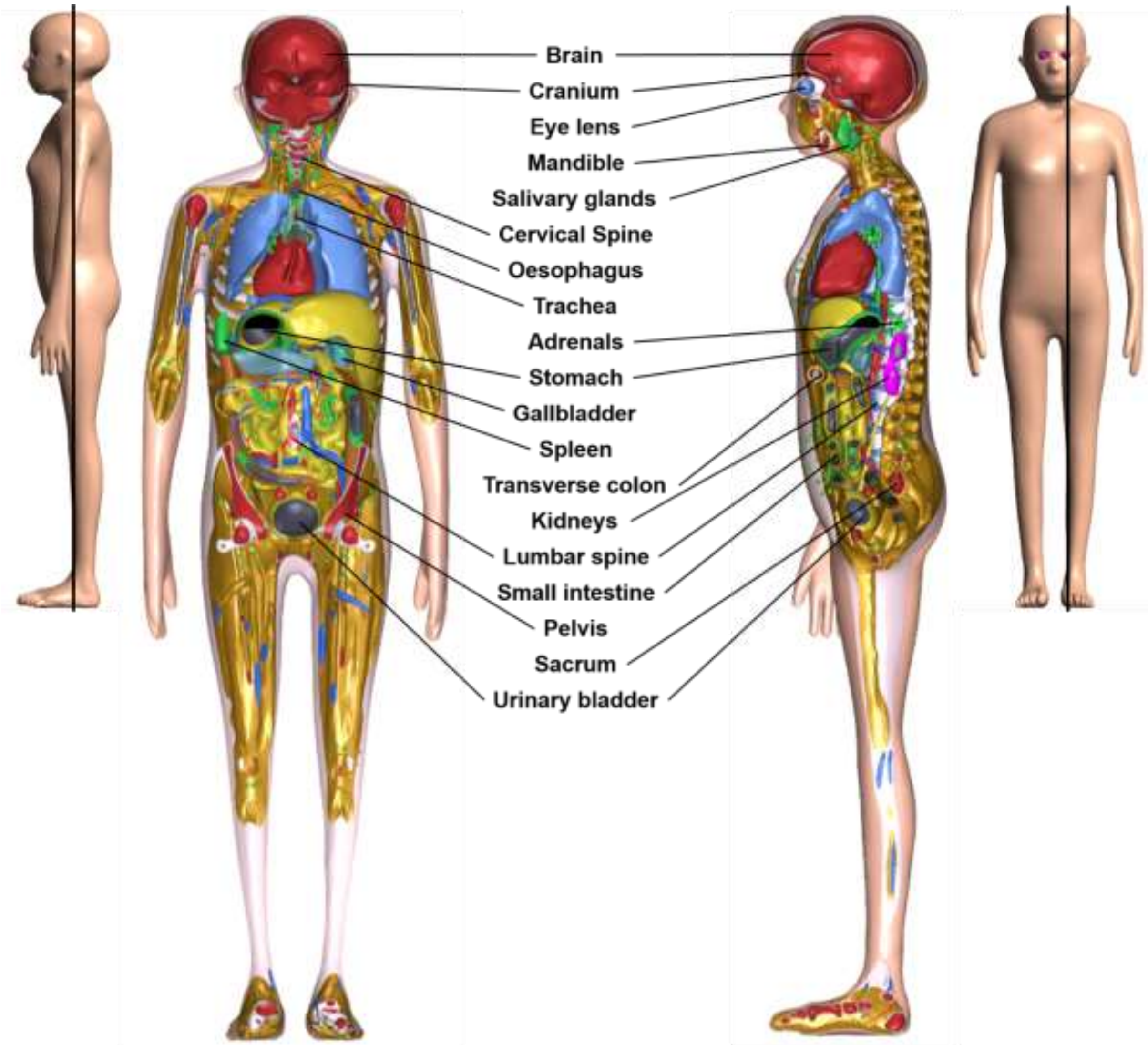

2285

2286 Fig. G.8.2. Coronal and sagittal images of the 10-year-old female mesh-type reference
2287 computational phantom.

2288

G.9. Images of the 15-year-old male mesh-type reference computational phantom

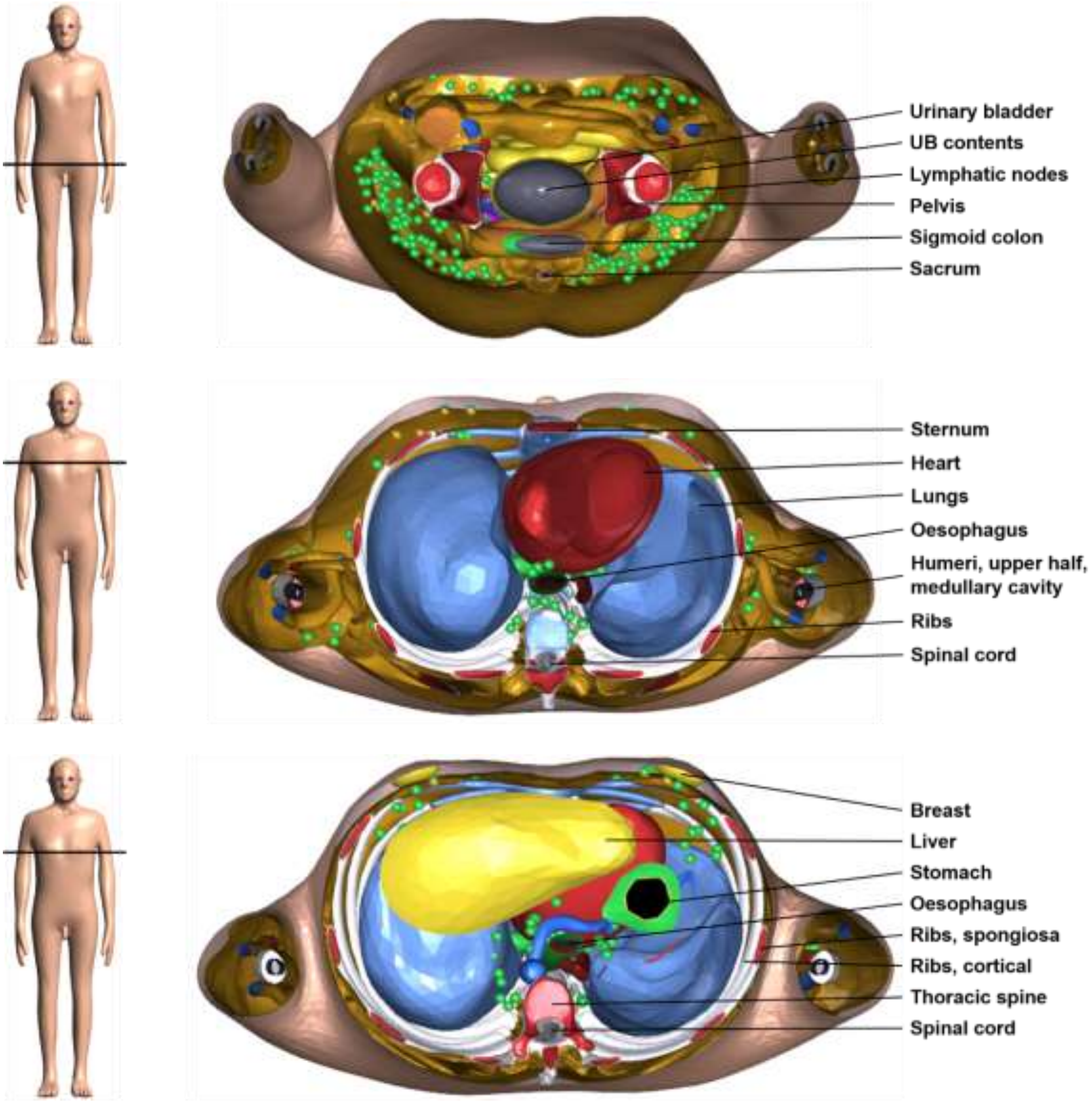

Fig. G.9.1. Transverse (axial) images of the 15-year-old male mesh-type reference computational phantom (*continued on next page*).

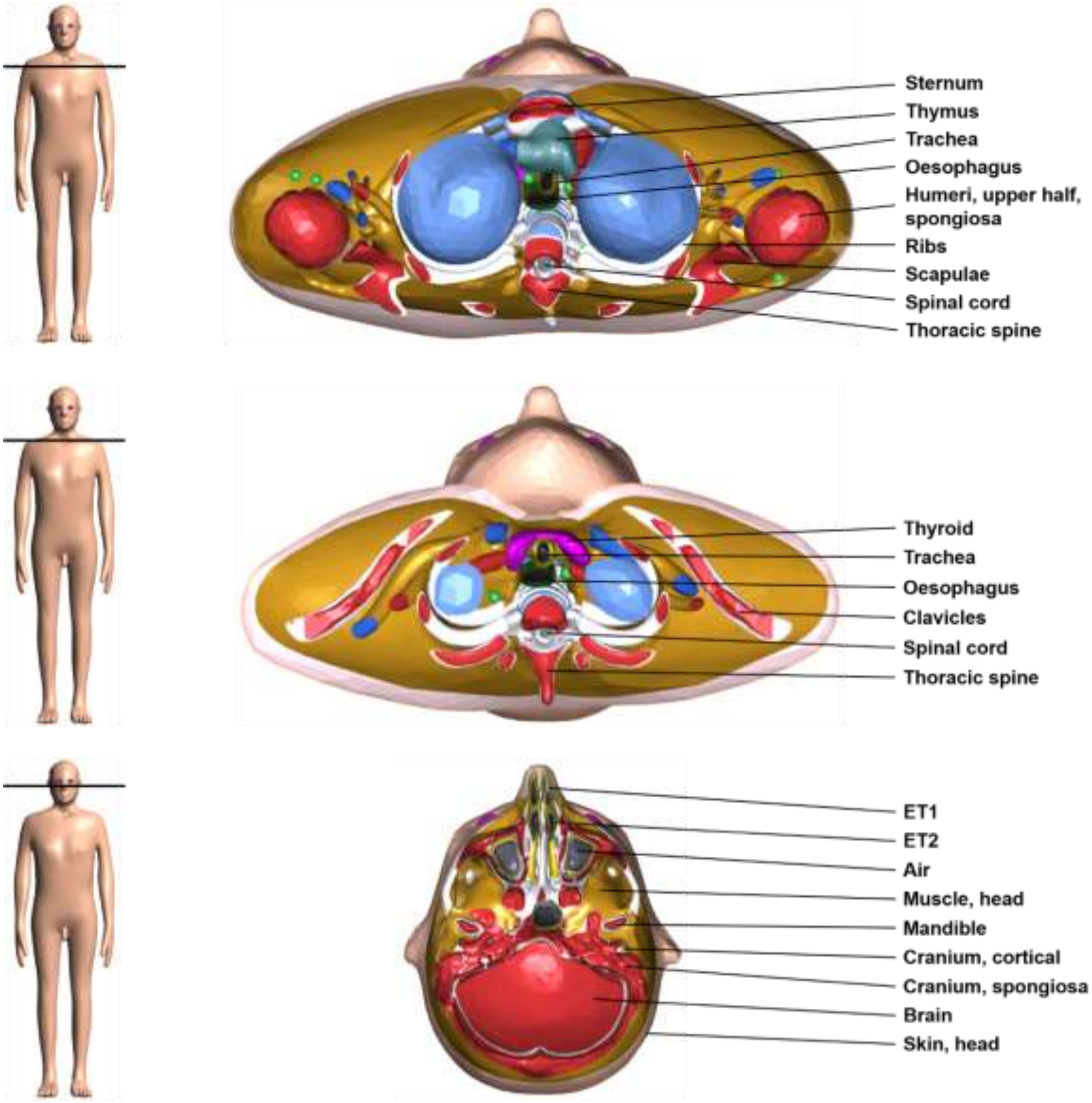

Fig. G.9.1. (*continued*)

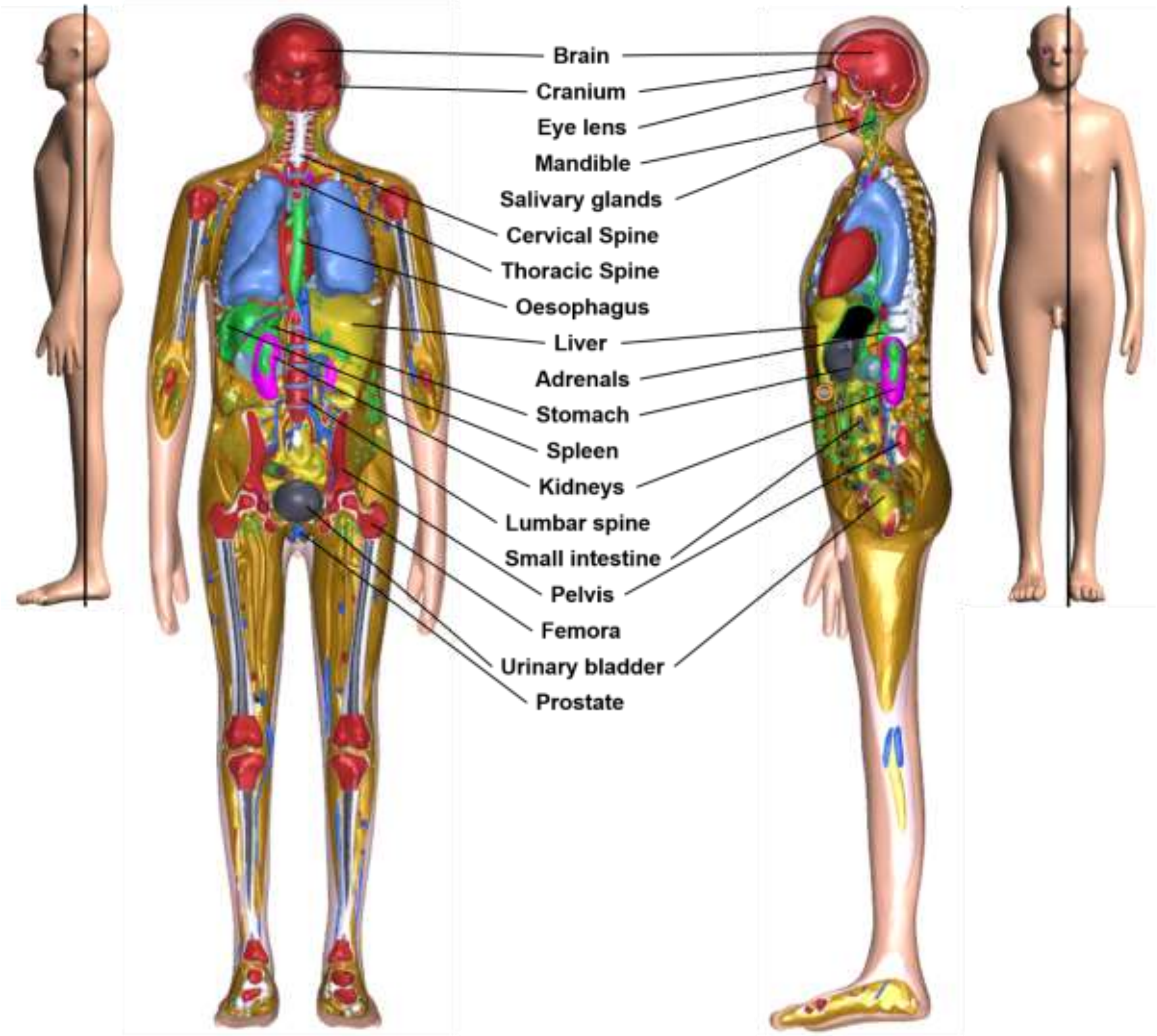

2302

2303 Fig. G.9.2. Coronal and sagittal images of the 15-year-old male mesh-type reference
2304 computational phantom.

2305

G.10. Images of the 15-year-old female mesh-type reference computational phantom

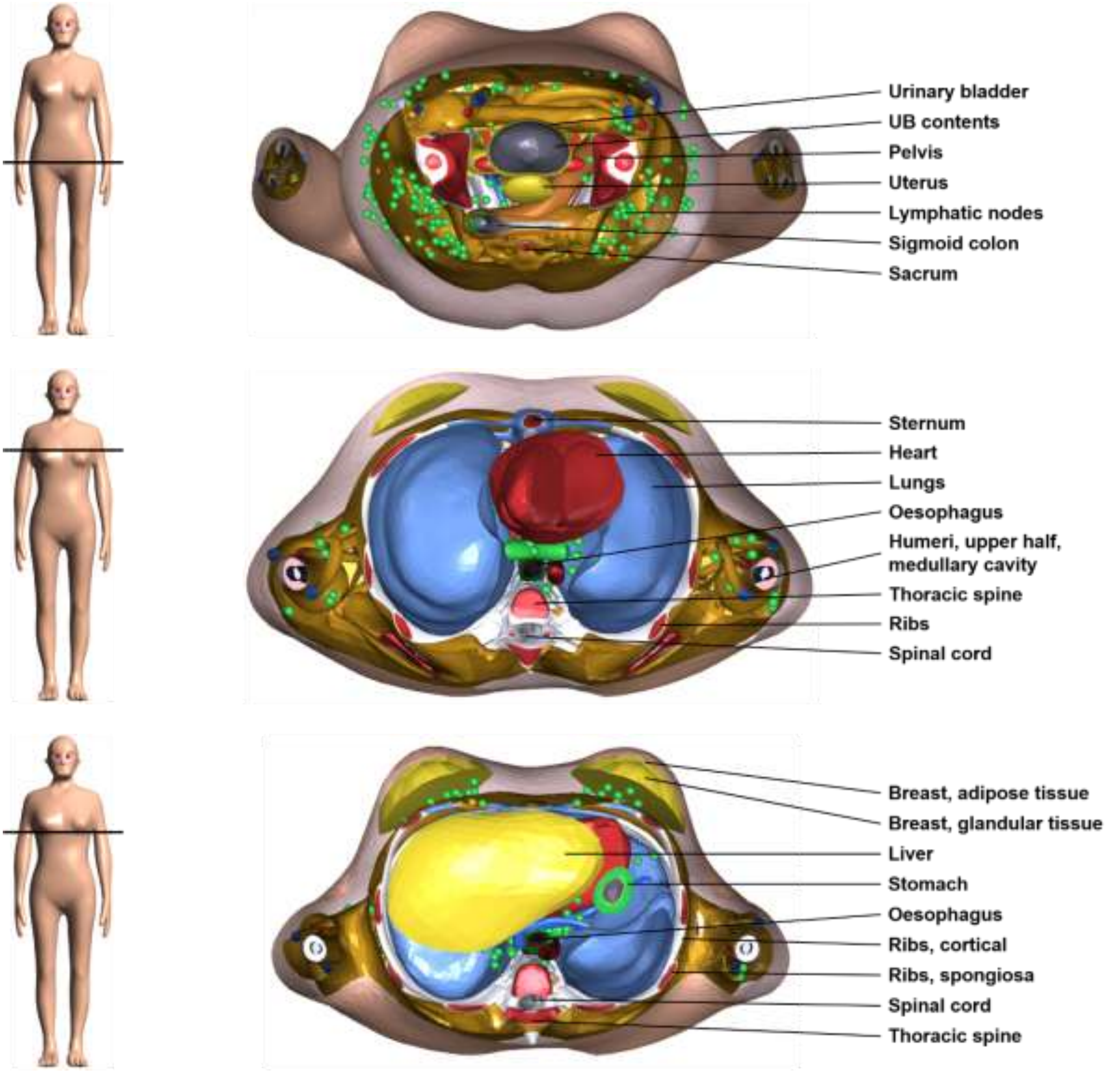

Fig. G.10.1. Transverse (axial) images of the 15-year-old female mesh-type reference computational phantom (*continued on next page*).

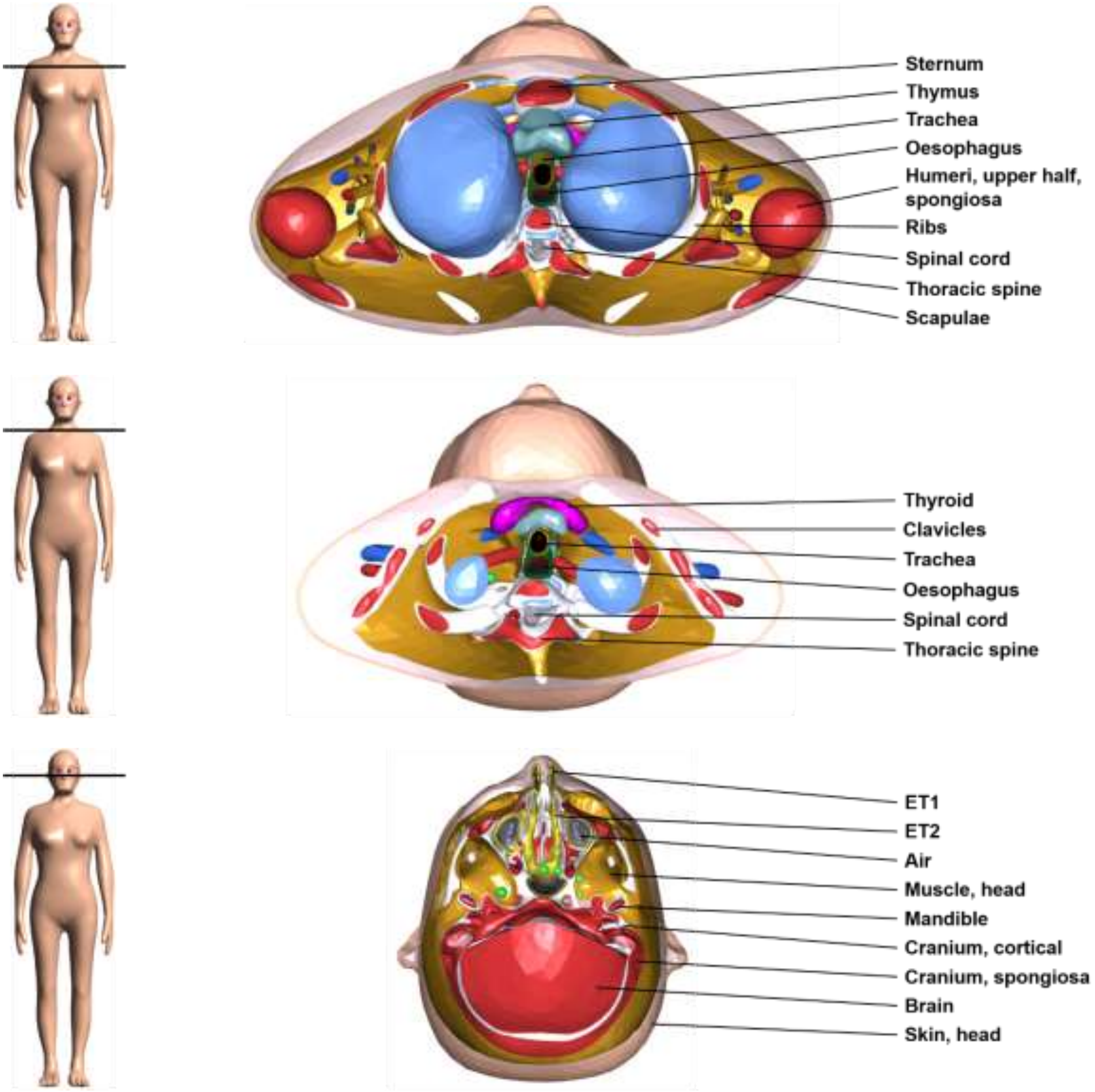

Fig. G.10.1. (*continued*)

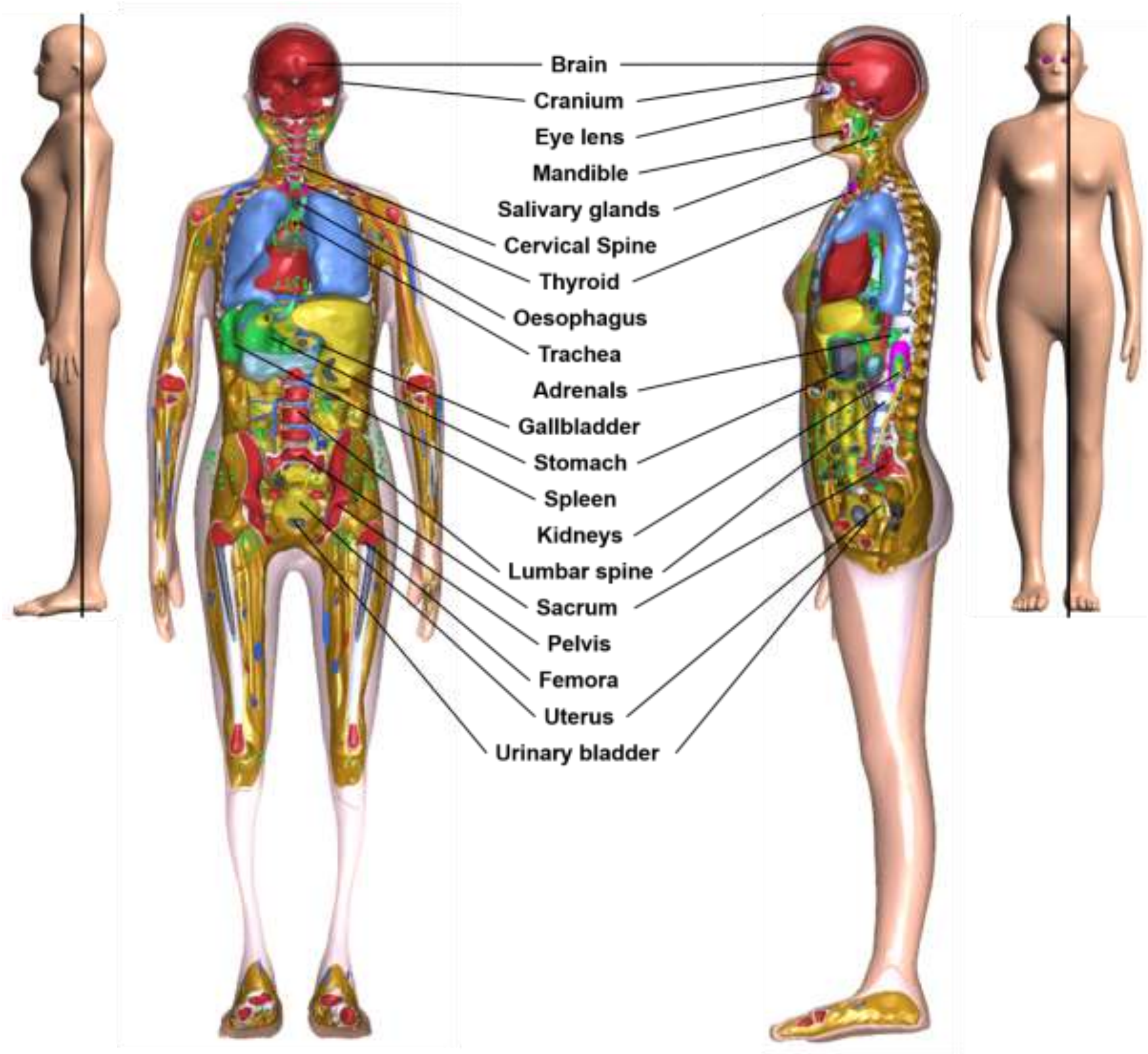

2319

2320 Fig. G.10.2. Coronal and sagittal images of the 15-year-old female mesh-type reference
2321 computational phantom.

2322

ANNEX H. COMPARISON OF DOSE COEFFICIENTS FOR EXTERNAL EXPOSURE

(H 1) This annex compares the dose coefficients (DCs) for organ dose of six organs (i.e. red bone marrow (RBM), colon, lungs, stomach, breast and skin) and effective dose for external exposures to photons, neutrons, electrons and helium ions calculated using the paediatric mesh-type reference computational phantoms (MRCPs) with those calculated with the *Publication 143* (P143) phantoms (ICRP, 2020). Note that the organs selected for the comparison of organ DCs, except skin, have the highest tissue-weighting factor (= 0.12) and the skin despite its small tissue-weighting factor (= 0.01) could significantly affect the effective dose calculation for external exposures to weakly penetrating radiations. To calculate the DCs, the MRCPs and P143 phantoms were implemented into the Geant4 code (version 10.06.p02) (Allisons et al., 2016) using the *G4Tet* and *G4VNestedParameterisation* classes, respectively. The phantoms were assumed to be in vacuum and irradiated by mono-energetic broad beams in six idealised irradiation geometries, i.e. antero-posterior (AP), postero-anterior (PA), left-lateral (LLAT), right-lateral (RLAT), rotational (ROT) and isotropic (ISO), for photons and neutrons and three irradiation geometries, i.e. AP, PA and ISO, for electrons and helium ions. The energy ranges considered are 10^{-2}–10^{4} MeV for photons and electrons, 10^{-9}–10^{4} MeV for neutrons and 1–10^{5} MeV/u for helium ions. The number of primary particles varied from 10^{7} to 10^{10} depending on the particle type and energy, keeping the statistical relative errors for the organ DCs below 5% and for the effective DCs below 0.5%. The particles were generated by using the *G4VUserPrimaryGeneratorAction* class. The physics libraries of *FTFP_BERT_HP* and *G4EmLivermorePhysics* were used to transport the neutrons and all other particles, respectively (Geant4 Physics Reference Manual). The thermal neutron scattering treatment S(α, β) for hydrogen in light water at 300 K was also activated to consider the thermal vibration of molecules. The kerma approximation was not applied. A range of 1 μm for the secondary production cut was applied to all particles. Note that for photons, the RBM and endosteum DCs were estimated using the fluence-to-absorbed dose response functions (DRFs). For spot-check purpose, the MCNP6 (version 2.0) (Martz et al., 2017) and PHITS (version 3.10) (Furuta et al., 2017) codes were additionally used to calculate the organ and effective DCs for some selected energy points, under the same simulation conditions (remaining spot-check DCs will be included prior to publication). For the MCNP6 code, the default physics library was used to transport all the particles (Martz et al., 2017) except for neutrons for which the *ENDF70* physic library was used (Trellue et al., 2009). For the PHITS code, the *EGS5* physics library was used for photons and electrons (Hirayama et al., 2005), the *JENDL-4.0* physics library and event generator mode version 2.0 were used for neutrons (Shibata et al., 2011) and the default physics library was used for helium ions (Furuta et al., 2017). The energy cut values, which are equivalent to the range cut value used in the Geant4 code, were applied to the MCNP6 and PHITS codes. Figs H.1–H.6 show the organ DCs for photons in the AP irradiation geometry, as examples, and Figs H.7–H.11 show the effective DCs for photons. Figs H.12–H.17 show the organ DCs for neutrons in the AP irradiation geometry, as examples, and Figs H.18–H.22 show the effective DCs for neutrons. Figs H.23–H.28 show the organ DCs for electrons in the ISO irradiation geometry, as examples, and Figs H.29–H.33 show the effective DCs for electrons. Figs H.34–H.39 show the organ DCs for helium ions in the ISO irradiation geometry, as examples, and Figs H.40–H.44 show the effective DCs for helium ions. Figs H.45–H.50 show the lens DCs for photons. For discussion of the comparisons, please see Section 7.1 of the main text.

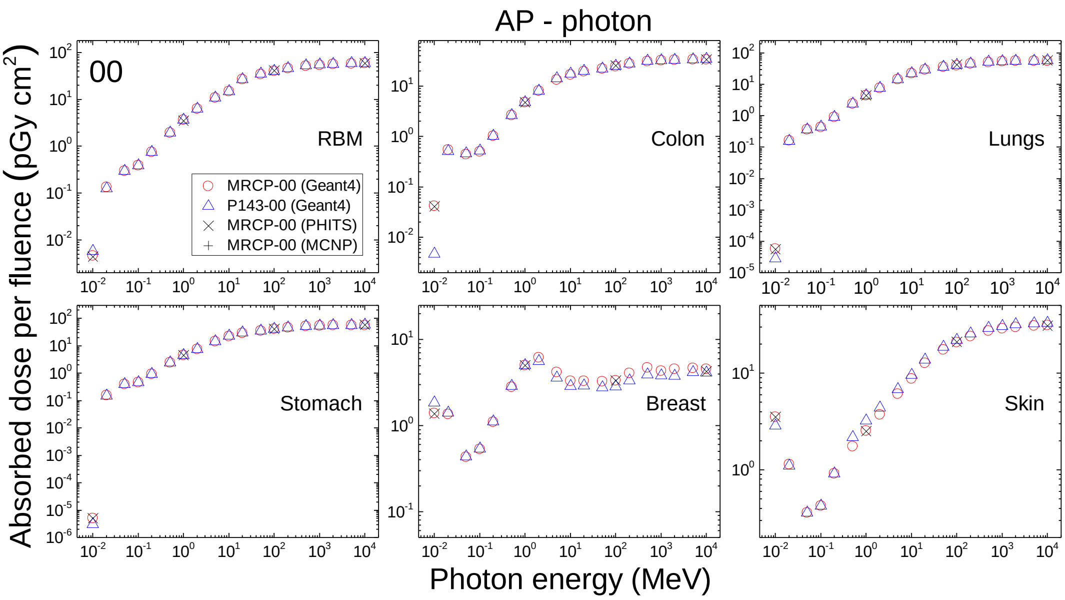

Fig. H.1. Absorbed dose per fluence (pGy cm^2) to the red bone marrow (RBM), colon, lungs, stomach, breast and skin in the antero-posterior (AP) irradiation geometry for photon exposures calculated with the newborn mesh-type reference computational phantoms (MRCPs), along with the values calculated with the P143 newborn phantoms. The values shown were averaged for the male and female phantoms.

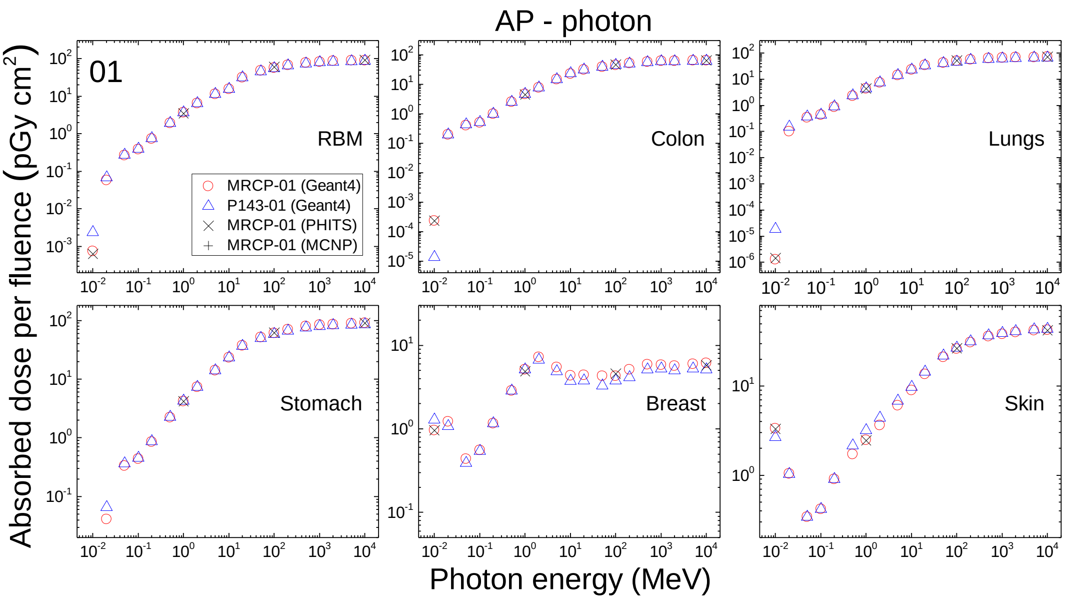

Fig. H.2. Absorbed dose per fluence (pGy cm^2) to the red bone marrow (RBM), colon, lungs, stomach, breast and skin in the antero-posterior (AP) irradiation geometry for photon exposures calculated with the 1-year-old mesh-type reference computational phantoms (MRCPs), along with the values calculated with the P143 1-year-old phantoms. The values shown were averaged for the male and female phantoms.

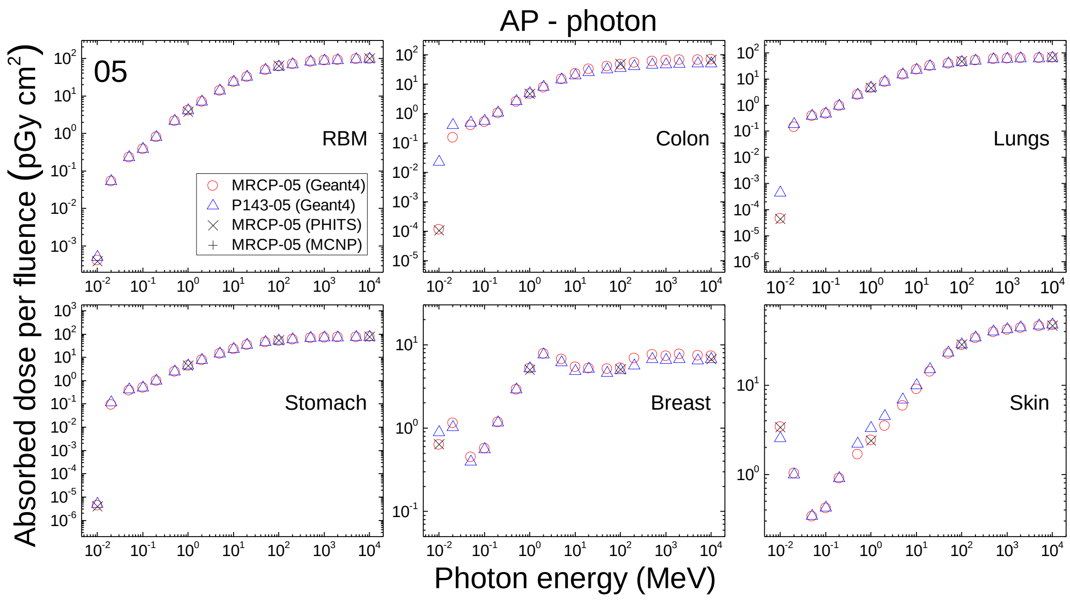

2384 Fig. H.3. Absorbed dose per fluence (pGy cm^2) to the red bone marrow (RBM), colon, lungs,
2385 stomach, breast and skin in the antero-posterior (AP) irradiation geometry for photon exposures
2386 calculated with the 5-year-old mesh-type reference computational phantoms (MRCPs), along
2387 with the values calculated with the P143 5-year-old phantoms. The values shown were
2388 averaged for the male and female phantoms.

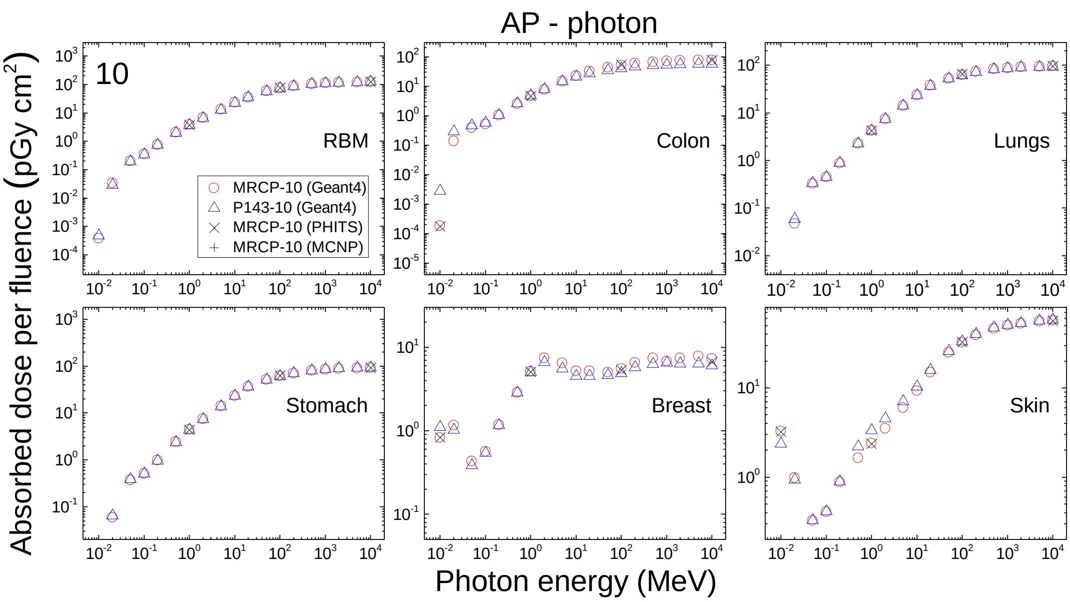

2390 Fig. H.4. Absorbed dose per fluence (pGy cm^2) to the red bone marrow (RBM), colon, lungs,
2391 stomach, breast and skin in the antero-posterior (AP) irradiation geometry for photon exposures
2392 calculated with the 10-year-old mesh-type reference computational phantoms (MRCPs), along
2393 with the values calculated with the P143 10-year-old phantoms. The values shown were
2394 averaged for the male and female phantoms.

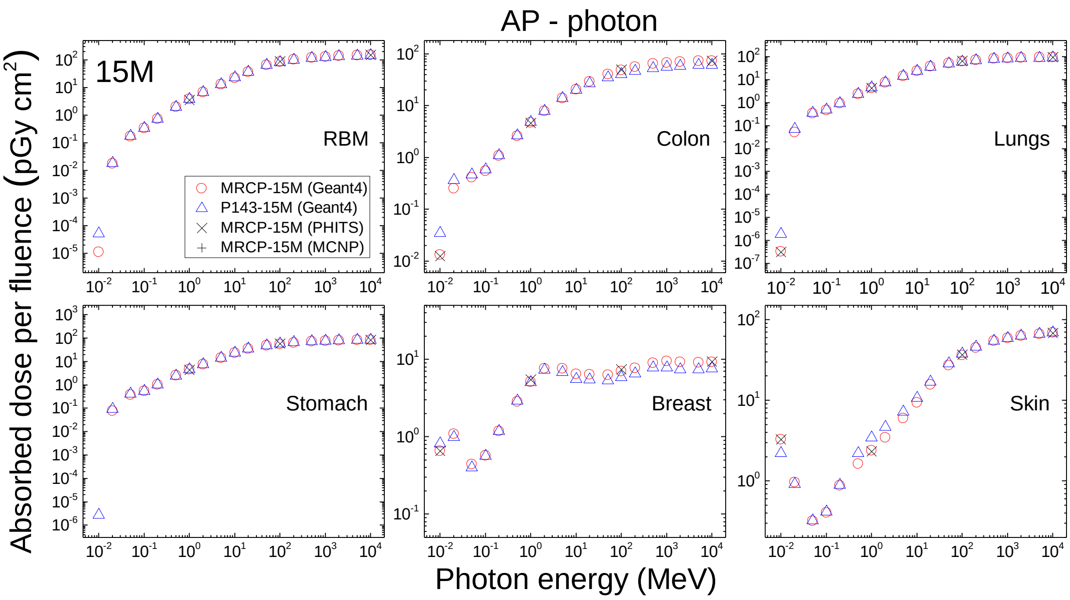

Fig. H.5. Absorbed dose per fluence (pGy cm^2) to the red bone marrow (RBM), colon, lungs, stomach, breast and skin in the antero-posterior (AP) irradiation geometry for photon exposures calculated with the 15-year-old male mesh-type reference computational phantom (MRCP), along with the values calculated with the P143 15-year-old male phantom.

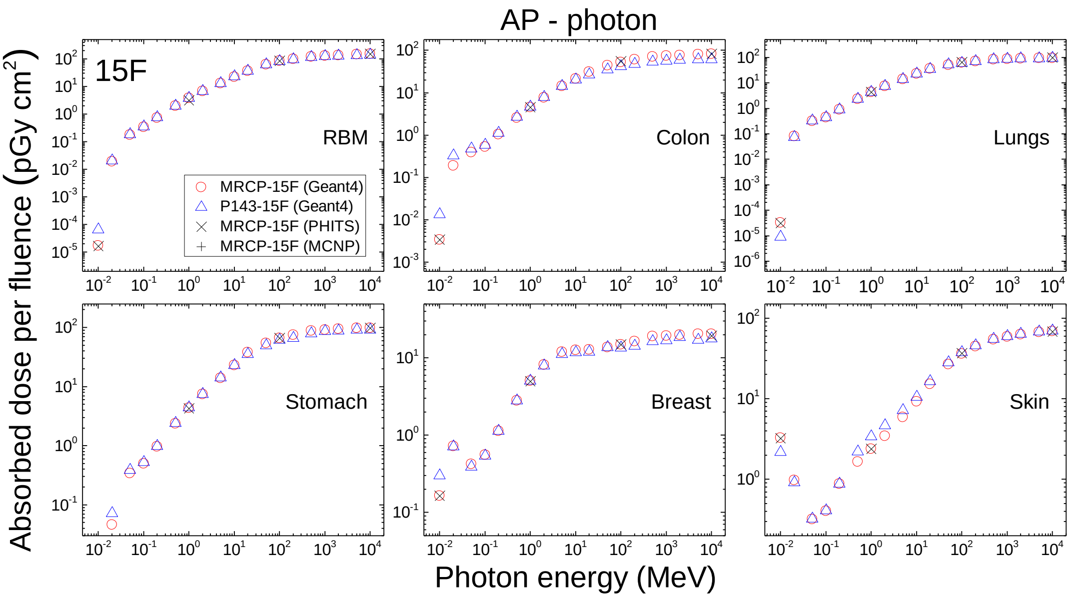

Fig. H.6. Absorbed dose per fluence (pGy cm^2) to the red bone marrow (RBM), colon, lungs, stomach, breast and skin in the antero-posterior (AP) irradiation geometry for photon exposures calculated with the 15-year-old female mesh-type reference computational phantom (MRCP), along with the values calculated with the P143 15-year-old female phantom.

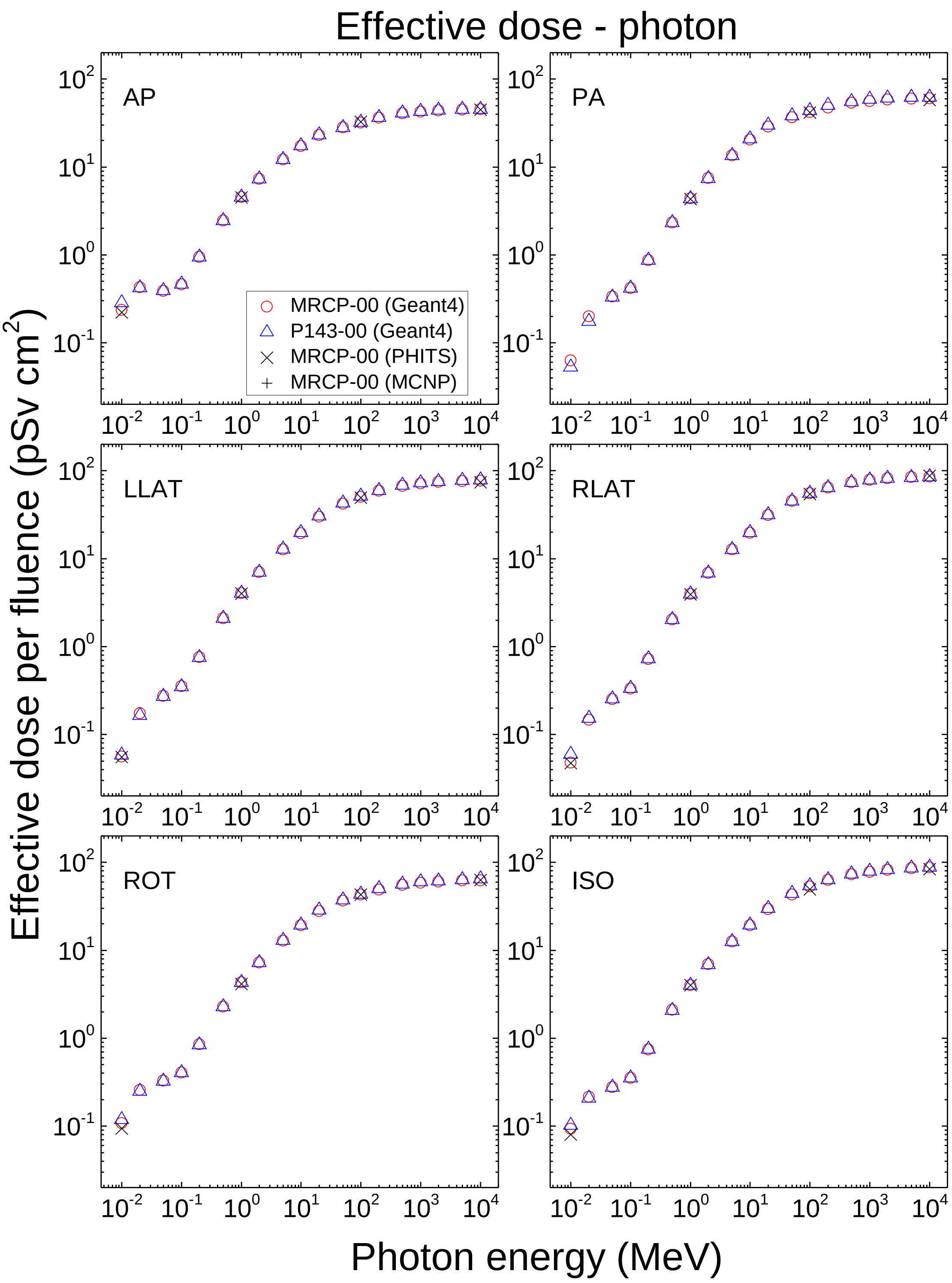

Fig. H.7. Effective dose per fluence (pSv cm^2) for photon exposures calculated with the newborn mesh-type reference computational phantoms (MRCPs), along with the values calculated with the P143 newborn phantoms.

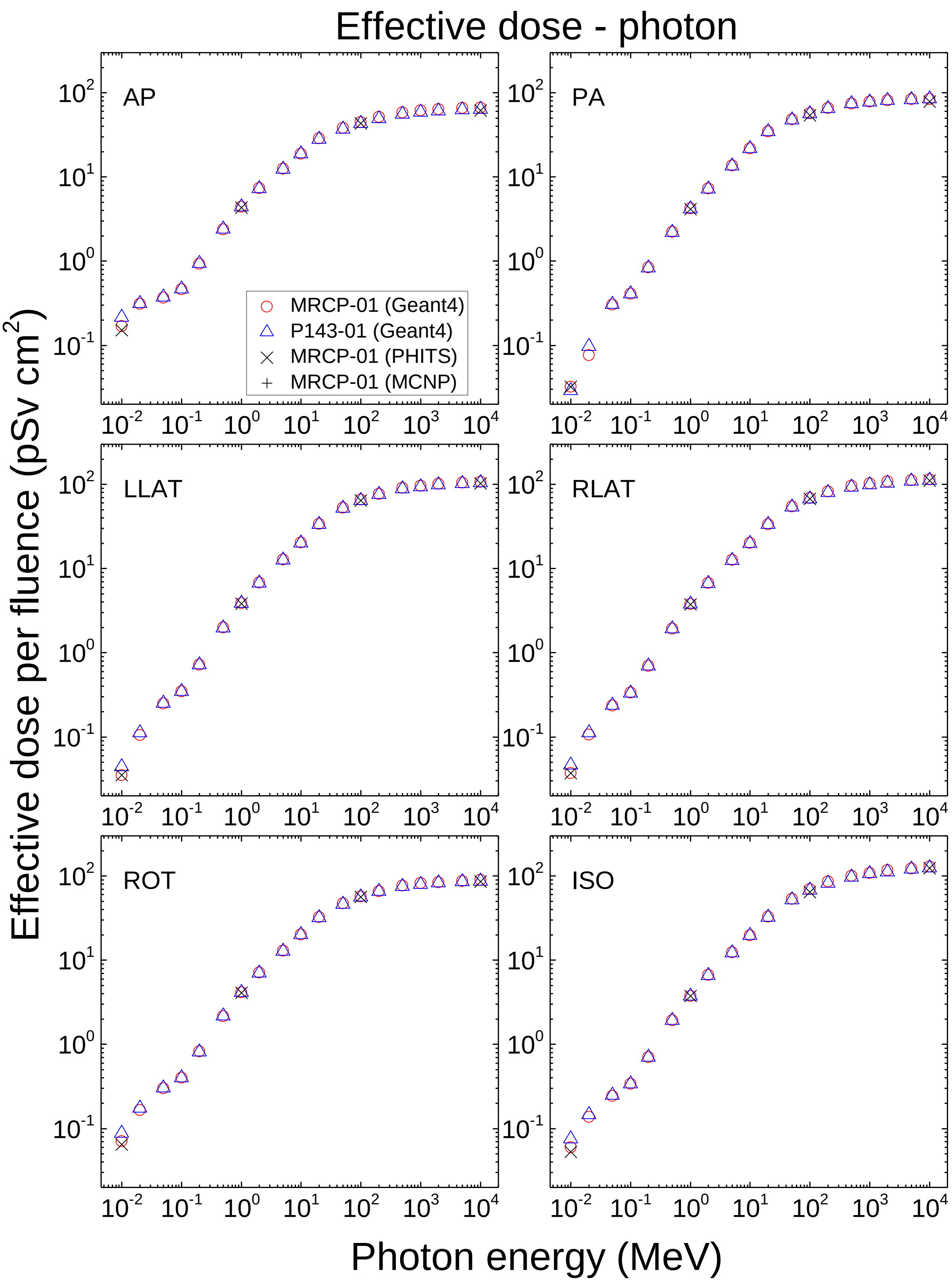

Fig. H.8. Effective dose per fluence (pSv cm^2) for photon exposures calculated with the 1-year-old mesh-type reference computational phantoms (MRCPs), along with the values calculated with the P143 1-year-old phantoms.

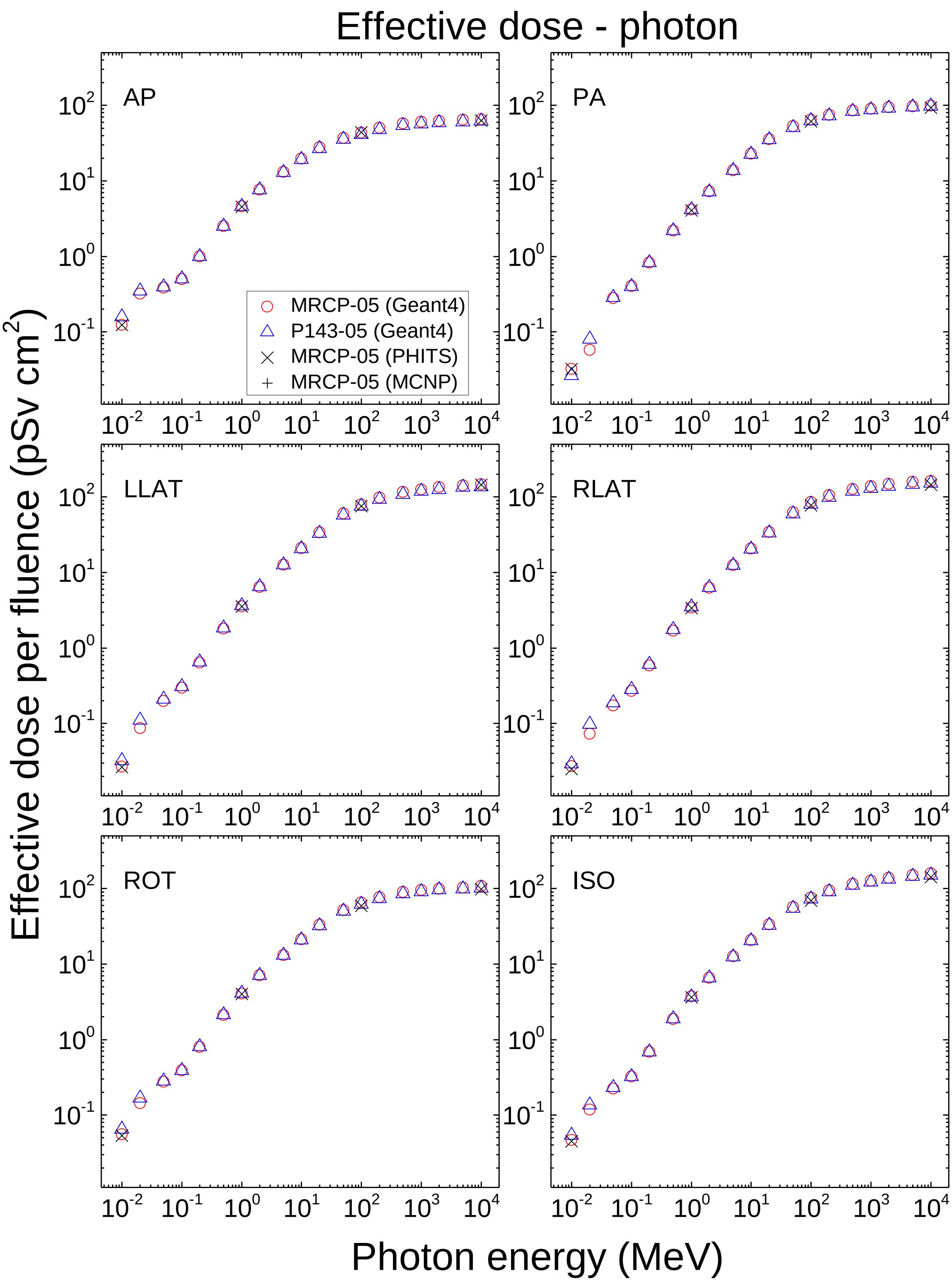

2418 Fig. H.9. Effective dose per fluence (pSv cm^2) for photon exposures calculated with the 5-year-
2419 old mesh-type reference computational phantoms (MRCPs), along with the values calculated
2420 with the P143 5-year-old phantoms.

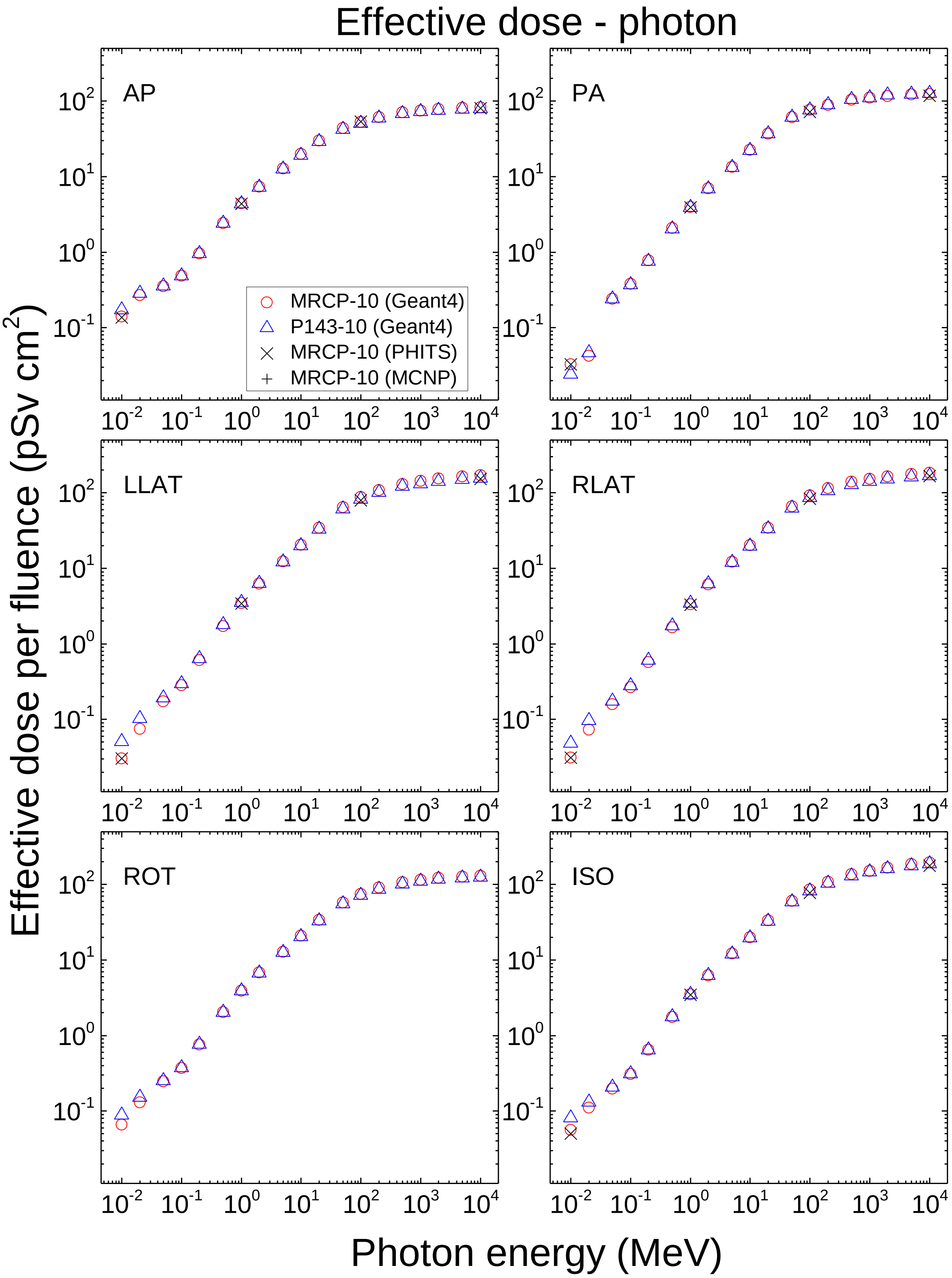

Fig. H.10. Effective dose per fluence (pSv cm^2) for photon exposures calculated with the 10-year-old mesh-type reference computational phantoms (MRCPs), along with the values calculated with the P143 10-year-old phantoms.

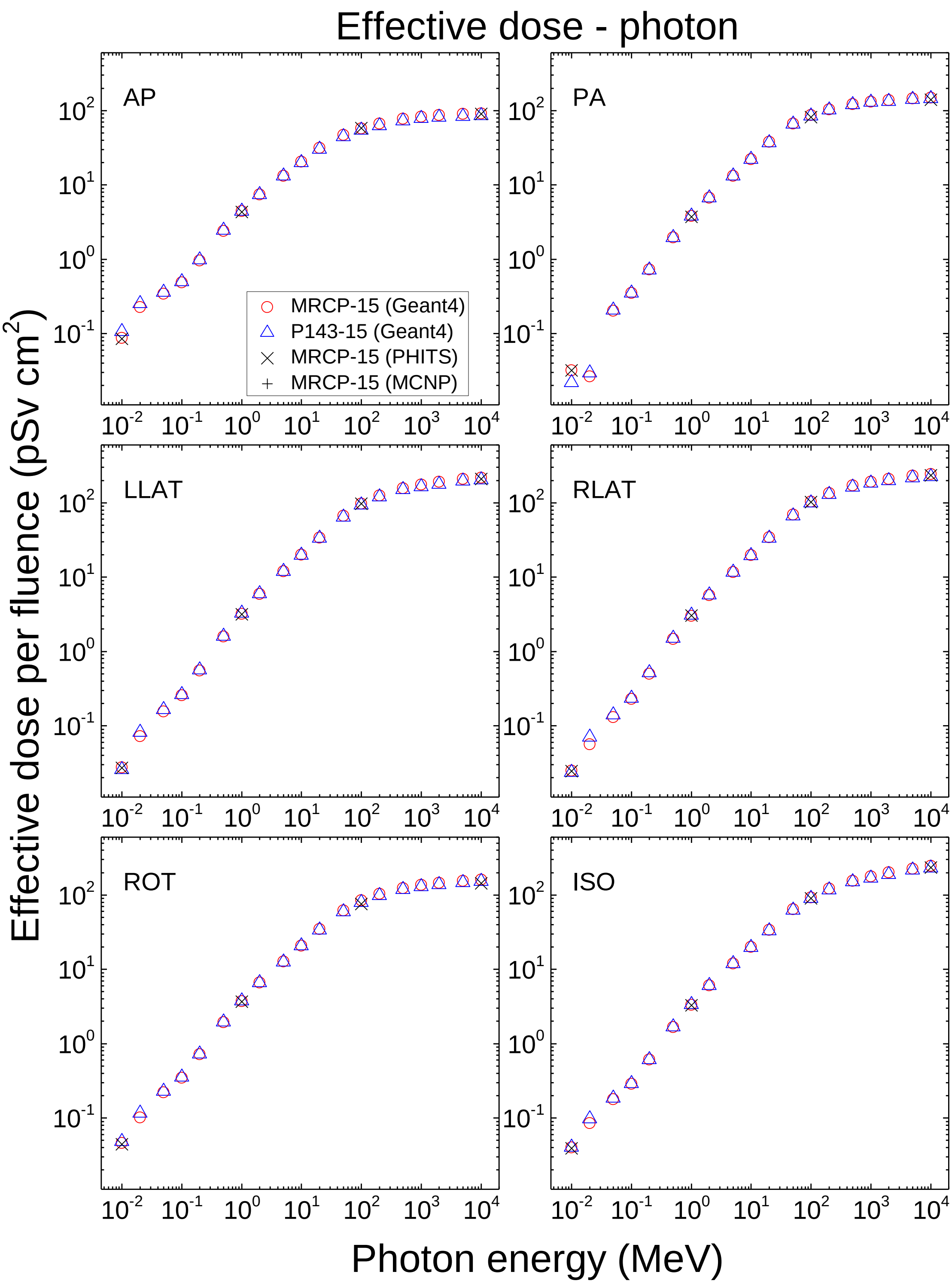

2428 Fig. H.11. Effective dose per fluence (pSv cm^2) for photon exposures calculated with the 15-
2429 year-old mesh-type reference computational phantoms (MRCPs), along with the values
2430 calculated with the P143 15-year-old phantoms.

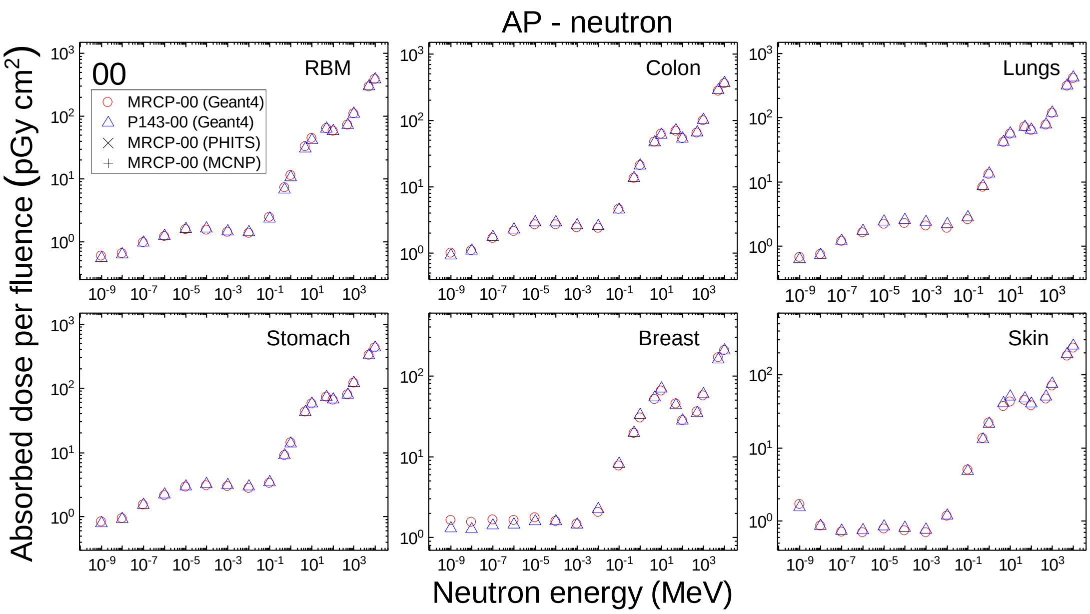

Fig. H.12. Absorbed dose per fluence (pGy cm^2) to the red bone marrow (RBM), colon, lungs, stomach, breast and skin in the antero-posterior (AP) irradiation geometry for neutron exposures calculated with the newborn mesh-type reference computational phantoms (MRCPs), along with the values calculated with the P143 newborn phantoms. The values shown were averaged for the male and female phantoms.

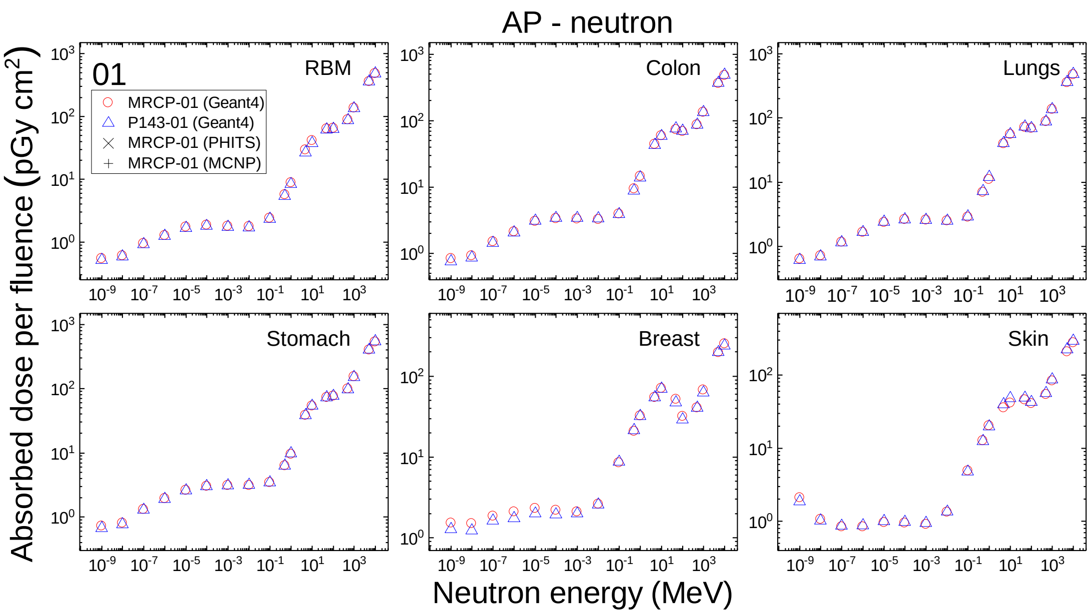

Fig. H.13. Absorbed dose per fluence (pGy cm^2) to the red bone marrow (RBM), colon, lungs, stomach, breast and skin in the antero-posterior (AP) irradiation geometry for neutron exposures calculated with the 1-year-old mesh-type reference computational phantoms (MRCPs), along with the values calculated with the P143 1-year-old phantoms. The values shown were averaged for the male and female phantoms.

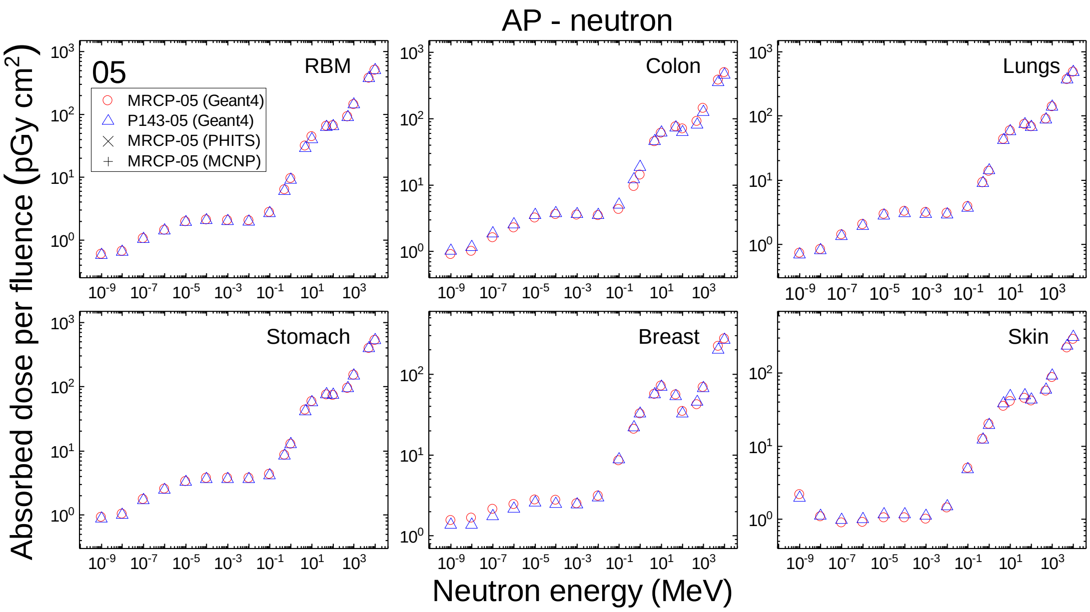

Fig. H.14. Absorbed dose per fluence (pGy cm^2) to the red bone marrow (RBM), colon, lungs, stomach, breast and skin in the antero-posterior (AP) irradiation geometry for neutron exposures calculated with the 5-year-old mesh-type reference computational phantoms (MRCPs), along with the values calculated with the P143 5-year-old phantoms. The values shown were averaged for the male and female phantoms.

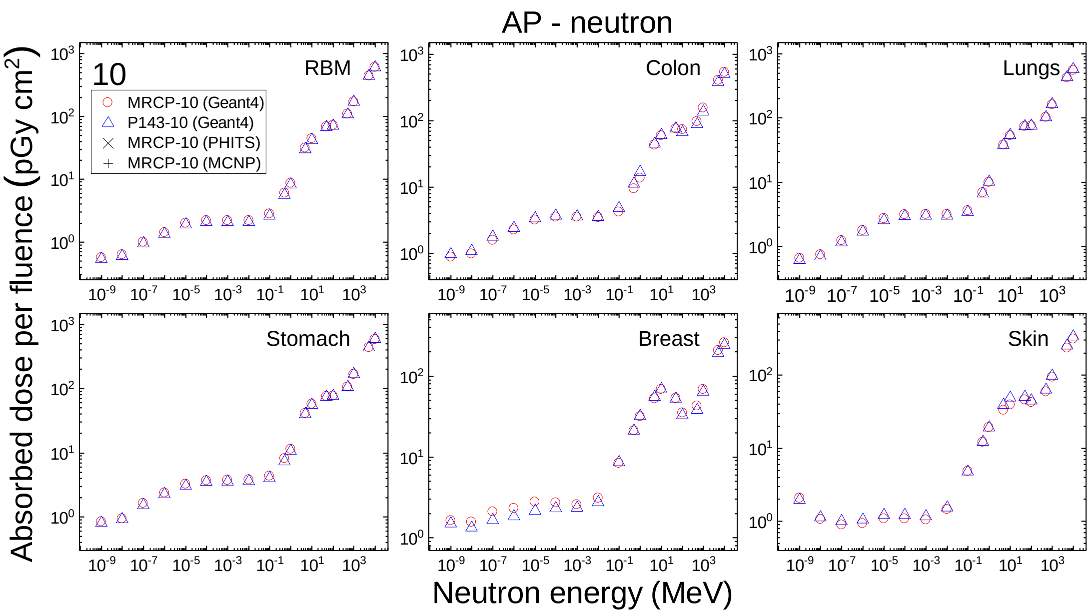

Fig. H.15. Absorbed dose per fluence (pGy cm^2) to the red bone marrow (RBM), colon, lungs, stomach, breast and skin in the antero-posterior (AP) irradiation geometry for neutron exposures calculated with the 10-year-old mesh-type reference computational phantoms (MRCPs), along with the values calculated with the P143 10-year-old phantoms. The values shown were averaged for the male and female phantoms.

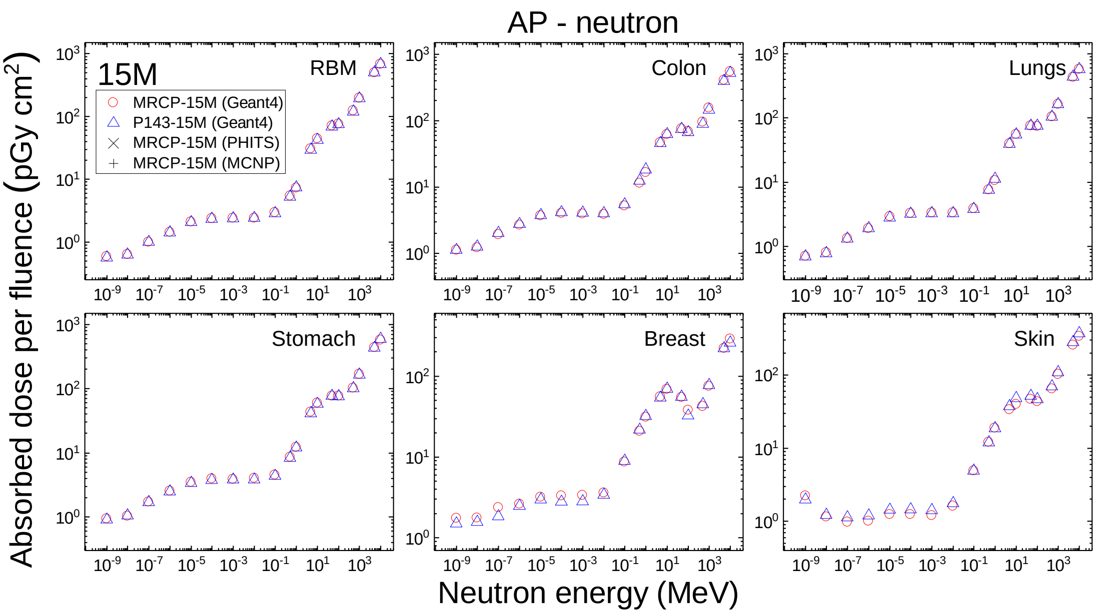

Fig. H.16. Absorbed dose per fluence (pGy cm^2) to the red bone marrow (RBM), colon, lungs, stomach, breast and skin in the antero-posterior (AP) irradiation geometry for neutron exposures calculated with the 15-year-old male mesh-type reference computational phantom (MRCP), along with the values calculated with the P143 15-year-old male phantom.

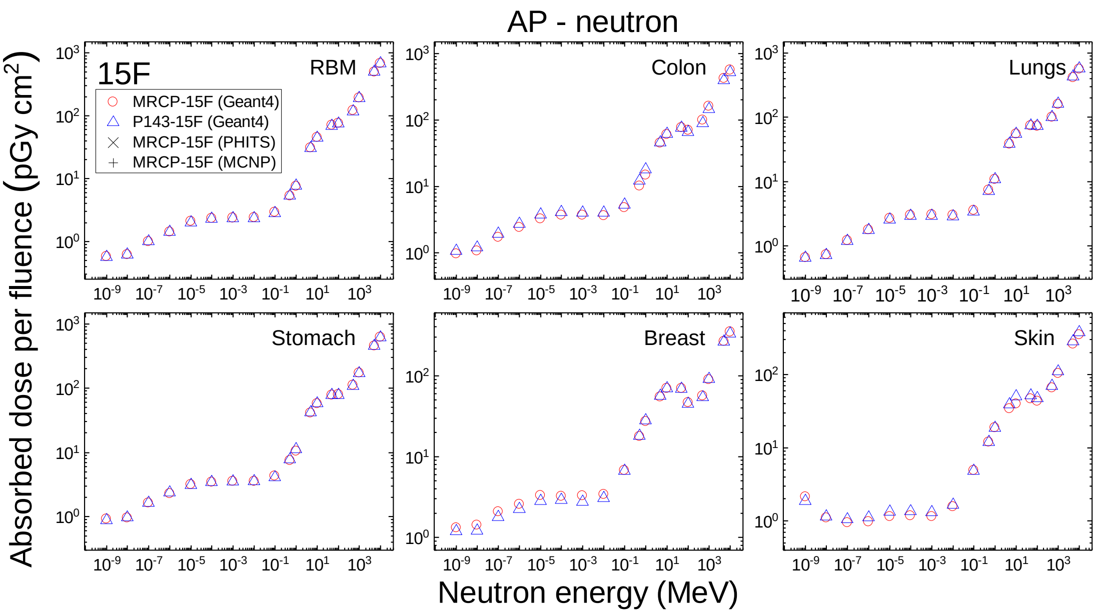

Fig. H.17. Absorbed dose per fluence (pGy cm^2) to the red bone marrow (RBM), colon, lungs, stomach, breast and skin in the antero-posterior (AP) irradiation geometry for neutron exposures calculated with the 15-year-old female mesh-type reference computational phantom (MRCP), along with the values calculated with the P143 15-year-old female phantom.

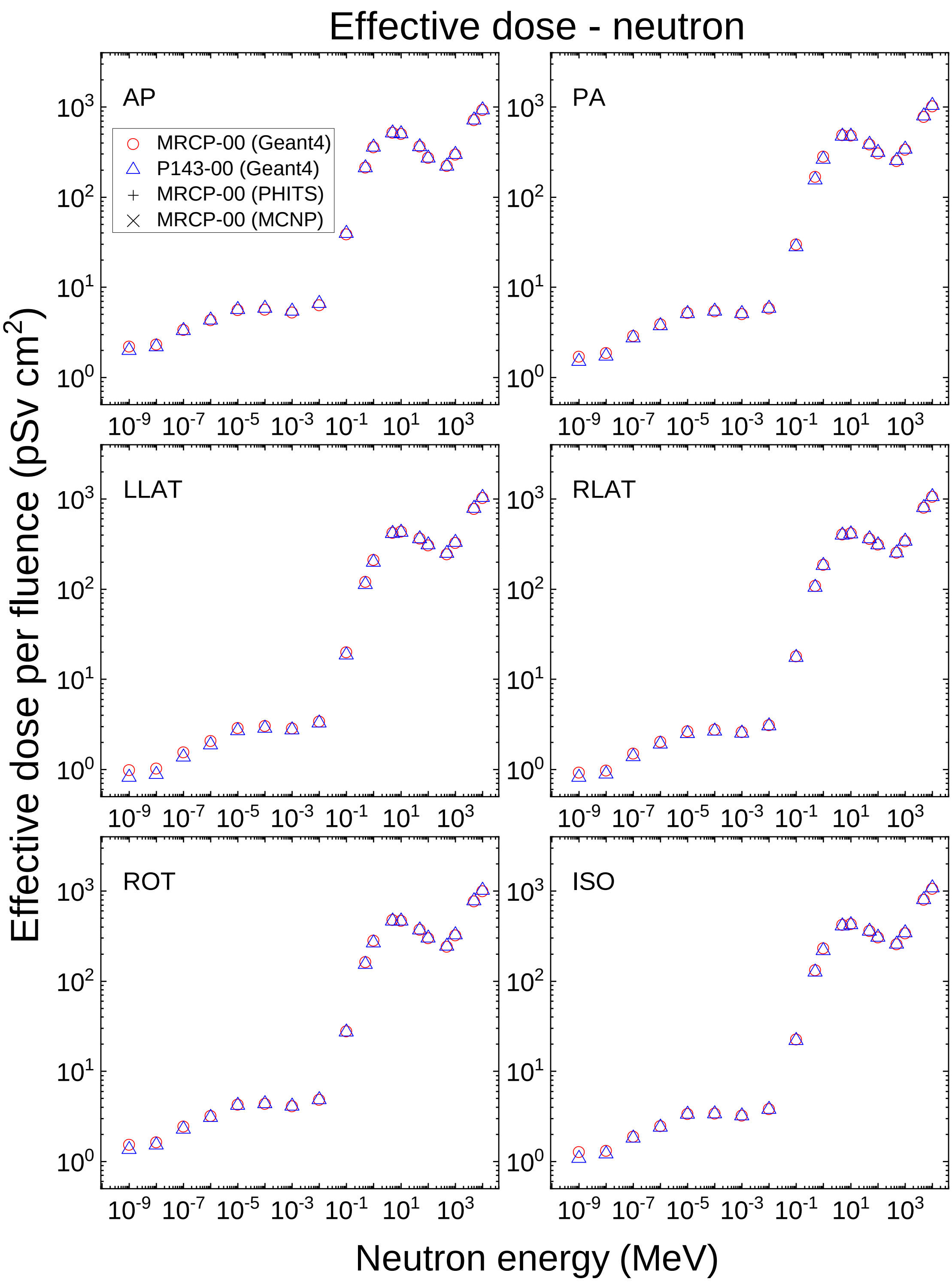

Fig. H.18. Effective dose per fluence (pSv cm^2) for neutron exposures calculated with the newborn mesh-type reference computational phantoms (MRCPs), along with the values calculated with the P143 newborn phantoms.

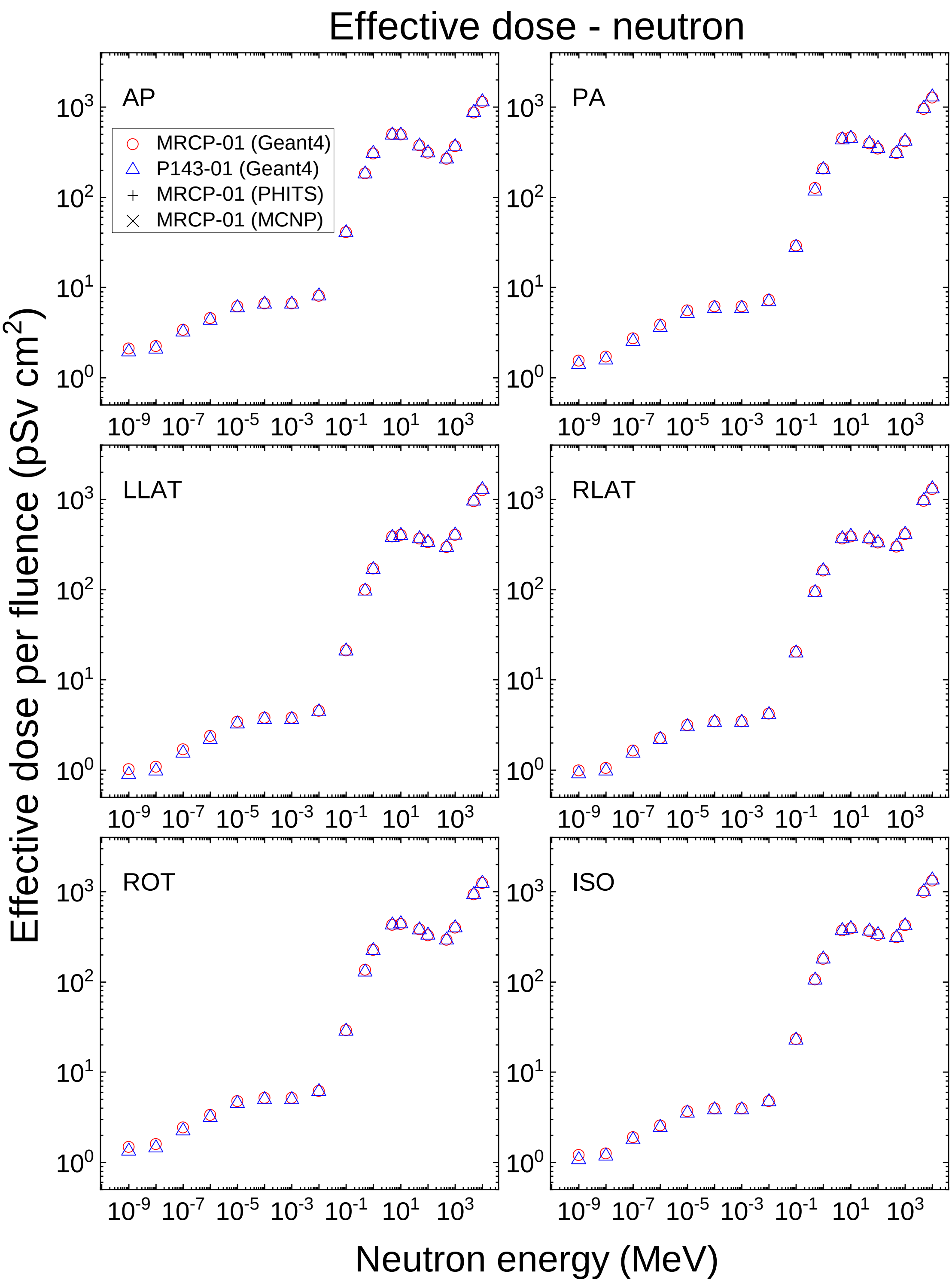

2475 Fig. H.19. Effective dose per fluence (pSv cm^2) for neutron exposures calculated with the 1-
2476 year-old mesh-type reference computational phantoms (MRCPs), along with the values
2477 calculated with the P143 1-year-old phantoms.

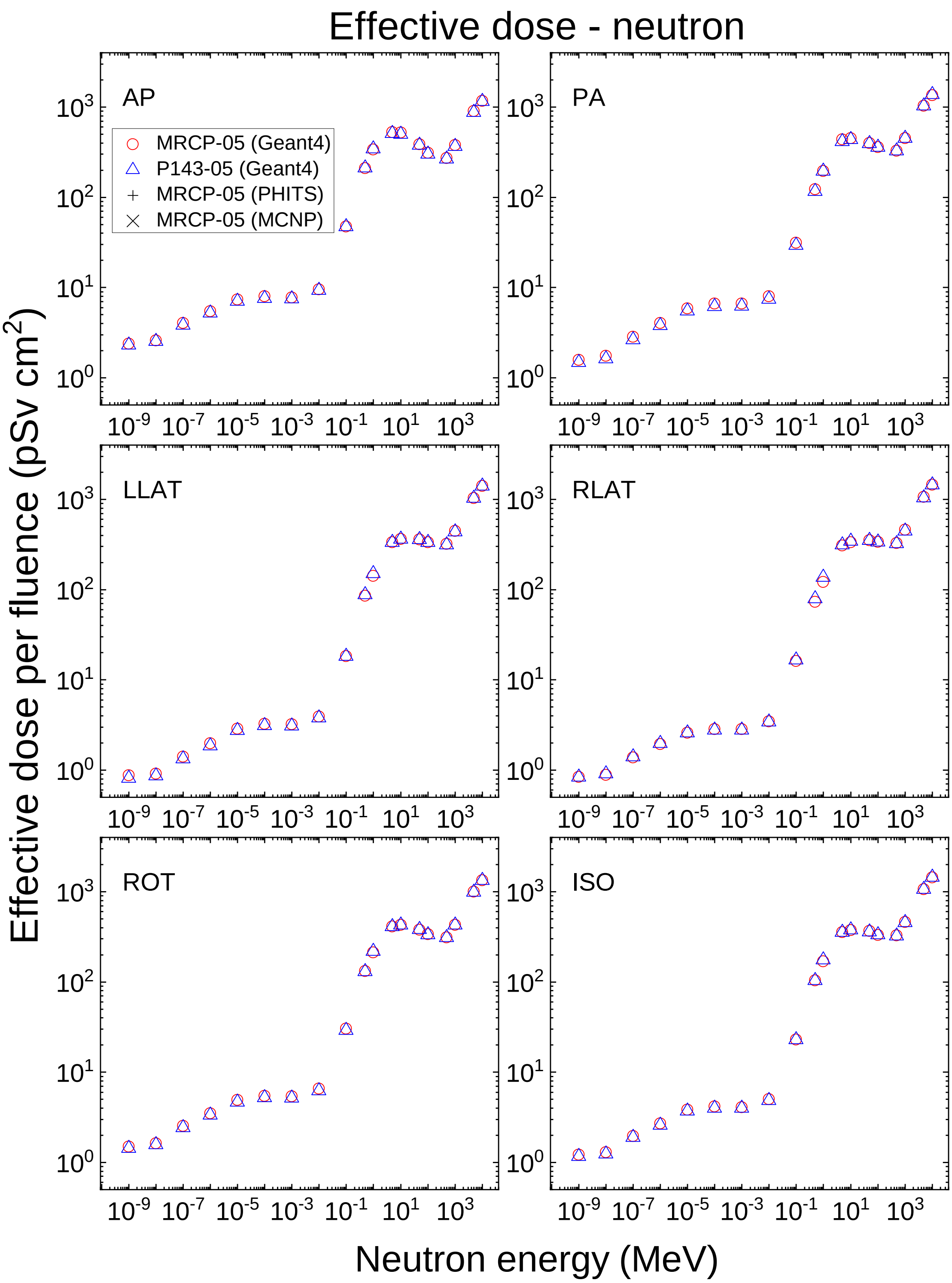

2479
2480 Fig. H.20. Effective dose per fluence (pSv cm^2) for neutron exposures calculated with the 5-
2481 year-old mesh-type reference computational phantoms (MRCPs), along with the values
2482 calculated with the P143 5-year-old phantoms.
2483

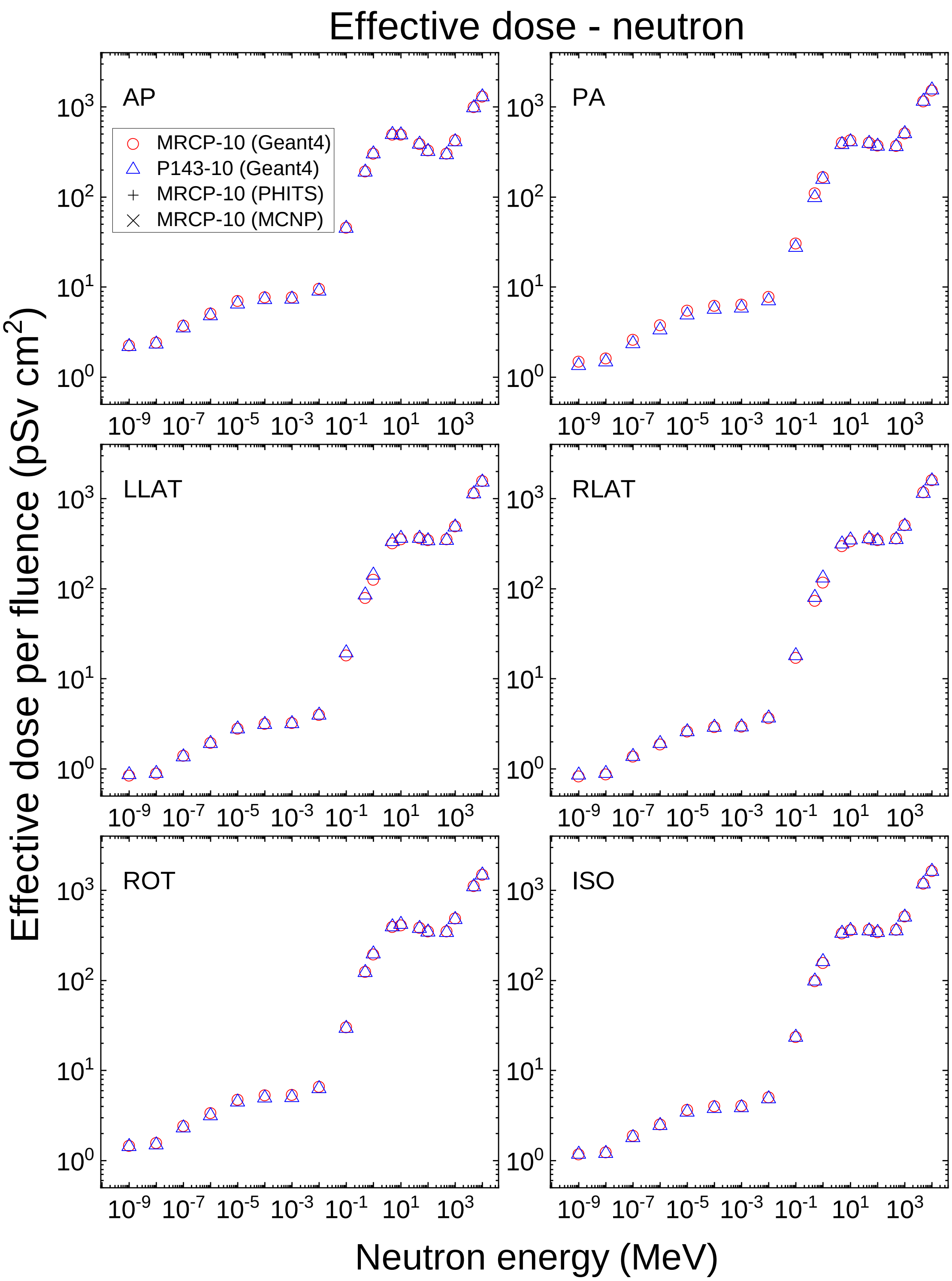

Fig. H.21. Effective dose per fluence (pSv cm^2) for neutron exposures calculated with the 10-year-old mesh-type reference computational phantoms (MRCPs), along with the values calculated with the P143 10-year-old phantoms.

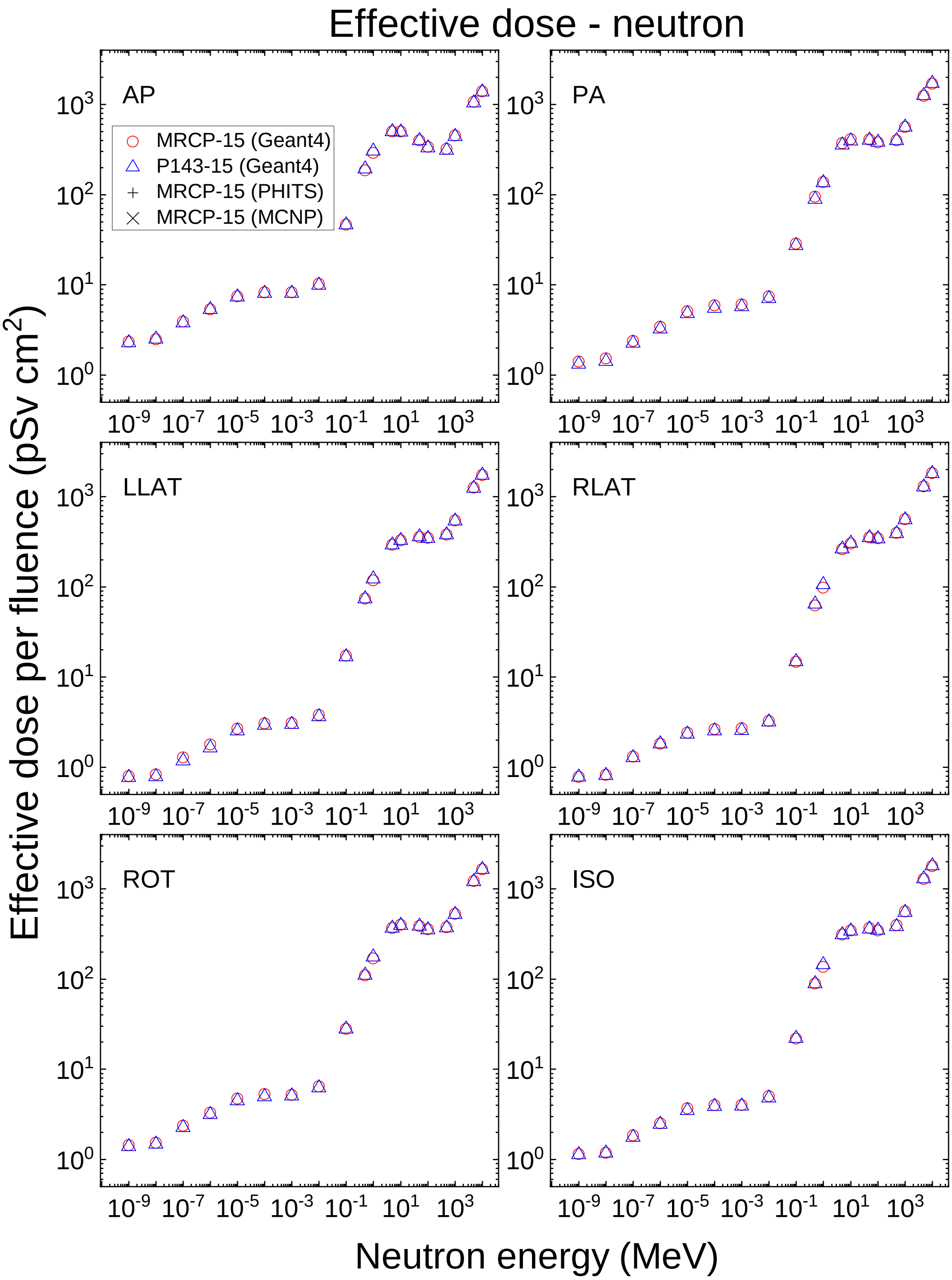

Fig. H.22. Effective dose per fluence (pSv cm^2) for neutron exposures calculated with the 15-year-old mesh-type reference computational phantoms (MRCPs), along with the values calculated with the P143 15-year-old phantoms.

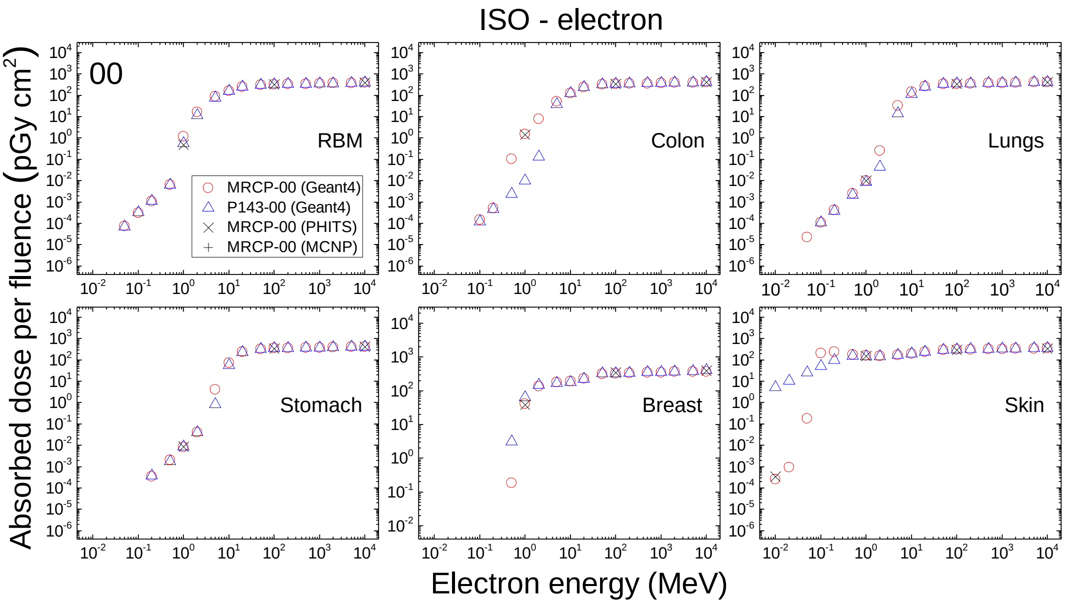

Fig. H.23. Absorbed dose per fluence (pGy cm^2) to the red bone marrow (RBM), colon, lungs, stomach, breast and skin in the isotropic (ISO) irradiation geometry for electron exposures calculated with the newborn mesh-type reference computational phantoms (MRCPs), along with the values calculated with the P143 newborn phantoms. The values shown were averaged for the male and female phantoms.

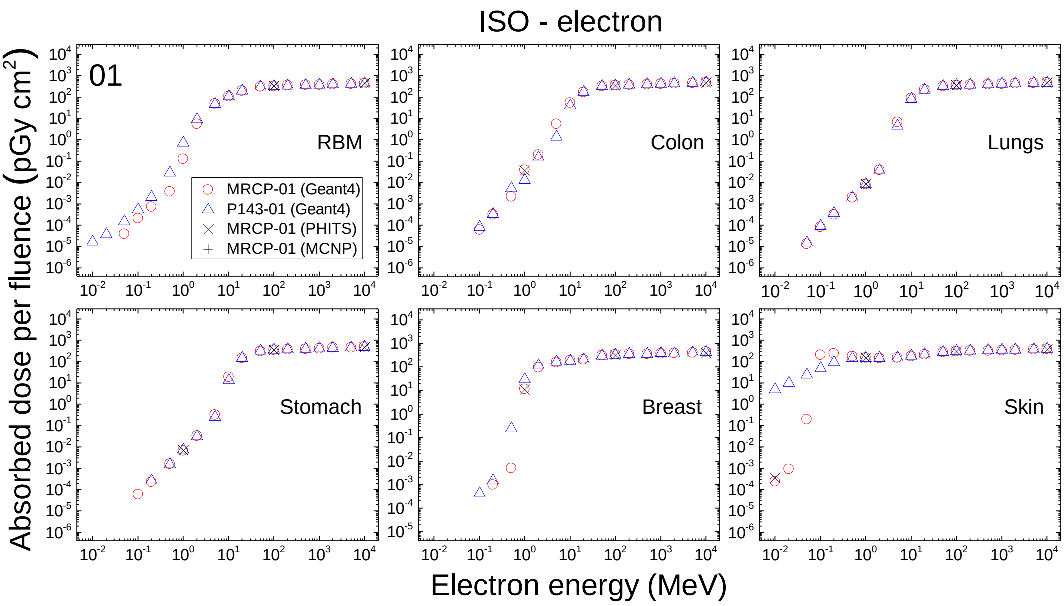

Fig. H.24. Absorbed dose per fluence (pGy cm^2) to the red bone marrow (RBM), colon, lungs, stomach, breast and skin in the isotropic (ISO) irradiation geometry for electron exposures calculated with the 1-year-old mesh-type reference computational phantoms (MRCPs), along with the values calculated with the P143 1-year-old phantoms. The values shown were averaged for the male and female phantoms.

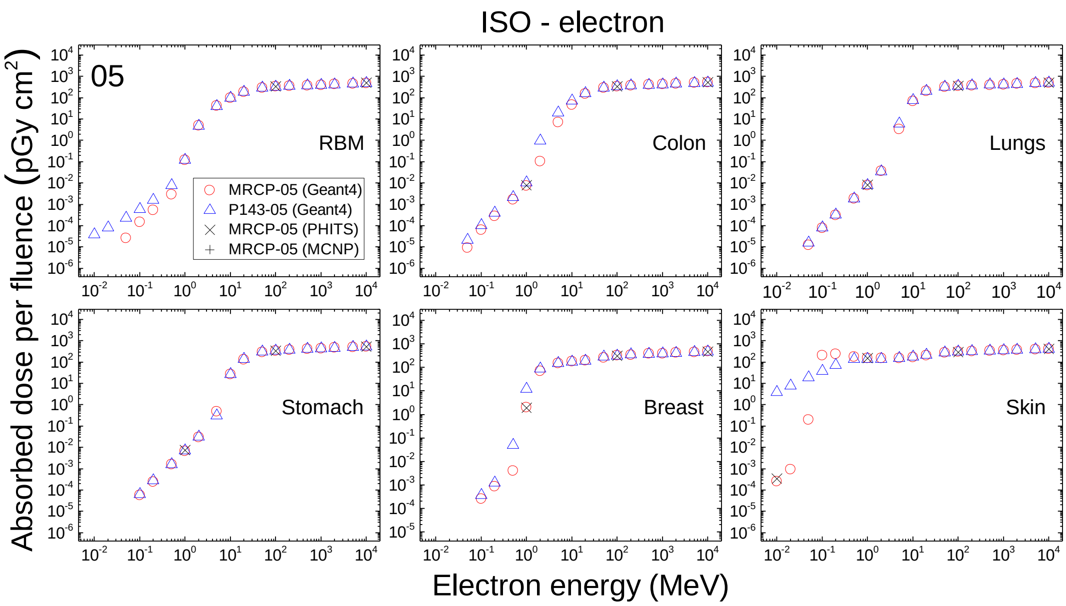

Fig. H.25. Absorbed dose per fluence (pGy cm^2) to the red bone marrow (RBM), colon, lungs, stomach, breast and skin in the isotropic (ISO) irradiation geometry for electron exposures calculated with the 5-year-old mesh-type reference computational phantoms (MRCPs), along with the values calculated with the P143 5-year-old phantoms. The values shown were averaged for the male and female phantoms.

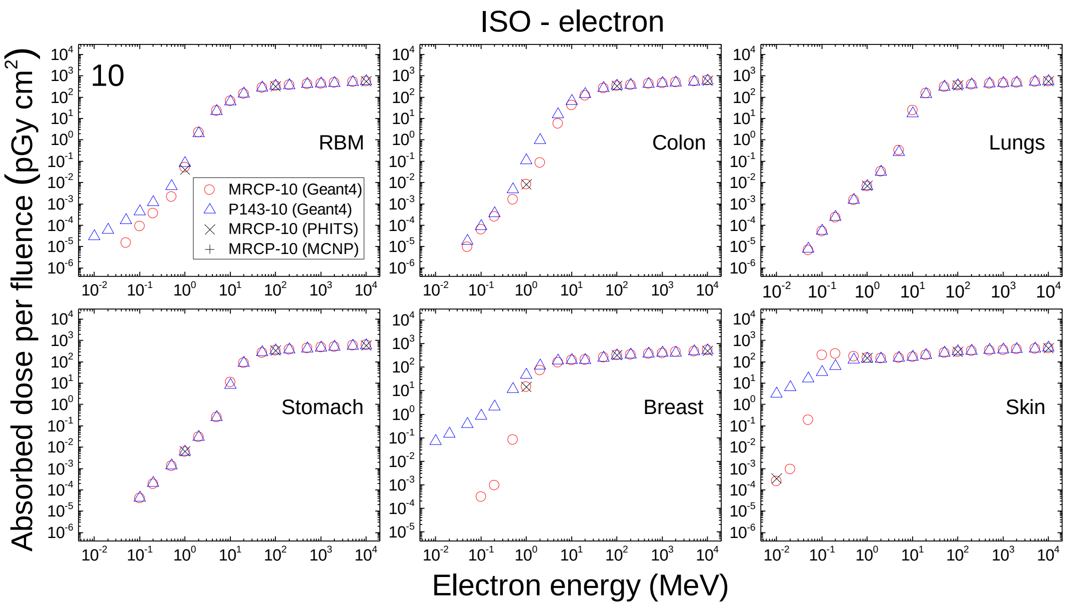

Fig. H.26. Absorbed dose per fluence (pGy cm^2) to the red bone marrow (RBM), colon, lungs, stomach, breast and skin in the isotropic (ISO) irradiation geometry for electron exposures calculated with the 10-year-old mesh-type reference computational phantoms (MRCPs), along with the values calculated with the P143 10-year-old phantoms. The values shown were averaged for the male and female phantoms.

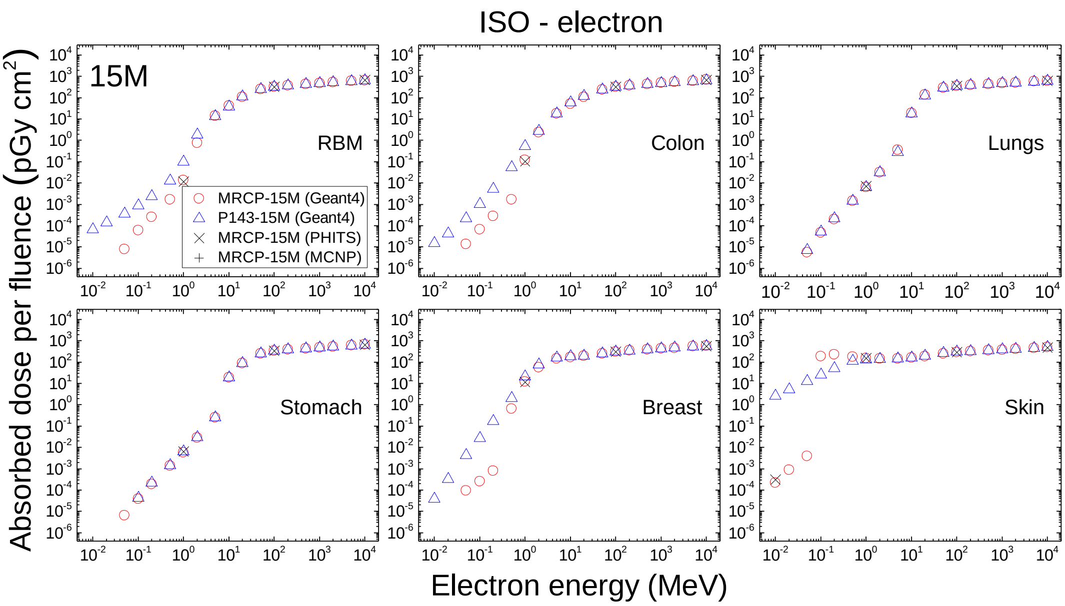

Fig. H.27. Absorbed dose per fluence (pGy cm^2) to the red bone marrow (RBM), colon, lungs, stomach, breast and skin in the isotropic (ISO) irradiation geometry for electron exposures calculated with the 15-year-old male mesh-type reference computational phantom (MRCP), along with the values calculated with the P143 15-year-old male phantom.

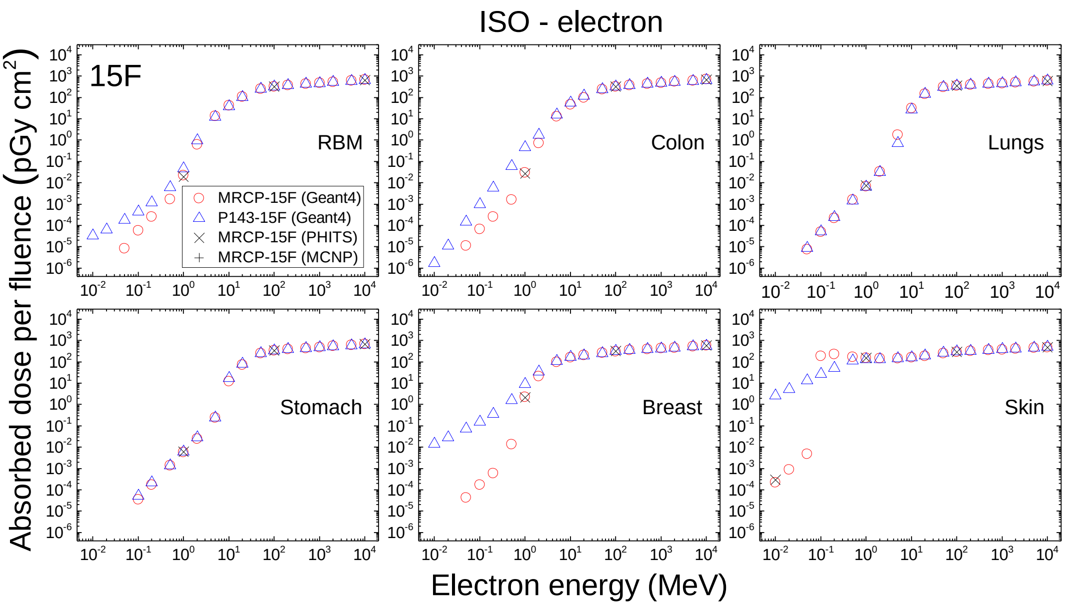

Fig. H.28. Absorbed dose per fluence (pGy cm^2) to the red bone marrow (RBM), colon, lungs, stomach, breast and skin in the isotropic (ISO) irradiation geometry for electron exposures calculated with the 15-year-old female mesh-type reference computational phantom (MRCP), along with the values calculated with the P143 15-year-old female phantom.

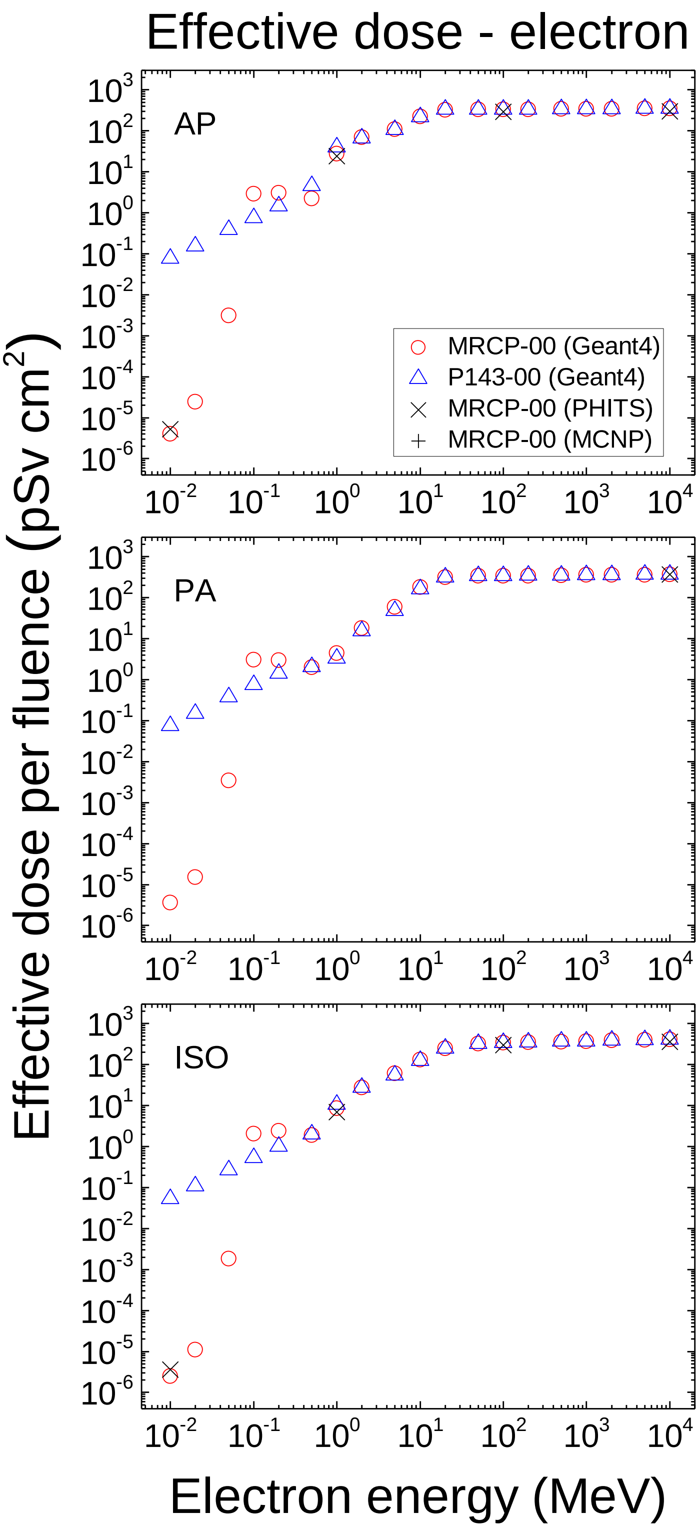

2531
2532 Fig. H.29. Effective dose per fluence (pSv cm^2) for electron exposures calculated with the
2533 newborn mesh-type reference computational phantoms (MRCPs), along with the values
2534 calculated with the P143 newborn phantoms.
2535

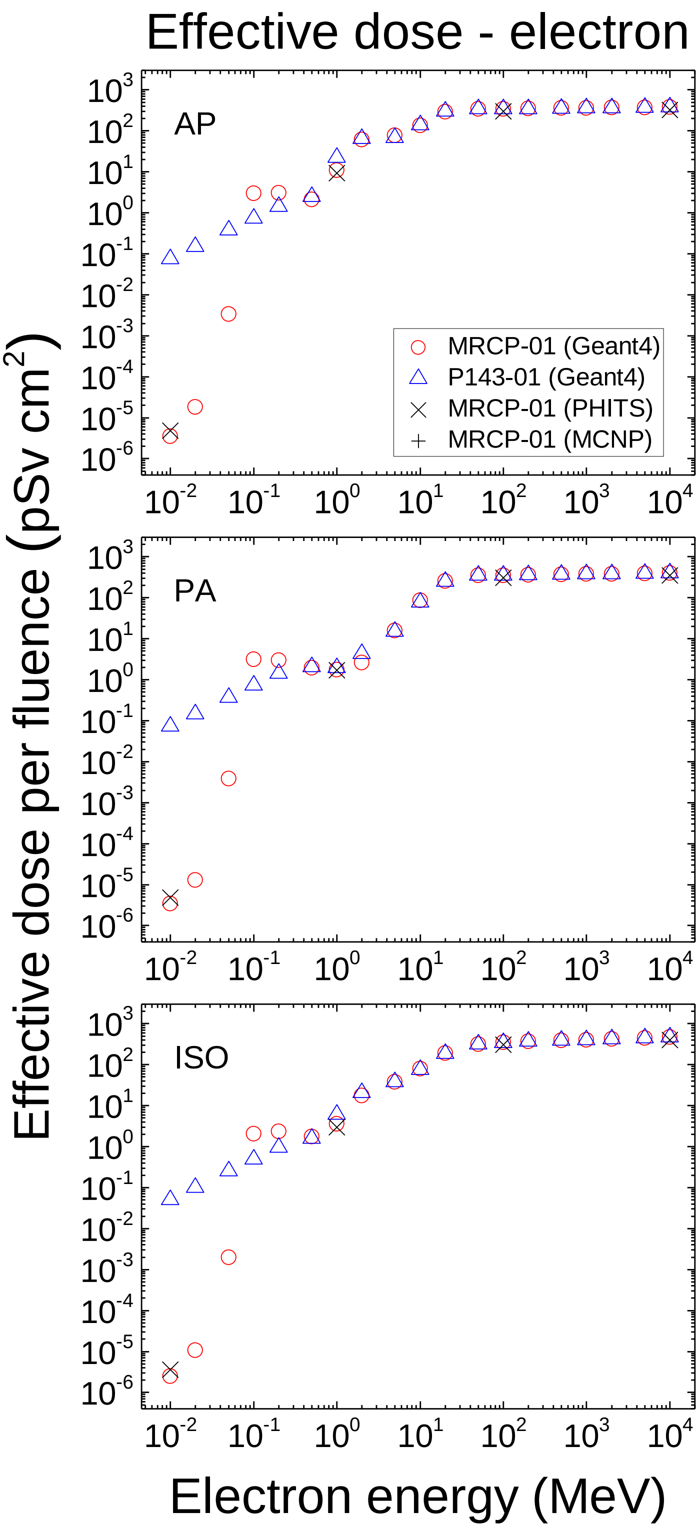

2536
2537 Fig. H.30. Effective dose per fluence (pSv cm^2) for electron exposures calculated with the 1-
2538 year-old mesh-type reference computational phantoms (MRCPs), along with the values
2539 calculated with the P143 1-year-old phantoms.
2540

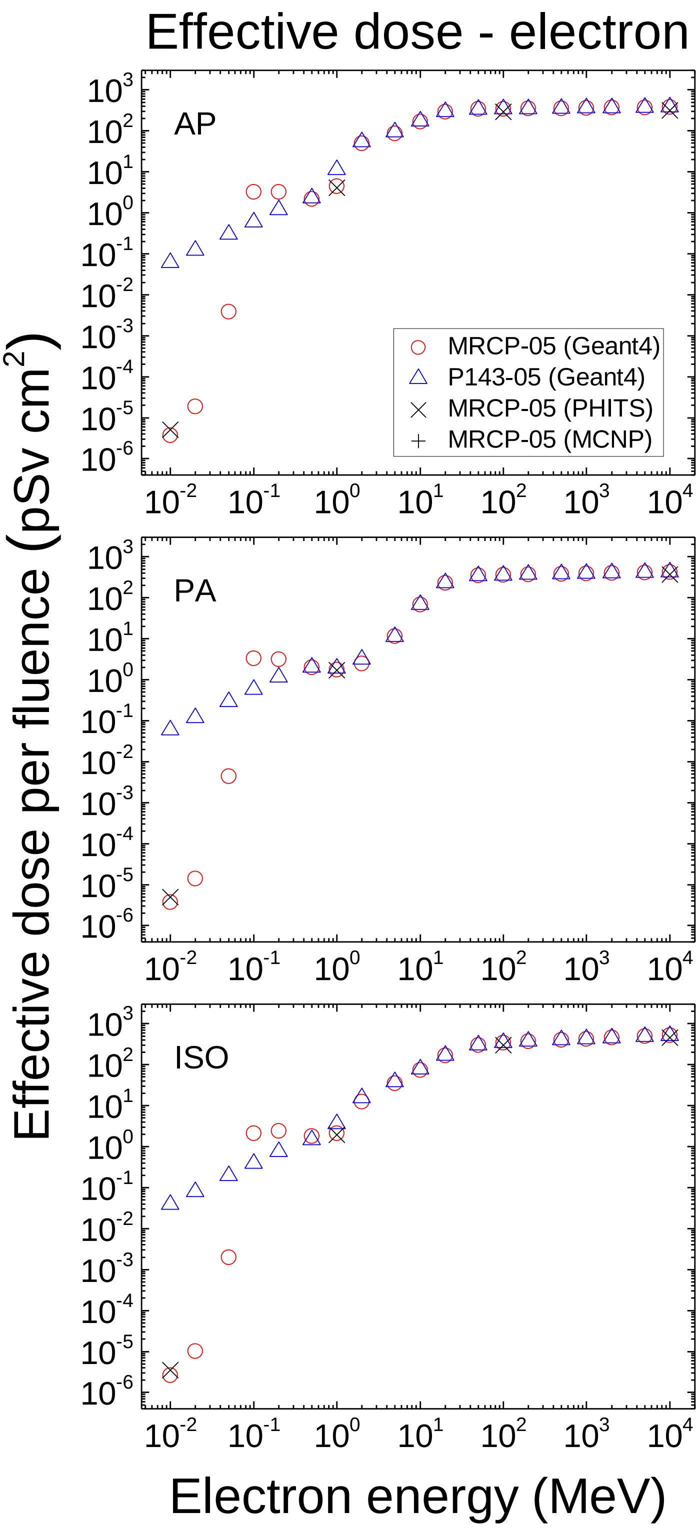

2541
2542 Fig. H.31. Effective dose per fluence (pSv cm^2) for electron exposures calculated with the 5-
2543 year-old mesh-type reference computational phantoms (MRCPs), along with the values
2544 calculated with the P143 5-year-old phantoms.
2545

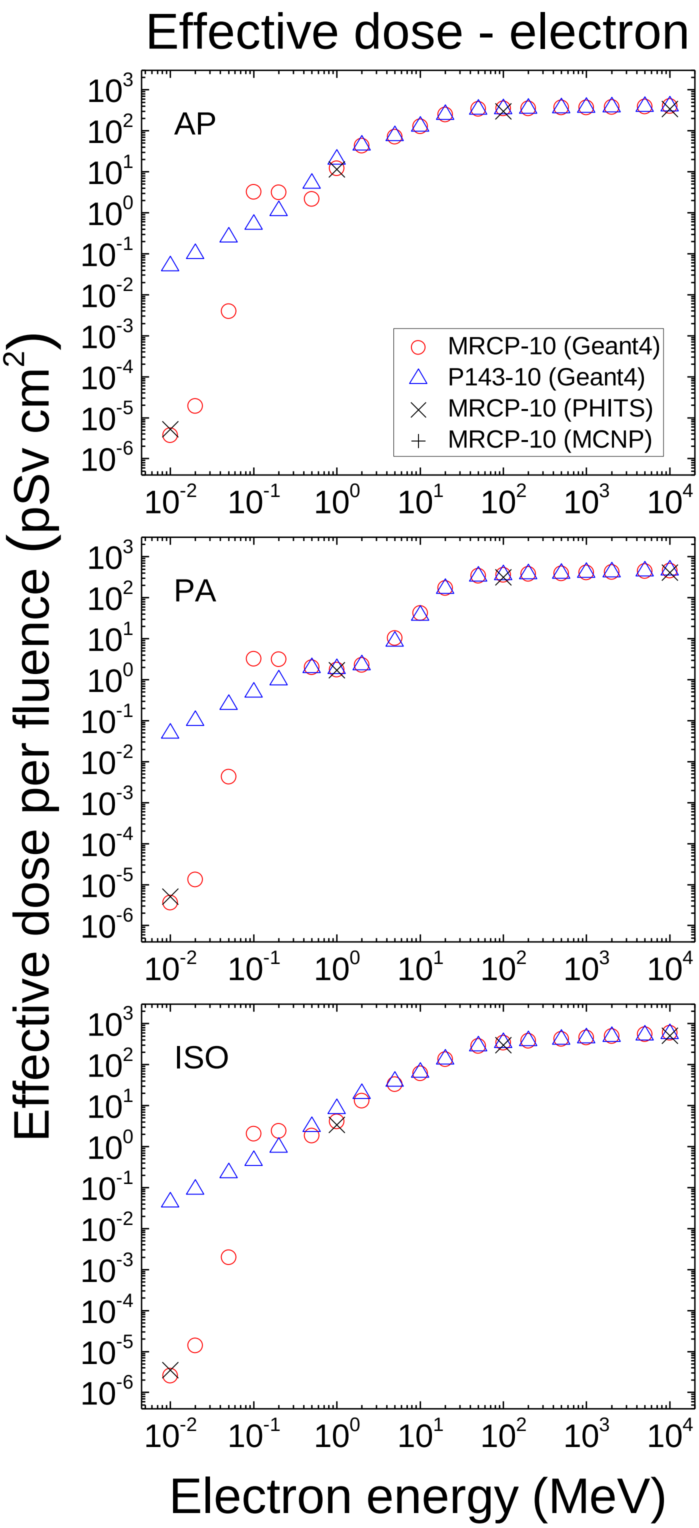

Fig. H.32. Effective dose per fluence (pSv cm^2) for electron exposures calculated with the 10-year-old mesh-type reference computational phantoms (MRCPs), along with the values calculated with the P143 10-year-old phantoms.

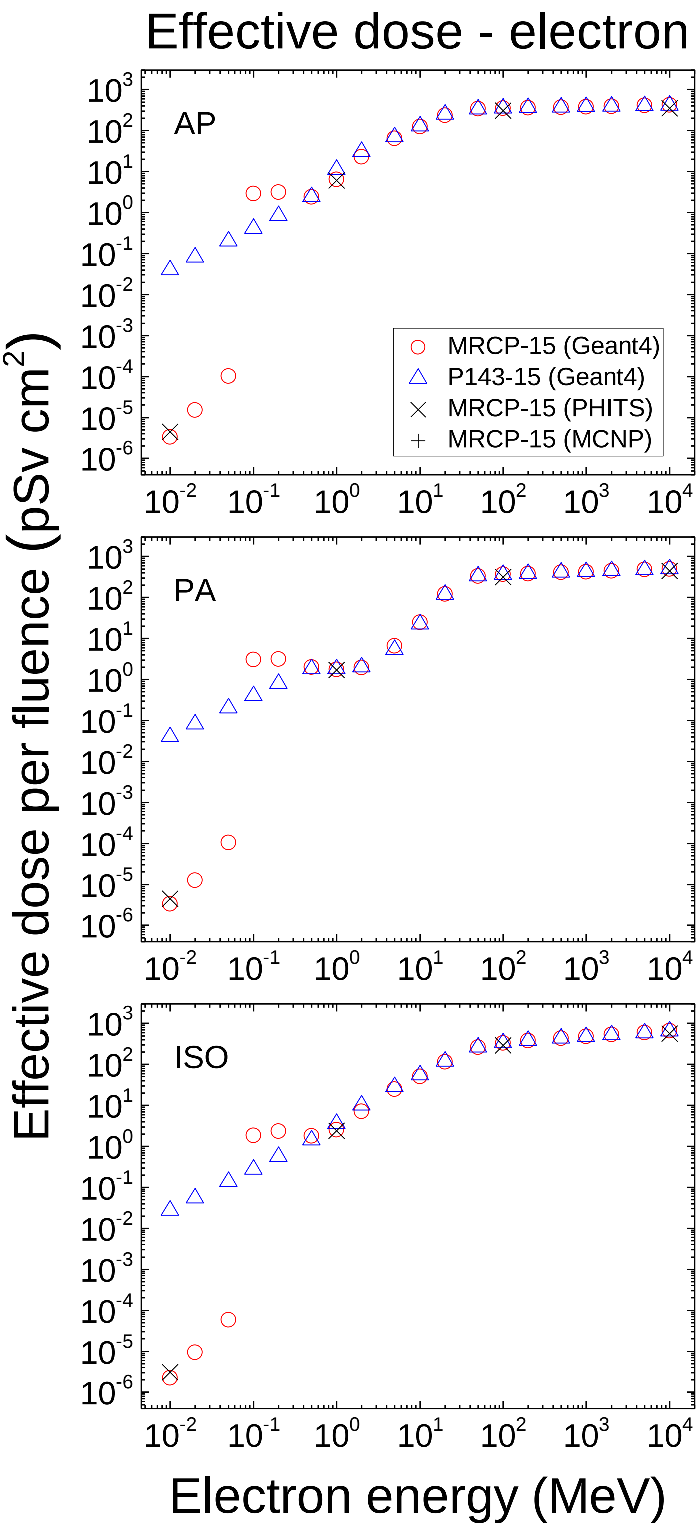

2551
2552 Fig. H.33. Effective dose per fluence (pSv cm^2) for electron exposures calculated with the 15-
2553 year-old mesh-type reference computational phantoms (MRCPs), along with the values
2554 calculated with the P143 15-year-old phantoms.
2555

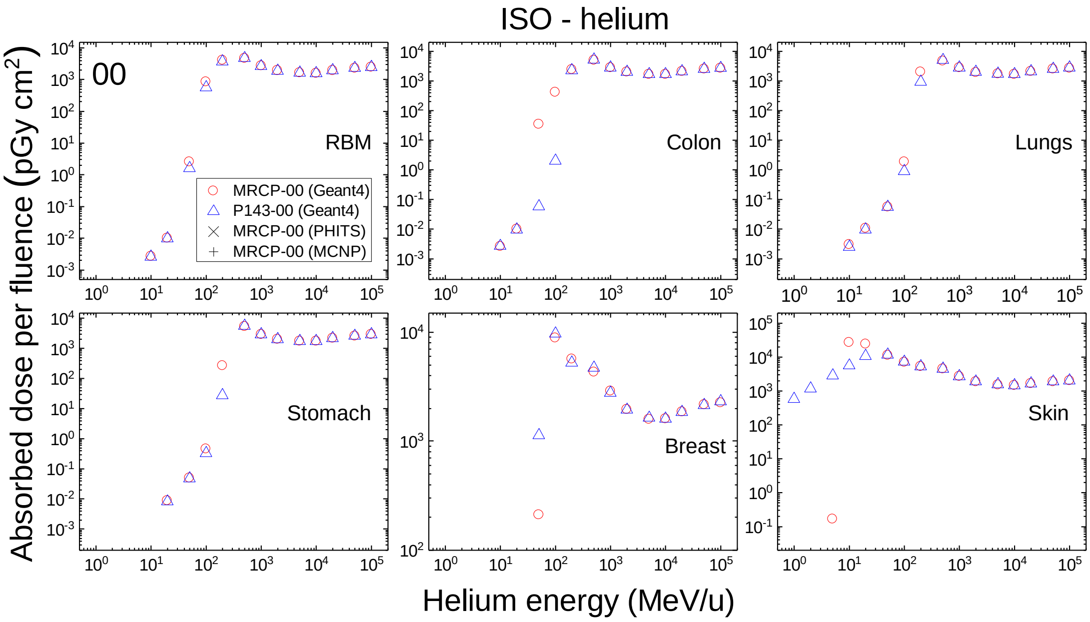

Fig. H.34. Absorbed dose per fluence (pGy cm^2) to the red bone marrow (RBM), colon, lungs, stomach, breast and skin in the isotropic (ISO) irradiation geometry for helium ion exposures calculated with the newborn mesh-type reference computational phantoms (MRCPs), along with the values calculated with the P143 newborn phantoms. The values shown were averaged for the male and female phantoms.

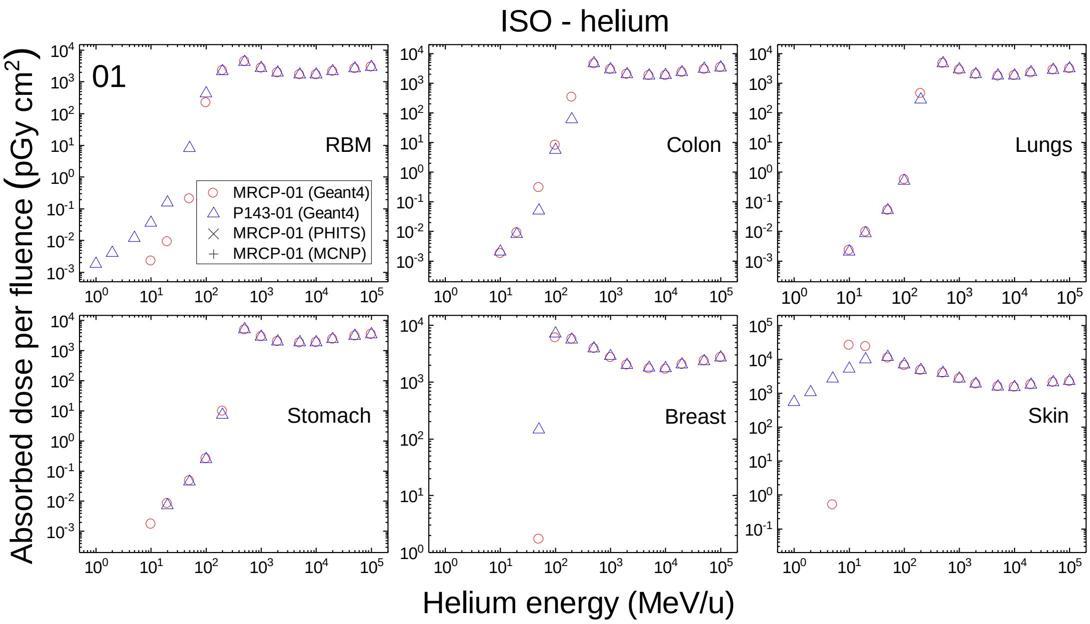

Fig. H.35. Absorbed dose per fluence (pGy cm^2) to the red bone marrow (RBM), colon, lungs, stomach, breast and skin in the isotropic (ISO) irradiation geometry for helium ion exposures calculated with the 1-year-old mesh-type reference computational phantoms (MRCPs), along with the values calculated with the P143 1-year-old phantoms. The values shown were averaged for the male and female phantoms.

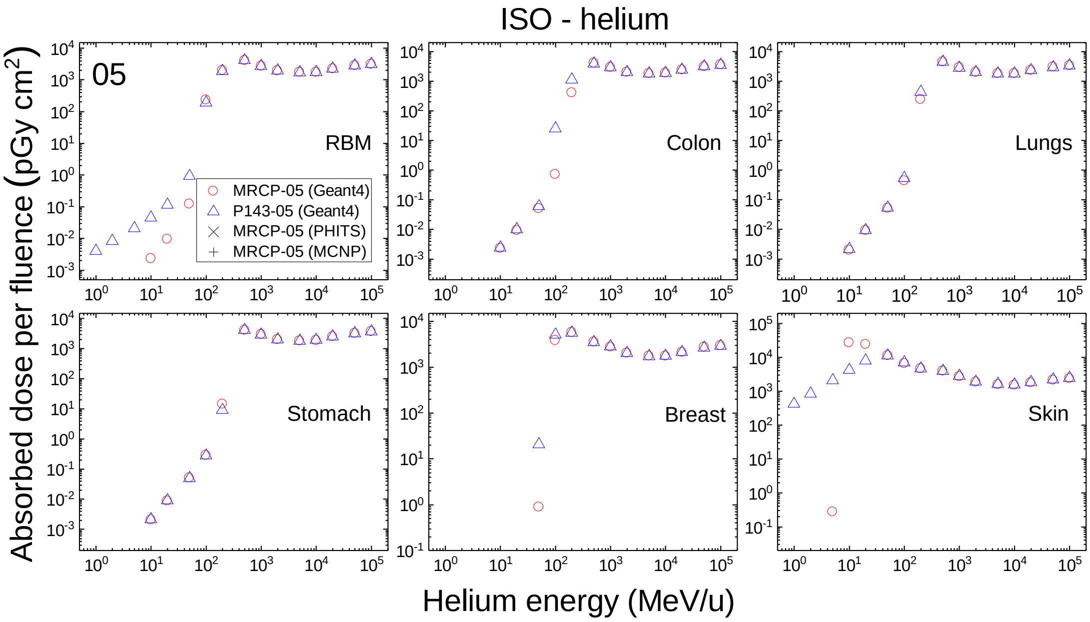

Fig. H.36. Absorbed dose per fluence (pGy cm^2) to the red bone marrow (RBM), colon, lungs, stomach, breast and skin in the isotropic (ISO) irradiation geometry for helium ion exposures calculated with the 5-year-old mesh-type reference computational phantoms (MRCPs), along with the values calculated with the P143 5-year-old phantoms. The values shown were averaged for the male and female phantoms.

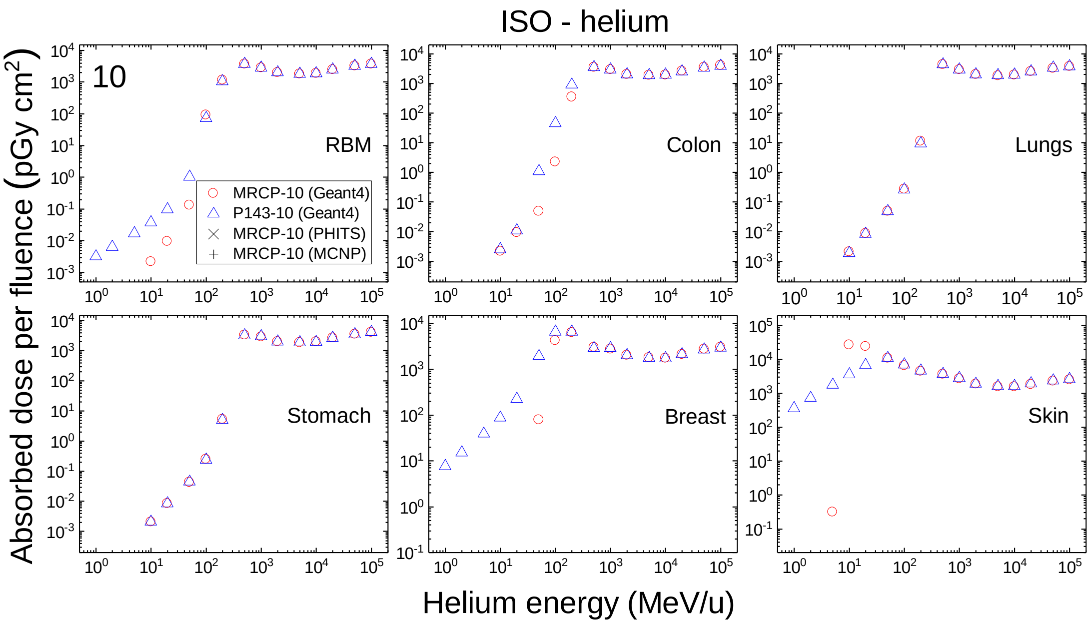

Fig. H.37. Absorbed dose per fluence (pGy cm^2) to the red bone marrow (RBM), colon, lungs, stomach, breast and skin in the isotropic (ISO) irradiation geometry for helium ion exposures calculated with the 10-year-old mesh-type reference computational phantoms (MRCPs), along with the values calculated with the P143 10-year-old phantoms. The values shown were averaged for the male and female phantoms.

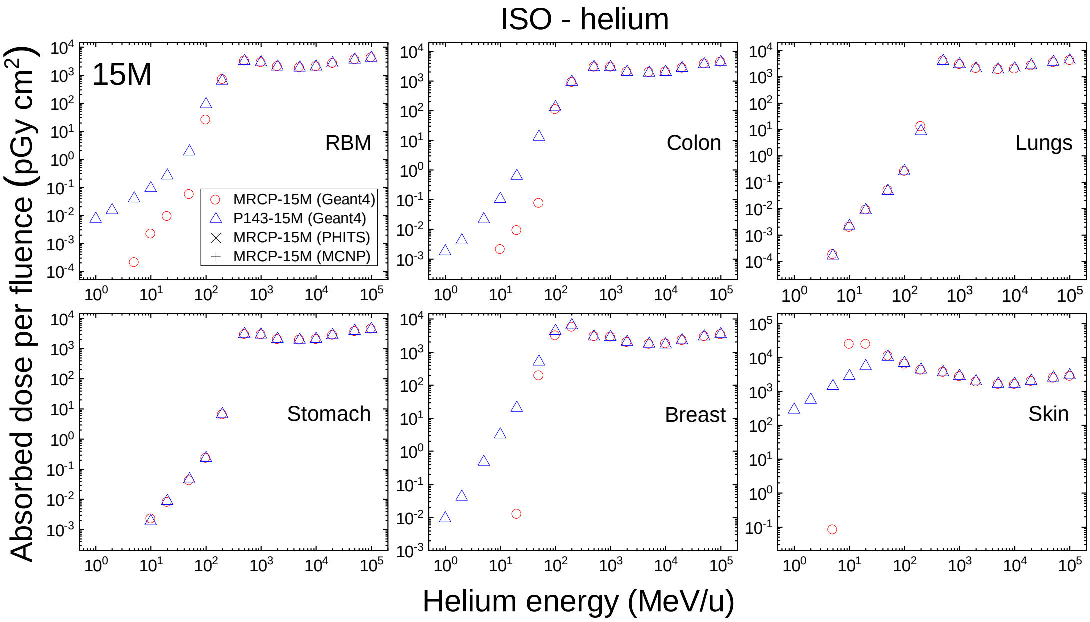

Fig. H.38. Absorbed dose per fluence (pGy cm^2) to the red bone marrow (RBM), colon, lungs, stomach, breast and skin in the isotropic (ISO) irradiation geometry for helium ion exposures calculated with the 15-year-old male mesh-type reference computational phantom (MRCP), along with the values calculated with the P143 15-year-old male phantom.

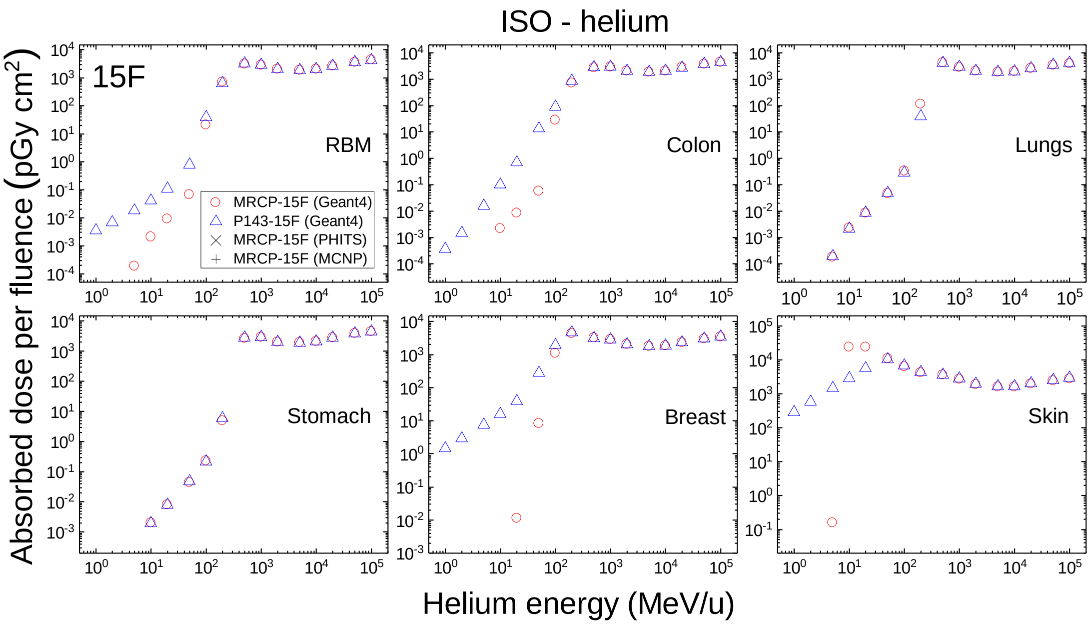

Fig. H.39. Absorbed dose per fluence (pGy cm2) to the red bone marrow (RBM), colon, lungs, stomach, breast and skin in the isotropic (ISO) irradiation geometry for helium ion exposures calculated with the 15-year-old female mesh-type reference computational phantom (MRCP), along with the values calculated with the P143 15-year-old female phantom.

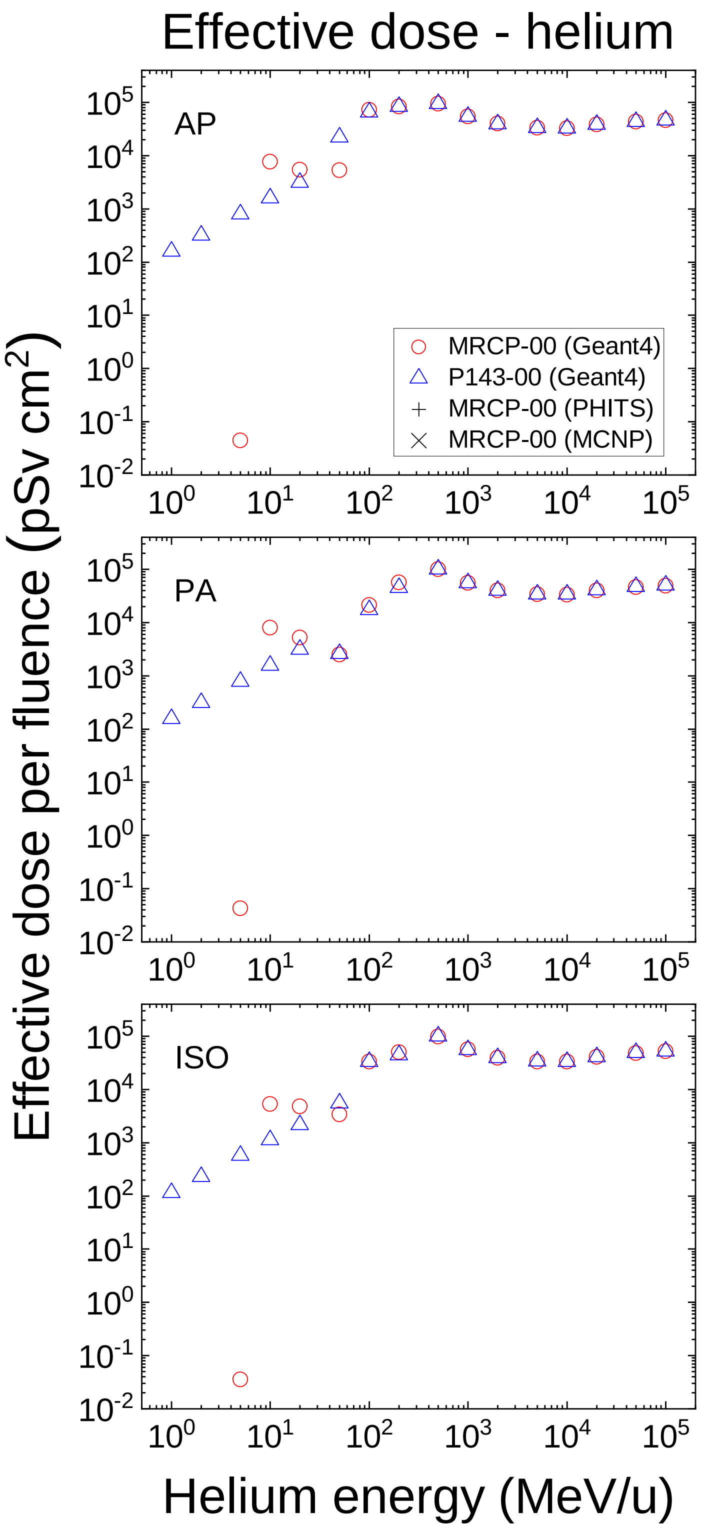

2593
2594 Fig. H.40. Effective dose per fluence (pSv cm^2) for helium ion exposures calculated with the
2595 newborn mesh-type reference computational phantoms (MRCPs), along with the values
2596 calculated with the P143 newborn phantoms.
2597

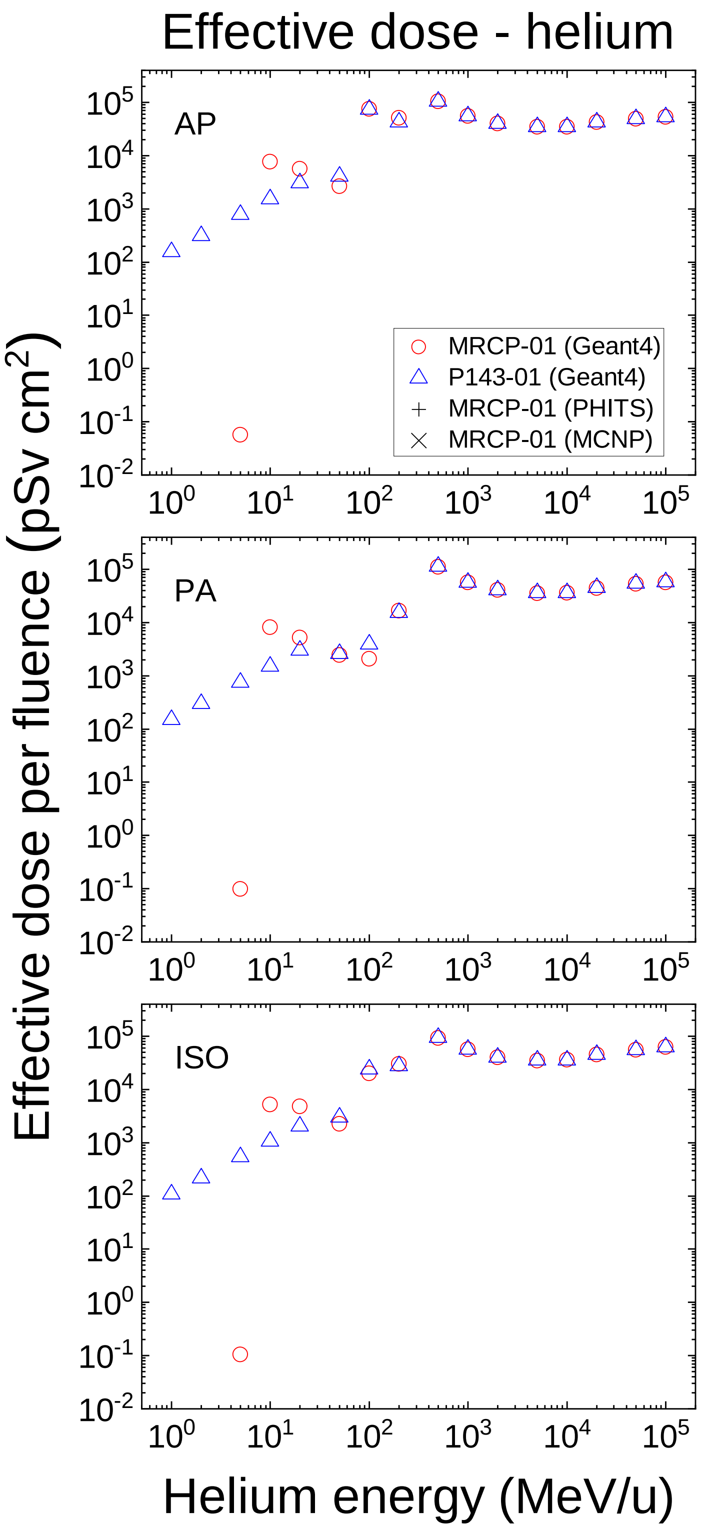

2598
2599 Fig. H.41. Effective dose per fluence (pSv cm^2) for helium ion exposures calculated with the
2600 1-year-old mesh-type reference computational phantoms (MRCPs), along with the values
2601 calculated with the P143 1-year-old phantoms.
2602

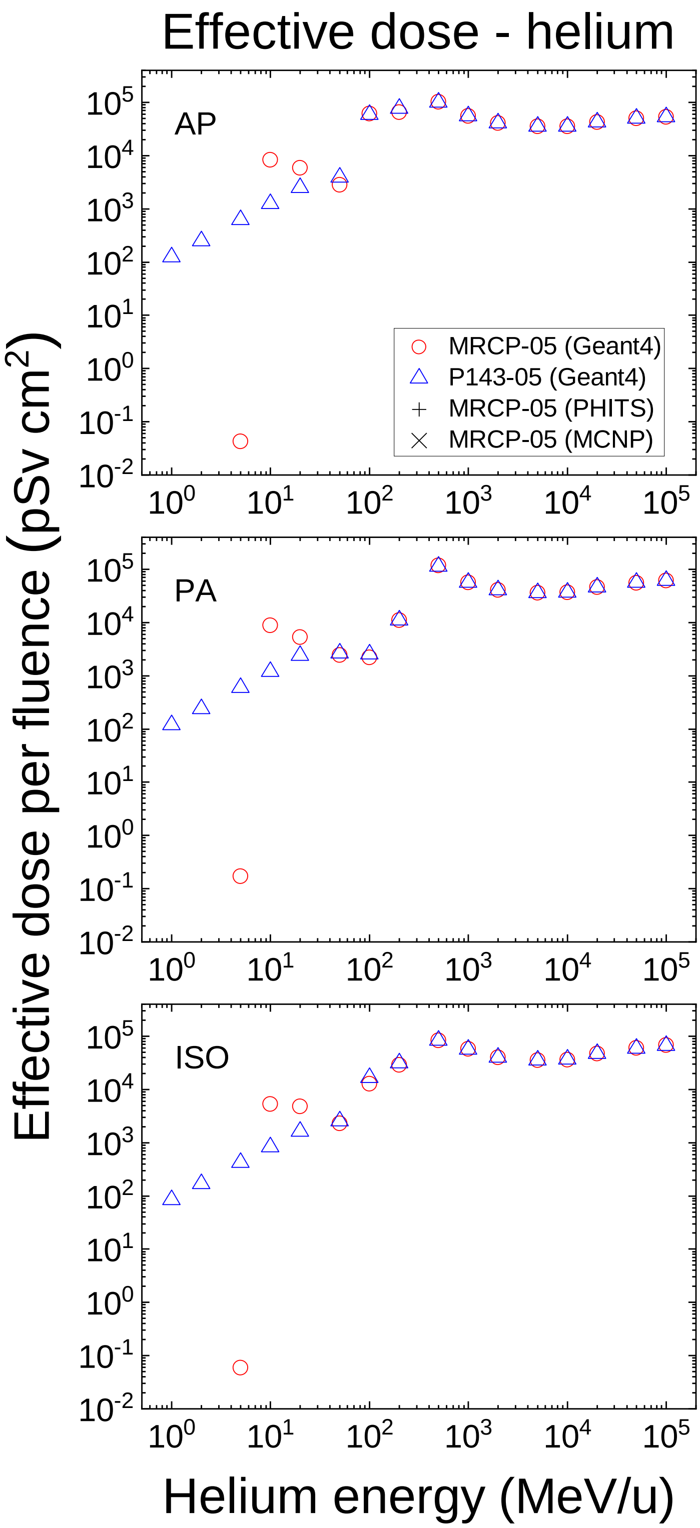

2603
2604 Fig. H.42. Effective dose per fluence (pSv cm^2) for helium ion exposures calculated with the
2605 5-year-old mesh-type reference computational phantoms (MRCPs), along with the values
2606 calculated with the P143 5-year-old phantoms.
2607

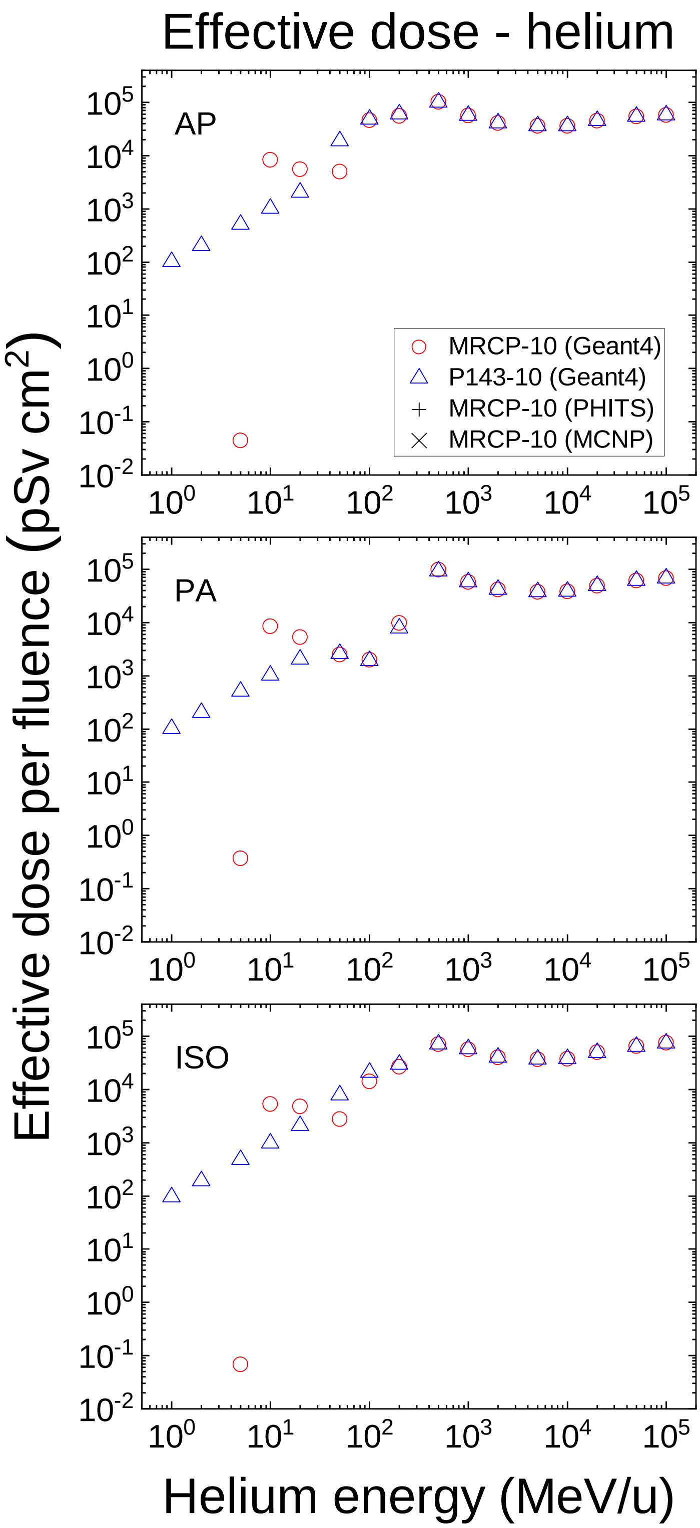

2609 Fig. H.43. Effective dose per fluence (pSv cm^2) for helium ion exposures calculated with the
2610 10-year-old mesh-type reference computational phantoms (MRCPs), along with the values
2611 calculated with the P143 10-year-old phantoms.

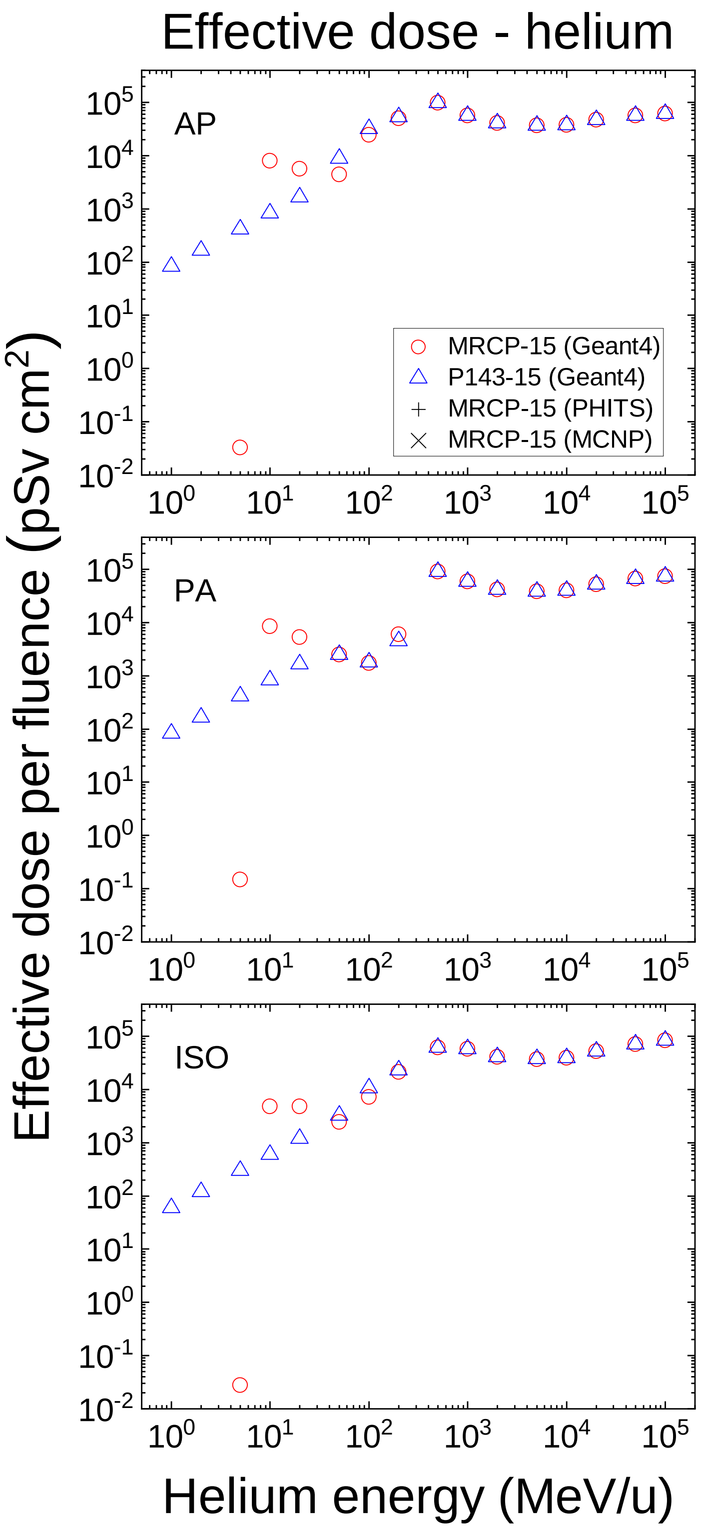

2613
2614 Fig. H.44. Effective dose per fluence (pSv cm^2) for helium ion exposures calculated with the
2615 15-year-old mesh-type reference computational phantoms (MRCPs), along with the values
2616 calculated with the P143 15-year-old phantoms.
2617

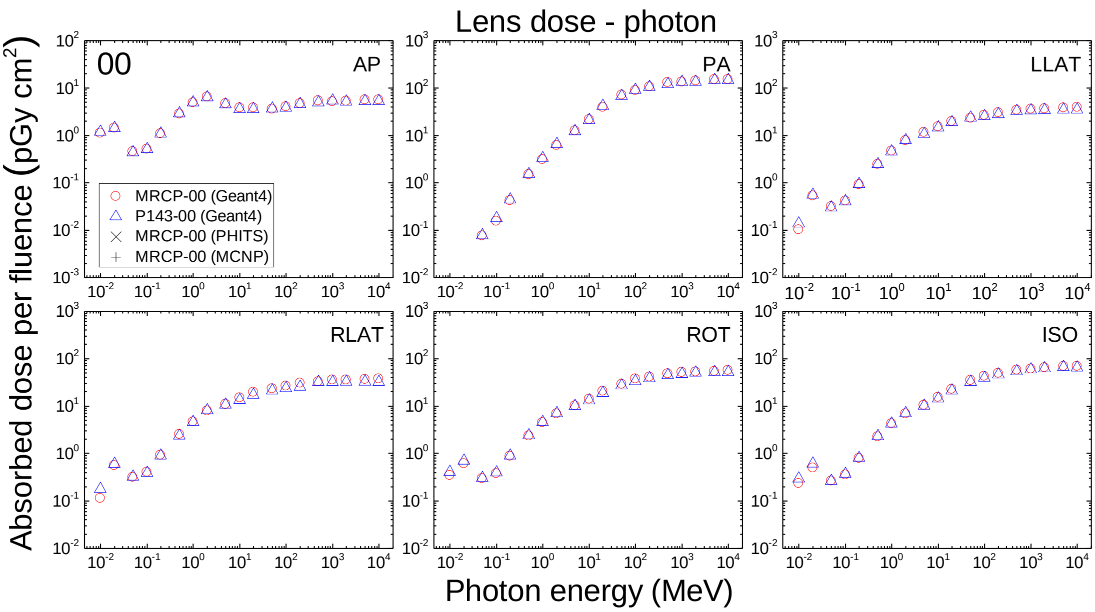

Fig. H.45. Absorbed dose per fluence (pGy cm^2) to the lens in the antero-posterior (AP), postero-anterior (PA), left-lateral (LLAT), right-lateral (RLAT), rotational (ROT) and isotropic (ISO) irradiation geometries for photon exposures calculated with the newborn mesh-type reference computational phantoms (MRCPs), along with the values calculated with the P143 newborn phantoms. The values shown were averaged for the male and female phantoms.

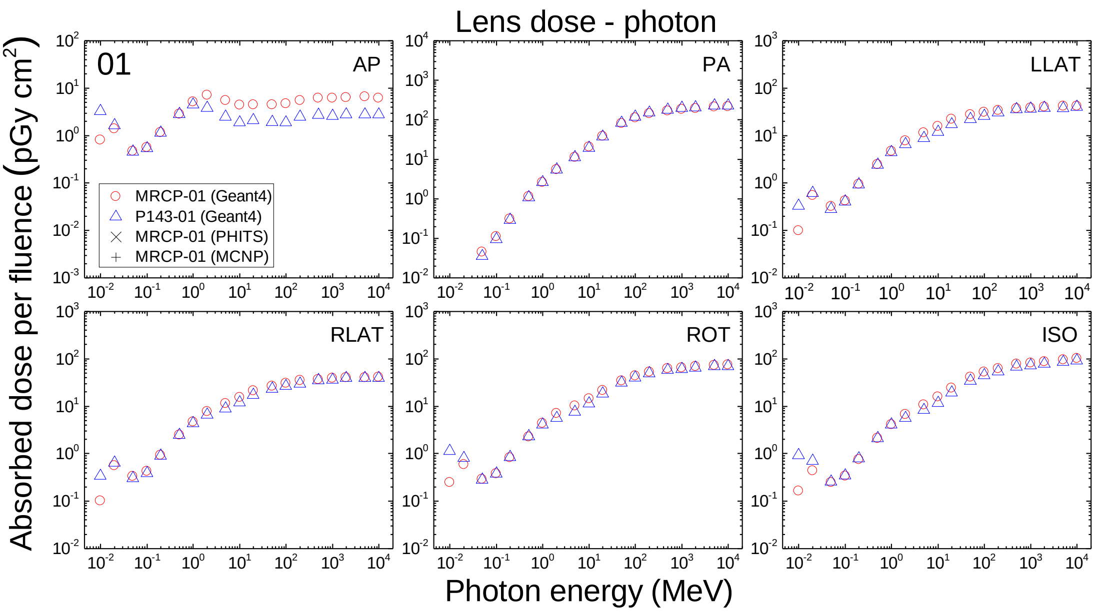

Fig. H.46. Absorbed dose per fluence (pGy cm^2) to the lens in the antero-posterior (AP), postero-anterior (PA), left-lateral (LLAT), right-lateral (RLAT), rotational (ROT) and isotropic (ISO) irradiation geometries for photon exposures calculated with the 1-year-old mesh-type reference computational phantoms (MRCPs), along with the values calculated with the P143 1-year-old phantoms. The values shown were averaged for the male and female phantoms.

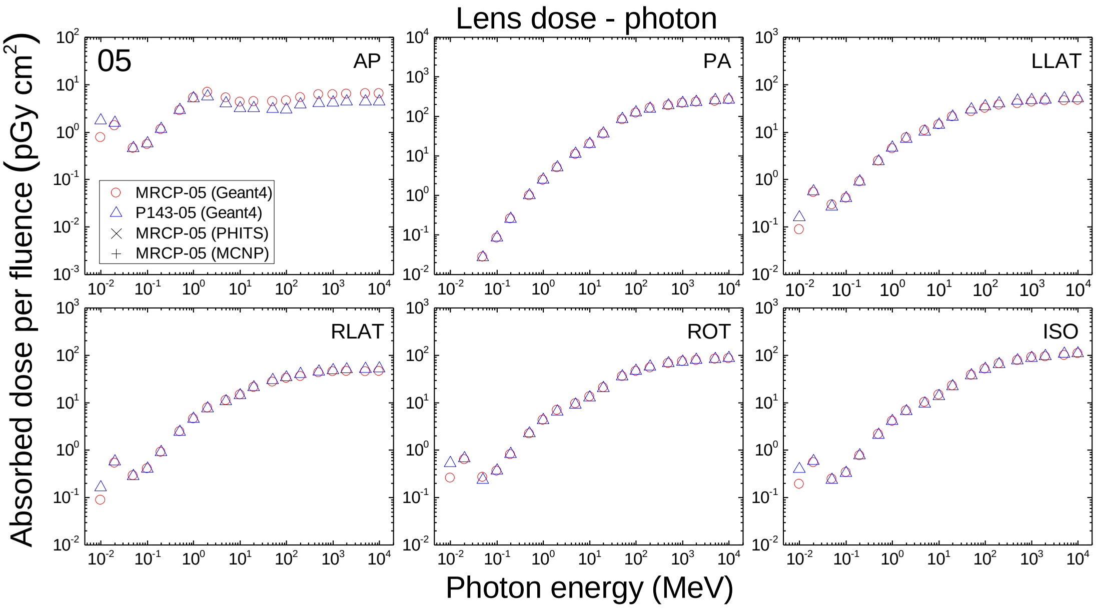

Fig. H.47. Absorbed dose per fluence (pGy cm^2) to the lens in the antero-posterior (AP), postero-anterior (PA), left-lateral (LLAT), right-lateral (RLAT), rotational (ROT) and isotropic (ISO) irradiation geometries for photon exposures calculated with the 5-year-old mesh-type reference computational phantoms (MRCPs), along with the values calculated with the P143 5-year-old phantoms. The values shown were averaged for the male and female phantoms.

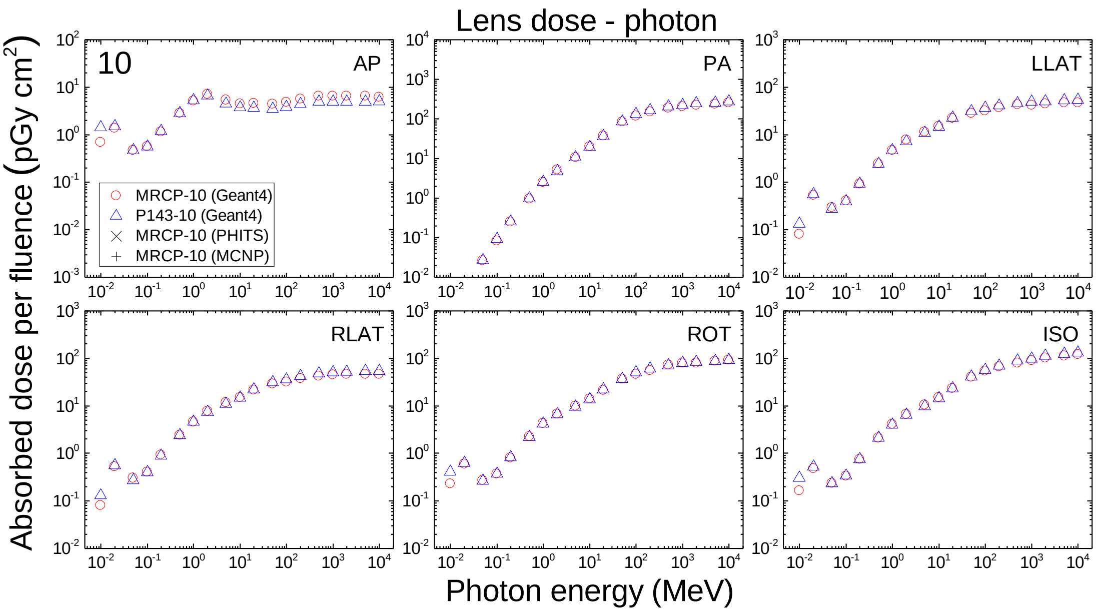

Fig. H.48. Absorbed dose per fluence (pGy cm^2) to the lens in the antero-posterior (AP), postero-anterior (PA), left-lateral (LLAT), right-lateral (RLAT), rotational (ROT) and isotropic (ISO) irradiation geometries for photon exposures calculated with the 10-year-old mesh-type reference computational phantoms (MRCPs), along with the values calculated with the P143 10-year-old phantoms. The values shown were averaged for the male and female phantoms.

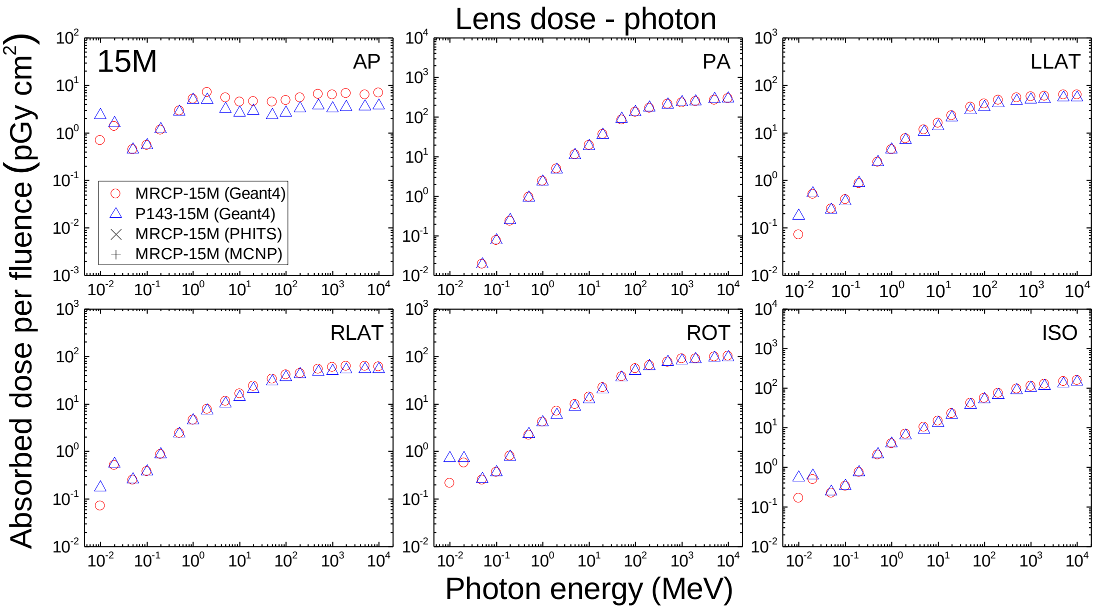

Fig. H.49. Absorbed dose per fluence (pGy cm^2) to the lens in the antero-posterior (AP), postero-anterior (PA), left-lateral (LLAT), right-lateral (RLAT), rotational (ROT) and isotropic (ISO) irradiation geometries for photon exposures calculated with the 15-year-old male mesh-type reference computational phantom (MRCP), along with the values calculated with the P143 15-year-old male phantom.

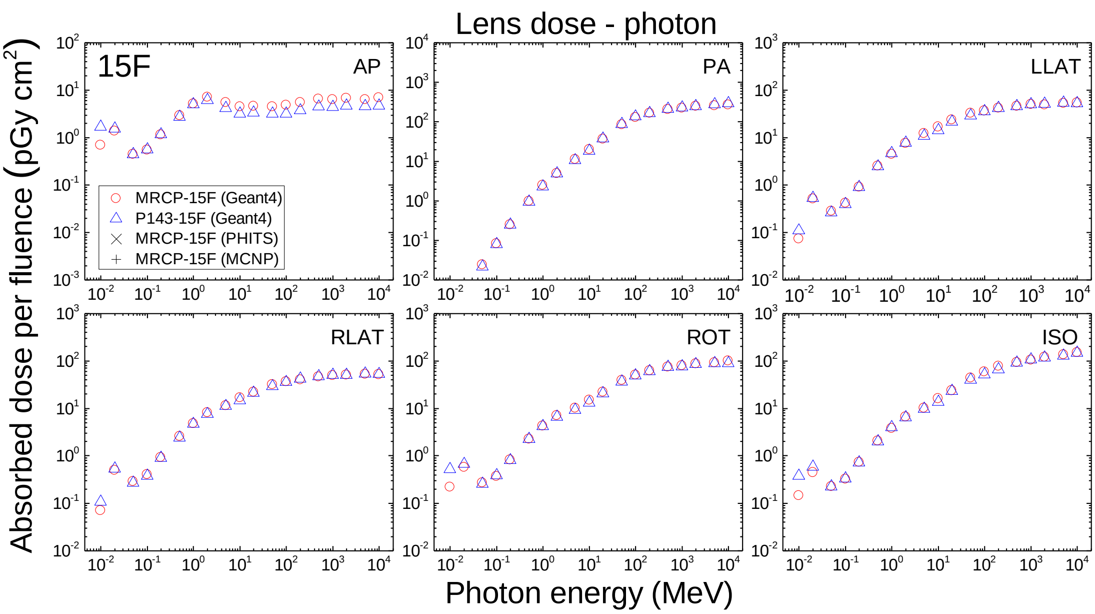

Fig. H.50. Absorbed dose per fluence (pGy cm^2) to the lens in the antero-posterior (AP), postero-anterior (PA), left-lateral (LLAT), right-lateral (RLAT), rotational (ROT) and isotropic (ISO) irradiation geometries for photon exposures calculated with the 15-year-old female mesh-type reference computational phantom (MRCP), along with the values calculated with the P143 15-year-old female phantom.

H.1. References

Allison, J., Amako, K., Apostolakis, J., et al., 2016. Recent developments in Geant4. Nucl. Instrum. Methods Phys. Res. Sect. A. 835, 186–225.

Furuta, T., Sato, T., Han, M.C., et al., 2017. Implementation of tetrahedral-mesh geometry in Monte Carlo radiation transport code PHITS. Phys. Med. Biol. 62, 4798–4810.

Hirayama, H., Namito, Y., Bielajew, A.F., et al., 2005. The EGS5 Code System. Menlo Park, USA and Tsukuba, Japan: SLAC National Accelerator Laboratory and High Energy Accelerator Research Organization (SLAC-R-730 and KEK Report 2005-8).

ICRP, 2020. Paediatric Reference Computational Phantoms. ICRP Publication 143. Ann. ICRP 49(1).

Martz, R.L., 2017. The MCNP6 book on unstructured mesh geometry: a user's guide for MCNP6.2. Report LA-UR-17-22442. Los Alamos National Laboratory, Los Alamos, NM.

Shibata, K., Iwamoto, O., Nakagawa, T., et al., 2011. JENDL-4.0: a new library for nuclear science and engineering. J Nucl Sci Technol. 48, 1–30.

Trellue, H.R., Little, R.C., White, M.C., et al., 2009. ENDF70: A Continuous-Energy MCNP Neutron Data Library Based on ENDF/B-VII.0. Nuclear Technol. 168, 832–836.

ANNEX I. COMPARISON OF SPECIFIC ABSORBED FRACTIONS

(I 1) This annex compares the specific absorbed fractions (SAFs) for photons and electrons calculated using the paediatric mesh-type reference computational phantoms (MRCPs) with the values calculated with the *Publication 143* (P143) phantoms (ICRP, 2020) and the values in *Publication 1XX* (ICRP, 2022). To calculate the values, the MRCPs and P143 phantoms were implemented into the Geant4 code (version 10.06.p02) (Allisons et al., 2016) using the *G4Tet* and *G4VNestedParameterisation* classes, respectively. The considered source organs are the liver, lungs, cortical bone and thyroid, in which mono-energetic photons and electrons, ranging from 10 keV to 10 MeV, were uniformly generated using the *G4VUserPrimaryGeneratorAction* class. The number of source particles varied from 10^7 to 10^{10}, depending on the particle type and energy, keeping the statistical relative errors of the calculated SAFs below 5%. The kerma approximation was not applied. The physics library of *G4EmLivermorePhysics* was used to transport the particles with the secondary range cut value of 1 μm (Geant4 Physics Reference Manual). Note that for photons, the SAFs for the red bone marrow (RBM) and endosteum were estimated using the fluence-to-absorbed dose response functions (DRFs). For spot-check purpose, the MCNP6 (Martz et al., 2017) and PHITS (version 3.10) (Furuta et al., 2017) codes were additionally used to calculate the SAFs for some selected energy points, under the same simulation conditions (remaining spot-check SAFs will be included prior to publication). The default physics library for the MCNP6 (Martz et al., 2017) and the *EGS5* physics library for the PHITS code (Hirayama et al., 2005) were used to transport photons and electrons. The energy cut values, which are equivalent to the range cut value used in the Geant4 code, were applied to the MCNP6 and PHITS codes. Figs I.1–I.24 and I.25–I.48 show the SAFs for the selected source and target organs for photons and electrons, respectively. Note that for each source organ, four target organs were selected considering the contribution to effective dose. For discussion of the comparisons, please see Section 7.2 of the main text.

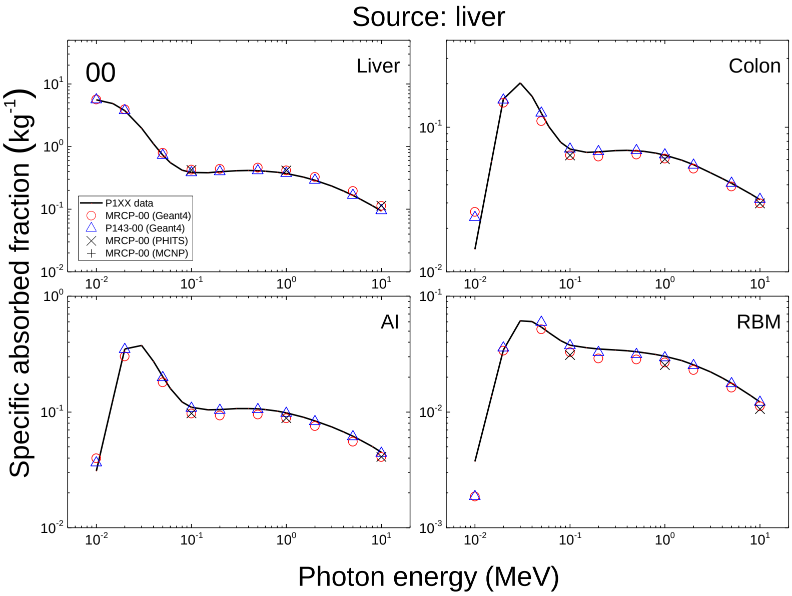

Fig. I.1. Specific absorbed fractions (SAFs) for liver as a source and liver, colon, alveolar-interstitium (AI) and red bone marrow (RBM) as a target for photon exposures calculated with the newborn mesh-type reference computational phantoms (MRCPs), along with the values calculated with the P143 newborn phantoms and the *Publication 1XX* values (ICRP, 2022). The values shown were averaged for the male and female phantoms.

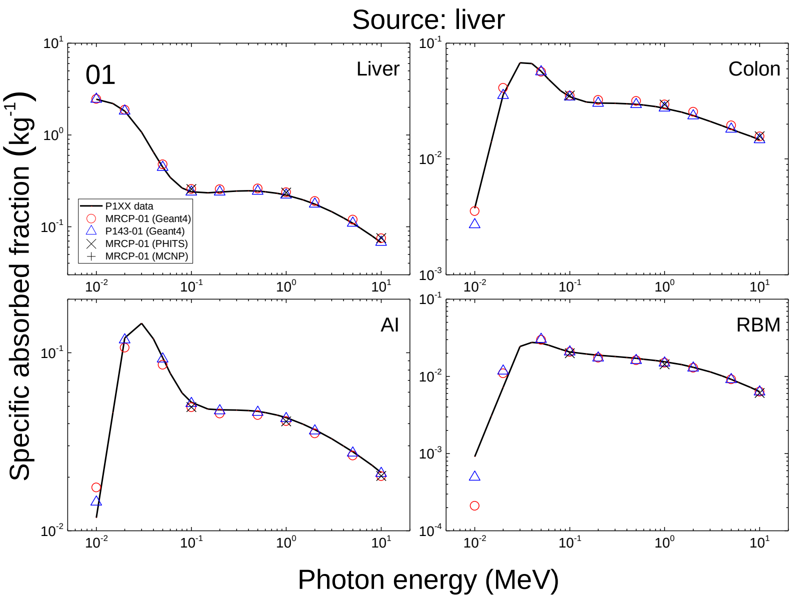

Fig. I.2. Specific absorbed fractions (SAFs) for liver as a source and liver, colon, alveolar-interstitium (AI) and red bone marrow (RBM) as a target for photon exposures calculated with the 1-year-old mesh-type reference computational phantoms (MRCPs), along with the values calculated with the P143 1-year-old phantoms and the *Publication 1XX* values (ICRP, 2022). The values shown were averaged for the male and female phantoms.

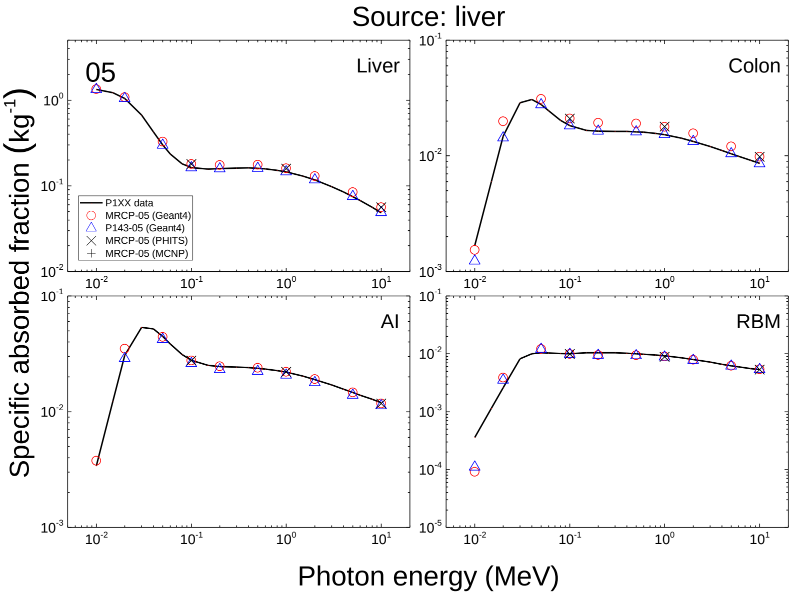

Fig. I.3. Specific absorbed fractions (SAFs) for liver as a source and liver, colon, alveolar-interstitium (AI) and red bone marrow (RBM) as a target for photon exposures calculated with the 5-year-old mesh-type reference computational phantoms (MRCPs), along with the values calculated with the P143 5-year-old phantoms and the *Publication 1XX* values (ICRP, 2022). The values shown were averaged for the male and female phantoms.

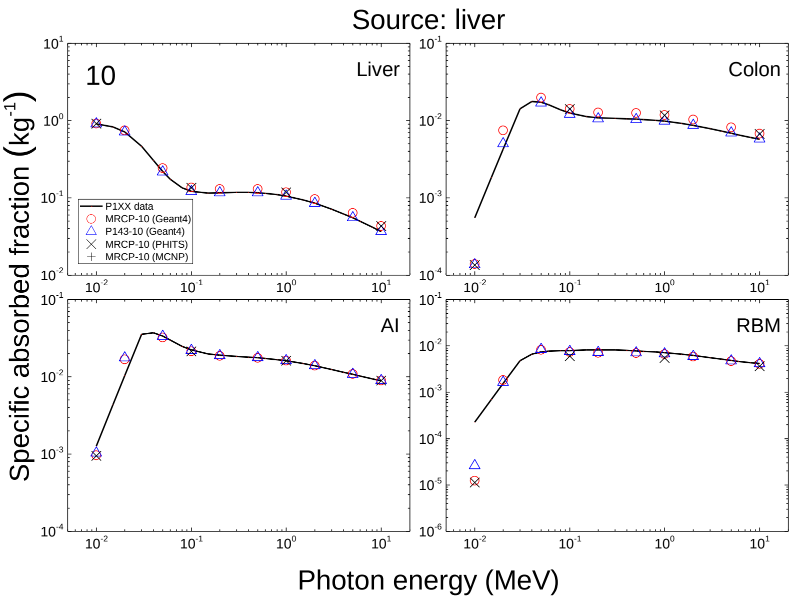

Fig. I.4. Specific absorbed fractions (SAFs) for liver as a source and liver, colon, alveolar-interstitium (AI) and red bone marrow (RBM) as a target for photon exposures calculated with the 10-year-old mesh-type reference computational phantoms (MRCPs), along with the values calculated with the P143 10-year-old phantoms and the *Publication 1XX* values (ICRP, 2022).

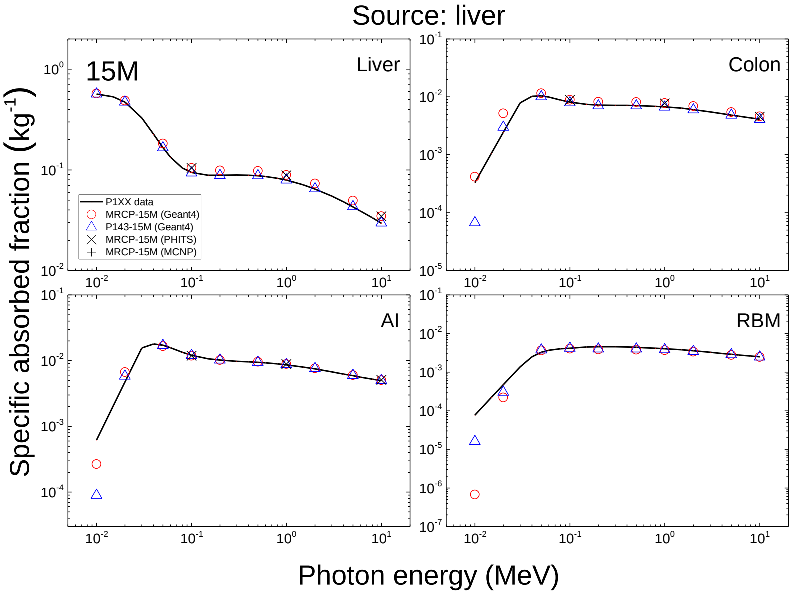

Fig. I.5. Specific absorbed fractions (SAFs) for liver as a source and liver, colon, alveolar-interstitium (AI) and red bone marrow (RBM) as a target for photon exposures calculated with the 15-year-old male mesh-type reference computational phantom (MRCP), along with the values calculated with the P143 15-year-old male phantom and the *Publication 1XX* values (ICRP, 2022).

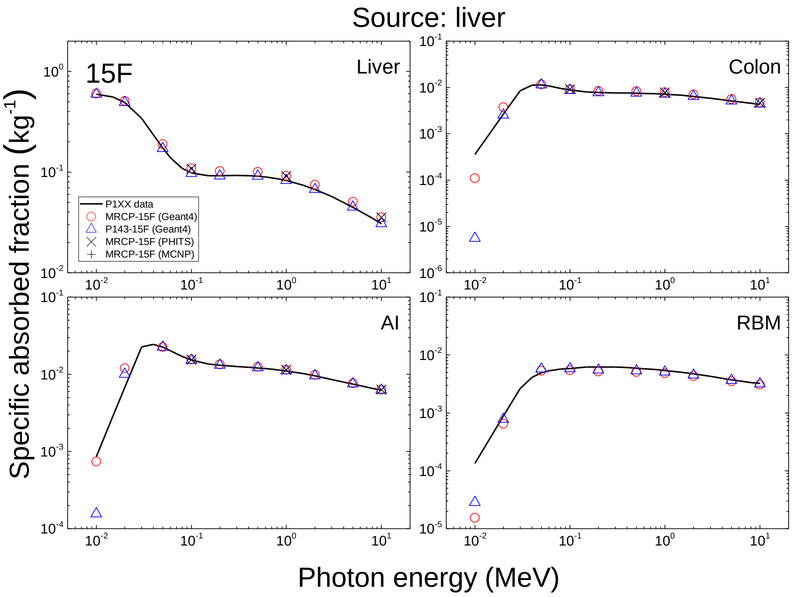

Fig. I.6. Specific absorbed fractions (SAFs) for liver as a source and liver, colon, alveolar-interstitium (AI) and red bone marrow (RBM) as a target for photon exposures calculated with the 15-year-old female mesh-type reference computational phantom (MRCP), along with the values calculated with the P143 15-year-old female phantom and the *Publication 1XX* values (ICRP, 2022).

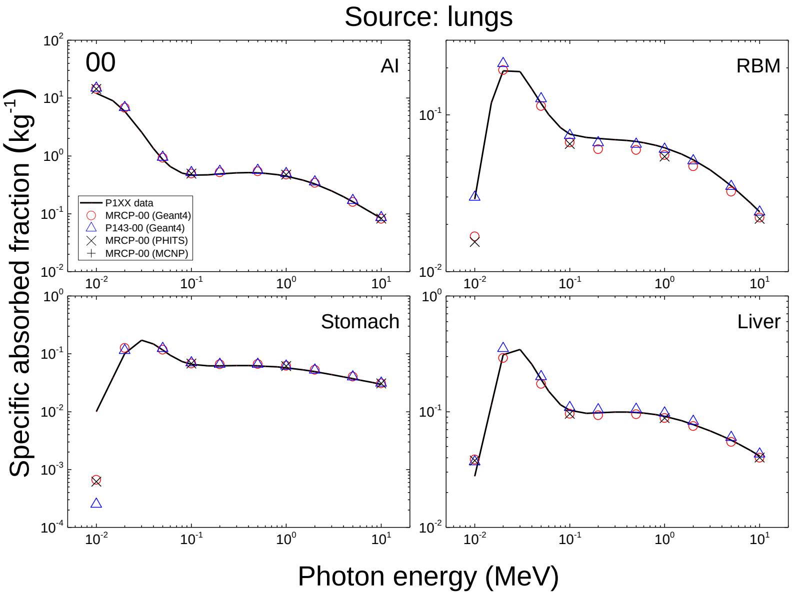

Fig. I.7. Specific absorbed fractions (SAFs) for lungs as a source and alveolar-interstitium (AI), red bone marrow (RBM), stomach and liver as a target for photon exposures calculated with the newborn mesh-type reference computational phantoms (MRCPs), along with the values calculated with the P143 newborn phantoms and the *Publication 1XX* values (ICRP, 2022). The values shown were averaged for the male and female phantoms.

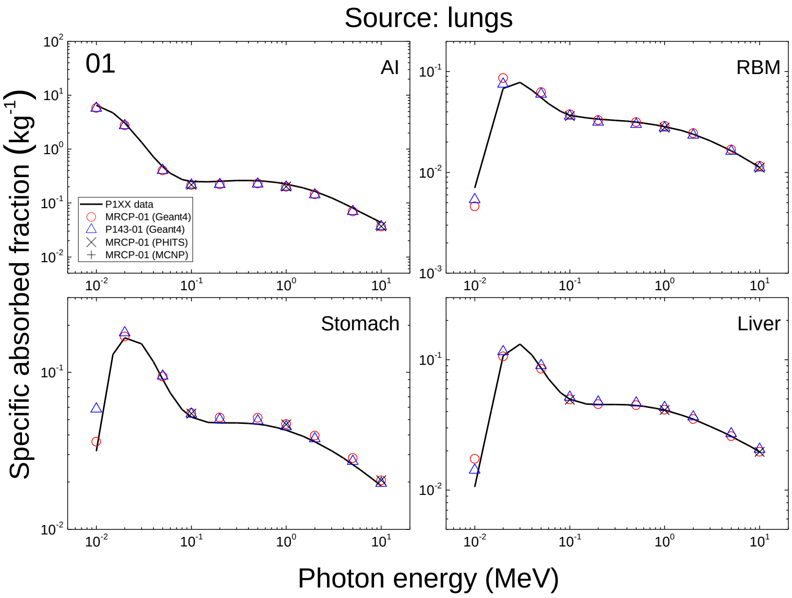

Fig. I.8. Specific absorbed fractions (SAFs) for lungs as a source and alveolar-interstitium (AI), red bone marrow (RBM), stomach and liver as a target for photon exposures calculated with the 1-year-old mesh-type reference computational phantoms (MRCPs), along with the values calculated with the P143 1-year-old phantoms and the *Publication 1XX* values (ICRP, 2022). The values shown were averaged for the male and female phantoms.

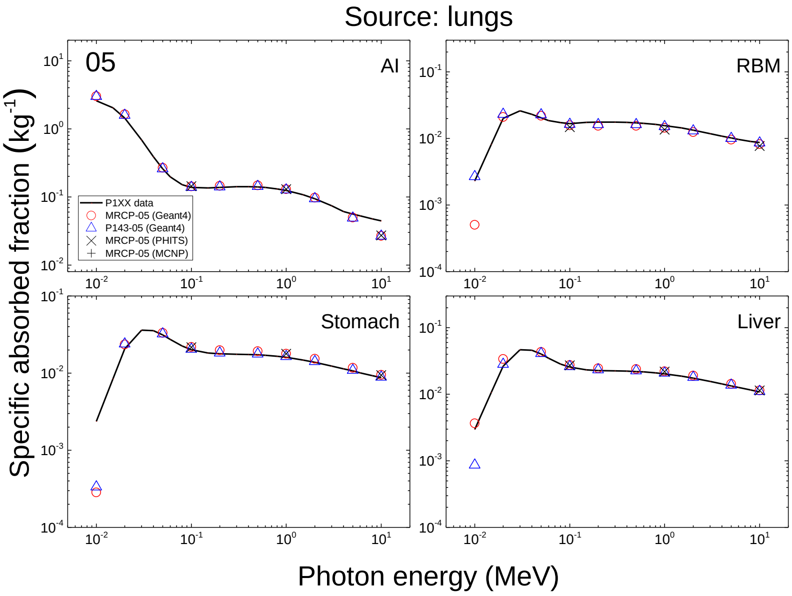

Fig. I.9. Specific absorbed fractions (SAFs) for lungs as a source and alveolar-interstitium (AI), red bone marrow (RBM), stomach and liver as a target for photon exposures calculated with the 5-year-old mesh-type reference computational phantoms (MRCPs), along with the values calculated with the P143 5-year-old phantoms and the *Publication 1XX* values (ICRP, 2022). The values shown were averaged for the male and female phantoms.

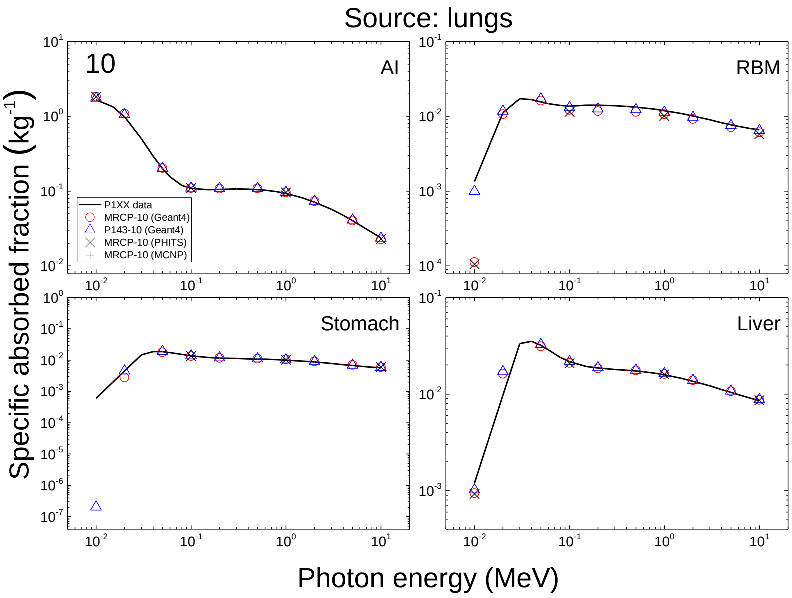

Fig. I.10. Specific absorbed fractions (SAFs) for lungs as a source and alveolar-interstitium (AI), red bone marrow (RBM), stomach and liver as a target for photon exposures calculated with the 10-year-old mesh-type reference computational phantoms (MRCPs), along with the values calculated with the P143 10-year-old phantoms and the *Publication 1XX* values (ICRP, 2022). The values shown were averaged for the male and female phantoms.

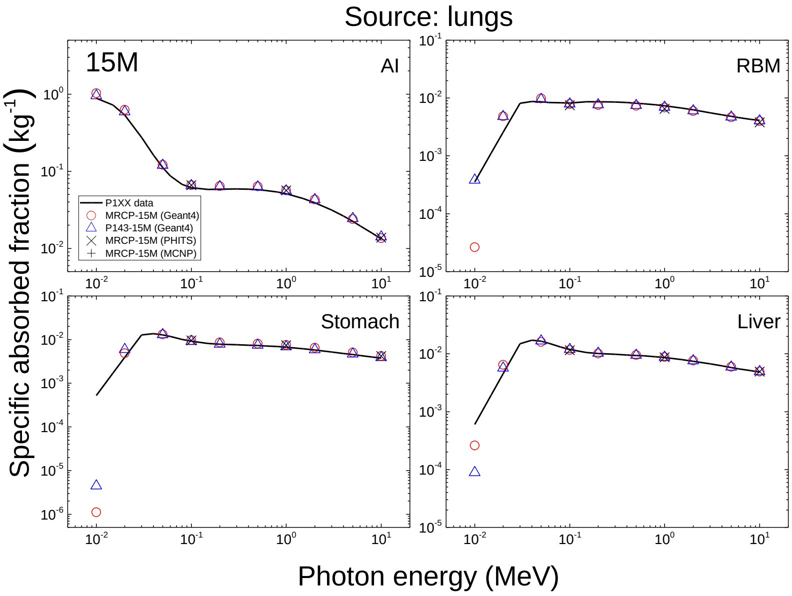

Fig. I.11. Specific absorbed fractions (SAFs) for lungs as a source and alveolar-interstitium (AI), red bone marrow (RBM), stomach and liver as a target for photon exposures calculated with the 15-year-old male mesh-type reference computational phantom (MRCP), along with the values calculated with the P143 15-year-old male phantom and the *Publication 1XX* values (ICRP, 2022).

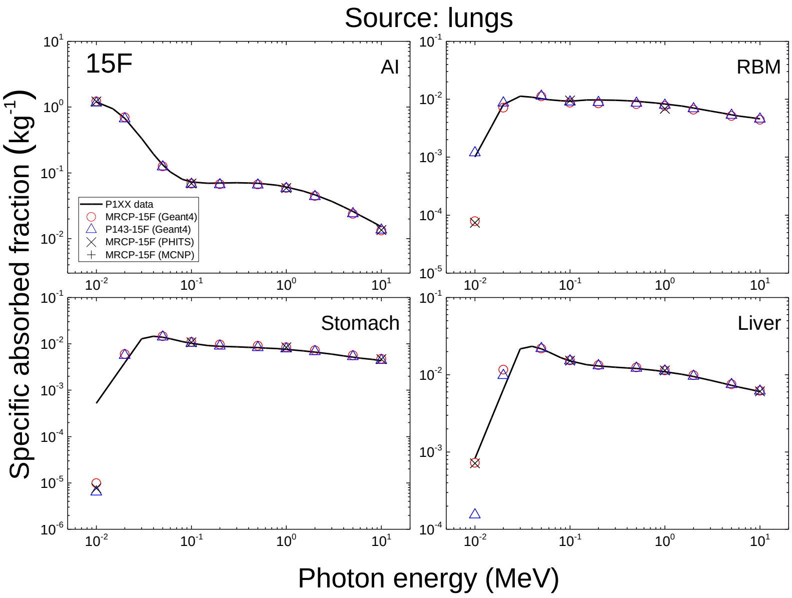

Fig. I.12. Specific absorbed fractions (SAFs) for lungs as a source and alveolar-interstitium (AI), red bone marrow (RBM), stomach and liver as a target for photon exposures calculated with the 15-year-old female mesh-type reference computational phantom (MRCP), along with the values calculated with the P143 15-year-old female phantom and the *Publication 1XX* values (ICRP, 2022).

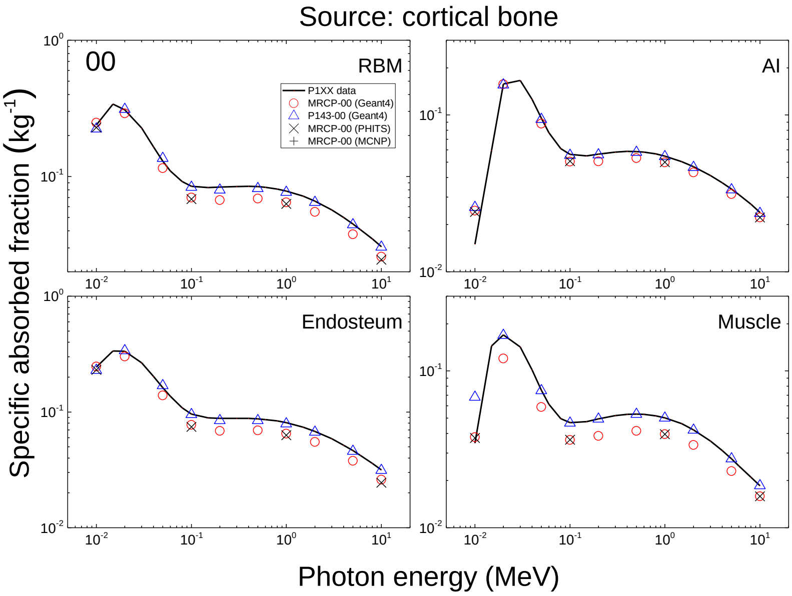

Fig. I.13. Specific absorbed fractions (SAFs) for cortical bone as a source and red bone marrow (RBM), alveolar-interstitium (AI), endosteum and muscle as a target for photon exposures calculated with the newborn mesh-type reference computational phantoms (MRCPs), along with the values calculated with the P143 newborn phantoms and the *Publication 1XX* values (ICRP, 2022). The values shown were averaged for the male and female phantoms.

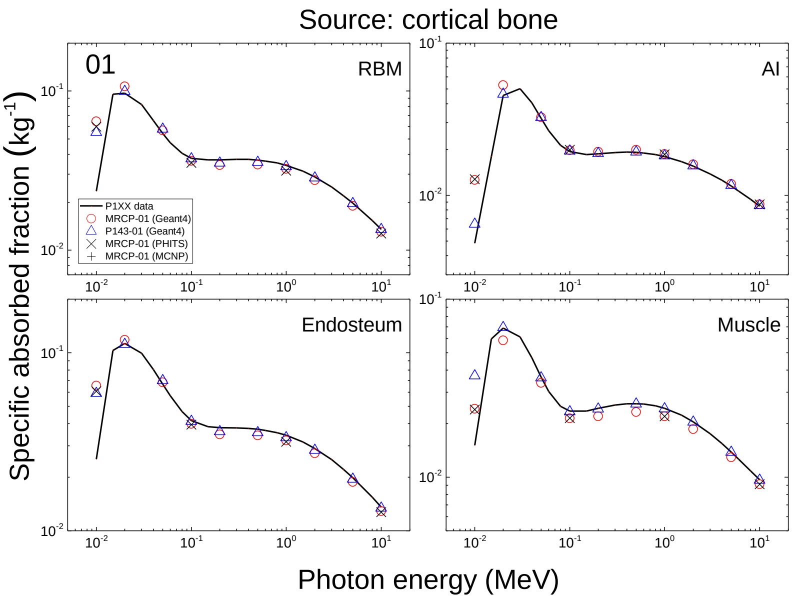

Fig. I.14. Specific absorbed fractions (SAFs) for cortical bone as a source and red bone marrow (RBM), alveolar-interstitium (AI), endosteum and muscle as a target for photon exposures calculated with the 1-year-old mesh-type reference computational phantoms (MRCPs), along with the values calculated with the P143 1-year-old phantoms and the *Publication 1XX* values (ICRP, 2022). The values shown were averaged for the male and female phantoms.

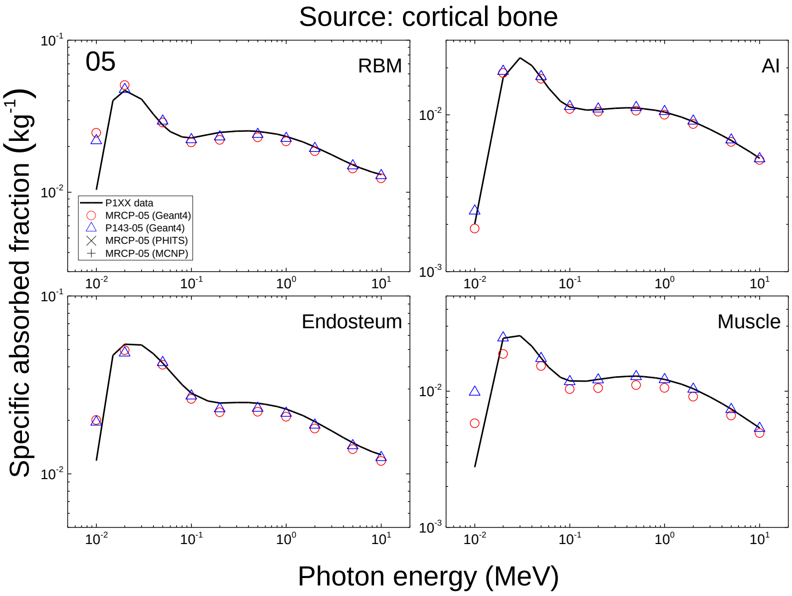

Fig. I.15. Specific absorbed fractions (SAFs) for cortical bone as a source and red bone marrow (RBM), alveolar-interstitium (AI), endosteum and muscle as a target for photon exposures calculated with the 5-year-old mesh-type reference computational phantoms (MRCPs), along with the values calculated with the P143 5-year-old phantoms and the *Publication 1XX* values (ICRP, 2022). The values shown were averaged for the male and female phantoms.

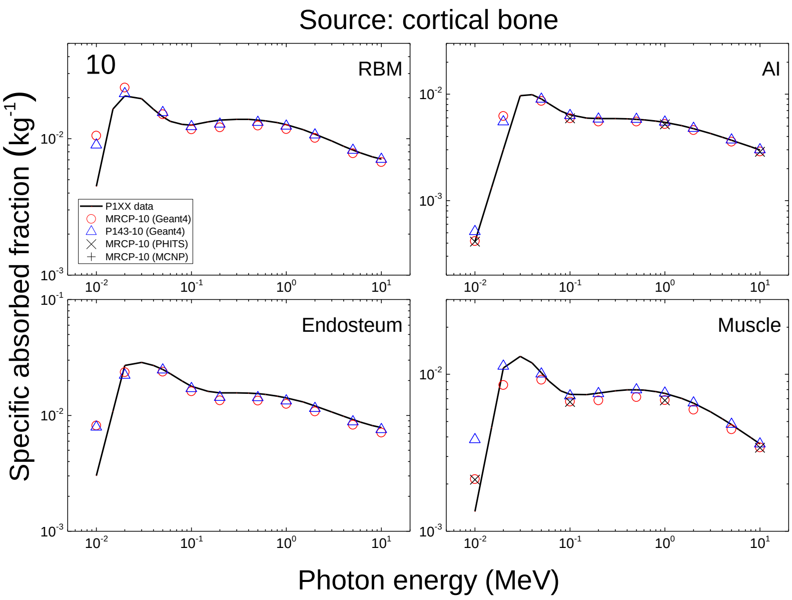

Fig. I.16. Specific absorbed fractions (SAFs) for cortical bone as a source and red bone marrow (RBM), alveolar-interstitium (AI), endosteum and muscle as a target for photon exposures calculated with the 10-year-old mesh-type reference computational phantoms (MRCPs), along with the values calculated with the P143 10-year-old phantoms and the *Publication 1XX* values (ICRP, 2022). The values shown were averaged for the male and female phantoms.

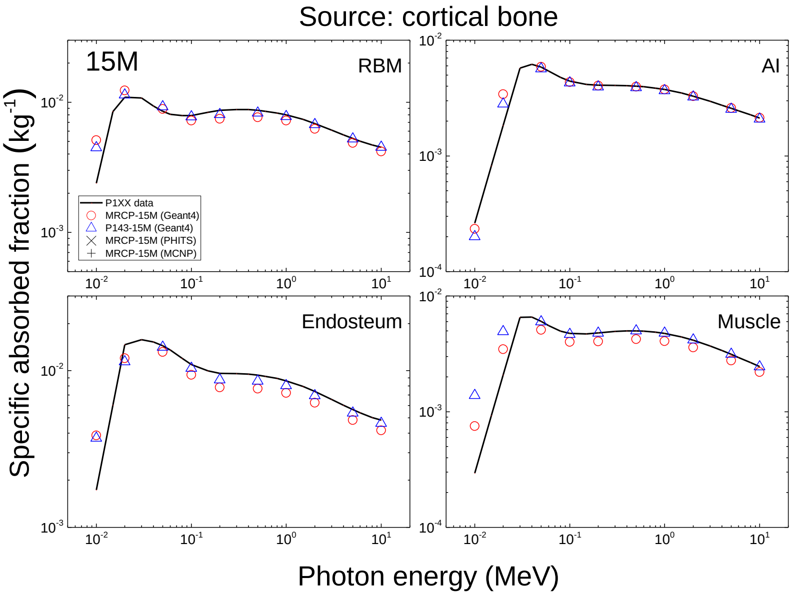

Fig. I.17. Specific absorbed fractions (SAFs) for cortical bone as a source and red bone marrow (RBM), alveolar-interstitium (AI), endosteum and muscle as a target for photon exposures calculated with the 15-year-old male mesh-type reference computational phantom (MRCP), along with the values calculated with the P143 15-year-old male phantom and the *Publication 1XX* values (ICRP, 2022).

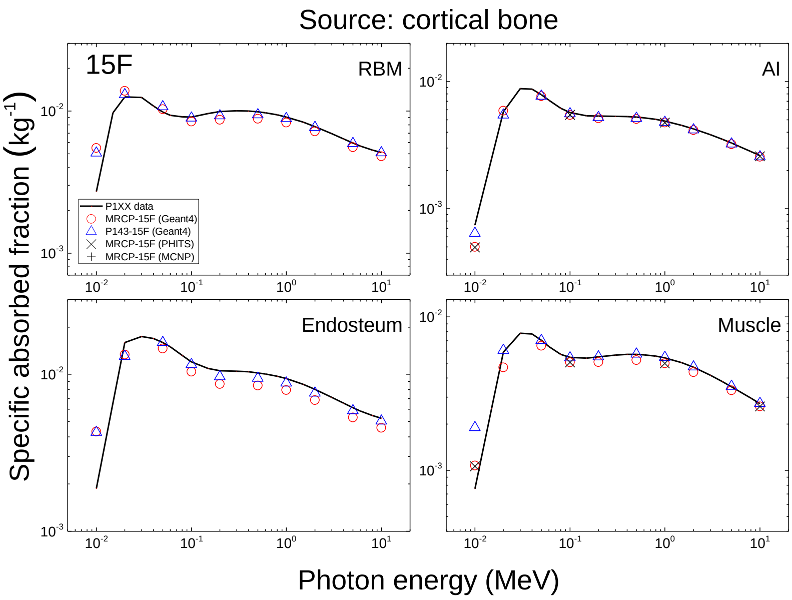

Fig. I.18. Specific absorbed fractions (SAFs) for cortical bone as a source and red bone marrow (RBM), alveolar-interstitium (AI), endosteum and muscle as a target for photon exposures calculated with the 15-year-old female mesh-type reference computational phantom (MRCP), along with the values calculated with the P143 15-year-old female phantom and the *Publication 1XX* values (ICRP, 2022).

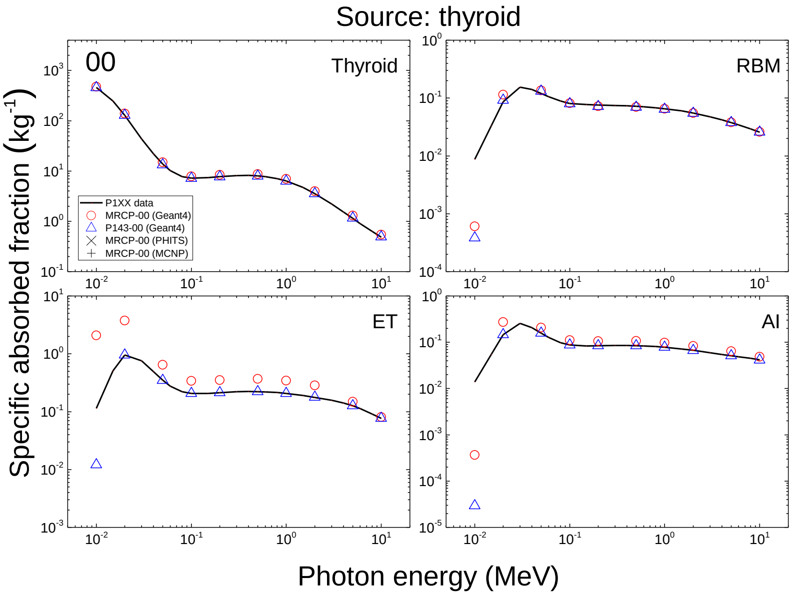

Fig. I.19. Specific absorbed fractions (SAFs) for thyroid as a source and thyroid, red bone marrow (RBM), extrathoracic (ET) region and alveolar-interstitium (AI) as a target for photon exposures calculated with the newborn mesh-type reference computational phantoms (MRCPs), along with the values calculated with the P143 newborn phantoms and the *Publication 1XX* values (ICRP, 2022). The values shown were averaged for the male and female phantoms.

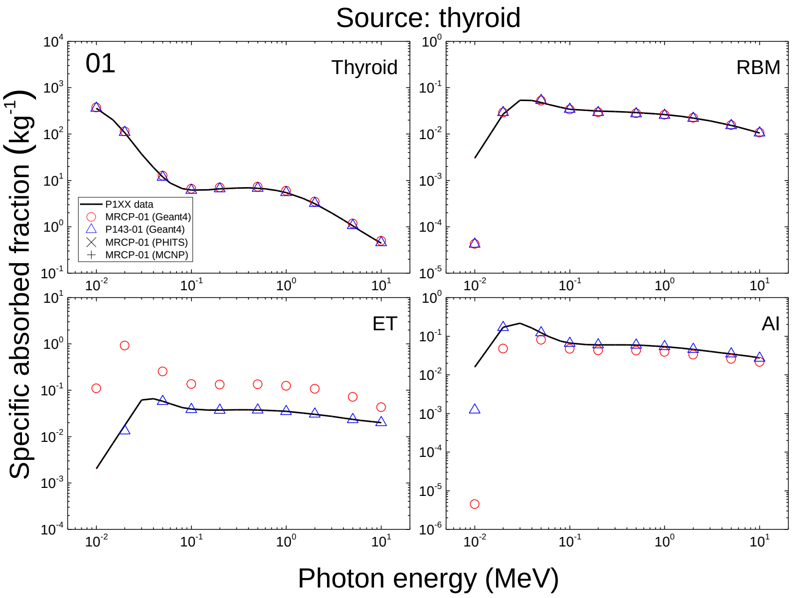

Fig. I.20. Specific absorbed fractions (SAFs) for thyroid as a source and thyroid, red bone marrow (RBM), extrathoracic (ET) region and alveolar-interstitium (AI) as a target for photon exposures calculated with the 1-year-old mesh-type reference computational phantoms (MRCPs), along with the values calculated with the P143 1-year-old phantoms and the *Publication 1XX* values (ICRP, 2022). The values shown were averaged for the male and female phantoms.

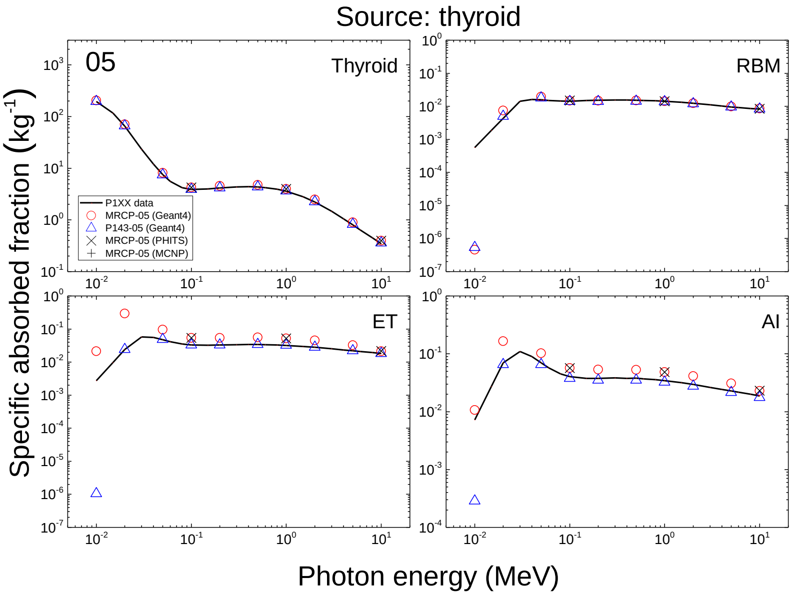

Fig. I.21. Specific absorbed fractions (SAFs) for thyroid as a source and thyroid, red bone marrow (RBM), extrathoracic (ET) region and alveolar-interstitium (AI) as a target for photon exposures calculated with the 5-year-old mesh-type reference computational phantoms (MRCPs), along with the values calculated with the P143 5-year-old phantoms and the *Publication 1XX* values (ICRP, 2022). The values shown were averaged for the male and female phantoms.

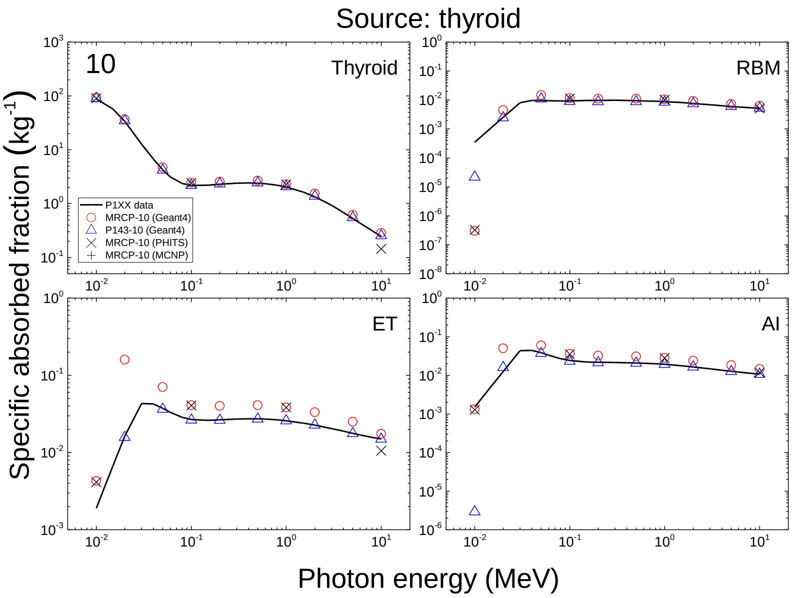

Fig. I.22. Specific absorbed fractions (SAFs) for thyroid as a source and thyroid, red bone marrow (RBM), extrathoracic (ET) region and alveolar-interstitium (AI) as a target for photon exposures calculated with the 10-year-old mesh-type reference computational phantoms (MRCPs), along with the values calculated with the P143 10-year-old phantoms and the *Publication 1XX* values (ICRP, 2022). The values shown were averaged for the male and female phantoms.

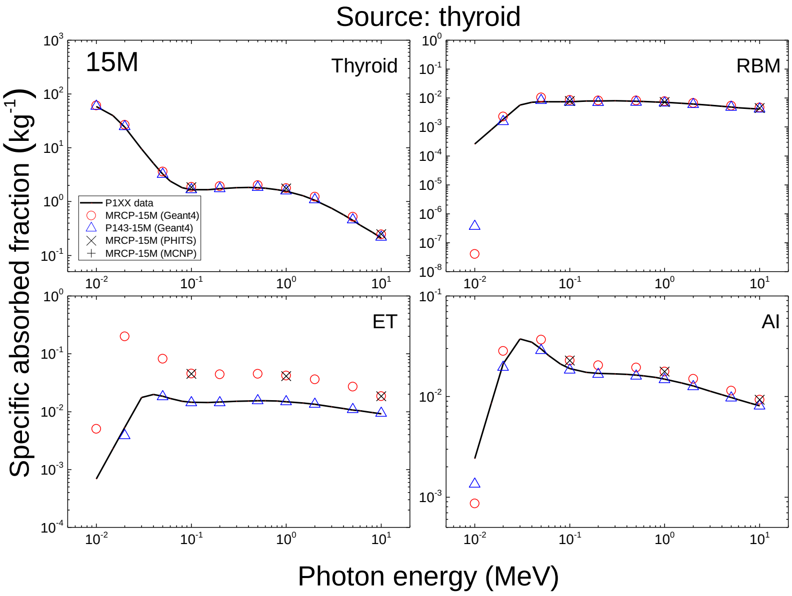

Fig. I.23. Specific absorbed fractions (SAFs) for thyroid as a source and thyroid, red bone marrow (RBM), extrathoracic (ET) region and alveolar-interstitium (AI) as a target for photon exposures calculated with the 15-year-old male mesh-type reference computational phantom (MRCP), along with the values calculated with the P143 15-year-old male phantom and the *Publication 1XX* values (ICRP, 2022).

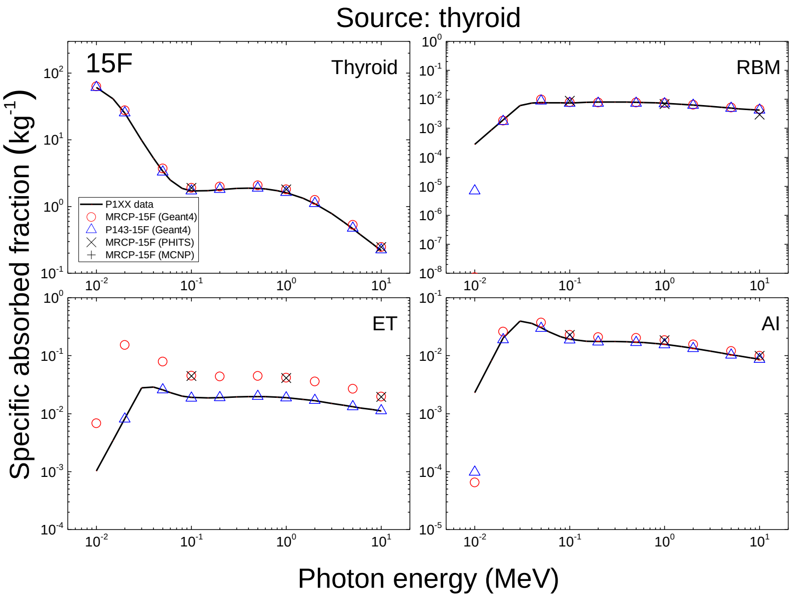

Fig. I.24. Specific absorbed fractions (SAFs) for thyroid as a source and thyroid, red bone marrow (RBM), extrathoracic (ET) region and alveolar-interstitium (AI) as a target for photon exposures calculated with the 15-year-old female mesh-type reference computational phantom (MRCP), along with the values calculated with the P143 15-year-old female phantom and the *Publication 1XX* values (ICRP, 2022).

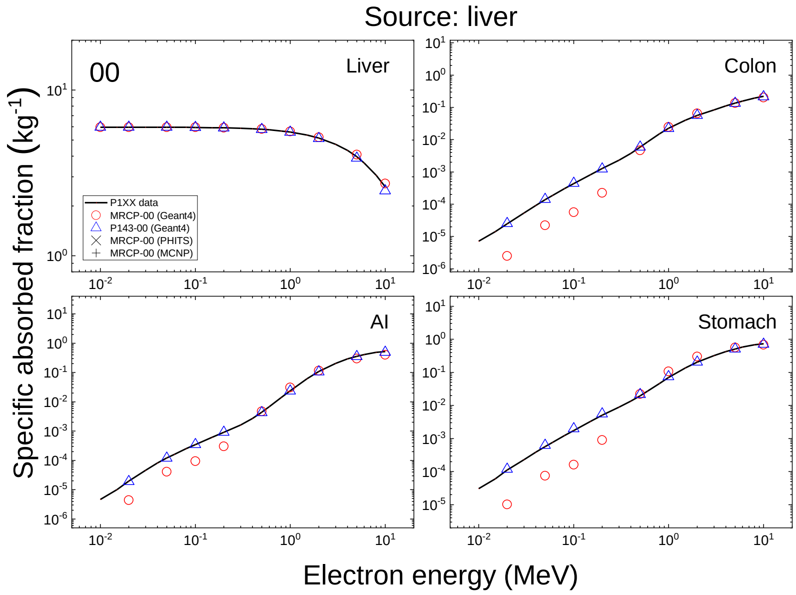

Fig. I.25. Specific absorbed fractions (SAFs) for liver as a source and liver, colon, alveolar-interstitium (AI) and stomach as a target for electron exposures calculated with the newborn mesh-type reference computational phantoms (MRCPs), along with the values calculated with the P143 newborn phantoms and the *Publication 1XX* values (ICRP, 2022). The values shown were averaged for the male and female phantoms.

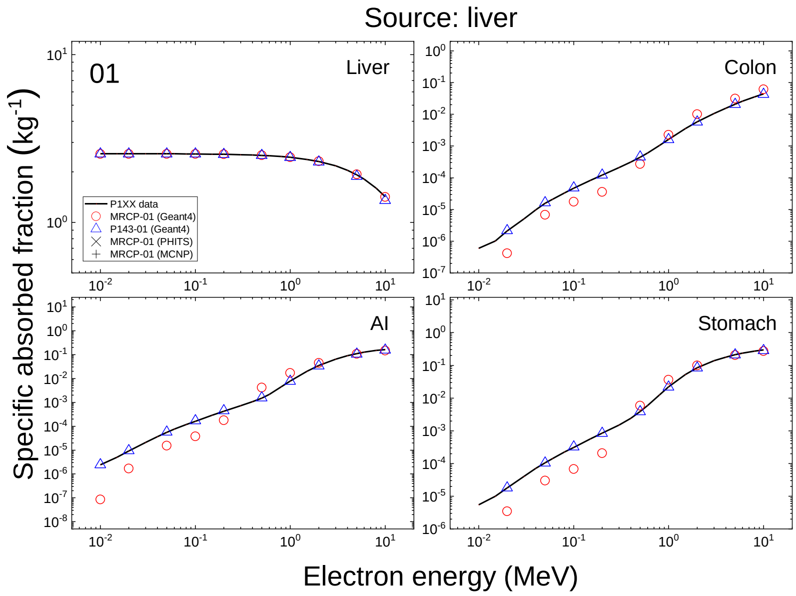

Fig. I.26. Specific absorbed fractions (SAFs) for liver as a source and liver, colon, alveolar-interstitium (AI) and stomach as a target for electron exposures calculated with the 1-year-old mesh-type reference computational phantoms (MRCPs), along with the values calculated with the P143 1-year-old phantoms and the *Publication 1XX* values (ICRP, 2022). The values shown were averaged for the male and female phantoms.

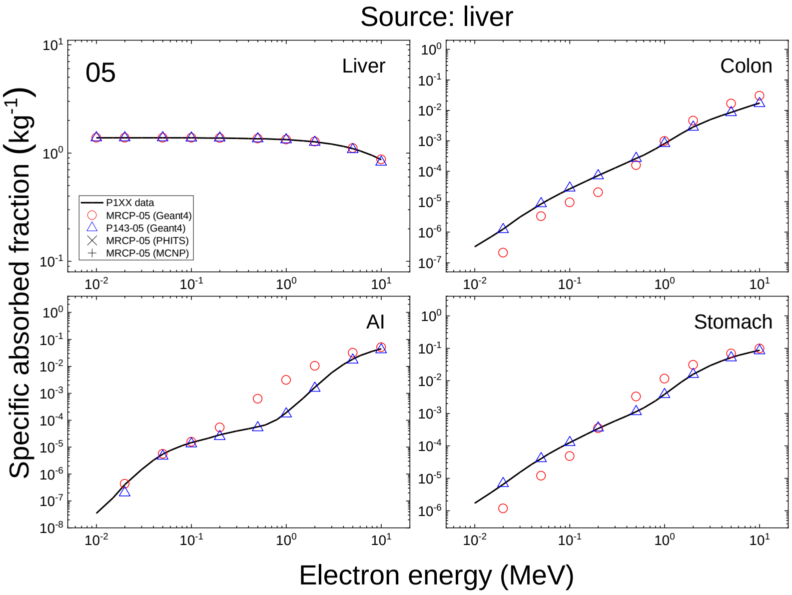

Fig. I.27. Specific absorbed fractions (SAFs) for liver as a source and liver, colon, alveolar-interstitium (AI) and stomach as a target for electron exposures calculated with the 5-year-old mesh-type reference computational phantoms (MRCPs), along with the values calculated with the P143 5-year-old phantoms and the *Publication 1XX* values (ICRP, 2022). The values shown were averaged for the male and female phantoms.

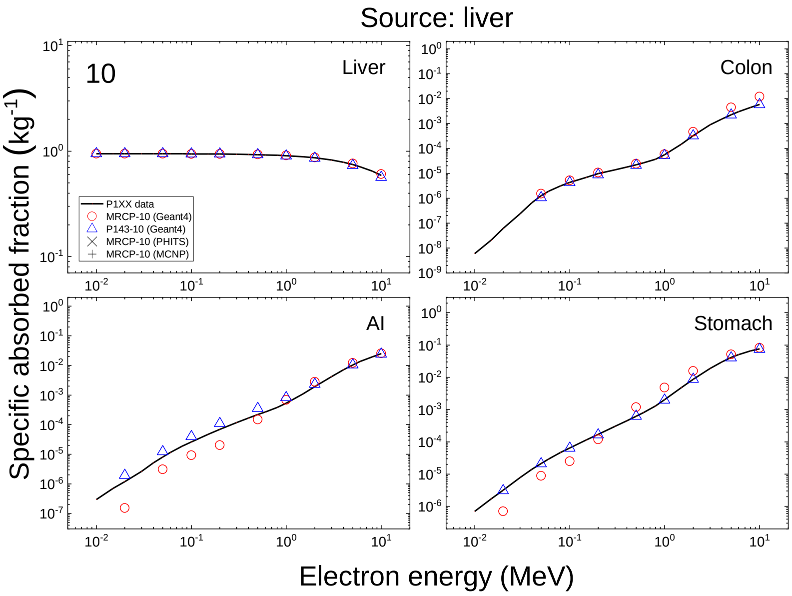

Fig. I.28. Specific absorbed fractions (SAFs) for liver as a source and liver, colon, alveolar-interstitium (AI) and stomach as a target for electron exposures calculated with the 10-year-old mesh-type reference computational phantoms (MRCPs), along with the values calculated with the P143 10-year-old phantoms and the *Publication 1XX* values (ICRP, 2022). The values shown were averaged for the male and female phantoms.

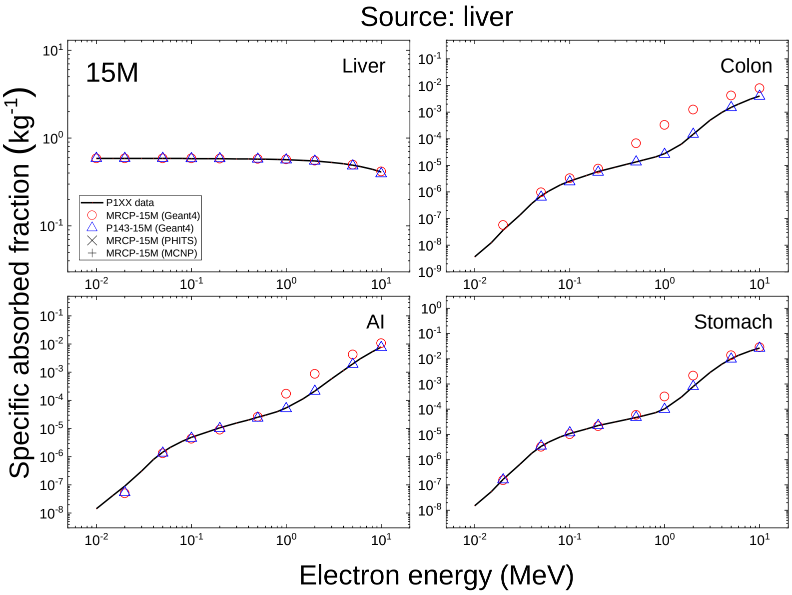

Fig. I.29. Specific absorbed fractions (SAFs) for liver as a source and liver, colon, alveolar-interstitium (AI) and stomach as a target for electron exposures calculated with the 15-year-old male mesh-type reference computational phantom (MRCP), along with the values calculated with the P143 15-year-old male phantom and the *Publication 1XX* values (ICRP, 2022).

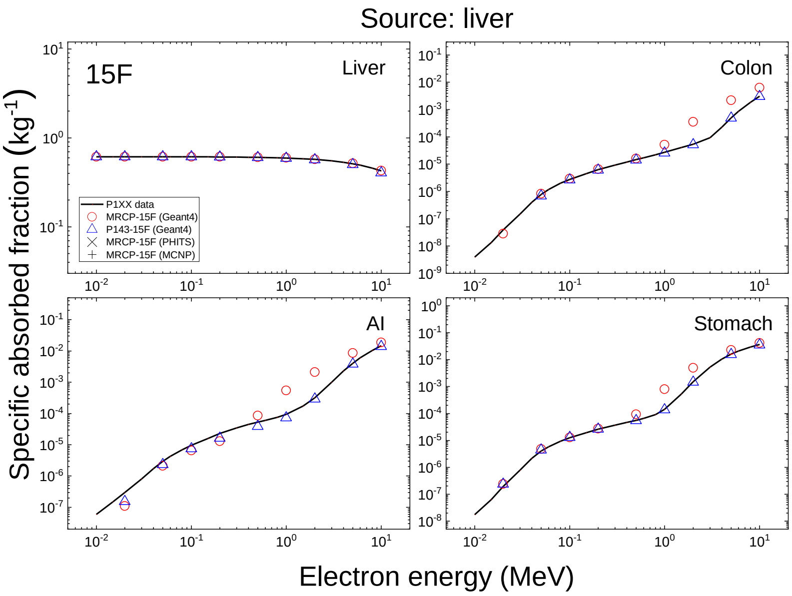

Fig. I.30. Specific absorbed fractions (SAFs) for liver as a source and liver, colon, alveolar-interstitium (AI) and stomach as a target for electron exposures calculated with the 15-year-old female mesh-type reference computational phantom (MRCP), along with the values calculated with the P143 15-year-old female phantom and the *Publication 1XX* values (ICRP, 2022).

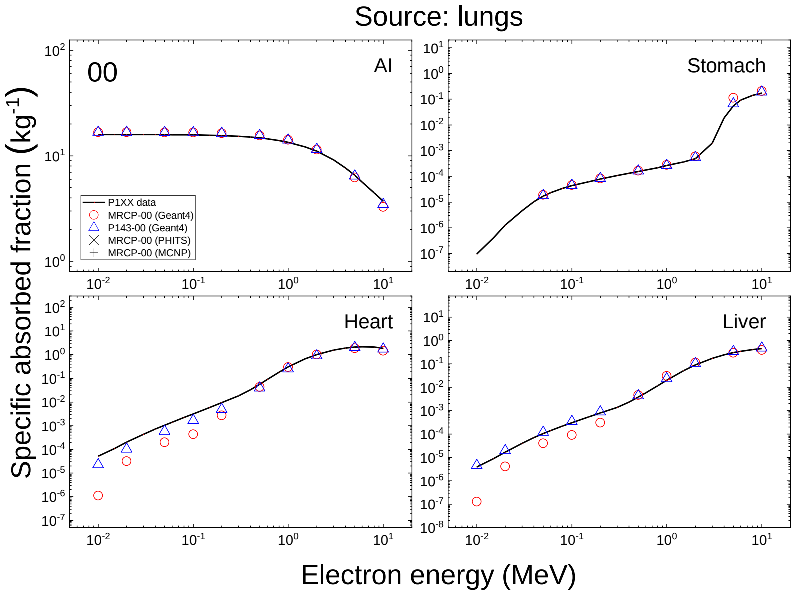

Fig. I.31. Specific absorbed fractions (SAFs) for lungs as a source and alveolar-interstitium (AI), stomach, heart and liver as a target for electron exposures calculated with the newborn mesh-type reference computational phantoms (MRCPs), along with the values calculated with the P143 newborn phantoms and the *Publication 1XX* values (ICRP, 2022). The values shown were averaged for the male and female phantoms.

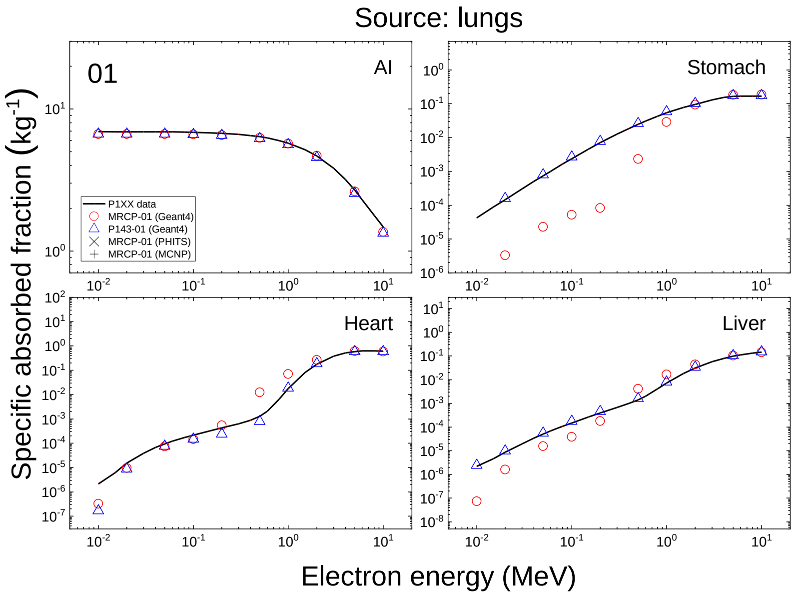

Fig. I.32. Specific absorbed fractions (SAFs) for lungs as a source and alveolar-interstitium (AI), stomach, heart and liver as a target for electron exposures calculated with the 1-year-old mesh-type reference computational phantoms (MRCPs), along with the values calculated with the P143 1-year-old phantoms and the *Publication 1XX* values (ICRP, 2022). The values shown were averaged for the male and female phantoms.

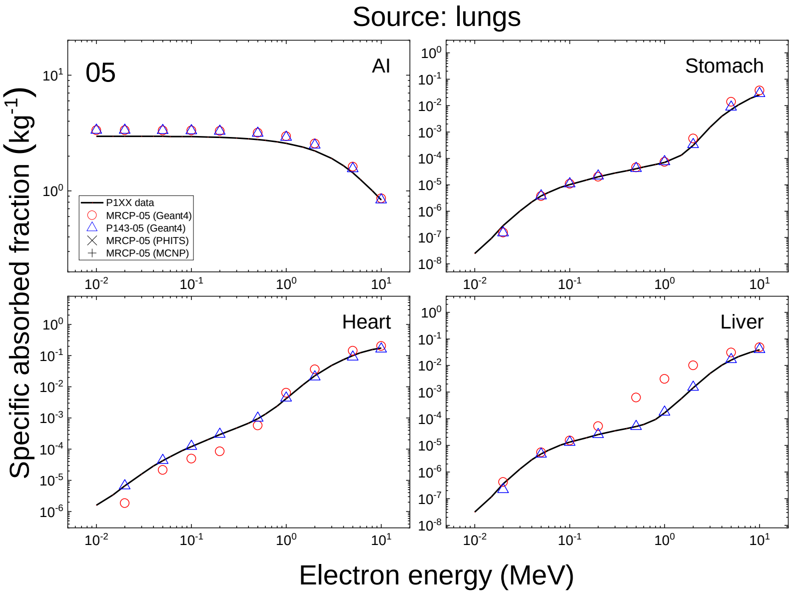

Fig. I.33. Specific absorbed fractions (SAFs) for lungs as a source and alveolar-interstitium (AI), stomach, heart and liver as a target for electron exposures calculated with the 5-year-old mesh-type reference computational phantoms (MRCPs), along with the values calculated with the P143 5-year-old phantoms and the *Publication 1XX* values (ICRP, 2022). The values shown were averaged for the male and female phantoms.

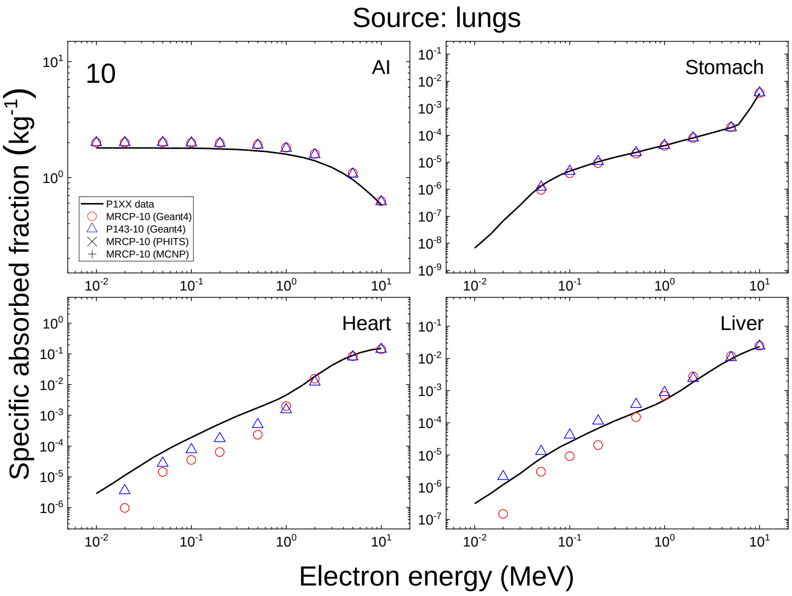

Fig. I.34. Specific absorbed fractions (SAFs) for lungs as a source and alveolar-interstitium (AI), stomach, heart and liver as a target for electron exposures calculated with the 10-year-old mesh-type reference computational phantoms (MRCPs), along with the values calculated with the P143 10-year-old phantoms and the *Publication 1XX* values (ICRP, 2022). The values shown were averaged for the male and female phantoms.

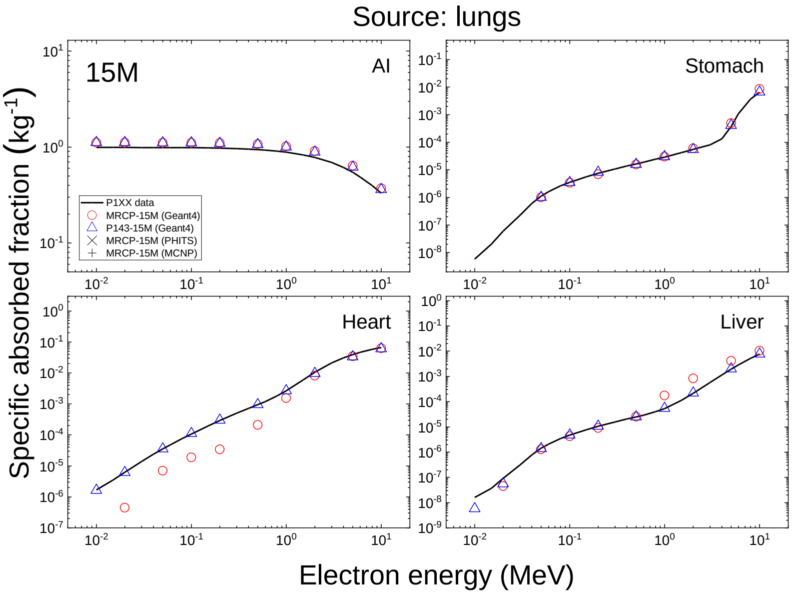

Fig. I.35. Specific absorbed fractions (SAFs) for lungs as a source and alveolar-interstitium (AI), stomach, heart and liver as a target for electron exposures calculated with the 15-year-old male mesh-type reference computational phantom (MRCP), along with the values calculated with the P143 15-year-old male phantom and the *Publication 1XX* values (ICRP, 2022).

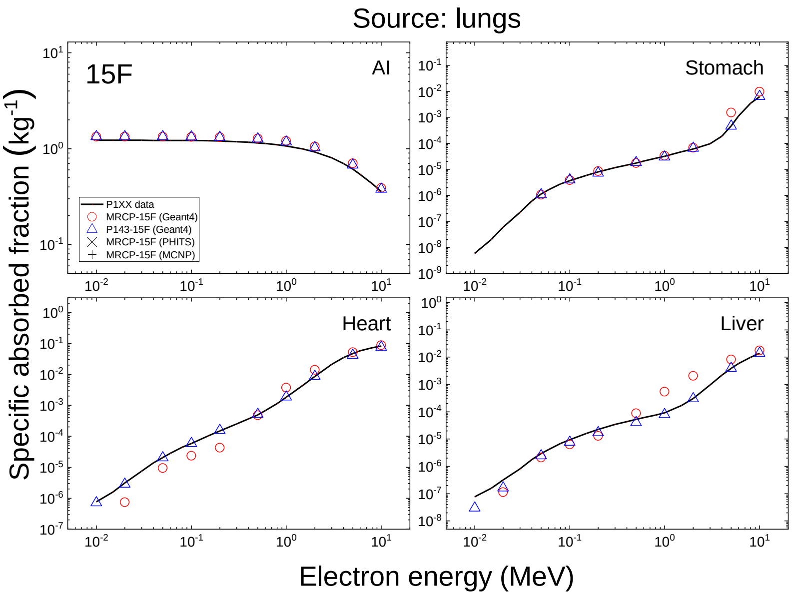

Fig. I.36. Specific absorbed fractions (SAFs) for lungs as a source and alveolar-interstitium (AI), stomach, heart and liver as a target for electron exposures calculated with the 15-year-old female mesh-type reference computational phantom (MRCP), along with the values calculated with the P143 15-year-old female phantom and the *Publication 1XX* values (ICRP, 2022).

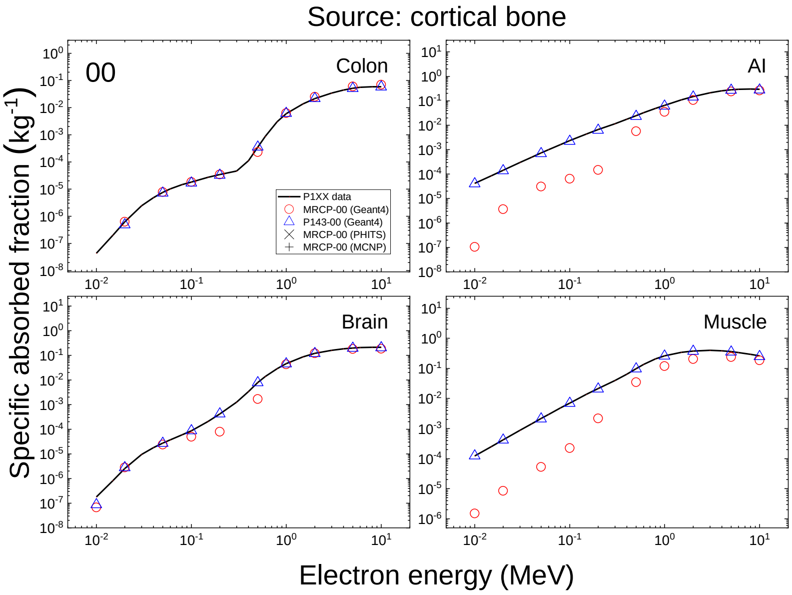

Fig. I.37. Specific absorbed fractions (SAFs) for cortical bone as a source and colon, alveolar-interstitium (AI), brain and muscle as a target for electron exposures calculated with the newborn mesh-type reference computational phantoms (MRCPs), along with the values calculated with the P143 newborn phantoms and the *Publication 1XX* values (ICRP, 2022). The values shown were averaged for the male and female phantoms.

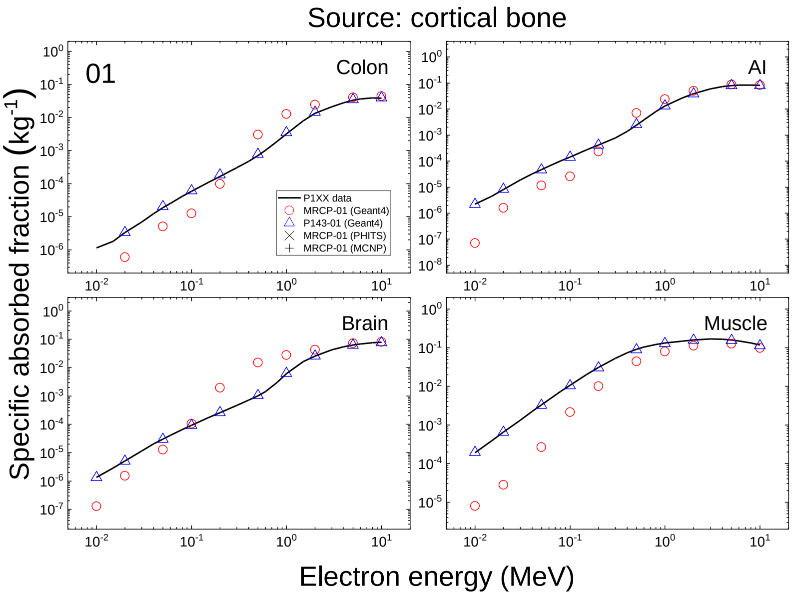

Fig. I.38. Specific absorbed fractions (SAFs) for cortical bone as a source and colon, alveolar-interstitium (AI), brain and muscle as a target for electron exposures calculated with the 1-year-old mesh-type reference computational phantoms (MRCPs), along with the values calculated with the P143 1-year-old phantoms and the *Publication 1XX* values (ICRP, 2022). The values shown were averaged for the male and female phantoms.

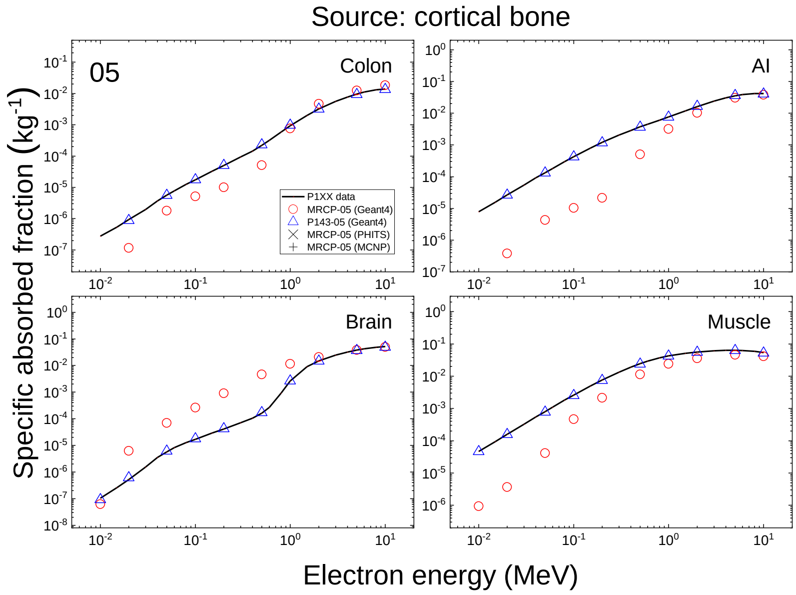

Fig. I.39. Specific absorbed fractions (SAFs) for cortical bone as a source and colon, alveolar-interstitium (AI), brain and muscle as a target for electron exposures calculated with the 5-year-old mesh-type reference computational phantoms (MRCPs), along with the values calculated with the P143 5-year-old phantoms and the *Publication 1XX* values (ICRP, 2022). The values shown were averaged for the male and female phantoms.

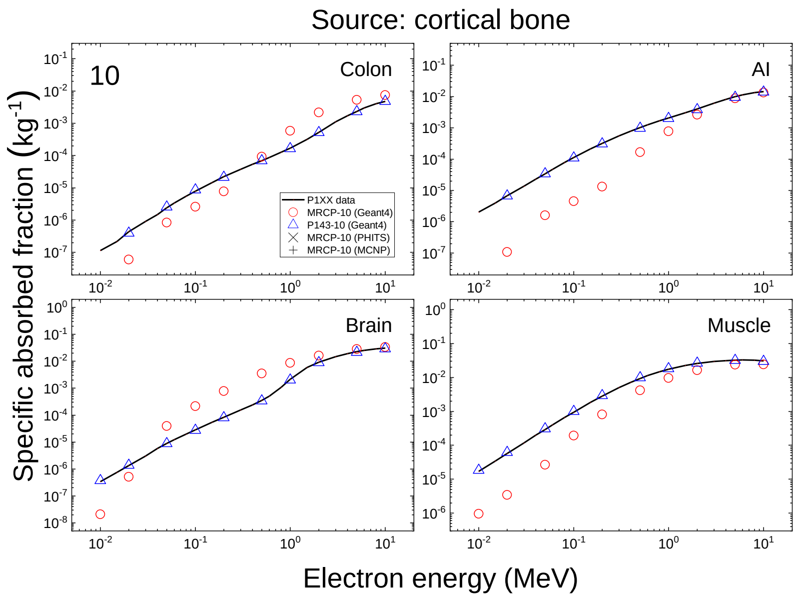

Fig. I.40. Specific absorbed fractions (SAFs) for cortical bone as a source and colon, alveolar-interstitium (AI), brain and muscle as a target for electron exposures calculated with the 10-year-old mesh-type reference computational phantoms (MRCPs), along with the values calculated with the P143 10-year-old phantoms and the *Publication 1XX* values (ICRP, 2022). The values shown were averaged for the male and female phantoms.

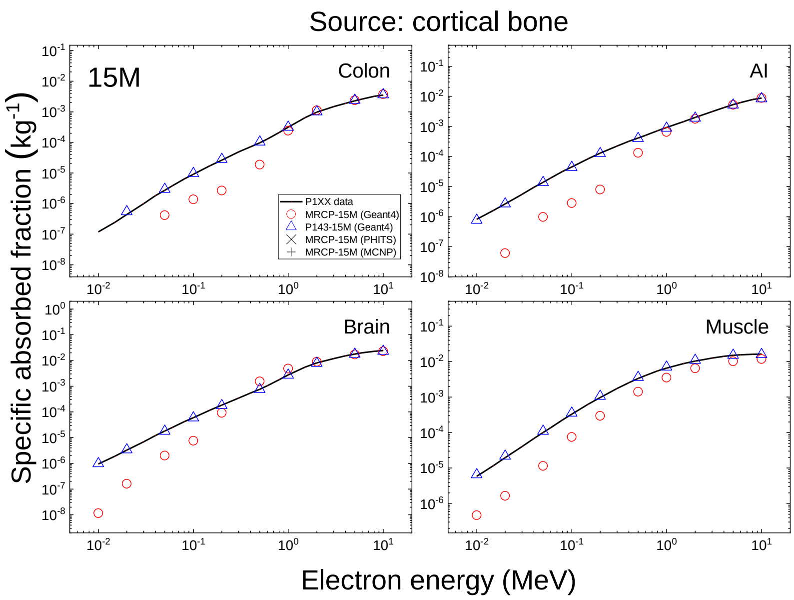

Fig. I.41. Specific absorbed fractions (SAFs) for cortical bone as a source and colon, alveolar-interstitium (AI), brain and muscle as a target for electron exposures calculated with the 15-year-old male mesh-type reference computational phantom (MRCP), along with the values calculated with the P143 15-year-old male phantom and the *Publication 1XX* values (ICRP, 2022).

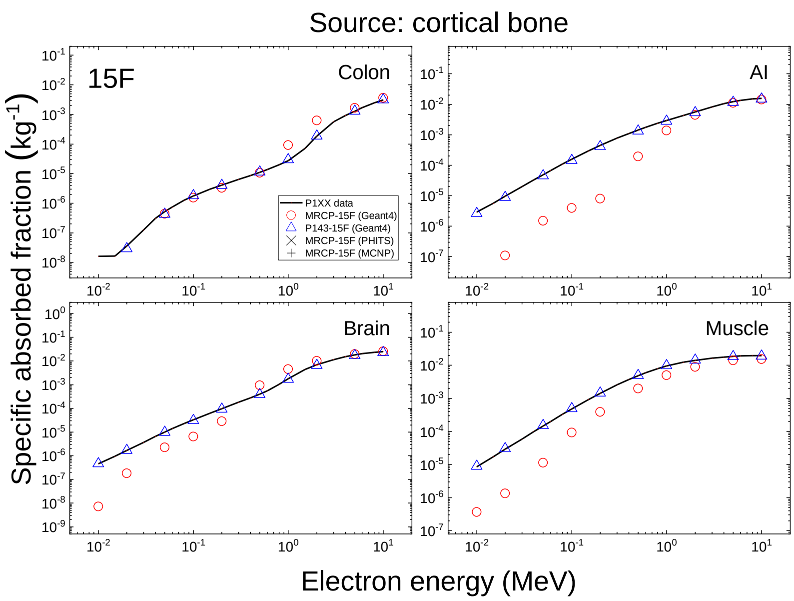

Fig. I.42. Specific absorbed fractions (SAFs) for cortical bone as a source and colon, alveolar-interstitium (AI), brain and muscle as a target for electron exposures calculated with the 15-year-old female mesh-type reference computational phantom (MRCP), along with the values calculated with the P143 15-year-old female phantom and the *Publication 1XX* values (ICRP, 2022).

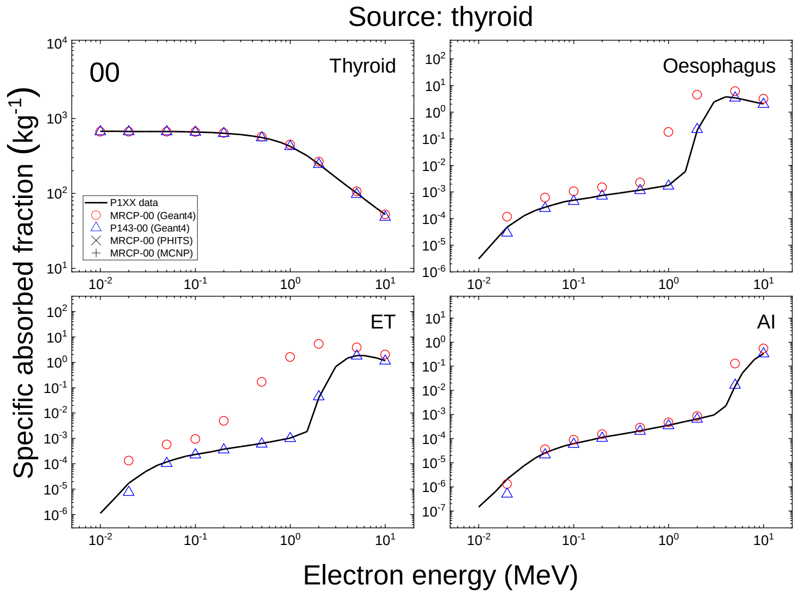

Fig. I.43. Specific absorbed fractions (SAFs) for thyroid as a source and thyroid, oesophagus, extrathoracic (ET) region and alveolar-interstitium (AI) as a target for electron exposures calculated with the newborn mesh-type reference computational phantoms (MRCPs), along with the values calculated with the P143 newborn phantoms and the *Publication 1XX* values (ICRP, 2022). The values shown were averaged for the male and female phantoms.

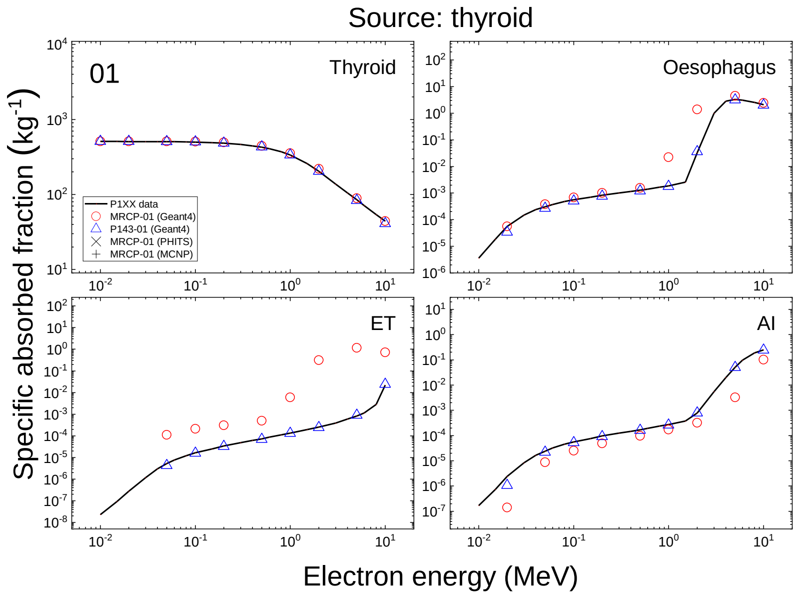

Fig. I.44. Specific absorbed fractions (SAFs) for thyroid as a source and thyroid, oesophagus, extrathoracic (ET) region and alveolar-interstitium (AI) as a target for electron exposures calculated with the 1-year-old mesh-type reference computational phantoms (MRCPs), along with the values calculated with the P143 1-year-old phantoms and the *Publication 1XX* values (ICRP, 2022). The values shown were averaged for the male and female phantoms.

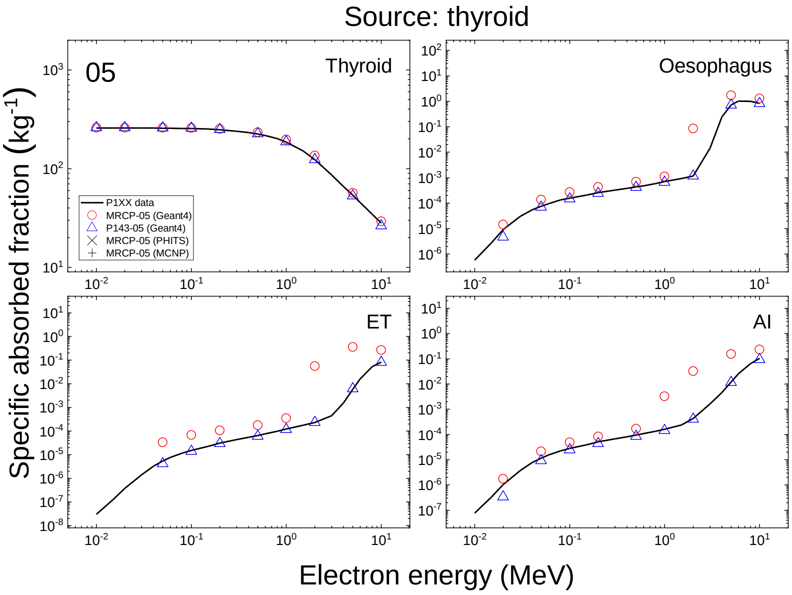

Fig. I.45. Specific absorbed fractions (SAFs) for thyroid as a source and thyroid, oesophagus, extrathoracic (ET) region and alveolar-interstitium (AI) as a target for electron exposures calculated with the 5-year-old mesh-type reference computational phantoms (MRCPs), along with the values calculated with the P143 5-year-old phantoms and the *Publication 1XX* values (ICRP, 2022). The values shown were averaged for the male and female phantoms.

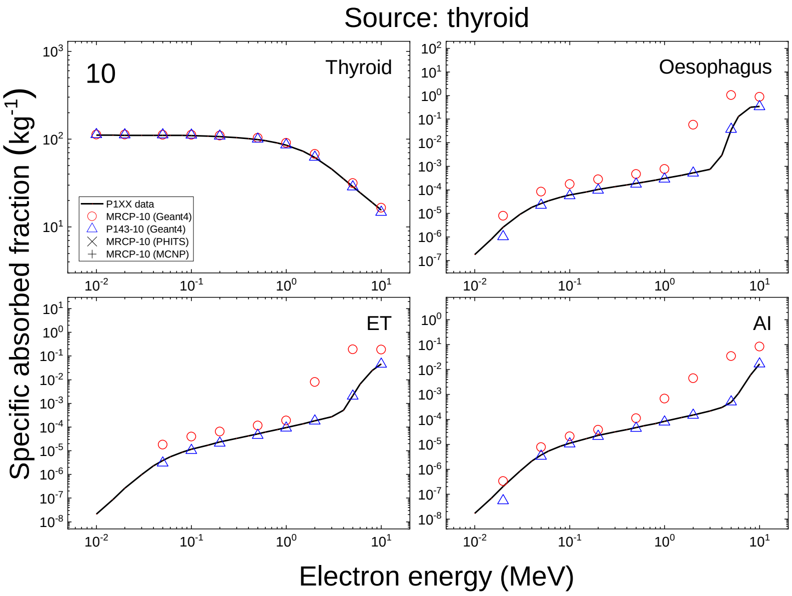

Fig. I.46. Specific absorbed fractions (SAFs) for thyroid as a source and thyroid, oesophagus, extrathoracic (ET) region and alveolar-interstitium (AI) as a target for electron exposures calculated with the 10-year-old mesh-type reference computational phantoms (MRCPs), along with the values calculated with the P143 10-year-old phantoms and the *Publication 1XX* values (ICRP, 2022). The values shown were averaged for the male and female phantoms.

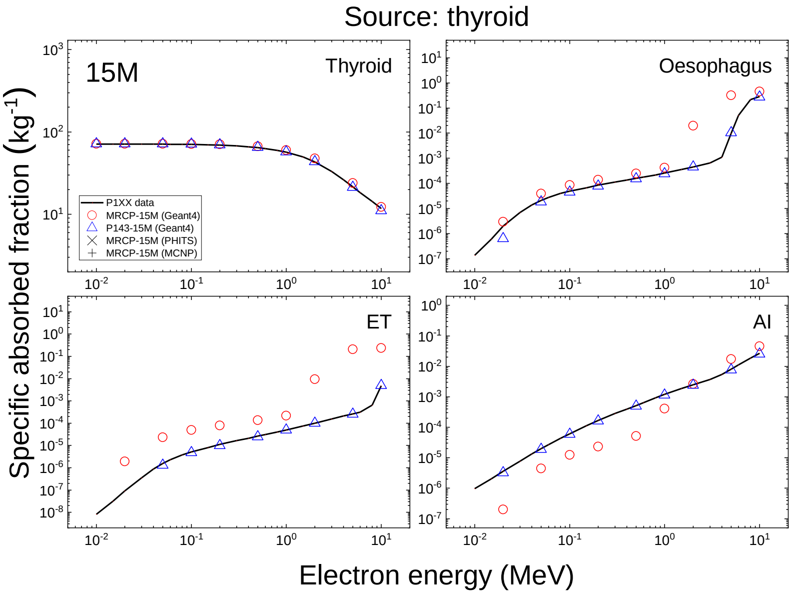

Fig. I.47. Specific absorbed fractions (SAFs) for thyroid as a source and thyroid, oesophagus, extrathoracic (ET) region and alveolar-interstitium (AI) as a target for electron exposures calculated with the 15-year-old male mesh-type reference computational phantom (MRCP), along with the values calculated with the P143 15-year-old male phantom and the *Publication 1XX* values (ICRP, 2022).

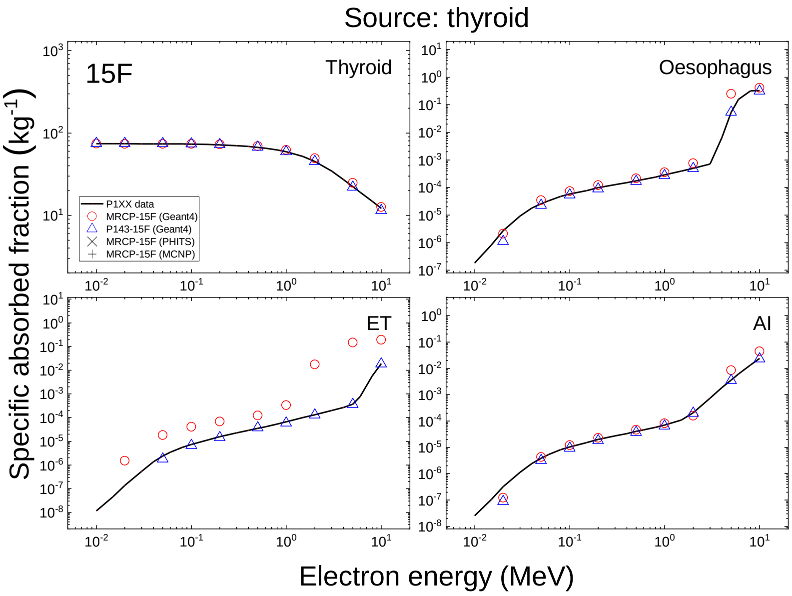

Fig. I.48. Specific absorbed fractions (SAFs) for thyroid as a source and thyroid, oesophagus, extrathoracic (ET) region and alveolar-interstitium (AI) as a target for electron exposures calculated with the 15-year-old female mesh-type reference computational phantom (MRCP), along with the values calculated with the P143 15-year-old female phantom and the *Publication 1XX* values (ICRP, 2022).

I.1. References

Allison, J., Amako, K., Apostolakis, J., et al., 2016. Recent developments in Geant4. Nucl. Instrum. Methods Phys. Res. Sect. A. 835, 186–225.

Furuta, T., Sato, T., Han, M.C., et al., 2017. Implementation of tetrahedral-mesh geometry in Monte Carlo radiation transport code PHITS. Phys. Med. Biol. 62, 4798–4810.

ICRP, 2020. Paediatric Reference Computational Phantoms. ICRP Publication 143. Ann. ICRP 49(1).

ICRP, 2022. Internal Dose Assessment for Reference Children: Specific Absorbed Fractions. ICRP Publication 1XX. Ann. ICRP XX(X) (will be published in 2022).

Martz, R.L., 2017. The MCNP6 book on unstructured mesh geometry: a user's guide for MCNP6.2. Report LA-UR-17-22442. Los Alamos National Laboratory, Los Alamos, NM.

Trellue, H.R., Little, R.C., White, M.C., et al., 2009. ENDF70: A Continuous-Energy MCNP Neutron Data Library Based on ENDF/B-VII.0. Nuclear Technol. 168, 832–836.

ANNEX J. DESCRIPTION OF ELECTRONIC FILES

(J 1) The package of electronic files containing the detailed data of the paediatric mesh-type reference computational phantoms (MRCPs) can be found in a downloadable data file. The package is organised in two folders: *Phantom_data and MC_examples*.

J.1. Data files in Phantom_data

(J 2) This folder is subdivided into ten folders, one for each of the ten reference phantoms (MRCP_00M: newborn male, MRCP_00F: newborn female, MRCP_01M: 1-year-old male, MRCP_01F: 1-year-old female, MRCP_05M: 5-year-old male, MRCP_05F: 5-year-old female, MRCP_10M: 10-year-old male, MRCP_10F: 10-year-old female, MRCP_15M: 15-year-old male, MRCP_15F: 15-year-old female). Each folder contains the following files:

- Data files for the tetrahedral mesh (TM) version MRCPs; the file names are:

NODE-format file	ELE-format file
MRCP_00M.node	MRCP_00M.ele
MRCP_00F.node	MRCP_00F.ele
MRCP_01M.node	MRCP_01M.ele
MRCP_01F.node	MRCP_01F.ele
MRCP_05M.node	MRCP_05M.ele
MRCP_05F.node	MRCP_05F.ele
MRCP_10M.node	MRCP_10M.ele
MRCP_10F.node	MRCP_10F.ele
MRCP_15M.node	MRCP_15M.ele
MRCP_15F.node	MRCP_15F.ele

The data files consist of NODE- and ELE-format files. The NODE-format files contain a list of node coordinates composing the TM-version phantoms. The NODE-format files are represented by:

- First line:
  <# of nodes> <dimension (= 3)> <n/a (= 0)> <n/a (= 0)>
- Remaining lines list # of points:
  <node ID> <x> <y> <z>

The ELE-format files contain a list of tetrahedrons composing the TM-version phantoms. Each tetrahedron is represented as four node IDs listed in the corresponding NODE-format files and an organ ID number with respect to the tetrahedron. The ELE-format files are represented by:

- First line:
  <# of tetrahedrons> <dimension (= 3)> <# of attributes (= 1, for organ ID)>

  - Remaining lines list # of tetrahedrons:
    <tetrahedron ID> <node 1> <node 2> <node 3> <node 4> <organ ID>

- Data files for the polygon mesh (PM) version MRCPs; the file names are:

OBJ-format file	MTL-format file
MRCP_00M.obj	MRCP_00M.mtl
MRCP_00F.obj	MRCP_00F.mtl
MRCP_01M.obj	MRCP_01M.mtl
MRCP_01F.obj	MRCP_01F.mtl
MRCP_05M.obj	MRCP_05M.mtl
MRCP_05F.obj	MRCP_05F.mtl
MRCP_10M.obj	MRCP_10M.mtl
MRCP_10F.obj	MRCP_10F.mtl
MRCP_15M.obj	MRCP_15M.mtl
MRCP_15F.obj	MRCP_15F.mtl

These files consist of OBJ- and MTL-format files, which contain data on PM and colours, respectively. They can be imported in various 3D commercial programs such as *3ds Max*™ (Autodesk, USA), *MAYA*™ (Autodesk, USA), *Rapidform*™ (INUS Technology INC., Korea) and *Rhinoceros 5.0* (Robert McNeel, USA).

- Lists of the media, elemental compositions and densities; the file names are:

MRCP_00M_media.dat
MRCP_00F_media.dat
MRCP_01M_media.dat
MRCP_01F_media.dat
MRCP_05M_media.dat
MRCP_05F_media.dat
MRCP_10M_media.dat
MRCP_10F_media.dat
MRCP_15M_media.dat
MRCP_15F_media.dat

- The mass ratios of bone constituents in the bone sites; the file names are:

MRCP_00M_bone.dat
MRCP_00F_bone.dat
MRCP_01M_bone.dat
MRCP_01F_bone.dat

MRCP_05M_bone.dat
MRCP_05F_bone.dat
MRCP_10M_bone.dat
MRCP_10F_bone.dat
MRCP_15M_bone.dat
MRCP_15F_bone.dat

- The mass ratios of blood in various body tissues; the file names are:

MRCP_00M_blood.dat
MRCP_00F_blood.dat
MRCP_01M_blood.dat
MRCP_01F_blood.dat
MRCP_05M_blood.dat
MRCP_05F_blood.dat
MRCP_10M_blood.dat
MRCP_10F_blood.dat
MRCP_15M_blood.dat
MRCP_15F_blood.dat

- PDF files for phantom visualisation; the file names are

MRCP_00M.pdf
MRCP_00F.pdf
MRCP_01M.pdf
MRCP_01F.pdf
MRCP_05M.pdf
MRCP_05F.pdf
MRCP_10M.pdf
MRCP_10F.pdf
MRCP_15M.pdf
MRCP_15F.pdf

The PDF files visualise the MRCPs in a 3D view, as shown in Fig. J.1. The PDF files can be opened in Acrobat program (Adobe Systems, San Jose, CA, USA) where one can navigate the phantoms in detail, e.g. by rotating or enlarging each of the organs/tissues. Detailed instruction on these 3D PDF files can be found in elsewhere (https://helpx.adobe.com/acrobat/using/displaying-3d-models-pdfs.html)

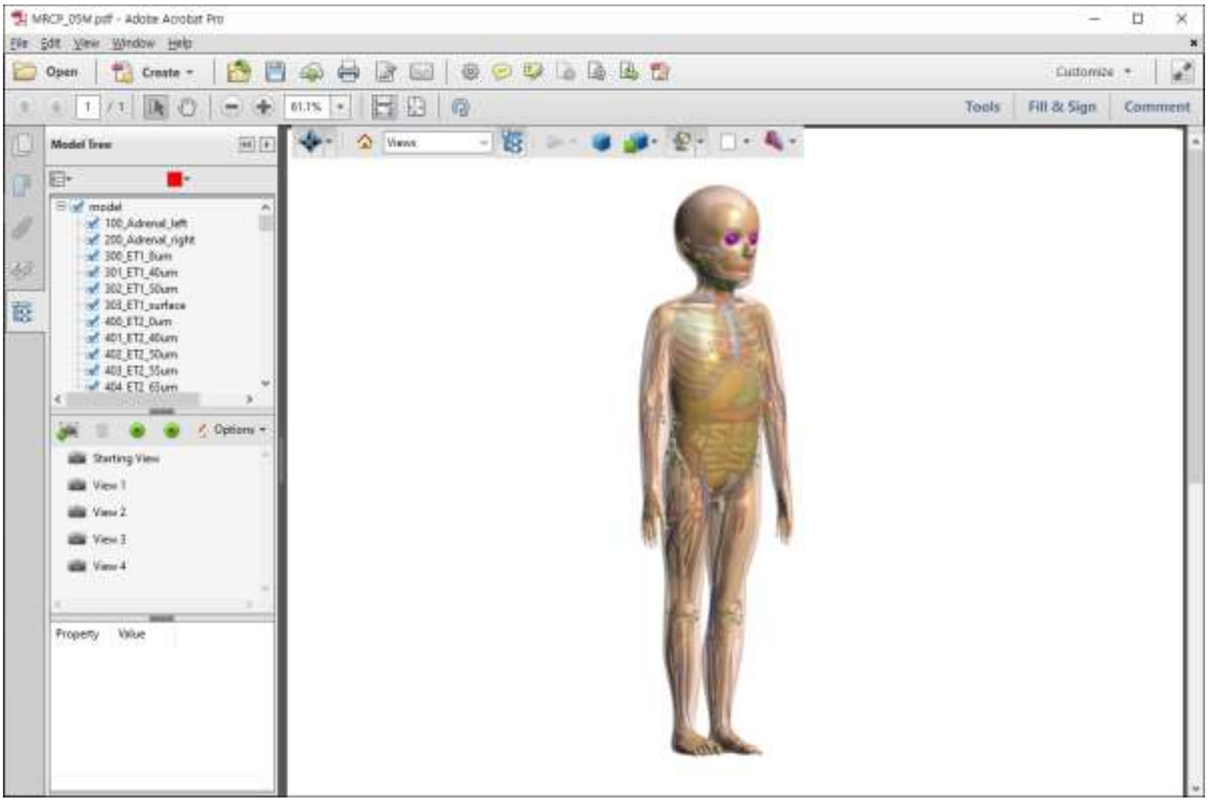

Fig. J.1. 3D view of the 5-year-old mesh-type reference computational phantom (MRCP) visualised in the Adobe Acrobat program importing the MRCP_05M.pdf file.

J.2. Data files in *MC_examples*

(J 3) This folder contains the following three compressed files:

MRCP_GEANT4.zip
MRCP_MCNP6.zip
MRCP_PHITS.zip

The data files contain input examples for implementation of the TM-version phantoms in the three Monte Carlo codes, i.e. Geant4 (Allison et al., 2016), MCNP6 (Martz et al., 2017) and PHITS (Furuta et al., 2017). Each of the compressed files includes examples for internal and external exposures. The internal exposure source is defined as a homogeneous liver source isotropically emitting 1-MeV photons. The external exposure source is defined as a point source isotropically emitting 1-MeV photons located at 1 m in front of the phantom. Detailed information on the implementation is described in the 'README.txt' file included in each compressed file.

J.3. References

Allison, J., Amako, K., Apostolakis, J., et al., 2016. Recent developments in Geant4. Nucl. Instrum. Methods Phys. Res. Sect. A. 835, 186–225.

Furuta, T., Sato, T., Han, M.C., et al., 2017. Implementation of tetrahedral-mesh geometry in Monte Carlo radiation transport code PHITS. Phys. Med. Biol. 62, 4798–4810.

Martz, R.L., 2017. The MCNP6 book on unstructured mesh geometry: a user's guide for MCNP6.2. Report LA-UR-17-22442. Los Alamos National Laboratory, Los Alamos, NM.

ACKNOWLEDGEMENTS

The Acknowledgements heading is a standard heading, but unnumbered. As such, it will appear in the Contents. This section begins with a brief description, generally one paragraph, about the establishment of the Task Group. The date the Task Group was established, its number, and its name, must be included. It then goes on as shown in the following way, with many parts serving both to acknowledge contributions and to preserve the record of membership for historical purposes, including:

- a sentence of thanks;
- a list of Task Group members and the years during which they were involved;
- where appropriate, the members of the working party (working party is not capitalised) that paved the way to establishment of the Task Group;
- the names of critical reviewers from the responsible Committee(s) and the Main Commission;
- the editorial members (Editor-in-Chief and Associate Editors);
- the members of the responsible Committee(s) during the preparation of the publication, including emeritus members;
- Main Commission members at the time of approval of the publication, including emeritus members; and
- a final sentence thanking individuals and organisations who participated in the public consultation process.

ICRP thanks all those involved in the development of this publication for their hard work and dedication over many years.

Task Group 103 members (2019–present)

C.H. Kim (Chair)	H. Han	B. Shin
W.E. Bolch	C. Lee	Y.S. Yeom
C. Choi	T.T. Nguyen	M. Zankl
B.S. Chung	N. Petoussi-Henss	
K. Eckerman	R. Qiu	

The authors from Hanyang University were:

S. Kim	G. Son

Committee 2 critical reviewers

D. Jokisch	T. Smith

Main Commission critical reviewers

K. Cho	S. Liu

Editorial members

C.H. Clement (Scientific Secretary and *Annals of the ICRP* Editor-in-Chief)
T. Yasumune (Assistant Scientific Secretary and *Annals of the ICRP* Associate Editor) *(2022-)*
H. Fujita (Assistant Scientific Secretary and *Annals of the ICRP* Associate Editor) *(2018–2022)*

Committee 2 members during preparation of this publication

(2017–2021)

J.D. Harrison (Chair)	A. Giussani	T. Sato
F. Paquet (Vice-Chair)	D. Jokisch	T. Smith
W.E. Bolch (Secretary)	C.H. Kim	A. Ulanowski
M. Antonia Lopez	R. Leggett	F. Wissmann
V. Berkovski	J. Li	
E. Blanchardon	N. Petoussi-Henss	

(2021–2025)

F. Bochud (Chair)	A. Giussani	J. Li
F. Paquet (Vice-chair)	D. Jokisch	J.W. Marsh
M. Antonia Lopez (Secretary)	C.H. Kim	N. Petoussi-Henss
M. Andersson	M.S. Kulkarni	T. Sato
V. Berkovski	S. Lamart	T. Smith
D. de Souza Santos	C. Lee	A. Ulanowski

Committee 2 emeritus members during preparation of this publication

K. Eckerman n

Main Commission members at the time of approval of this publication

Chair: W. Rühm, *Germany*
Vice-Chair: D.A. Cool, *USA*
Scientific Secretary: C.H. Clement, *Canada*; *sci.sec@icrp.org**

K.E. Applegate, *USA*
F. Bochud, *Switzerland*
S. Bouffler, *UK*
K.W. Cho, *Korea*
G. Hirth, *Australia*
M. Kai, *Japan*
D. Laurier, *France*
S. Liu, *China*
S. Romanov, *Russia*
T. Schneider, *France*
A. Wojcik, *Sweden*

Emeritus members
R.H. Clarke, *UK*
F.A. Mettler Jr, *USA*
R.J. Pentreath, *UK*
R.J. Preston, *USA*
C. Streffer, *Germany*
E. Vañó, *Spain*

*Although formally not a Main Commission member since 1988, the Scientific Secretary is an integral part of the Main Commission.